NGU
Norges geologiske undersøkelse
Geological Survey of Norway

GEOLOGI FOR SAMFUNNET
GEOLOGY FOR SOCIETY

NGU Rapport 2013.002

Coop Phase I
Crustal Onshore-Offshore Project


bayerngas


BKK


ConocoPhillips


DETNORSKE


Eni
Eni Norge


e·on


GDF SUEZ


Lundin


MAERSK
OIL


NGU
Geology for Society since 1858


NORECO


OLJEDIREKTORATET


REPSOL


RWE The energy to lead


Statoil


TOTAL


Verbundnetz
Gas AG


wintershall

Geological Survey of Norway
NO-7491 Trondheim, Norway
Tel.: 47 73 90 40 11
Telefax 47 73 92 16 20

REPORT

Report no.: 2013.002 | ISSN 0800-3416 | Grading: Confidential to 22.01.2018

Title:
Coop Phase I - Crustal Onshore-Offshore Project

Authors:
Odleiv Olesen, Marco Brönner, Jörg Ebbing, Harald Elvebakk, Jomar Gellein, Janusz Koziel, Torleif Lauritsen, Ole Lutro, Yuriy Maystrenko, Christian Müller, Aziz Nasuti, Per Terje Osmundsen, Trond Slagstad and Gaute Storrø

Client:
BayernGas, BKK, ConocoPhillips, Det norske, Eni, E.ON, GdF Suez, Lundin, Maersk, NGU, Noreco, Oljedirektoratet, Repsol, RWE-Dea, Statoil, Total, VNG and Wintershall.

County:
Vest-Agder, Rogaland, Hordaland and Sogn & Fjordane

Commune:

Map-sheet name (M=1:250.000)
Mandal, Stavanger, Haugesund, Bergen and Måløy

Number of pages: 359 Price (NOK): 1450
Map enclosures:

Fieldwork carried out:	Date of report:	Project no.:	Person responsible:
2010-2012	22.01.2013	3366.00	Øystein Nordgulen

Summary: The five-year Crustal Onshore-Offshore Project (Coop) is an integrated data acquisition and interpretation project established to study the onshore-offshore relationships in the northeastern North Sea and Møre-Haltenbanken area. The Coop Phase I Report summarises the results from the Norwegian North Sea and western Norway. New aeromagnetic, gravity and petrophysical data as well as heat flow data have been acquired. All new data were compiled with existing data. Information on mainland basement structures, deep weathering and heat production has been extrapolated to the offshore region. We conclude that the Norwegian strandflat is an exhumed weathered and peneplaned surface of Late Triassic to Early Jurassic age that has been modified and levelled during Pleistocene erosion. This surface was preserved beneath Late Jurassic and Cretaceous strata until the Neogene. Support for this conclusion comes from the AMAGER mapping and the occurrence of a relatively flat and gently westward-dipping top of basement beneath the Jurassic sedimentary rocks close to the coastline. The heat generation of the mainland basement rocks has been calculated from the chemical analyses of the U, Th and K contents in c. 2000 bedrock samples and airborne radiometric measurements along the coast of western Norway. The heat generation varies with almost one order of magnitude. Temperature logging has been carried out in Fyllingsdalen (Bergen) and Ullandhaug (Stavanger). The heat flow was calculated based on temperature logging and thermal conductivity data. The observed thermal gradients are 16.5 °C/km in Fyllingsdalen and 13 °C/km at Ullandhaug. Tentative palaeoclimatic corrections for Fyllingsdalen and Ullandhaug vary from 15 to 30 mW/m² (i.e., 20-40 % of the original heat-flow values). Two different scenarios show corrected heat-flow values which vary from 43 to 51 mW/m² at Ullandhaug and from 59 to 74 mW/m² in Fyllingsdalen. The increased heat flow in Fyllingsdalen is attributed to high values of radiogenic heat production within the Løvstakken granite. Crustal models of the Norwegian North Sea and western Norway have been established from gravity, magnetic, seismic, well log and bedrock mapping data. By attributing thermal properties (e.g., radiogenic heat production and thermal conductivity) to the individual basement bodies we have calculated the heat flow from the basement into the sedimentary basins. The observed and modelled heat flow is strongly controlled by the lithology and structures in the crust. The temperature at a depth of 5 km in the Egersund and Stord basins is, for example, estimated to c. 155 °C and 170 °C, respectively. A map of Quaternary sand channels in the Norwegian North Sea has been produced. Plans for Coop Phase II are summarised at the end of the report.

Keywords: Geofysikk (Geophysics)	Kontinentalsokkel (Continental shelf)	Tolkning (Interpretation)
Berggrunnsgeologi (Bedrock geology)	Magnetometri (Magnetometry)	Varmestrøm (Heat flow)
Petrofysikk (Petrophysics)	Gravimetri (Gravimetry)	Fagrapport (Scientific report)

TABLE OF CONTENTS

1. INTRODUCTION

The Geological Survey of Norway (NGU) launched in 2010 an integrated data acquisition and interpretation project to study the onshore-offshore relationships along the coast of western Norway. The Coop project was originally financed by NGU, Oljedirektoratet (NPD) and the petroleum companies BayernGas, ConocoPhillips, Det norske, Lundin, Noreco, Statoil, Total and Wintershall with the goal to improve our knowledge of onshore-offshore tectonic links, deep weathering and heat flow along the coast of western Norway. The energy and petroleum companies BKK, Eni, E.ON, GdF Suez, Maersk, Repsol, RWE-Dea and VNG joined the project in 2011 and 2012 as late participants and the project was extended to a Phase II including the Møre margin, the Møre-Trøndelag Fault Complex and the Haltenbanken area. The total Coop area includes at the present stage the Viking and Central grabens and the Froan, Møre, Stord, Egersund and Norwegian-Danish basins.

Aeromagnetic and gravity data provide continuous coverage of the mainland and offshore areas and act as a bridge between areas traditionally investigated by two different methods: field bedrock mapping and seismic interpretation. High-resolution aeromagnetic surveys are particularly useful for detailed mapping of basement lithology and basement depth, igneous bodies, sand channels, salt diapirs, fault systems and deep weathering.

The Coop project includes acquisition of five new airborne surveys acquired in the years 2010-2013 in addition to new gravity and heat-flow data. The aeromagnetic surveys (CNAS-10 and STAS-13) have a profile spacing of 1 km while the combined aeromagnetic and radiometric surveys along the coast of western and mid Norway (BESTAS-10, SAS-11 and TRAS-13) have a line spacing of 250 m. The TRAS-13 and STAS-13 will be reported in the Phase II report. In Phase I NGU has compiled both new surveys (CNAS-10, BESTAS-10 and SAS-11) and existing aeromagnetic surveys on the mainland and offshore to provide a comprehensive and state-of-the-art aeromagnetic grid. New petrophysical data such as magnetic properties, density and the K, U and Th contents from spectrometer measurements on outcrops are acquired to facilitate the interpretation of the new surveys.

Information on deep weathering and heat production of mainland basement rocks can be extrapolated from the mainland to the offshore region. By attributing thermal properties (e.g., radiogenic heat production and thermal conductivity) to the individual basement bodies from potential field modelling, it is possible to calculate the heat flow from the basement into the sedimentary basins. Understanding heat-flow variation in sedimentary basins is of vital importance for the success of petroleum exploration campaigns. Temperature is critical for both source rock maturation and the diagenesis and quality of reservoir rocks. Petroleum reservoirs occur mainly within the Golden Zone (60-120^{o}C) (Bjørkum et al. 1998, Nadeau et al. 2005). The depth to this temperature interval depends to a large degree on the basement heat production which contributes approximately 50% of the heat-flow values offshore Norway (Ritter et al. 2004).

Only c. 10% of the heat is produced within the sedimentary rocks of the basins. The heat production within the crystalline basement depends on the content of radioactive elements such as potassium, uranium and thorium. The contents of these elements show a wide

variation within the mainland crystalline basement of Norway. Partly due to a lack of systematic data compilation, our knowledge of the basement rock composition below the Norwegian continental shelf is very poor or almost non-existent over large areas.

The products of the Coop project include a basement characterisation as well as full 3D crustal and thermal models. Relatively felsic rocks such as the Precambrian gneisses and granites generate more heat than the intermediate-mafic rocks within the Caledonian nappes and high-grade metamorphic units (e.g., the Lofoten gneiss complex). The latter rock units are representative for middle and lower crust. Assuming a constant heat production from the continental crust in basin modelling studies offshore Norway will lead to considerable errors in the calculation of the temperature regime in sedimentary basins. Analysis of offshore and onshore well data is a fundamental step to obtaining a detailed input for heat flow and thermal gradients.

Recent petroleum discoveries on the Utsira High have further demonstrated that deeply weathered basement rocks constitute a viable petroleum reservoir.

The Coop study has aimed at compiling lithogeochemical information on basement rocks along the coast of western Norway with emphasis on characterising the U, Th and K contents. Geophysical information such as seismic, aeromagnetic and gravity data, together with well penetrations of basement, will provide a basis for extending this information below the offshore sedimentary basins. The Geological Survey of Norway (NGU) holds complete gravity and aeromagnetic databases from the whole of the Norwegian mainland and offshore areas in addition to detailed information on the mainland bedrock geology. The onshore-offshore geophysical interpretations can also be constrained by age-dating and petrophysical analysis of basement core samples obtained from offshore exploration wells (Appendix C and D).

Seismic velocity and seismic-reflection patterns from offshore basement rocks help in distinguishing between Caledonian nappe complexes and more massive Precambrian granites and gneisses. Hence an updated version of the Slagstad et al. (2009) basement-related heat-flow map has been produced (Chapter 14 of the present report). New heat-flow data have been optained from the northern North Sea (2010) and the Halten area (Appendix A)

An additional element of relevance to the heat flow in sedimentary basins is the structural relief of the basement; basement highs most likely act as focusing points for fluids that are being driven out from the overlying sediments. The basement highs will also most likely focus the heat flow since the thermal conductivity in basement rocks is usually higher than in sedimentary sequences. An element of the project has therefore been to map the basement structure and to combine this with the mapped rock-type distribution.

Temperatures from bottom hole measurements and drill stem tests (DST) from selected wells have been used to calibrate the crustal and temperature model.

2. AEROMAGNETIC PROCESSING AND COMPILATON OF THE COOP DATA

Aziz Nasuti, Marco Brönner, Torleif Lauritsen and Odleiv Olesen

2.1 Introduction

The delineation of gravity and magnetic anomalies should normally be the first geophysical method to be applied to a new basin or region under evaluation or re-evaluation. In frontier and under-explored areas, where seismic data are sparse or non-existent, the acquisition of aeromagnetic data still remains the cheapest and easiest way to obtain and/or refine a picture of the structural setting of the study area. Aeromagnetic data can also be useful for the strategic planning of new seismic and electromagnetic acquisitions and help to define potential prospects. Large aeromagnetic surveys can be carried out efficiently and safely almost everywhere, in a short period of time and at a reasonable cost.

When integrated with seismic and gravity interpretations, modern aeromagnetic information can also reduce the risk of making faulty geological interpretations. Both gravity and magnetic data are independent of seismic data, both physically and from the technical measurement point of view. A joint interpretation that combines seismic and potential field data thus produces a synergy that helps to significantly improve and validate the geological and structural interpretation of potential prospects.

Modern aeromagnetic data are usually applied as a relevant complement for basin and geodynamic interpretation in Norway. If the seismic coverage is poor, it can be jointly combined with gravity data to confirm and/or estimate the lateral extent of basement features, lava flows, magmatic intrusions, salt structures or sand channels that may be observed in the sparse seismic sections (Figure 2.1). High-resolution aeromagnetic surveys also represent relatively inexpensive tools for the 3D mapping of faults and fracture systems propagating through hydrocarbon-bearing sedimentary successions.

A variety of modern techniques to process, display and model the magnetic anomalies is available for basin analysis. Several magnetic techniques can support the basin analysis and permit geoscientists: 1) to identify and delineate mafic intrusions and volcanic rocks at depth, 2) to quantify and evaluate the top of the magnetic basement and infer the location of the thickest sedimentary section, 3) to detect subtle, intra-sedimentary, ‘micro-magnetic’ anomalies, and 4) to evaluate, to some extent, the temperature of the crust (Curie temperature).

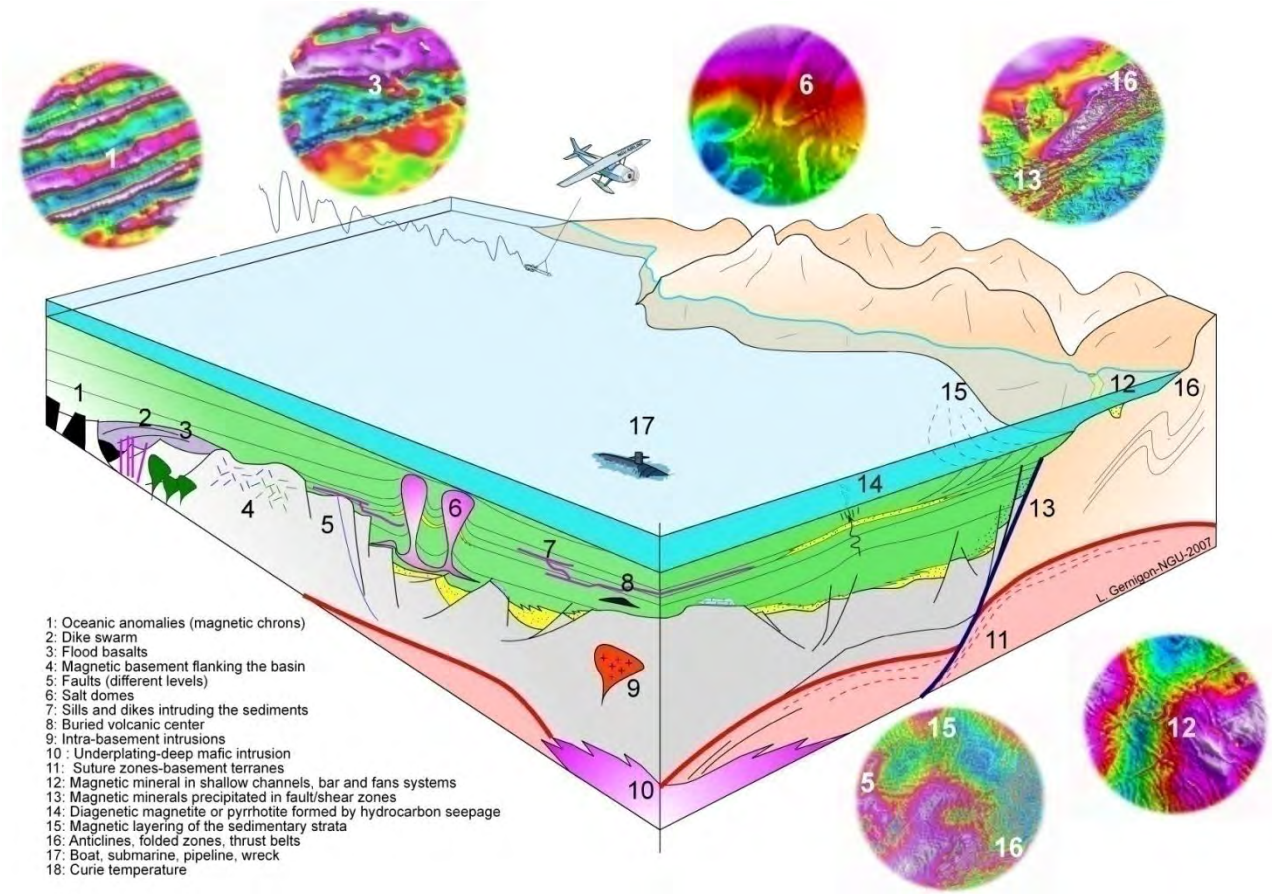

Figure 2.1. 3D cartoon and examples of the application of modern NGU aeromagnetic surveys to basin or geodynamic studies. The cartoon illustrates structures and geological units that can cause of the observable magnetic responses (Gernigon et al. 2007a).

2.2 COOP – The Crustal Onshore-Offshore Project

The Geological Survey of Norway (NGU) has launched an integrated data acquisition and interpretation project to study the onshore-offshore relations along the coast of western and mid Norway. The project area includes the Viking and Central grabens and the Froan, Møre, Stord, Egersund and Norwegian-Danish basins (Figure 2.2).

Aeromagnetic and gravity data provide continuous coverage of the mainland and offshore areas and act as a bridge between areas traditionally investigated by two different methods: field bedrock mapping and seismic interpretation. Information on deep weathering and heat production of mainland basement rocks can consequently be extrapolated to the offshore region. By attributing thermal properties (e.g., radiogenic heat production and thermal conductivity) to the individual basement bodies from potential field modelling, it is possible to calculate the heat flow from the basement into the sedimentary basins.

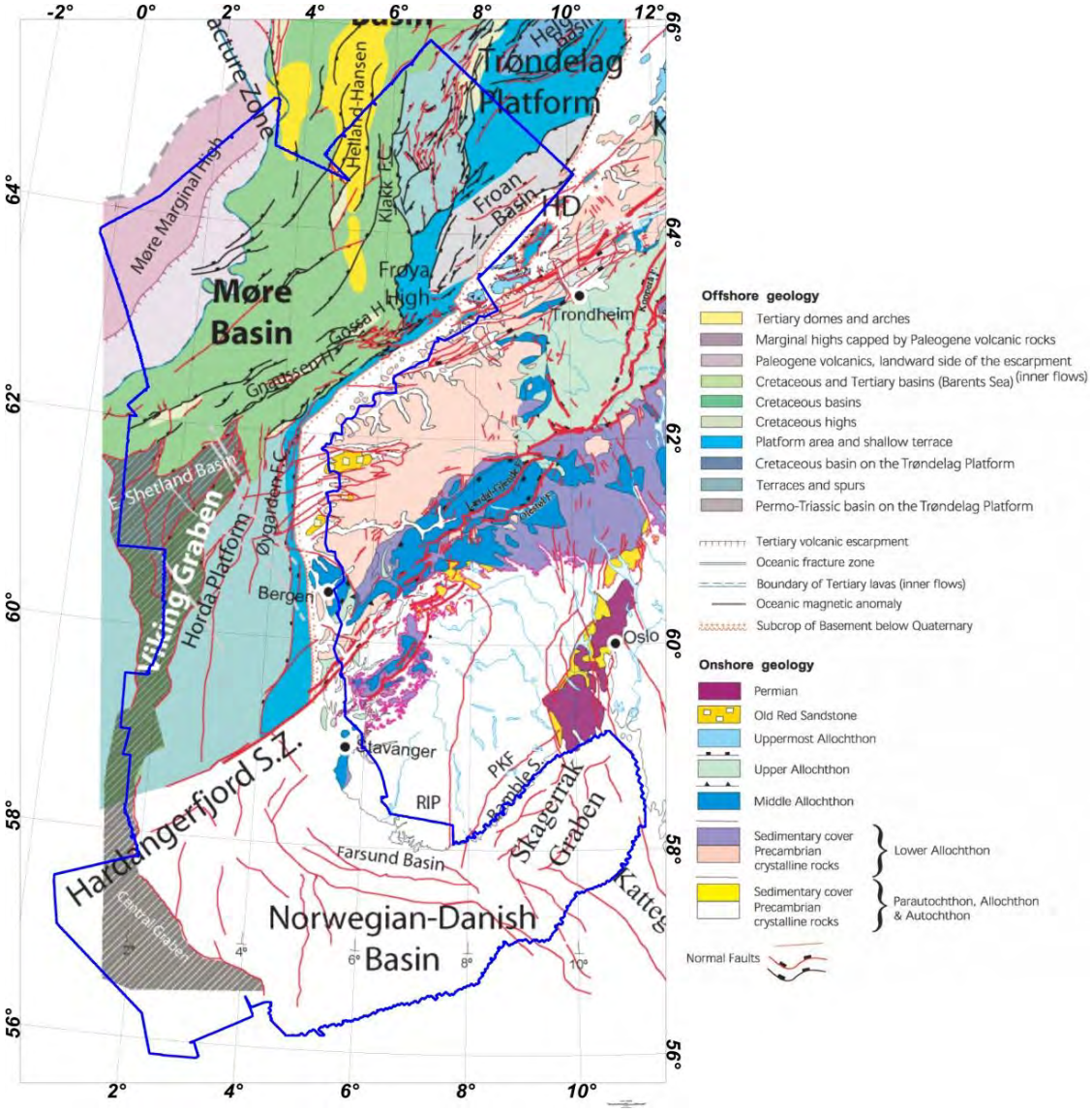

Figure 2.2. Outline of the study area. The blue polygon shows the study area superimposed on a simplified geological map (modified from Mosar et al., 2002).

2.3 Data processing and profile levelling

RAW-magnetic data cannot be used directly for gridding and require a number of processing steps before the production of the final aeromagnetic grid and the map of the total magnetic intensity (TMI) can be used for interpretation. For example, the raw data from the Viking-93 survey (Figure 2.3) cannot be used without further processing. Noise filtering and statistical levelling processing were carried out using the commercial Oasis montaj software (Geosoft 2010a). Microlevelling was performed using the MAGMAP FFT package from Oasis montaj (Geosoft 2010a). The raw data have been processed using standard procedures and methodologies used in many other geological surveys (Luyendyk 1997). In the year 2012, some of the old surveys have been reprocessed and a new microlevelling process was applied to some of the compiled surveys in order to improve the quality of the final product (Table 2.1). The various processing steps and standard procedures are outlined below.

2.3.1 Preliminary noise filtering and basic corrections

Noise filtering

High-frequency noise is often created as the aeroplane is manoeuvring. After acquisition, initial raw data were imported directly into an Oasis montaj database and subsequently interpolated to a regular grid, normally 1/4 of flight-line spacing cell size, to check the quality of lines and tie-lines. Spikes due to minor noise and artefacts were smoothed with a light low-pass filter in order to keep the signal intact. For the offshore aeromagnetic measurements the spikes associated with boats and platforms were removed from the data. For example, the Viking-93 survey is shown after spike removal in Figure 2.4.

Systematic lag corrections

A systematic lag correction for the different surveys was tested but not applied as it did not affect the reprocessed data quality.

The TMI RAW data reflect the recorded magnetic field, including the Earth's geomagnetic main field and all disturbances. The data are dominated by the Earth's geomagnetic field, observable by the increasing magnetics to the northeast.

2.3.2 International Geomagnetic Reference Field (IGRF correction)

As part of the processing, the total magnetic intensity (TMI) field is computed from the recorded magnetic field after subtraction of the International Geomagnetic Reference Field (IGRF) model (Fig. 2.5). The IGRF is a mathematical representation of the undisturbed Earth's geomagnetic field.

The IGRF-corrected data are represent the so-called total field magnetic anomaly, which can be presented either on individual magnetic profiles or on gridded data and illustrated as a magnetic anomaly map. The changes in the geomagnetic field are unlikely to be entirely predictable and differences between the predictive IGRF and the true geomagnetic field grow over the course of each epoch. In the long term, the old IGRF models improve by incorporating measured data. Therefore, the geomagnetic field periodically adopts models for past epochs, called Definitive Geomagnetic Reference Field (DGRF) models. DGRF models will not be available until datasets are significantly improved. DGRF models, therefore, become the official record on how the geomagnetic field has evolved in past epochs (Blakely 1995).

As mentioned before, in the COOP project several old and new surveys have been processed or reprocessed. For those surveys for which DGRF were available, their DGRF has been calculated and subtracted from the raw magnetic data in order to compute the total magnetic anomalies. A DGRF model for Viking-93 is shown in Figure 2.5.

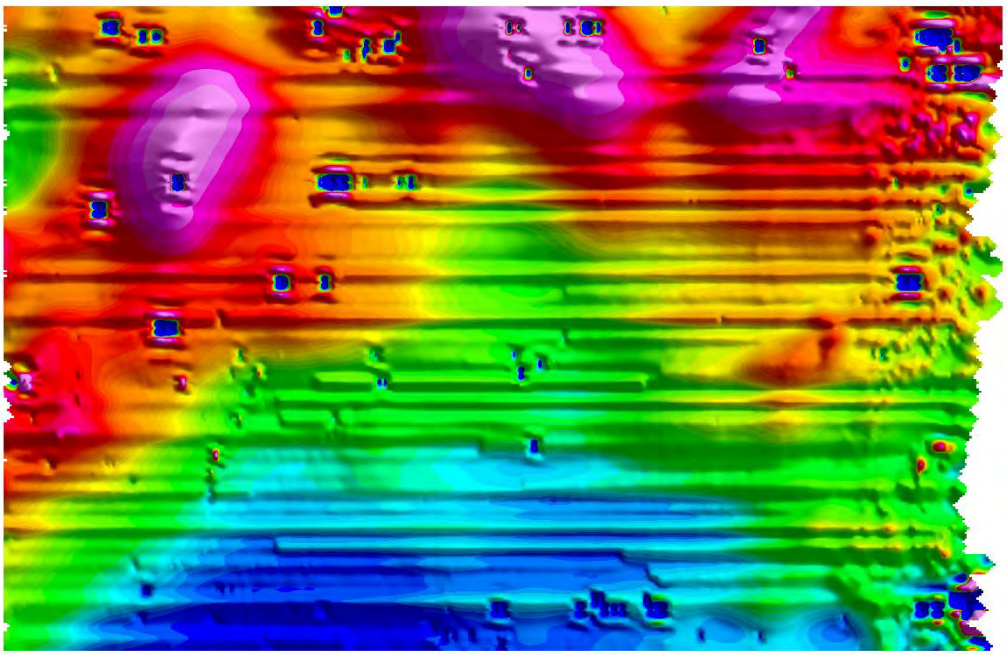

Figure 2.3. Viking-93 TMI RAW magnetic profile data (without levelling and noise filtering) gridded by means of the minimum curvature algorithm (grid cell size at 500 x 500 m). Note that the artefacts are mostly parallel to the line profiles due to diurnals. Projection UTM zone 31N, ED50.

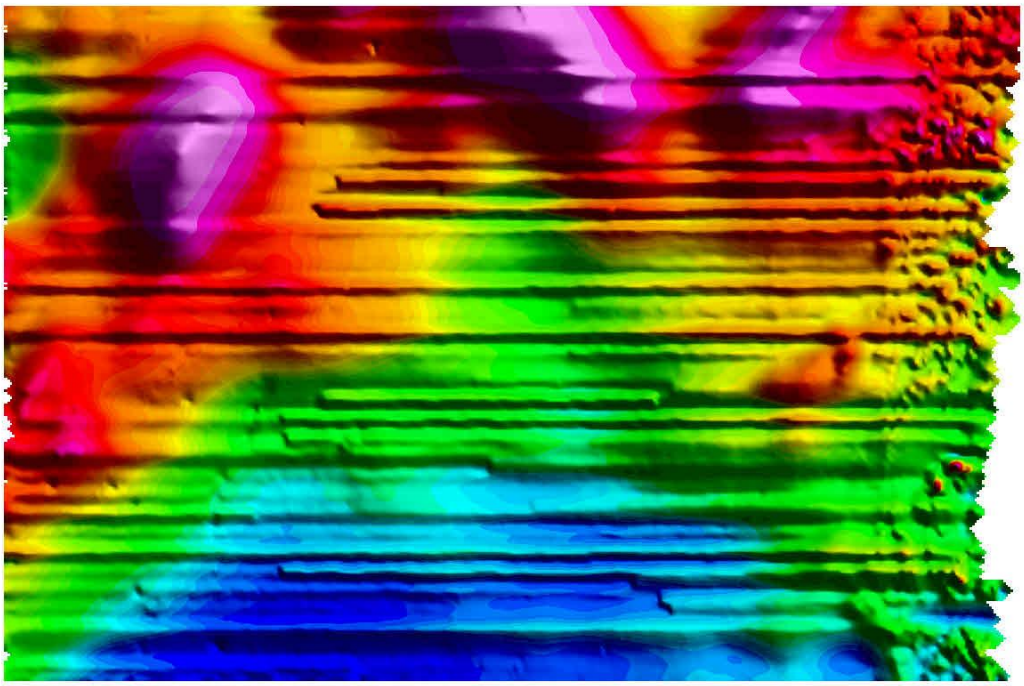

Figure 2.4. Viking-93 TMI RAW magnetic profile data with noise filtering gridded by means of the minimum curvature algorithm (grid cell size at 500 x 500 m). Spikes from platforms and boats have also been removed. Illumination from the northeast.

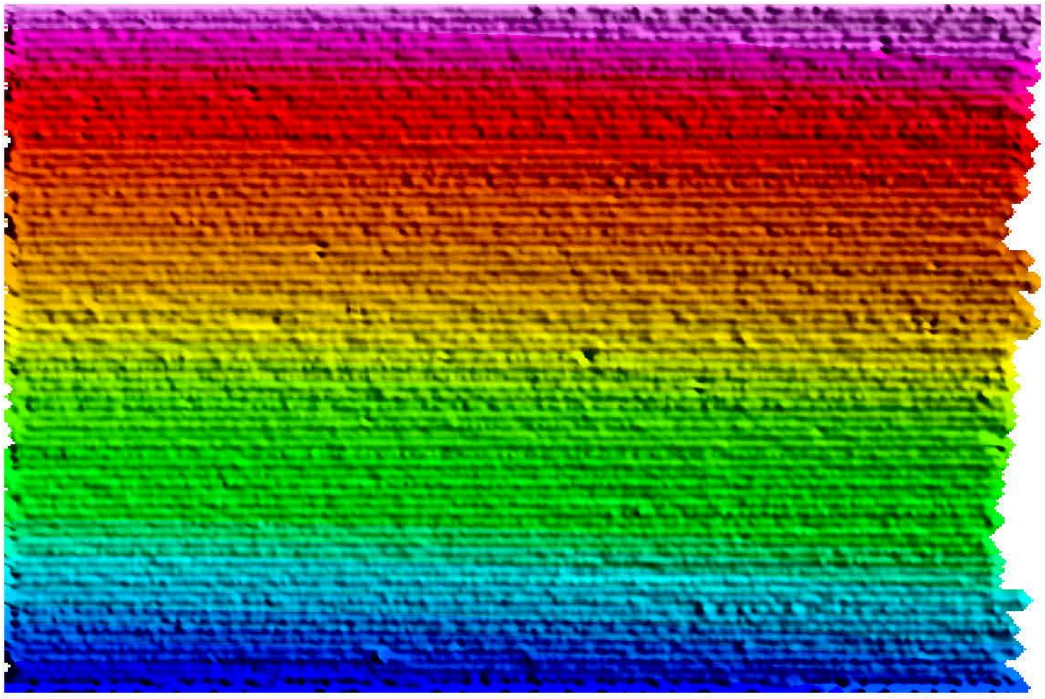

Figure 2.5. The DGRF-1993 model within the Viking-93 survey area. The small and high-frequency anomalies are due to varying flight altitude (see Figure 2.8 for location).

2.4 Levelling and microlevelling of the magnetic profiles

2.4.1 Diurnal variation and use of base-magnetometer readings

A variety of external, time-varying, field factors usually influence and cause errors during aeromagnetic acquisition. These include time variation (diurnal effects) in the magnetic field, altitude variation, ground clearance variation and magnetic effects of seawater swells. These factors are usually sufficient to explain the errors at crossover points between lines and tie-lines.

Even if they are small, these long-wavelength effects can be visually distracting, particularly on image-enhanced displays. Such misfits can also produce artifacts during interpolation and, consequently, erroneous interpretation if no suitable corrections have been applied. The most important reason for this is the time shift in the Earth's magnetic field variations between the offshore survey area and the onshore base station. There is normally a spatial difference in amplitude and frequency of these diurnals.

2.4.2 Statistical levelling

The purpose of levelling is to minimise the residual differences in a coherent way by proportioning them between lines and tie-lines. Proper levelling or microlevelling algorithms usually require close and proper line spacing, and the quality of the final result is generally a function of this crucial parameter. The wide line spacing of previous surveys did not allow proper levelling, and interpolation of raw data produced erroneous or factitious anomalies.

For this project, levelling was undertaken using a standard statistical levelling method of the tie-lines and survey lines, provided as part of the Geosoft Oasis montaj (Geosoft 2010b). The new aeromagnetic survey was processed using a statistical levelling method by which the discrepancies between the readings at each crossover point were reduced by systematically proportioning them between the tie and line profiles. 'Suspicious' crossover differences (outliers) were first removed manually before levelling and full-levelling of the tie-lines and line profiles. A first-order (linear) trend removal was applied during the tie-line levelling, but for one line in the central part of the survey an additional tension spline (b-spline) correction was necessary after several preliminary tests. The tie-lines located in the northern survey area and extending from north to south were also microlevelled before performing line levelling. This was to remove noise along the flight lines before adjusting the in-lines (Figure 2.6). Extreme mis-tie values (outliers) were checked and removed again manually before calculating the next full-levelling correction, until convergence was achieved. The final result has to be considered as the best compromise between the removal of levelling errors and anomaly preservation.

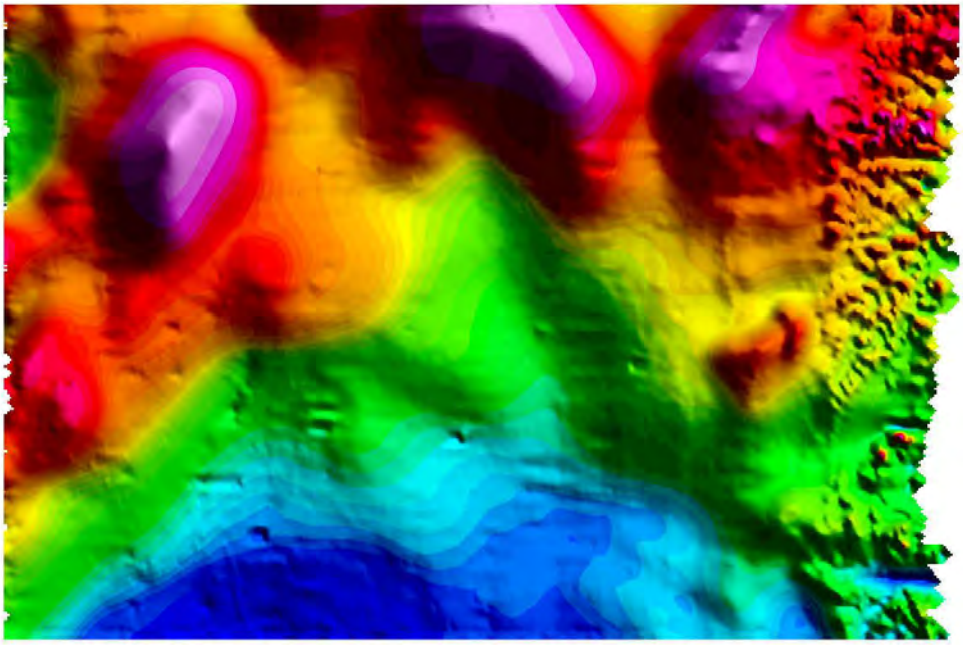

Figure 2.6. Statistical levelling of the magnetic profiles in the Viking-93 survey. Illumination from the northeast.

2.4.3 Microlevelling

We performed microlevelling to remove minor ('micro') levelling errors still remaining along parts of some profiles after the statistical levelling. To improve the levelling, the Geosoft microlevelling approach using the PGW GX system of the available MAGMAP processing package of the Oasis montaj (Geosoft 2010a) was adopted. This proved to be better adapted to preserving geological information for this specific case where the remaining levelling errors are irregularly distributed. The PGW GX system applies a decorrugation process in the frequency domain to isolate the levelling corrections before applying them to the original

data. The Viking-93 data have been decorrugated to reduce line-to-line levelling errors, which are visible as linear magnetic features parallel to the flight lines. Decorrugation is simply a frequency domain procedure based on a directional cosine filter. This filter retains anomalies, from gridded data, in the flight-line direction only. First, a Butterworth high-pass filter is set to four times the line spacing to pass wavelengths in the order of two to four line separations. Such a process results from a line-to-line levelling error. In a second step, a directional cosine filter is set to pass wavelengths only in the direction of the lines. The microlevelled data are shown in the Figure 2.7.

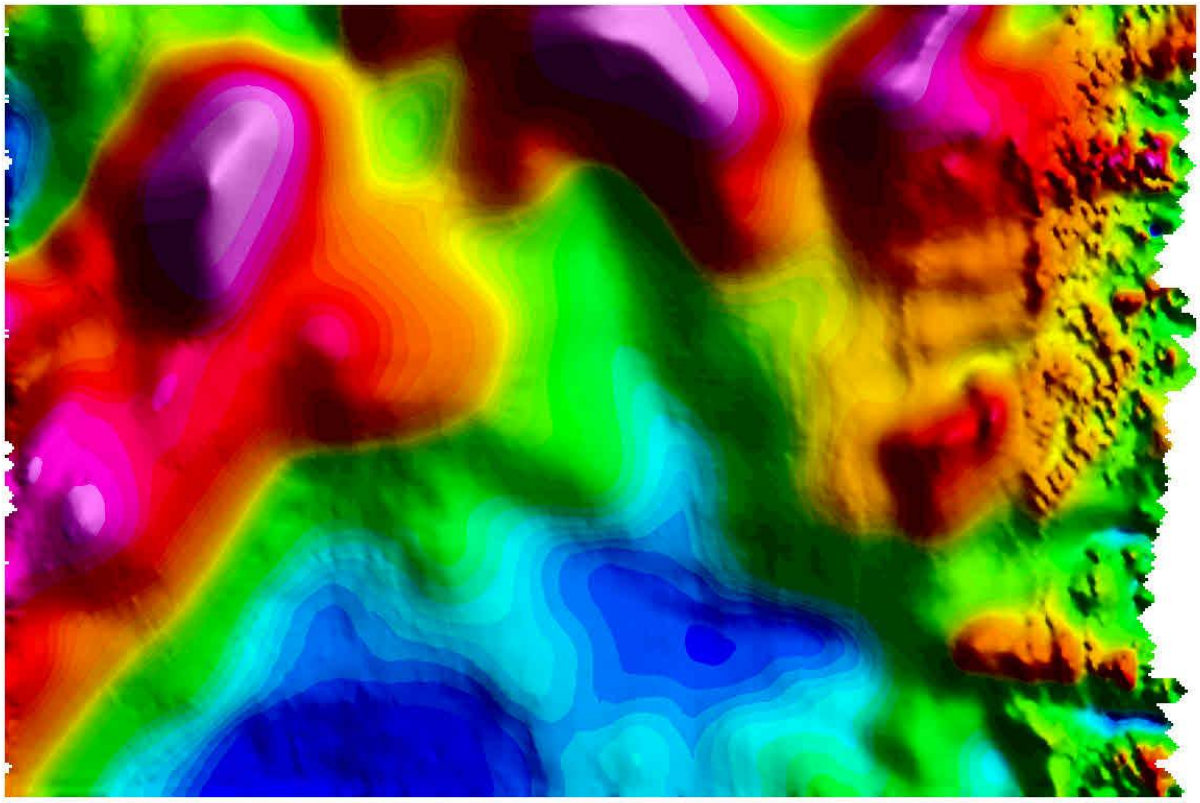

Figure 2.7. Microlevelling of the magnetic data after statistical levelling of the Viking-93 survey. Gridding of the profiles was carried out using the minimum curvature algorithm (grid resolution: 500 x 500 m).

2.5 Final merging and comparison with previous compilations

2.5.1 Merger of the COOP grids

With the completion of new and state-of-the-art aeromagnetic surveys covering the study area (Figure 2.8), we assembled a new compilation by merging every single survey together from scratch. For merging, we used the Geosoft software Grid knitting (Geosoft 2010a) which allows the merging of multiple grids in a selected order, considering the quality and resolution of the various surveys (***Table 2.1***). However, in order to have a full control on the merging grids, grids have been merged one by one. After microlevelling the data were still contaminated by some noise. Subsequent to gridding, we used the 5×5 symmetrical convolution filter to remove very short-wavelength noise. The final product of the survey is shown in Figure 2.9.

The grid-merge of data with different quality can locally decrease the resolution of high-quality datasets (in particular in the overlapping areas). For local interpretation and modelling, we consequently recommend using the original grids for a local study. The complete compilation grid can only be provided to the partners that also purchased the TGS UHAM-09 magnetic datasets, which were used for this compilation. For other sponsors, we have substituted the modern grid with the vintage NGU 74/45 surveys.

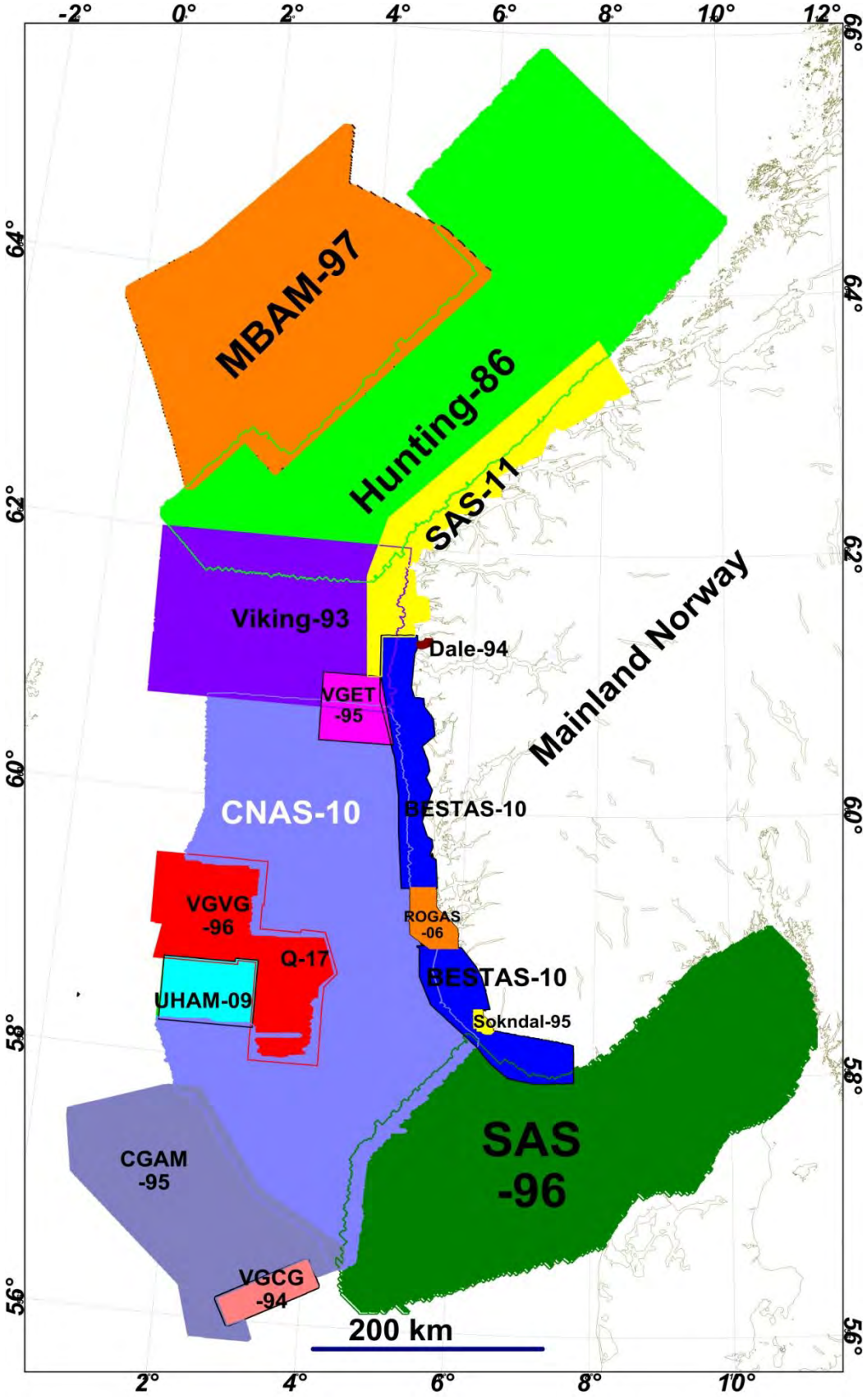

Figure 2.8. Magnetic surveys. Outlines of the various magnetic surveys that have been compiled for the COOP project.

Table 2.1. Aeromagnetic surveys that have been used for magnetic compilation.

Year	Area	Operator, Reference	Survey name	Sensor elevation m	Line spacing km	Length km	Reprocessing
1986	Trøndelag Platform	Hunting, Skilbrei & Kihle 1995	Hunting-86	200	2	57.000	Reprocessed partly and microlevelled
1993	N. Viking Graben	NGU, 20	Viking-93	150	0.5-2	28.000	Reprocessed totally
1994	Helicopter measurements over the Gjølanger area	NGU Report, 95.053	Dale-94	30-40	0.1		-
1994	Vøring Basin	Amarok/TGS, 22	VGVB-94	140	1-3	31.800	-
1994	S. Viking Graben	Amarok/TGS, 24	VGVG-94	160	0.2	44.800	Partly processed and microlevelled
	Central Graben, North Sea	TGS, 1994	VGCG-94	-	0.6-0.8	11,904	-
1995	Central Graben, North Sea	TGS, 1995	CGAM-95	-	2.5-7.5	17,327	-
1995	East Troll, North Sea	TGS,1995	VGET-95	-	0.2-0.6	21,866	-
1995	Helicopter measurements over Sokndal	NGU Report, 95.120	Sokndal-95	30-40	0.1		-
1996	Quadrant 17, North Sea	TGS, 1996	Q17		0.45-1.2	21,347	Reprocessed
1996	Skagerrak	NGU, Olesen et al. 2004	SAS-96	150	2	42.000	Microlevelled
1997	Møre Basin	Amarok/TGS, 26	MBAM-97	220	1-2	46.600	Reprocessed totally
2006	Geological and geophysical investigations for the ROGFAST project.	NGU report, 2006.076	ROGAS-06	60	0.25		-
2009	Utsira high, North Sea	TGS,2009	UHAM-09				-
2010	Central North Sea	NGU Report, 2012.023	CNAS-10	115	1	82.000	Totally reprocessed
2010	Bergen-Stavanger Region	FUGRO, 2010	BESTAS-10				-
2011	Stad region (western coast of Norway)	Novatem *C11089, 2012*	SAS-11	140-1450	0.25		New data

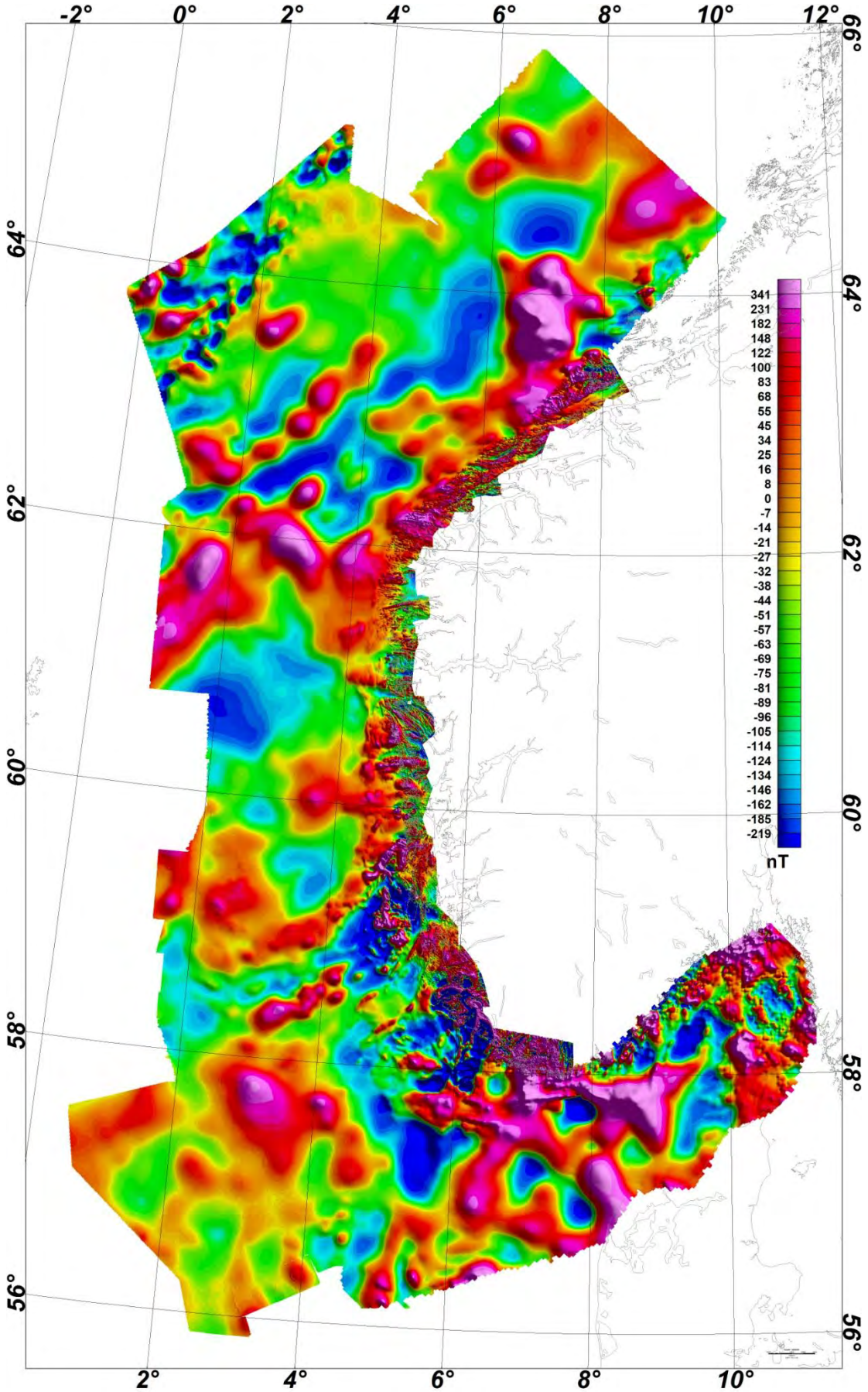

Figure 2.9. TMI field after microlevelling and noise reduction.

2.5.2 Comparison with the previous compilation

In comparison to the previous compilation by Olesen et al., 2010 the new compilation, including the most recent surveys UHAM-09, CNAS-10, BESTAS-10 and SAS-11 datasets reveals a significant improvement in data quality and resolution. The acquisition of the new data during the last four years also, and in particular wanted, to close the gap between offshore and onshore observations to allow a combined interpretation and correlation of the onshore geology to the offshore regions in the western coasts of Norway. A number of additional linear features, which can be linked with structures observed onshore could be followed into offshore regions and were thus allowing a better onshore-offshore correlation and provide a better basis for the interpretation of particular features. For example the SAS-11 survey is compared with old datasets from NGU (74-75) in Figure 2.10.

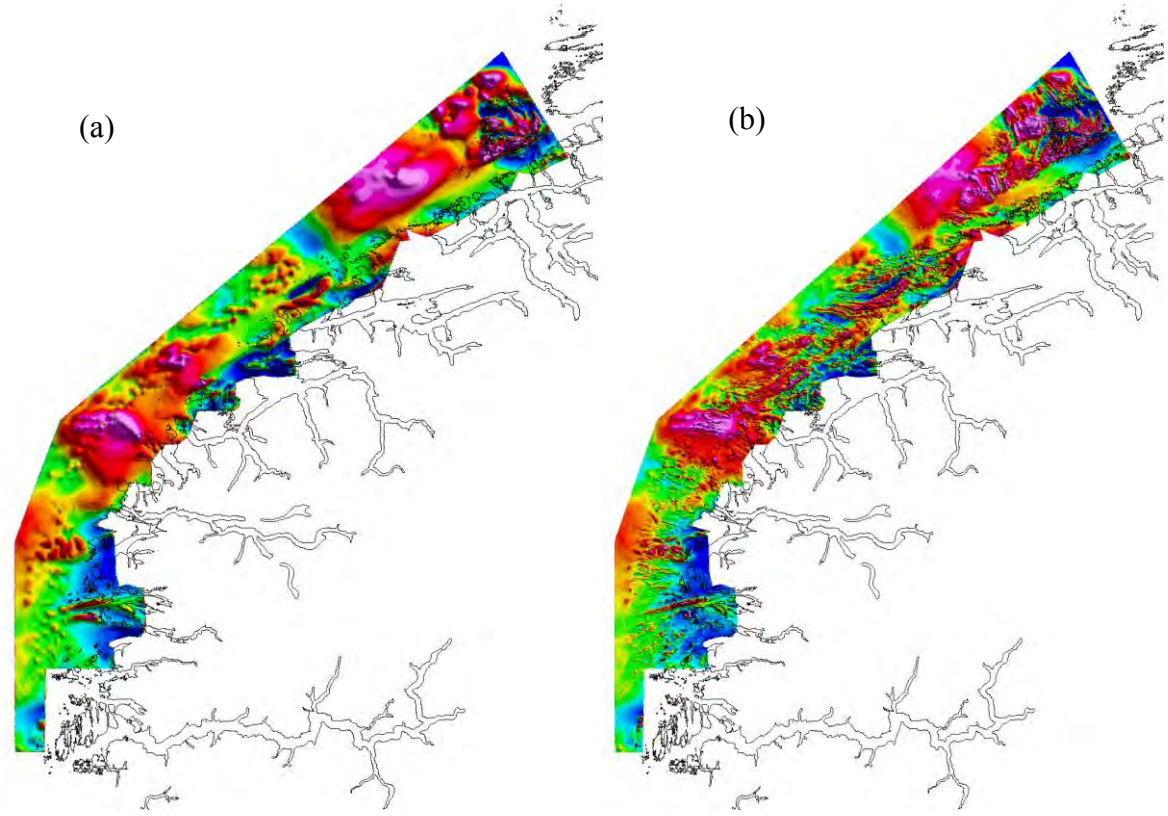

Figure 2.10. Comparison of old and new datasets; (a) old NGU dataset, (b) new SAS-11 survey.

2.6 Data enhancement

In order to detect the main geological structures and trends the aeromagnetic data are filtered as a qualitative aspect of interpretation. Horizontal gradient, analytical signal and the tilt-derivative method are utilised to enhance magnetic anomalies associated with faults and other structural discontinuities.

The total horizontal gradient (THG) method is considered as one of the simplest approaches to estimate the contact locations (e.g. faults). The method is the less susceptible to noise in the data, because it requires only the two, first-order, horizontal derivatives of the magnetic field.

If T (x, y) is the magnetic field and the horizontal derivatives of the field are (∂T / ∂x *and* ∂T / ∂y), then the horizontal gradient HG (x, y) is given by:

$$THG = \sqrt{(\frac{\partial T}{\partial x})^2 + (\frac{\partial T}{\partial y})^2}$$

The derived horizontal gradient map is shown in Figure 2.11 and its shaded relief version is depicted in Figure 2.12.

The analytic signal, although often more discontinuous than the horizontal gradient, can, however, generate a maximum directly over discrete bodies as well as along their edges. The width of a maximum, or ridge, is an indicator of the depth to the contact, as long as the signal arising from a single contact can be resolved. The analytical signal is formed through a combination of horizontal and vertical gradients of a magnetic anomaly (Blakely 1996).

$$AS = \sqrt{(\frac{\partial T}{\partial x})^2 + (\frac{\partial T}{\partial y})^2 + (\frac{\partial T}{\partial z})^2}$$

The analytical signal maps in coloured and shaded relief are shown in Figure 2.13 and Figure 2.14.

We also used the tilt-derivative method (TDR) in order to enhance the edges of sources. The tilt derivative is the angle between the total horizontal derivative (x and y directions) and the first vertical derivative and is defined by Miller and Singh (1994) as:

$$TDR = tan^{-1}(\frac{\frac{\partial T}{\partial z}}{\sqrt{(\frac{\partial T}{\partial x})^2 + (\frac{\partial T}{\partial y})^2}})$$

where T (x, y) is the magnetic field and the horizontal derivatives of the field are (∂T / ∂x *and* ∂T / ∂y) and the vertical derivative is ∂T / ∂z. Tilt angle responses vary between positive values over the source, zero over or near the edge, and negative values outside the body (Cooper & Cowan 2006). The results are depicted in Figure 2.15 and Figure 2.16.

The aeromagnetic grids and images can be downloaded from NGUs ftp2.ngu.no server. User names and passwords have already been distributed to the Coop partners.

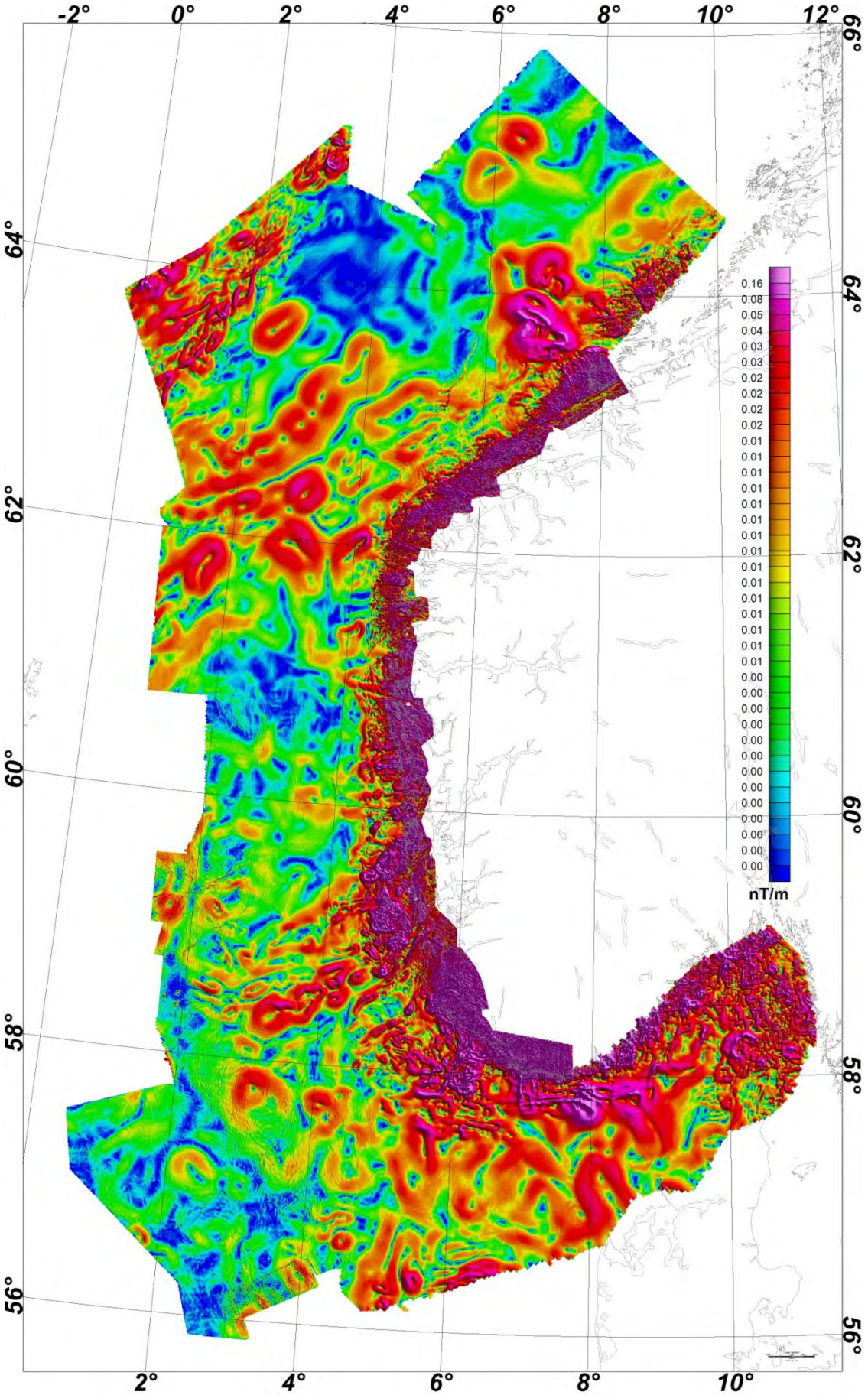

Figure 2.11. Total horizontal gradient map of the microlevelled data.

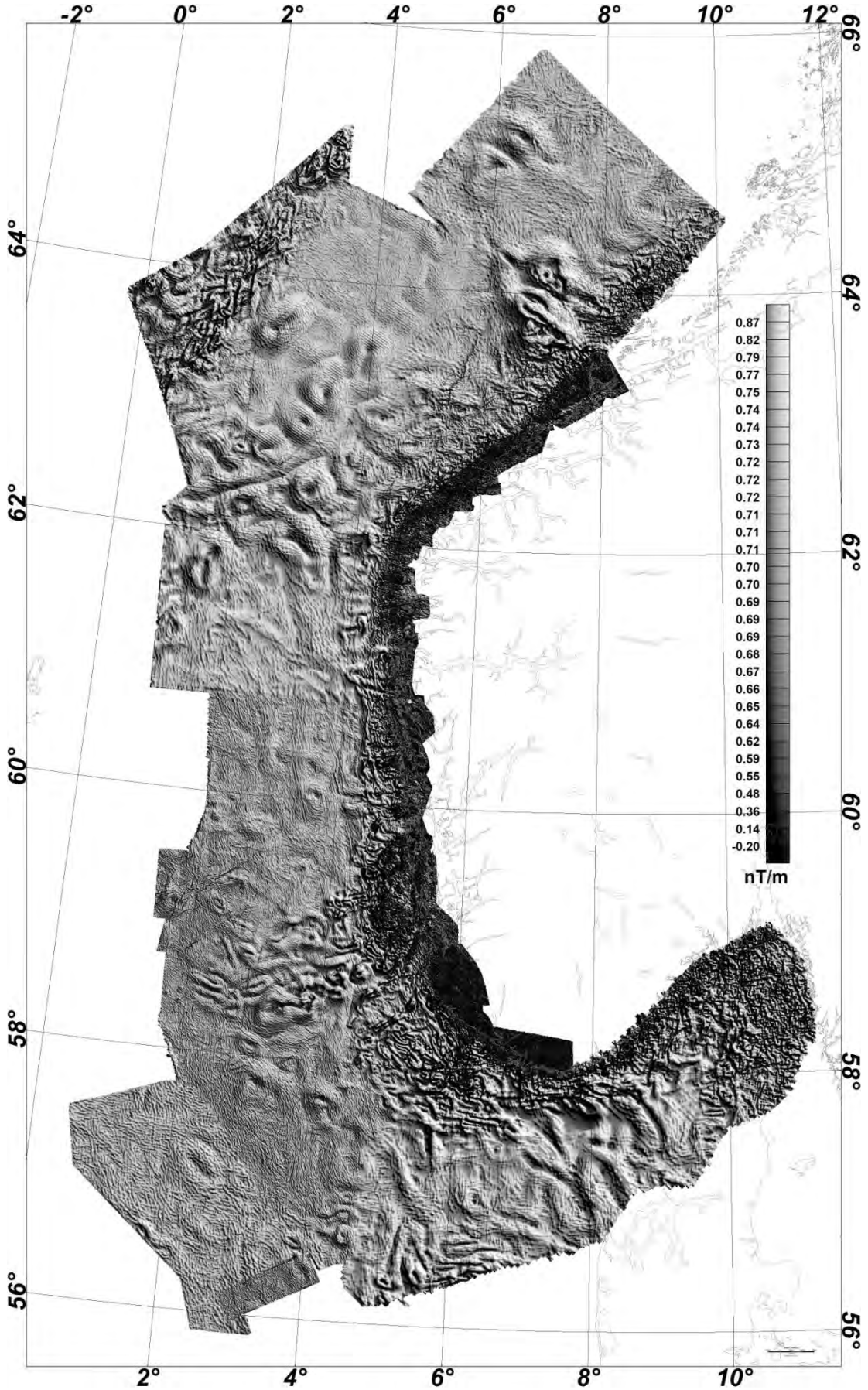

Figure 2.12. Grey tone shaded relief map of the total horizontal gradient of the magnetic data.

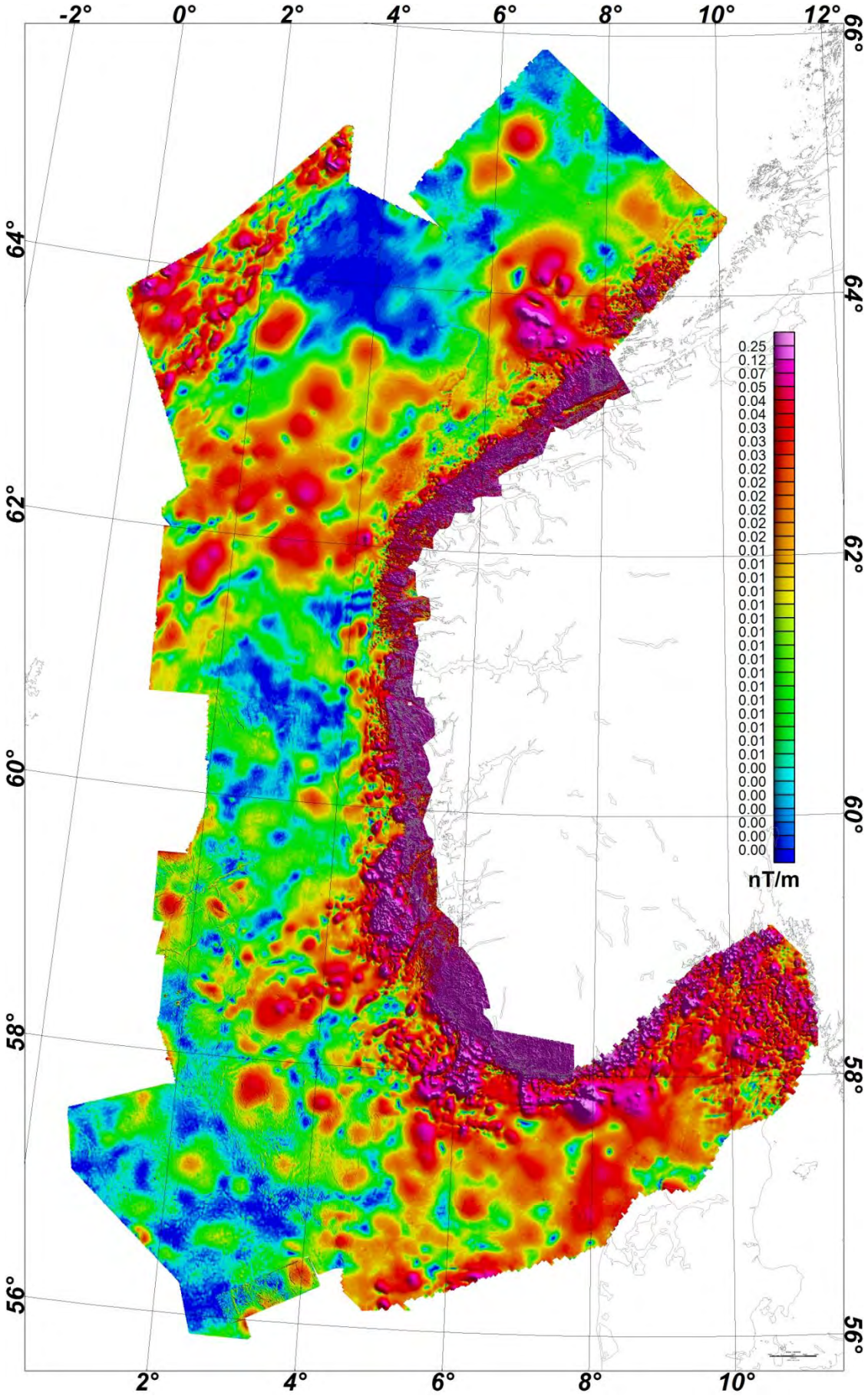

Figure 2.13. Analytical signal map of the aeromagnetic surveys in the study area.

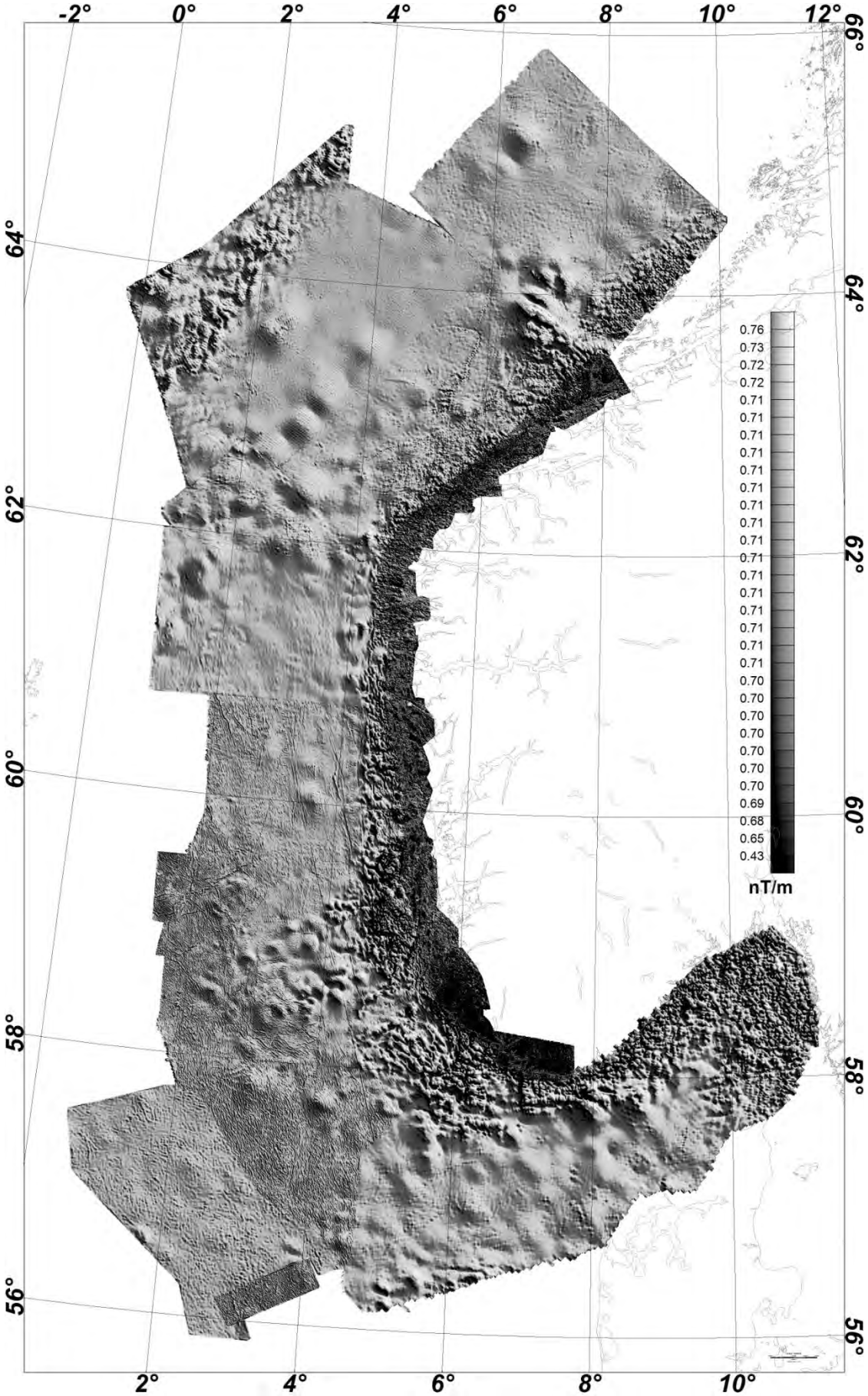

Figure 2.14. Grey tone shaded relief map of the analytical signal (total gradient amplitude).

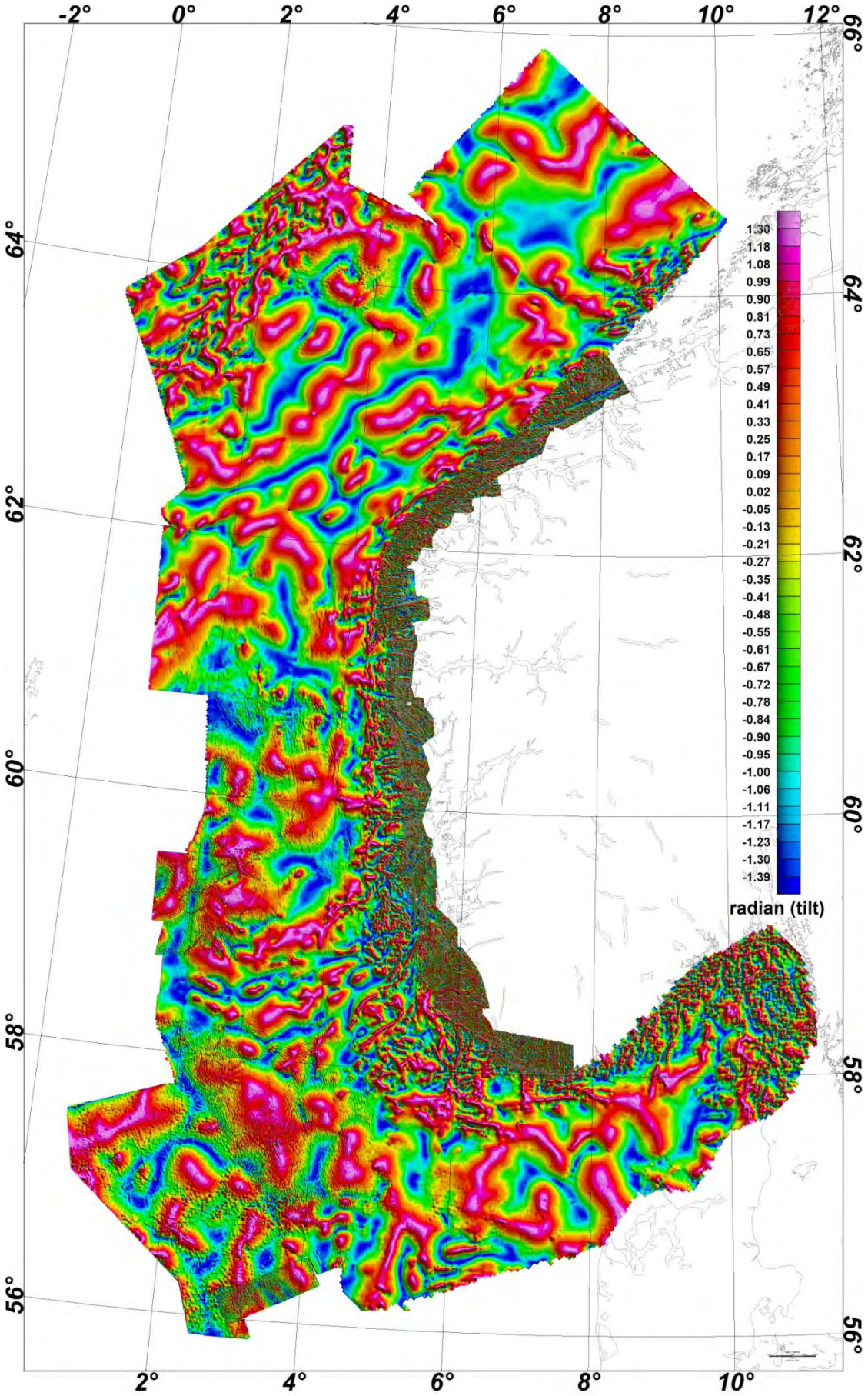

Figure 2.15. Tilt-derivative map of the aeromagnetic surveys in the study area.

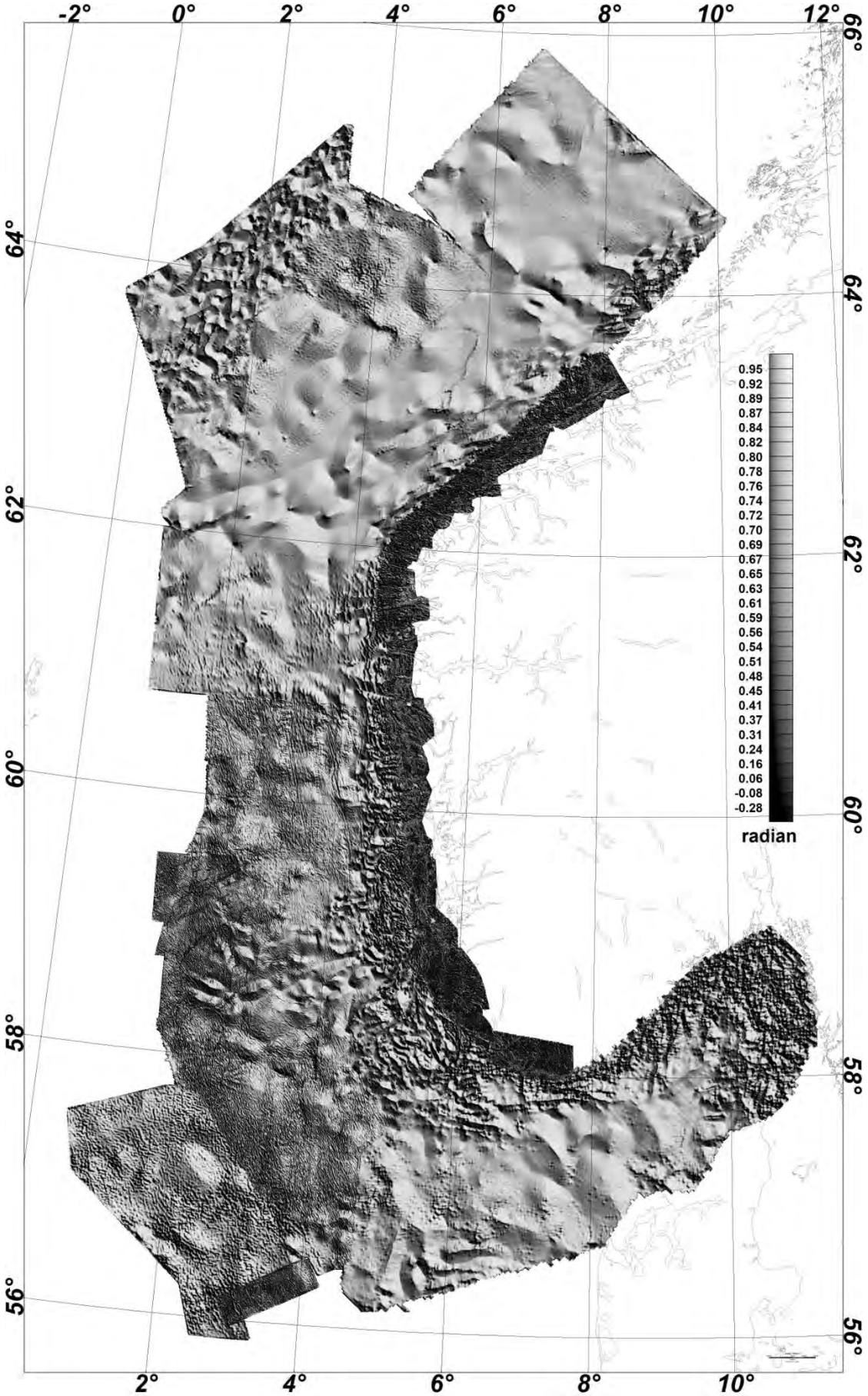

Figure 2.16. Grey tone shaded relief map of the tilt-derivative.

2.7 Merger of the COOP grid with the vintage mainland data

The new compiled surveys have been merged with the regional grid of the mainland area of Norway (Olesen et al. 2010) and the results are shown in Figure 2.17.

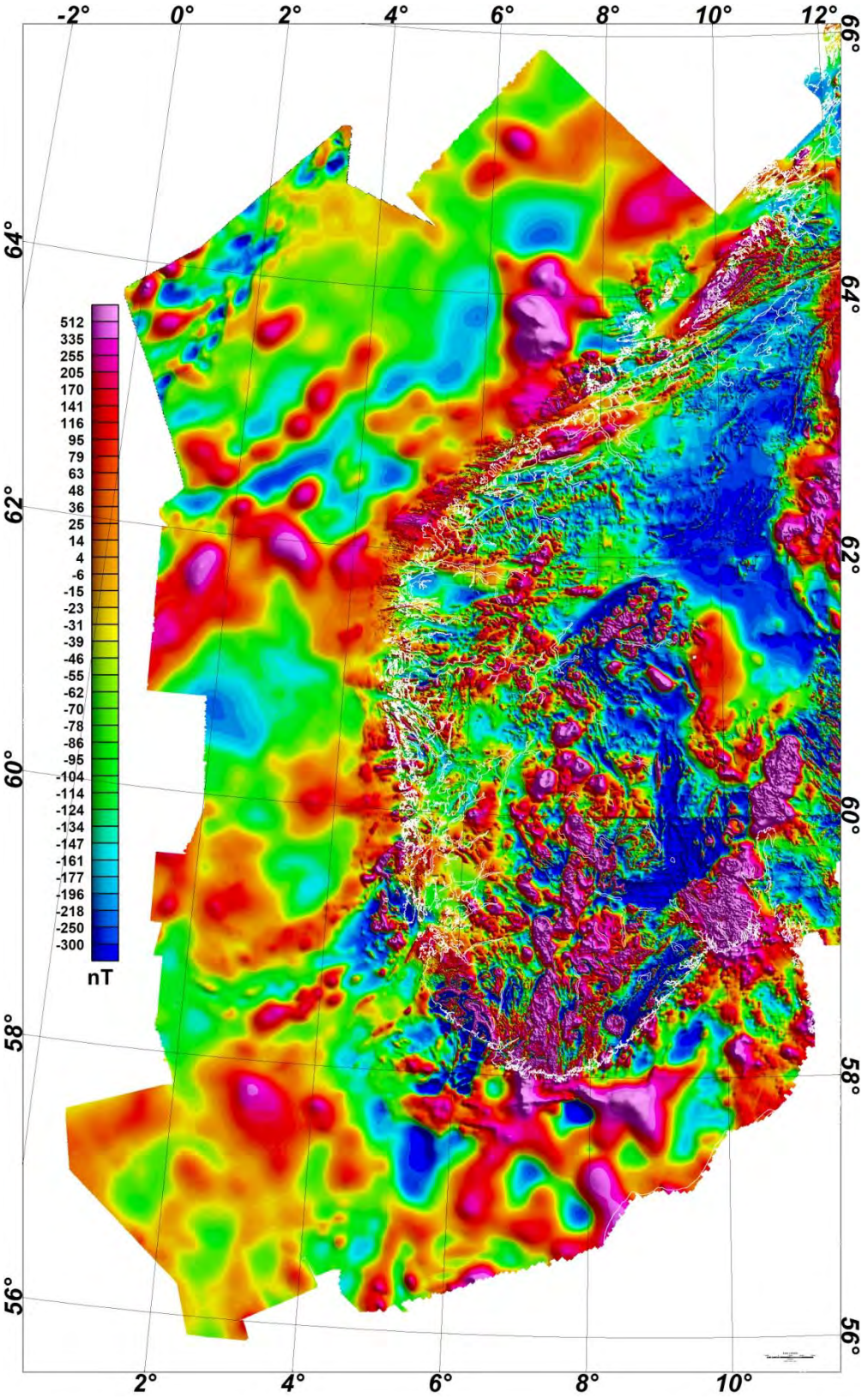

Figure 2.17. Updated regional magnetic compilation with the data from COOP project.

3. GRAVITY DATA - NEW MEASUREMENTS AND COMPILATIONS

Jörg Ebbing & Jomar Gellein

NGU has recently released a new gravity anomaly map for the North Atlantic (Fig. 3.1, Olesen et al. 2010). For the entire shelf, the marine gravity database consists of 554,000 km of ship profiles collected by the Norwegian Petroleum Directorate (NPD), TGS-NOPEC Geophysical Company (TGS), the Norwegian Mapping Authority (SK) and various commercial companies. From the Norwegian mainland, c. 68,000 land gravity stations measured by NGU, SK and several Norwegian and foreign universities have been included in the compilation. For the mainland, a Bouguer correction with density 2670 kg/m3 has been calculated, and special attention has been given to the terrain correction, which significantly reduced the effect of the fjords (Olesen et al. 2010).

The profile data offshore Norway have been levelled using the median levelling technique (Mauring & Kihle 2006), and gravity data from DNSC08 satellite altimetry (Andersen & Knudsen 2010) were used to fill in data gaps in the deep ocean area. The resolution of the shipboard surveys is estimated to be ~1 mGal over 5–10 km wavelengths (Dragoi-Stavar and Hall 2009). Here, free-air data have been used and interpolated to a square grid of 2 x 2 km.

In 2010, a new Earth gravity model, DTU10, was released as an update to DNSC08 (Andersen et al. 2008, 2010), which for the North Atlantic is based on a similar dataset as in Olesen et al. (2010). The compilation has a resolution of 1 x 1 minute, and onshore DTU10 relies on a corrected version of EGM2008 (Pavlis et al. 2012), which in turn is based on a subset of the Norwegian gravity database. Therefore, we did not compare the compilations here in detail, as they are based on the same dataset and differences can probably be explained by the number of data used, their resolution and accuracy.

For the oceanic areas and most of the shelf, the DTU10 model is based mainly on satellite altimetry and only on a limited amount of shipborne surveys. Such high-resolution, satellite-derived, free-air data are estimated to have a resolution of ~3 mGal over 10–15 km wavelengths for the North Atlantic (Andersen et al. 2010). The resolution is assumed to increase with higher latitudes because of improved crossing angles between satellite tracks. Overlapping satellite and marine gravity measurements in the Arctic Ocean differ by 2.64–3.11 mGal (Childers et al. 2001).

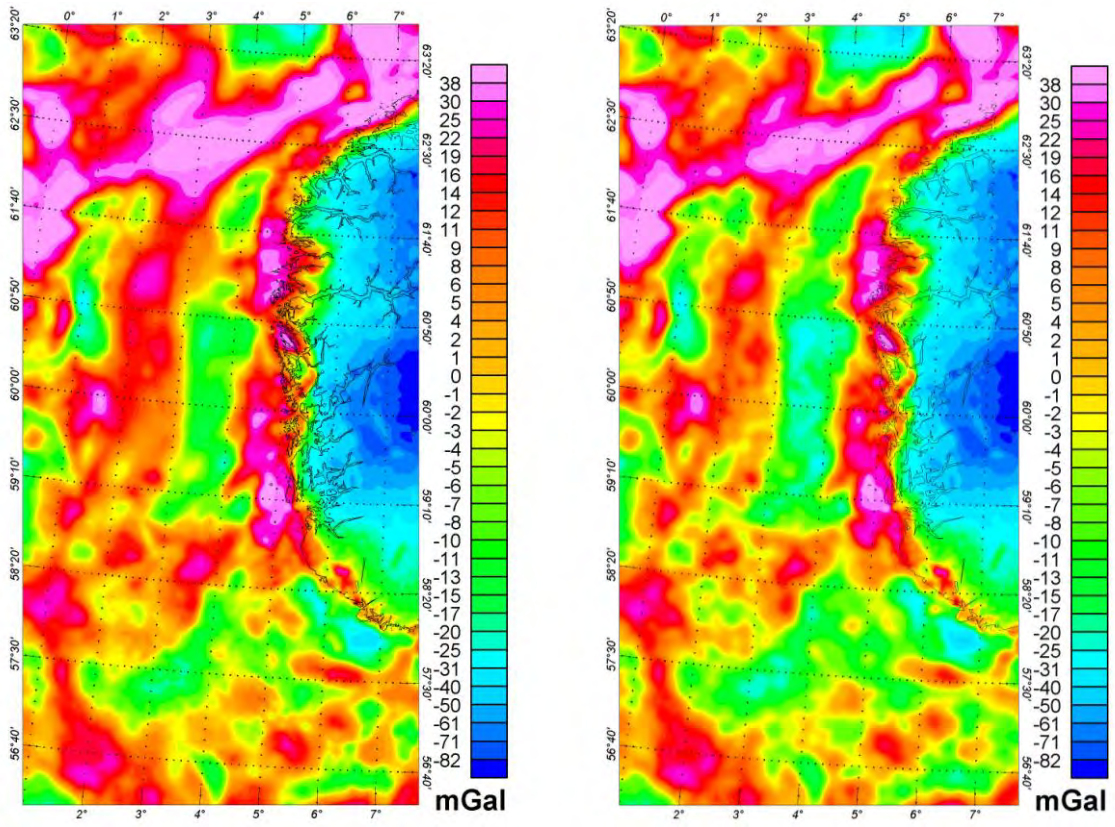

Figure 3.1 Regional gravity compilations: (Left) NGU compilation after Olesen et al. (2010), (Right) DTU10 (offshore) and NGU compilation (onshore). Offshore: free-air anomaly, onshore: Bouguer anomaly. For more details see text.

In Figure 3.1 both the free-air anomaly from Olesen et al. (2010) and the DTU10 compilation are shown. In general the fields look quite similar, but some differences can be observed which are clearer on a difference map (Fig. 3.2).

The differences are not in the order of +/-3 mGal, as would be expected from the data accuracy, but show maximum differences up to 15 mGal (neglecting local higher amplitudes), and in general a difference of 2.5-7.5 mGal over the northern North Sea, and slightly higher on the Møre margin. Comparison of the DT10 dataset with other shipborne surveys of the North Atlantic shows a difference in the range of the expected standard deviation (not shown here). The reason for the differences between the two datasets on the shelf can most likely be explained by the levelling procedure. Both at the coast and towards the oceanic part, the models are consistent, as they are linked here. In between a long-wavelength misfit is introduced, as no direct control on the long wavelength is available. The difference maps also show a form of ringing, which is caused by short-wavelength features (<15 km) which have a poor resolution in the satellite altimetry.

For the modelling in Chapter 12, we use the combined NGU-DTU10 model, as we are not particurlarly interested in the short wavelength, but rather in the intermediate- to long-wavelength field which, on the shelf is better expressed in the DTU10.

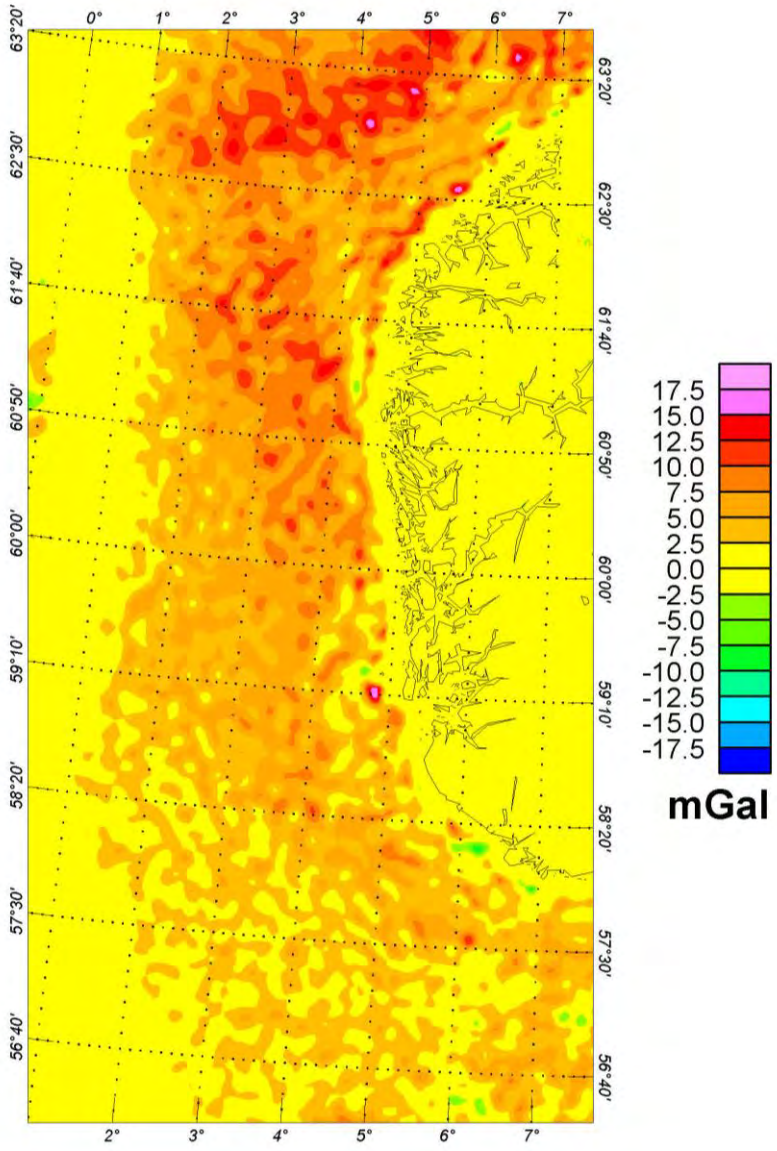

Figure 3.2 Difference map for the compilations in Figure 3.1, left and right.

A better control and improved version of the NGU compilation can be provided by integration with satellite models (e.g., GRACE, GOCE). This work is in progress, and the improved compilation is planned to be released in 2013.

3.1 New gravity measurements – acquisition and processing

To bridge the gap between the densely measured mainland and the marine surveys, new gravity measurements have been carried out along the coast from Haugesund to Florø, in western Norway (Fig. 3.3). The objective was to measure with a denser spacing of points and closer to the open sea on islands and skerries. In 2010, the gravity measurements were

extended with 260 new stations using helicopter transport. Data acquisition was carried out using a Scintrex CG-3 gravimeter in the period from 19.09 to 29.09. 2010.

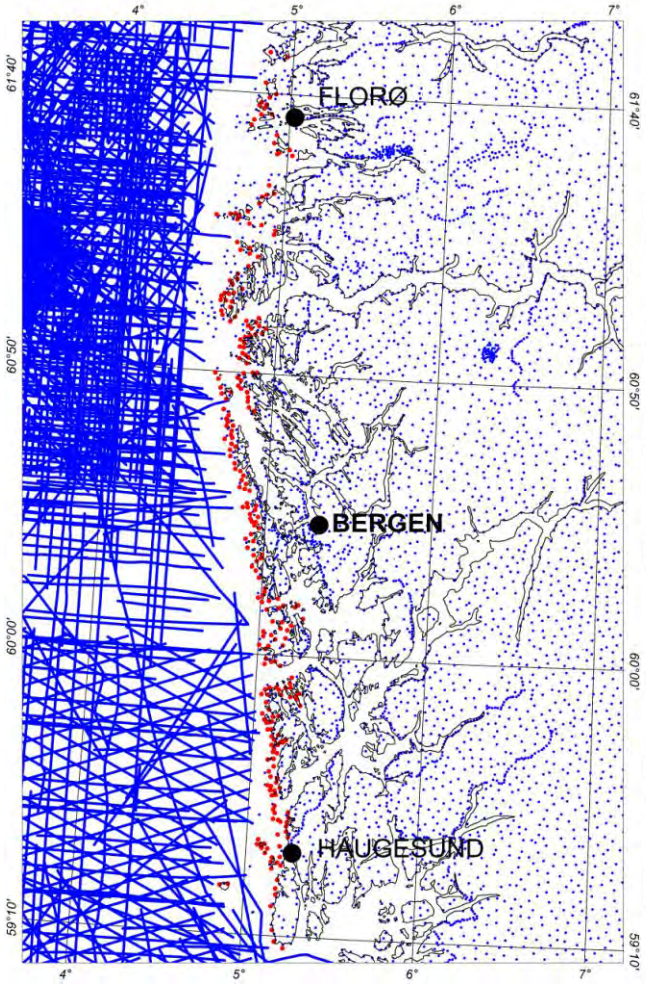

Figure 3.3 Newly acquired (red) and previous gravity points and marine surveys (blue).

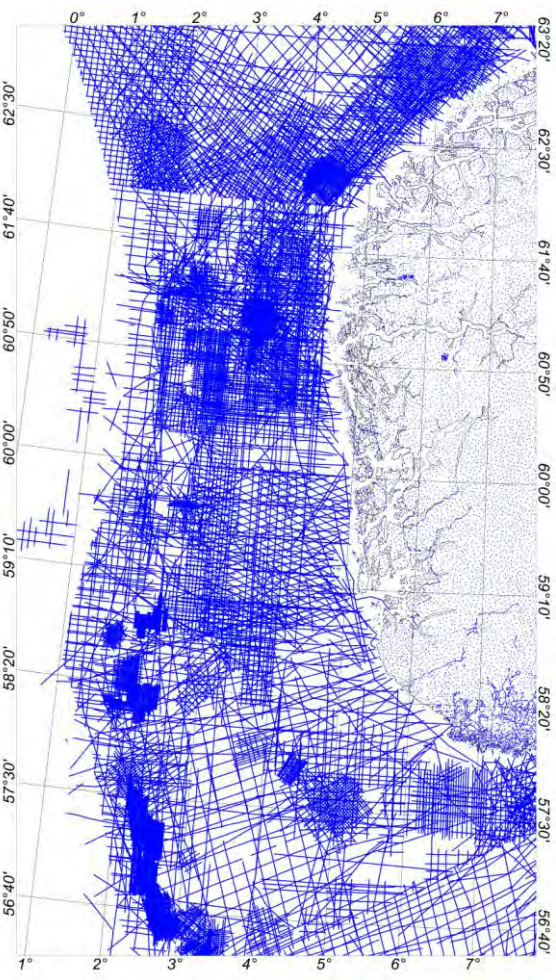

Figure 3.4 Total data coverage.

3.1.1 Processing

Bouguer anomaly values were calculated using software (Mathisen 1976) from the Norwegian Mapping Authority (Kartverket). Bouguer and terrain corrections were carried out using a standard density of 2670 kg/m^3. Terrain corrections were performed using 8 points with known elevation at five circles around each gravity station. Circle radii were 50, 100, 200, 400 and 800 m. The elevations were extracted from the Norwegian Mapping Authority's database. In addition to the stations measured in this project, several stations from NGUs database, the Norwegian Mapping Authority, the Norwegian Petroleum Directorate, Norwegian and foreign institutions and commercial companies are included in the gridding of the Bouguer values (Fig. 3.4). Bouguer (Fig. 3.5) and residual (Fig. 3.6) maps were made using the Oasis montaj system from Geosoft (2010, 2011). A high-pass filtered residual map has been produced by subtracting wavelengths <200 km to enhance regional features. Both Figures 3.5 and 3.6 show a coastal gravity high, which is terminating against the Hardangerfjord Shear Zone.

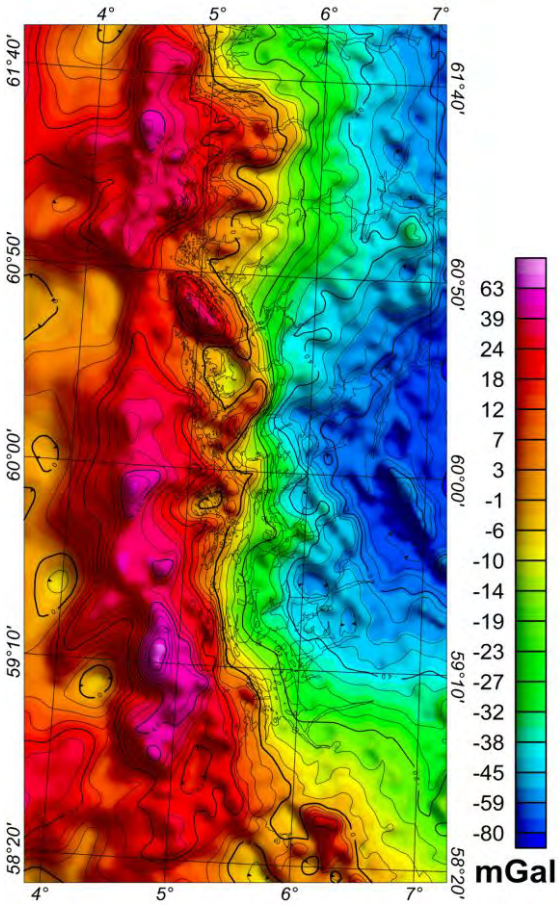

Figur 3.5 *Bouguer anomaly map, 2 x 2 km grid.*

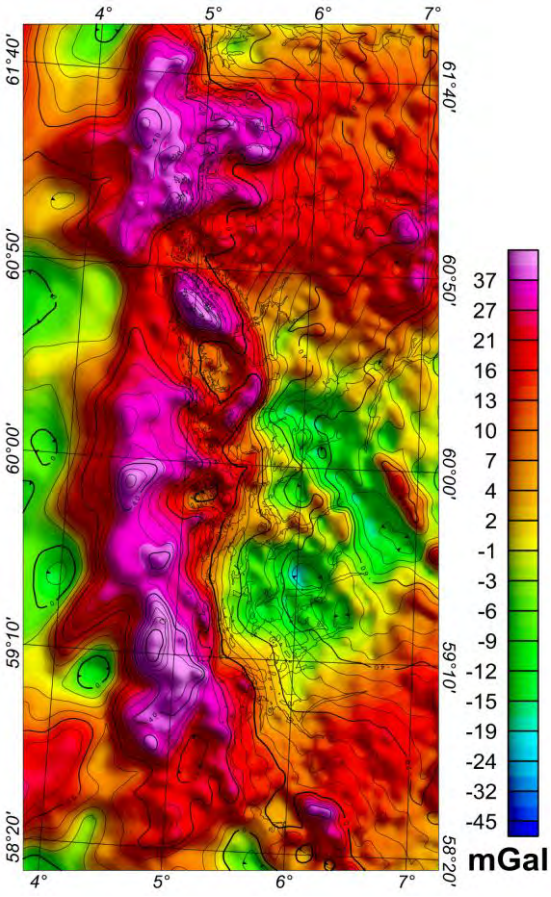

Figure 3.6 *High-pass filtered residual map, 200 km cutoff.*

3.2 Comparison with regional compilations

Figure 3.7 shows the difference between the newly acquired gravity data (2010) and the compilation in Figure 3.1 (right). The standard deviation is 1.75 mGal with a mean difference of -0.79 mGal. This is in the range of the uncertainty of the regional compilation. However, the general difference is negative, and these values must be included when levelling the marine shipborne data from the coast towards the oceanic domain in order to avoid an incorrect tie to the Norwegian mainland data.

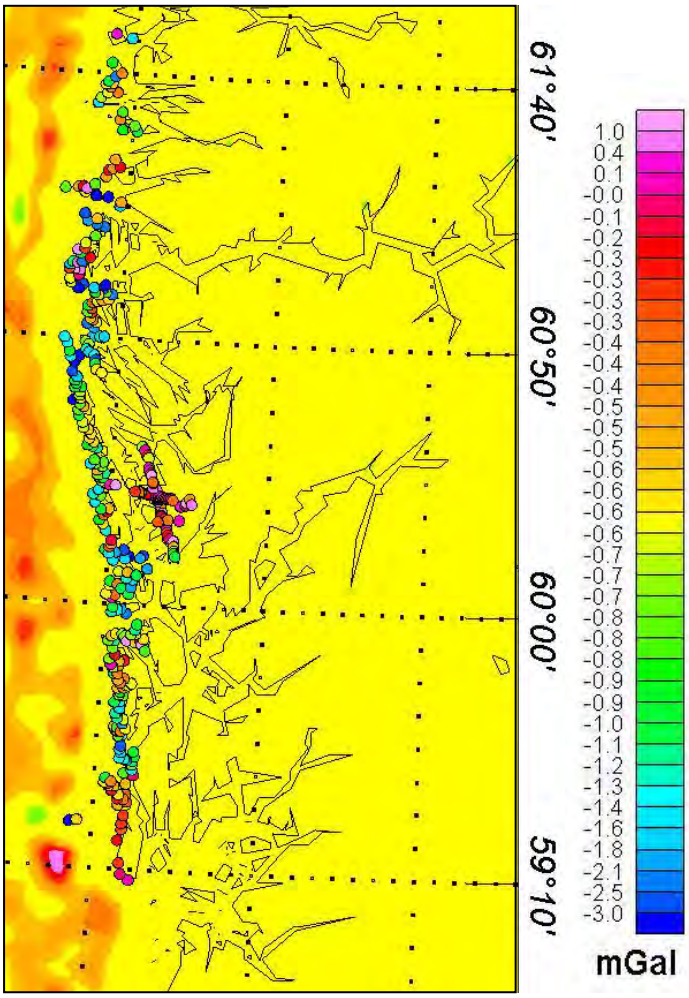

Figure 3.7 Gravity difference for the new gravity points (circles) relative to regional compilation (Fig. 3.1) plotted on top of the difference map from Figure 3.2.

4. CORRECTION AND COMPILATION OF AIRBORNE RADIOMETRIC DATA

Torleif Lauritsen

There are many naturally existing radioactive elements. However, only three have isotopes that emit gamma radiation of sufficient intensity to be measured by airborne gamma ray spectrometry. The three major sources of gamma radiation are Potassium-40, daughter products in the ^{238}U decay series and daughter products in the ^{232}Th series.

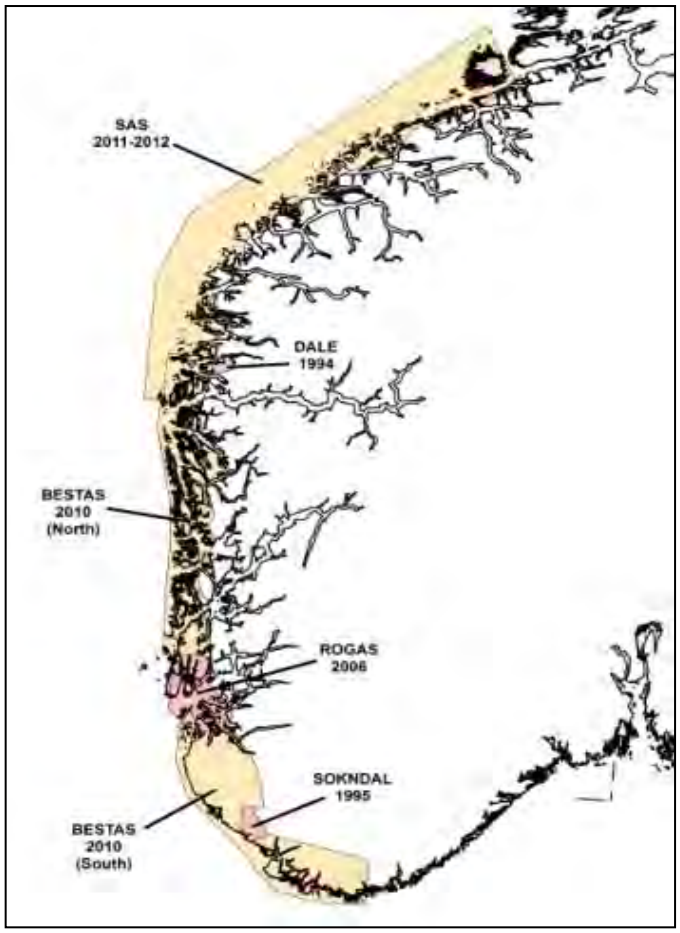

Figur 4.1. Airborne gamma ray spectrometry surveys within the COOP project.

The multi-channel gamma spectrometry data used in the present study were acquired from fixed wing and helicopter surveys (1994-2012). Figure 4.1 shows their locations.

In addition to the BESTAS10 and SAS11 surveys initiated in the COOP project, we included the three minor surveys Dale94, ROGAS06 and Sokndal95. Acquisition details can be seen in Table 4.1.

Normally, the count rates in the K, U and Th windows will be converted to apparent radioelement concentrations, K %, eU ppm and eTh ppm. For the older surveys at Sokndal (1995) and Dale (1994) this was not done. These two datasets occur simply with count rates in the K, U and Th windows. However, both NGU surveys partially overlap the FUGRO survey from 2010, and have thus enabled the making of scatter diagrams and calculations of regression equations.

In Figures 4.2, 4.3 and 4.4 we present the scatter diagrams for the relationships between the Dale94 survey and the BESTAS10 North survey with regard to uranium, thorium and potassium. Similar scatter diagrams for the Sokndal and BESTAS10 South surveys were also produced.

The regression equations are then used to convert count rates to radioelement concentrations in the two helicopter surveys. For the Dale94 survey the regression equations are:

Uranium (ppm) = 0.70573 + (Uranium (cps) * 0.066677)
Thorium (ppm) = 2.5066 + (Thorium (cps) * 0.27726)
Potassium (%) = 0.28467 + (Potassium (cps) * 0.010141)

The regression equations for the Sokndal95 survey are:

Uranium (ppm) = 0.6249 + (Uranium (cps) * 0.057904)
Thorium (ppm) = 2.3448 + (Thorium (cps) * 0.2696)
Potassium (%) = 0.25998 + (Potassium (cps) * 0.0088748)

Table 4.1. Acquisition details.

Survey	Year	Contractor	Platform	*Flying height (m)*	Line spacing (m)	cps/ppm
Dale	**1994**	**NGU**	**Helicopter**	**60**	**100**	**cps**
Sokndal	**1995**	**NGU**	**Helicopter**	**60**	**100**	**cps**
ROGAS	**2006**	**SGU**	**Fixed wing**	**60-100**	**250**	**ppm/%**
BESTAS	**2010**	**FUGRO**	**Fixed wing**	**60**	**250**	**ppm/%**
SAS	**2011-2012**	**NOVATEM**	**Fixed wing**	**60**	**250**	**ppm/%**

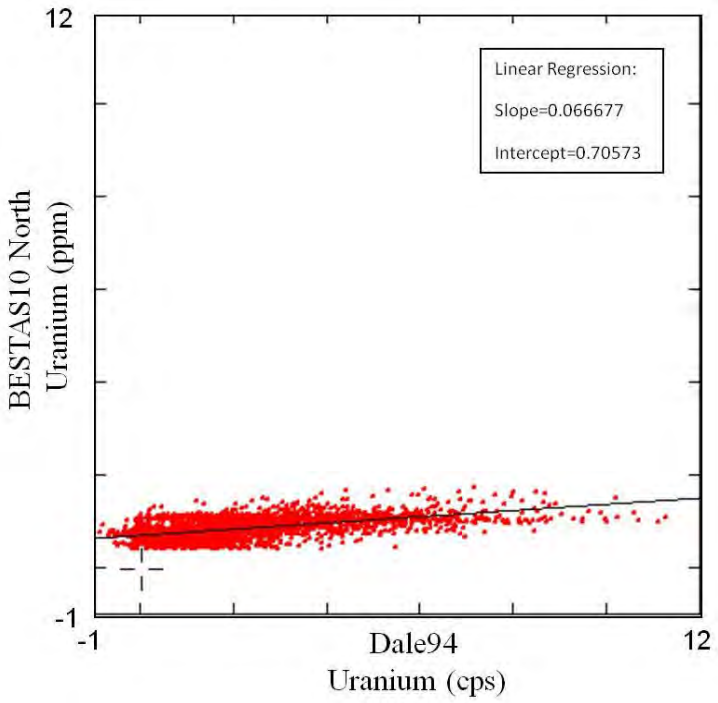

*Figure 4.2 Scatter diagram for uranium in BESTAS North (ppm) vs. DALE (cps). The regression equation is Y=0.70573+(X*0.066677).*

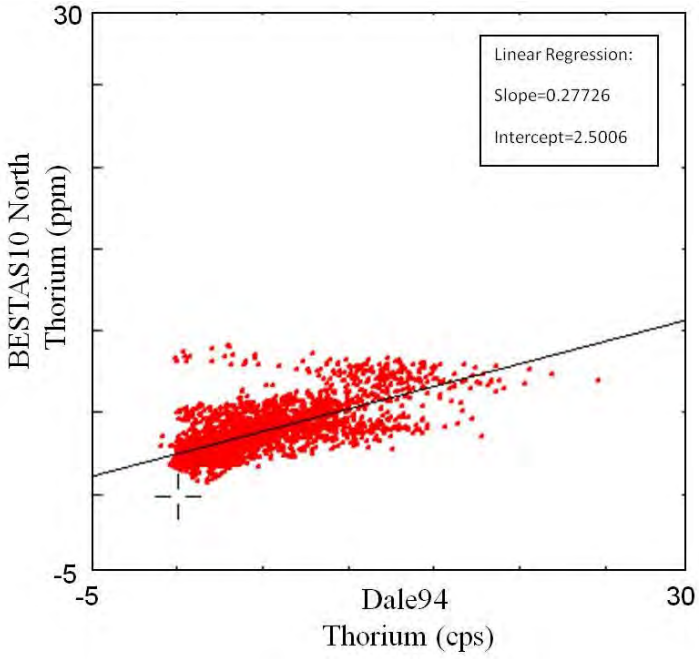

*Figure 4.3. Scatter diagram for thorium in BESTAS North (ppm) vs. DALE (cps). The regression equation is Y=2.5066+(X*0.27726).*

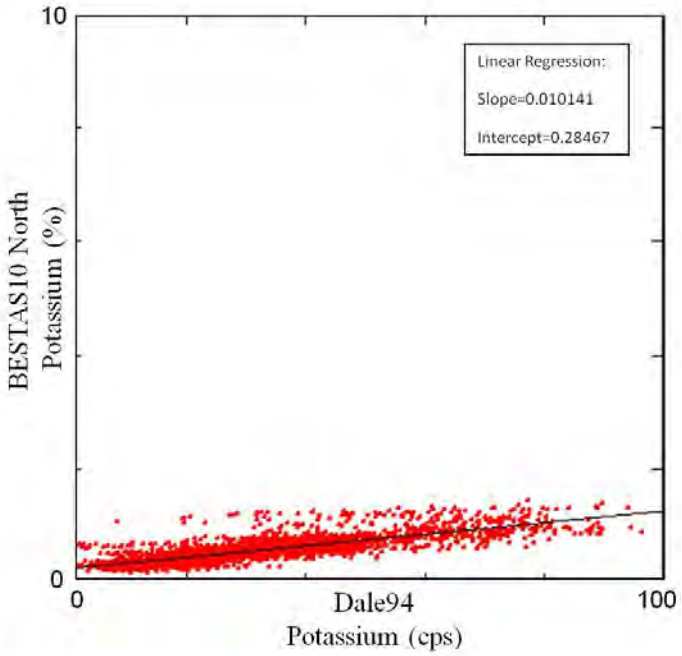

*Figure 4.4. Scatter diagram for potassium in BESTAS North (ppm) vs. DALE (cps). The regression equation is Y=0.28467+(X*0.010141).*

The uranium, thorium and potassium data from each survey were gridded with a grid cell size of 50 x 50 metres. The six surveys were then knitted together with respect to each radioactive element. The results of this combination are presented in Figure 4.5.

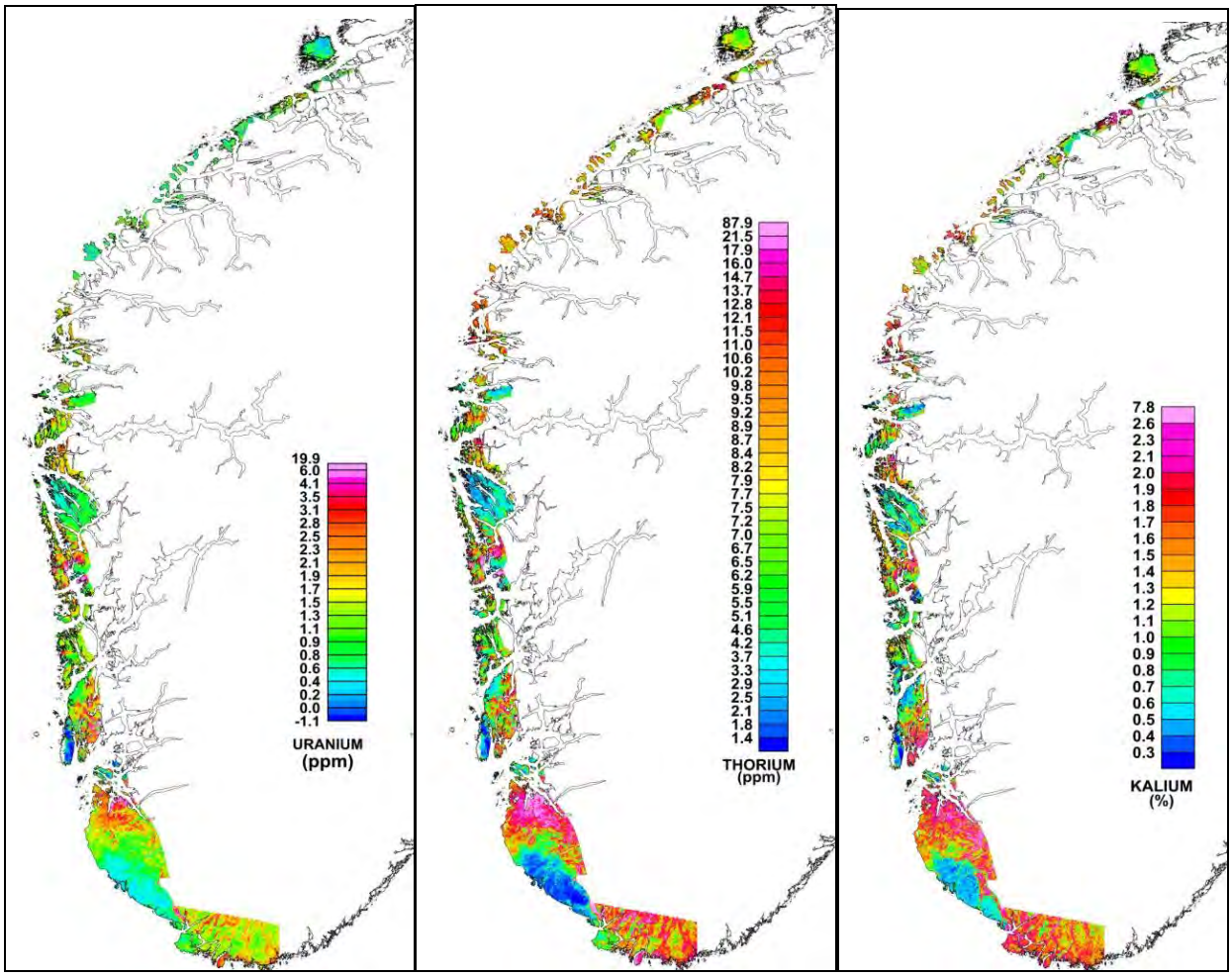

Figure 4.5. The results of the radiometric measurements: apparent radioelement concentrations of uranium (ppm), thorium (ppm) and potassium (%).

5. COMPILATION OF PETROPHYSICAL DATA

Torleif Lauritsen

Approximately 28,000 rock samples from the whole of Norway, collected during geological mapping and geophysical studies, have been measured with respect to density, susceptibility and remanence (Torsvik & Olesen 1988). The data are stored in NGUs petrophysical database (Olesen et al. 1993). Figure 5.1a displays the geographical distribution of a selection of these petrophysical samples on the mainland of southern Norway.

We have produced maps of susceptibility and density by calculating the average values within each geological unit present in the geological map (Sigmond 1996) (Fig. 5.1b).

Non-representative samples (e.g., sulphide mineralisations, hydrothermal alterations, mylonites, dolerite and eclogite) were removed from the dataset before map production. We then selected points within each polygon on the bedrock map. An average of these points was attributed to each polygon. The applied colour scale for the susceptibility map is logarithmic in order to depict the several magnitude-wide distributions for each rock unit.

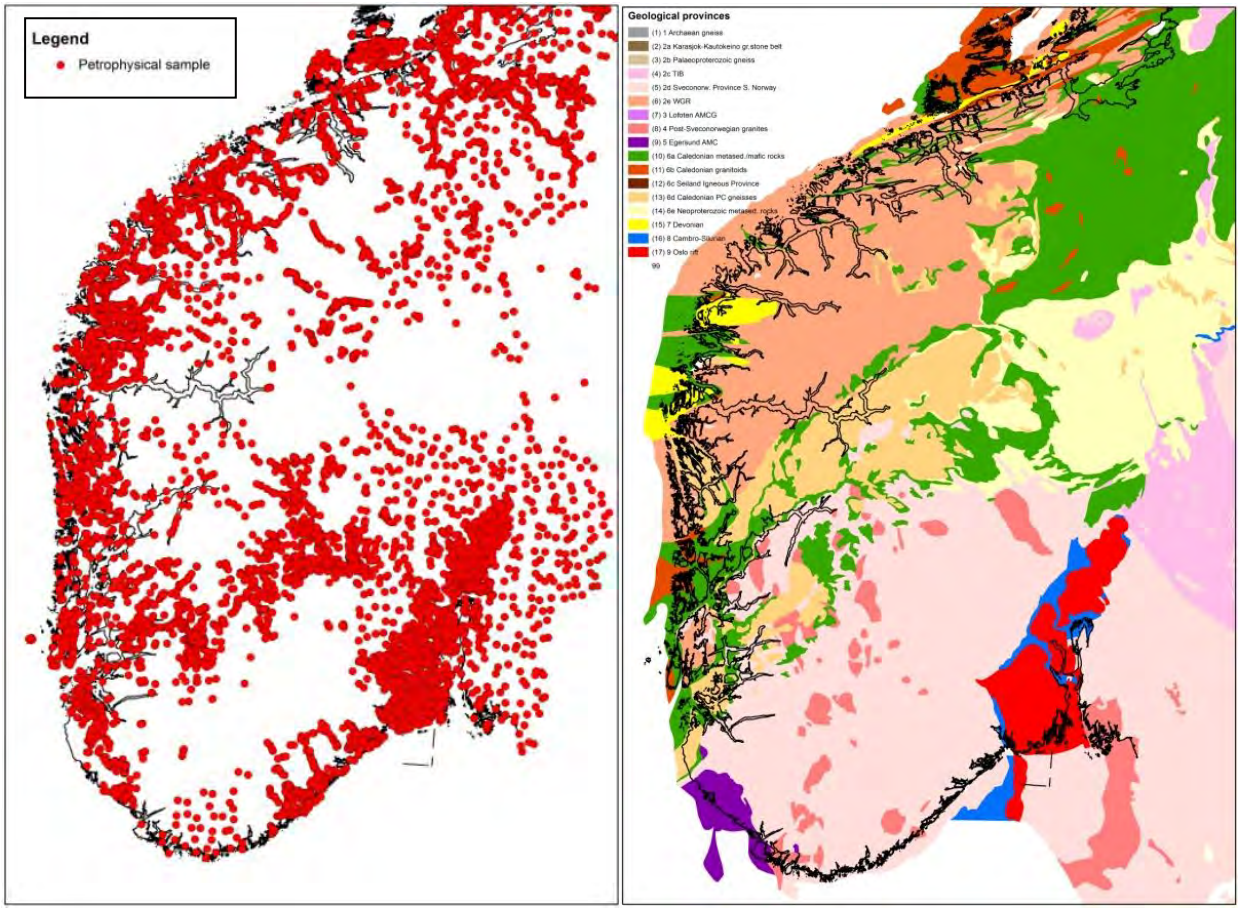

Figure 5.1 a) Geographical distribution of the petrophysical samples on the south Norwegian mainland. b)Simplified bedrock map of southern Norway (Sigmond 1996).

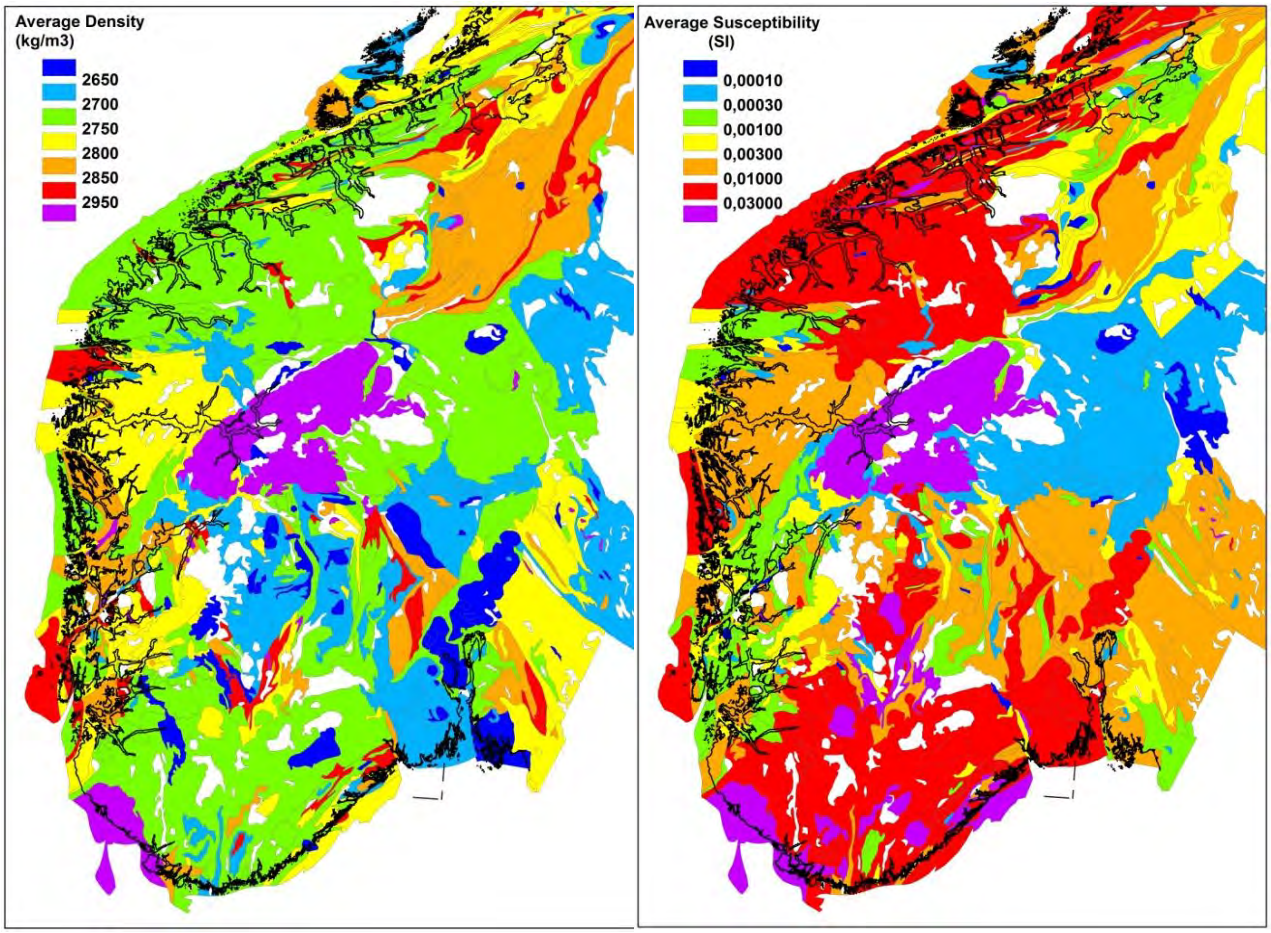

Figure 5.2 a) and b). Average density and average susceptibility of surface bedrock samples within each geological unit on the bedrock map of southern Norway (Sigmond 1996). Average density in kg/m3 and average susceptibility in SI units. The applied colour scale for the susceptibility data is logarithmic in order to depict the wide distribution of the mean values.

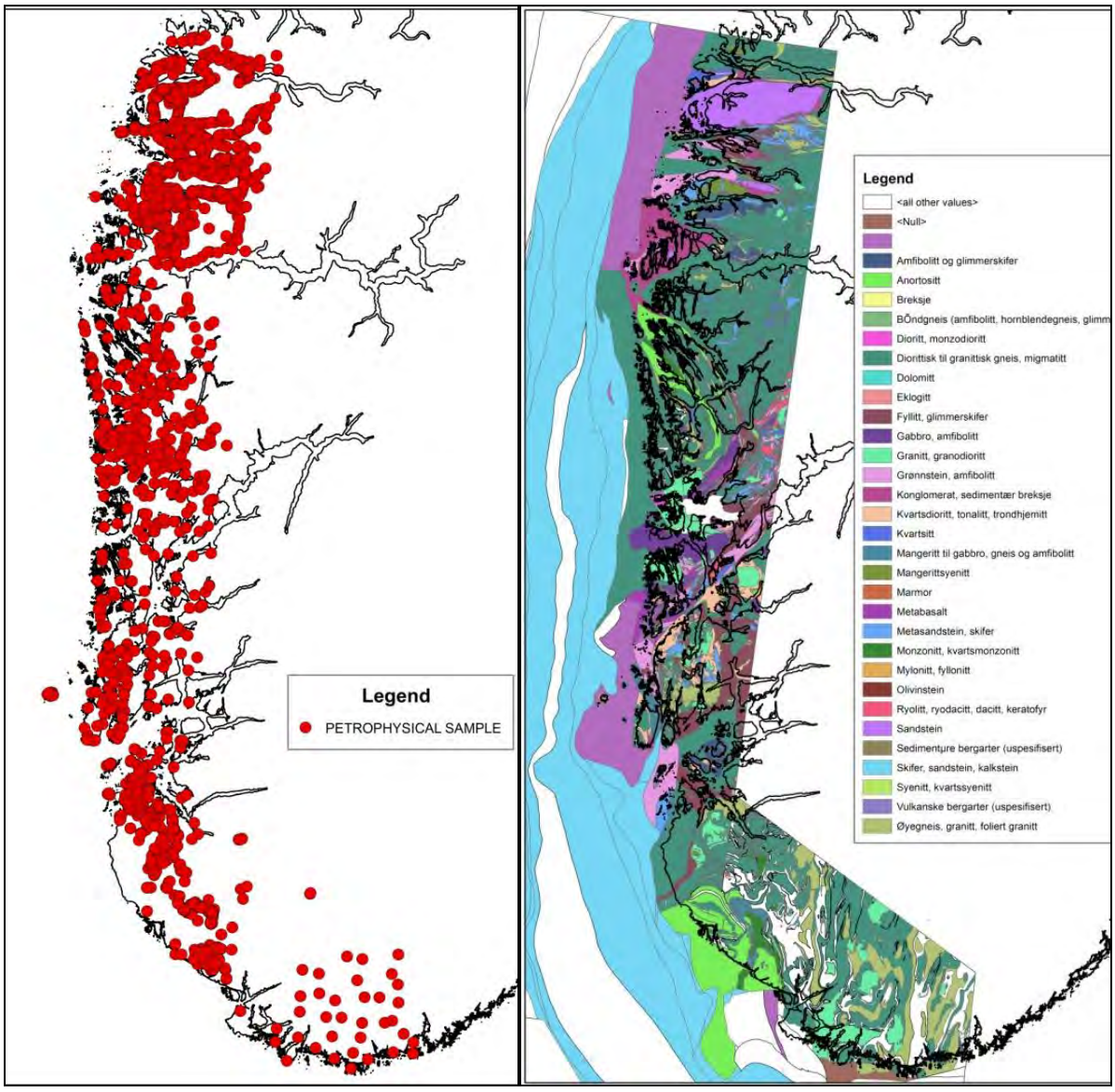

Figure 5.3 a) A selection of petrophysical bedrock samples situated within the outline of the detailed bedrock map. A total of 2515 surface bedrock samples have been measured in this area. b) COOP project bedrock map (Lutro 2013, Chapter 9 of the present report).

The samples have an even and dense geographical distribution within the area of this project (Fig. 5.3 a). Thus, the level of detail in the bedrock map defines the resolution of the density and average susceptibility maps. We have therefore decided to combine these samples with a more detailed geological map (Fig. 5.3 b).

Figure 5.4 presents the average density (a) and average susceptibility (b) of bedrock samples within each geological unit on the COOP project bedrock map (Lutro 2013, Chapter 9).

The average density map shows the highest values (> 2950 kg/m^3) in the basic extrusive rocks (greenstones) of the Sunnfjord area, and relatively high values (> 2850 kg/m^3) in the monzonites, migmatites and anorthosites of the Lindås Nappe and the metabasalts and amphibolites of the Hardangerfjord Nappe (both nappes are located in the Bergen Arc). High values (2850 - 2950 kg/m^3) are also recorded in the migmatites and amphibolites of the Boknafjord Nappe.

The granitic gneisses of the Øygard complex (to the west of the Bergen Arc) are visible as a low-density area (< 2650 kg/m^3), similar to the banded gneisses of the Mandal area. Furthermore, the gneisses north-northeast of Fensfjord appear to have lower densities (2650-2700 kg/m^3) than the surrounding bedrock units.

Granites and gneisses of the Farsund-Mandal area and the anorthosites of the Egersund area show higher magnetisation (susceptibility > 0.01 SI) than the surrounding bedrock, but also the Western Gneiss Region has relatively high values (0.003-0.03 SI).

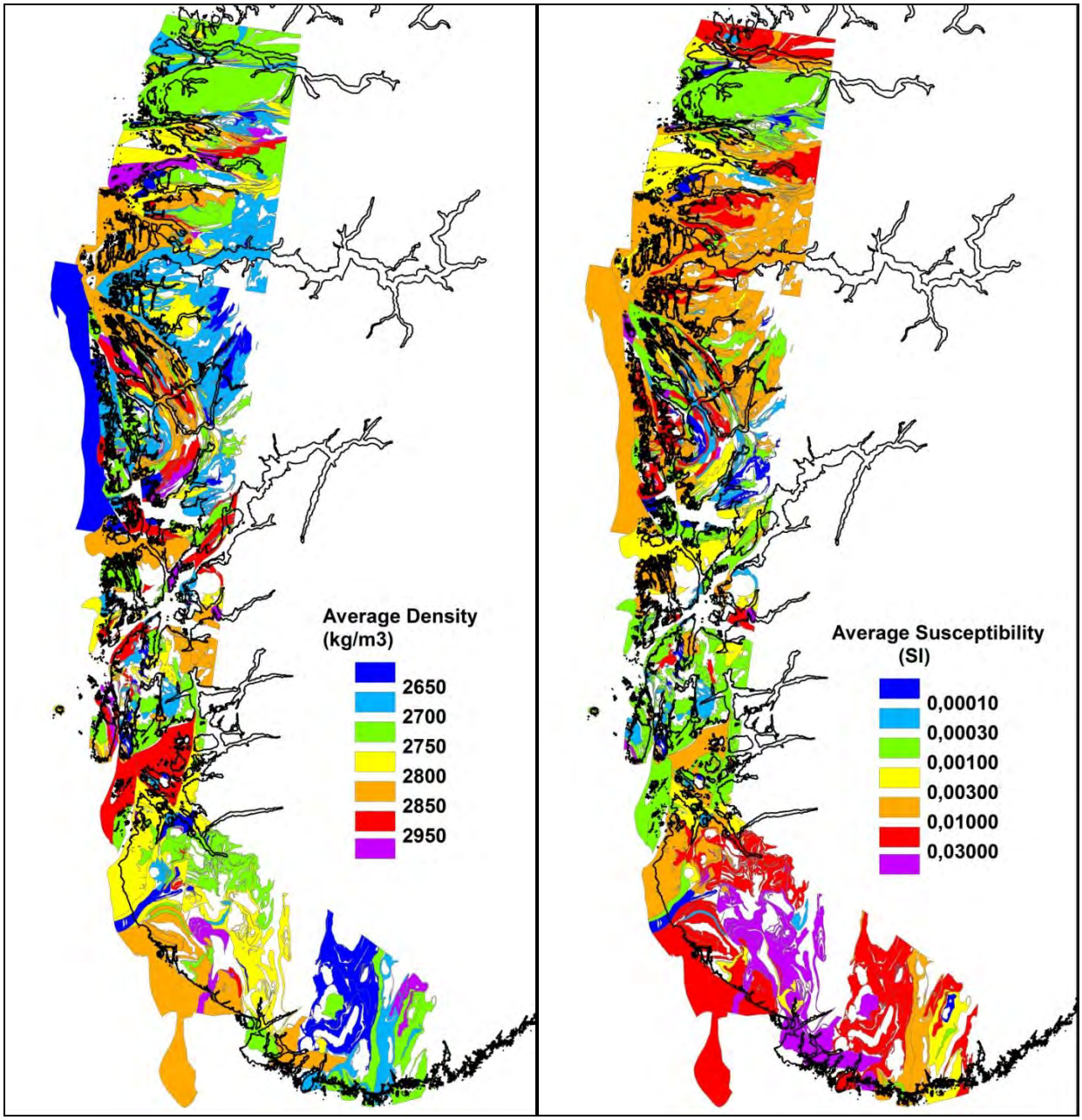

Figure 5.4 a) and b). Average density and average susceptibility of bedrock samples within each geological unit of the COOP project bedrock map (Lutro 2013, Chapter 9). Average density in kg/m3 and average susceptibility in SI units. The applied colour scale for the susceptibility data is logarithmic in order to depict the wide distribution of the mean values.

6. LOGGING OF THE FYLLINGSDALEN, ALSTEIN AND ULLRIGG BOREHOLES

Harald Elvebakk & Gaute Storrø

6.1 Introduction

During 2011 and 2012 thermal logging was carried out in three boreholes in the Bergen and Stavanger areas. In Fyllingsdalen, Bergen, a 516 m-deep borehole was drilled in a granitic rock and logging was performed in March 2012 and June 2012. In Stavanger, a 2010 m-deep well at Ullrigg (IRIS) was logged to 1045 m vertical depth. A 300 m-deep borehole on the small island Alstein in Boknafjord was logged in March 2011 (Elvebakk 2011). This borehole was drilled for investigations of rock quality for the planned tunnel beneath the Boknafjord. Figure 6.1 shows the locations of the Alstein and Ullrigg boreholes, and a geological map of the Stavanger area.
Table 6.1 shows the borehole data. The logging was performed by Harald Elvebakk, NGU.

Table 6.1. Borehole data, Fyllingsdalen, Alstein and Ullrigg.

Borehole	North wgs 84	East wgs 84	Metres a.s.l.	Zone	Logging date	Incl.	Diam. (cm)	Depth (m)
Fyllingsdalen	6695267	294648	17	32 V	28.03.12 15.06.12	Vertical	6.0	510
Alstein	6549227	300588	8	32 V	07.03.11	Vertical	7.6	300
Ullrigg	6537345	310499	40	32 V	10.03.11	90 – 58 ^{o}	17.5”	1038 vert depth

Besides temperature, the following parameters were logged: Water conductivity, natural gamma radiation, rock resistivity (SHN and LON) and seismic velocity (P- and S-wave).

The Water Quality Sonde (WQS) and TCN sonde, Robertson Geologging Ltd., with high-resolution sensors, were applied for the temperature measurements, see below.

WQS

Parameter	Range	Accuracy	Resolution	Time constant
Pressure	0 – 2000 dbar	0.05 %	0.0015 %	50 ms
Temperature	-1 – 50 ^{o}C	0.00 5 ^{o}C	0.001 ^{o}C	50 ms
Conductivity				
Salt water	0 – 64 mS/cm	0.005 mS/cm	0.001 mS/cm	50 ms
Fresh water	0 – 6400 µS/cm	1 µS/cm	0.1 µS/cm	50 ms

TCN

Parameter	Range	Accuracy
Temperature	0 – 70 oC	0. 5 oC
Conductivity	0 – 50,000 µS/cm	+/- 2.5 % at 500 µS/cm
Natural Gamma	50 mm x 25 mm NaI scintillation crystal	

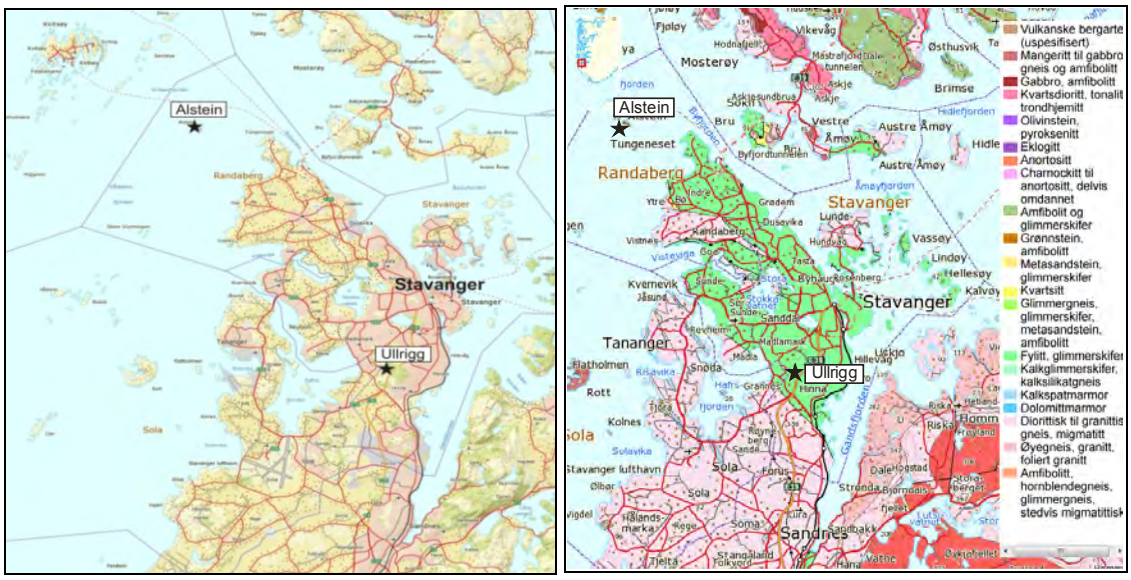

Figure 6.1. Overview map (left) and geological map of the Stavanger area (right), including locations of the Alstein and Ullrigg boreholes.

6.2 Alstein

The Alstein borehole is located in a gabbro. Figure 6.2 shows the borehole site on the little island of Alstein in Boknafjord, northwest of Randaberg.

Figure 6.2. The Alstein borehole and borehole site.

The logged parameters in the Alstein borehole were temperature, electrical conductivity of water, total natural gamma radiation, rock resistivity and seismic velocity (P- and S-wave). From the resistivity measurements, the apparent porosity is calculated using a simplified version of Archie's law (Archie 1942). Figure 6.3 shows the logs of all these parameters and a geological log based on cores. The borehole was also logged by optical televiewer for fracture mapping (Elvebakk 2011).

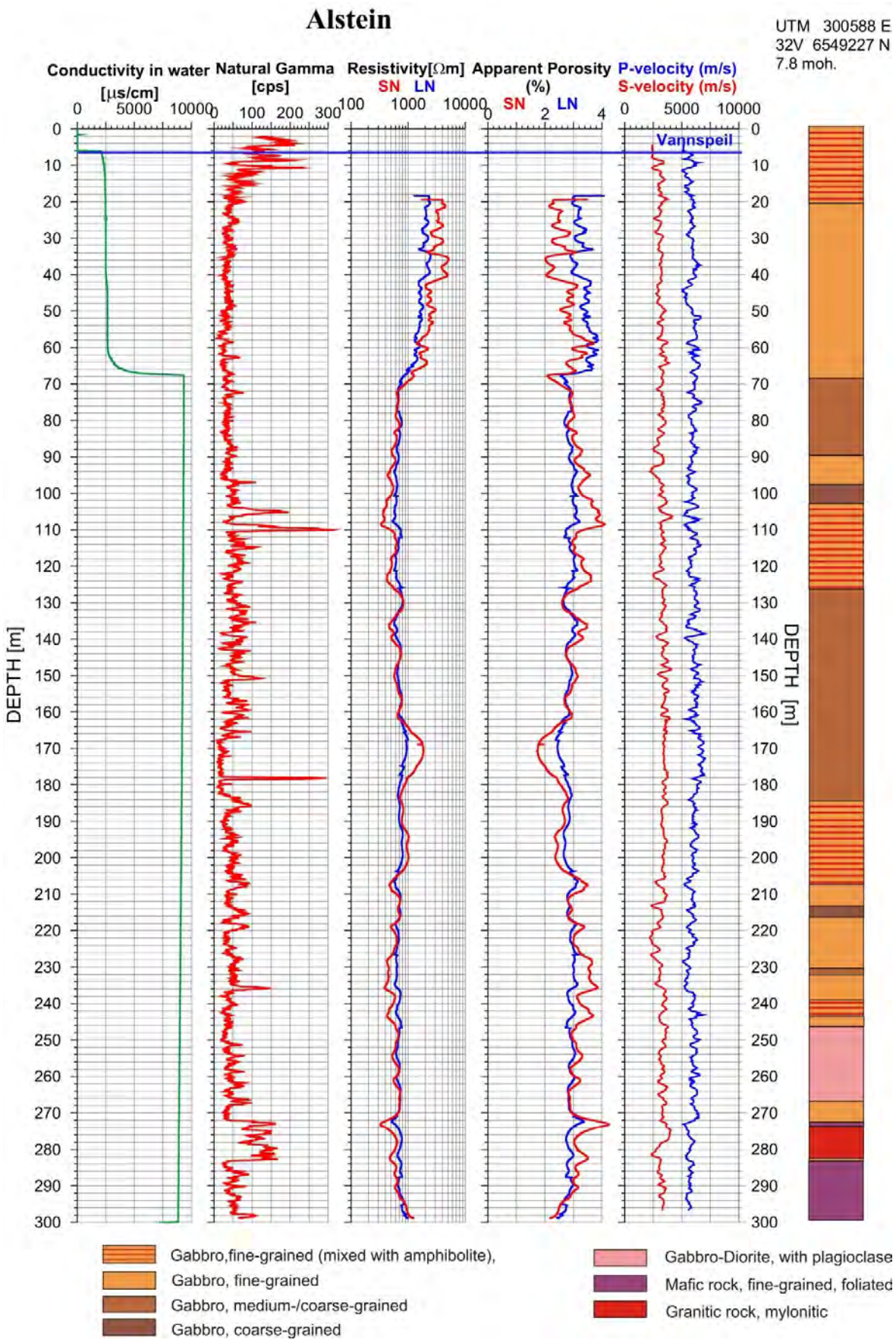

Figure 6.3 Alstein borehole. Conductivity, gamma, resistivity, porosity, seismic velocity and geological log.

Figure 6.4 shows the temperature and thermal gradient in the Alstein borehole. The temperature at the bottom of the borehole at300 m-depth is 10.7 ^{o}C. The thermal gradient seems to have stabilised from 200 m depth and is calculated to be 10.4 ^{o}C/km in the deepest part of the borehole. The gradient was lower than expected.

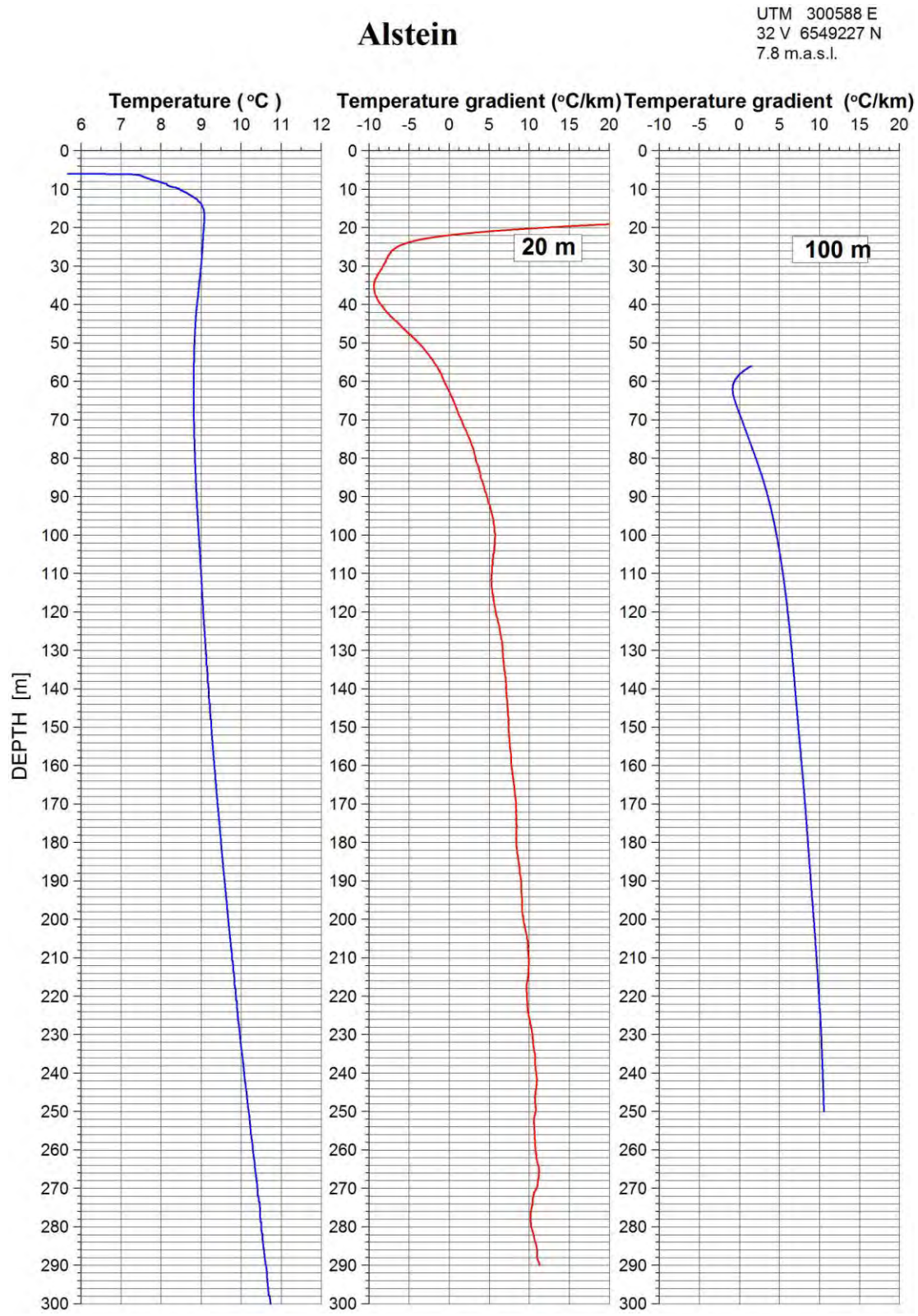

Figure 6.4. Alstein borehole. Temperature and thermal gradients at 20 m and 100 m intervals.

6.3 Ullrigg

Figure 6.5 shows the Ullrigg site at IRIS, Stavanger, and logging in the well U2, and Figure 6.6 shows the main features of well U2. The well was logged to a vertical depth of 1038 m. The logged depth was limited by the capacity of the winch.

Figure 6.5. The Ullrigg well site and logging in U2.

Figure 6.7 shows the temperature log and calculated gradients. The thermal gradients are calculated using running least-squares of a straight line with depth intervals of 20 m and 100 m. The average thermal gradient below 100 m is 13.0 ^{o}C/km. The bottom temperature at 1038 m depth is 20.6^{o}C.

Figure 6.8 shows logs of temperature, water conductivity and natural gamma radiation. It is difficult to explain the change in conductivity recorded at about 300 m depth. The well is cased and such changes are often caused by fractures and inflow of water. The change in gamma radiation at 800 m depth relates to a geological boundary between phyllite and gneiss. The radiation from phyllite is very low, 25 – 30 cps, whereas the higher radiation in the gneiss is probably caused by an increased content of potassium (K^{40}), most likely in the feldspar.

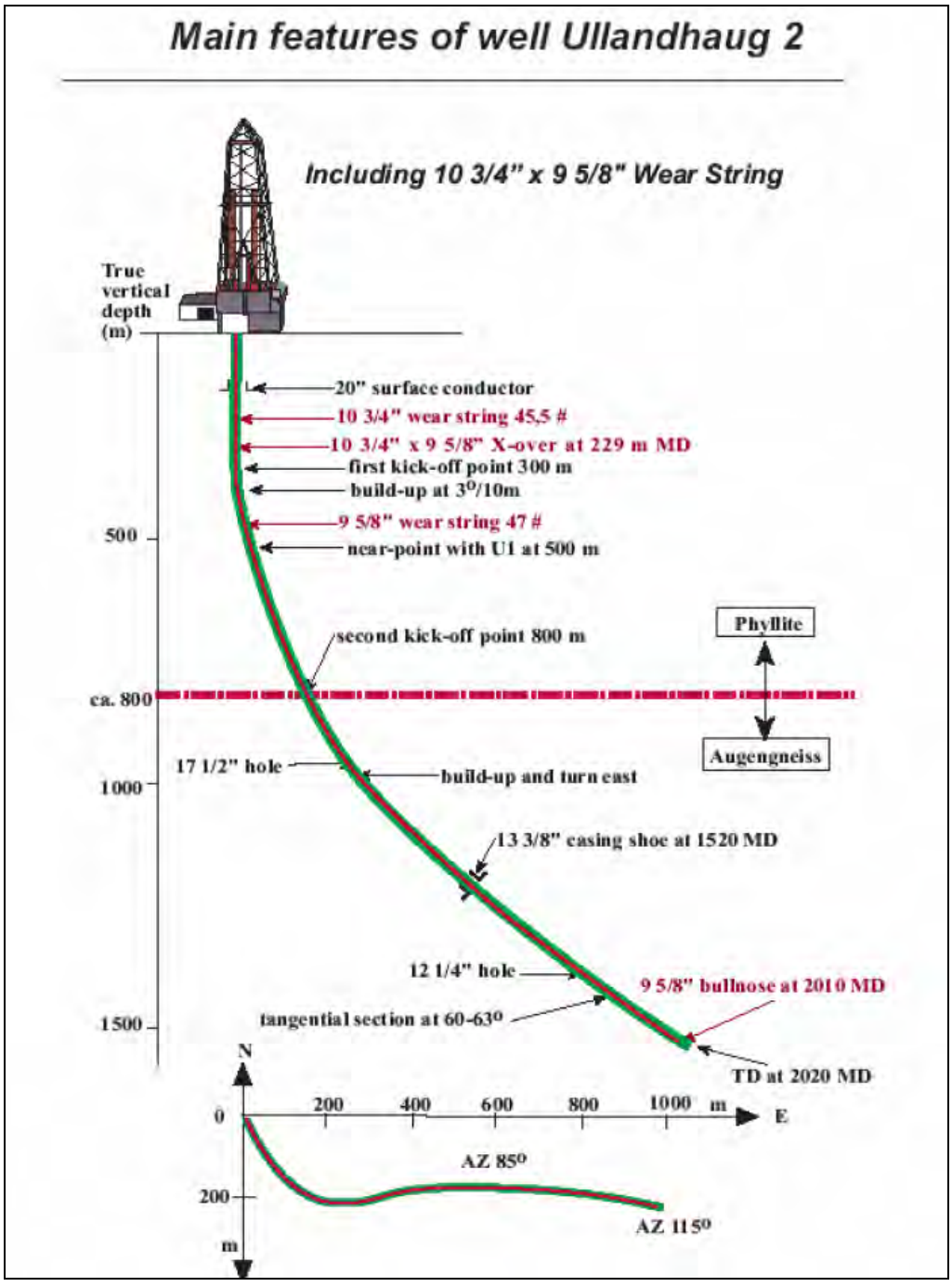

Figure 6.6. Main features of Well U2 at Ullrigg.

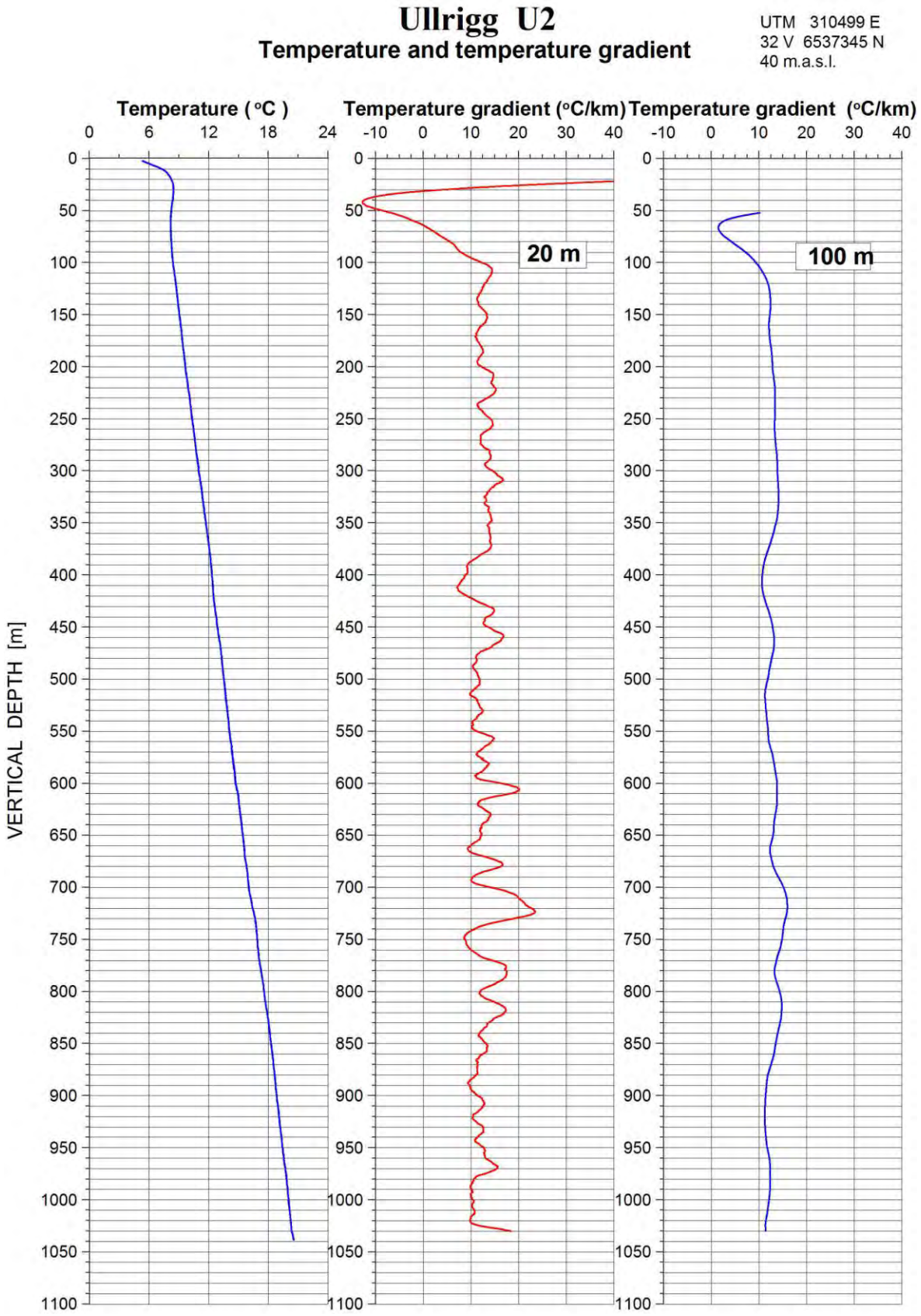

Figure 6.7. Ullrigg U2 borehole, temperature and thermal gradients at 20 m and 100 m intervals.

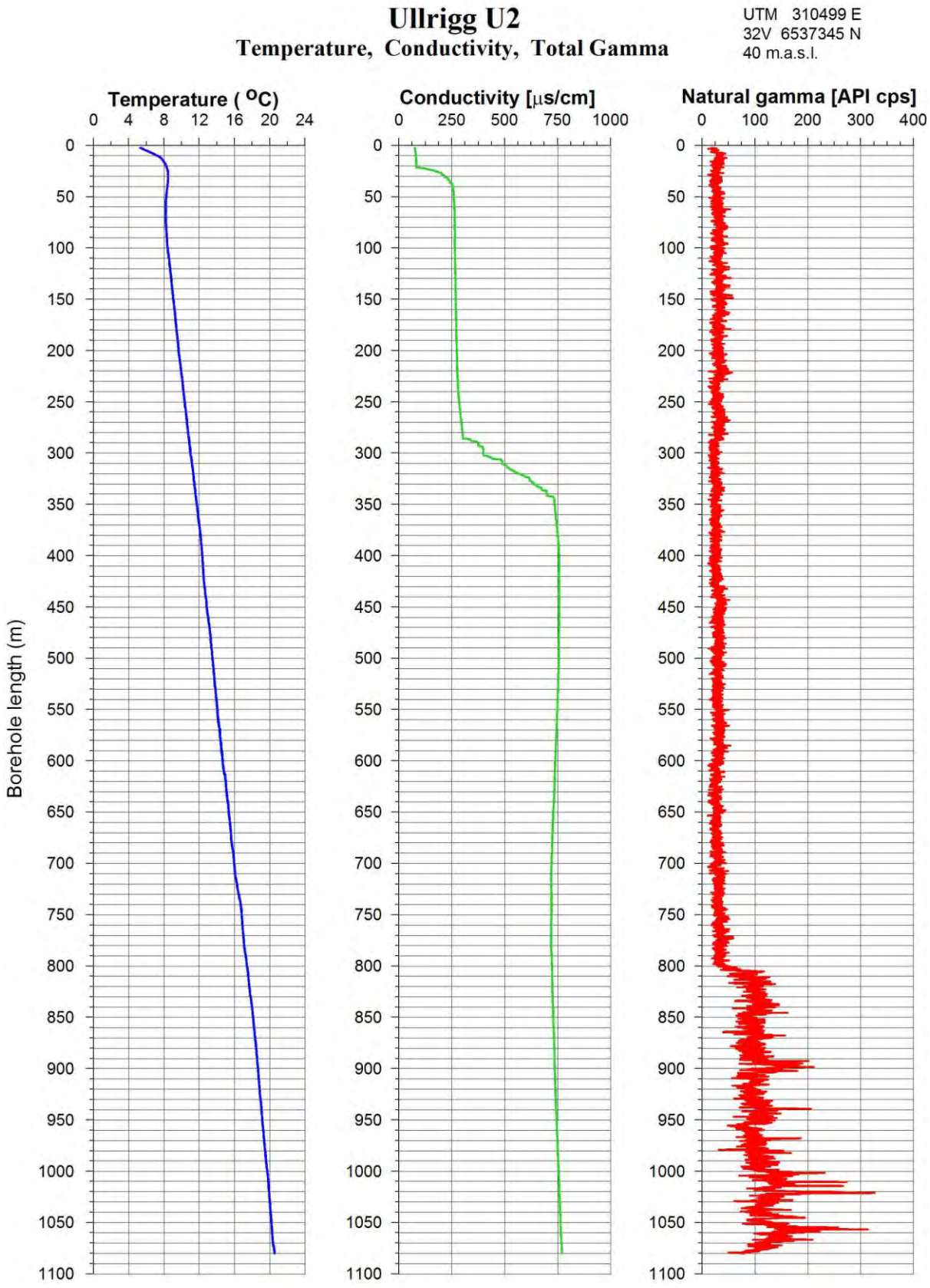

Figure 6.8. Ullrigg U2 borehole, temperature, water conductivity and natural gamma radiation.

6.4 Fyllingsdalen

Figure 6.9 shows pictures from the drilling and logging in the Fyllingsdalen borehole. Figure 10 shows the geological and gravity map of the Bergen area with the borehole located in a granitic rock indicating a rather low gravity anomaly. The borehole was drilled by Drillcon in September 2011 down to a depth of 516 m. The upper 120 m of the borehole was cased because of the highly fractured bedrock. The borehole was originally planned to reach a depth of 800 m, but the fractured bedrock caused problems for the drilling operation. The first logging took place in February 2012 but the sensor was stuck at a depth of 120 m. A new drilling company (Geodrilling) was hired to reopen the hole and in late March the borehole was logged to a depth of 480 m. In June 2012 a new logging was performed down to 510 m depth and water samples were taken at four different levels in the borehole.

Figure 6.9. Drilling and logging site in Fyllingsdalen, Bergen.

The logging parameters recorded in Fyllingsdalen were temperature, water conductivity, total natural gamma, rock resistivity and seismic velocity (P- and S-wave). The measured thermal gradient was lower than expected. Four water samples were therefore collected at different depths for analysis of the chemical elements and ions in the water. It transpired that cold water was flowing through the bedrock and thus producing the low thermal gradient. This will be discussed later.

Figure 6.11 shows all logs from the Fyllingsdalen borehole. The water conductivity is quite high with some small variations at different levels which can be related to water inflow. The small change at 495 m depth coincides with a small increase in temperature at the same depth, which supports an occurrence of open fractures and water inflow at this level.

The gamma radiation is quite high which is normal for granite, 300 – 500 cps. This is caused by a high content of potassium, but also radioactive minerals containing U and Th will affect the levels of radiation. This is common in granites and will produce heat.

The rock resistivity is much lower than normal values for granite. Large variations in the resistivity indicate a fractured bedrock. This is supported by a low seismic velocity in some of the low-resistivity zones. Normal resistivity values for granite are 6000 – 8000 ohmm. (Elvebakk 2011). In Fyllingsdalen, borehole resistivity varies from 300 to 3000 ohmm. Saline groundwater (pore water) will also influence the measured resistivity.

As mentioned above, some low-velocity zones are present. Normal P-velocity for granite is 5000 – 6000 m/s (Elvebakk 2011). Lower values indicate a fractured bedrock.

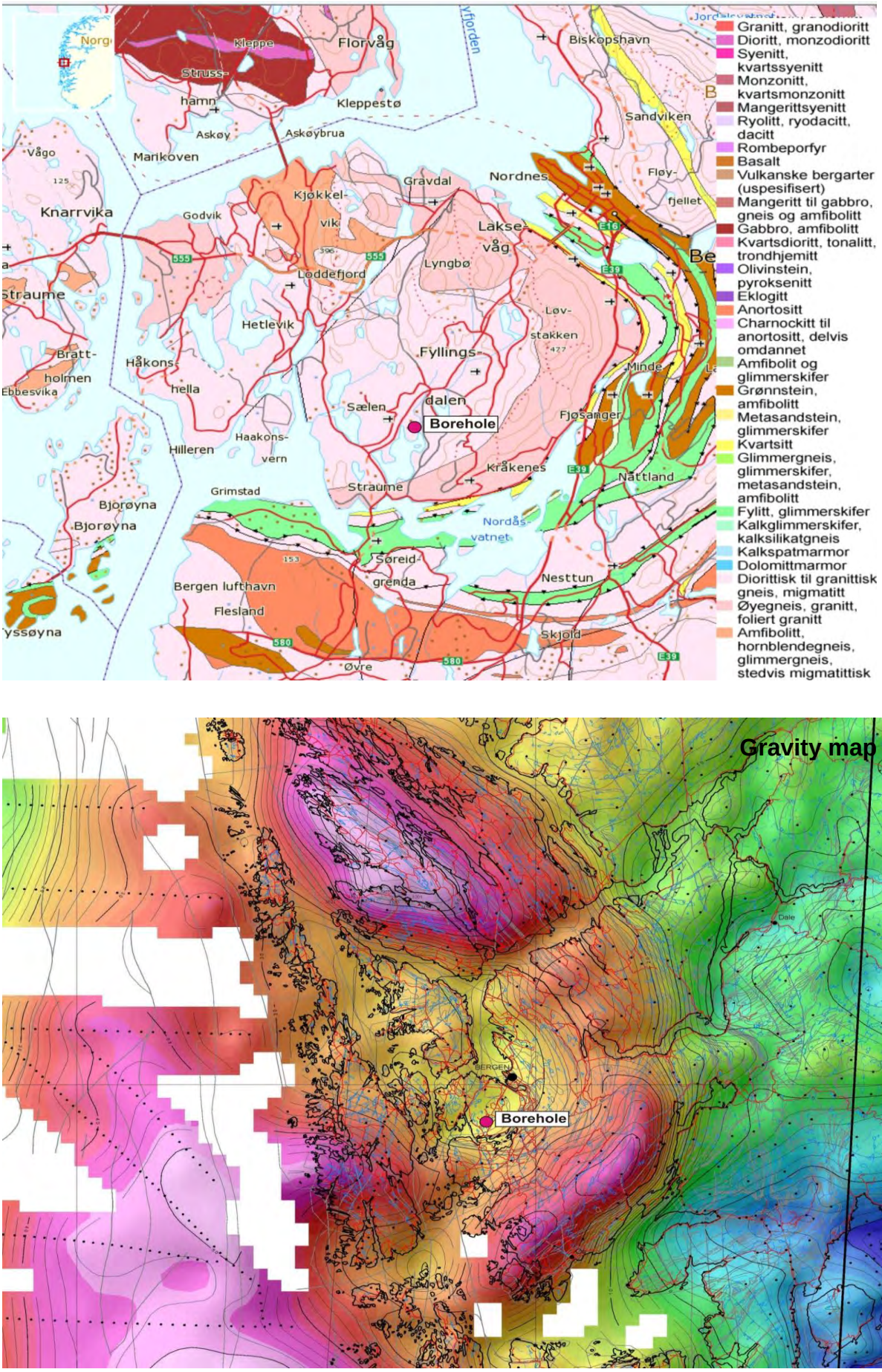

Figure 6.10. Geological and gravity map of the Bergen area. Red represents high and blue low gravity anomalies.

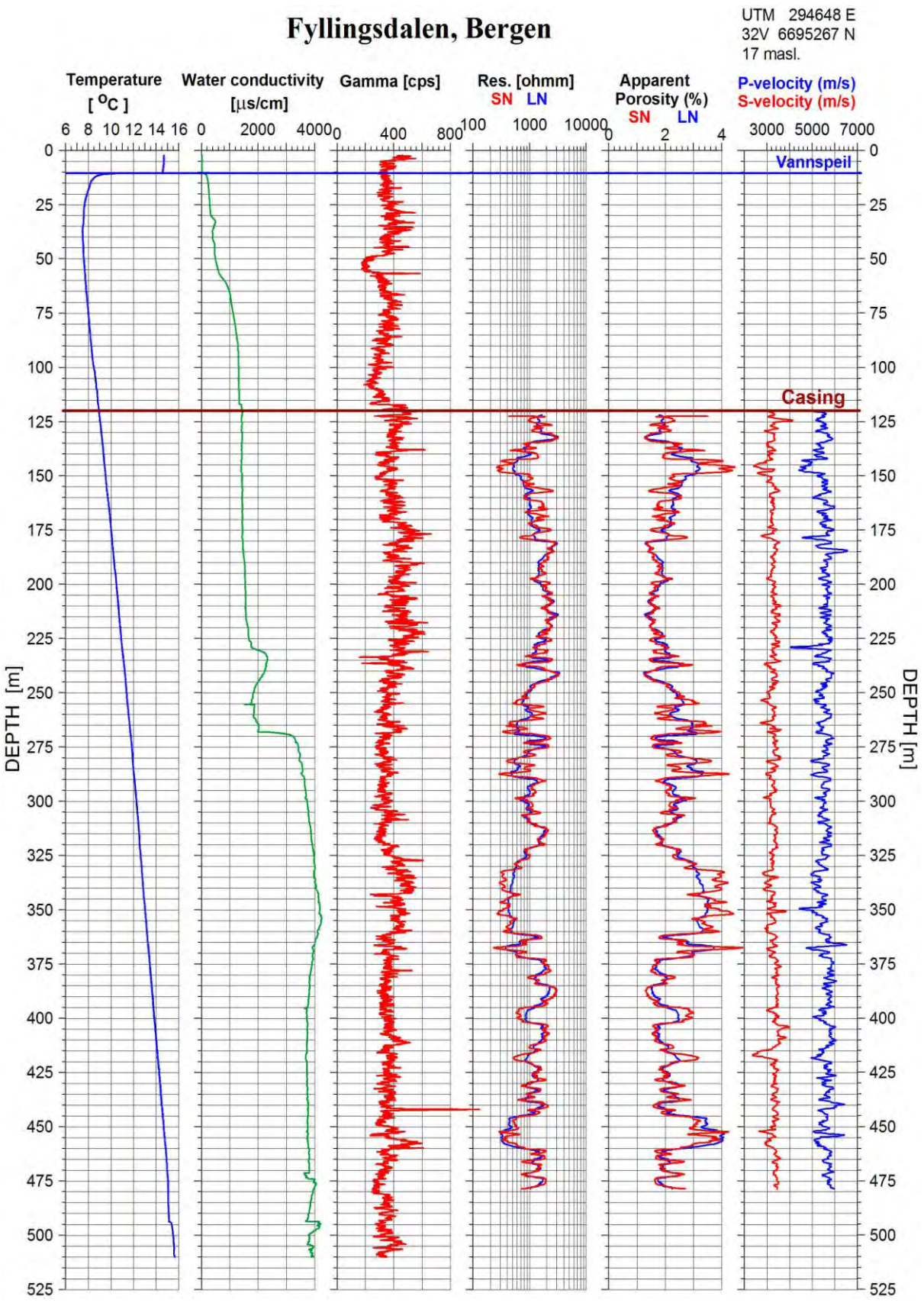

Figure 6.11. Fyllingsdalen. Temperature, water conductivity, natural gamma, resistivity, apparent porosity and seismic velocity.

Figure 6.12 shows temperature and thermal gradients in the Fyllingsdalen borehole. The bottom temperature at 510 m depth is 15.6 °C. From a depth of 275 to 510 m the thermal gradient is 16.2 °C/km, and 16.5 °C/km for the complete borehole. The large variation in gradients close to the bottom is caused by the temperature increase at 495 m depth. Variations in the 20 m interval gradient (which shows more details than the 100 m interval) may be related to variations in the thermal conductivity.

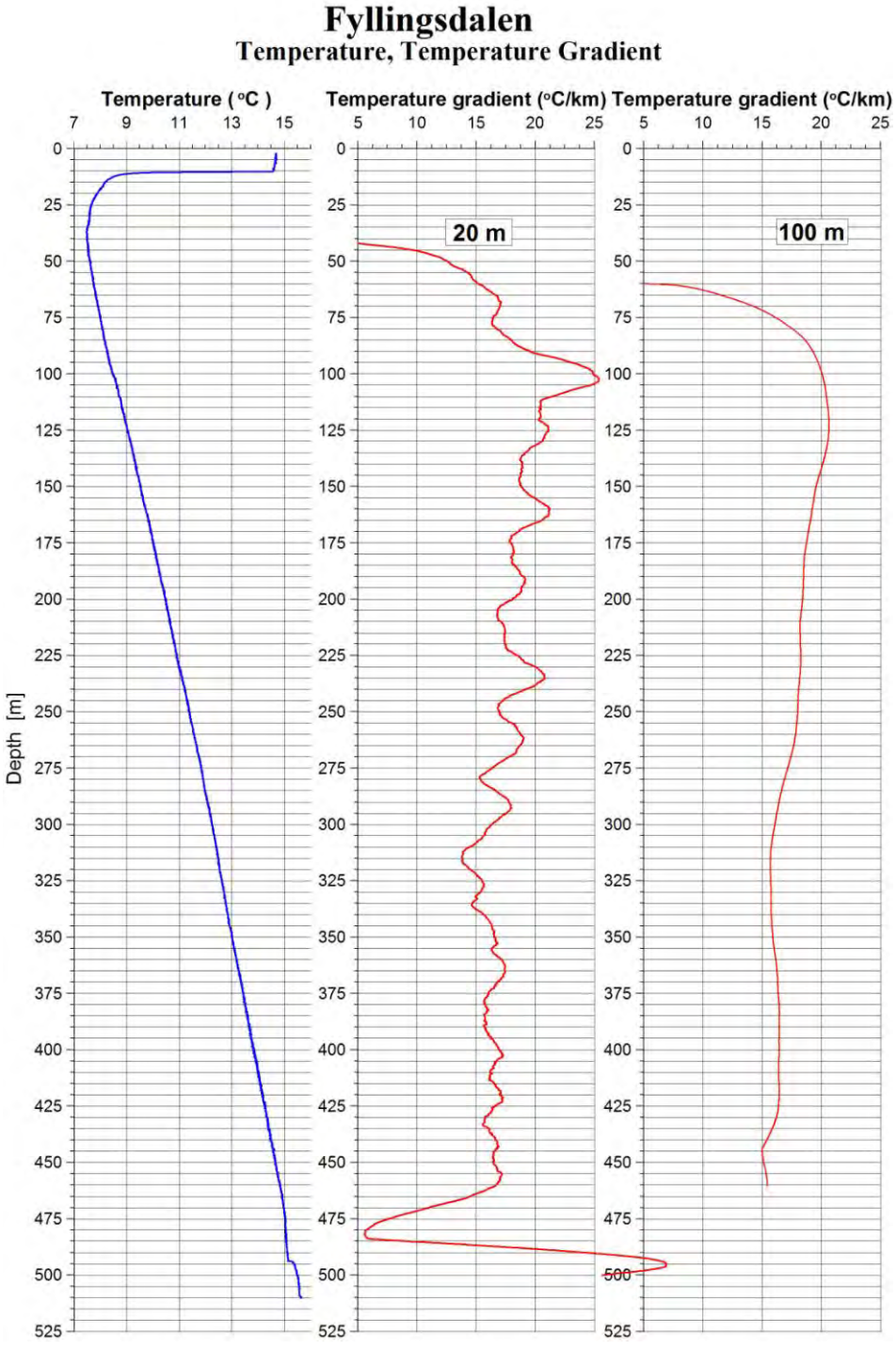

Figure 6.12. Fyllingsdalen borehole, temperature and thermal gradients at 20 m and 100 m intervals.

6.5 Discussion: thermal gradients

The measured temperatures and calculated thermal gradients in the Alstein, Ullrigg and Fyllingsdalen boreholes are lower than expected. Table 6.1 shows the gradients from the three boreholes and Figure 6.13 shows the temperature logs from the same boreholes. The explanation for the low gradients will be discussed in Chapter 12, Thermal modelling. However, a likely explanation for the Alstein and Ullrigg boreholes can be paleoclimatic effects, cooling from former ice ages. In Fyllingsdalen, the thermal gradient was expected to be higher, especially because the granitic bedrock contains small amounts of radioactive elements which produce heat. The granite was found to be highly fractured at several levels in the borehole. Both the temperature and the water conductivity logs indicated inflow of water. Groundwater flow in the granite can also have influenced the temperature and thermal gradients.

Table 6.1. Thermal gradients in the Alstein, Ullrigg and Fyllingsdalen boreholes.

Borehole	**Average thermal gradient [^{o}C/km]**	**Vertical depth [m]**
Alstein	10.4	300
Ullrigg	13.0	1038
Fyllingsdalen	16.2 – 16.5	510

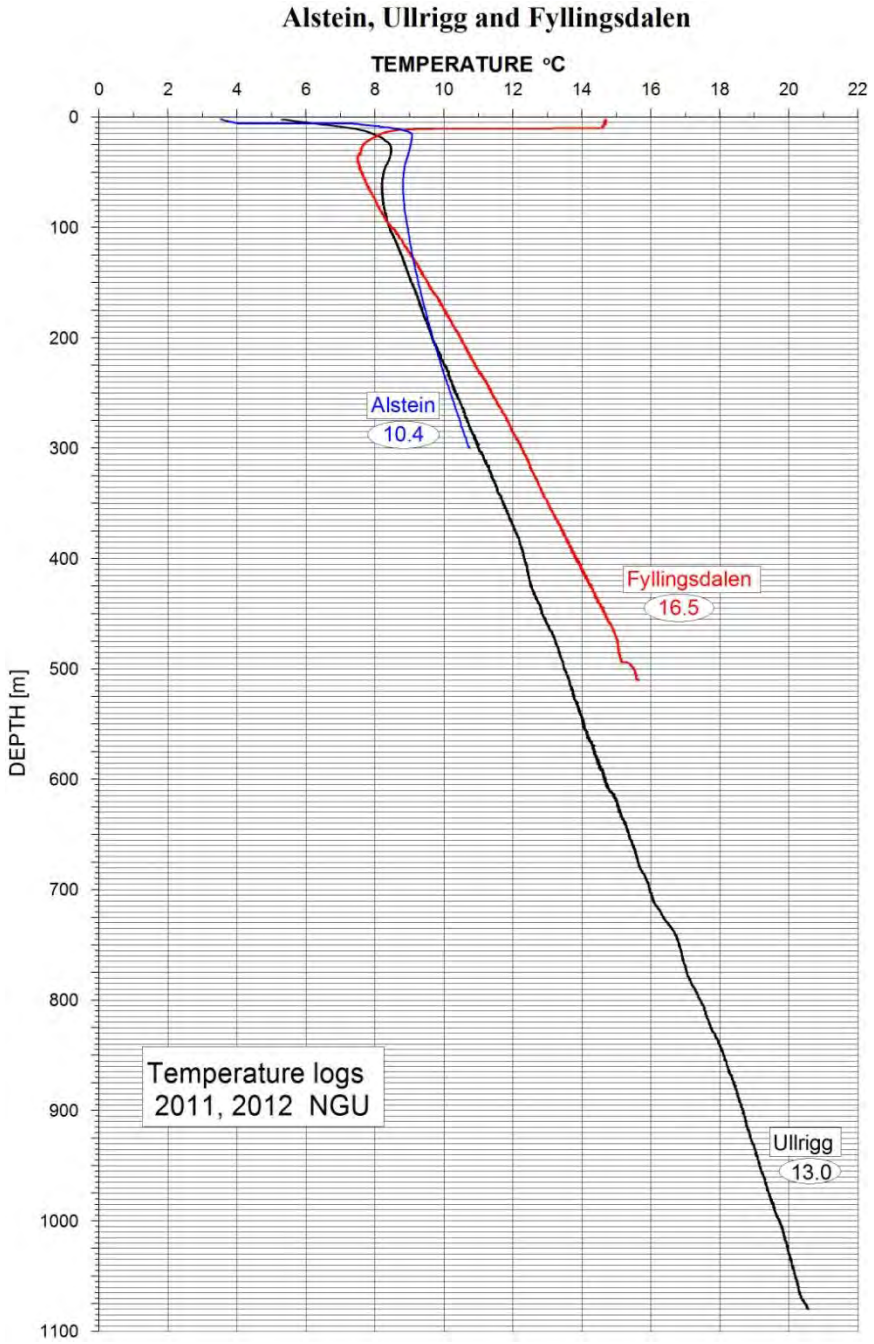

Figure 6.13. Temperature logs for the Alstein, Ullrigg and Fyllingsdalen boreholes.

6.5.1 Water sampling in the Fyllingsdalen borehole

Because of the low thermal gradient and indicated water inflow in the borehole, water samples were collected at four different depths with large variations in water conductivity. Samples were taken at 35 m, 110 m, 450 m and 496 m depths. The chemical composition of the water may differ from "fresh" sea water to fossil water. "Fresh" sea water, or diluted sea water with the same relative composition as pure sea water, might be an indicator of sea water flow within the granite. Regarding the salinity of the water, the main ions are Mg^{2+}, Ca^{2+}, Na^{+}, K^{+}, Cl^{-} and SO_4^{2+}. The chemical composition of the water samples from Fyllingsdalen is shown in Figure 14. In Figure 15, the analyses from a borehole at Hamar are shown for comparison. The Hamar borehole is located far inland. Units in the figures are meq (mill equivalents).

Fyllingsdalen

The chemical composition of the groundwater is quite stable all the way down to a depth of 500 m, with sodium (90-95 meq%) and chloride (85-90 meq%) as the main components. The overall composition is very much the same as that of standard mean ocean water (SMOW), although the salinity of the groundwater is much lower (0.1-0.5 %) than that of SMOW (3.5 %).

Hamar

Hamar borehole is located in southeastern Norway, c. 100 km north of Oslo in Cambro-Silurian limestones and shales and Precambrian gneiss. The chemical composition (meq%) of the groundwater changes gradually from a sodium-bicarbonate dominated water at the uppermost sampling level (100 m), to a sodium-chloride dominated water at the lowermost sampling level (800 m). At 800 m, the relative composition of the groundwater is very much the same as that of standard mean ocean water (SMOW), although the salinity of the groundwater is much lower (0.6 %) than that of SMOW (3.5 %).

The results of the chemical analyses from the Fyllingsdalen borehole are shown in Appendix B.

6.6 Conclusions and further plans

The measured thermal gradients in the Stavanger and Bergen areas are quite low and lower than expected. It is considered that the low gradients in the Alstein and Ullrigg boreholes are influenced by a paleoclimatic effect and that the area has been exposed to deep permafrost. In Fyllingsdalen, water flow in the granite can have caused the low gradient in addition to the paleoclimatic effect. Figure 6.16 shows a composite temperature log with data from numerous deep boreholes acquired by NGU and the University of Aarhus since 2006.

NGU has ordered a new winch with a 2000 m cable to extend the temperature logging in the Ullrigg hole to a vertical depth of c. 1500 m. It is expected that the thermal gradient will be relatively undisturbed at this depth.

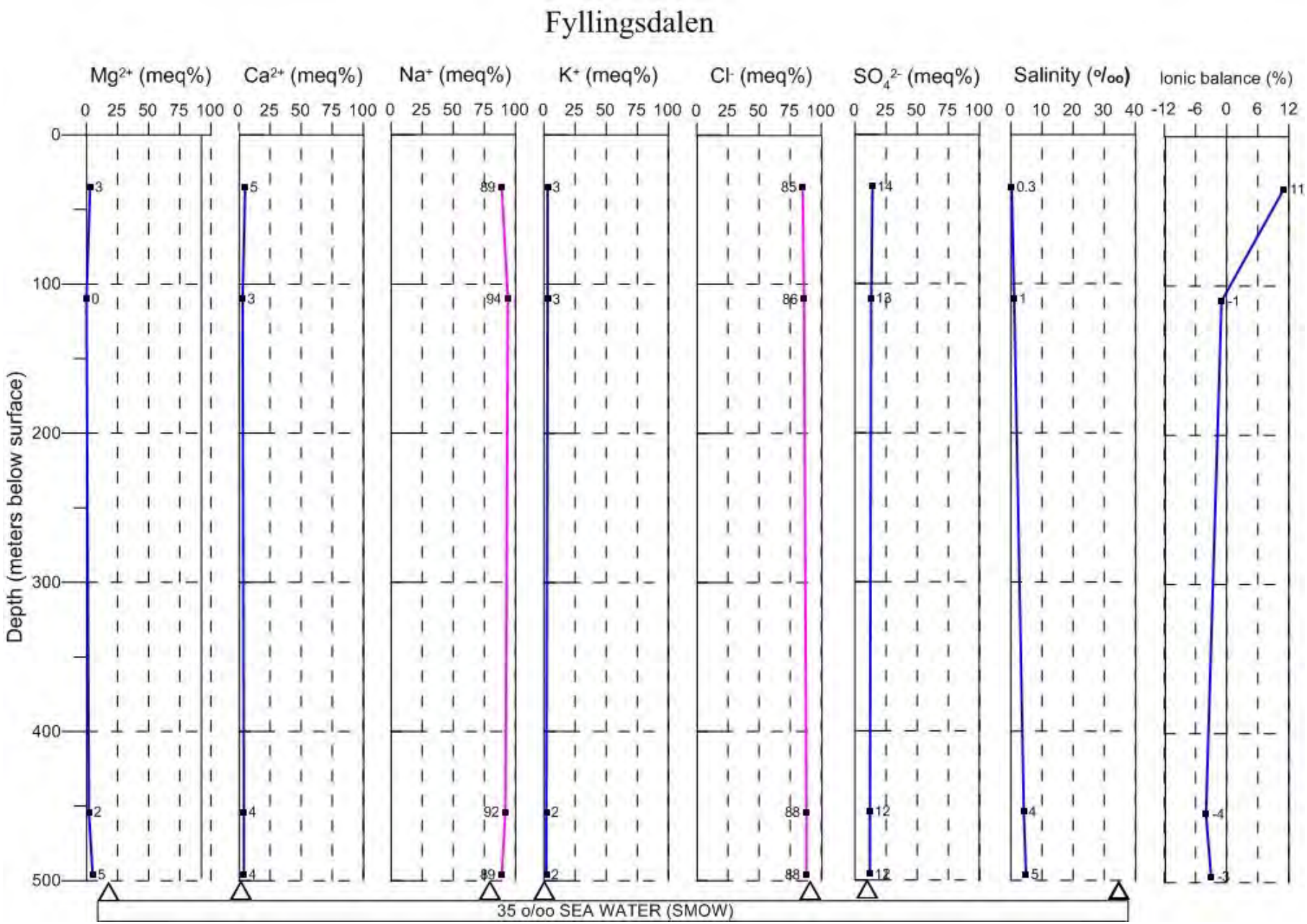

Figure 6.14. Chemical composition of samples from the Fyllingsdalen borehole and composition of standard mean ocean water (SMOW).

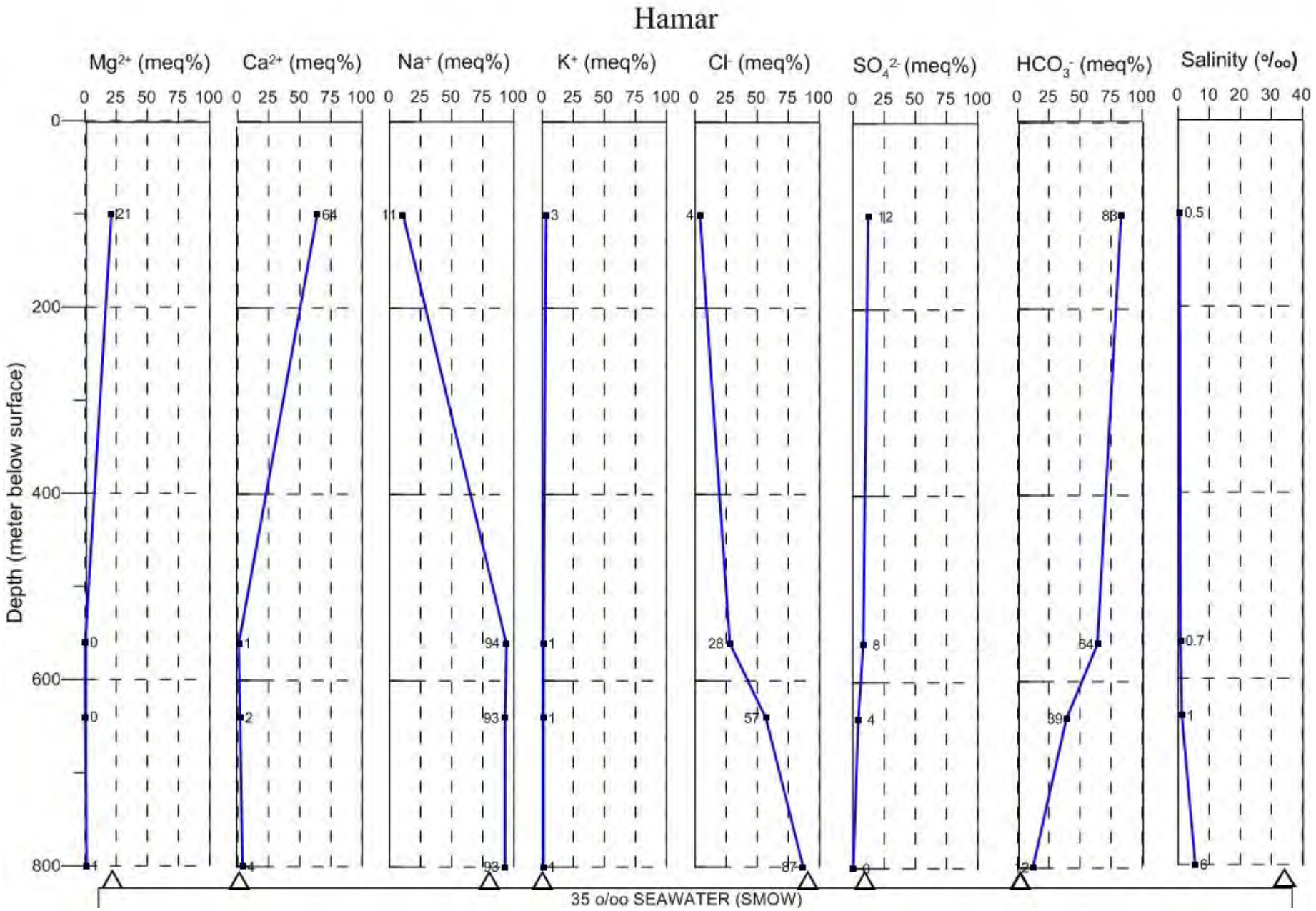

Figure 6.15, Chemical composition of samples from the Hamar borehole and composition of standard mean ocean water (SMOW).

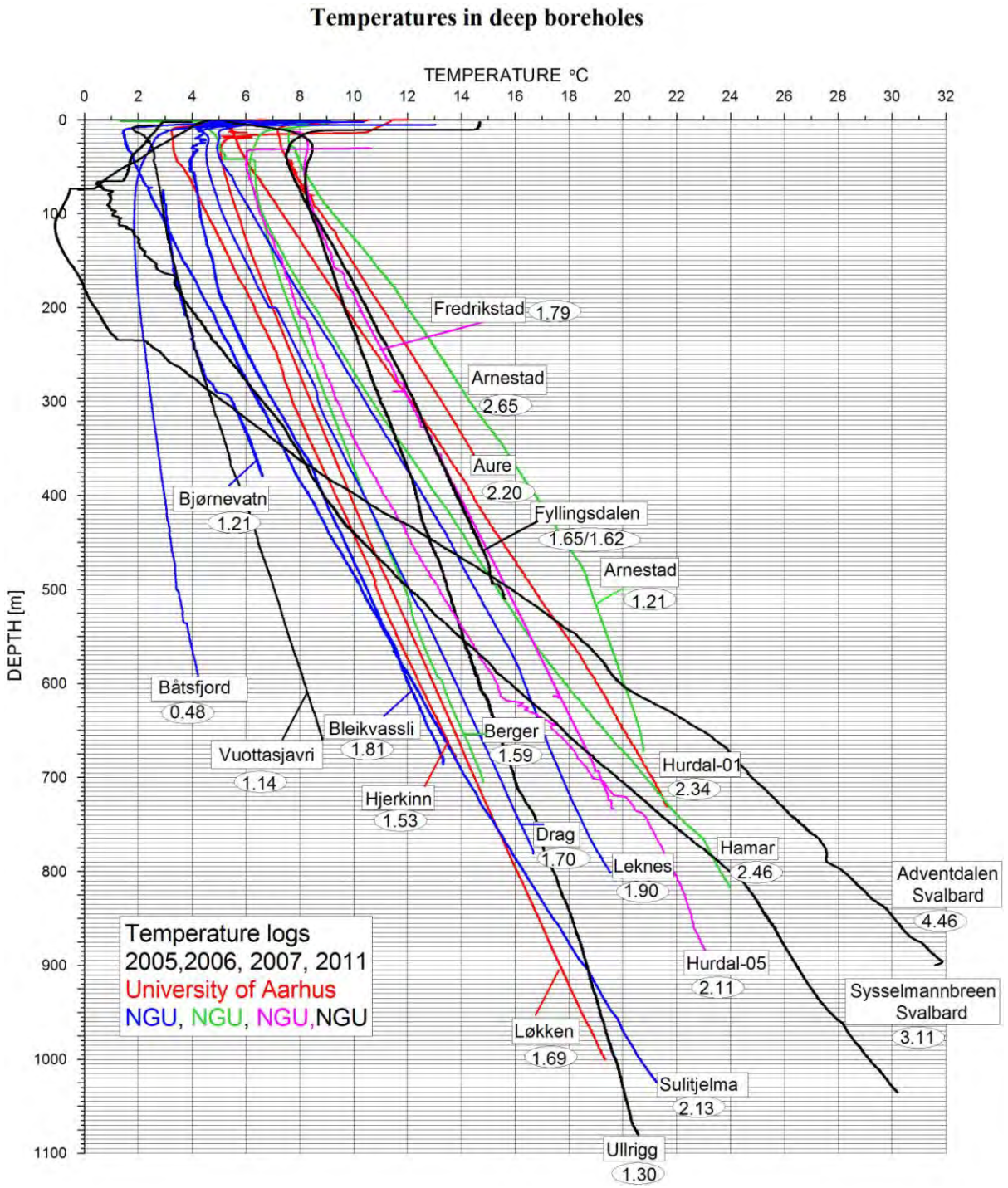

Figure 6.16. Temperature logs in deep boreholes measured by NGU and the University of Aarhus. Average thermal gradients are shown as ^{o}C/100 m.

7. ESTIMATION OF MAGNETIC DEPTHS

Aziz Nasuti and Marco Brönner

7.1 Introduction

Depth to magnetic source calculation is a challenging and important task in magnetic interpretation. A complete and quantitative interpretation of potential field data aims at estimating information about the depth, dimension and contrast of the relevant geological units. Magnetic depth estimates are often a reasonable approximation to depth to the magnetic basement (i.e., metamorphic, igneous, oceanic), and the crystalline basement depth (or alternatively, the sedimentary thickness) is a primary exploration risk parameter. Furthermore, estimating basement depths is directly useful for thermo-kinematical modelling and thermal maturity applications (e.g., heat-flow estimation, source-rock burial depth, distribution and volume).

It is noticeable, however, that such an interpretation of depth to basement suffers from an inherent ambiguity. As a matter of fact, it is not possible to obtain all three types of information simultaneously without other *a priori* information (e.g., the geological context or seismic data). These methods are usually applicable for simplified source geometries (dimensions) and are most of the time independent of the susceptibility contrast. The depths estimated by some methods can be used as the final, quantitative solution in some ideal situations (i.e., where the anomaly is well isolated and the noise is insignificant or removed).

In this chapter, we present the results obtained using the 3D-located Euler deconvolution of the magnetic total field.

7.2 Euler deconvolution

The Euler method applies the Euler's homogeneity equation to construct a system of linear equations, and then determines, through a least-squares inversion for one window, the (vertical and horizontal) position of a single source for a given source geometry (Reid *et al.* 1990). Euler deconvolution was first presented by Thompson (1982) for profile data and developed for gridded data by Reid *et al.* (1990).

The method requires the use of the calculated horizontal and vertical derivatives of the magnetic field. Thompson (1982) called the fall-off rate (i.e., the negative of the degree of homogeneity) the structural index (N). Synthetic tests (Silva & Barbosa 2003, Keating & Pilkington 2004, Stavrev & Reid 2007) indicate (1) that the Euler method can locate the outline and depth of a variety of simple geometrical shapes; and 2) that the structural indices will cluster and thus determine the best structural interpretation. Although expressed as vertical contacts, faults with a large throw may be best displayed with a structural index of zero (Table 7.1).

Euler's homogeneity equation is valid for bodies of arbitrary shape, characterised by these indices. In practice, the Euler method assumes idealised structures such as contacts, thin sheets (dykes), vertical or horizontal cylinders and a 3D sphere. In this section of the report we therefore briefly describe the theory, advantages and limitations behind the technique and present its applications for the COOP project.

Structural Index	Magnetic field	Gravity field
0	contact	sill/dyke/step
0.5	thick step	ribbon
1	sill/dyke	pipe
2	pipe	sphere
3	sphere	

Table 7.1. Summary of the structural indices for simple geometric models from magnetic or gravity anomalies (Reid et al. 1990, Marson & Klingele 1993, Bainbridge et al. 2002).

Euler 3D deconvolution is a semi-automated technique enabling rapid qualitative interpretation and depth estimation of source depths from large gridded gravity and magnetic datasets (Reid *et al.* 1990, Barbosa *et al.* 2000, Pilkington *et al.* 2000, Hsu 2002, Mushayandebvu *et al.* 2004, Florio *et al.* 2006). The technique has considerable advantages.
1) It can be applied to large datasets extremely quickly; 2) it provides a qualitative interpretation of geological structures; 3) it can provide depth estimates for the sources of the anomalies; 4) magnetic data do not need to be reduced to the pole (Reid *et al.* 1990); and 5) it is also insensitive to magnetic inclination, declination and remanence since these become part of the constant in the anomaly function of a given model.

7.3 Interpretation of the structural indices

Careful consideration of the distribution and clustering of Euler solutions is, however, required in order to determine which solution best represents the causative source at depth within the crust. Although in theory, interpretation of the Euler solutions requires no prior geological knowledge, Reid *et al.* (1990) acknowledged that this can be significantly beneficial. Reid *et al.* (1990) claimed that the choice of structural index remains the prime limitation of the traditional Euler technique. This and other limitations arise as a product of some of the simplifying assumptions of the technique, which assume that the source is (1) equivalent to a simplified geometrical feature, (2) spatially homogeneous, (3) independent of neighbouring magnetic sources and (4) has a heterogeneous magnetisation or density.

In the COOP survey, as in the entire North Sea, most of the geological structures are most likely arbitrarily shaped sources, and are therefore not simply modelled or defined by the structural index. The fact that the sources may not be internally or spatially homogeneous (i.e., the magnetisation and shape of the source change with depth or along strike), or the source-to-observation distance increases (thus, the anomaly shape changes with depth), or other sources impinge on each other's spatial positions, are inherent sources of scatter (Reid *et al.* 1990, Keating & Pilkington 2004). Consequently, it is necessary to examine a number of structural indices to compare the results and clustering of solutions for several individual features. Alternatively, in such situations, geological constraints from external data sources would be beneficial to the interpretation of the COOP dataset in the future.

Complexities also arise with respect to the depth of burial of the source. Ravat (1996) noted that there was a strong inter-dependency between the choice of the structural index and the distance of the source-to-observation, and that with increased distance the results were biased towards the higher structural indices, explained by the exponential decay of a source anomaly with depth. It can be predicted that with increasing depth the attenuation rate of the anomaly is less; deeper sources may therefore only be represented by higher values (Ravat 1996). The relationships between the source type and the observation level are considerably altered following upward continuation of the observation level, thus increasing the possibility of mis-identification of the true structural index (Ravat 1996).

7.4 Located 3D Euler method

Euler deconvolution usually assumes a 'moving window' technique (Reid *et al.* 1990). This standard technique produces a mathematical solution for each position of the window, estimating the unknowns after each sequential movement. The minimum and maximum depths that can be resolved are related to the grid cell size and the window size selected, highlighting the importance of the quality of the dataset and the nature of the investigations.

For this report, we preferred the 'Located 3D Euler method', which is a modified version of the standard Euler deconvolution (Bainbridge *et al.* 2002). The located 3D Euler method refines the standard method by first running a peak-finding routine (Blakely & Simpson 1986), which locates peaks and estimates an appropriate window size before the deconvolution. This method produces far fewer solutions because only a small subset of the grid will be at the centre of peaks in the dataset. Combined with discrimination techniques, we can obtain more reliable Euler solutions. Peak detection was obtained automatically using the Blakely grid peak-picking algorithm of Blakely & Simpson (1986).

Normally, for the pre-processing of the dataset, the analytical signal will be used as the primary grid for Euler deconvolution. However, we found that the tilt-derivative method can extract more anomalies than the analytical signal. Such procedures may increase the ratio of noise to signal within the grid; therefore, such pre-processing is limited by the initial quality

of the dataset, because noise will contribute to the scattering of solutions. In the present project, we tried different upward continuations to remove some of the remaining noise within the magnetic compilation. Finally, data were 1000 m upward continued and depth estimations show that sources shallower than 500 m have been eliminated.

To estimate the reliability of the method, the depth-to-basement results from Euler deconvolution were compared with observed basement depths from well logs, and we found that we could achieve similar results from Euler deconvolution with a SI=0.5. Basement was reached in 39 wells, which are listed in the **Table 7.2**. The results of located Euler deconvolution are depicted in Figure 7.1. The data from the wells are compared to the Euler solutions in Figure 7.2.

Some Euler solutions could also be linked to the presence of sills within the sedimentary successions. Nevertheless, we consider the study area not to be well adapted to the Euler techniques. Thick successions of sedimentary rocks (5-10 km or more), and consequently a small magnetic sediment-basement contrast over wide areas of the survey, blur the magnetic signature from the basement and reduce the applicability of the Euler deconvolution in terms of a depth-to-magnetic basement calculation. Here, modelling rather than Euler techniques is definitely the method of choice in order to obtain a better hand on the depth-to-basement.

Table 7.2 Wells reaching assumed crystalline basement were used to constrain the Euler deconvolution results. The well information was provided by NPD (http://www.npd.no). The wells have been sorted by increasing depth from the bottom of the table to the top.

Well name	**Depth-to-drilled-basement**	Oldest penetrated age
35/3-2	4400	Pre-Devonian
35/3-5	4114	Pre-Devonian
35/3-4	4089	Pre-Devonian
31/6-1	4070	Pre-Devonian
2/6-3	4060	Pre-Devonian
25/7-1	3592	Pre-Devonian
16/1-3	3498	Pre-Devonian
2/6-5	3260	Pre-Devonian
36/1-2	3255	Pre-Devonian
3/7-1	3227	Pre-Devonian
32/4-1	3186	Pre-Devonian
25/10-2	3181	Pre-Devonian
8/3-1	3015	Pre-Devonian
16/1-2	2919	Pre-Devonian
16/4-1	2909	Pre-Devonian
35/9-2	2885	Pre-Devonian
25/6-1	2881	Pre-Devonian
17/3-1	2852	Pre-Devonian
36/7-1	2841	Pre-Devonian
35/9-3	2783	Pre-Devonian
36/4-1	2717	Pre-Devonian
16/1-5	2460	Pre-Devonian
25/11-1	2459	Pre-Devonian
16/2-5	2373	Pre-Devonian
35/9-1	2350	Pre-Devonian
35/9-1	2350	Pre-Devonian
25/11-17	2256	Pre-Devonian
18/11-1	2086	Pre-Devonian
16/6-1	2060	Pre-Devonian
16/1-12	2055	Pre-Devonian
16/3-2	2019	Pre-Devonian
16/1-4	2010	Pre-Devonian
16/2-4	2000	Pre-Devonian
16/5-1	1943	Pre-Devonian
16/2-1	1906	Pre-Devonian
16/2-3	1905	Pre-Devonian
10/5-1	1843	Pre-Devonian
36/1-1	1596	Pre-Devonian
36/7-2	1435	Pre-Devonian

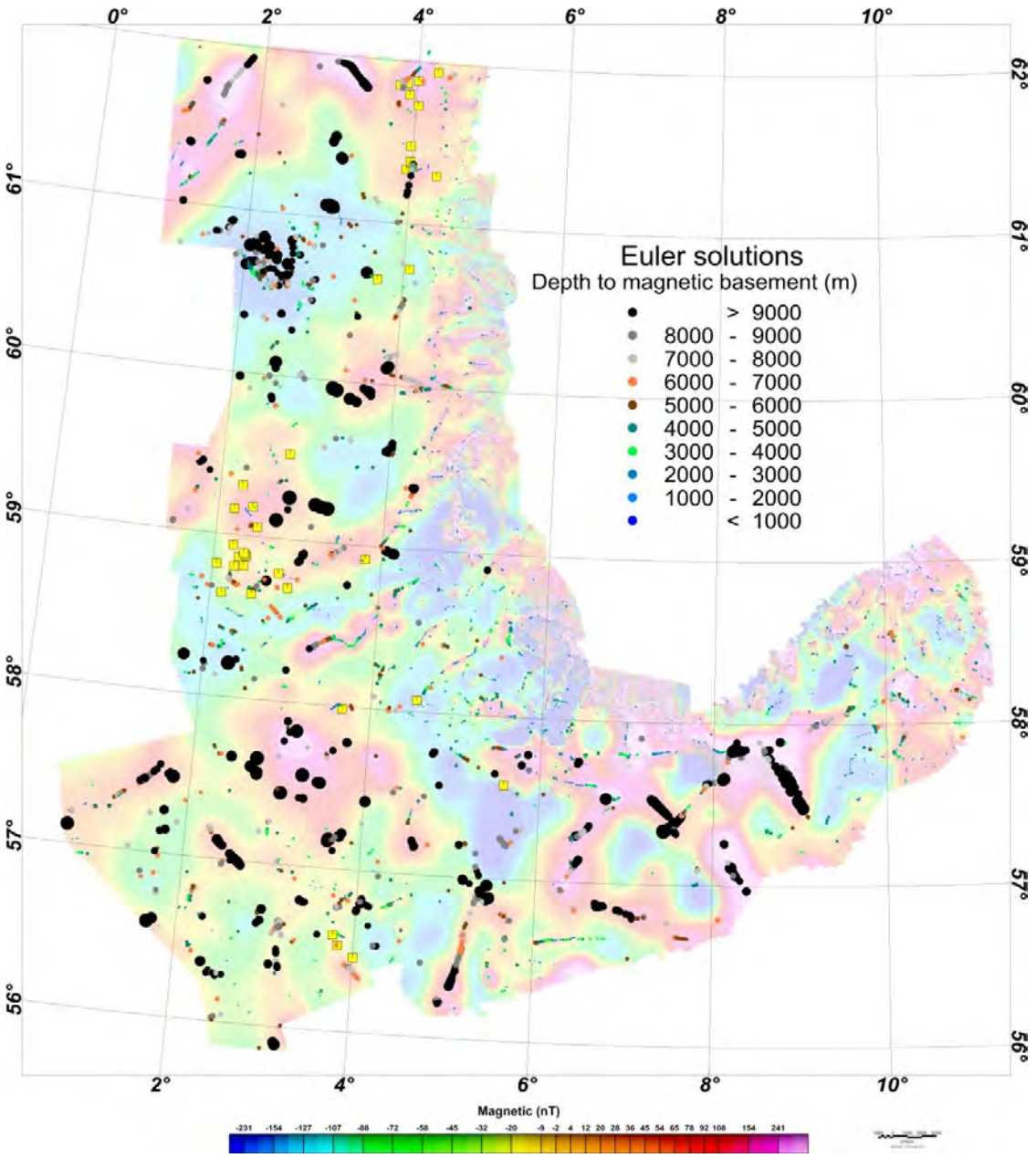

Figure 7.1. Result from the located Euler deconvolution data. The solutions were derived by using a structural index of 0.5. The locations of the wells are shown as small yellow boxes.

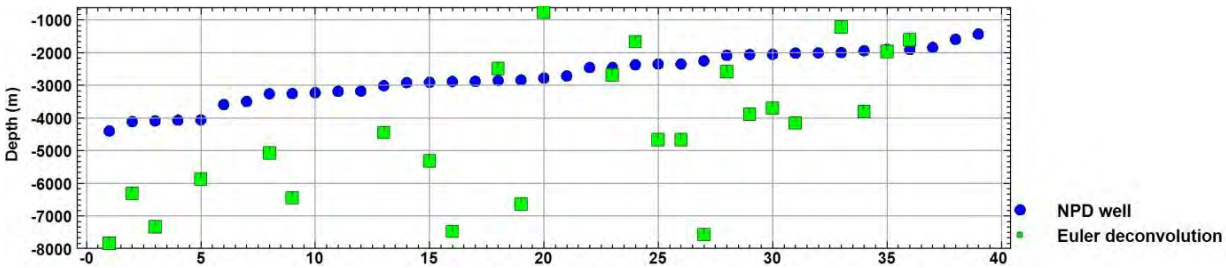

Figure 7.2. Comparision of well data and located Euler deconvolution data. The wells have been sorted according to their depth (see Table 7.2).

7.5 Werner deconvolution

The Werner deconvolution method (Werner 1953, Gunn 1997) was applied to the new magnetic dataset to support the modelling and interpretation in 2D and 3D. The Werner deconvolution was applied only to the 2D profiles. The tilt-derivative map has been used to define the magnetic anomalies and the locations of a large number of profiles crossing these anomalies (Figure 7.3). The Werner deconvolution method has been used to estimate and/or underline the potential depth of magnetic sources along these specific profiles (Figure 7.4). The basic assumption of the Werner deconvolution is that all magnetic anomalies are the result of the presence of either a series of dykes or edge interfaces. The strike lengths and depths of the source bodies are also assumed to be infinite, whereas the width of each body is assumed to be either: (1) finite, representing a dyke; or (2) approaching zero, such that it represents a vertical interface between two bodies of differing magnetic susceptibility. The robustness of the technique is such that no reduction to the pole is required, and it works effectively with both induced and remanent magnetisations.

Werner (1953) recognised that analysing magnetic anomalies could be complicated because of the superposition from adjacent anomalies and the effect of noise (e.g., diurnal variations, non-two-dimensionality and induced versus remanent magnetism). For this reason, the Werner deconvolution algorithm uses simple models for the sources and a quadratic form for the source/noise interference to determine the magnetisation properties of the causative bodies. To reduce the noise we applied first an upward continuation filter to smooth the magnetic data. If the deconvolution is successful in defining a 'real' source, then depth estimates should define either the edges of the causative body or the depth range of an interface or the upper boundary of an intrusion. These results were compared with the Euler solutions computed in the previous part of the chapter (Figure 7.5). This comparison shows that, in some places, the Werner deconvolution method shows a better estimation of the basement depth ,wheras, in other places the Euler deconvolution solutions are closer to the actual depthws from the well data. Also in some areas both methods show equally good estimations of the depth-to-basement. Therefore we suggest using both methods in order to achieve a more reliable modelling. We made a grid out of the solutions to visualise the results (Figure 7.6). This map shows the depth to magnetic basement which can be used for comparison with other available datasets in the area (e.g., seismic data), and also shows the difference between the Werner deconvolution estimates and the top-basement according to the well data. As is evident from this map, for some particular areas, for example in the Utsira High, the difference is relatively greater than in the other areas which might be an indication of less magnetic basement. Such a low-magnetic basement has been encountered in all exploration wells that reach basement in the North Sea and the Møre-Haltenbanken area (Appendix D and Slagstad et al. 2008) and has also been reported from Denmark to the south of the SAS-96 survey by Olesen et al. (2004).

As mentioned earlier, in order to better understand the structures and to reduce the ambiguity in our depth-to-basement interpretations, we suggest that more efforts should be directed to

forward and inversion modelling. In this respect, the results from the Euler and Werner deconvolution can be modified in an interactive 3D geological and geophysical modelling, and especially by incorporating additional geophysical datasets (e.g., reflection seismics) for constraining the models.

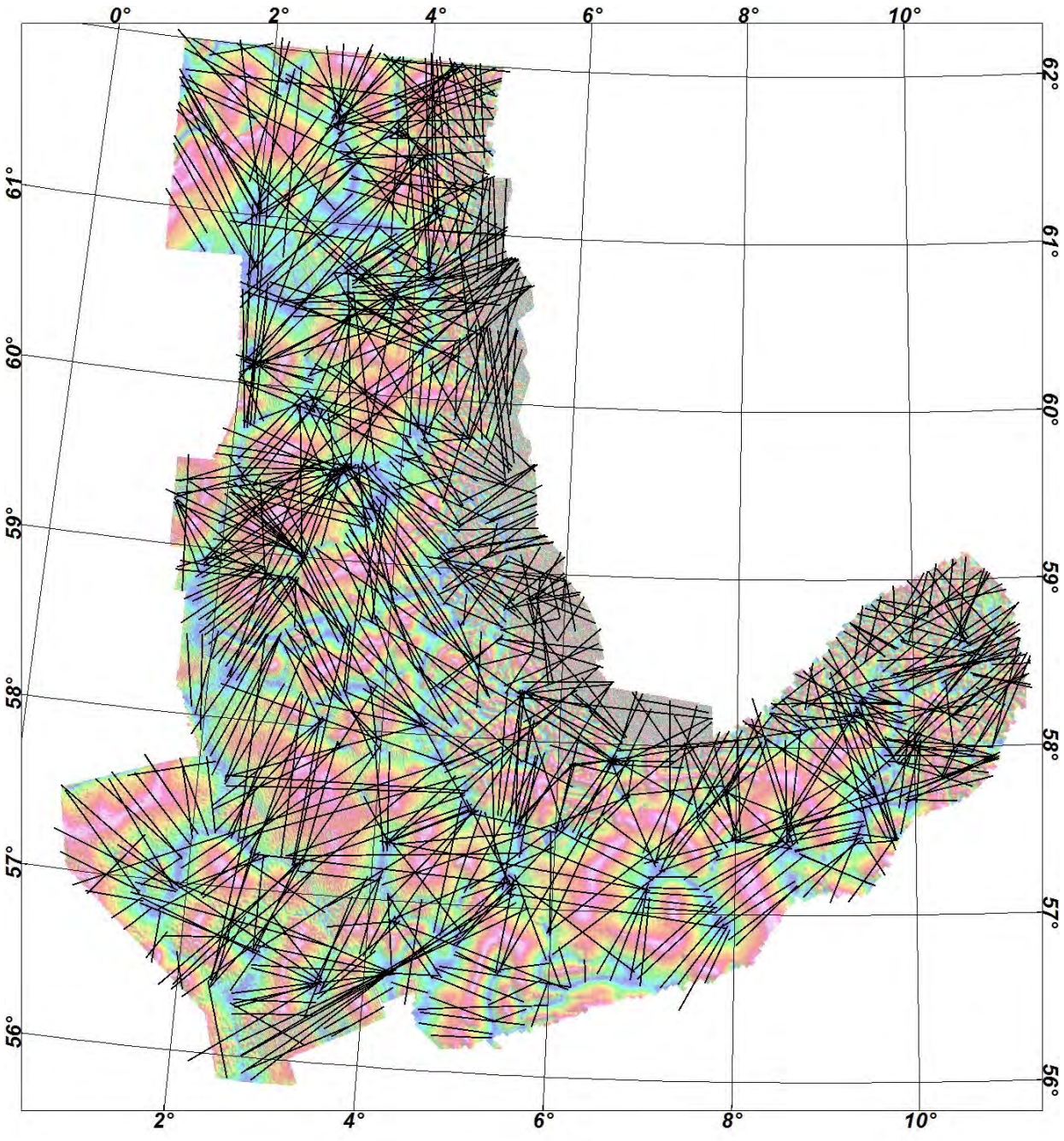

Figure 7.3 A total of 867 magnetic profiles were extracted over the magnetic anomalies for using depth estimation by the Werner deconvolution method. The background map is the magnetic tilt derivative map.

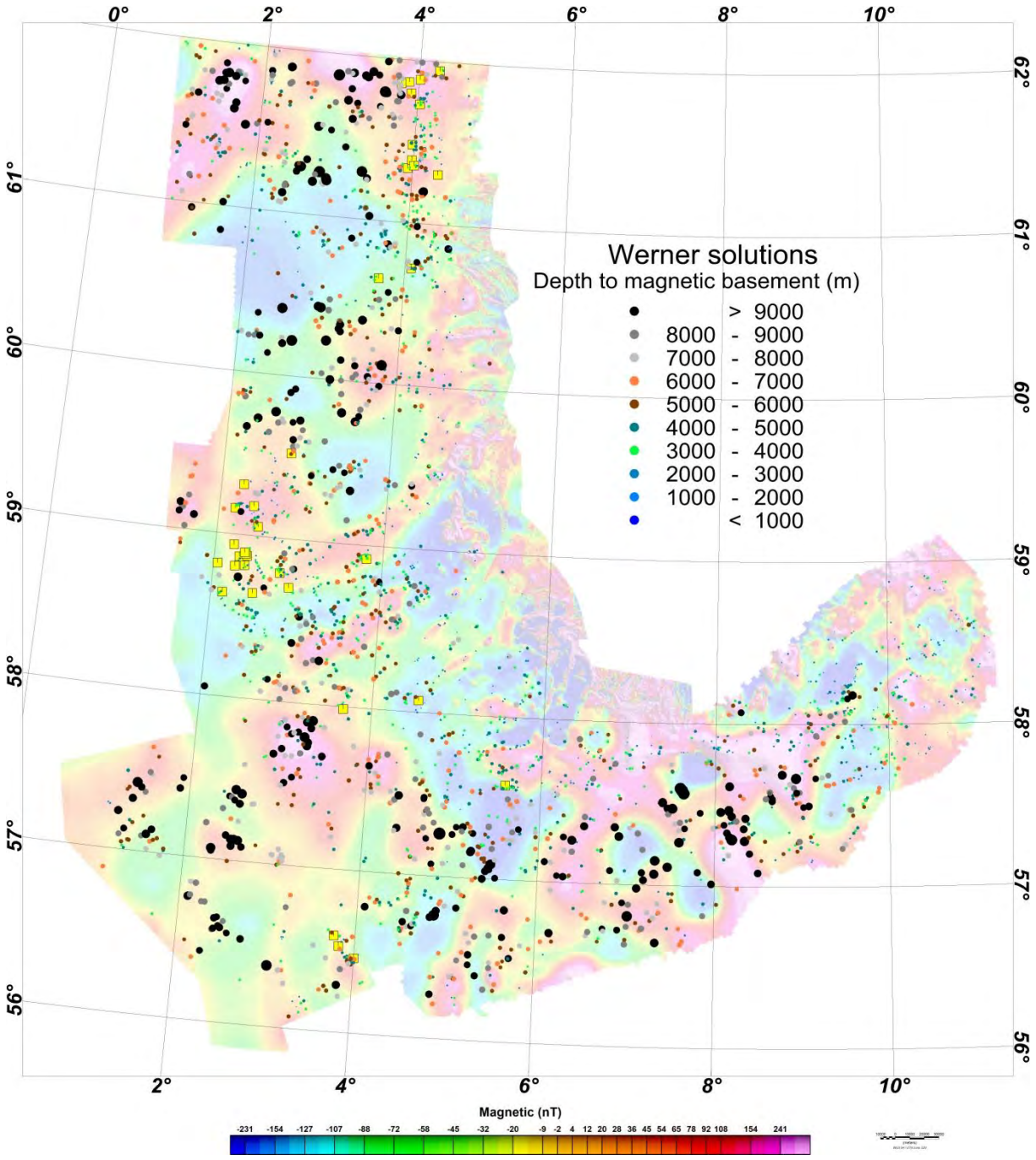

Figure 7.4. Result from the Werner deconvolution method. The locations of the wells are depicted as small yellow boxes. The background map represents the magnetic map.

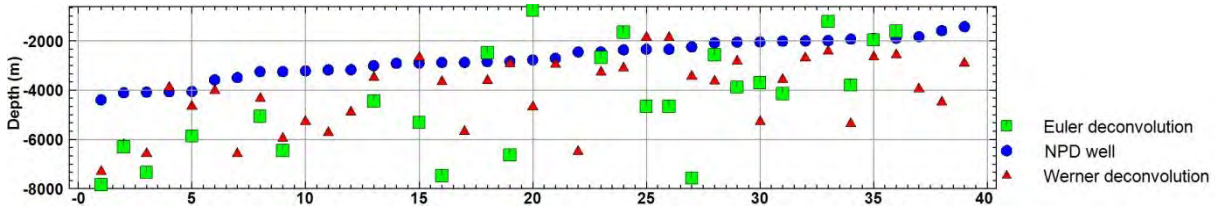

Figure 7.5. Comparison of the depth-to-basement from well data, located Euler deconvolution and Werner deconvolution methods. The wells have been sorted by their depth (see Table 7.2).

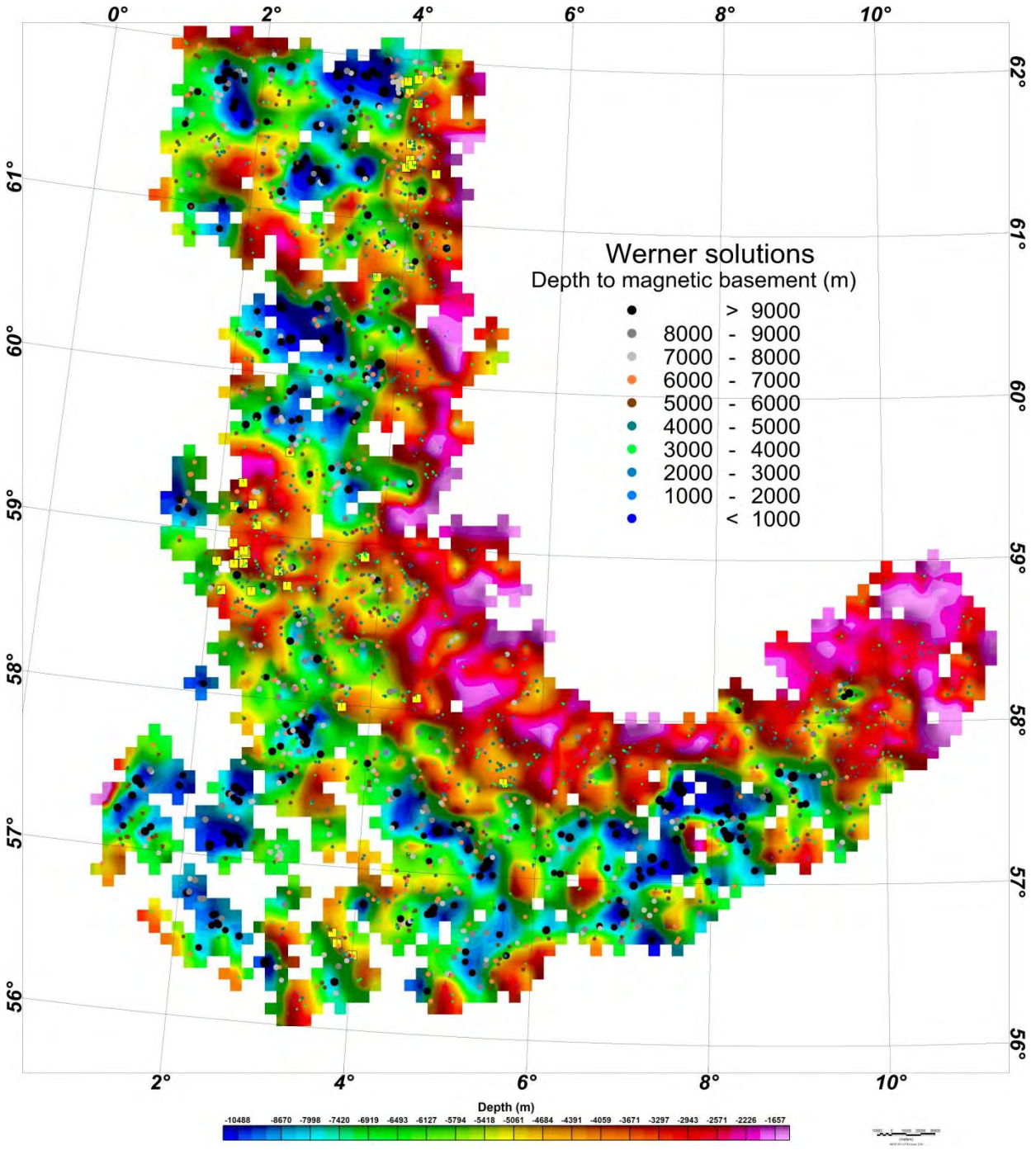

Figure 7.6. Gridded map of the Werner deconvolution solutions. The Werner solutions are shown on top of the gridded map (grid resolution: 8000 x 8000 m). The locations of the wells are shown as small yellow boxes.

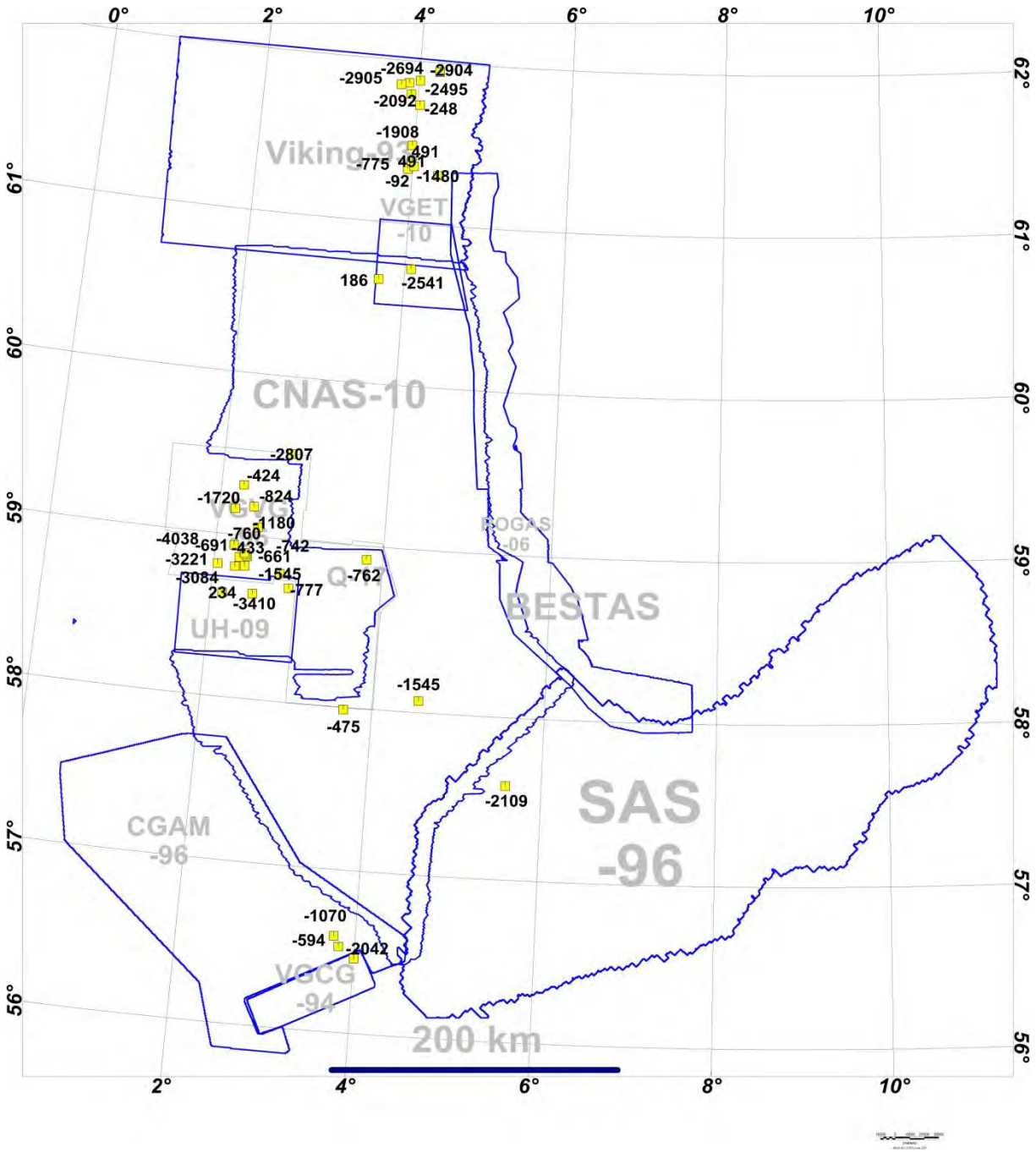

Figure7.7. Depth residual map. The differences between the depth-to-basement of the NPD well data (yellow boxes) and the Werner deconvolution method results are shown as numbers. The negative values show that the Werner estimation is located deeper than the depth-to-basement indicated by the well logging.

8. HEAT PRODUCTION CALCULATIONS

Trond Slagstad & Torleif Lauritsen

8.1 Introduction

Internal radiogenic heat production is a major factor determining the thermal structure of continental crust (e.g., Turcotte & Schubert 1982), and variation in internal heat production may have important implications for temperature-dependent crustal processes such as metamorphism, magmatism and deformation (Bea et al. 2003, Andreoli et al. 2006, Sandiford & McLaren 2006). Regional investigations of heat production at the surface, coupled with heat flow data that provide information about heat production at depth in the crust (e.g., Jaupart & Mareschal 2003), are necessary for understanding the present-day thermal structure of the crust, which in turn may be used to reconstruct the thermal structure of the crust prior to, during and after past tectonic events (Ranalli & Murphy 1987, Karlstrom & Williams 1998).

This part of the COOP phase 1 report presents the results of radiogenic heat-production calculations based on measurements of U, Th and K on rock samples, as well as airborne radiometric measurements. These data are integral in understanding the thermal and geological structure of the continent-ocean transition of the Norwegian continental margin. The first part of this section deals with heat-production data from chemical analyses of rock samples whilest the second part deals with heat-production data from airborne gamma ray measurements.

8.2 Sources of heat-production data

The chemical data used to calculate heat production originate from various sources, and are presented in Table 8.1 and Fig. 8.1. The majority of the samples have been analysed by XRF (K) and LA–ICP–MS (U, Th); thus, a complete set of major and trace element data exists for each of these samples. Flem et al. (2005) described the procedures for LA–ICP–MS analysis in detail. The remaining samples have been analysed by γ-ray spectrometry, and for these samples only the concentrations of heat-producing elements are available. The analytical procedure, detection limits, accuracy and precision of the γ-ray spectrometry method are described by Raade (1973) and Killeen & Heier (1975). For several geological units, heat-production estimates based on both XRF/LA–ICP–MS and γ-ray spectrometry exist. Average heat-production rates for such units are similar regardless whether they are based on the older γ-ray data or more modern XRF/LA–ICP–MS data, suggesting that the quality of the former is good. For the majority of the samples, densities have been determined using Archimedes' principle by weighing the samples in air and immersed in water, or, if geometrically simple samples are available (e.g., drill-cores), by weighing the samples and dividing by the calculated volume. For samples where the original authors reported densities,

these densities have been used. If density data are unavailable, density was estimated based on lithology.

Table 8.1. Sources of heat-production data.

Source	n	Analytical method
LITO-project	2755	XRF, LA–ICP–MS
Other NGU data	623	XRF, LA–ICP–MS
Killeen & Heier (1975)	629	γ-ray spectrometry
Raade (1973)	967	γ-ray spectrometry
Ormaasen (1976)	102	γ-ray spectrometry

8.3 Heat-production calculations

More than 98% of present-day heat production is the result of the decay series ^{238}U and ^{232}Th and the single-step decay of ^{40}K. The isotope ^{235}U has a significantly shorter half-life than ^{238}U (c. 0.7 billion years and 4.5 billion years, respectively) and is now reduced to 0.7% of the total naturally occurring uranium. Other, short-lived radioactive isotopes may have made significant thermal contributions in early stages of the Earth's history, but they are not detected now. Other long-lived radioactive isotopes also exist, but their decay rates are so slow that they have never made any significant contribution to the Earth's heat (e.g., ^{87}Rb with a half-life of c. 49 billion years and ^{147}Sm with a half-life of c. 106 billion years). The heat-production rate of a rock can thus be calculated based on the rock's K, U and Th concentrations and density (Rybach 1988), as shown in Equation 8.1. C_U and C_{Th} represent U and Th concentrations in ppm, respectively, C_K represents K concentration in wt.%, and δ is density.

$$A = \delta * (9.52C_U + 2.56C_{Th} + 3.48C_K) * 10^{-5} \qquad (8.1)$$

8.4 Heat production of Norwegian bedrock

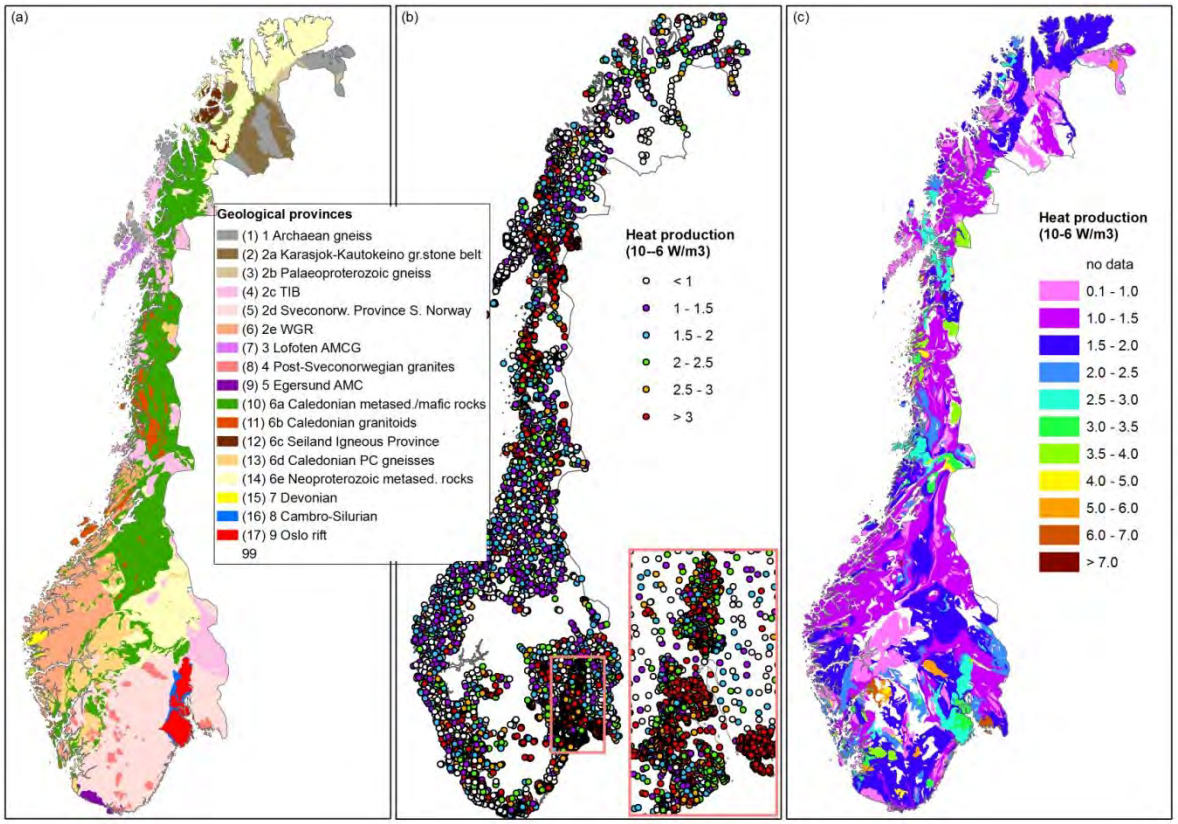

Figure 8.1 (a) Simplified geological map, modified after Sigmond (1996). (b) Heat-production data. (c) Average heat-production rates for geological units where data are available.

A number of factors, of which lithology, tectonic setting, tectonometamorphic history and age are the most obvious, may influence the heat production of a geological unit or province. The work presented here is part of a larger effort to enhance our understanding of the geological and thermal structure of the continental margin of Norway (and the Baltic Shield). This means that heat-production values must be assigned to geological units onshore that can be correlated offshore onto the continental margin using seismic or potential field data. With these objectives in mind, Slagstad (2008) presented and discussed the then available heat-production data with reference to specific geological provinces, subdivided based on lithology, tectonic setting, tectonometamorphic history and age. The subdivision includes nine major and several minor provinces, ranging in age from Archaean to Permian. Table 8.2 and Fig. 8.1 present a summary of geological and heat-production information currently available. The table and figure are updated from that presented by Slagstad (2008), and include additional data acquired in this project. For a detailed discussion of the various geological provinces and the heat-production data, see Slagstad (2008). Fig. 8.2 presents a more detailed view of the area covered in the COOP project.

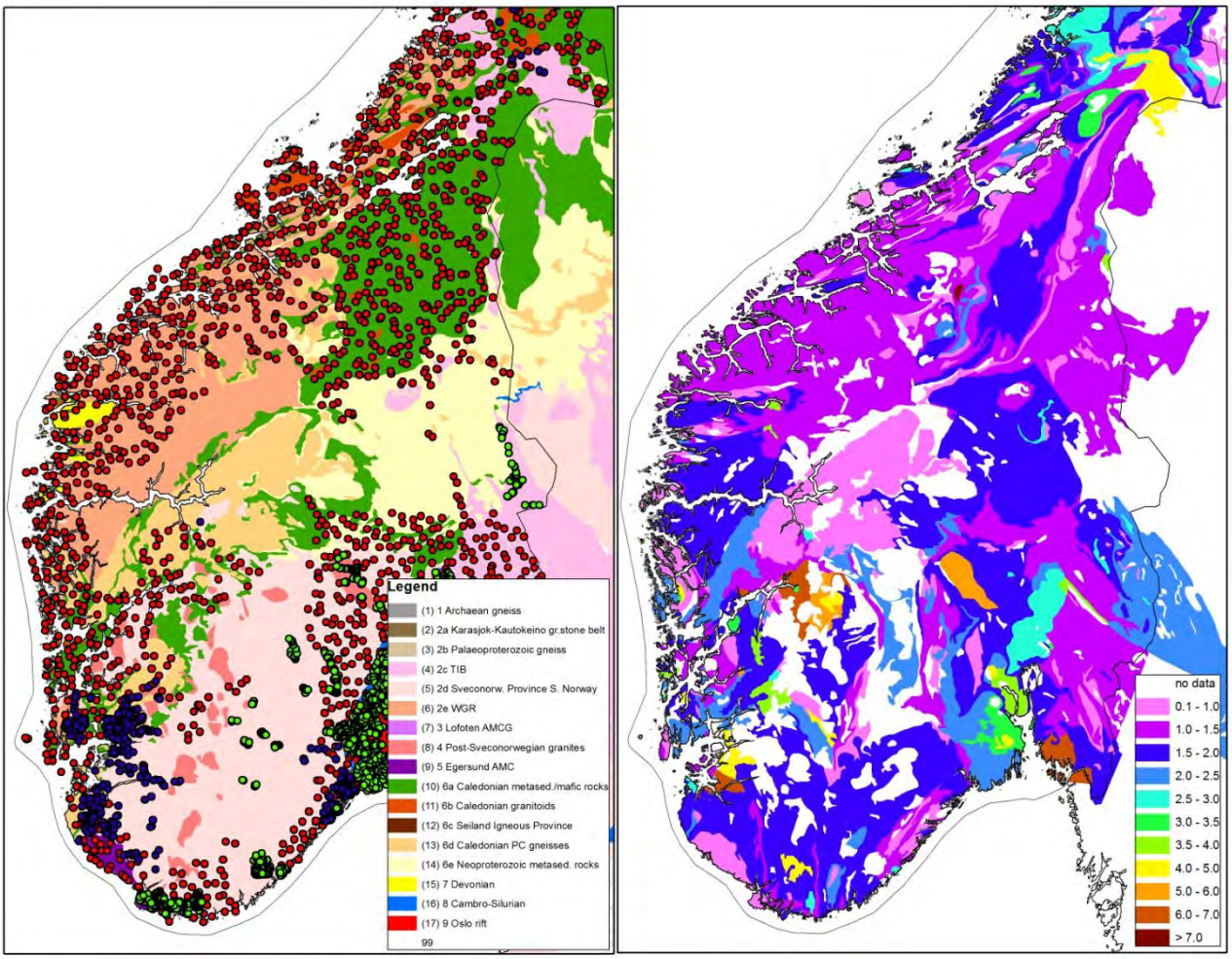

Figure 8.2. Heat production in the COOP project area.

Table 8.2. Simplified geological history and heat-production rates of geological provinces in Norway. See text for details and references.

	Geological province	n	Age (Ma)	Lithology	Tectonic setting	Tectonometamorphic history	Heat production rate (μW m^{-3})	
							Area wtd. mean[1]	Median ±1σ
1	Archaean gneisses	176	3000–2500	Dominantly tonalitic to granitic gneisses		Palaeoproferozoic (c. 2.0–1.8 Ga) amphibolite- to granulite-facies metamorphism.	0.93	0.81 ± 1.36
2	Proterozoic gneissic rocks							
2a	Karasjok-Kautokeino greenstone belts, NE Norway	63	2100-2000	Tholeiitic metabasalts, amphibolites and interlayered metasedimentary rocks	Continental rifting and oceanic subduction	Metamorphosed under greenschist- to amphibolite-facies conditions during obduction onto the Karelian craton at c. 1.9 Ga.	0.45	0.35 ± 0.44
2b	Palaeoproterozoic gneisses	38	2000–1900	Garnet-quartz-feldspar paragneiss and hypersthene-plagioclase orthogneiss	Deposition in continental back-arc basin	High-grade metamorphism during continent-continent collision at c. 1900 Ma	0.83	0.70 ± 1.22
2c	Transscandinavian Igneous Belt (TIB)	686	1810–1770	Alkali-calcic to calc-alkaline quartz monzonites to granites	Active continental margin, back-arc extension	Deformation and metamorphism at c. 1.46–1.42 and 1.0 Ga in SW Sweden. Variable Caledonian effects in NW Norway at c. 420 Ma.	2.61	2.43 ± 2.01
2d	Sveconorwegian Province, S Norway	1138	1500–1000	Tholeiitic to calc-alkaline, intermediate to felsic, metavolcanic and plutonic suites	Active continental margin and continental back-arc.	Local crustal reworking at 1.26–1.16 Ga. Continent-continent collision and associated medium- to high-grade metamorphism at c. 1.0 Ga. Very low-grade Caledonian metamorphism at c. 400 Ma in western areas.	1.88	1.55 ± 1.60
2e	Western Gneiss Region, W Norway	444	1750–1000	Dominantly tonalitic to granitic gneisses	Active continental margin	Sveconorwegian and Caledonian high-grade metamorphism at c. 1000 and 400 Ma, respectively.	1.49	1.46 ± 1.34
3	Lofoten anorthosite-mangerite-charnockite-granite (AMCG) complex	137	1800–1790	Mangerite, smaller volumes of gabbro, anorthosite, charnockite and granite	Related to TIB 1 magmatism	Crystallised under low-P granulite-facies conditions. No significant later metamorphic events.	0.67	0.62 ± 0.38
4	Post-Sveconorwegian granites, S Norway	505	930–920	Dominantly granite, locally grading to diorite	Extensional, post-tectonic magmatism	Generally no significant metamorphic overprinting.	4.15	3.81 ± 2.53
5	Egersund anorthosite-mangerite-charnockite (AMC) complex	62	930	Massive anorthosite, lesser volumes of leuconorite, mangerite and charnockite	Extensional, post-tectonic magmatism	Very low-grade Caledonian metamorphism at c. 400 Ma.	0.61	0.70 ± 1.33
6	Caledonian thrust-sheets							

	Geological province	n	Age (Ma)	Lithology	Tectonic setting	Tectonometamorphic history	Heat production rate (μW m^{-3})	
							Area wtd. mean[1]	Median ±1σ
6a	Late Proterozoic to Palaeozoic metasedimentary and metamafic rocks	965	500–450	Metagreywacke, phyllite, mica schist, lesser volumes of marble and greenstone.	Passive margin sequences. Greenstones formed in oceanic arc / back-arc.	Low- to high-grade metamorphism during the Caledonian orogeny at c. 450–400 Ma.	1.44	1.32 ± 1.29
6b	Caledonian intrusive rocks	183	480–430	Dominantly calc-alkaline diorite, tonalite, granodiorite and granite. Minor trondhjemitic intrusions.	Active continental margin.	Variable overprinting during the Caledonian orogeny at c. 430–410 Ma.	1.85	1.74 ± 1.83
6c	Seiland igneous province	15	570–560	Gabbro, lesser volumes of ultramafic and alkaline rocks, and intermediate granitoid rocks.	Intracontinental rift.	Variable overprinting during the Caledonian orogeny at c. 420 Ma.	1.16	0.69 ± 0.98
6d	Precambrian gneissic rocks	113	1690–950	Syenitic to monzonitic gneisses, anorthosite-mangerite-charnockite-granite suites	Active continental margin. AMCG suite formed in intraplate setting (?)	Late Sveconorwegian, high-grade metamorphism at c. 930 Ma. Variable, but locally high-grade metamorphism at c. 450 Ma.	1.23	1.18 ± 1.91
6e	Neoproterozoic metasedimentary rocks	268	1000–500	Quartzitic to arkosic sandstone, mica schist, pelite and volumetrically subordinate carbonate	Continental shelf	Variable high- to low-grade Scandian and pre-Scandian metamorphism in Finnmark. Low-grade overprinting in Lillehammer during the Scandian phase at c. 430-400 Ma.	1.52	1.41 ± 0.96
7	Devonian sedimentary rocks	21	400–390	Fluvial sandstones, conglomerate, breccia	Post-orogenic extension	No metamorphic overprinting.	1.12	1.12 ± 0.48
8	Cambro–Silurian sedimentary rocks	39	540–420	Marine shales, carbonates, sandstones	Epicontinental basin, later foreland basin	Low-grade metamorphism and deformation during the Caledonian orogeny at c. 420 Ma; local contact metamorphism during formation of Oslo rift at c. 300–280 Ma.	1.86	1.58 ± 1.43
9	Oslo Rift	1052	300–280	Tholeiitic basalts, monzonite, syenite and granite	Intracontinental rift.	No metamorphic overprinting.	2.92	2.49 ± 1.64

[1]The area-weighted heat production of a geological province is calculated by first calculating the average heat production of all polygons on Sigmond's (1996) map from which heat-production data are available. The average value for each polygon is then multiplied by the area of the polygon and divided by the total area of all polygons belonging to a particular geological province, giving the area-weighted heat production.

8.5 Airborne gamma ray spectrometry

In addition to the laboratory measurements, we have applied the airborne gamma ray spectrometer measurements in order to calculate the heat-production from the different rock units exposed at the surface. We have, in this case, also calculated heat generation rates (A in $\mu W/m^3$) using Rybach's formula (8.1) (Rybach 1988).

While gamma rays in the energy range used for the mapping of natural sources of radiation can penetrate several hundred metres of air, they are completely impeded by about 30-50 cm of rock or soil. This has several implications for the mapping of natural sources of radiation.

The airborne gamma ray spectrometry method is thus a surface mapping method, because most of the gamma rays emanating from the Earth's surface originate in the top 30 cm of the surface. This means that the interpretation of these data requires an understanding of surface processes such as weathering, and the relationship between surface materials and bedrock geology.

The flight altitude above ground level is an important operational variable, because gamma rays are attenuated by air, and corrections must be made for variations in flight altitude. As a general rule, spectrometric data obtained at an altitude greater than 250 m will be of little value. Thus, data from a flight altitude greater than 250 m have been masked out.

Finally, we corrected the heat generation map for the effect of the sedimentary cover and lakes. Lakes and the Quaternary sediments act as a blanket, absorbing gamma particles generated in the rocks that they overlie. In order to obtain a reliable heat generation map of the bedrock, we carefully checked the locations where the bedrock is exposed and filtered out the other areas where it is covered by sediments and lakes.

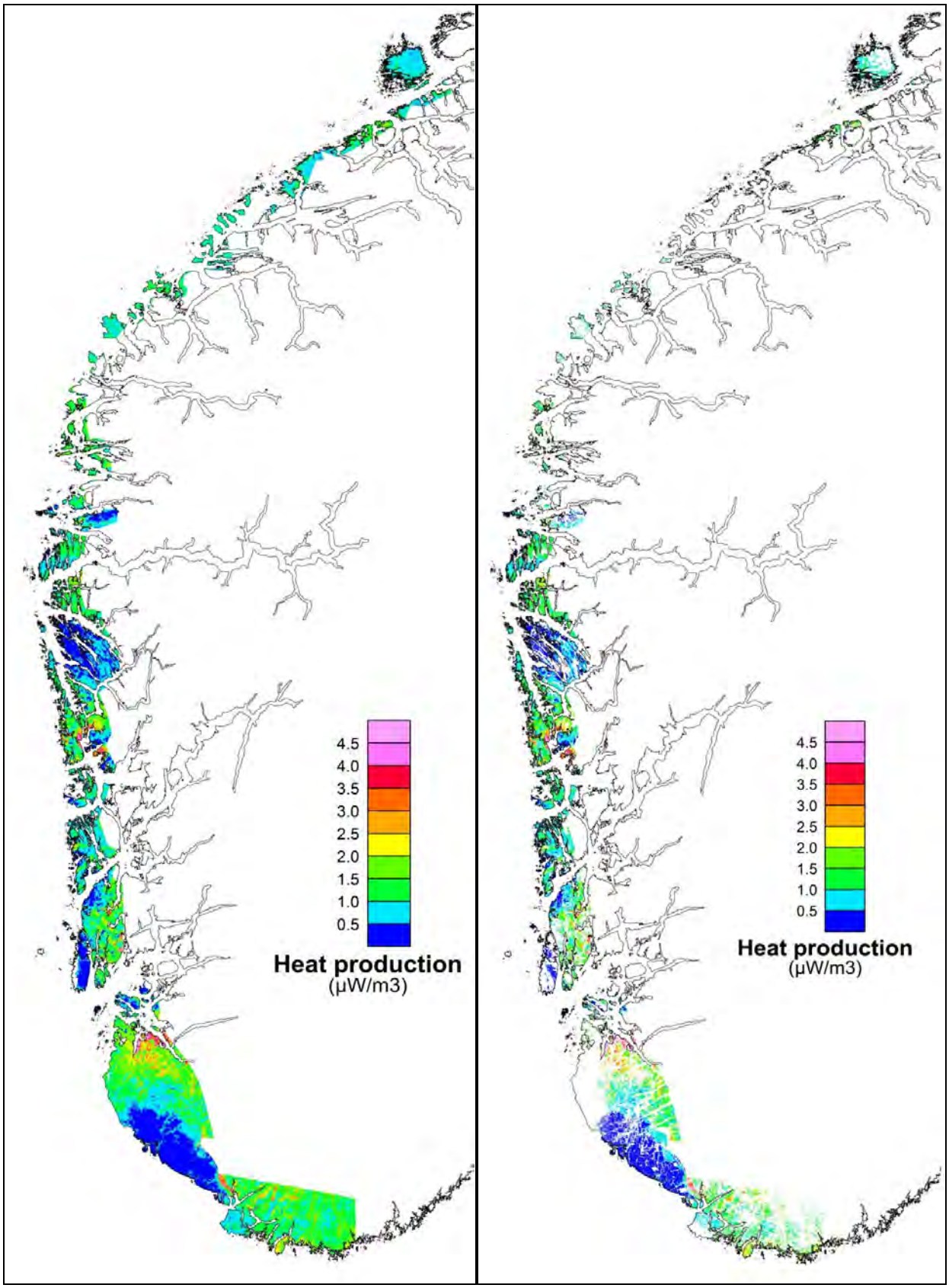

Figure 8.3 a) and b). Heat generation values calculated from airborne multi-channel gamma spectrometry surveys. Note that the results shown in figure a) are not corrected for the attenuation effect of the lakes and the Quaternary sediments, attenuation effect of the lakes and the Quaternary sediments, and a flight altitude over 250 m. Figure b) shows the corrected values.

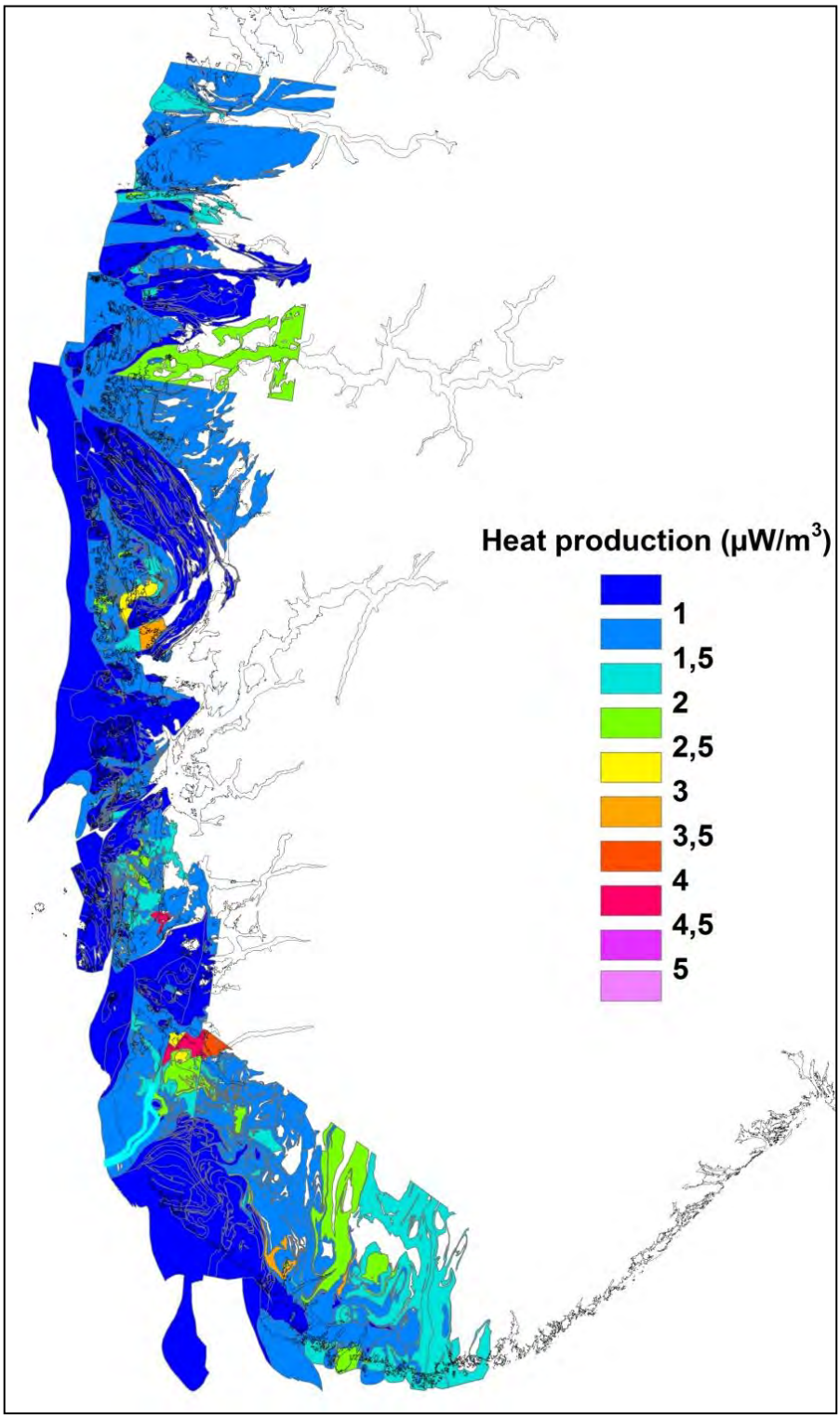

Figure 8.4. Average heat generation map of the western Norway region as derived from airborne gamma spectrometry surveys and corrected for the attenuation effect of sedimentary overburden and lakes, and masked for a flight altitude higher than 250 m.

The final corrected heat production grid (Fig. 8.3 b) was then converted to a raster (in ArcMap). A raster is a digital image composed of rows and columns, where each element is assigned one value. The raster values were then converted to a point-shape file. We then joined these points to the detailed bedrock map polygons. Each polygon was given an average value of the points that fell within it. By this process we thus produced an average heat production map.

Normally, the rock density (ρ) is assumed to be equal to 2700 kg/m^3 (Equation 8.1). Having produced an average density map (Chaper 5, Figure 5.4 a), we then had the possibility of joining this map to the average heat production map, and thus multiplying the average heat generation values by a correction factor based on the real average density values within each bedrock unit. Where we had no petrophysical samples the correction factor was set to 1.

The final heat generation map is shown in Figure 8.4.
The most evident areas of heat-producing bedrock are the Korsnes granite (3.0-3.5 µW/m^3) and the granitic gneisses from Fyllingsdalen to Sotra (2.5-3.0 µW/m^3), commonly referred to as Løvstakken granite. We have observed even higher values in the augen gneisses (metamorphosed porphyritic granites) east of Gandsfjorden and across Høgsfjord (3.5-4.5 µW/m^3), and also in the granites across Hervikfjorden (4.0-4.5 µW/m^3). Beyond these areas the major part of the COOP project area is characterised by very low heat-production values (< 1.5 µW/m^3).

We have compared the heat-production values calculated from the chemical analyses of LITO-project samples with those calculated from the airborne gamma ray spectrometer surveying. This is done by merging the airborne heat-generation grid into the database of heat-generation from the chemical analyses (Oasis Montaj). This gives us a dual heat generation dataset for any mutual pair of coordinates (Fig. 8.5).

A scatter diagram in Figure 8.6 shows the regression equation between the two datasets: Y = 0.79919 + 0.25898*X.

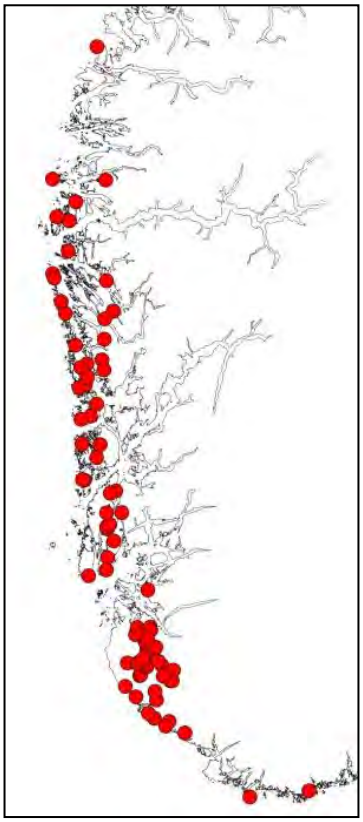

Figure 8.5. Chemically analysed LITO-project samples that have mutual coordinates with airborne gamma spectrometer measurements.

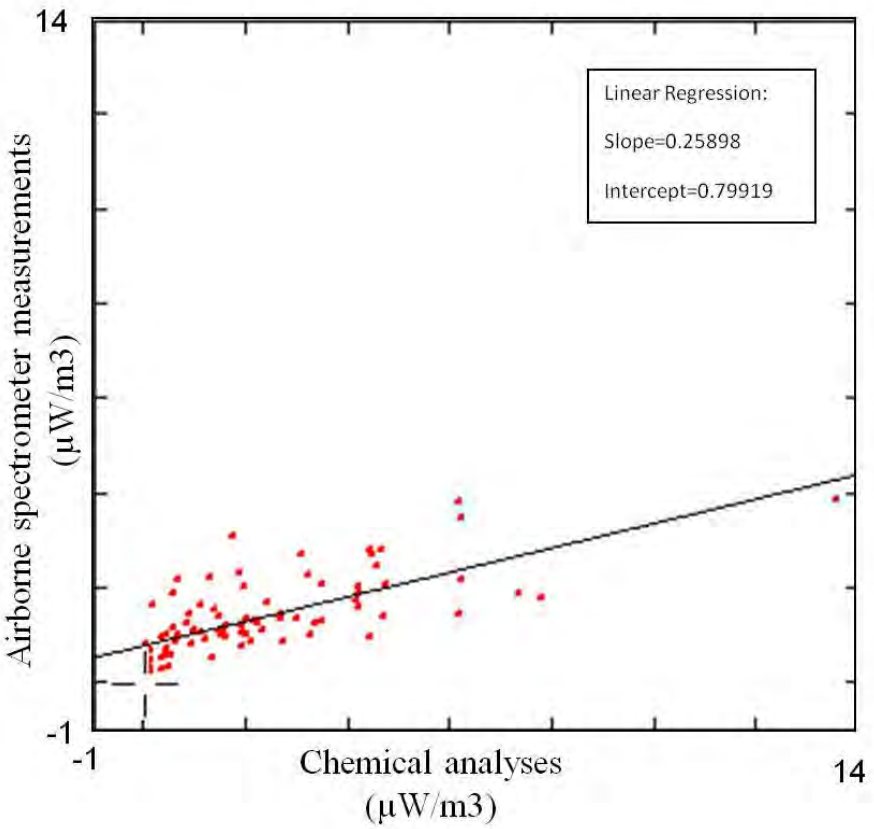

Figure 8.6. Scatter diagram: heat-production from chemical analyses of LITO-project samples vs heat-production from airborne gamma ray spectrometer surveying.

We find a reasonably good agreement between heat-generation values calculated from the airborne gamma ray spectrometer surveying and those calculated from the chemical analyses (Fig. 8.7). Because the aircraft moves forward during the accumulation time, the area of ground sampled is elongated. A rule of thumb indicates that 60-70% of the counts originate in a rectangle with a width of twice the flying altitude, and a length of twice the flying altitude plus the distance travelled during accumulation. For a typical fixed-wing survey, at an altitude of 60 m, speed 225 km/h and accumulation time 0.5 s, the area represented by each sample is about 120 m x 150 m. Thus, airborne surveys normally result in lower heat-generation values, because they average contributions from a variety of radioactive sources.

Another reason why airborne surveys may record lower heat generations is the ground moisture. Waterlogged surfaces reduce the amount of radiation emanating from the ground. Areas of recent heavy rain should therefore be avoided during surveying.

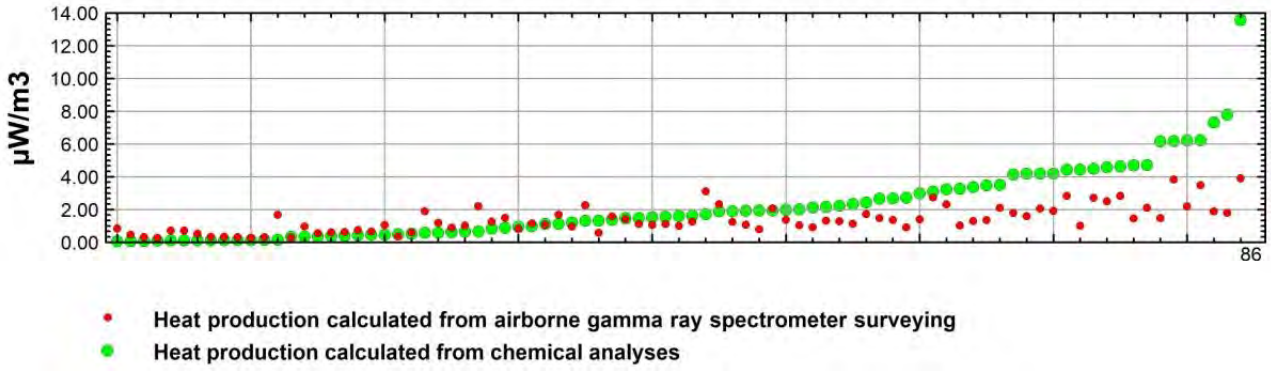

Figure 8.7. Comparison of heat production calculated from chemical analyses and airborne gamma ray spectrometer surveying. The chemical values are presented in an ascending sequence.

Another way of showing the relationship between the two datasets is by illustrating their ratio (Fig. 8.8).

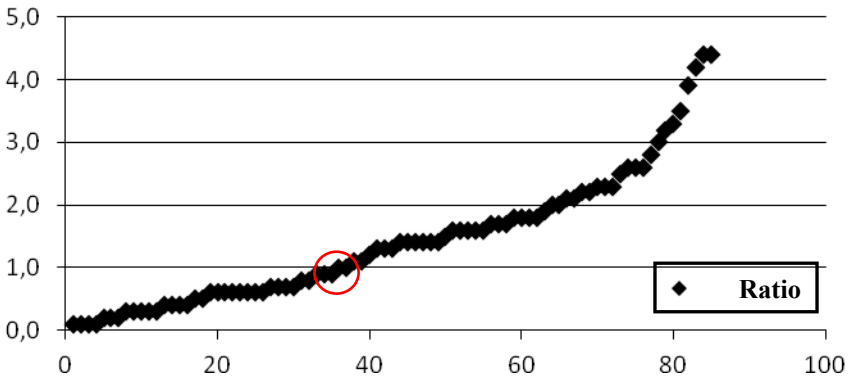

Figure 8.8. Calculated heat production ratio of chemical analyses to airborne surveying. A total of 85 samples are included in the analysis. The red circle represents a 1:1 ratio.

The ratio shows the relationship between the calculated heat productions from chemical analyses and those derived by congruent airborne gamma ray spectrometer surveying, using a total of 85 samples. The highest ratio of chemical analyses to airborne surveying is 4.5 to 1. Furthermore, this figure shows that c. 38 ratios, i.e. c. 45 %, are less than 1. This means that 45 % of the LITO-project samples have a heat generation calculated from chemical analyses that is smaller than the ones calculated from airborne measurements. This is a large and unexpected number that may indicate that a large number of LITO-project samples were collected from rock types that are not representative of the average or main bedrock type, i.e., from lenses of an uncommon bedrock or from dykes that have minor contents of heat-producing radioactive elements. Another reason for this mismatch might be that some of the airborne values could have been influenced by Quarternary deposits with higher than average radio-activities.

As in the case of the airborne gamma ray spectrometry study, we used the concentrations of uranium, thorium and potassium derived from portable gamma spectrometry measurements in the Bergen area, and calculated heat-generation values according to Equation (8.1). Figure 8.9 shows the portable spectrometry measurements that have mutual coordinates with the airborne gamma spectrometer measurements.

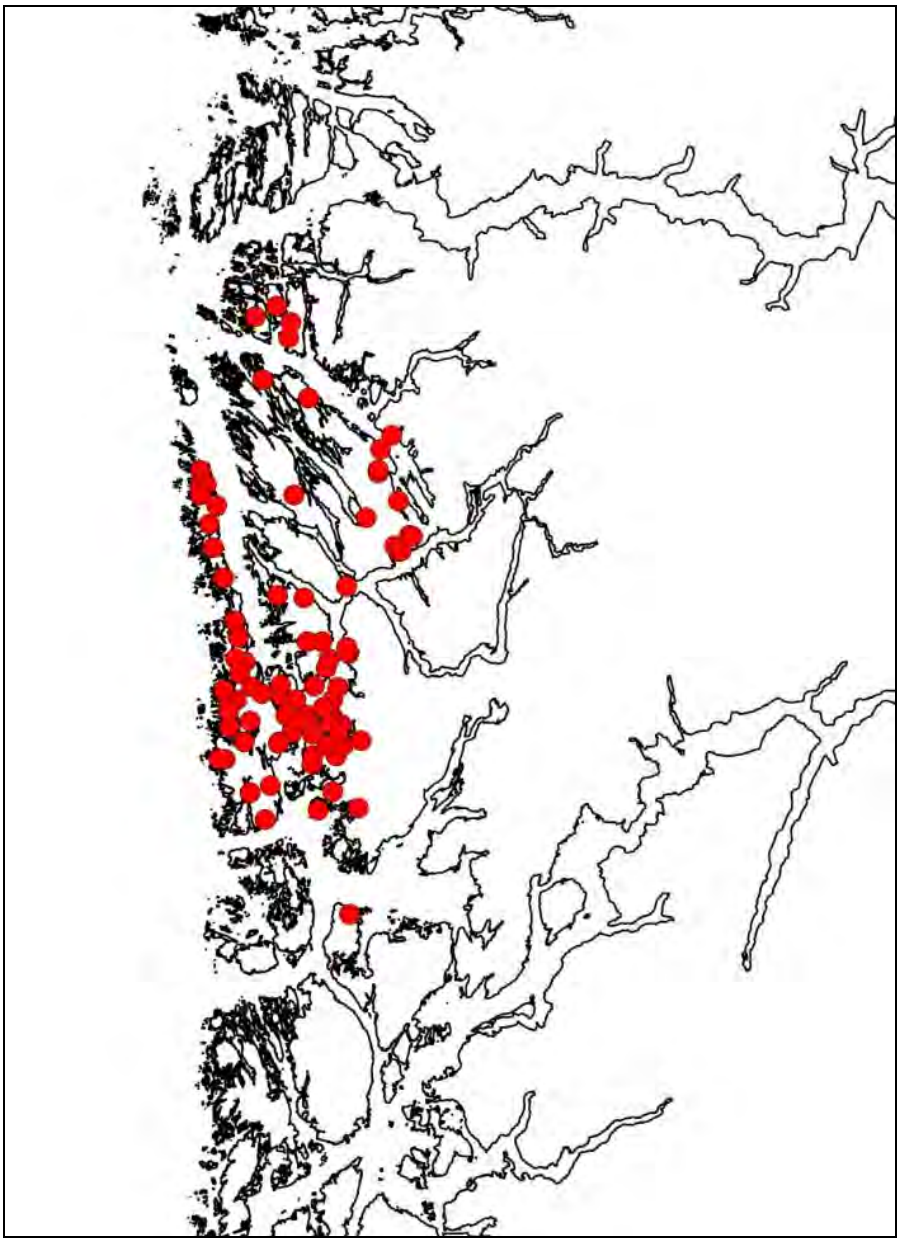

Figure 8.9. Portable spectrometer measurements that have mutual coordinates with the airborne gamma spectrometer measurements in the Bergen area.

A scatter diagram in figure 8.10 shows the regression equation between the two datasets:
Y = 0.71872 + 0.22676*X.

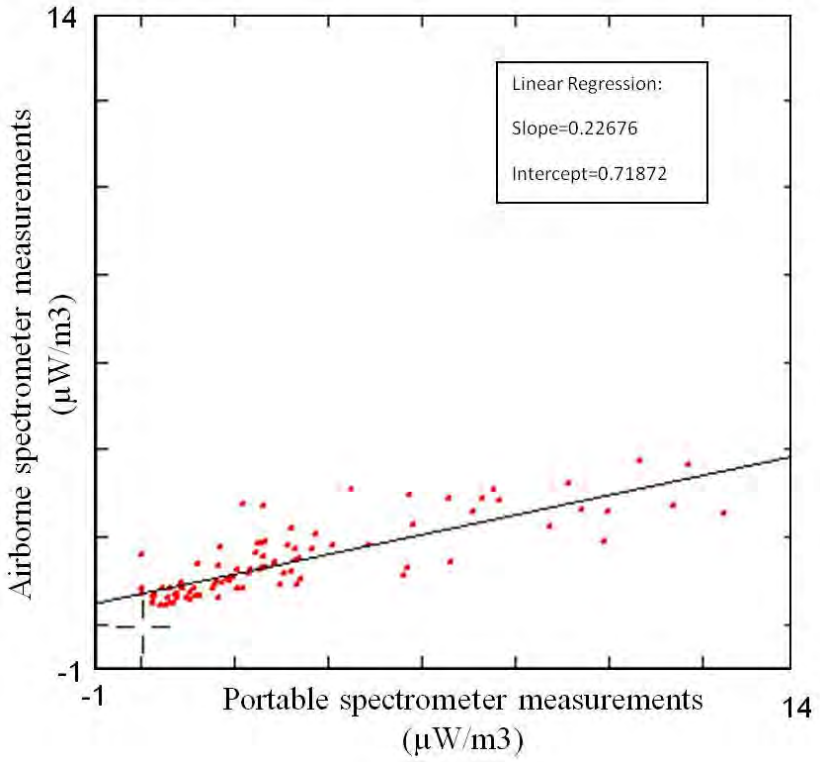

Figure 8.10. Scatter diagram: heat-production from portable spectrometer ground measurements vs heat-production from airborne gamma ray spectrometer surveying.

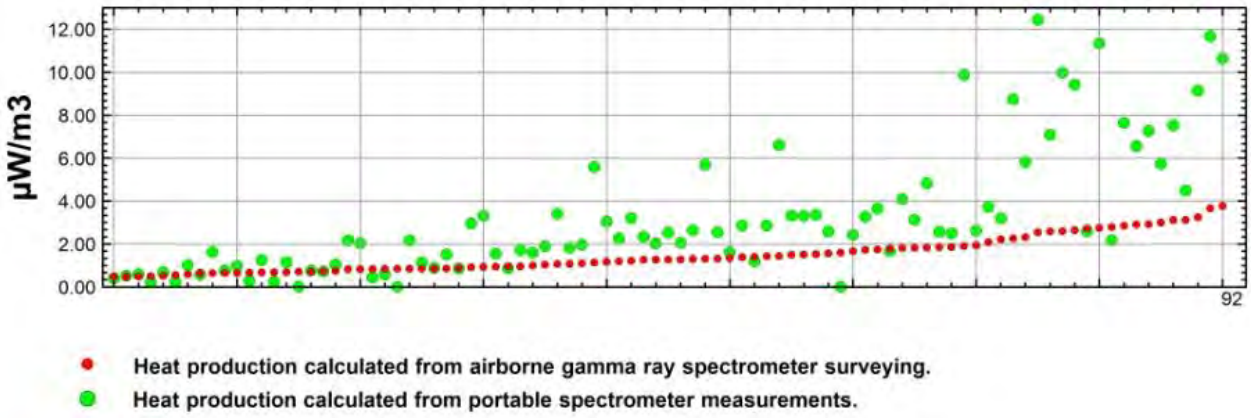

Figure 8.11. Comparison of heat- production calculated from portable spectrometer measurements and airborne gamma ray spectrometer surveying. The heat- production values calculated from the airborne measurements are presented in an ascending sequence.

As for the chemical measurements, we find a reasonably good agreement between heat-generation values calculated from airborne gamma spectrometer surveying and those calculated from portable spectrometer measurements (Fig. 8.11). Nevertheless, the portable spectrometer values show a considerable spread as compared with the airborne values. This can be due to the actual number of portable spectrometer readings; the more readings that are taken the more accurate will be the calculated ground concentration.

However, with respect to ground surveys, airborne surveys result in lower heat generations, because they average the contributions from various radioactive sources. This is typical for bedrock units with high radioactivity but limited surface exposure.

Figure 8.12 shows the calculated heat production ratio of the portable spectrometry to the airborne surveying.

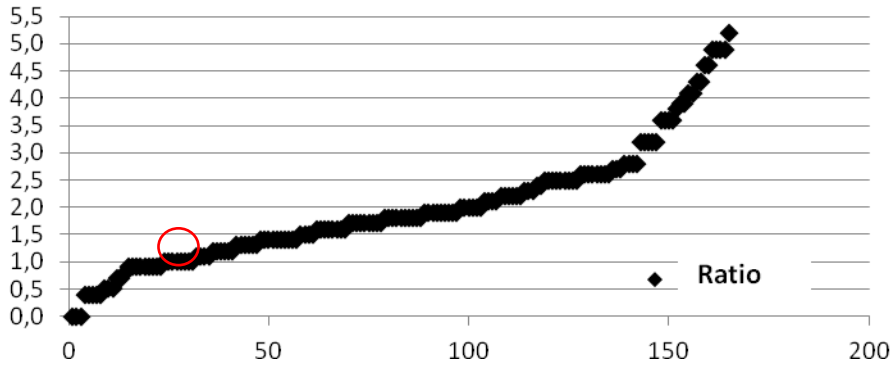

Figure 8.12. Calculated heat production ratio of the portable spectrometry to the airborne surveying. The red circle represents a 1:1 ratio.

9. COMPILATION OF GEOLOGICAL MAPS

Ole Lutro

9.1 Data

The bedrock geology map of the area covered by the first part of the COOP project has been compiled by combining five published maps at the scale of 1:250.000. They have been published over a considerable time span. The first one, Måløy, now called Florø, was published in 1970 (Kildal 1970), Mandal came out in 1982 (Falkum 1982), Stavanger in 1995 (Jorde et al. 995), Bergen in 1997 (Ragnhildstveit & Helliksen 1997) and Haugesund in 1998 (Ragnhildstveit et al. 1998). These maps were digitised after publication and have been published on the NGU web site where both raster and vector versions are displayed. However, they have only a generalised legend in the vector version. The map produced for the COOP project has been made seamless in the central part where the maps were compiled at roughly the same time and partly by the same authors. This version of the map contains as much information as is possible to obtain from the legend of the printed maps, such as rock names, tectonic and stratigraphic names and ages. The 1:250.000 map sheets were published with a description printed on the left-hand side. These have been converted to text-files and are included as Appendix E to the present report (they can also be found on the Ftp2.ngu.no - server as pdf-files). There is also an item in the map called strat_base which is a hyperlink to the stratigraphic database of Norway (http://aps.ngu.no/pls/oradb/geoenhet_SokiDb.Startapp). By clicking this you can obtain information on the stratigraphic names used in the map.

9.2 Geology

The area of interest stretches from Vest-Agder in the south to Sogn og Fjordene in the north (Fig. 9.1). It comprises both autochthonous and parautochthonous, Precambrian basement rocks and Caledonian thrust sheets containing both Lower Palaeozoic sedimentary rocks and Precambrian gneisses. Devonian sedimentary rocks were deposited at the end of the Caledonian orogeny on top of the Caledonian thrust sheets. The youngest rocks found are scattered, N-S-trending, dolerite dykes of Permian and Jurassic age (Fossen & Dunlap 1999).

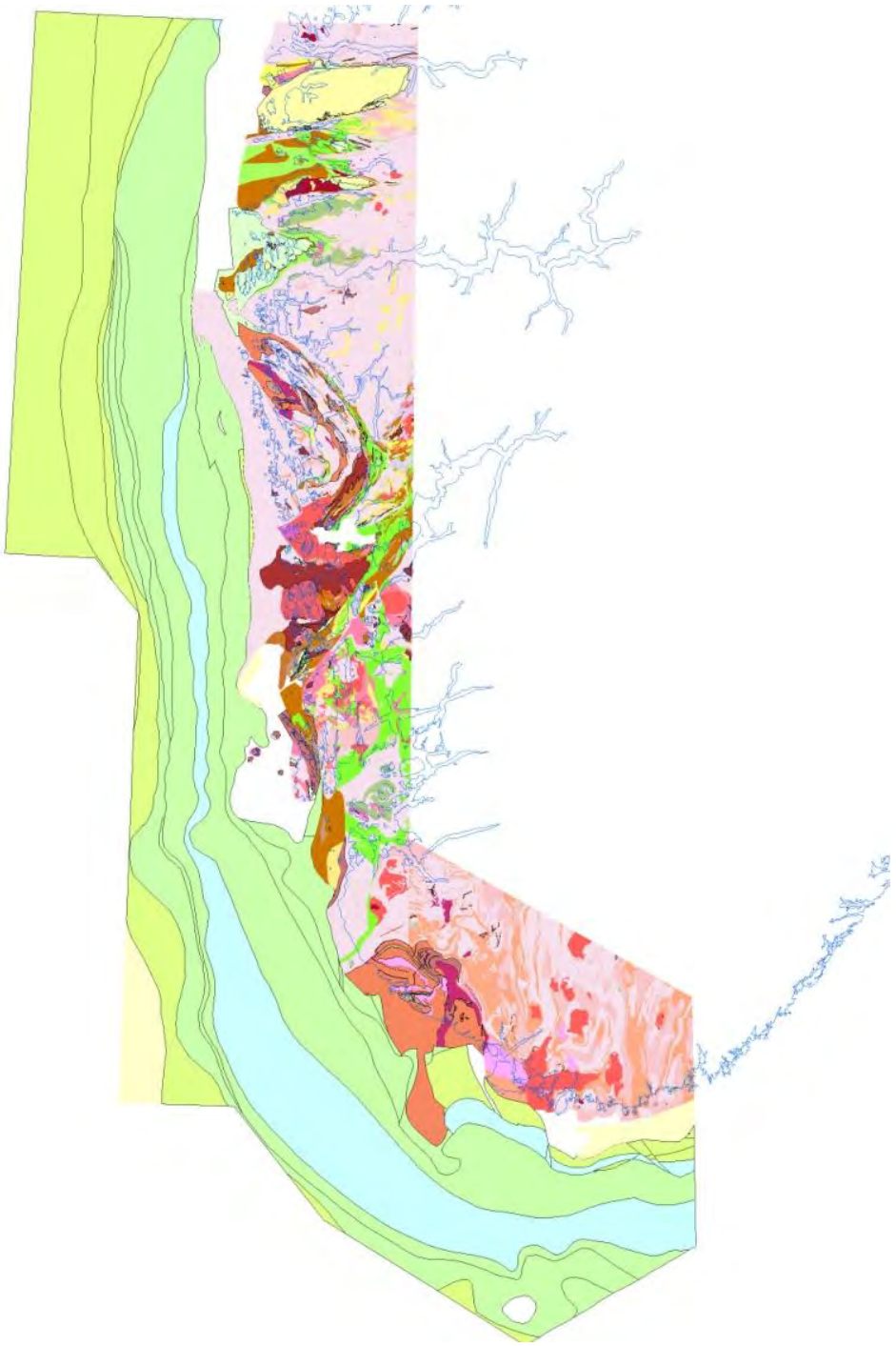

Figure 9.1. Geological map of the COOP 1 area.

Precambrian basement

The Precambrian basement occurs mainly in three areas: (1) In the northern part of the map, in the Western Gneiss Region, (2) in the Øygarden Complex west of Bergen and (3) in the extensive Precambrian area of southern Norway. All three areas belong to the Mesoproterozoic Sveconorwegian province of southern Norway. They consist mainly of granitic orthogneisses with minor amounts of metasedimentary rocks, in many places migmatitic. These rocks were formed during both the Gothian orogeny (1700-1500 Ma) and the Sveconorwegian orogeny (1200-900 Ma). Intruding the gneisses are large syntectonic

(1050-1020 Ma) and post-tectonic granites (990-920 Ma) (Slagstad et al. in press and references therein).

The Rogaland Igneous Complex represents part of the post-tectonic igneous activity in the area. Large bodies of anorthosite, mangerite and charnockite were intruded between 950 and 920 Ma. The magnetic map indicates that the complex continues offshore and the onshore part may constitute only a small part of the complex (Fig. 9.2). Around the intrusions there is a contact metamorphic aureole in granulite facies.

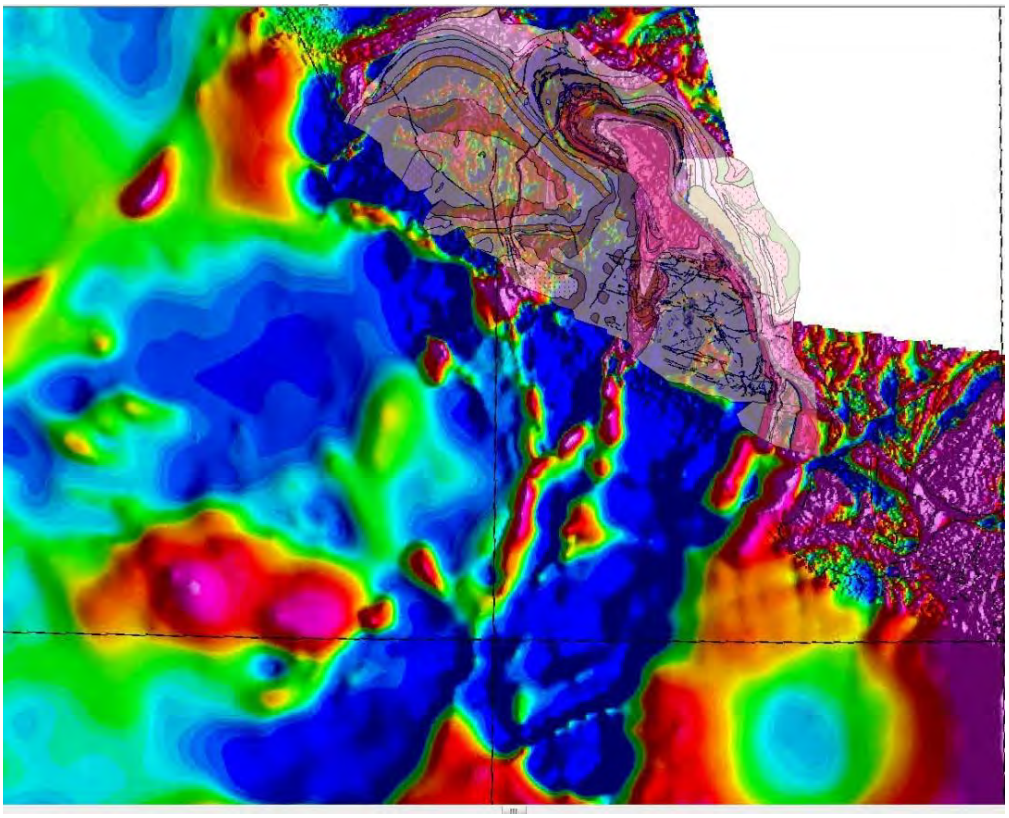

Figure 9.2. The onshore Rogaland Igneous Complex shown on the magnetic map, The magnetic low areas offshore are assumed to represent an offshore continuation of the Rogaland Igneous Complex.

The Øygarden Complex is probably connected to the Western Gneiss Region (WGR). This link is buried underneath the younger Caledonian nappes and has been modified by Caledonian structures.

The WGR and Øygarden Complex are separated from the autochthonous basement of southern Norway by Caledonian thrust sheets. The rocks of the WGR and possibly the Øygarden Complex took part in the Caledonian orogeny and were partly subducted to considerable depth during the collision between Baltica and Laurentia. This led to the formation of HP and UHP eclogites. The pressure increases toward northwest indicating that Baltica was subducted under Laurentia (Krogh 1977).

Caledonian rocks

Autochthonous, parautochthonous rocks

At the end of the Neoproterozoic era, the Precambrian basement was transgressed and covered by Late Neoproterozoic to Ordovician sediments (Bockelie & Nystuen 1985). In this area only thin layers of autochthonous sediments are found above the Baltican basement. On Haugalandet, these sedimentary rocks are Late Neoproterozoic(?) quartzites and arkoses and overlying Early Palaeozoic phyllites.

Allochthonous rocks

The majority of Caledonian rocks in the area are found in thrust-sheets, thrust on top of the autochthonous rocks. These rocks have been grouped into four major allochthons (Roberts & Gee 1985). In this area rocks assigned to the Lower, Middle and Upper allochthons are found (Bryhni & Sturt 1985). As well as the Mesoproterozoic basement gneissic rocks, the Lower allochthon contains mainly Neoproterozoic to Ordovician sedimentary successions from the margin of Baltica. The Middle Allochthon consists of minor Neoproterozoic to Ordovician sedimentary rocks and slices of Precambrian crystalline rocks from the outer margins of Baltica. The Upper Allochton includes island arcs and ophiolitic successions and associated sedimentary rocks formed outboard of Baltica in the Iapetus Ocean.

Lower allochthon

In the map area, the Lower Allochthon is represented by Cambrian to Ordovician schists in Ryfylke, usually called the Ryfylke schists.

Middle allochthon

The thrust-sheets in the middle allochthon contain Mezo- to Neoproterozoic rocks, gneisses and intrusive rocks with a thin cover of Neoproterozoic arenites and Cambrian and Ordovician schists. These include the Boknfjorden and Storheia Nappes in Rogaland and the Blåmannen, Mjånes, Slettafjellet and Grasberget Nappes in the Bergen area. The Lindås Nappe might be regarded as part of the Middle Allochthon and contains granulite-facies rocks such as charnockite, mangerite, gabbro and anorthosite. These rocks are similar to those in the Rogaland Igneous Complex and also in the Jotun Nappe Complex which is regarded as middle allochthon. Strongly deformed and retrograded anorthosites and related rocks are found in Sunnfjord and Nordfjord in the Eikefjord Group. The Dalfjorden suite, which consists mainly of syenite and gabbro, is also regarded as Middle Allocthon. In Sunnfjord, the crystalline rocks are overlain by schist and quartzites of the Høyvik and Lykkjebø groups.

Upper Allochthon

The thrust-sheets in the Upper Allochthon consist of ophiolite fragments and island-arc complexes overlain by oceanic sediments. The ophiolite complexes found on Karmøy, Bømlo, Gullfjellet and in the Bergen area are of early Ordovician age. They are all part of the Hardangerfjord Nappe Complex. Associated with the ophiolite fragments are intrusive rocks

such as the Utsira complex and the West Karmøy Igneous Complex. The Solund-Stavfjorden ophiolite complex is of Late Ordovician age.

Intruded into these rocks are several intrusive complexes such as the Sunnhordland Intrusive Complex and the Sygneskollen granodiorite. The age of these intrusions is around 430 Ma.

The emplacement of the allochthonous units took place towares the end of the Silurian period (generally called the *Scandian* phase of the Caledonian orogeny) as they were thrusted onto the Baltican continental margin from a west-northwest source (present-day coordinates).

Nordfjord-Sogn Detachment Zone

At the end of the Caledonian orogeny, the compressional pevent was followed by a phase of extensional collapse probably due to tectonic instability. In this part of Norway this extensonal phase was first described by Hossack (1984) and Norton (1986) coined the term Nordfjord-Sogn Detachment Zone (NSDZ) for a major extensional detachment zone found between Sogn and Nordfjord. The detachment is a low-angle normal fault-zone which reaches up to 6 km in thickness and started to develop under amphibolites-facies conditions (Johnston et al. 2007). Structures within the zone show late-Scandian top-to-the-west movements.

Later brittle faults are more localised structures and involve low-angle faults beneath the eastern margins of the Devonian deposits of western Norway and steeper E-W-trending normal faults.

The NSDZ is, in part, responsible for the exhumation of a great part of the lower crust. In the hanging-wall of the fault there are low-grade Caledonian rocks and Devonian deposits. In its footwall one finds eclogites that formed at depths of 80-90 km (Johnston et al. 2007).

The Bergen Arc Shear Zone (BASZ) along the Fensfjorden is described as an extensional shear zone (Wennberg et al. 1998) and most probably represents a continuation of the NSDZ . The most southern observation of the NSDZ is on the northern shore of Sognefjorden in the Solund area. An interpretation of how it probably continues and links up with the BASZ is shown in Fig. 9.3.

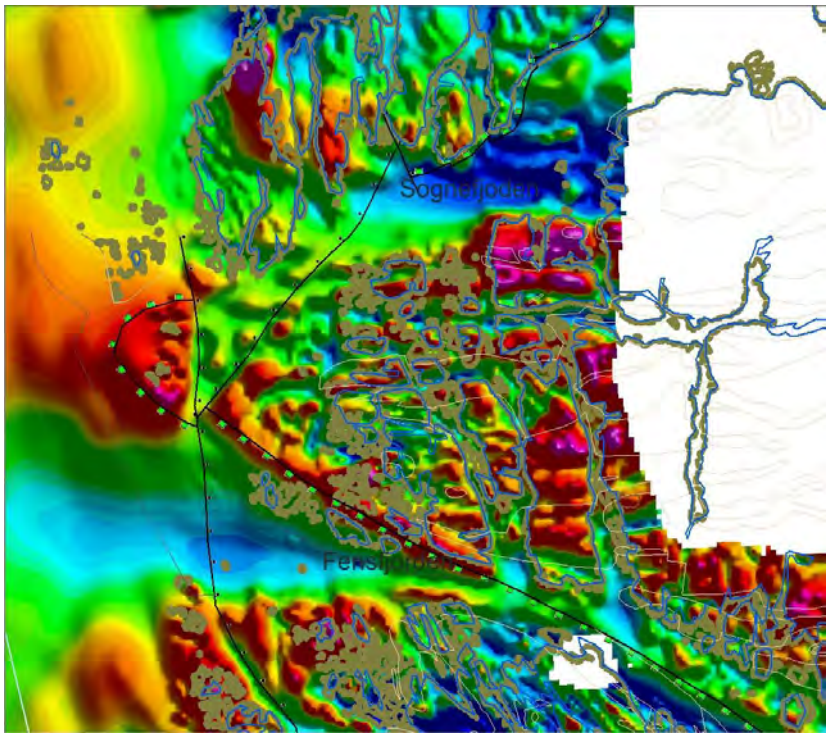

Figure 9.3. The possible continuation of the Bergen Arc Shear Zone northwest of Fensfjorden into the Sognefjorden area where the Nordfjord Sogn Detachment Zone starts.

A third major detachment feature is the Hardangerfjord Shear Zone which has a total length of 600 km (Andersen & Hurich 2006). This shear zone might have both a Precambrian and a Palaeozoic history (Andersen & Hurich 2006).

Devonian sedimentary rocks

Devonian deposits are found in four areas that have been considered to represent four, separate, fault-bounded, sedimentary basins. The four basins are the Solund, Kvamshesten, Håsteinen and Hornelen basins. The Solund basin is dominated by conglomerates but also contains intermediate to acid lavas (Furnes & Lippard 1983) interpreted as landslides (Hartz et al. 2002) that probably originated from the Solund-Stavfjord Ophiolite Complex. The Kvamshesten basin consists of both sandstones and conglomerates (see descriptions by, e.g. Osmundsen et al. 2001). The Håsteinen basin is dominated by conglomerates. The Hornelen basin exposes a marginal conglomerate deposited by debris flows which interfingers with sandstone layers. The sandstone strata occur in upward coarsening sequences dipping at around 20 to 30° towards the west producing a characteristic step-wise landscape (Fig. 9.4).The apparent stratigraphic thickness of the Hornelen basin succession is in excess of 20 km, and the metamorphic grade is similar in the oldest western part of the basin and in the eastern youngest part.

Figure 9.4. The Hornelen basin. The figure is an ortho-photo from "Norge i bilder" (http://www.norgeibilder.no/)

Offshore subcrop units

Geophysical data indicate that the subcrop of the Eocene is slightly misinterpreted west of Bergen. The analytic signal of the magnetic compilation shows pipelines and sand channels as symmetric linear features whereas the asymmetric linear features are interpreted as the subcrop of Eocene strata dipping west (Fig. 9.5). See also Chapter 11 in the present report. The corrected subcrop units are shown in Figures 9.1 and 9.6B

ArcGIS database

The digital geological map, coop_1_pl, can be found on the ftp2.ngu.no/database directory in the coop_geology.gdb File Geodatabase. There is also an associated layer file, coop_1_pl.lyr. This file uses the feature hovedbergart to symbolise the map.

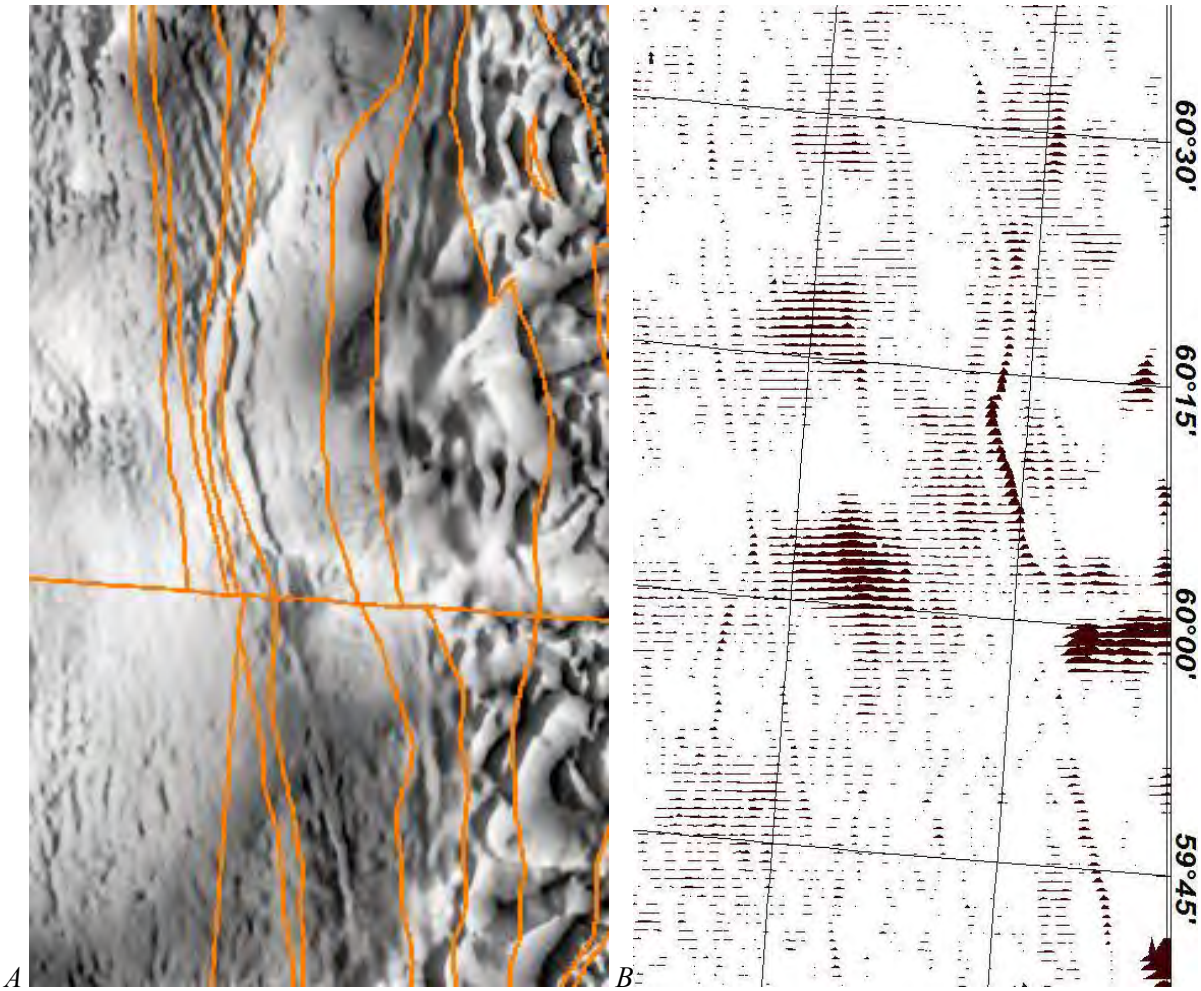

Figure 9.5 A) The original Cenozoic subcrop units on the 1:250.000 bedrock maps Haugesund and Bergen (Ragnhildstveit et al. 1998 and Ragnhildstveit & Helliksen 1997, respectively) plotted on the analytical signal of the aeromagnetic data compilation reveal a misinterpretation of the seismic reflectors; the subcrop pattern crosses the magnetic anomalies. B) Part of Fig. 11.4 showing a stackplot of the 8 km high-pass filtered profile data. The asymmetry of the coast-parallel anomalies with a steep gradient to the east and a gentler gradient to the west shows that the sources of the anomalies dip gently towards the west, consistent with interpretations of seismic data (Ragnhildstveit & Helliksen 1997).

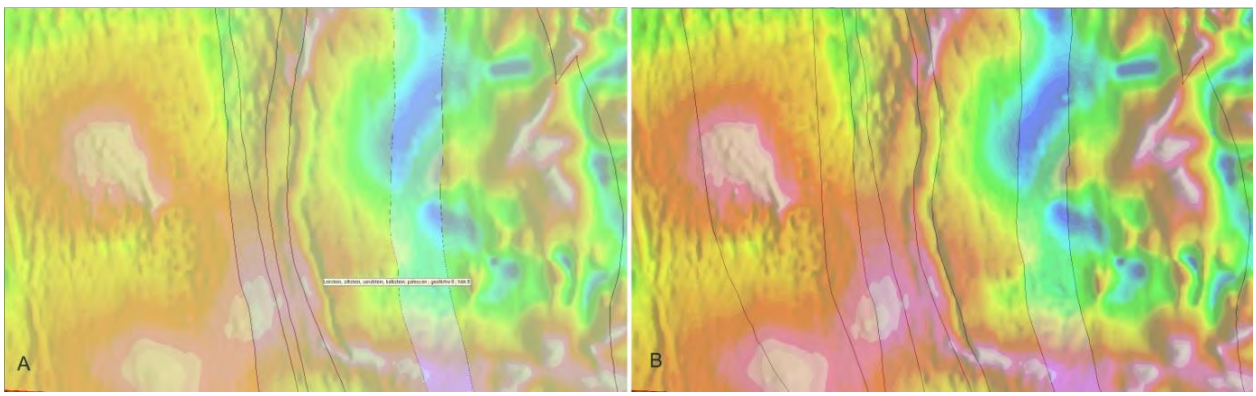

Figure 9.6 A. The original map of the subcrop of Cenozoic strata to the west of Bergen; B The reinterpreted subcrop of the Eocene strata.

10. 2D PROFILES

Jörg Ebbing and Per Terje Osmundsen

The following chapter presents 2D modelling performed along the two seismic reflection lines released to the project (NSR06-31174 and NSR06-31142-2, see Fig. 10.1). The interpretation of the long-offset seismic lines was carried out with the objective to identify the main structural elements and to provide an independent interpretation of the top basement and crustal structure as an input for the 3D modelling (see Chapter 12).

The crustal-scale architecture of the North Sea has been featured only in a few published studies, and we compare our interpretations especially with those of Christiansson et al. (2000) and Fichler et al. (2011).

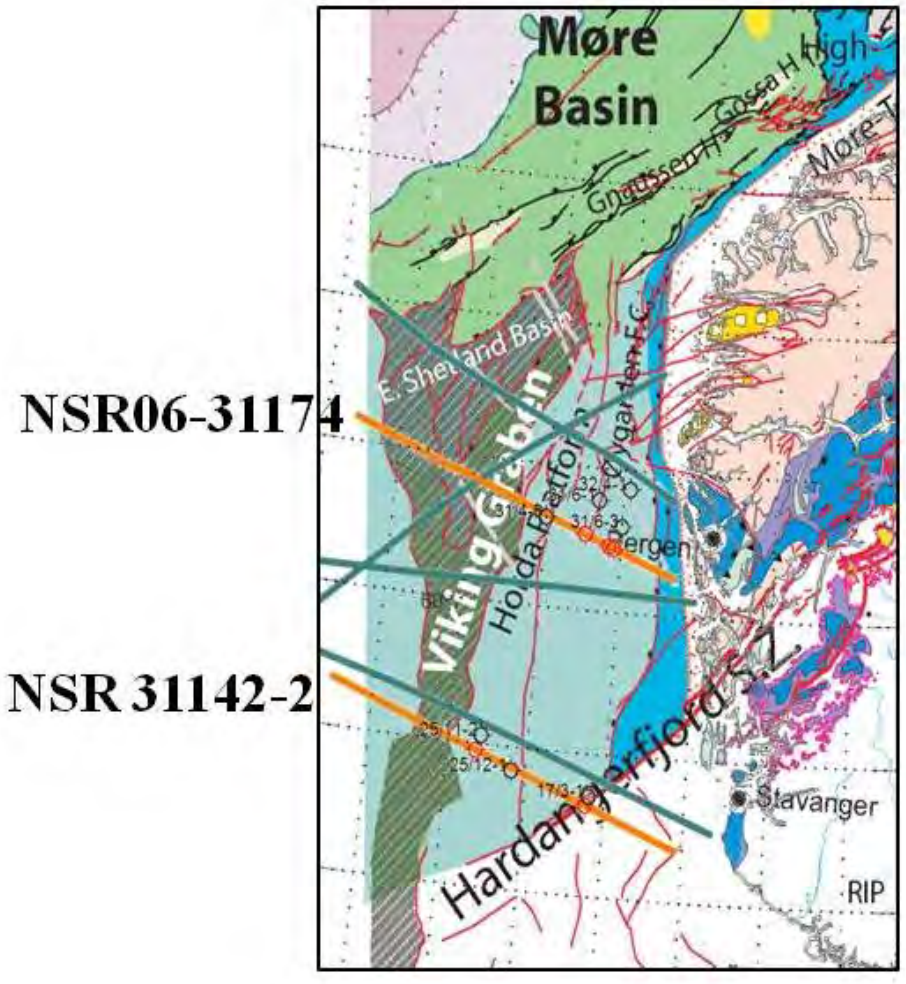

Figure 10.1 Location of the NSR profiles (orange lines) on top of structural map of western Norway and the Viking Graben (modified after Mosar 2003). The green lines indicate the locations of 4 geoseismic sections from Christiansson et al. (2000). The northernmost profile has also been interpreted by Fichler et al. (2011). Also indicated with black circles are the wells close to the NSR lines.

The workflow in the interpretation of the 2D lines included seismic interpretation using the information from a number of available wells and depth conversion of the twt-interpretation as a basis for gravity and magnetic modelling. Modelling of the gravity and magnetic field was relatively straightforward from the seismic interpretation (see detailed description) and no modifications of the seismic interpretations were needed. In the last step, we discuss the interpretation of the 2D lines with onshore analogues, the magnetic depth estimates in Chapter 7 and the structural and lithological interpretations by Christiansson et al. (2000) and Fichler et al. (2011), respectively.

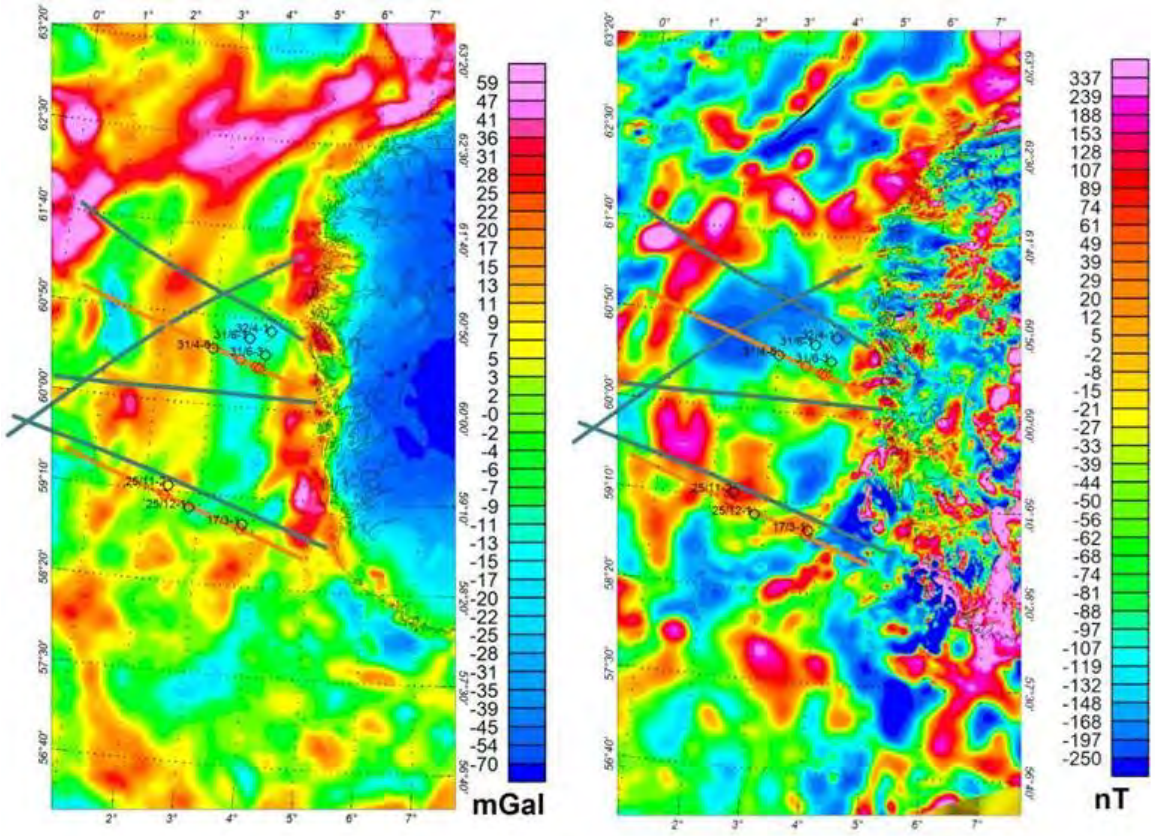

Figure 10.2 (Left) Bouguer anomaly, (right) magnetic anomaly map after Olesen et al. (2010) The locations of the NSR lines, profiles from Christiansson et al. (2000) and used wells are also shown.

The two profiles cross different features of the study area, and notably the southern profile is running perpendicular to the offshore expression of the Hardangerfjord Shear Zone (Fig. 10.1). This is also seen in the location of the profiles with respect to the magnetic and gravity map in Figure 10.2.

The two profiles cross different features of the study area, and notably the southern profile is running perpendicular to the offshore expression of the Hardangerfjord Shear Zone (Fig. 10.1). This is also seen in the location of the profiles with respect to the magnetic and gravity map in Figure 10.2.

10.1 Seismic interpretation

Interpretation and depth conversion of the seismic reflection data was performed using the Easydepth (R) module of Temis, a software package provided by Franlab-Beicip. The NSR 06-31142 and NSR 06-31174 lines were acquired by TGS-NOPEC and recorded to 9 s twt. The data quality is good to excellent down to between 4 and 6 seconds two-way time (twt). This allows for a detailed interpretation of deep structures and basins in a number of areas. Inside the basement, information is limited, and reflectivity in the middle and lower crystalline crust could rarely be interpreted with confidence.

Key horizons interpreted in the seismic lines include the near base of Tertiary (BT in Figure 10.3), the northern North Sea Unconformity Complex (Kyrkjebø et al. 2004), abbreviated here by the more traditional BCU, the near base Jurassic (NBJ) and the top of the seismic basement (SB). The top of the seismic basement is locally underlain by reflectors that may indicate the presence of deep-seated, Palaeozoic basins. In some selected areas, we have outlined some alternatives for the top of the basement. The upper alternative is, however, the one that can be traced with the least difficulty across the sections, and has been chosen as the basis for the potential field modelling. In both profiles, unconformities are imaged in the Triassic or pre-Triassic successions of deep basin areas. These have been mapped in restricted areas. The top of basement could be interpreted with some confidence in parts of the sections, whereas in other parts, a well-defined top basement reflector is lacking. In addition to the colour-coded key horizons, a large number of other reflectors were traced to illustrate stratal patterns in the different stratigraphic units, such as downlap and onlap relationships. This includes, for instance, reflectors that outline major progradational units in the Cenozoic.

For the depth conversion, velocity models were constructed using the velocities reported by Christiansson et al. (2000) in combination with velocities calculated from nearby wells. The Moho interpretation results from the modelling and was added to the profiles after depth conversion. It is not our objective to describe the stratigraphy of the North Sea in any detail; this has been done in a number of published works as well as by studies carried out in the partner companies. We focus on the large-scale structure and on certain observations that are pertinent to the potential field modelling or the geological interpretation below the BCU.

10.1.1 The southern section (NSR06-31142-2)

The section crosses the Åsta Graben, the Utsira High and the Viking Graben. Figure 10.3 presents our interpretation in two-way time (twt) and depth, respectively. The modelled Moho shown in the depth-converted section rises from a depths of between 28 and 30 kilometres at the ends of the section to c. 25-26 km beneath the Viking Graben and under the area of 17/3-1. Thus, the Moho is 2-3 kilometres deeper than that interpreted by Christiansson et al. (2000) for their transect located 20 km to the north of the present section.

The Viking Graben is markedly asymmetric in this location, with the larger downthrow on the northwest side (Fig. 10.3). In the Viking Graben, sediment thicknesses are in the order of 10-12 kilometres in our interpretation, depending on the pick of top basement. High-amplitude reflectors, interpreted to represent deep parts of the basin stratigraphy occur down to between 5 and 6 s twt (c. 8 and 10 kilometres depth in the depth-converted section). The age and origin of these layers are uncertain but it is likely that they represent either Permian salt (e.g. Thomas & Coward 1996, Jackson & Larsen 2008) or volcanic rocks. Throw on the master fault complex on the west side of the graben is correspondingly in the order of several kilometres, perhaps as much as 8-10 kilometers. It is flanked by a growth section that is c. 4 kilometres thick measured from the base of the `synrift´section (gold reflector) to the BCU. On the eastern side of the graben, the thickness of this section is reduced to 1-2 km orless.

A broad, gentle anticline occupies central parts of the Viking Graben, including lower parts of the Cretaceous succession. The crest of the anticline is relatively sharp at the level of the golden reflector but the amplitude decreases stratigraphically upwards into low levels in the Cretaceous. Thus, the stratigraphic growth interval for the anticline largely overlaps with that of the main synrift growth section and thus with extensional faulting along the main, western graben-bounding fault. Normal faults are also observed across the anticline and in particular at 4-4.5 s twt between the anticlinal crest and the western flank of the Utsira High, where they cut and offset a deep-seated, high-amplitude, reflector package. A smaller anticline occurs at the base Cretaceous level close to the main graben boundary fault.

Formation of the anticline was related to sliding on Zechstein salt by Thomas & Coward (1996). Zechstein salt was encountered in wells on the southwestern flank of the Utsira High (e.g. Jackson & Larsen 2008, Jackson et al. 2010). Jackson & Larsen (2008) used biostratigraphic data and detailed seismic interpretation to constrain the timing of inversion to the interval between the late Early Volgian and the Late Albian. From our section, it can be argued that a gentle anticline also shows at the lowermost Cenozoic levels and that inversion as such may not have ceased in the Early Cretaceous.

To the east of the Utsira High, the basement topography is characterised by horsts and grabens that are associated with Triassic and possibly pre-Triassic basins. Internal unconformities are identified that relate to the rotation history of the half-graben. The present project did not include a regional correlation study of the deep levels of the rift, and thus the ages of these deep unconformities are not well constrained. They must, however, be Triassic or older, based on the wells used to constrain the stratigraphy of the section. Our southern profile is outside of, but close to the northern boundary for Permian Zechstein salt as it is drawn in, for instance, the Millennium Atlas (Glennie et al. 2003). Thus, the possibility exists that Permian salt may come into the section also east of the Utsira High. The interpreted sections are therefore shown with alternative top basement interpretations in the southeastern parts of the line. In the most shallow basement alternative, the convex-up reflector package observed at c. 3.8 s twt represents a warped shear zone in the basement, similar to that

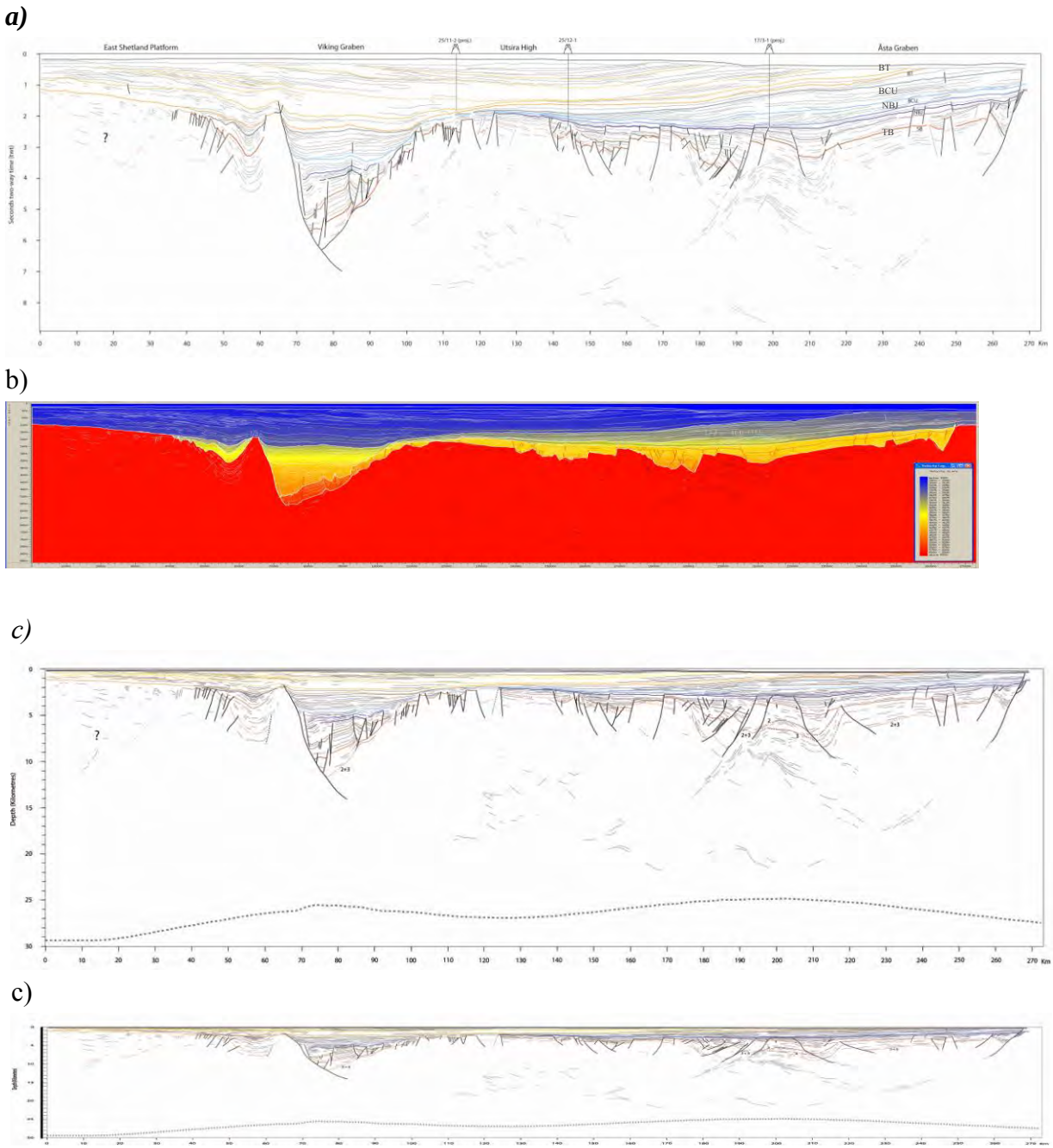

Figure 10.3. *Line-drawing interpretation of seismic reflection line NSR06-31142-2. (a): interpretation in two-way time (twt), (b) Velocity model based on Christiansson et al. (2000), (c) Depth-converted interpretation (vertically exaggerated) and (d) Depth-converted interpretation with no vertical exaggeration. The red line represents the top of seismic basement, and brown lines are deep-seated unconformities in the pre-Jurassic synrift fill under the Horda Platform. Dark blue reflectors represent near base Jurassic and medium Bluethe near base of Upper Jurassic. Light blue: `Base Cretaceous´. Green: Lower Cretaceous reflector. Orange: Base of Tertiary. Yellow reflectors are unconformities in the Cenozoic succession. See text for more explanation.*

observed onshore in the footwall of the Hardangerfjord Shear Zone (HSZ, Fig.10.7). The lower top basement alternative would open for interpretation of the convex-upwards reflectors in the vicinity of 17/3-1 as a salt pillow; in this scenario, parts of the upper basement alternative could tentatively represent the top of a Permian succession. However, 17/3-1 encountered metamorphic basement directly under Triassic strata at a measured depth of 2852

m. The deeper basin alternative would thus require Permian rocks to pinch out between the seismic line and 17/3-1.

East of the Utsira High, two (N)W-dipping major faults can be identified in the pre-Jurassic succession. One is positioned close to the end of the section and has a throw of about 1 s twt at the interpreted top basement level. Strongly SE-dipping reflectors are observed underneath gently northwest-dipping Triassic reflectors in the flanking half-graben basin, The other is located just west of 17/3-1, and bounds a c. 20 km wide half-graben basin with SE-dipping Triassic and pre(?)-Triassic strata. Reflectors interpreted to represent a fault or a fault-related shear zone can be traced to c. 6 s twt, well inside the basement in our interpretation. It is possible that this reflector band could represent faulting along the continuation of the Hardangerfjorden Shear Zone (Fig. 10-7), as the HSZ does enter the general area. However, consulting the NPD structure map of the area, the southernmost Øygarden Fault Complex (ØFC) is an equally good or better canditate. The hangingwall cutoff to the adjacent half-graben basin is at c. 3.5 s (upper basement alternative) or close to 5 s (lower top basement alternative). The sediment thickness in the resultant pre-Jurassic half-graben would be between 3 and 6 kilometres.

The large-scale geometry of the Utsira High resembles that of a faulted rollover in the hanging wall of the western graben boundary fault. The high is densely faulted in a horst-and- graben pattern that largely pre-dates the base of the Cretaceous. A number of small Triassic and Jurassic `mini´-basins on the southwestern parts of the high were related to salt withdrawal by Jackson et al. (2010). Along our section, the stratigraphy identified in the deep half-graben basin to the east of the high can be traced with some confidence towards the well 25/12-1. An array of faults to the east of this well does, however, complicate the interpretation of the pre-Cretaceous stratigraphy onto the main part of the Utsira High. The well 25/12-1 was reported to terminate in coarse Devonian clastics. However, the assessment of age for these basal deposits was based entirely on sedimentary facies (see NPD fact pages and Completion report for 25/12-1). Thus, it is possible that these rocks may be of an age other than Devonian, for instance Triassic or Permian.

10.1.2 The northern line (NSR06-31174)

The northern section crosses the Horda Platform, the Viking Graben, the Tampen Spur/East Shetland Basin and the easternmost parts of the East Shetland Platform. In this section, the modelled Moho rises from between 29 and 30 kilometres depth at the ends of the section to c. 23 km under the Viking Graben and western parts of the Horda Platform. This is deeper than the Moho interpreted by Christiansson et al. (2000) for their northern transect, located c. 60 kilometres north of the present line. Correspondingly, the crust is c. 3 kilometres thicker beneath the Viking graben under our northern transect compared to their northern section. The interpretation of the top basement under the Viking Graben, however, is not well constrained.

a)

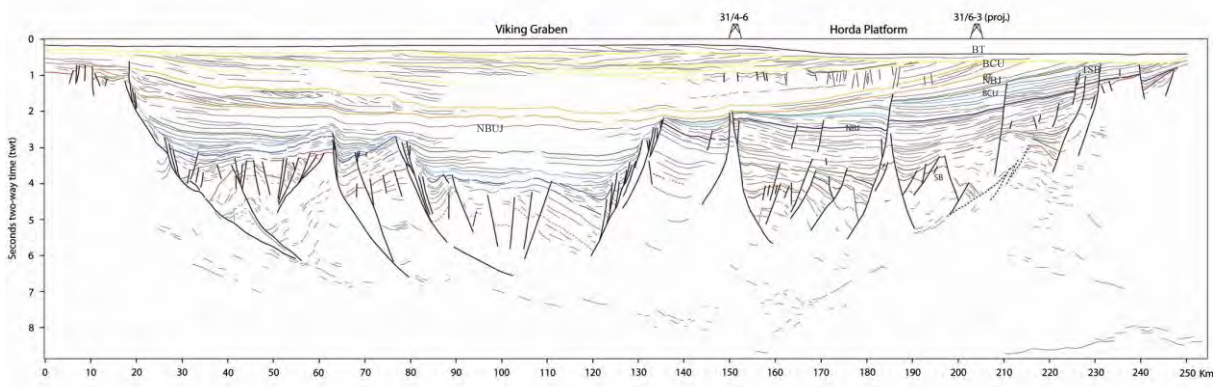

b)

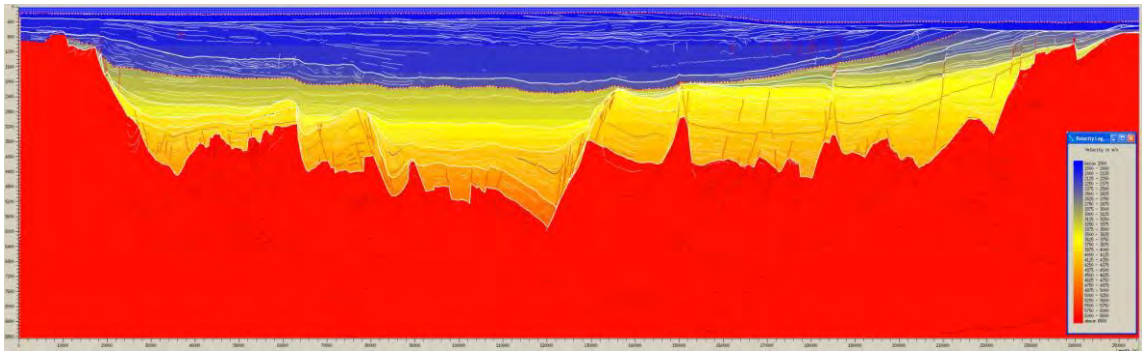

c)

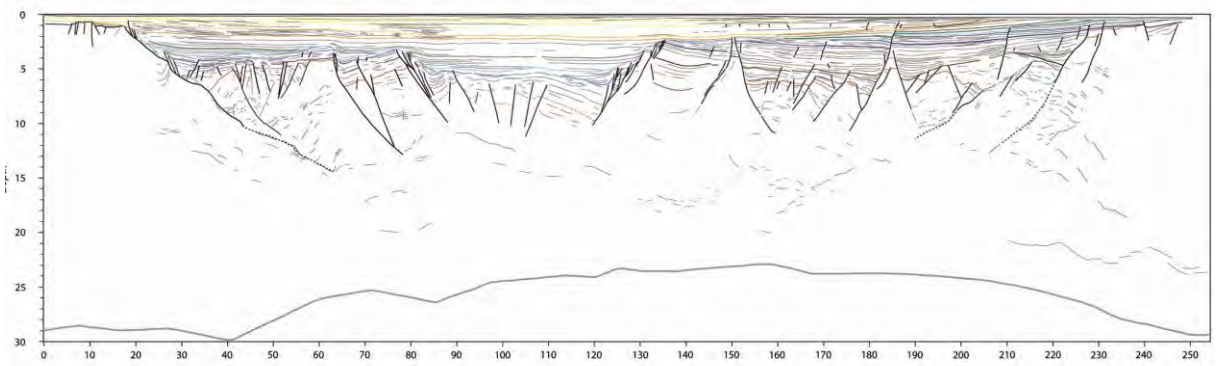

d)

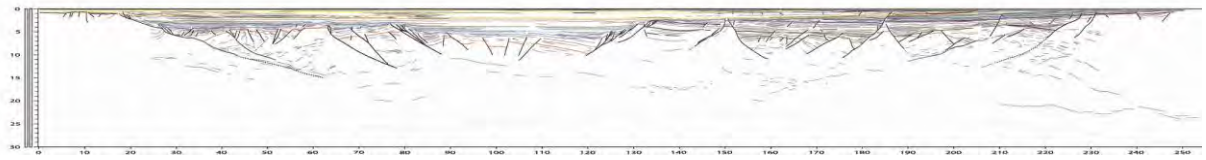

Figure 10.4. Line-drawing interpretation of seismic reflection line NSR06-31174. (a) interpretation in two-way time (twt), (b) Velocity model based on Christiansson et al. (2000), (c) Depth-converted interpretation (vertically exaggerated) and (d) Depth-converted interpretation with no vertical exaggeration. The red line represents the top of seismic basement, and brown lines are deep-seated unconformities in the pre-Jurassic synrift fill under the Horda Platform. Dark blue reflector represent near base Jurassic and medium blue near base of Upper Jurassic. Light blue: `Base Cretaceous´. Green: Lower Cretaceous reflector. Orange: Base of Tertiary. Yellow reflectors are unconformities in the Cenozoic succession. See text for further details.

In the eastern parts of our section, deep pre-Jurassic basins under the Horda Platform are well imaged. As is the case with the southern line, the top of the seismic basement locally occurs above reflectors that may represent deep basin strata and the top of seismic basement may thus not everywhere coincide with the top of true metamorphic basement. The Øygarden Fault Complex (ØFC) is well imaged close to the southeast end of the section. In this location, the main strand of the ØFC barely affects the Jurassic and Cretaceous strata, and the upper parts of our pre-Jurassic succession, which includes units in the Upper Triassic, show a marked thinning towards the southeast and small offsets across the ØFC.

On the contrary, a pre-Jurassic syn-rift unit below this level displays a c. 3 km thick growth section towards the ØFC and also thickens towards the antithetic fault located c. 40 km to the northwest of the ØFC. Some 10 km northwest of the ØFC, a deep-seated fault or fault array appears to produce c. 3 kilometres of additional throw of the top of seismic basement. The lower parts of the stratigraphy preserved in the hanging wall of this fault do not display much reflectivity and could, tentatively, represent a Palaeozoic basin.

The Viking Graben appears to be relatively symmetric as compared to our southern profile. Wedge-shaped, Upper Jurassic deposits flank the graben with reflectors that downlap on older and more planar strata, that are likely to be Mid Jurassic in age. Reflectivity indicates rotated fault-blocks to 6 s twt or at least 10 km, but the top of the crystalline basement is difficult to assess in the graben. Again, the top of the seismic basement does not necessarily correspond to the top of the crystalline basement.

10.2 Modelling of the gravity and magnetic field

Based on the line drawings and the seismic velocity model, in the next step we modelled the magnetic and gravity field along the two profiles. The applied densities are in agreement with the velocity model using empirical relations as used in Ebbing et al. (2009) or Fichler et al. (2011). Susceptibility values have also been used from these studies, and remanence has been largely been ignored and is here included as part of the susceptibility. The magnetic field has been modelled with an inclination of 73º, declination of -1.5º and total field strength of 51030 nT.

10.2.1 The southern profile

Using the geometry from the seismic interpretation and, for the deep part, from Christiansson et al. (2000), allowed us to adjust the modelled gravity field to the observed Bouguer anomaly with little crustal internal variation (Fig. 10.5). The Bouguer anomaly shows only amplitudes +/-15 mGal and can mostly be addressed by the geometry of the top basement and variations in crustal density in the order of 2700 +/- 50 kg/m^3. Such a variation is within the errors of velocity-density conversions.

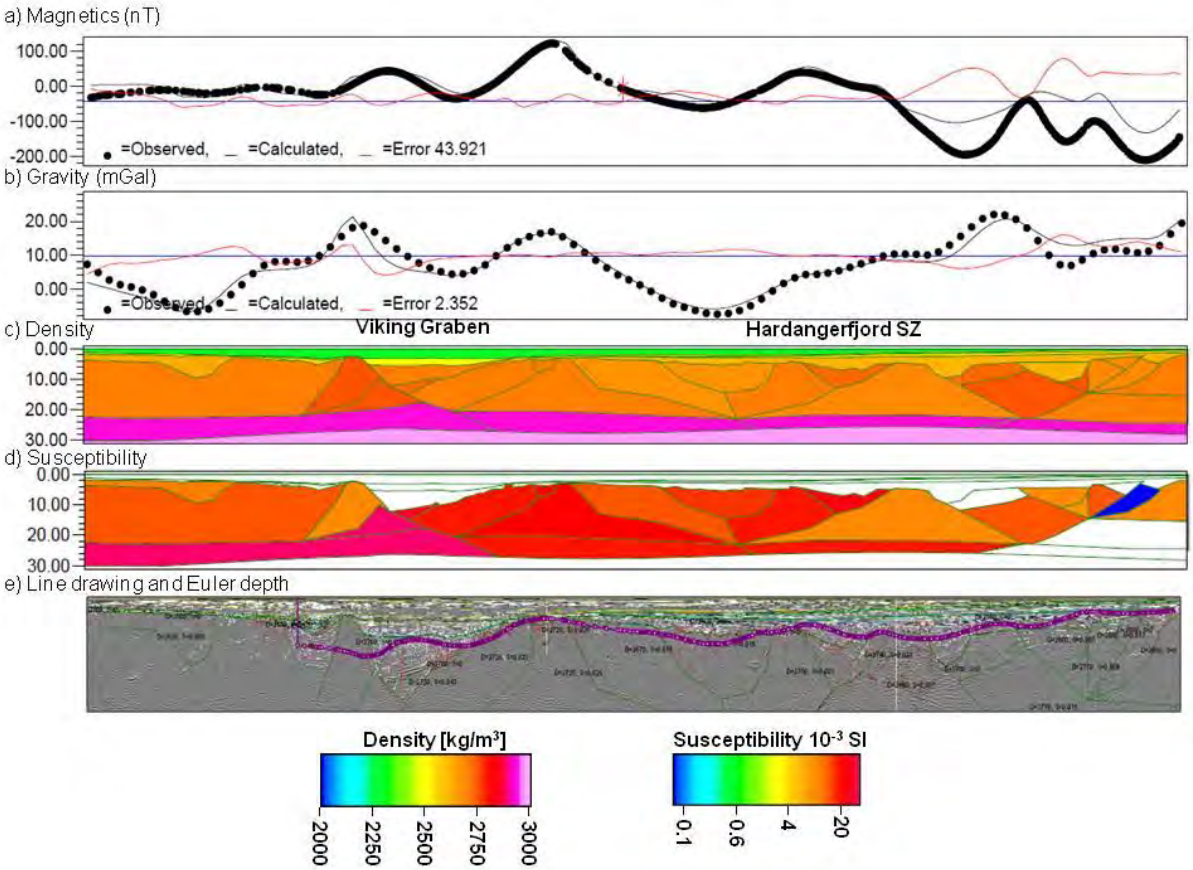

Figure 10.5 3D modelling of the southern profile NSR31142-2. (a) Observed, modelled and residual magnetic anomaly, (b) Observed, modelled and residual gravity anomaly, (c) Density structure, (d) Susceptibility structure, (e) Seismic line drawing and magnetic depth estimates using Euler deconvolution.

The magnetic field was more complicated to address: (1) the lower crust west of the Viking Graben required high susceptibility. Such high magnetisation is unusual for lower crustal rocks, but in agreement with similar observations by Fichler et al. (2011). (2) The main magnetic high east of the Viking Graben did not correlate with the top basement geometry. However, the magnetic high corresponds to a gravity high, which made it reasonable to address this high by a slightly increased susceptibility in the basement. (3) At the eastern end of the profile, landwards from the Hardangerfjord Shear Zone, the magnetic field could not be addressed with reasonable magnetic parameters. Comparison with Figure 10.2 shows that the profile is located at the transition between magnetic low to the north and a magnetic high to the south. In this case, the 3D geometry has to be modelled in order to address the changes in magnetic properties, which cannot be achieved by 2D modelling.

10.2.2 The northern profile

For the northern profile, both the gravity and magnetic field could be addressed, but the properties of the crust had to be varied more significantly. For the gravity field, the lower crust west of the East Shetland basin has a slightly lower density than the lower crust on the rest of the profile. This lower crust also has a higher susceptibility than in the central part of

the profile. Beneath the East Shetland Basin and extending beneath the Viking Graben a crustal feature (sliver) has been introduced, which has an unusually low susceptibility and a relatively high density. This sliver had to be introduced to be able to present the prominent magnetic low and gravity high, which extend from the East Shetland Basin to the Horda Platform. As will be discussed in section 1.3.4, this might indicate the presence of metasedimentary rocks.

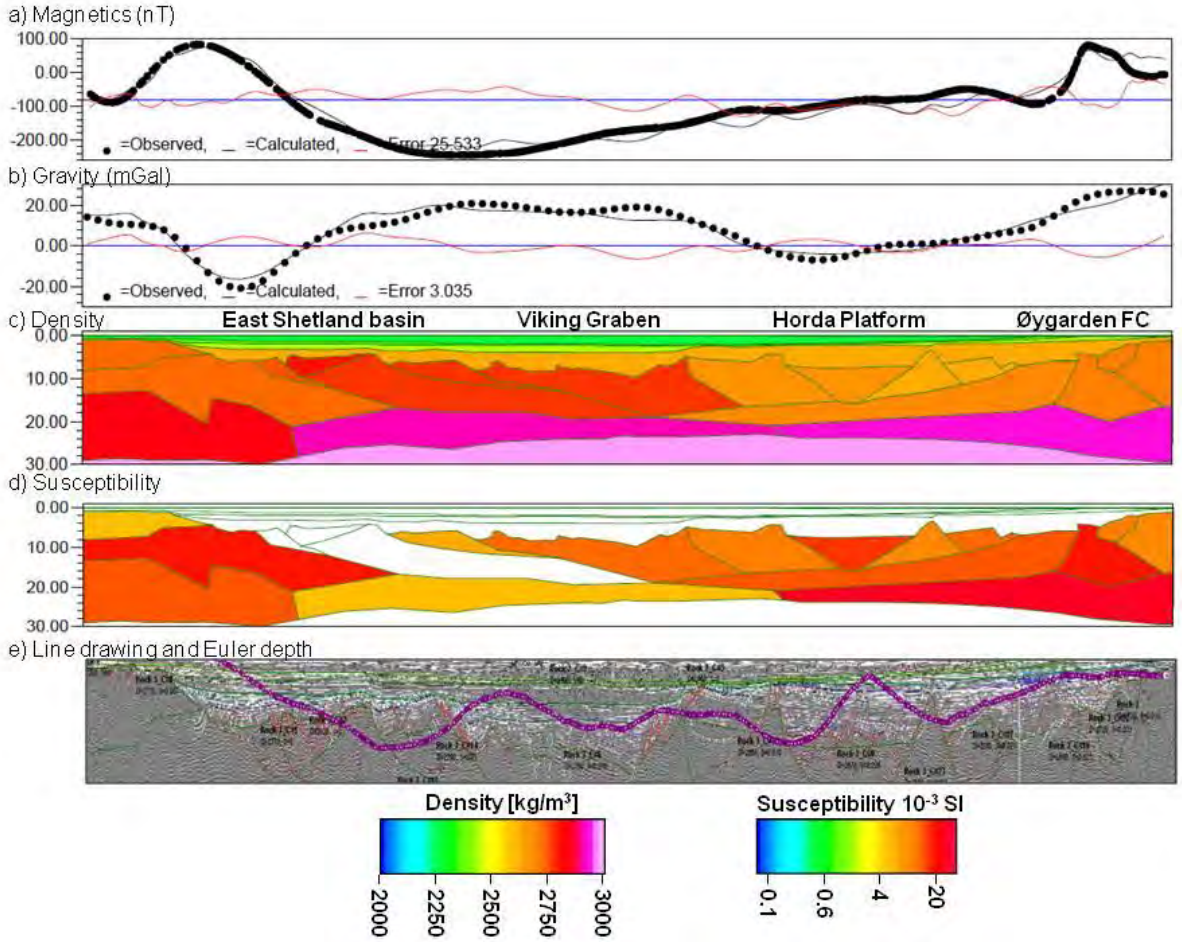

Figure 10.6 Density and susceptibility structure along the northern profile NSR06-31174. (a) Observed, modelled and residual magnetic anomaly, (b) Observed, modelled and residual gravity anomaly, (c) Density structure, (d) Susceptibility structure, (e) Seismic line drawing and magnetic depth estimates using Euler deconvolution.

10.3 Interpretation

The main task of the 2D interpretation was to provide a structural input file to the 3D model (see Chapter 12). However, already from the results presented here, some interesting conclusions can be made.

10.3.1 Comparison to onshore geology

The continuation of the Hardangerfjord Shear Zone (HSZ) into the area of the Stord Basin/Ling depression has been proposed by several authors and linked to the evolution of Permo-Triassic and younger basins in the offshore areas (e.g. Færseth 1996, Andersen et al. 1999). The HSZ is characterised onshore by a c. 5 km-thick succession of footwall mylonites

(Fossen & Hurich 2005). Along its northeastward continuation, brittle faults such as the Lærdal-Gjende Fault follow the main trend of the HSZ and are characterised by mylonitic footwalls (Andersen et al. 1999). Down-to-the northwest movements of the hanging wall have resulted in up to 10-15 km of normal displacement across the shear zone. The footwall is characterised by a culmination defined by warped gneissic foliation and lithological boundaries, whereas the hanging wall is characterized by a gentle synform defined by deflected Caledonian nappes (Fig. 10.7). The aeromagnetic map in Figure 10.8 indicates that the ductile Hardanger Shear Zone does not extend into the Ling Graben but bends southwards into Karmsundet between Karmøy and Haugalandet on the mainland. In the offshore, the seismic reflection data (NSR06-31142-2) indicate the presence of a convex-upwards feature at depth in the vicinity of 17/3-1. The area is one of structural complexity as the Øygarden Fault Complex merges with the northwest boundary of the Ling depression to the southwest of 17/3-1 (NPD structural map). Several authors have suggested that the extrapolated HSZ would arrive in this area and the culmination observed in our section is clearly flanked by a large fault with a significant down-to-the-northwest throw. The half-graben basin to the northwest of the culmination contains pre-Jurassic synrift rocks, likely to be Early Triassic or Permian in age (see for instance Færseth, 1996). This would be consistent with the ages obtained from the onshore Lærdal-Gjende Fault, which has documented Permian and Jurassic faulting events (Andersen et al. 1999).However, the fault and culmination may equally well be be related to the southernmost part of the Øygarden Fault Complex, as indicated by the NPD structural map of the area. In this case, the question arises where the Hardangerfjord Shear Zone continues. One possible explanation may be found in the magnetic data, which show a southwards deflection of the strong reflectivity that emerges from Hardangerfjorden and that may represent mylonites of the type described by Fossen & Hürich from the HSZ.

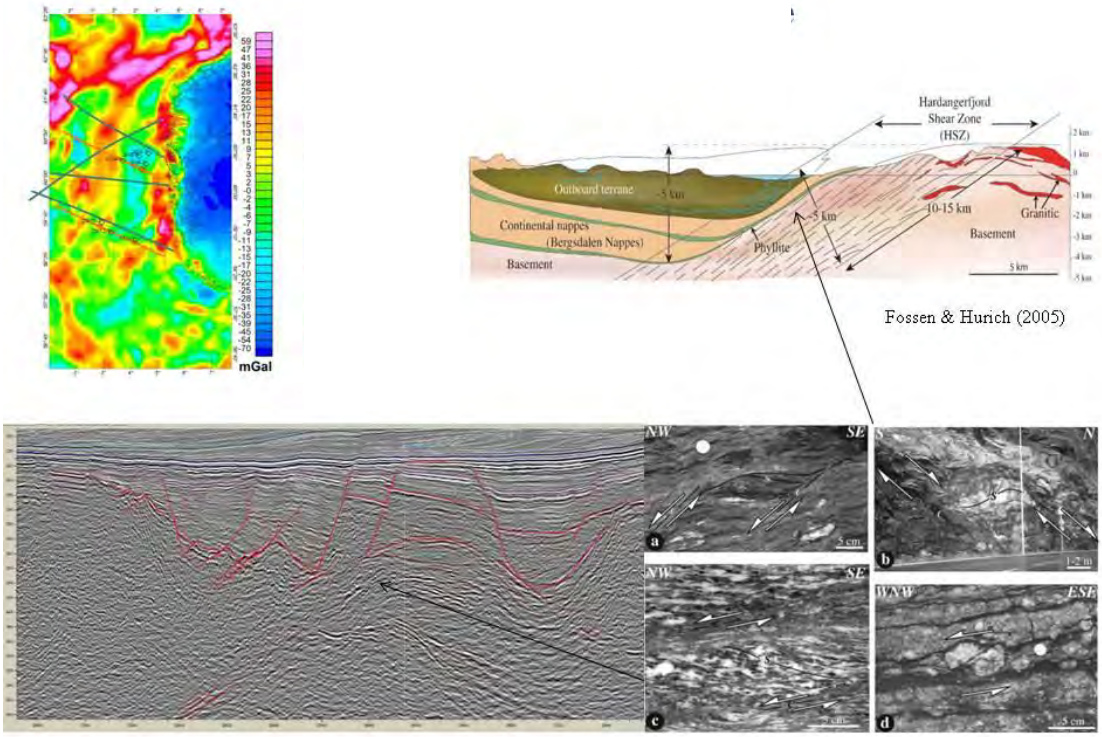

Figure 10.7 Comparison between onshore structural geometries related to the Hardangerfjord Shear Zone (Fossen & Hurich 2005) and geometries observed in the area southeast of the Utsira High in the vicinity of 17/3-1. It is tempting to interpret the subsurface culmination observed in the seismic data in the area beneath 17/3-1 as the continuation of the footwall of the HSZ, but the Øygarden Fault appears to be an equally good candidate. See text for more details.

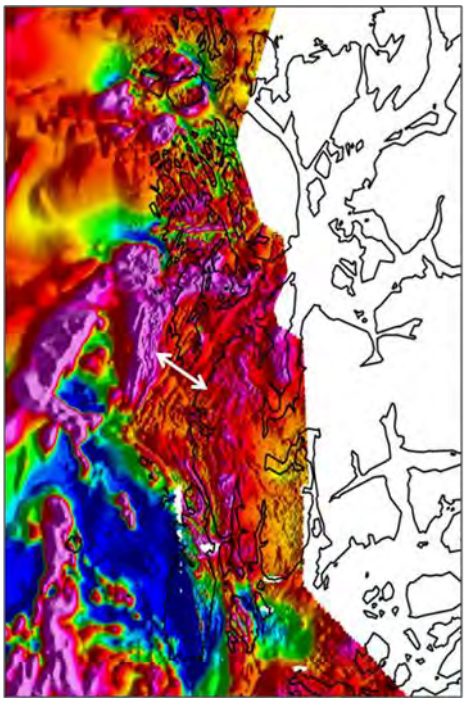

Figure 10.8 Aeromagnetic map depicting the southward bend of the Hardanger Shear Zone into the Karmsundet between Karmøy and Haugalandet. The white arrow shows the width of the sear zone.

10.3.2 Comparison to magnetic depth estimates

In Figures 10.5 and 10.6, the interpretation of the top basement is also compared to the magnetic depth estimates from Chapter 7. In the southern profile, the magnetic depth estimates are within reasonable limits of the top basement from the combined seismic-gravity-magnetic interpretation. Especially, the changes in the top basement are imaged, which shows the effect of the susceptibility contrast at the top basement on the magnetic field. This is a good example of the usefulness of magnetic depth estimates, as these can provide reliable results in areas where the 2D modelling fails, due to geometrical variations perpendicular to the profile. Towards the west and the Viking Graben, the magnetic depth estimates are too shallow compared to the seismic top basement. This can be explained by the very deep top basement, which is not associated with a magnetic low. The reason is that intra-crustal variations in magnetic properties now govern the shape and amplitudes of the magnetic field.

For the northern profile the magnetic depth estimates vary significantly from the integrated top basement along the entire profile. This can be explained by the absence of local variations in the magnetic field and again, the dominant role of the intra-crustal variations in the magnetic properties. This shows that magnetic depth estimates are useful tools when local variations are observed, but should only be used with uttermost care, when such short-wavelength anomalies do not exist and deep crustal sources dominate the magnetic field. Both 2D modelling and magnetic depth estimates provide useful information, which should be considered as input when establishing a 3D model of the magnetic properties.

10.3.3 Depth to Moho

Our profiles feature a relatively constant Moho depth with little variations in lower crustal density, except for the western part of the northern profile. Christiansson et al. (2000) and subsequently Mjelde et al. (2012) however, introduced a high-velocity LCB beneath the coast line. The reasoning for its introduction was the presence of a peculiar band of reflections ~5 km beneath a first band of reflections, which conventionally would have been picked as the Moho. The P-velocities are the same as those normally associated with the upper mantle (>8.1 km/s). and Christiansson et al. (2000) modelled the LCB with densities of 2950 kg/m^3, which produced a good fit to the gravity field (see Figure 10 in Christiansson et al. 2000). However, they also used a density of 2700 and 2730 kg/m^3 from the top basement to the Moho with a density contrast of ~500 kg/m^3 to a mantle with a constant density of 3200 kg/m^3. Such a high density contrast is not in agreement with the observed step in seismic velocities. Similar to the seismic velocities, the basement density increases with depth to ~3000 kg/m^3 above the Moho (see Figs. 10.5 & 10.6). The LCB with velocities of > 8 km/s would be associated with a density of 3300 kg/m^3, which is necessary in order to adjust the gravity field and to achieve an isostatically balanced cross-section. The LCB of Christiansson et al. (2000) is interpreted by us as part of the upper mantle. Similar double reflections are observed beneath western Norway on the MAGNUS-Rex profiles (Stratford et al. 2009), which might imply a Moho doubling during the Caledonian orogeny. On the contrary, the velocity and density structure

does not support the existence of enclosed domains of an eclogitised lower crust beneath the coastline of western Norway.

10.3.4 A tentative crustal lithology

Figure 10.9 shows a tentative interpretation of the lithology of the northern North Sea following the classification of Fichler et al. (2011). The main portion of the basement consists of granites and gneisses, which have similar density and magnetic properties. Differentiation between these two is, in general, difficult with the uncertainties of their applied properties. Two structures are of particular interest. On the southern profile, the western portion of the lower crust corresponds to mafic intrusions similar to the observation by Fichler et al. (2011). Whilst the presence of such a feature is reasonable at the edge of the North Sea, it cannot be confirmed that this feature is continuous, as it is not modelled/present on our northern profile. The structure may, however, be present, but without a significant volume that, allows us to image it.

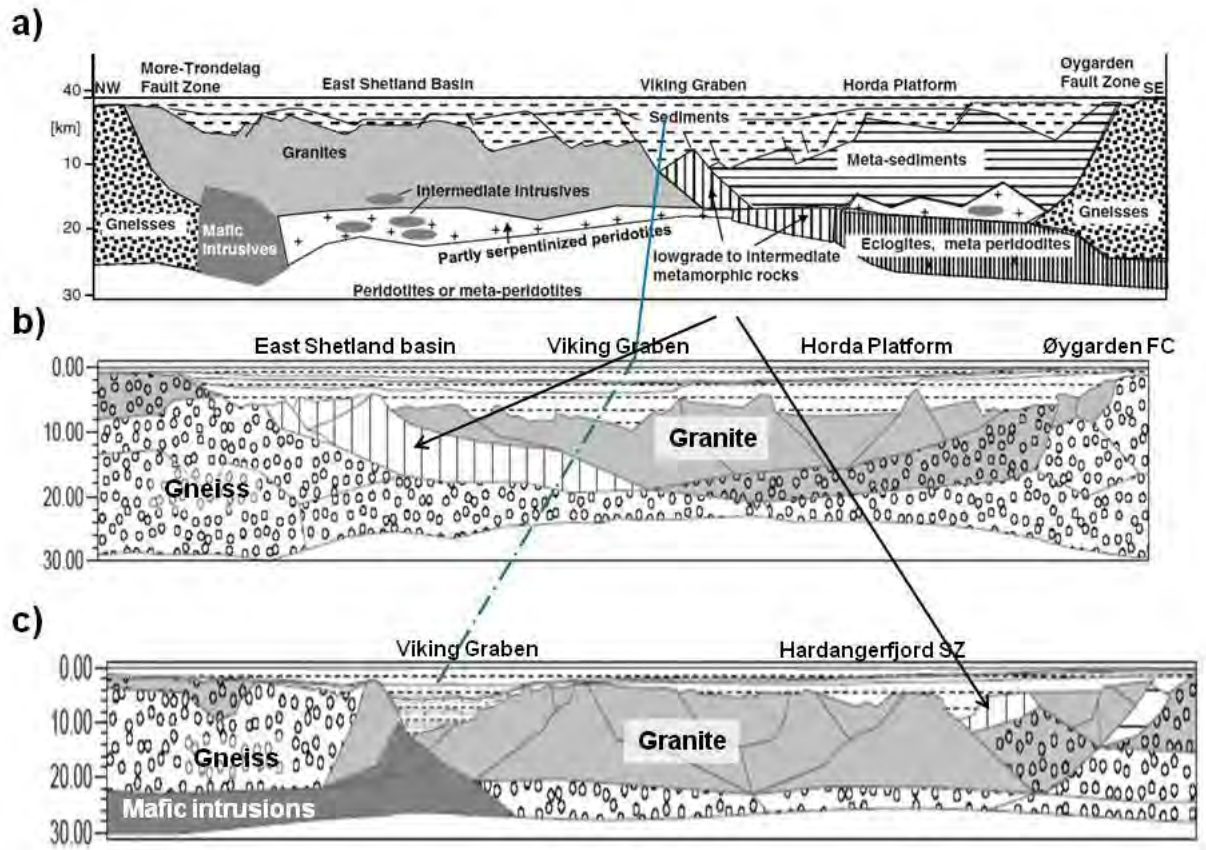

Figure 10.9 Tentative lithologies of the northern North Sea based on the interpretation of gravity and magnetic data. The upper profile shows the cross-section from Fichler et al. (2011) and their classification has been applied to the northern (central panel) and southern (bottom) NS line.

In the northern profile, the situation is further complicated by the presence of a sliver of metasedimentary rocks. In Fichler's et al. (2011) interpretation, these are located east of the Viking Graben, whereas we place them to the west of the Viking Graben. Fichler et al. (2011), moreover, inserted a serpentinised lower crust beneath the Horda Platform. This

observation cannot be confirmed by our modelling, but is within reasonable limits of the uncertainties of our modelled structures. These differences in characterising the lithologies of the crust emphasise the need for a 3D model, which would link the different observations and allow us to assess and describe the lithologies in a more reliable manner.

11. ONSHORE-OFFSHORE AEROMAGNETIC INTERPRETATION

Marco Brönner, Odleiv Olesen & Aziz Nasuti

11.1 Quaternary morphology indicated from aeromagnetic data

Buried channels of Quaternary age as they are observed in the North Sea and also in other parts of the world, e.g., North America and Eurasia, are shallow geological features, which were imprinted in the underlying undisturbed sedimentary strata by sub-glacial meltwater (Kellett 2007, Davies et al. 2004). In North Africa and the Middle East, examples of such channels from the late Ordovician actually provice evidence for a major glaciation on the super-continent Gondwana (Ghienne & Deynoux1998, Smart 2000). Some of these channels are today productive oil and gas reservoirs.

The Quaternary channels, however, attracted scientific and economical interest since they are commonly filled with highly porous and permeable sediments, such that they resemble water or hydrocarbon reservoirs. Furthermore, shallow gas deposits can be an indicator for hydrocarbon leakage from deeper reservoirs (Bauer & Fichler 2002) and may therefore provide information about migration paths. Fichler et al. (2005) investigated craters in the vicinity and at the heads of such channels in the North Sea, and argued that they are products of gas expulsions, triggered by melting gas hydrates. The existence of such shallow methane deposits presents a serious drilling hazard (Ahmad & Schmitt 2006) and a risk for blow-outs when drilling for deeper targets. Knowledge of the locations and possibly the depth and thickness of these morphological structures is therefore important a *priori* information for exploration activity in such areas (Salisbury et al. 1996).

Several studies have shown the capability to map these channels with geophysics (e.g., Ahmad & Schmitt 2006, Bauer & Fichler 2002). The most comprehensive picture of such systems derives from 3D seismic, but also state-of-the-art, high-resolution gravity and aeromagnetic data can image Quaternary channels. From the gravity data these features appear as small-scale gravity lows due to the less compacted, highly porous and perhaps gas-bearing infill. In the magnetic data, both positive and negative anomalies can be ascribed to Quaternary channels, whilst some of them do not have any imprint at all. The reasons for this are discussed in detail in Fichler et al. (2005) and Olesen et al. (2010) and are mainly due to a heterogenic infill of sand, gravel and boulders of crystalline rocks compared to the surrounding fine-grained sedimentary rocks (Fig. 11.1). A secondary change in magnetic mineralogy from biological and chemical processes cannot be ruled out.

However, the key to identifying and distinguishing these features from other source anomalies is mainly the pattern, which shows the typical vein-like character of fluvial systems with meanders, drainage channels and rivers. The wavelength and gradients can give a qualitative indication of the channel depth. For a more accurate depth estimation or modelling, a joint

interpretation with seismic and/or a detailed knowledge of the infill and its density/magnetisation is necessary (Ahmad & Schmitt 2006, Bauer & Fichler 2002, Fichler et al. 2005, Olesen et al. 2010).

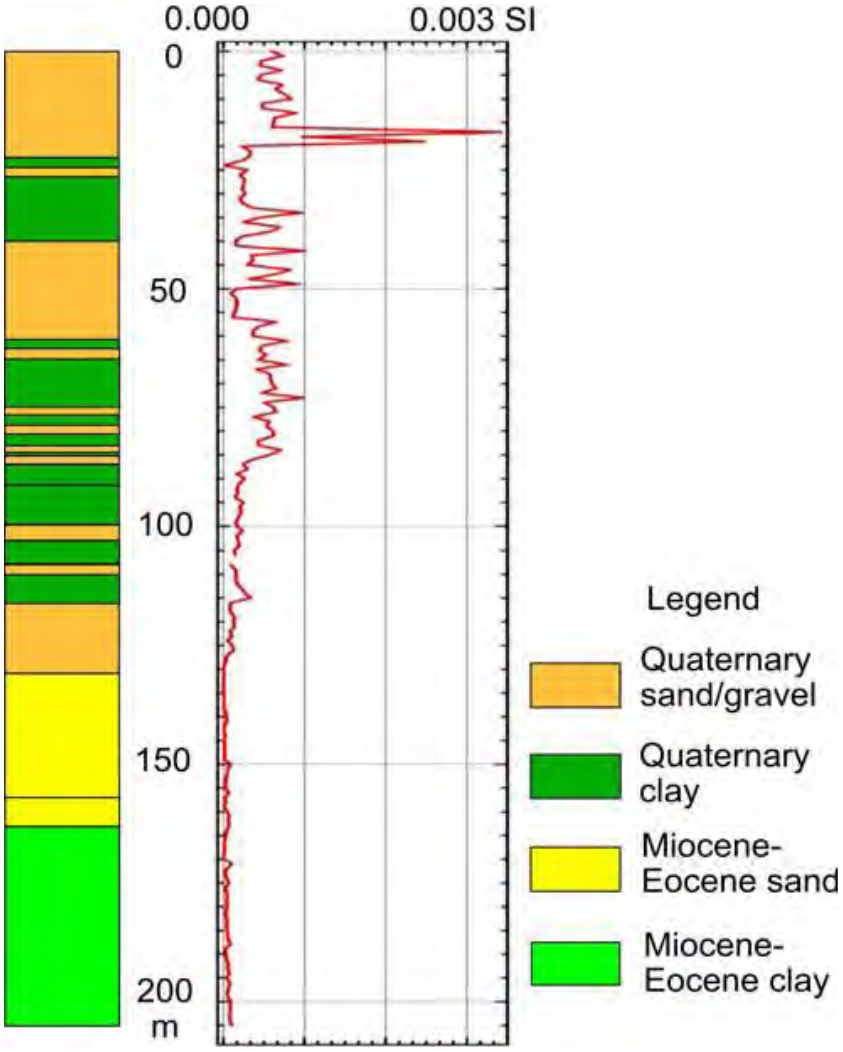

Figure 11.1 Lithological and susceptibility log from a borehole in southern Jutland (GEUS borehole no. 160.1526) reveals that magnetic anomalies are caused by Quaternary channels containing sand and gravel derived from the Fennoscandian Shield (Olesen et al. 2010). Low-magnetic Miocene sediments were encountered at a depth of c. 129 m. The deepest part of the Quaternary sand channel consists of low-magnetic sand and clay.

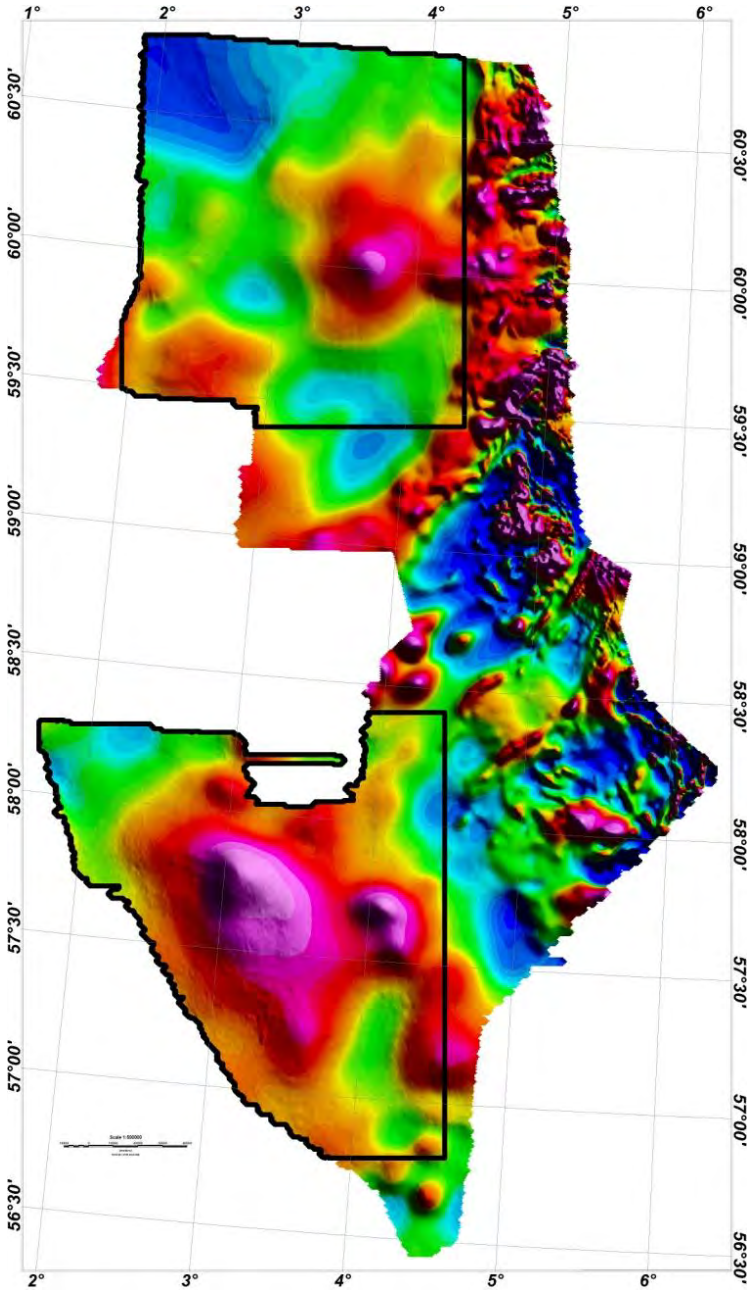

Figure 11.2 Aeromagnetic data acquired during the CNAS-10 survey (Nasuti et al. 2012). The black frames show the location of Figures 11.4 and 11.5.

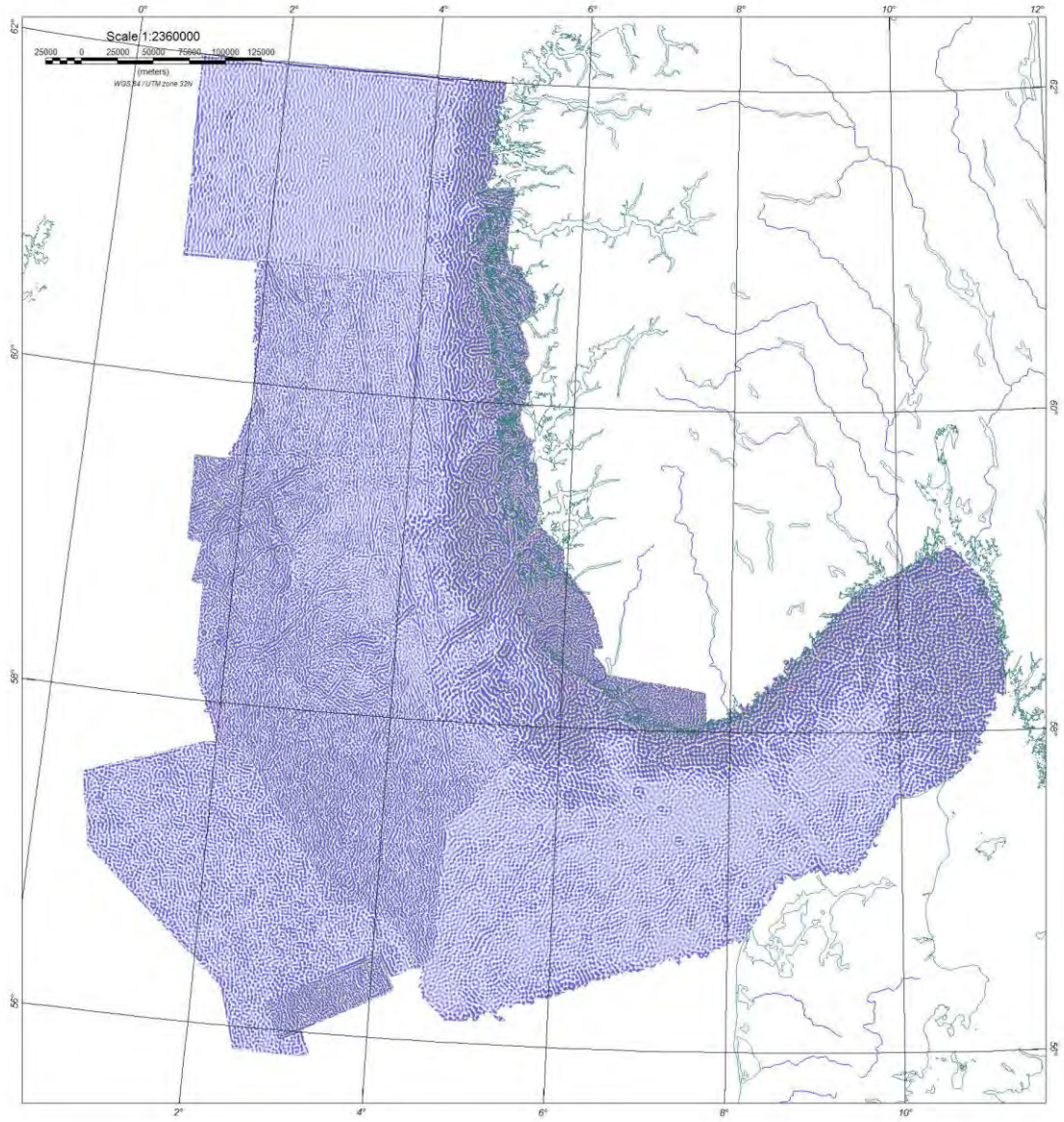

Figure 11.3. Band-pass filtered magnetic data (wavelength: 0.8-3 km) of the new aeromagnetic compilation. The filtered data reveal the different resolutions of the various surveys in this compilation, but also show an area of significantly denser lineaments in the western and southwestern parts of the CNAS-10 area, which appears to continue to the north and south, but is not obvious in the SAS-96 and CGAM-96 surveys due to larger line spacing and a reduced resolution.

To highlight the magnetic responses of these shallow features we produced various high-pass filtering (Fig. 11.3) of the new aeromagnetic compilation including the CNAS-10 and BESTAS-10 data. The high-pass filtering clearly shows the different resolutions from the different surveys, obviously related to acquisition parameters such as flight altitude and profile distance, but also to water depth and distance-to-magnetic source. As discussed above, the magnetic signal of these imprinted channels can be rather small and the higher the resolution of the magnetic data the better resolved they are, thus providing a more comprehensive picture of the system. However, from the high-pass filtered data, a region with a different and denser pattern of lineaments is observed in the WSW part of the CNAS-10

area, which continues into the VGVG-96 and UHAM-09 survey areas as well as to the VGCG-94 area.

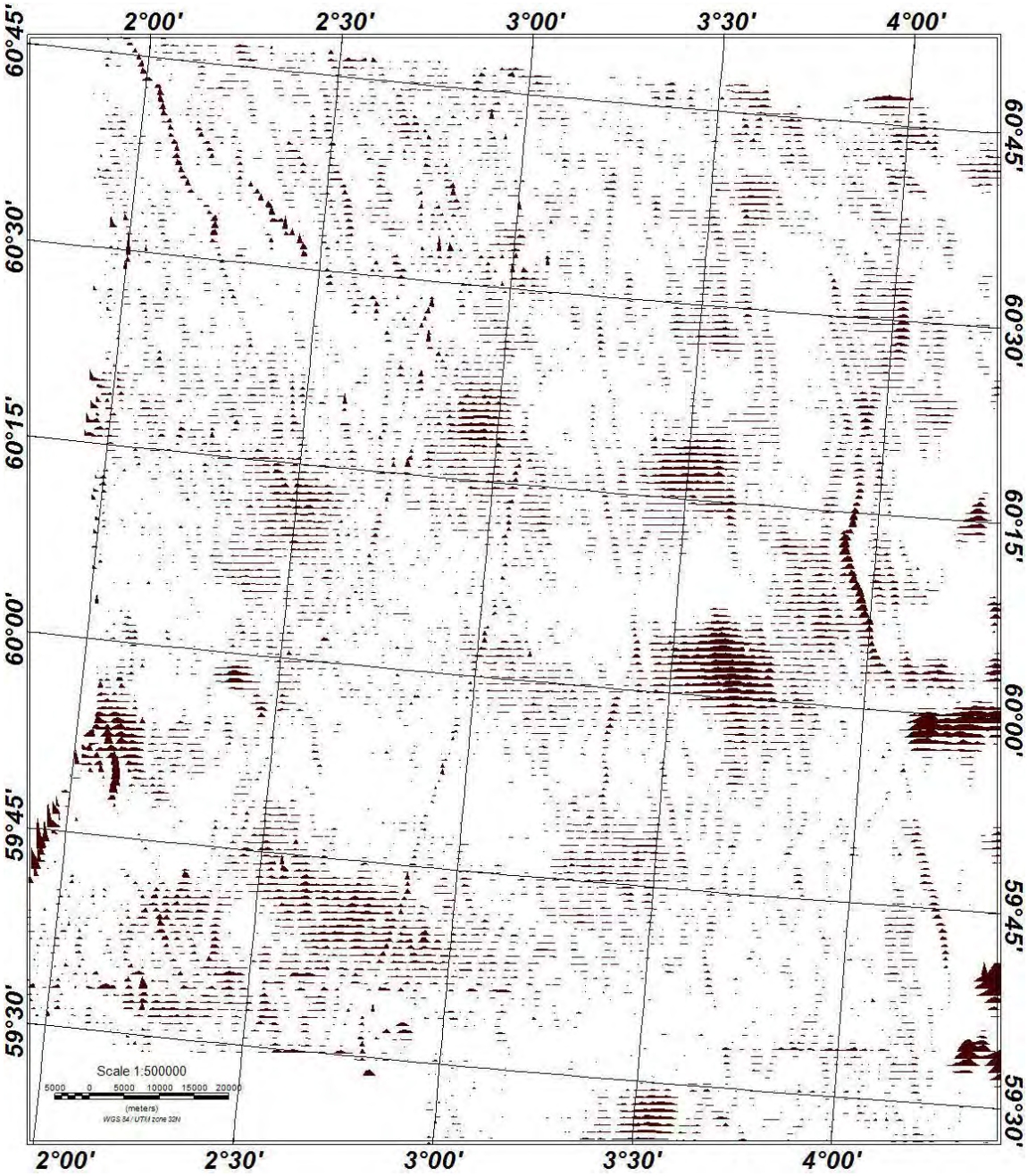

Figure 11.4 Magnetic stack plot of 8 km Gaussian high-pass filtered profile data from the northern CNAS survey. The northern black frame in Fig. 11.2 shows the location of the map. The asymmetry of the coast-parallel anomalies to the east – with a steep gradient to the east and a gentler gradient to the west – shows that the sources of the anomalies dip gently towards the west, consistent with interpretations of seismic data (Ragnhildstveit & Helliksen 1997). The linear symmetric anomalies to the west represent Quaternary sand channels and pipe lines.

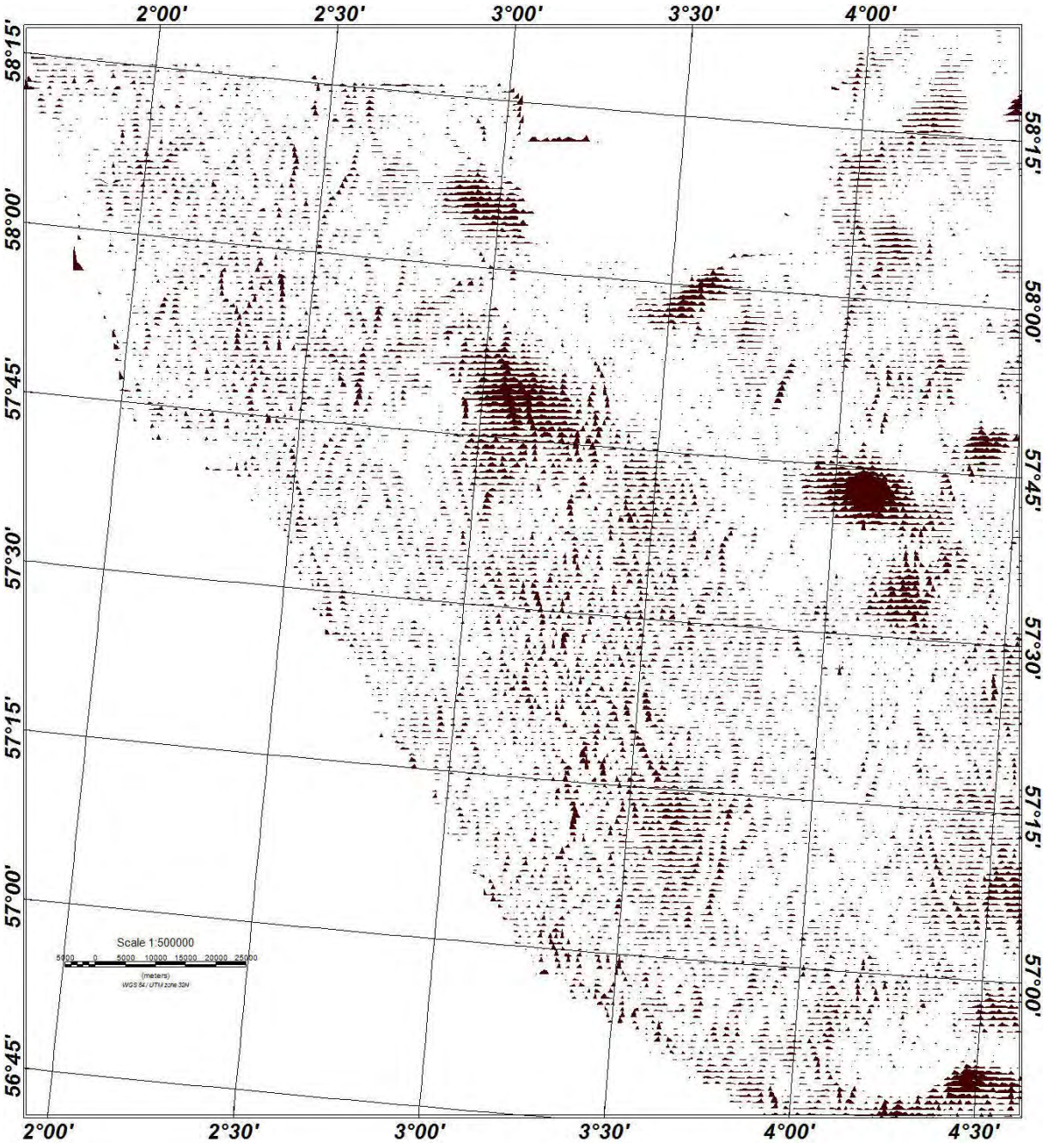

Figure 11.5. Magnetic stack plot of 8 km Gaussian high-pass filtered profile data from the southern CNAS survey. The southern black frame in Fig. 11.2 shows the location of the map. The linear symmetric anomalies to the west represent Quaternary sand channels. There are no asymmetric anomalies in this area representing subcrop units.

We assume there is a similar density of lineaments in the SAS-96 and CGAM-96 survey areas, but due to the lower resolution of these data, the channel signature there is less clear.

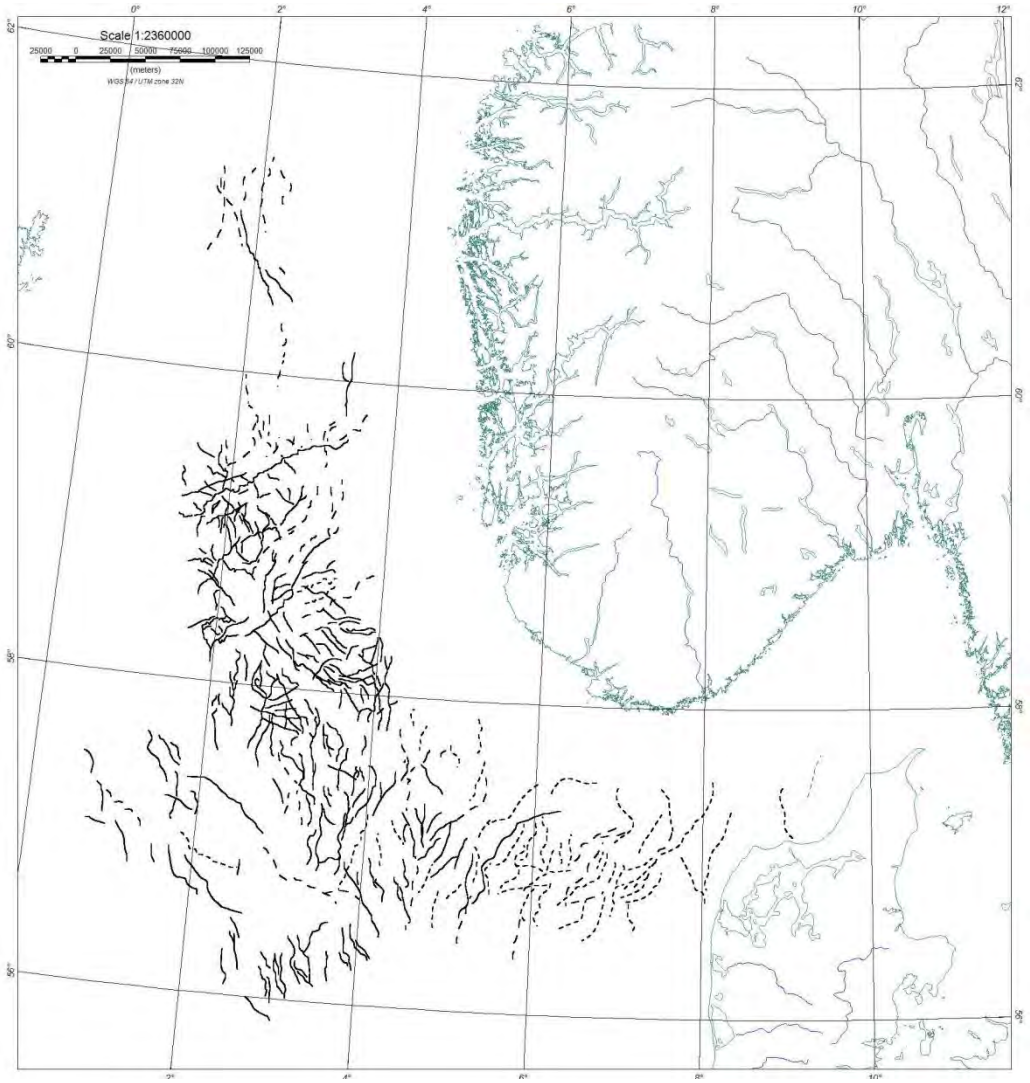

Figure 11.6. Quaternary sand channels interpreted from the new aeromagnetic data compilation. At least two systems of sand channels were observed, where the younger one is orientated perpendicular to the Norwegian coast and the older one has a predominant NNW-SSE trend.

As described above, a detailed interpretation of the high-pass filtered magnetic data was subsequently carried out, looking for patterns with fluvial system characteristics. The results are displayed in Figure 11.6. Solely based on magnetic data this technique certainly has some uncertainties and might not detect the entire system, but the aeromagnetic data provide a very quick overview of the distribution of sand channel systems in a study area. Quite a few of the anomalies are obviously related to Quaternary channels, whilst some features have greater uncertainties and were consequently drawn with dashed lines. The observed channels are concentrated in the southwestern area of the new compilation with more sparse channels farther to the north, southwest and southeast. The channels could not be observed all the way to the Norwegian coast. There is a rather sharp boundary towards the Norwegian Channel and a c. 90-100 km-wide corridor without sand channels parallel to the coast (Fig. 11.3).

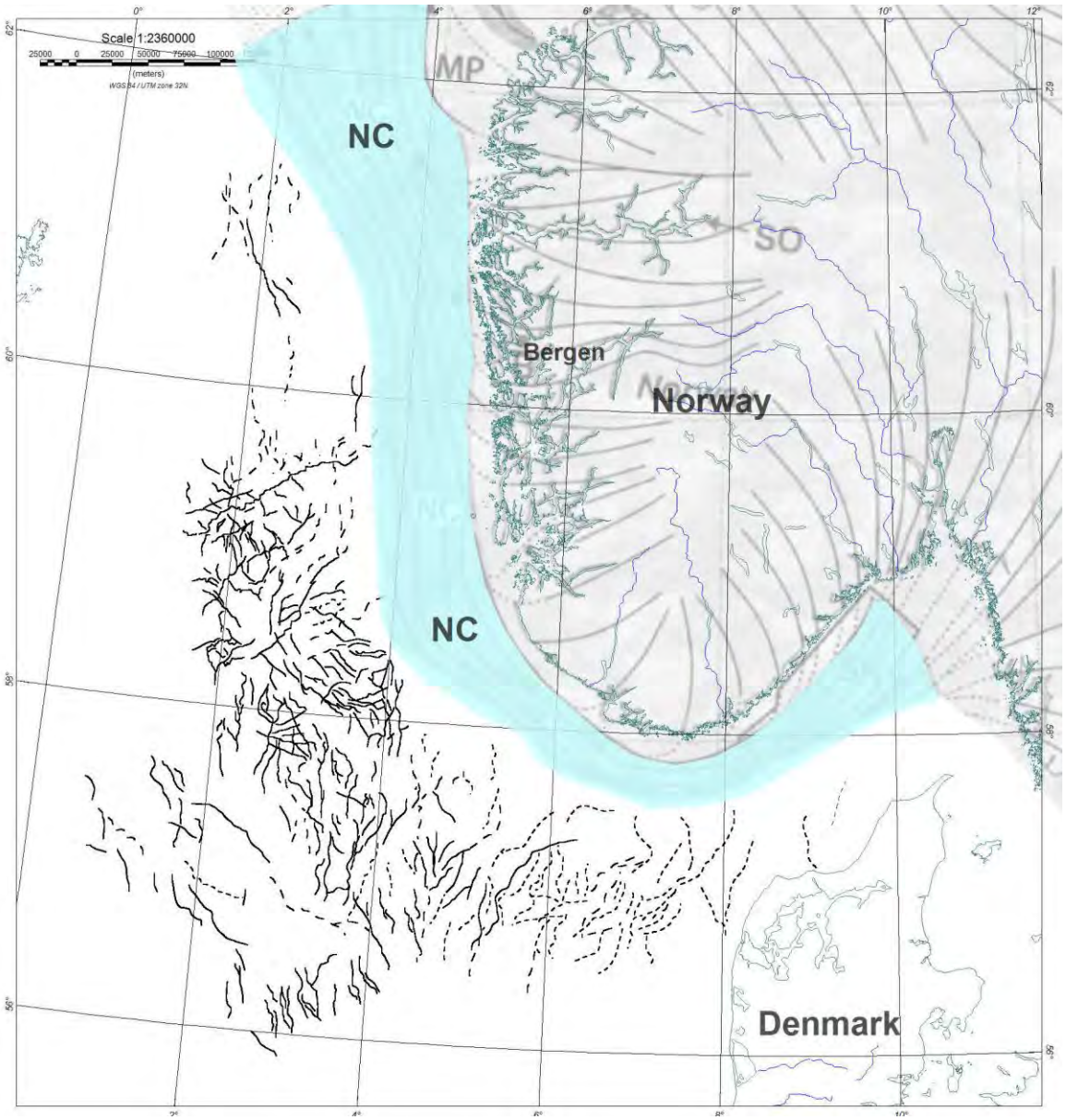

Figure 11.7. Correlation between the Norwegian Channel and the corridor lacking any indication of sand channels from the magnetic data.

However, from the interpreted structures a well developed meandering drainage system with a predominant orientation approximately perpendicular to the Norwegian coast can be observed. The system cross-cuts or overlies at least one other, most likely older system of sand channels, which has a more NNW-SSE orientation. The different trends document the extension and shape of the front of the ice sheet during various melting and freezing cycles. The observed NNW-SSE 'older' channels indicate a greater ice-sheet extension in an E-W orientation, whereas the younger one records a much later stage of the last ice age, where the ice-sheet was concentrated onshore Scandinavia and with a retreating front of the ice sheet parallel to the Norwegian coast.

The observed corridor without sand channels correlates well with the Norwegian Channel (Fig. 11.7). The new interpretations of Quaternary sand channels fit into the area in the Norwegian North Sea with no reported channels in the recently published review map of

northern Europe (Fig. 11.8) by van der Vegt et al. (2012). Buried Quaternary channels represent the offshore analogues to mainland eskers.

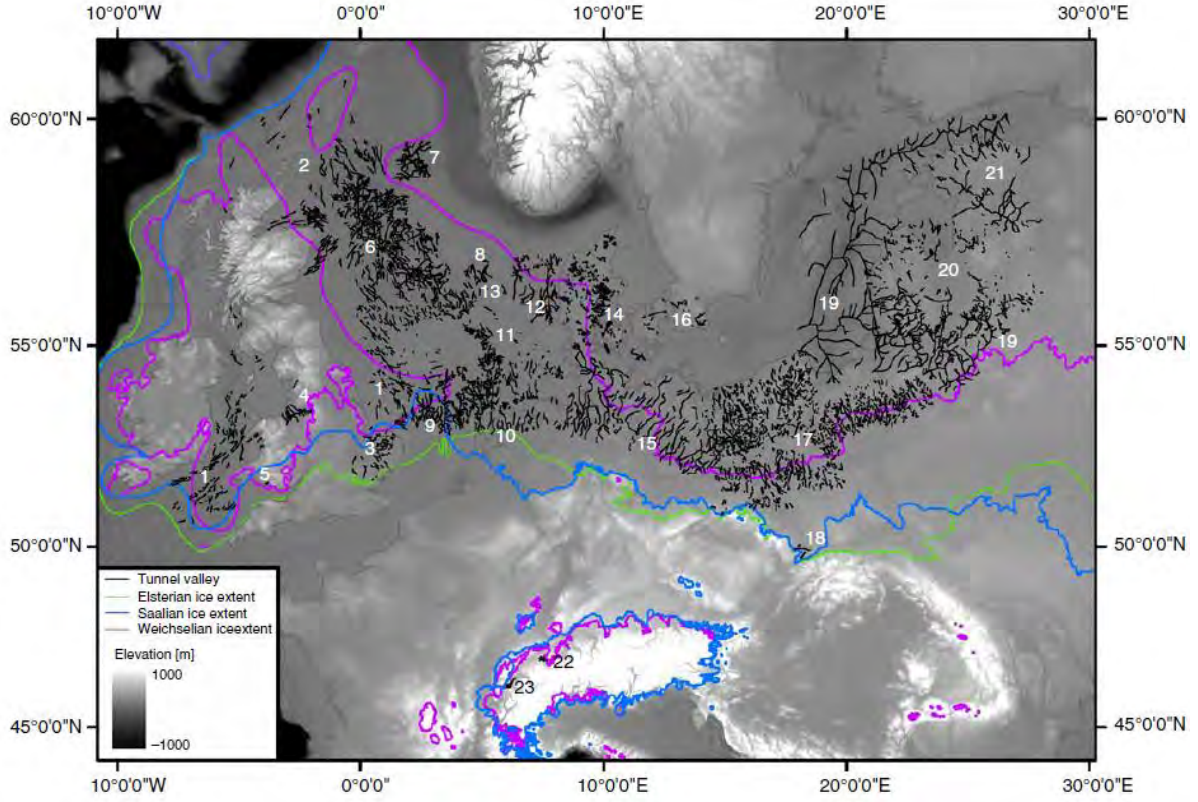

Figure 11.8. Compilation of Quaternary channels in northern Europe by van der Vegt et al. (2012). Our new interpretations fill in the gap with no reported channels to the west and south of the Norwegian Channel.

The Norwegian Channel is the imprint of a huge or repeated ice stream around southern Norway during the Quaternary period (Helland 1885, Rokoengen & Rønningsland 1983, Rise & Rokoengen 1984, Sejrup et al. 1996, 2003, Longva & Thorsnes 1997, Larsen et al. 2000, Stalsberg et al. 2003), which has a prominent bathymetrical expression and increased water depth of c. 400 m (compared to c. 200 m outside the channel).

The greater water depth accounts for a lower resolution of the magnetic data and could be a reason why there are no indications from aeromagnetic data for the presence of sand channels in this area. On the other hand, Rise et al. (2004) interpreted shallow-seismic horizons from 3D seismic data. They observed a lineated relief pattern with a fan-shaped structure (Fig. 11.9) and interpreted it as the footprint of a moving ice sheet. Therefore, it seems likely that possible pre-existing sand channels were repeatedly eroded such that no or very few remains of these channels can now be seen in this area.

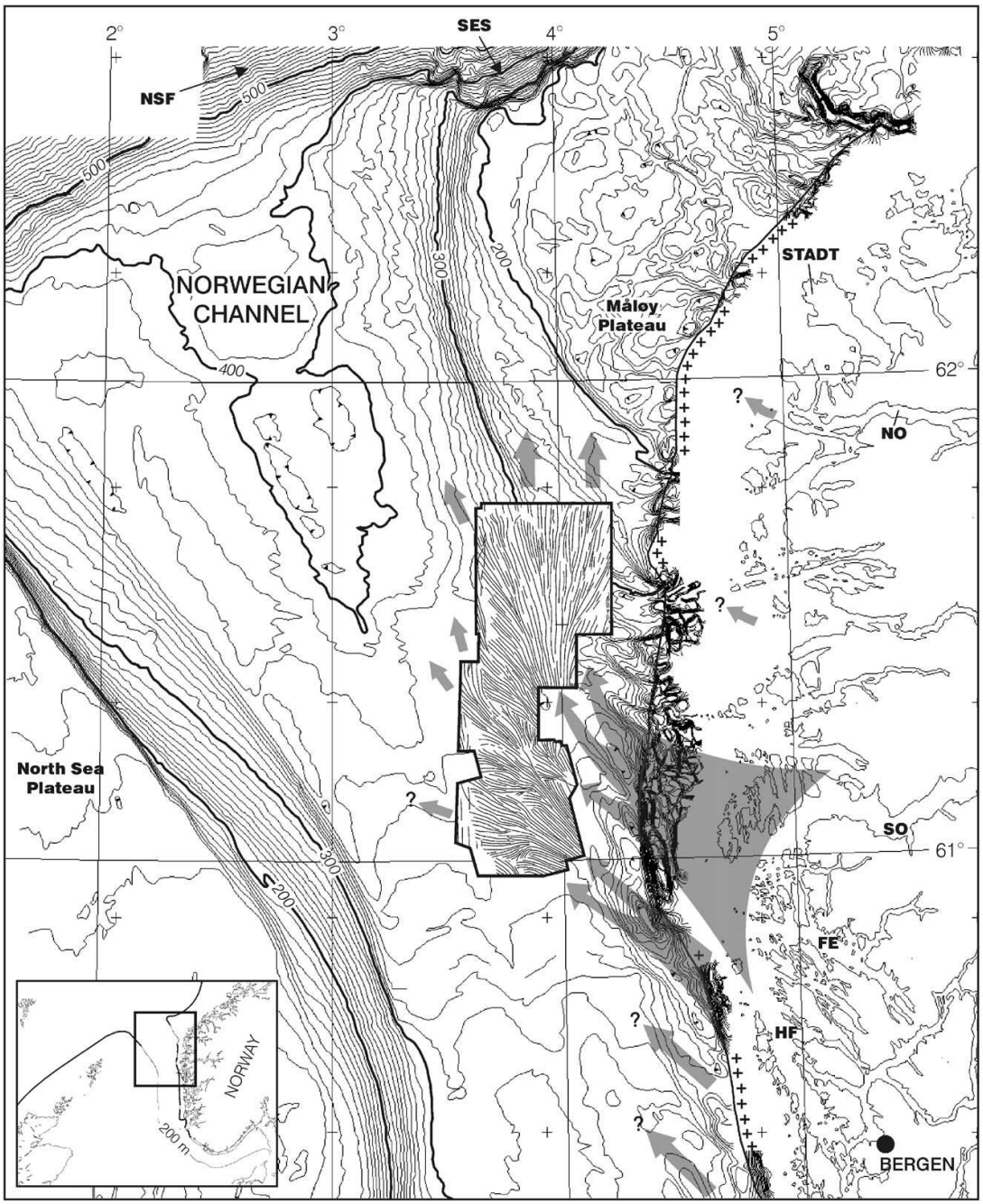

Figure 11.9. After Rise et al. (2004): Sketch of ice-flow lineaments formed at the initial stage of a mid-Pleistocene glaciation, interpreted from the 3D seismic image. The present bathymetry is depicted with contours. The main supply of ice to the study area was between Sognefjorden (SO) and Hjeltefjorden (HF). A substantial volume of ice from Sognefjorden appears to have been deflected northwards, probably because the area below the present shallow Måløy Plateau was a deep part of the Norwegian Channel at this time. The westerly trending lineations in the southwestern part of the study area show that the Norwegian Channel Ice Stream was not yet established at this time.

11.2 Mapping of deep-weathering onshore Norway and its offshore extensions

Fractured and deeply weathered basement is a well known phenomenon, which can be observed all over the world, where basement rocks are exhumed. However, the processes which trigger and maintain fracturing/weathering are still controversial. Climateic conditions and CO_2 concentration in the atmosphere are recognised to have an impact on weathering, and warm and humid conditions are obviously beneficial for increasing weathering rates, but also under Arctic conditions, physical and chemical weathering is observed. Uplift and denudation have also been discussed as an important factor, as well as the rock composition and mineral content of the basement. However, it is still poorly understood how these different factors interact with each other and if any one factor is more important than the others. This lack of understanding makes it difficult to locate and estimate the amount of fracturing/weathering in the basement where it is not observable or easily accessible and thus to develop a technique for systematic mapping.

Scandinavia was exposed to several ice ages and different epochs of glaciations onshore Norway eroded and removed almost entirely the overlying sedimentary successions. The preglacial landscape is consequently masked by glacial erosion but still reflects the impact of deep weathering. The numerous sounds and islands along the Norwegian coast could therefore to a large extent be conditioned by exhumation and erosion of a weathered basement. Onshore Norway and in wells on the Norwegian continental shelf, quite a few examples of deeply weathered and fractured basement have been observed. Saprolites in narrow fracture zones a couple of hundred metres deep were, for example, observed on the mainland of southeastern Norway. Several tunnel projects turned into economic disasters because of the unstable and leaking bedrock (Olesen et al. 2007a). Furthermore, along the Norwegian coast several places such as Lista, Karmøy, Vågsøy, Melfjorden and in the Lofoten-Vesterålen archipelago are well known for significant amounts of deeply weathered basement. These features raise an important question for the E&P industry as to where and how much fractured/weathered basement might exist offshore on the Norwegian shelf. For exploration, fractured basement is definitely both a blessing and a curse. For reservoirs where underlying basement is supposed to act as a bottom seal, fracturing within the basement might act as migration paths, causing a leakage from the reservoir into the basement; or, on the other hand, the basement itself could act as a reservoir.

NGU together with the Norwegian Petroleum Directorate have carried out an extensive project during the last three years to gain a better knowledge of deep-weathering locations and processes onshore mainland Norway (Olesen et al. 2012) and in the Lofoten-Vesterålen archipelago. As one outcome of this project, geophysical methods like magnetic, gravity, seismics and resistivity profiling are generally capable of mapping structures of deep weathering and fractured basement, but because of little economic interest for such basement structures in the past, the existing data were barely explored to gain a better knowledge and to assist in developing an improved mapping technique.

Figure 11.10. Magnetic measurements of weathered and unweathered bedrock on Hamarøya. The remaining magnetisation of the altered rocks is c. 30% lower than the parent material. Observations at other locations show a reduction of magnetisation by 50% and up to one order of magnitude.

Onshore Norway the AMAGER method (AeroMagnetic And GEomorphological Relations) was successfully applied in Southeast Norway. The method was developed and published by Olesen et al. (2007a) and comprises a correlation of morphological depressions and magnetic lows. The method is based on the not necessarily, but for Norway, common observation that deeply weathered basement shows a noticeably reduced magnetisation of the parent material (Fig. 11.10) and is moreover easily erodable. Relative magnetic lows correlating with topographic depressions in eroded and exposed basement landscapes are thus likely to indicate the location and distribution of deep weathering. Forward modelling of the aeromagnetic data shows that substantial volumes of low-magnetic material (down to 300 m) is needed to explain the magnetic lows (Olesen et al. 2007a). The method requires high-quality aeromagnetic data and digital elevation grids to achieve reliable results. Furthermore, detailed geological maps and a profound knowledge of the geology are useful for delineating areas with Quaternary overburden.

With the acquisition of the BESTAS-10 data onshore western Norway, high-resolution aeromagnetic data are on hand with sufficient resolution to be used for the AMAGER technique and for the mapping of possible deep weathering and fractured basement.

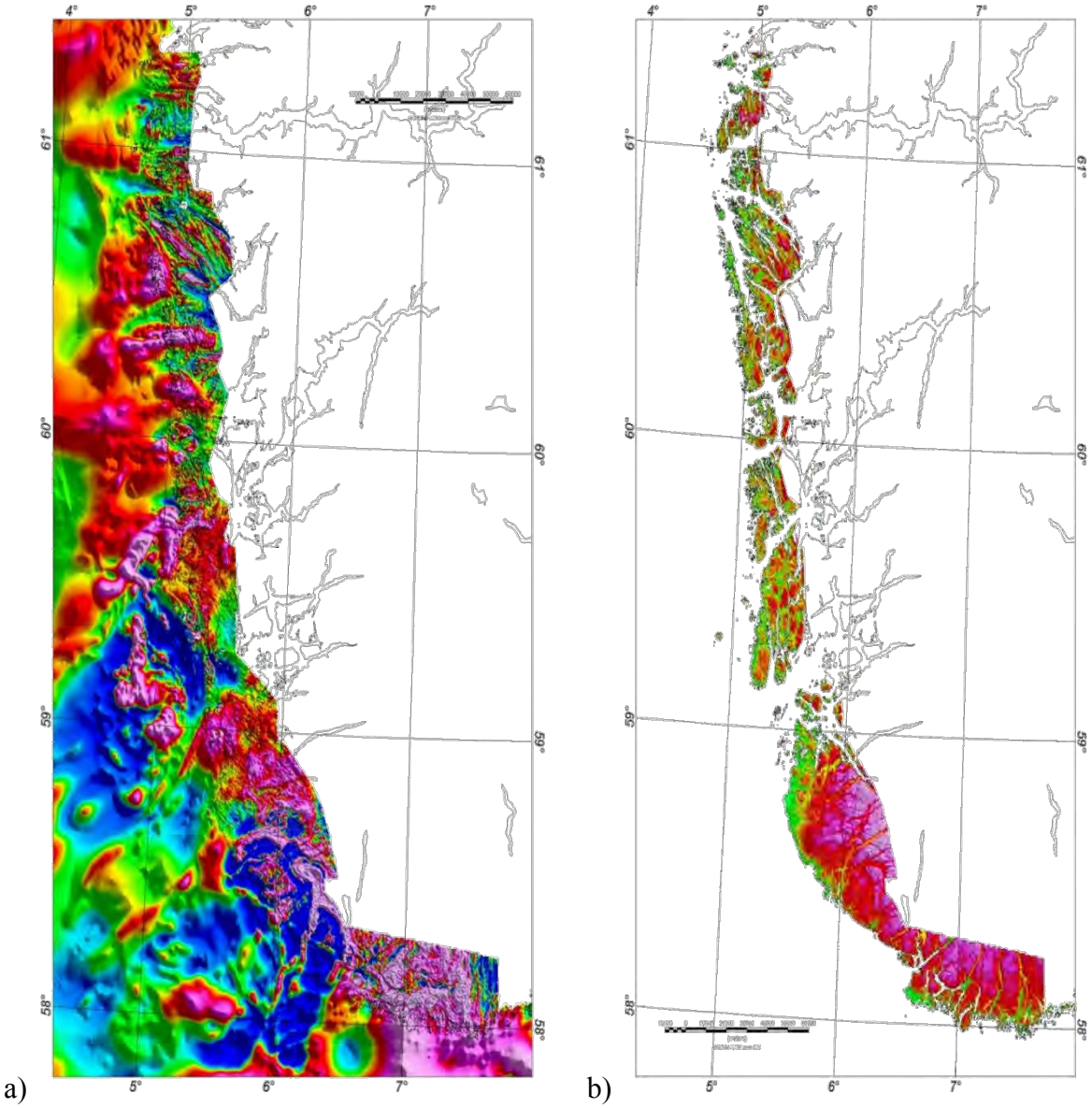

Figure 11.11 a) New magnetic data with BESTAS-10 and CNAS-10 and b) 50 m topographic grid, clipped to the onshore area of the BESTAS-10 data.

The AMAGER technique was applied to 1 km high-pass filtered data of both the aeromagnetic and the topography grid. The large size of the area and the different basement structures with partly significant changes in amplitude and orientation of the magnetisation made it very difficult to find a common correlation function, which could give reliable results. The reliability was estimated from a comparison of the calculated solution and known deep-weathering sites (e.g., on Lista and Karmøy) and fine-tuned if necessary. Locations with deeply weathered bedrock and low-resistivity zones on geoelectric profiles were also used as quality control. Furthermore, for the Egersund area, the anorthosite is known to have very high remanent magnetisation with inverse polarity with regard to the present magnetic field. This basement rock consequently produces a significant negative magnetic anomaly, whilst a reduction in magnetic minerals due to weathering appears as positive features in the magnetics. For the AMAGER approach, not one but two correlation functions were necessary to account for both phenomena. The correlation functions, which are considered to be most

reliable but do not produce too many solutions, were a correlation between a topographic depression of 5 m or more and a magnetic low of 5 nT or more, which could be observed over a distance of more than 1 km in areas with normal or no magnetic remanence. For the Egersund area with negative magnetic remanence, solutions were accepted for a correlation between a topographic depression of 5 m or more and a magnetic high of 5 nT or more, which could accordingly be observed over a distance of more than 1 km.

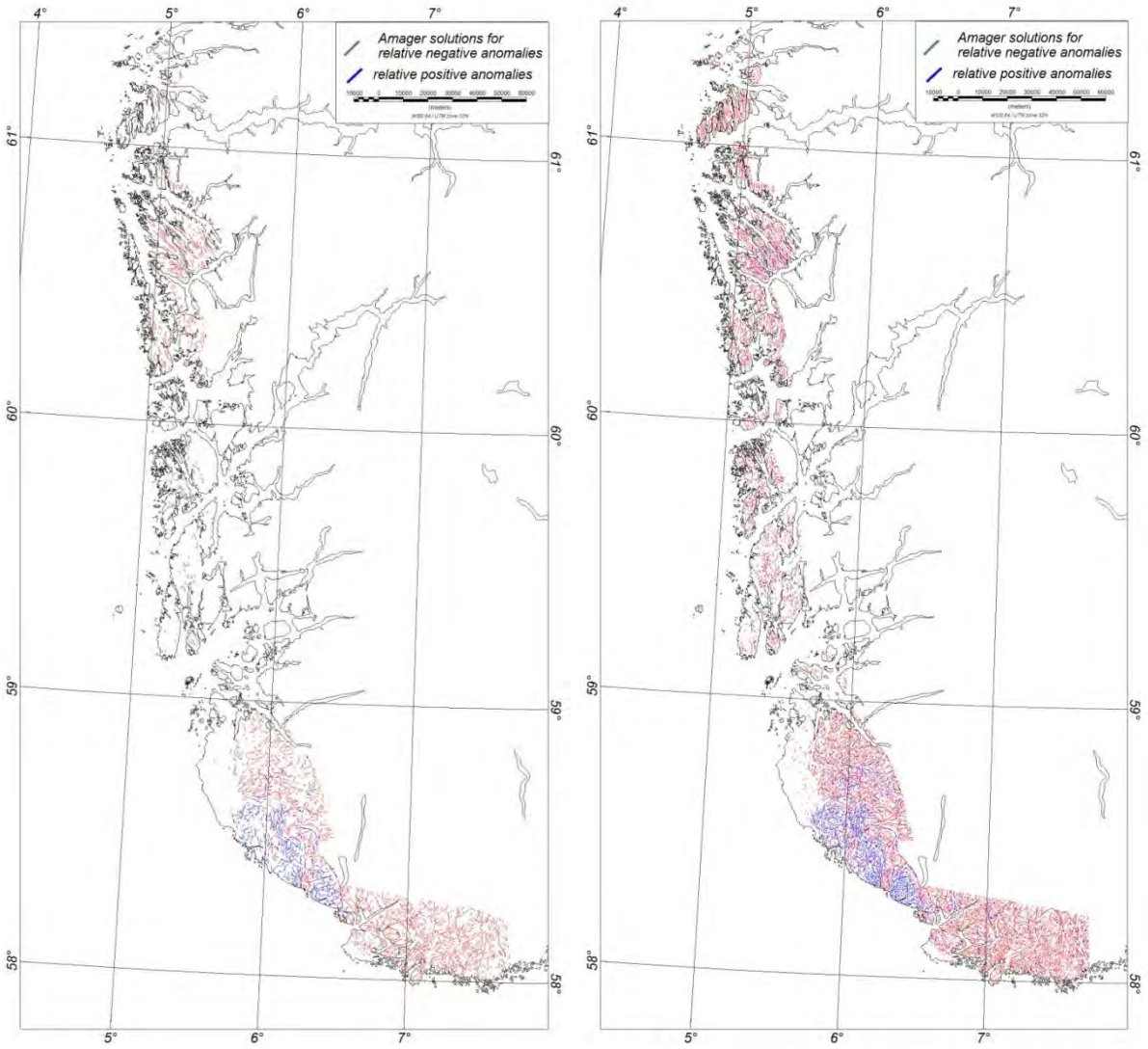

Figure 11.12 a) AMAGER solutions for BESTAS-10 data without and b) with AGC filter applied.

From the solution density, an obvious correlation with the basement magnetisation is observed and was also expected, since the magnetic contrast is larger as the unweathered basement becomes more magnetic. Low-magnetic gneiss regions show very sparse or no solutions, whilst high-magnetic norites and mangerites have a high density of solutions. However, to compensate – at least partly – for this effect, we applied an AGC filter to increase the low-magnetic anomalies in the gneiss regions.

The results indicate significant remains of deep weathering and/or fractured basement in these areas onshore Norway, which had previously barely been reported or published. An exception

is the weathering of the Rolfnes granite on the island of Bømlo located 70 km to the south of Bergen (Lie et al. 2012). The common occurrence of deep weathering on the strandflats of western Norway may imply that they represent a rejuvenation of surfaces of originally Mesozoic age.

The distribution of the possible weathering sites appears to be partly parallel to lithological boundaries and could be correlated with bedrock foliation (Fig. 11.12). Examples from Nordland show that in metamorphic and/or intrusive rocks, regolith remains can be found along their foliations (Gjelle et al. 1985, Wilberg 1989, Peter Ihlen pers. comm. 2012, Terje Solbakk pers. comm. 2012). However, a large number of the AMAGER solutions appear to have a rather irregular distribution and are likely to predominately reflect the system of fractures and thrusts in the basement onshore Norway. A correlation between the topography of southwestern Norway with a seismic time slice from the Utsira High (Lie et al. 2012) shows noticeable similarities (Fig. 11.13) which supports the AMAGER approach, but furthermore it also indicates a significant impact of weathering and erosion of the regolith for the development of the Norwegian landscape.

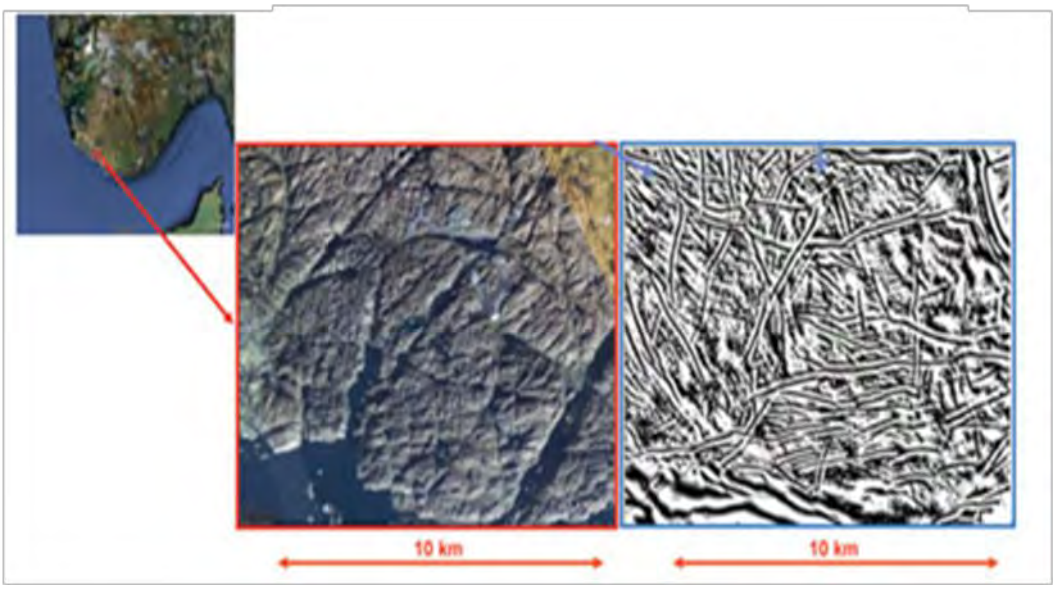

Figure 11.13. Correlation between a topographic map of southwest Norway and a fracture pattern observed from seismic at Utsira High, offshore Norway (Lie et al. 2012).

If the distribution of the valleys and mountain ridges, and the sounds and fjords are to some extent the visible expression of deep weathering and subsequent erosion during the ice ages, the remains of deep weathering onshore Norway are likely to be comparatively old. K/Ar dating in the 1970s and 1980s of assumed hydrothermal clay alteration associated with Permian fluorite and sulphide vein deposits, as well as regional fault zones in eastern and southern Norway (e.g., at Lassedalen, Gjerpen, Heskestad, Skreia and Feiring), yielded Mid and Late Triassic ages (Ineson et al. 1975, 1978, Ihlen et al. 1978, 1984). These ages most likely represent the same phase of deep weathering as has recently been reported from two exploration wells on the Utsira High (Fredin et al. 2012), and not hydrothermal alteration associated with the formation of the mineral deposits.

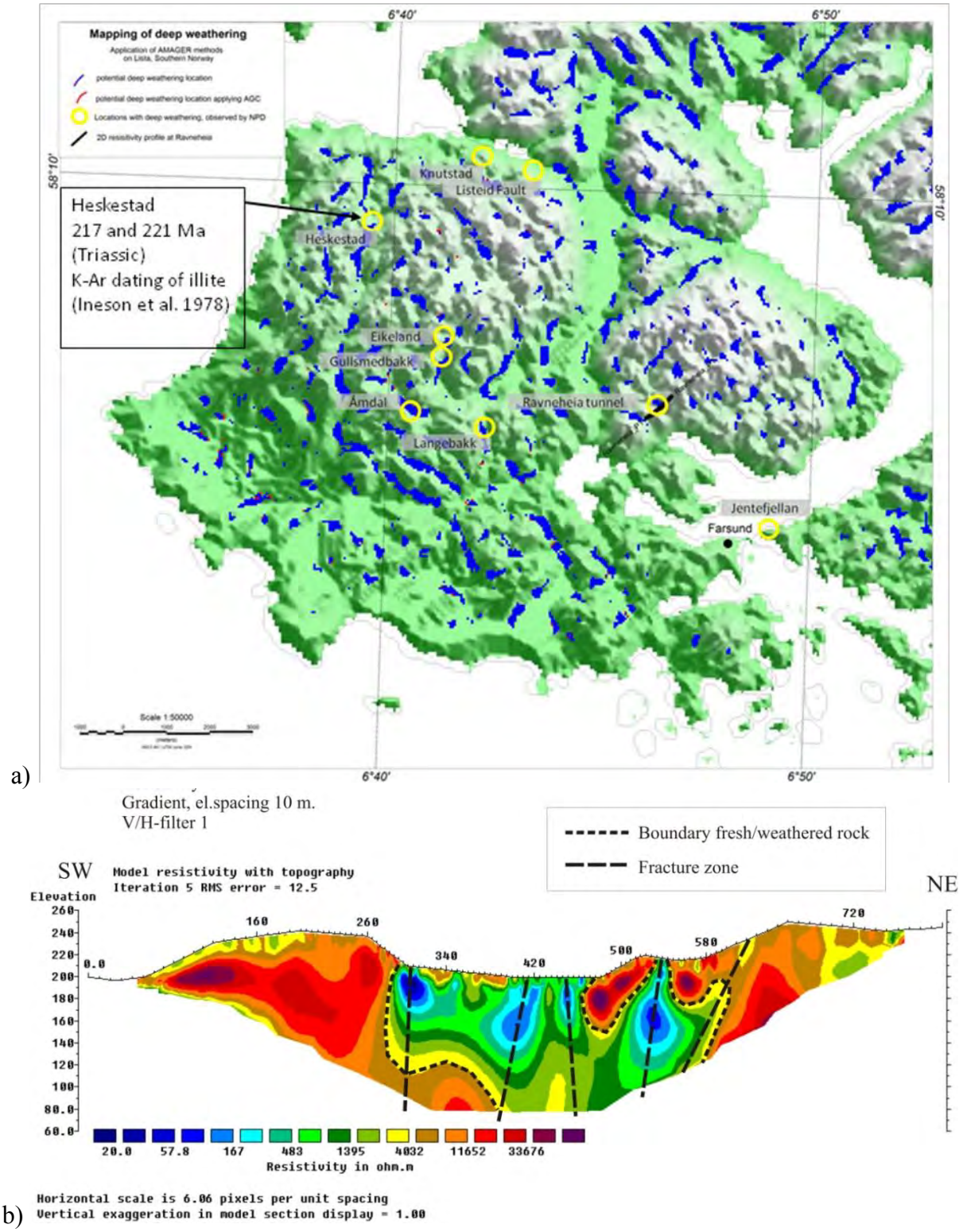

Figure 11.14 a) Potential deep weathering on Lista interpreted using the AMAGER method. Yellow circles show locations with observed deep weathering (Øverland et al. 2012). Note that K-Ar dating of illite in a fluorite-barite-bearing fault breccia at Heskestad yielded a Late Triassic age (217 and 221 Ma, Ineson et al. 1978). The clay alteration was previously associated with magmatism in the Skagerrak Graben, but was most likely formed during tropical weathering. b) Interpreted resistivity profile across a weathered weakness zone cutting the Ravneheia tunnel (from Rønning et al. 2009). The low-resistivity zones are interpreted to represent fractured and weathered bedrock.

Observed deep weathering on Lista (Øverland et al. 2012) coincides with the AMAGER solutions (Fig. 11.14a). K-Ar dating of illite in a fluorite-barite-bearing fault breccia at Heskestad on the northwestern part of the Lista peninsula (Fig. 11.14a) yielded a Late Triassic age (217 and 221 Ma; Ineson et al. 1978). The clay alteration was previously associated with magmatism in the Skagerrak Graben, but was most likely formed during a period of tropical weathering. A resistivity profile (Fig. 11.14b) across a 100 m-wide and weathered weakness zone in the Ravneheia tunnel reveals fractured and weathered bedrock extending to a depth of c. 100 m (Rønning et al. 2009, Øverland et al. 2012).

Considering the amount of possible weathering together with locally thick piles of saprolite onshore Norway (Olesen et al. 2012) it seems plausible to expect fractured and deeply weathered basement also on the basement highs offshore on the Norwegian shelf. Utsira High is a first proof of this hypothesis, but the observation and production of hydrocarbons from the basement on the UK continental shelf might raise the question, as to whether deep weathering and fracturing is a common occurrence on various basement highs along the entire Norwegian shelf. The AMAGER method is unfortunately less reliable offshore due to the sedimentary coverage, which can conceal depressions in the basement morphology. 3D seismic is probably the most effective method to map fracturing in offshore domains. Folded and fractured basement and the alteration of basement rocks by weathering processes, however, also change noticeably the characteristics of a rock's physical parameters such as rock resistivity, density and magnetisation, which are also likely to be detected by marine geophysical methods. Lundin Norway compared the 3D seismic pattern from a distinct seismic time-slice with the topography onshore southwestern Norway and discussed their similarities (Fig. 11.13). From onshore-offshore, high-resolution aeromagnetic data we correlated noticeable onshore deep weathering/fractured basement lineaments with magnetic features offshore (Fig. 11.11). For one area offshore Karmøy, where 2D seismic data were on hand, we could confirm the character of the interpreted magnetic features as fractured basement (Fig. 11.16).

Mapping of the deeply weathered bedrock on the strandflat along the coast of western Norway indicates that this mostly horizontal surface close to sea level was originally an exhumed pre-Quaternary surface. The deeply weathered and fractured basement rocks could have facilitated effective glacial erosion during the c. 40 glaciations in the Pleistocene. Freezing and thawing combined with abrasion by ocean waves during non-glaciated periods would have assisted in the formation of a relatively wide strandflat along the coast from Rogaland to Troms. Resistivity profiling has revealed a more than 100 m-thick unit of deep weathering in the Lofoten-Vesterålen-Hamarøya area in northern Norway and in the Oslofjord area (Olesen et al. 2012).

A Late Triassic or Early Jurassic age for the exhumed surface is likely. The occurrence of downfaulted Jurassic rocks to the east of the Øygarden Fault Zone on Bjorøy south of Bergen (Fossen et al. 1997), and along the inner part of the Møre-Trøndelag Fault Zone in the Griptarane area (Bøe & Skilbrei 1998) and Edøyfjord (Bøe & Bjerkli 1989), and in the Frøya-

Frohavet area (Bøe et al. 2005, 2010), suggests the presence of a boundary between basement rocks and overlying Mesozoic sediments which was situated not far above the present surface (Holtedahl 1998). Bøe et al. (2005) reported extensive weathering of the fault rocks and the Early Palaeozoic igneous rocks within the Frøyfjorden fault zone between Hitra and Frøya. Carstens (2012) and Lauritzen (2013) have further reported that deep weathering has facilitated the formation of coastal caves along the Norwegian coast (e.g., the Torghatten cave in Nordland). These reports support the conclusion that the Norwegian strandflat is an exhumed weathered and peneplaned surface of Late Triassic to Early Jurassic age that has been modified and levelled during Pleistocene erosion. The surface was preserved beneath Late Jurassic and Cretaceous sediments until the Neogene. This conclusion is also supported by the occurrence of a relatively flat and gently westward-dipping basement surface beneath the Jurassic sedimentary rocks close to the Norwegian coast (Fossen et al. 1997, Fossen 1998). The relatively high mountains on the Nordland standflat (e.g., Trollvasstinden 799 m, Lovund, 623 m Trænstaven 338 m, Landgode 802 m) most likely represent inselbergs on the Mesozoic peneplain.

Olesen et al. (2013) have also suggested that the Pleistocene erosion and unloading along the coast and loading in the central part of the North Sea and along the outer shelf in the North Sea Fan and the Naust Formation farther north constitute the main agent for the present-day seismicity on the shelf and along the coast. Pressure decrease associated with removal of sedimentary overburden along the coast may have caused an expansion of gas and resulted in expulsion of oil from the traps. Where uplift and tilting resulted in local extension, seal breaching and spillage may also have occurred, as in the Barents Sea (Nyland et al. 1992).

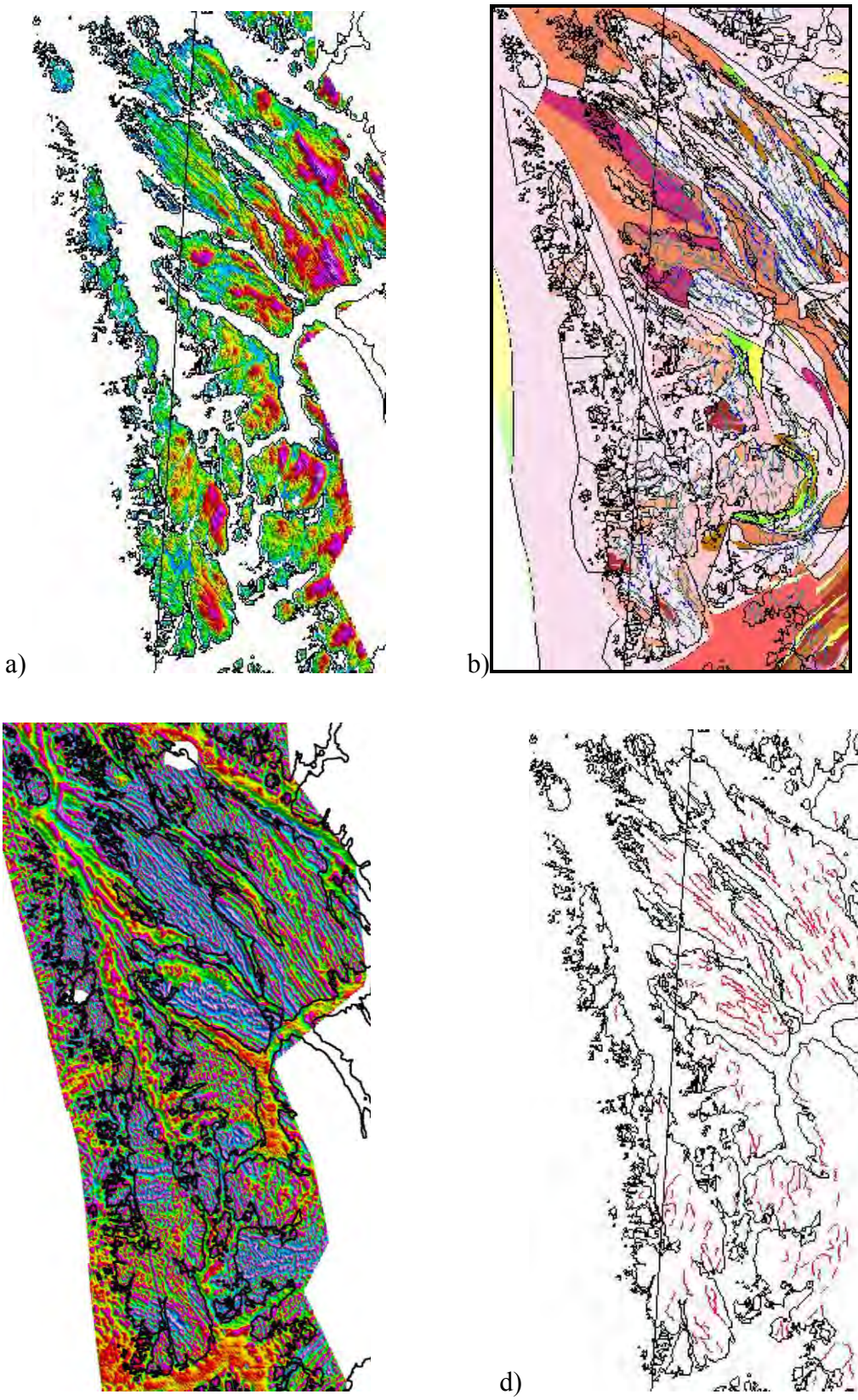

Figure 11.15 a) Topographic data of the Bergen area, b) geological map of the area with AMAGER solutions, c) 1 km high-pass filter of the aeromagnetic data and d) AMAGER solutions for the Bergen area). The AMAGER solution north of the Osterfjorden in Nordhordland shows a noticeable correlation with the structural trend of the geology and adjacent different basement types, which can indicate that saprolite remains may occur along the dominant foliation. To the SW on Sotra and Askøy, however, the solutions are rather irregular.

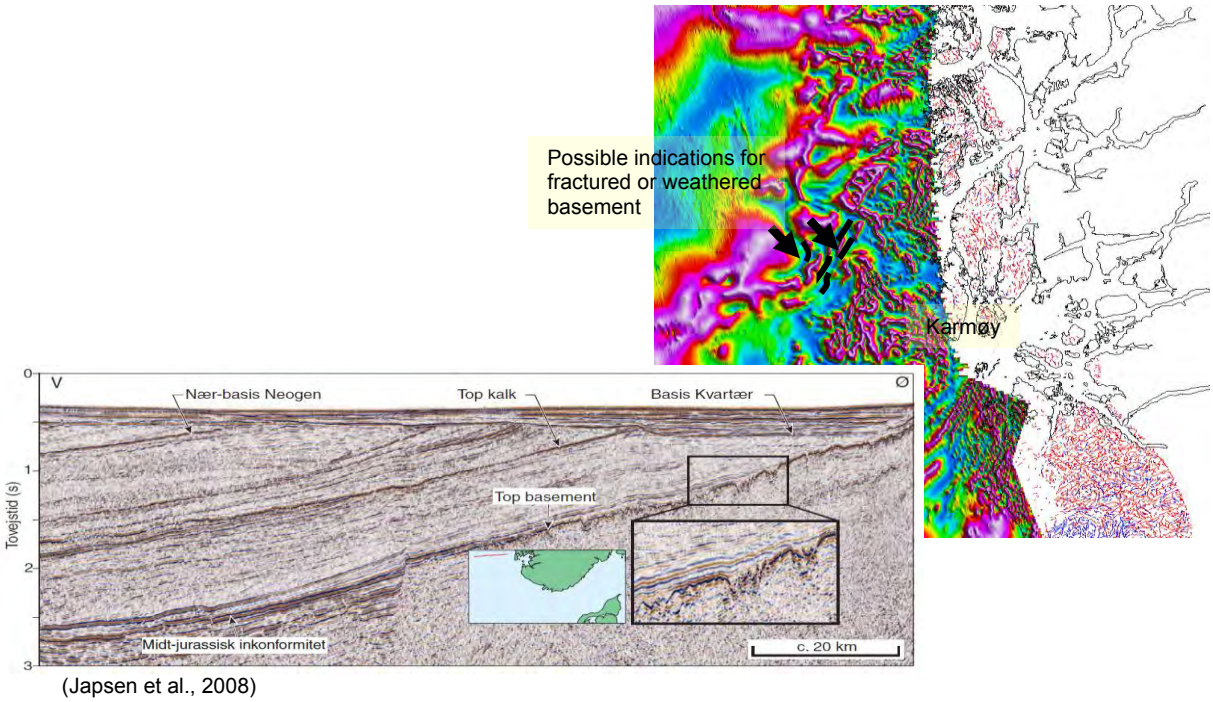

(Japsen et al., 2008)

Figure 11.16 Correlation of seismic data west of Karmøy, which indicate a significant amount of weathered and/or fractured basement (interpreted by Lars Nørgård-Jensen and presented in Japsen et al. 2008), and lineaments observed from the TILT derivative of the aeromagnetic data.

Depending on the depth to the basement and its magnetic response and, consequently, the magnetic contrast of unweathered and weathered/fractured basement, the correlation of magnetic and seismic data can be useful as a first approach for the systematic mapping of deeply weathered and/or fractured basement offshore.

11.3 Basement+ structures

Aeromagnetic and gravity data combined with petrophysical data (Figs. 2.11-2.17, 3.1, 3.6 & 5.2-5.4) fund a significant basis for mapping crustal structures both on mainland Norway and in the adjacent offshore regions. The new aeromagnetic and gravity compilations reveal Caledonian structures continuing from Great Britain across the North Sea to mainland Norway. Extrapolations of Late-Caledonian detachment structures occurring on the mainland can be traced on aeromagnetic and gravimetric images towards the SW across the North Sea. The footwall blocks of the detachments usually constitute magnetic Precambrian gneisses and intrusives while the hanging wall blocks of the detachments contain Caledonian nappes in the Upper and Uppermost Allochthon and post-Caledonian sediments which generally are low-magnetic.

Negative and positive anomalies on the continental shelf reflect to a large extent sedimentary basins and structural highs, respectively. Fig. 11.17 shows the spatial relationship between core complexes, low-angle detachments and the Transscandinavian Igneous Belt (TIB). The lower crustal rocks were exhumed along the low-angle detachments during a late phase of the Caledonian orogeny (Osmundsen et al. 2002, Olesen et al. 2002, 2010).

Of particular interest is the recognition of the structurally denuded basement culminations onshore Norway, and their bounding detachments. These major detachments formed during orogen-parallel extension, i.e., at a high angle to the orogenic front (Fig. 11.7). Detachments of a similar age and style have been mapped in East Greenland, e.g., the Fjord Region and Ardencaple Detachments (Hartz et al. 2002).

The asymmetry of the gravity anomalies within the Kongsberg–Bamble Complex, combined with the steep gradient, points to the overthrusted high-density granulites as being the main source of the observed anomalies (Olesen et al. 2010). The Kongsberg–Bamble anomalies can be traced southwards through the Kattegat to southern Sweden. A combined interpretation of the potential field and seismic data shows that the gravity anomalies previously suggested as relating to Permian igneous activity in the Kongsberg-Bamble, Skagerrak, central Jutland and Scania, to a large degree represent density variations and regional structures in the Sveconorwegian basement.

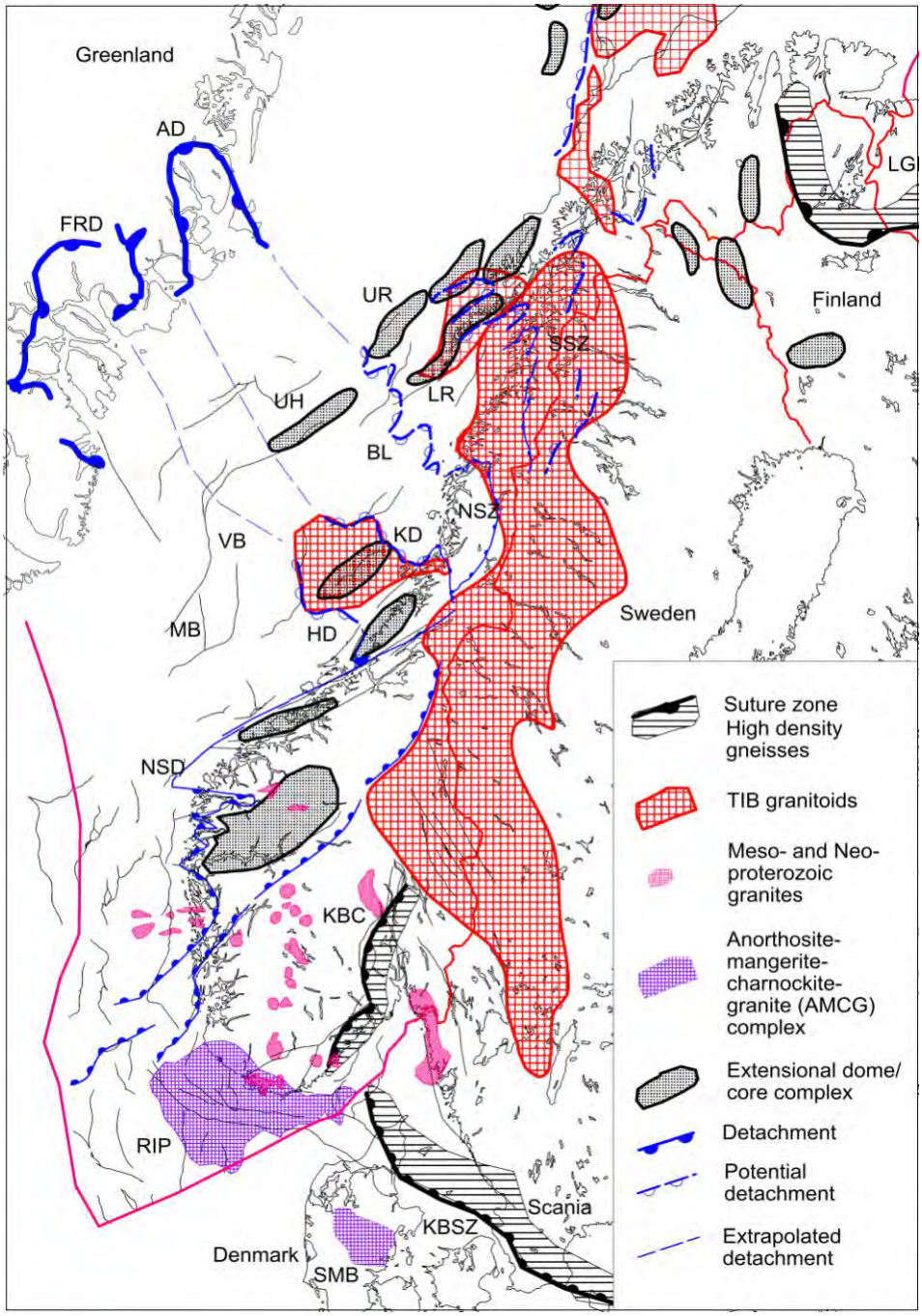

Figure 11.17. Regional structures compiled from interpretations of potential field data and bedrock mapping (Braathen et al. 2002, Hartz et al. 2002, Osmundsen et al. 2002, Ebbing et al. 2007, Barrère et al. 2009, Olesen et al. 2010). Greenland is rotated back to its pre-opening of the Atlantic position in the Eocene. AD – Ardencaple Fjord Detachment; BL – Bivrost Lineament, FRD—Fjord Region Detachment system; KBSS – Kongsberg-Bornholm Suture Zone; KBC – Kongsberg-Bamble Complex; KD – Kollstraumen Detachment, LGB – Lapland Granulite Belt; LR – Lofoten Ridge, MB – Møre Basin; NSZ – Nesna Shear Zone, NSD – Nordfjord-Sogn Detachment Zone, RIP – Rogaland Igneous Province; SSZ – Sagfjord Shear Zone; SMB – Silkeborg Magmatic Body; UR – Utrøst Ridge; VB – Vøring Basin.

A map showing the depth to the base of the 'Caledonian nappes' or a depth to autochthonous Precambrian basement in southern Norway was compiled in the Kontiki Project (Olesen et al.

2007b) (Fig. 11.18). The greatest depths can be found in the Faultingsgraben (6-10 km, Skilbrei 1989) to the north of the Hardangerfjord Shear Zone and in the Trøndelag area (8-12 km, Skilbrei et al. 2002). We assume that these nappes extend into the North Sea along the Hardangerfjord Shear Zone and can account for the relatively large discrepancies between depths to crystalline and magnetic basement (See Chapters 7 & 12). This conclusion receives support from the dating of basement rocks in the North Sea which revealed the same age and type of widespread magmatism related to the final closing of the Iapetus Ocean (Slagstad & Davidsen 2007, Slagstad et al. 2011).

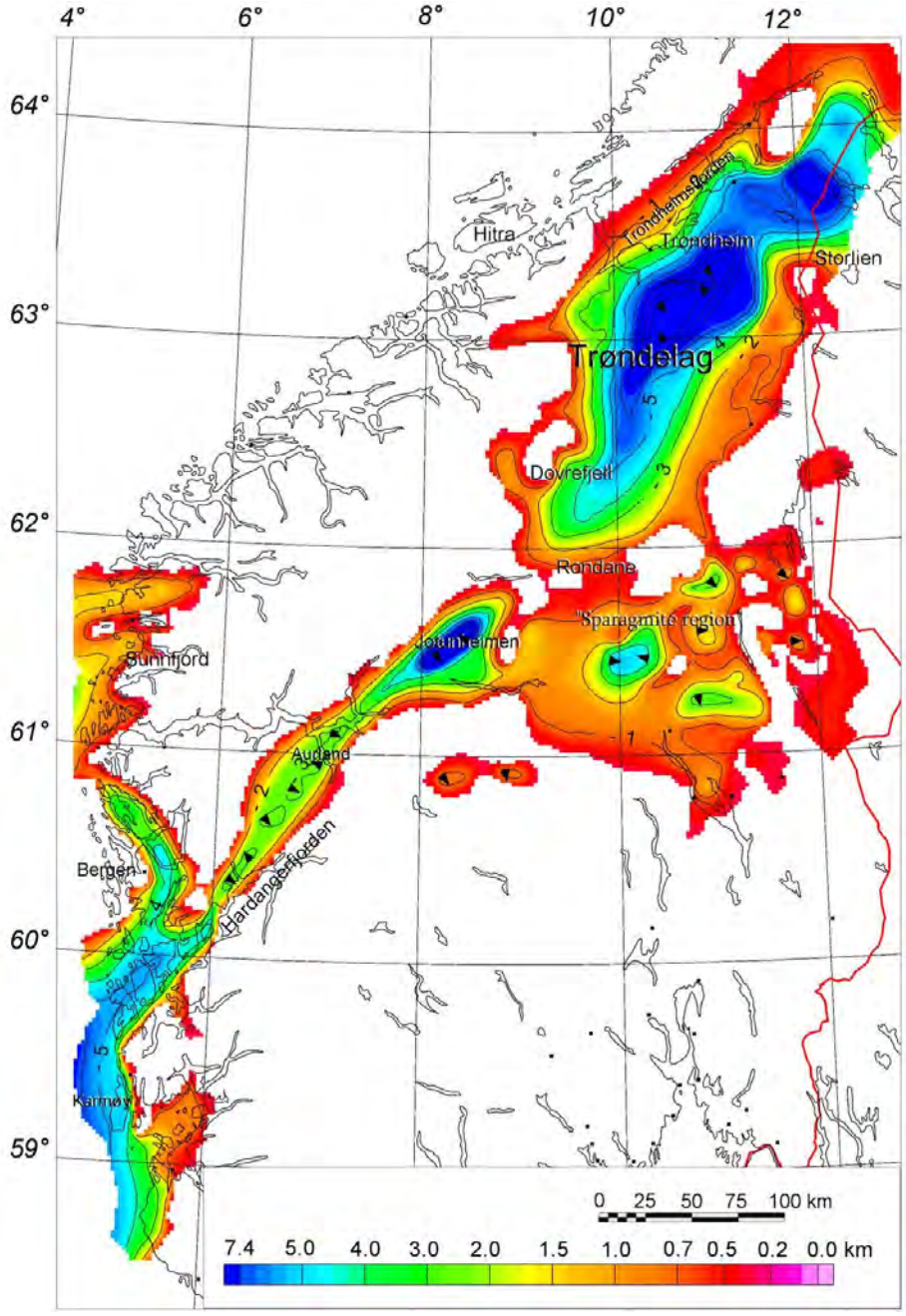

Figure 11.18. Estimated depths to the base of the Caledonian nappes from sea level, South and Central Norwegian Caledonides (Olesen et al. 2007b). Because the tectonic position of rocks of Precambrian age is uncertain in some areas (parautochthonous/allochthonous), the surface is kept close to rocks of Cambro-Silurian age, where possible. Note the deep synformal depressions in western Norway, Jotunheimen and particularly in Trøndelag and a more detailed basement topography in eastern Norway (Sparagmite region).

12. 3D CRUSTAL AND THERMAL MODELLING

Yuriy Maystrenko, NGU

12.1 Introduction

In order to analyse the regional configuration of the crystalline crust within the northern North Sea and adjacent areas of the continent, a lithosphere-scale 3D structural model has been constructed, covering the area of interest in the frame of the COOP project. The 3D model covers the area from 55.9°N-56.2°N to 61.9°N-62.2°N latitude and from 0.5°W-1°E to 8.8°E-8.9°E longitude (see red frame in Fig. 12.1). The study area covered by the 3D model is characterised by a smoothed bathymetry within most parts of the North Sea. Exceptions are observed only along the southern coast of Norway and within some fjords where depths to the sea floor reach 700-1300 m. Changes in topography are pronounced on the mainland. There, the relief is locally more than 2,000 m above mean sea level.

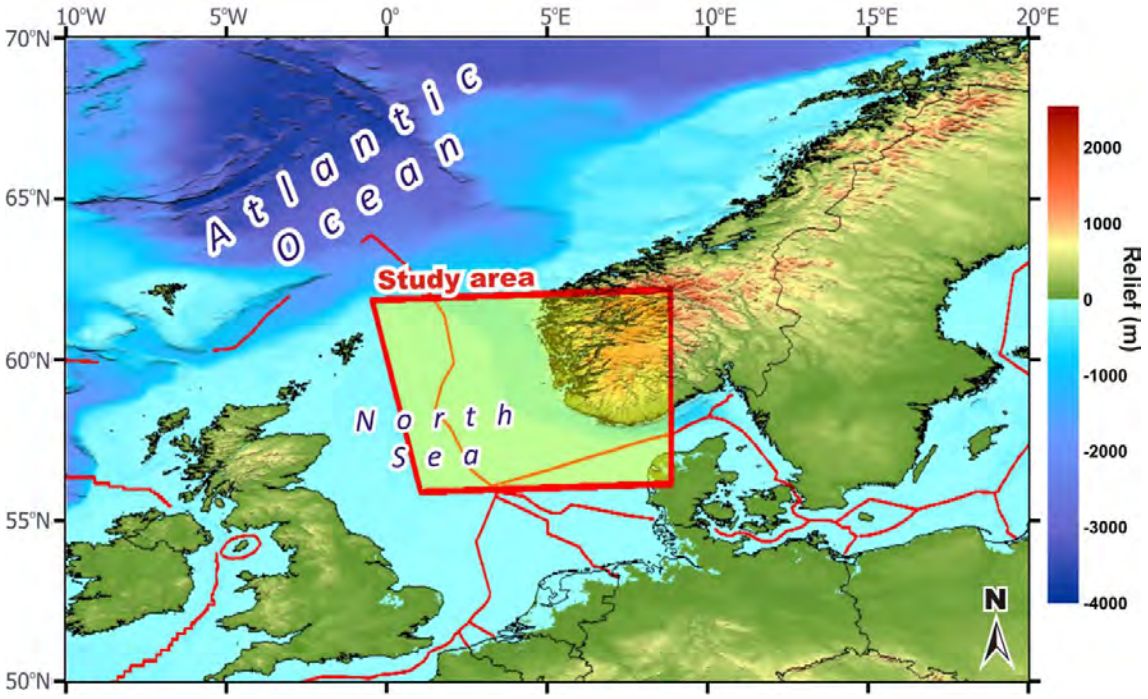

Figure 12.1. Overview map of northwestern Europe (bathymetry and topography from IOC, IHO, BODC 2003).

The 3D structural model covers the main tectonic units of the northern North Sea and the adjacent areas. Offshore, this includes major sedimentary depocentres within the Central and Viking grabens, the East Shetland and Norwegian-Danish basins, as well as the East Shetland and Horda platforms (Fig. 12.2). In addition, the model partially covers northern parts of the uplifted Mid North Sea and Ringkoebing-Fyn highs. Onshore, the sediments are relatively thin or mostly absent and, therefore, the crystalline rocks crop out at the surface within a large part of the continent.

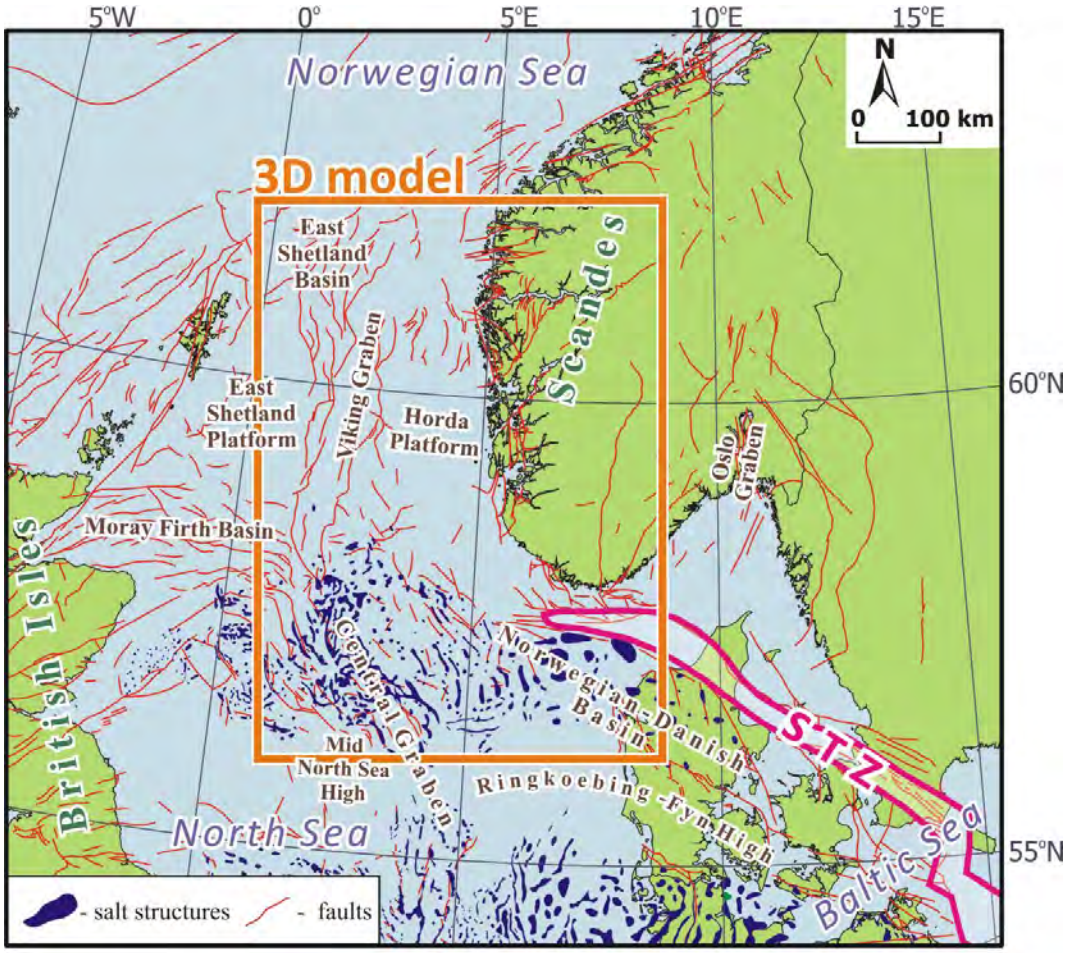

Figure 12.2. Tectonic settings within the study area with location of the 3D structural model of the northern North Sea and adjacent areas of the continent (after Ziegler 1990, Vejbæk & Britze 1994, Lokhorst 1998, Pharaoh 1999, Baldschuhn et al. 2001, Sigmond 2002, Maystrenko et al. 2012). STZ - Sorgenfrei-Tornquist Zone.

During construction of the 3D model, all available structural data have been integrated into an initial 3D model with help of 3D density modelling to obtain a lithosphere-scale 3D model of the area under consideration. This gravity-consistent 3D model was used as a structural base to evaluate the 3D conductive thermal field within the sedimentary infill, the underlying crystalline crust and the uppermost mantle.

The final 3D structural model is 672 km long and 488 km wide (Fig. 12.3), having a horizontal grid spacing of 4 km. The final constructed model consists of 21 layers from the base of the lithosphere to the present-day Earth´s surface: (1) sea water; (2) Tertiary; (3) Upper Cretaceous; (4) Lower Cretaceous; (5) Jurassic; (6) Triassic; (7) Zechstein salt;

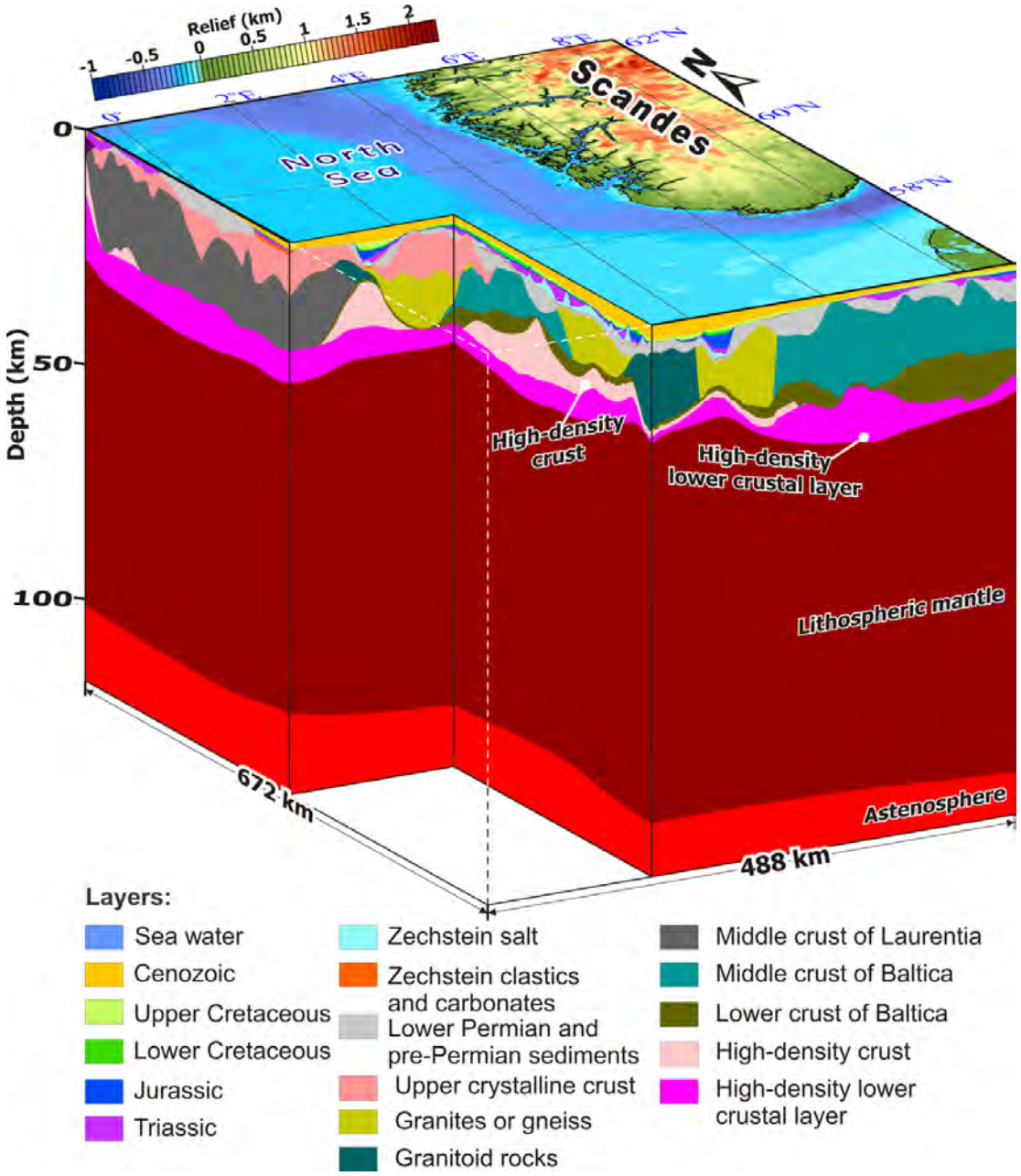

Figure 12.3. Lithosphere-scale 3D model of the northern North Sea and adjacent areas of the continent (four times vertically exaggerated).

(8) Zechstein clastics, carbonates and anhydrites; (9) pre-Permian sediments; (10) intrusions; (11) upper crustal magmatic rocks; (12) low-dense upper crustal layer; (13) upper crustal regional layer; (14) middle crust of Baltica; (15) eastern central North Sea rocks; (16) western central North Sea rocks; (17) middle crust of Laurentia and Avalonia; (18) lower crust of Baltica; (19) high-density crust; (20) high-density lower crustal layer; and (21) lithospheric upper mantle. Model coordinates are based on the Universal Transverse Mercator (UTM) coordinate system zone 32 (Northern Hemisphere), using the World Geodetic System (WGS) 84 datum.

12.2 Datasets

12.2.1 Structural data for the sedimentary cover

Construction of the 3D model has been carried out using recently published/released structural data. For the sedimentary cover, the largest dataset was the North Sea Digital Atlas (PGS Reservoir 2003) which covers the entire North Sea (Fig. 12.4).

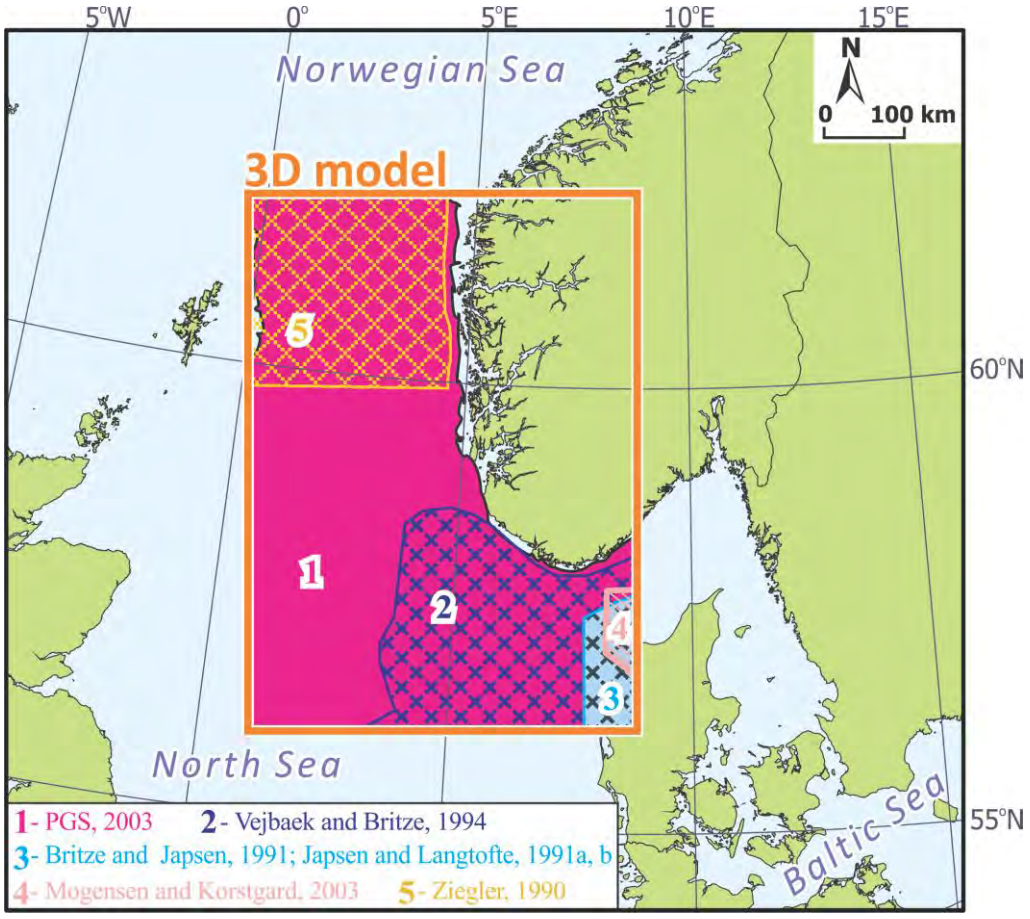

Figure 12.4 Datasets used for the sedimentary infill.

The TWT thickness maps of the Cenozoic, Upper Cretaceous, Lower Cretaceous, Jurassic, Triassic and Upper Permian (Zechstein) have been derived from the North Sea Digital Atlas (PGS Reservoir 2003). Subsequently, the obtained TWT thickness maps have been depth-converted by use of interval velocities. The interval velocities of the Upper Permian (Zechstein) (Fig. 12.5a) have been calculated according to NITG (2004) by use of equation (12.1).

$$V_i = a + c/(\Delta T - b) \quad (12.1)$$

where V_i is the interval velocity [m/s], a is the asymptote interval velocity (4410 m/s), c is a constant (47.36 m), ΔT is the one-way time thickness [s] and b is the asymptote (-0.018 s).

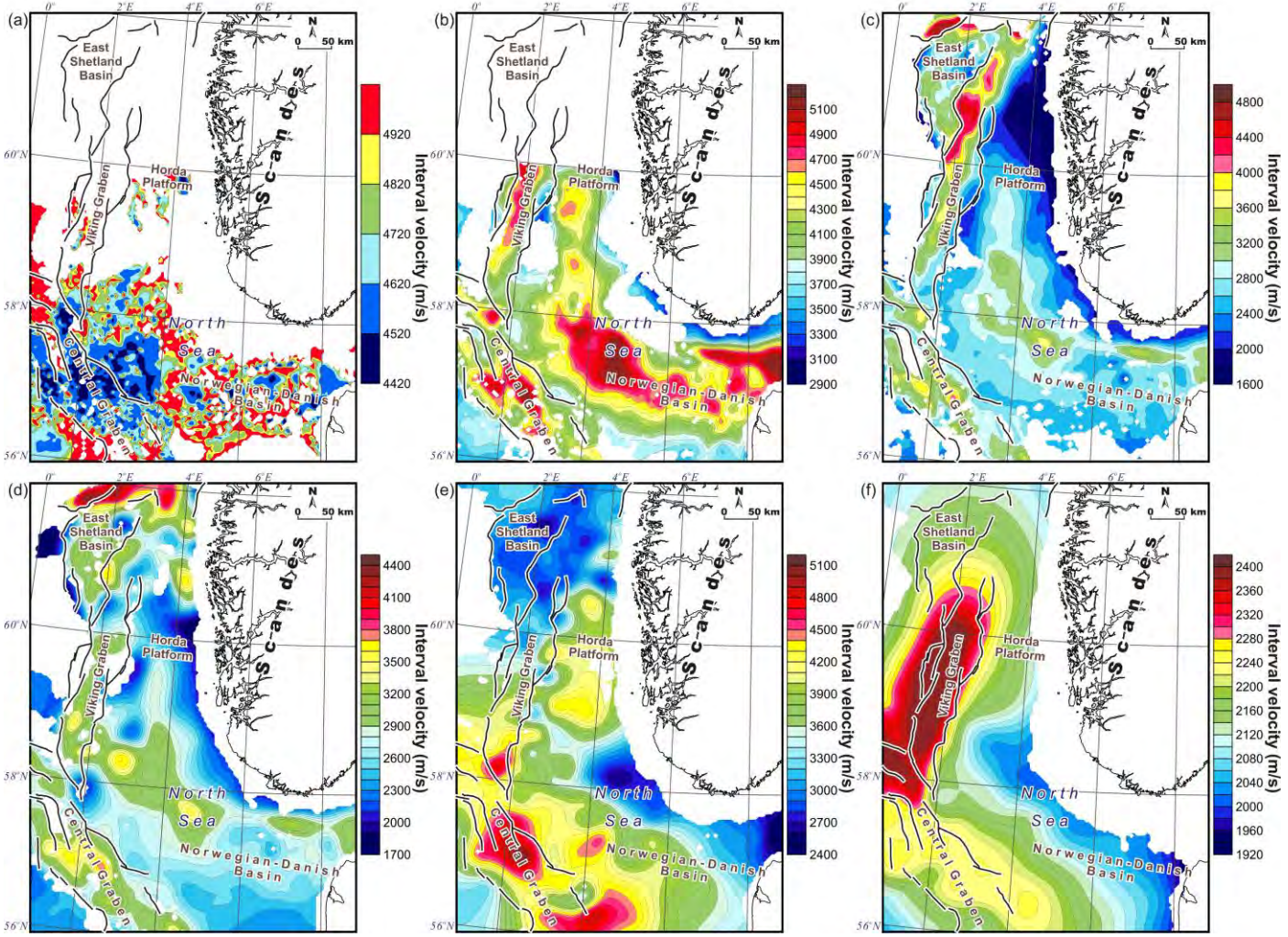

Figure 12.5. Interval velocities used for depth conversion of the data from the PGS Reservoir North Sea Digital Atlas (PGS Reservoir 2003): (a) Upper Permian (Zechstein); (b) Triassic; (c) Jurassic; (d) Lower Cretaceous; (e) Upper Cretaceous; (f) Cenozoic.

Equation (1) has the physical meaning that the interval velocities decrease with thickening of Upper Permian (Zechstein) sequence, allowing to take into account the lithological heterogeneity of the Zechstein sediments. The thick Zechstein is mostly represented by rock salt which was mobilised during several phases of salt tectonics to form various salt structures within the study area. On the other hand, the relatively thin sediments correspond to high-velocity carbonates and anhydrates which dominate within the thin Zechstein succession either as a result of differences in depositional conditions or due to post-Permian salt withdrawal.

In order to obtain Triassic and Jurassic interval velocities, the burial anomaly of the Chalk Group (Japsen 1998) has been adopted for the calculation of velocity anomalies in the case of both Jurassic and Triassic strata. Particularly, the interval velocities of the Triassic (Fig. 12.5b) and the Jurassic (Fig. 12.5c) have been derived according to the equation (12.2).

$$V_i = \Delta Z / \Delta T \quad (12.2)$$

where V_i is the interval velocity [m/s], ΔZ is the thickness of the layer [m] and ΔT is a one-way time thickness [s]. The thickness of the layer (ΔZ) according to Japsen (1993) is given as

$$\Delta Z = 1/k(V_o + dV + kZ_t)(e^{k\,\Delta T/2} - 1) \quad (12.3)$$

where k is the velocity gradient [m/s/m], V_o is the surface velocity [m/s], dV is the velocity anomaly [m/s], Z_t is depth to the top of the layer [m] and ΔT is a one-way time thickness [s]. Values of the velocity gradient (k) and the surface velocity (V_o) have been taken from Japsen (1994). The velocity anomaly (dV) has been calculated by use of equation (12.4).

$$dZ_b = -dV/k \quad (12.4) \text{ (according to Japsen 1998)}$$

where dZ_b is the burial anomaly [m].

The burial anomaly is the difference between the present-day burial of the sediments and the normalised depth, corresponding to normal compaction. In other words, the burial anomaly indicates the fact that the depth of the rock is anomalous relative to a reference trend (Japsen 1998). The burial anomaly is positive within the central part of the North Sea which rapidly subsided during the Cenozoic. In contrast, the burial anomaly is negative close to the coastline of Norway where Triassic and Jurassic sediments were affected by uplift and subsequent erosion towards the end of the Cretaceous and into the Cenozoic.

The interval velocities of the Lower Cretaceous (Fig. 12.5d) have been calculated by use of one-way time thickness of the Lower Cretaceous and the thickness of the Lower Cretaceous in metres from the deep wells (NPD 2011). On the other hand, the interval velocities of the Upper Cretaceous (Fig. 12.5e) are based on available interval velocities of the Chalk Group from borehole measurements (Japsen 1998). To remove some local peaks and/or artifacts

from the calculated interval velocities of the Lower and Upper Cretaceous, low-pass filtering has been applied.

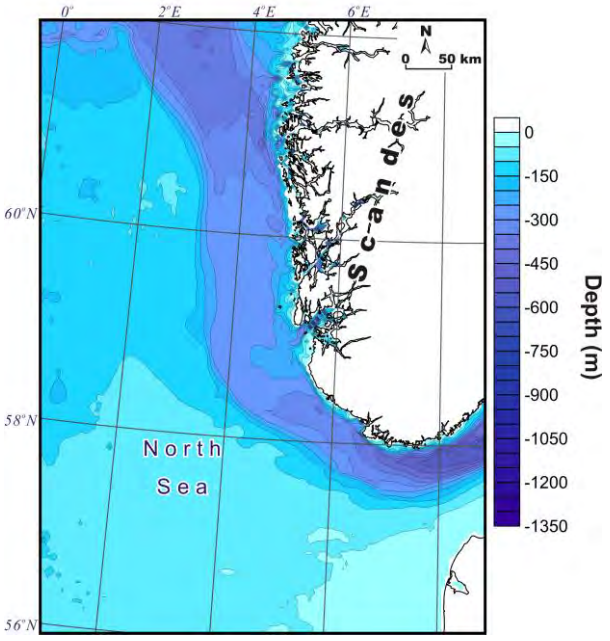

Figure 12.6. Bathymetry of the model area (from IOC, IHO, BODC 2003).

The obtained interval velocities of the Triassic, Jurassic, Lower Cretaceous and Upper Cretaceous (Figs. 12.5 a, b, c, d, e) have been cross-checked with available published data (Britze & Japsen 1991, Japsen & Langtofte 1991a, 1991b, Storvoll et al. 2005).

The interval velocities of the Cenozoic (Fig. 12.5f) have been taken from post-Chalk interval velocities according to values provided in Japsen (1999).

In addition to the data from the North Sea Digital Atlas (PGS Reservoir 2003), several thickness and structural depth maps, published by the Geological Survey of Denmark (GEUS), have been used for the southeastern part of the 3D model area within the Norwegian-Danish Basin (Fig. 12.4). These include thickness maps of the Triassic (Britze & Japsen 1991), Jurassic-Lower Cretaceous (Japsen & Langtofte 1991b), Chalk Group (Japsen & Langtofte 1991a) and structural depth maps of the top pre-Zechstein (Vejbaek & Britze 1994), top Zechstein (Britze & Japsen 1991) and base Chalk (Japsen & Langtofte 1991a) as well as the thickness of the Lower Cretaceous from Mogensen & Korstgard (2003).

The thickness of the Triassic deposits has also partially been taken from the Geological Atlas of western and central Europe (Ziegler 1990) for the northern part of the study area (Fig. 12.4).

The bathymetry has been derived from the General Bathymetric Chart of the Oceans (GEBCO) Digital Atlas (IOC, IHO, BODC 2003).

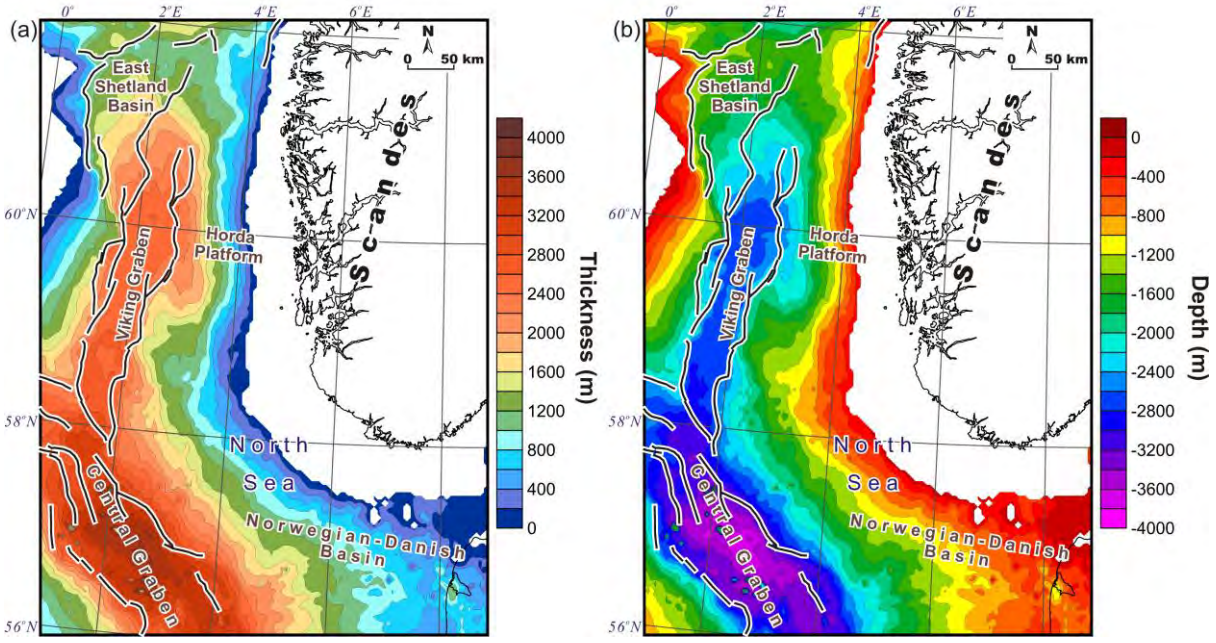

Figure 12.7. (a) Thickness map and (b) structural depth map (base of the layer) of the Cenozoic.

All mentioned datasets were gridded and compiled together in terms of thickness maps for the following intervals (Figs. 12.6-12.13): sea water, the Cenozoic, the Upper Cretaceous, the Lower Cretaceous, the Jurassic, the Triassic, the Upper Permian (Zechstein) salt and, finally, Upper Permian (Zechstein) clastics and carbonates.

The depth to sea floor is generally in the range of 100-400 m (Fig. 12.6) with prominent increases of depth along the southern coast of Norway and within the fjords. The uppermost sedimentary layer of the 3D structural model is the Cenozoic (Fig. 12.7). The wide region of thick Cenozoic is observed within the central part of the North Sea along the axial parts of the Central and Viking grabens. There, the depth to the base of the Cenozoic is more than 3,000 m. The thickness map of the Upper Cretaceous (Fig. 12.8a) shows that sediments are strongly thickened within the northern part of the Viking Graben and within the East Shetland Basin. Additionally, thickening of the Upper Cretaceous is locally observed within the Central Graben and the eastern part of the Norwegian-Danish Basin. The Lower Cretaceous (Fig. 12.9a) is characterised by pronounced thickening within the northernmost part of the study area where deposits reach more than 5,000 m in thickness. Distribution of the Jurassic sediments (Fig. 12.10a) demonstrates that the regional Jurassic depocentre is located within the Viking Graben. Several local depocentres are observed within the Central Graben and the eastern part of the Norwegian-Danish Basin. Configuration of the Central and Viking grabens is clearly recognisable at the bases of the Upper Cretaceous, Lower Cretaceous and Jurassic compared to the base of the Cenozoic (cf. Figs. 12.9b & 12.10b with Fig. 12.7), reflecting the fact that the major phase of subsidence within these grabens occurred during the Late Jurassic-Early Cretaceous interval. At that time, the Jurassic-Cretaceous North Sea rift

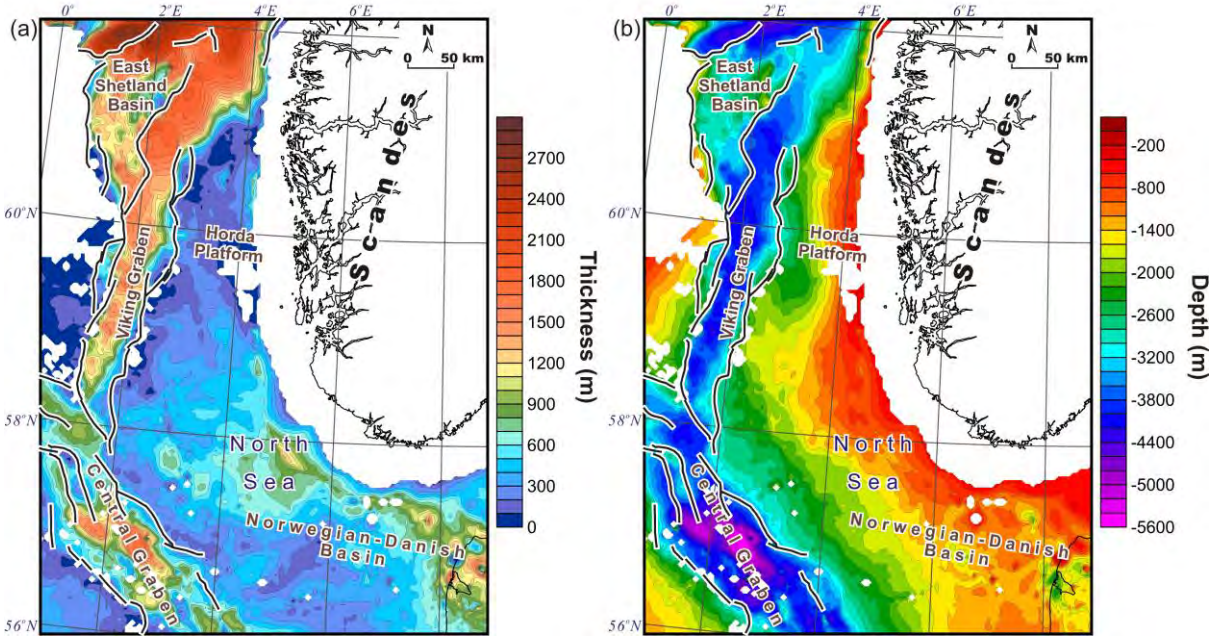

Figure 11.8. (a) Thickness map and (b) structural depth map (base of the layer) of the Upper Cretaceous.

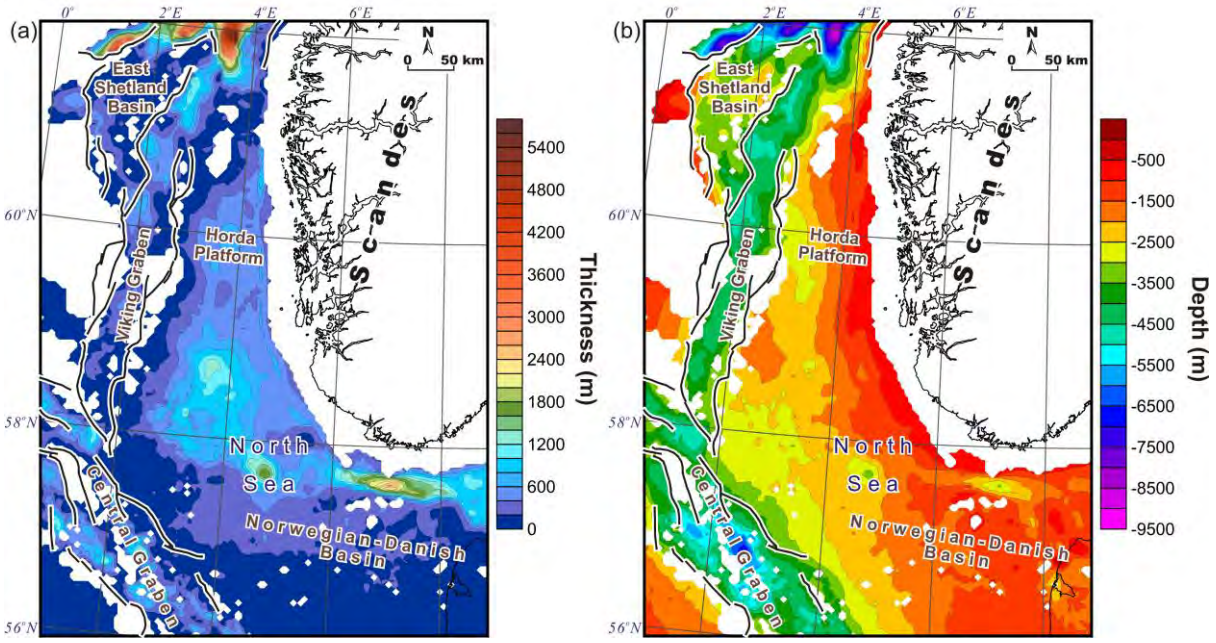

Figure 12.9. (a) Thickness map and (b) structural depth map (base of the layer) of the Lower Cretaceous.

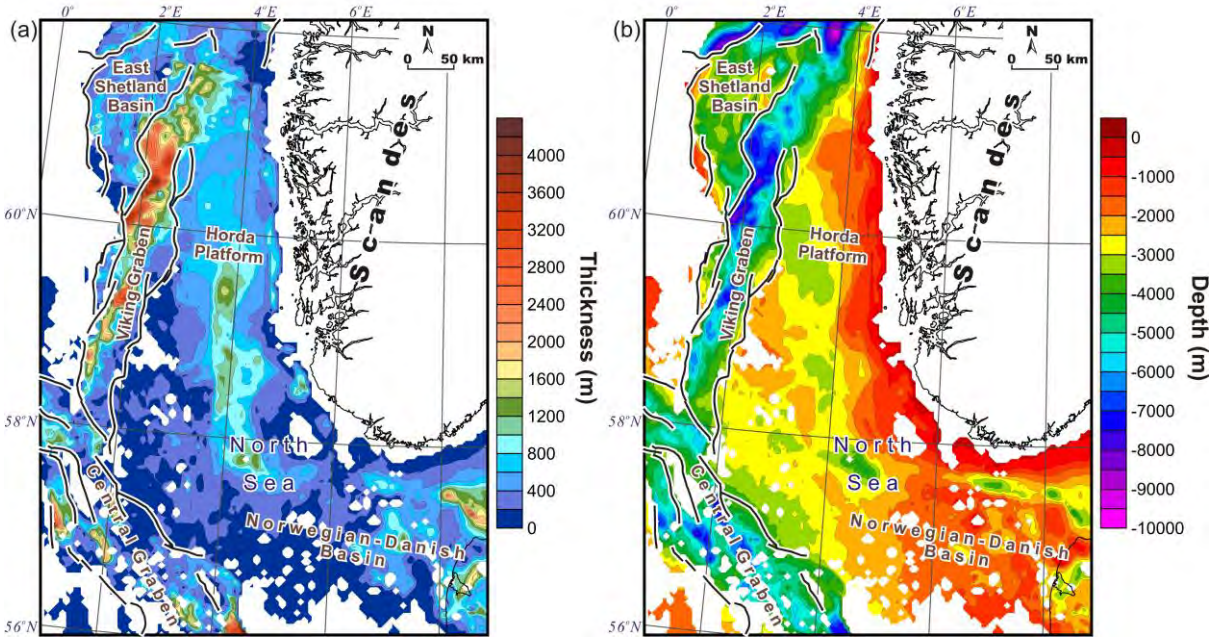

Figure 12.10. (a) Thickness map and (b) structural depth map (base of the layer) of the Jurassic.

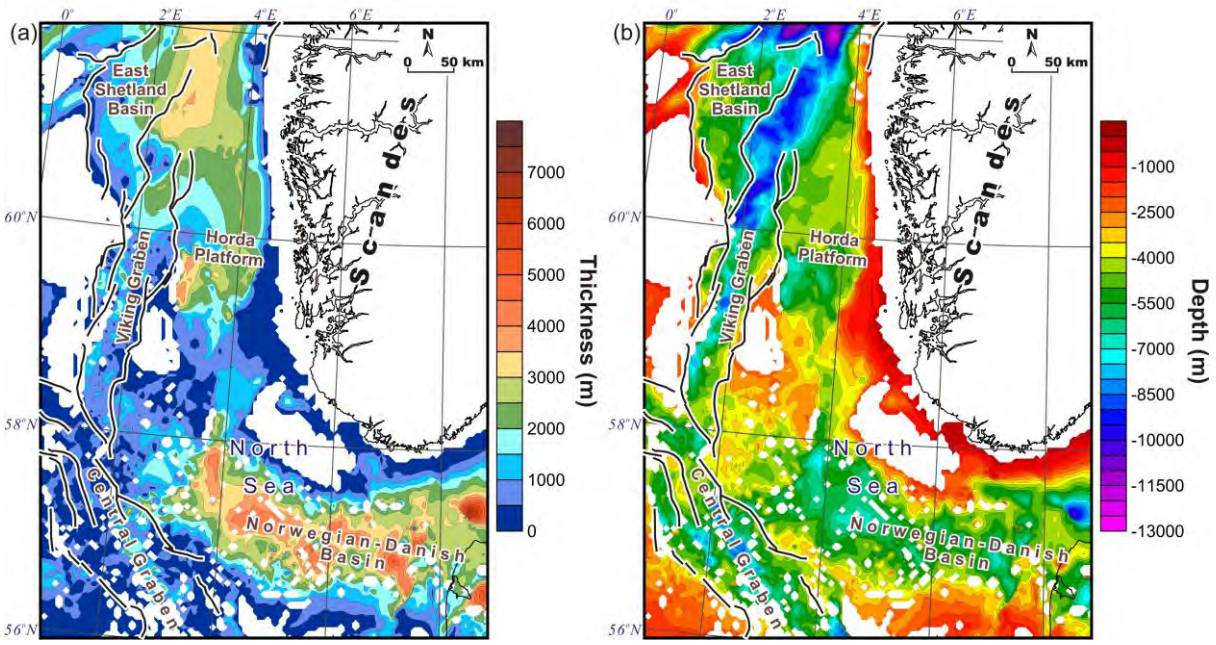

Figure 12.11. (a) Thickness map and (b) structural depth map (base of the layer) of the Triassic.

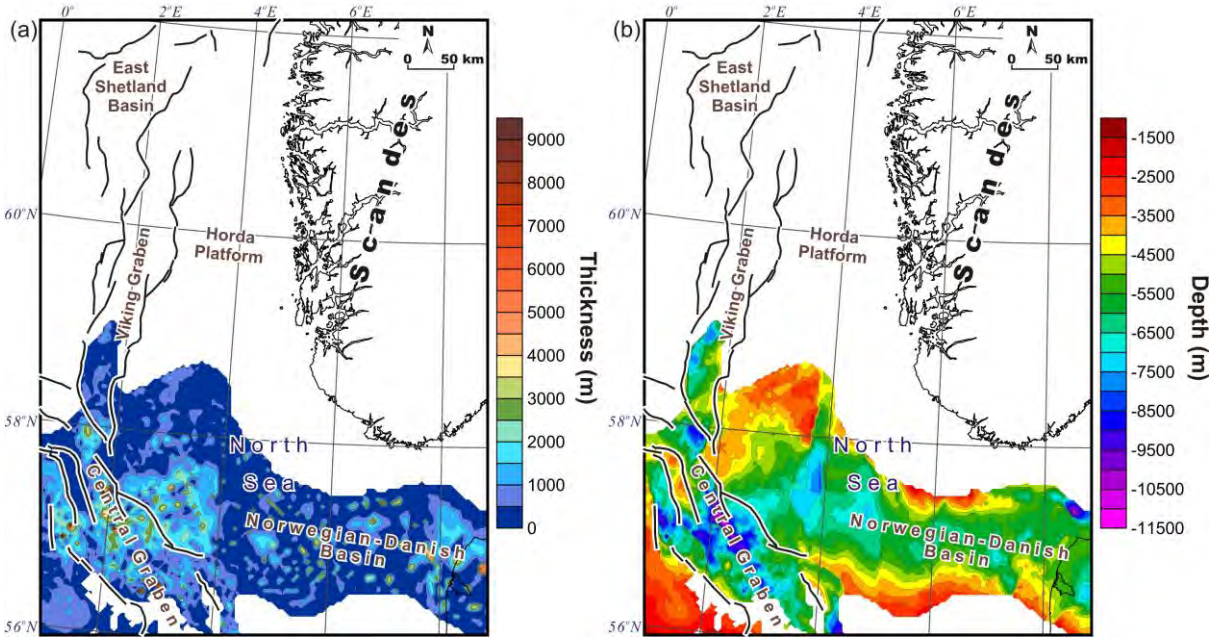

Figure 12.12. (a) Thickness map and (b) structural depth map (base of the layer) of the Upper Permian (Zechstein) salt.

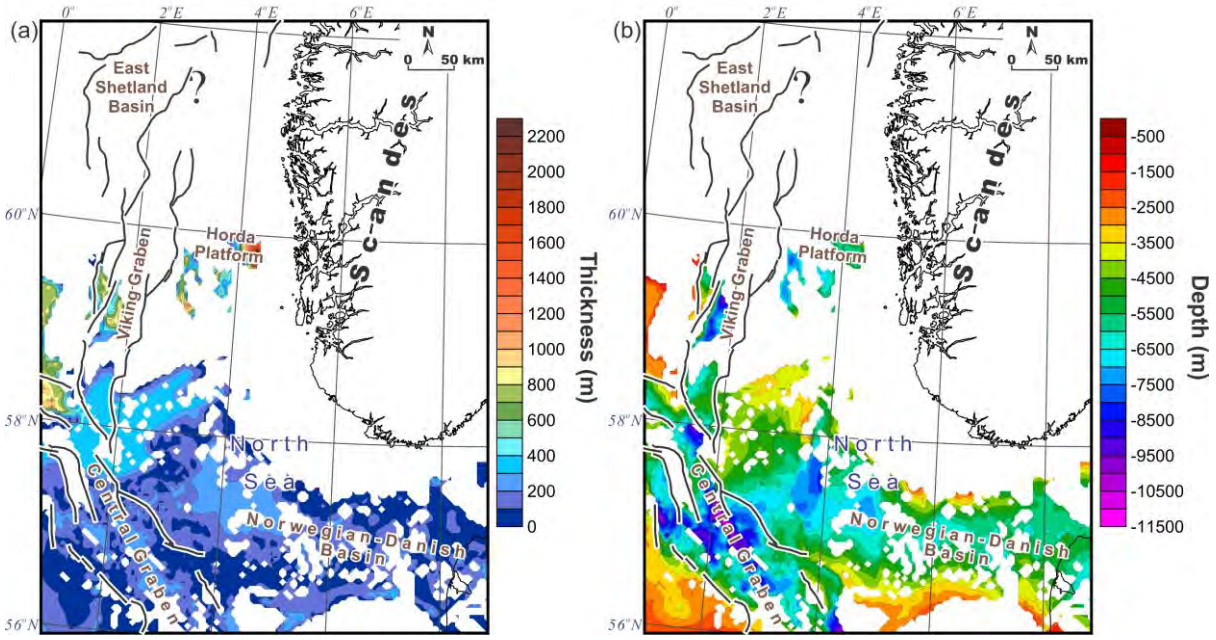

Figure 12.13. (a) Thickness map and (b) structural depth map (base of the layer) of the Upper Permian (Zechstein) clastics and carbonates. The detailed distribution of Upper Permian sediments is unknown within the northern parts of the Viking Graben and the East Shetland Basin.

system was formed within deep and relatively narrow grabens which form a triple junction of the Central and Viking grabens and the Moray Firth Basin. The next layer of the 3D model is the Triassic (Fig. 12.11a) which has a significantly thickened succession within the Norwegian-Danish Basin, the northern part of the Viking Graben and the East Shetland Basin. Depth to the base of the Triassic (Fig. 12.11b) is approximately 5,000-7,000 m within the Norwegian-Danish Basin and reaches more than 12,000 m in the north of the Viking Graben.

The thickness of the Upper Permian (Zechstein) salt (Fig. 12.12a) indicates that Zechstein salt was strongly mobilised during phases of salt tectonics which took place within the former Northern Permian Basin in response to major pulses of tectonic activity (e.g. Maystrenko et al. 2012). As a result of salt movements, the thickest Zechstein salt is localised within the areas where salt structures (walls, diapirs and pillows) were formed during post-Permian time. On the other hand, a thinning of Zechstein salt is observed within the areas where salt is strongly depleted. The Upper Permian (Zechstein) clastics and carbonates succession (Fig. 12.13a) strongly thickens considerably within the local areas of the northern part of the Northern Permian Basin. There, the non-saliferous Zechstein sequence is up to 2300 m thick.

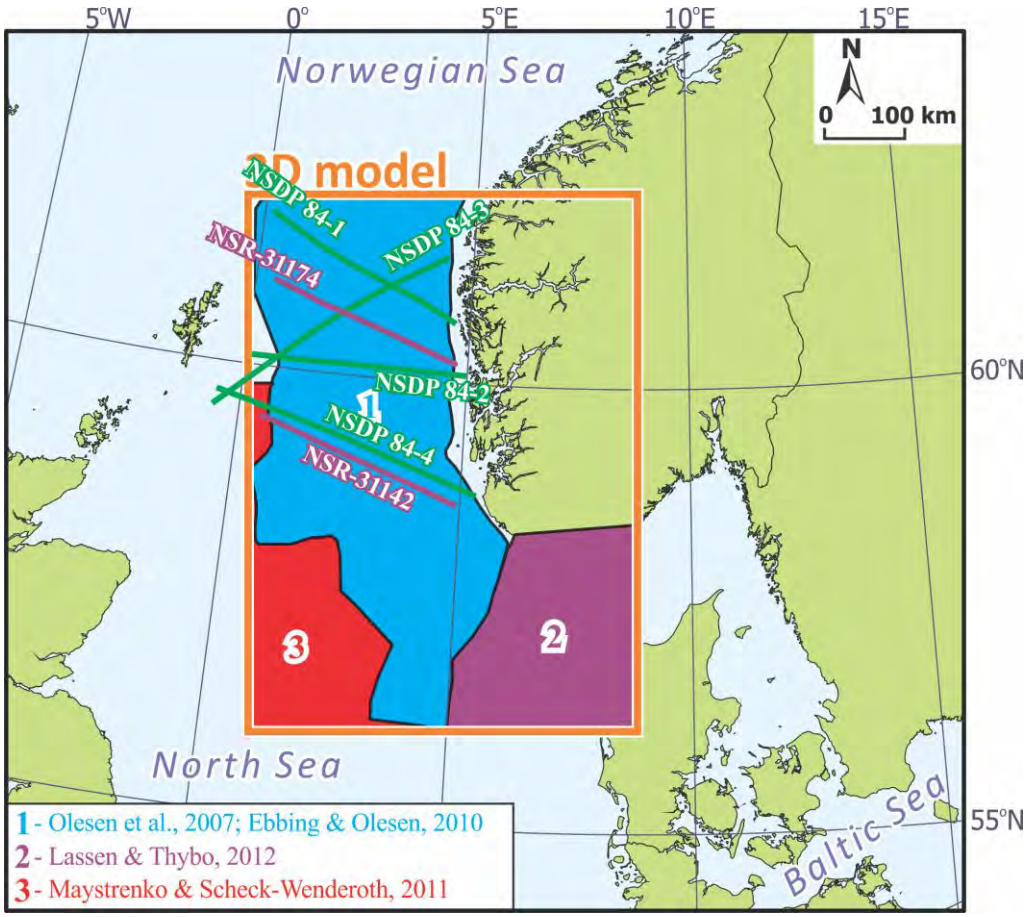

Figure 12.14. Datasets used for the top of the crystalline basement.

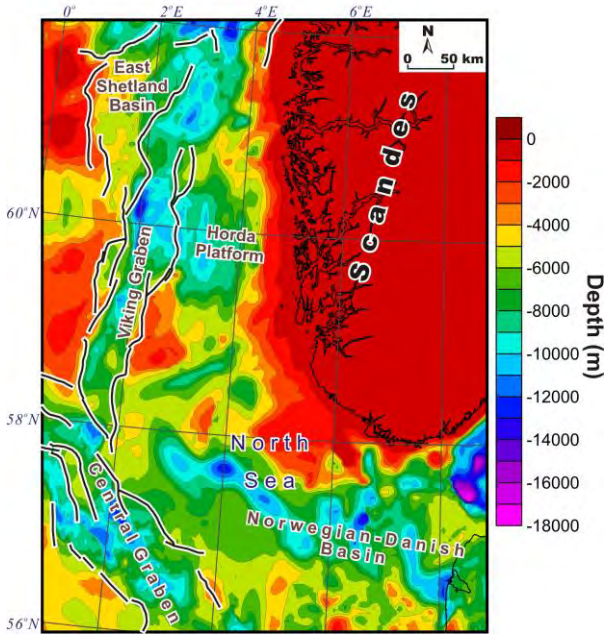

Figure 12.15. Depth to the top of the crystalline basement.

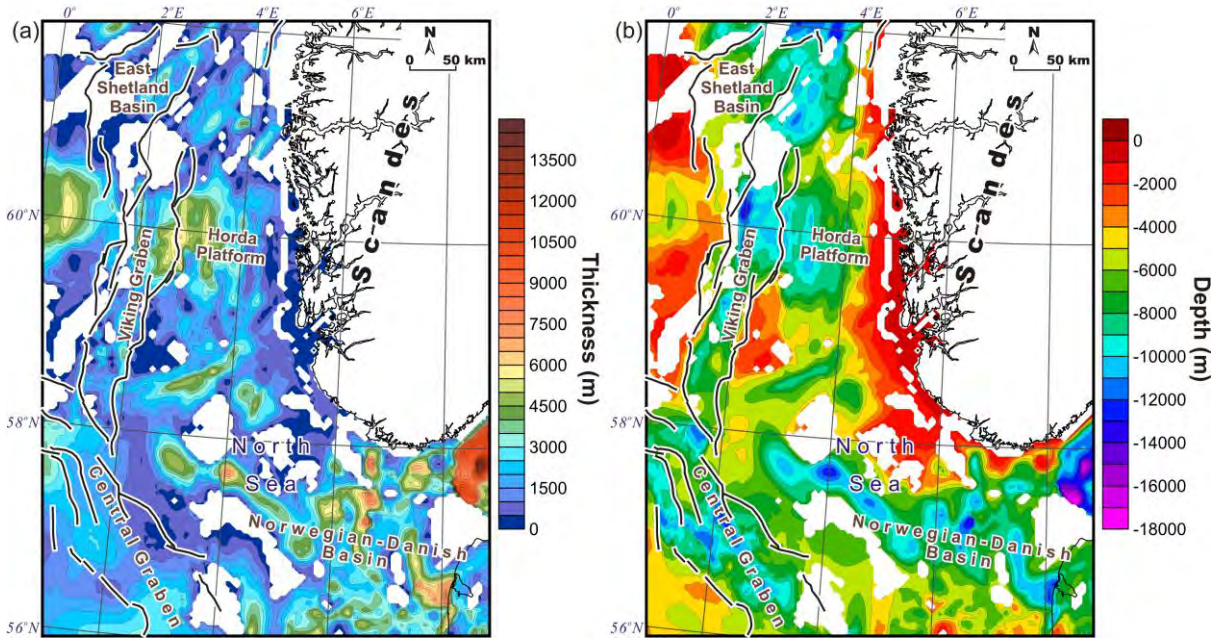

Figure 12.16. (a) Thickness map and (b) structural depth map (base of the layer) of Lower Permian and pre-Permian sedimentary rocks (Upper Permian sediments are partially included in the north of the study area).

Furthermore, well data (NPD 2011) and three datasets of depth to the top of crystalline basement (Fig. 12.14; Ebbing and Olesen 2010, Lassen et al. 2012, Maystrenko & Scheck-Wenderoth 2011) represent the main datasets for the top of the crystalline basement (Fig. 12.15) within the area under consideration. This top of the crystalline basement has been used to assess the configuration of Lower Permian and pre-Permian sediments (Fig. 12.16). The initial thickness of Lower Permian and pre-Permian sediments has been calculated as the

difference between the base of the Upper Permian-Meso-Cenozoic sediments and the top of the crystalline basement.

Configuration of the top of the crystalline basement (Fig. 12.15) reflects the superimposed effects of all tectonic events that have affected the study area and, therefore, this surface is characterised by a complicated structure. The depth to the top of the crystalline basement is almost 18 km within the northeastern part of the Norwegian-Danish basin (the Skagerrak Graben) where a marked thickening of pre-Permian sediments is observed (Lassen et al. 2012, Fig. 12.15a). The topography of the base of the sediments is relatively complex throughout the rest of the North Sea where several lows and highs are observed. The most prominent basement highs are easily recognisable within the southern flanks of the Viking Graben as well as in the northwestern corner of the model area.

The distribution of the pre-Permian sediments (Fig. 12.16) bears larger uncertainties than that of the Permian, Mesozoic and Cenozoic intervals within the areas where the depth to the top of the crystalline basement is great. The thickness map of the Lower Permian-pre-Permian (Fig. 12.16a) is characterised by areas of appreciable thickening within the Norwegian-Danish Basin. Within the northern part of the Norwegian-Danish Basin (the Skagerrak Graben), the pre-Permian layer is locally more than 13.5 km thick. Two Lower Permian-pre-Permian thickness maxima are located within the Horda and East Shetland platforms, reaching more than 6 km in thickness. The rest of the study area is characterised by a relatively thin Lower Permian-pre-Permian succession or even by an absence of sedimentary rocks.

The data obtained from these various sedimentary layers provide an excellent basis for an evaluation of the deep structure of the crystalline crust within the study area.

12.2.2 Structural data for the deep part of the study area

In contrast to the sedimentary cover, information on the depth to the Moho and the lithosphere-asthenosphere boundary is much less constrained by available data. During the last six years, four regional compilations of the Moho have been published by Ziegler & Dèzes (2006) (Fig. 12.17a), Kelly et al. (2007) (Fig. 12.17b), Davis (2010) (Fig. 12.17c), Tesauro et al. (2008) (Fig. 12.17d) and Grad et al. (2009) (Fig. 12.17e). The major structural trend of the crust-mantle boundary is always consistent within the study area, demonstrating that the crust is thick beneath the Norwegian mainland and is relatively thin beneath the sedimentary basins within the central part of the North Sea (Fig. 12.17). However, these Moho topographies represent only a general trend of the regional pattern of Moho

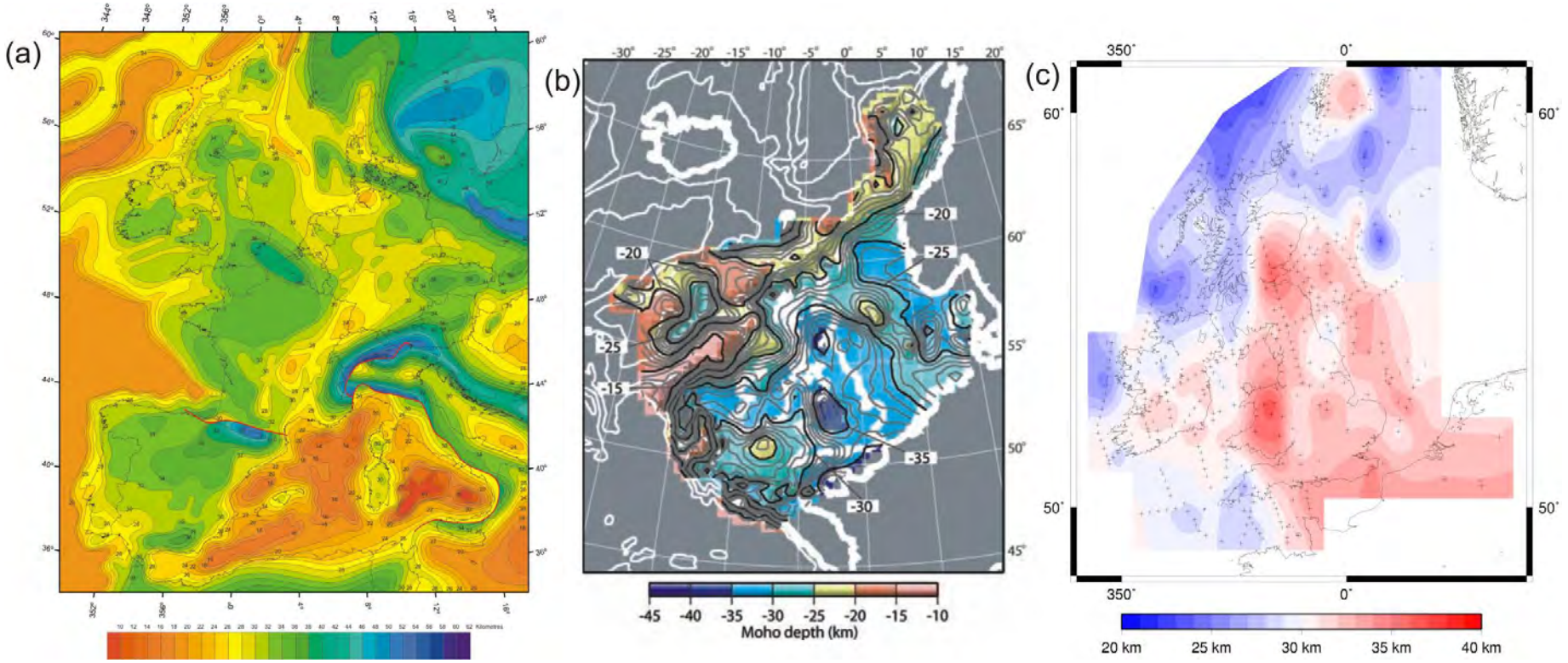

Figure 12.17. Moho topographies based on regional-scale compilations by (a) Ziegler & Dèzes (2006), (b) Kelly et al. (2007), (c) Davis, (2010), (d) Tesauro et al. (2008) and (e) Grad et al. (2009).

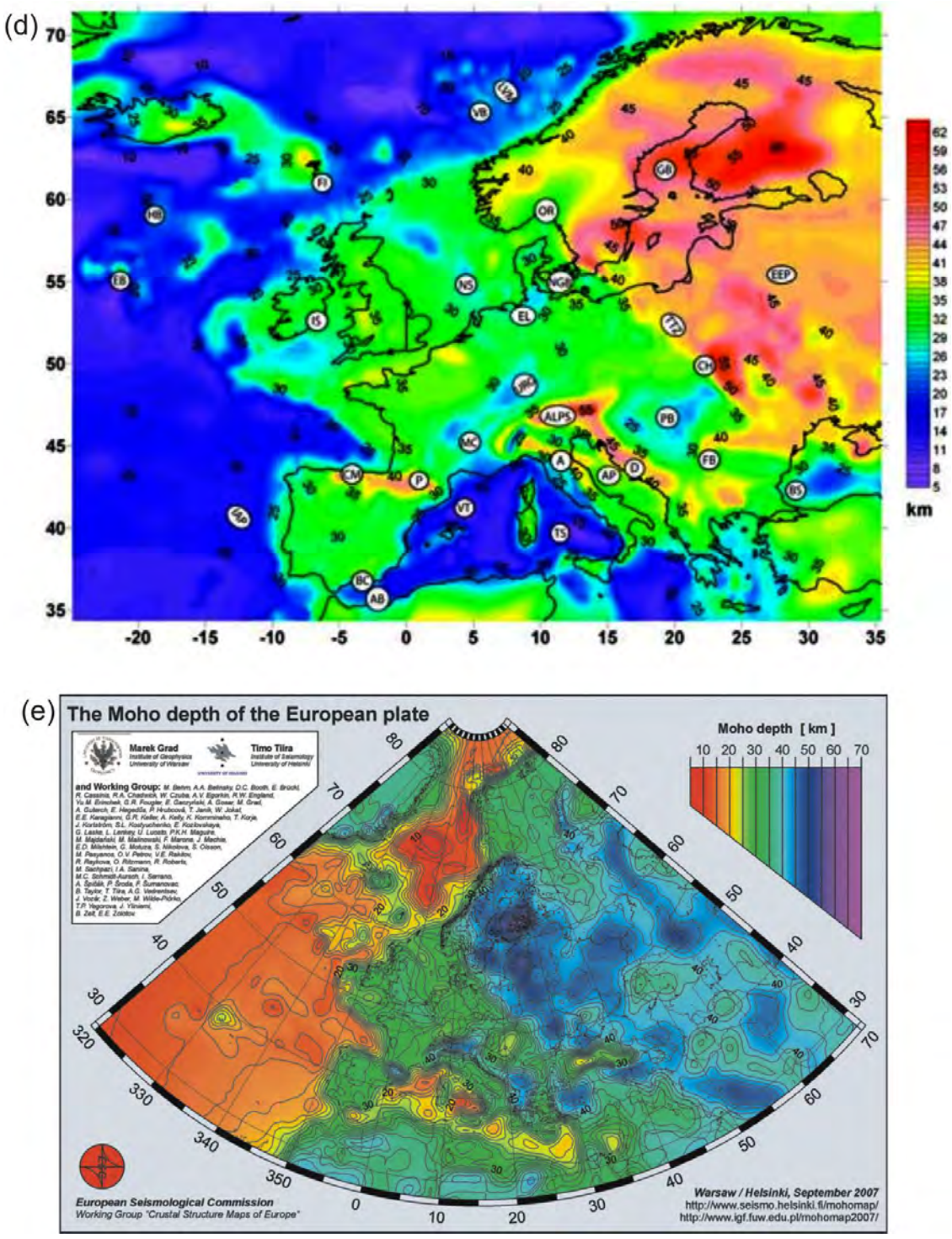

Figure 12.17. continued. Moho topographies based on regional-scale compilations by (a) Ziegler & Dèzes (2006), (b) Kelly et al. (2007), (c) Davis, (2010), (d) Tesauro et al. (2008) and (e) Grad et al. (2009).

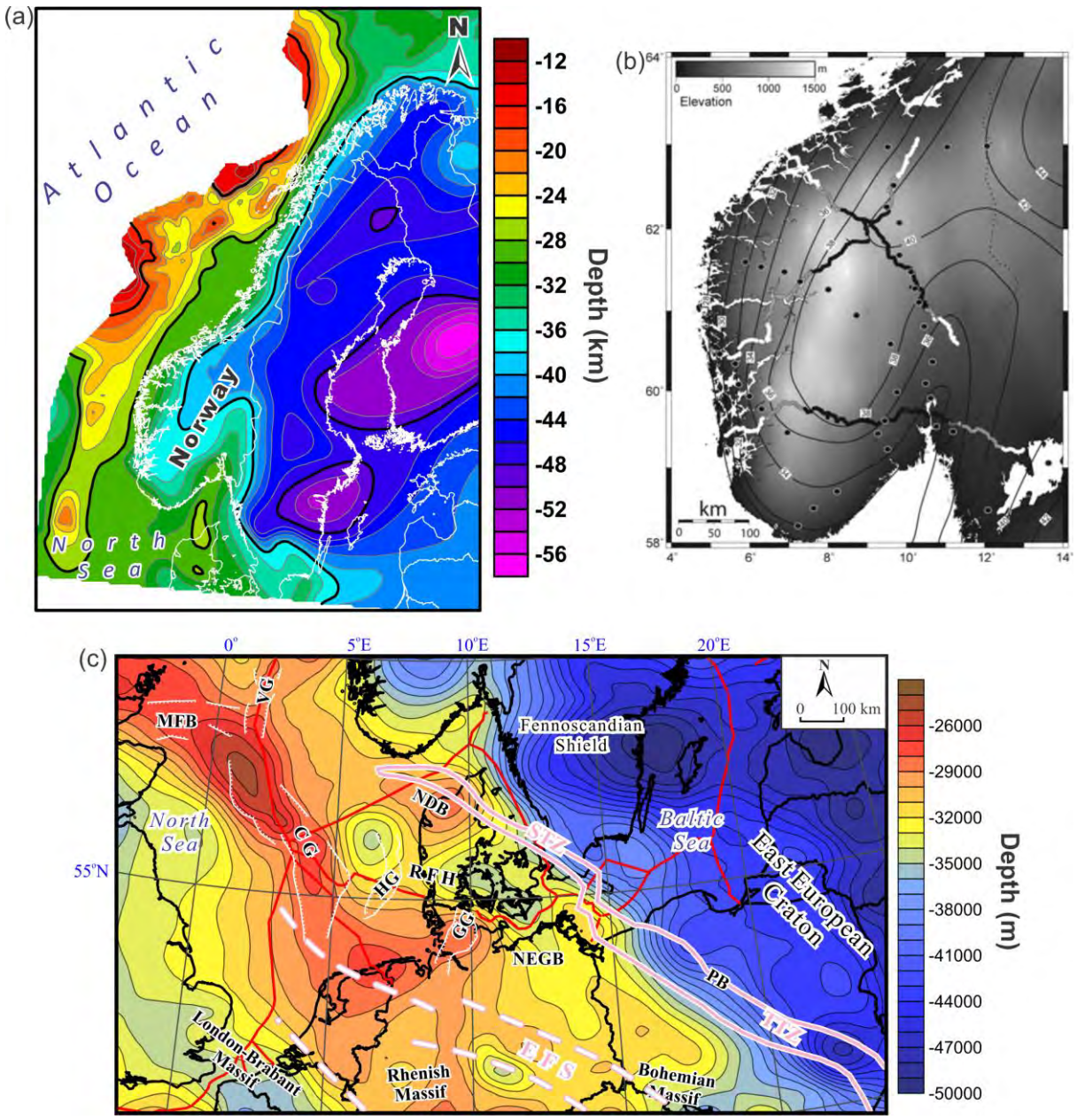

Figure 12.18. Three regional compilations of Moho topography used to constrain the input Moho within the area under consideration: (a) Ebbing & Olesen (2010), (b) Stratford et al. (2009), (c) Maystrenko & Scheck-Wenderoth (2011).

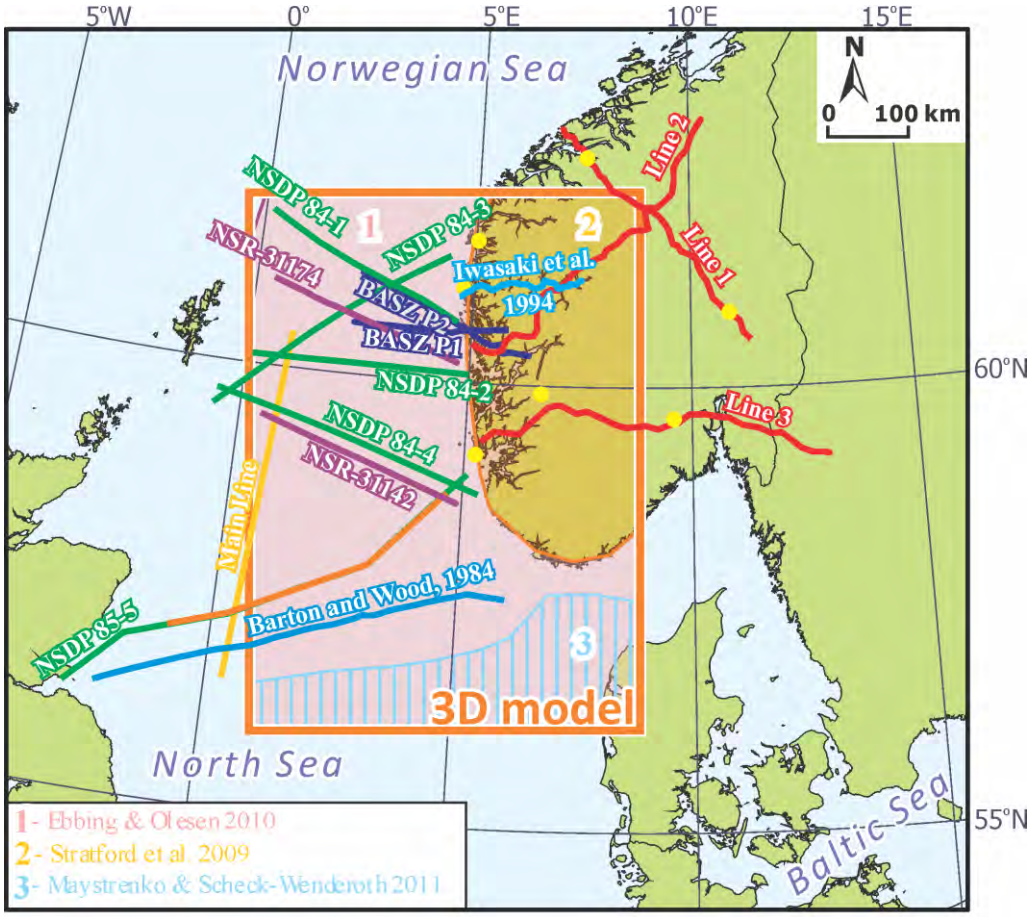

Figure 12.19. Datasets used for the internal structure of the crystalline crust and for the Moho topography.

configuration within the northern North Sea and, therefore, these maps are not sufficiently detailed for our present study. To construct a new Moho map, the most recent compilations (Fig. 12.18) by Stratford et al. (2009), Ebbing & Olesen (2010) and Maystrenko & Scheck-Wenderoth (2011) have been used as input data for 3D gravity modelling. In addition, Moho topography and configuration of the crystalline crust have locally been constrained by the results of interpretation of deep seismic lines which are located within the area covered by the 3D structural model (Fig. 12.19; Christie 1982, Barton & Wood 1984, Klemperer & White 1989, Iwasaki et al. 1994, McBride & England 1999, Christiansson et al. 2000, Erickson 2004, Fichler et al. 2011, Ebbing & Osmundsen 2012 this report).

The lithosphere-asthenosphere boundary has been derived from previously published data (Fig. 12.20), such as the seismically derived base of the lithosphere by Calcagnile et al. (1997) as well as depth to the base of the lithosphere based on integrated studies by Artemieva et al. (2006) and Maystrenko & Scheck-Wenderoth (2011). In addition, depth to the lithosphere-asthenosphere boundary from Geissler et al. (2010) has been used to constrain

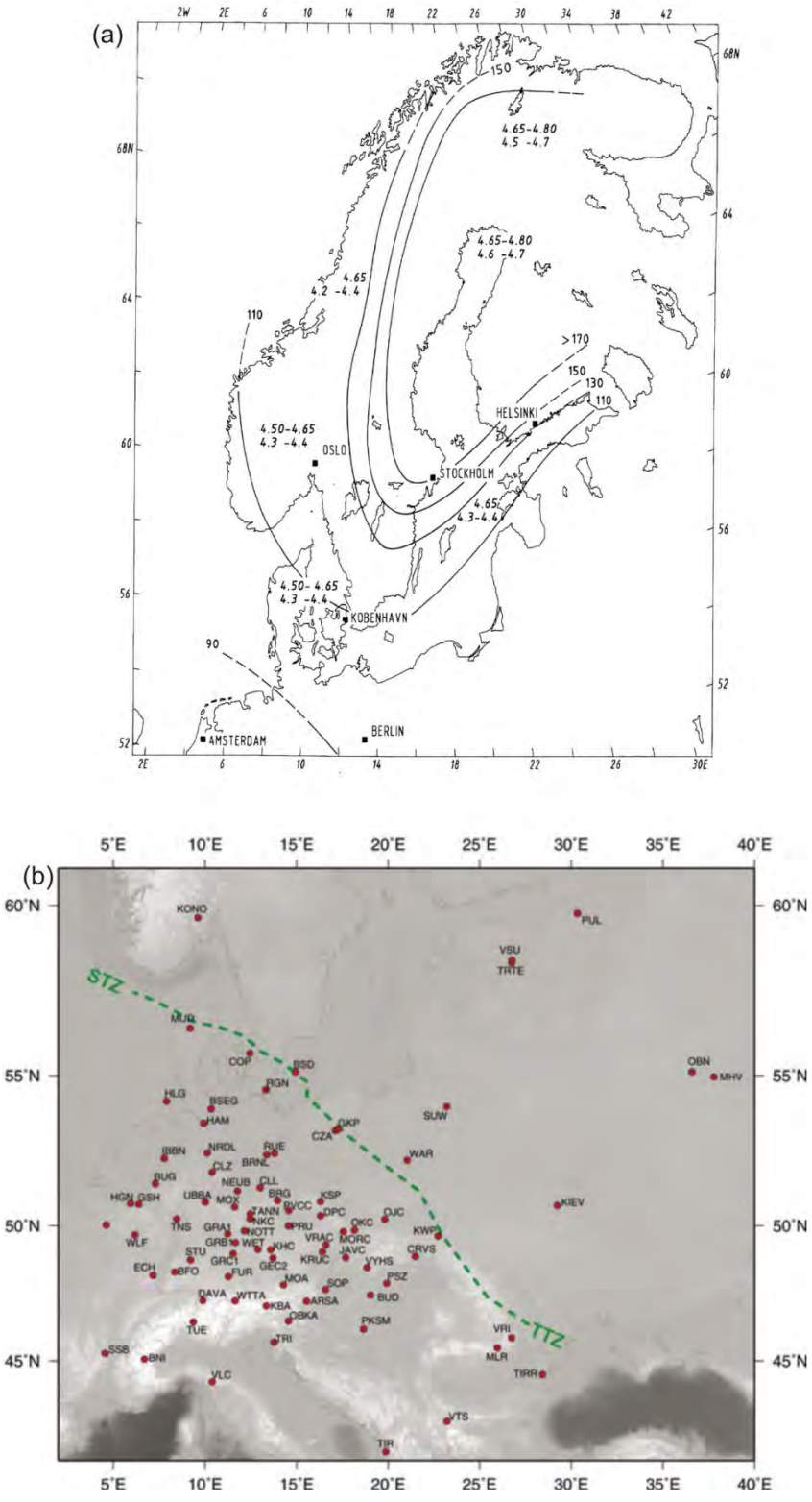

Figure 12.20. Depth to the lithosphere-asthenosphere boundary according to (a) Calcagnile et al. (1997), (b) Geissler et al. (2010), (c) Artemieva et al. (2006) and (d) Maystrenko & Scheck-Wenderoth (2011).

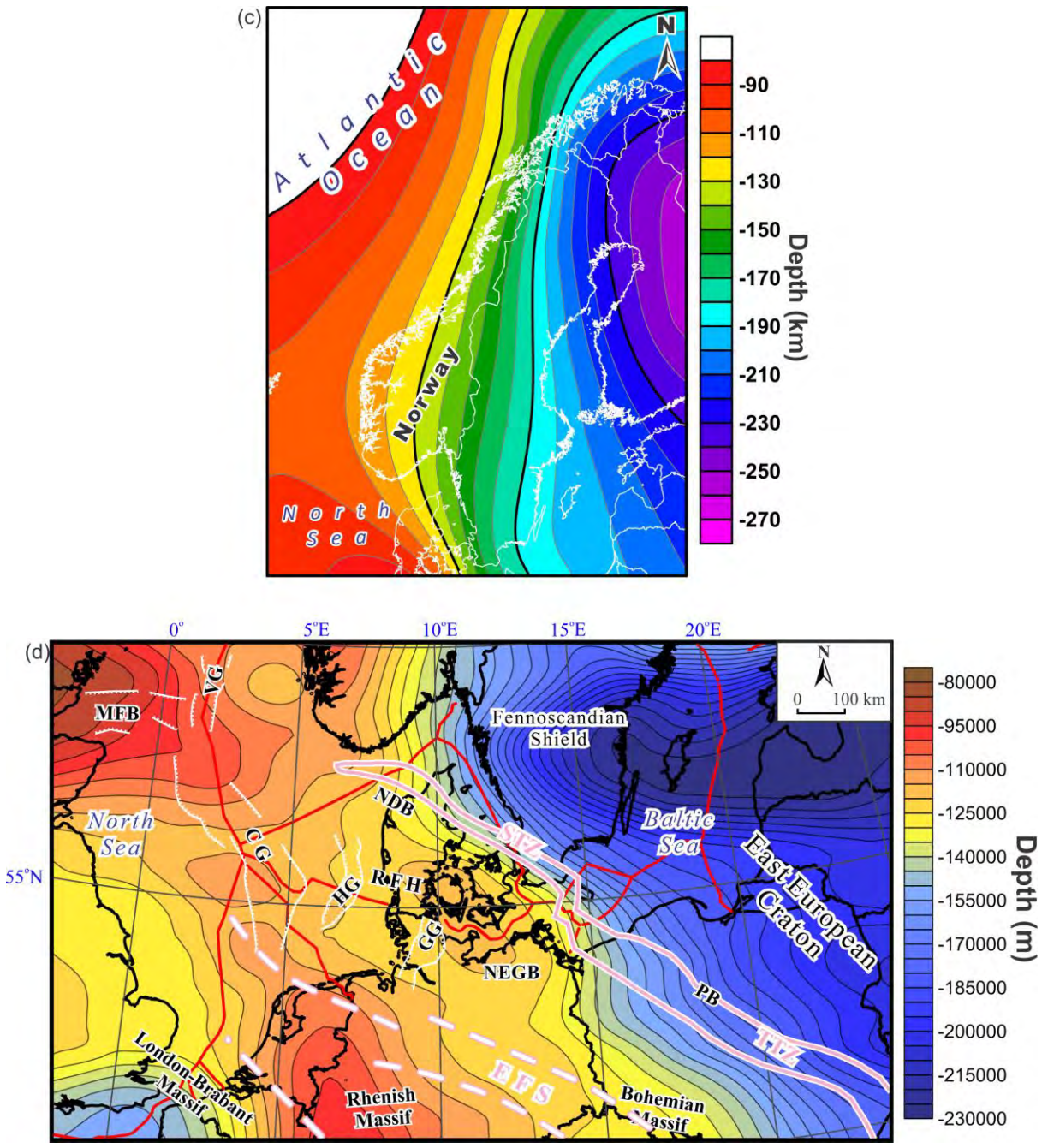

Figure 12.20. continued. Depth to the lithosphere-asthenosphere boundary according to (a) Calcagnile et al. (1997), (b) Geissler et al. (2010), (c) Artemieva et al. (2006) and (d) Maystrenko & Scheck-Wenderoth (2011).

this surface beneath the mainland where a KONO broad-band station is located (Fig. 12.20b). This estimate of the thickness of the lithosphere is based on S receiver functions.

Finally, the initial, lithosphere-scale, 3D structural model has been constructed based on the previously described data in order to reveal the deep structure of the northern North Sea and the adjacent continent.

12.3 3D density modelling

The main goal of the 3D density modelling was to evaluate the internal structure of the crystalline crust within the northern North Sea and adjacent areas of the continent. The above-described input data have provided a starting point for the 3D density modelling.

12.3.1 Observed gravity field

The Bouguer gravity anomalies onshore (Olesen et al. 2010) and the free air gravity anomalies offshore (Andersen et al. 2010) were used for the 3D density modelling. The gravity anomaly data over the mainland have been taken from the national gravity database at NGU (Olesen et al. 2010). For the Bouguer correction, a density of 2670 kg/m^3 has been applied (Olesen et al. 2010). The free air gravity anomalies are represented by the new global marine gravity field DNSC08GRA from double retracked satellite altimetry (Andersen et al. 2010). The observed gravity field (Fig. 12.21) is characterised by the presence of positive gravity anomalies over the Central and Viking grabens. The observed field over the Norwegian-Danish Basin is also complicated by local positive gravity anomalies. A prominent chain of positive anomalies along the western coast of Norway bounds the regional gravity low which is pronounced over the continent. In addition, the northwestern corner of the 3D model area is characterised by a high positive gravity anomaly (Fig. 12.21).

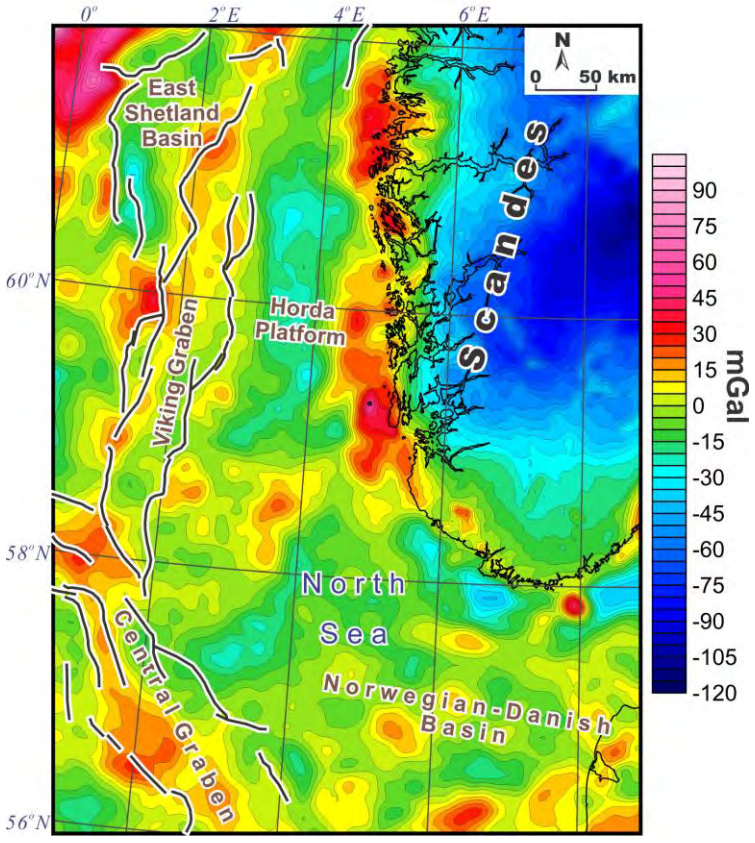

Figure 12.21 Observed gravity anomalies within the northern North Sea and adjacent areas of the continent. Gravity data are from the NGU compilation over the continent (Olesen et al. 2010) and the DNSC08GRA global marine gravity field (Andersen et al. 2010).

12.3.2 Densities

During the 3D density modelling, densities have been assigned constant values within each layer (Table 12.1). The uppermost sedimentary layer is represented by low-compacted Cenozoic clastic sediments and, therefore, has the lightest average density of 2210 kg/m^3. The dominance of chalky limestones in the Upper Cretaceous has raised the average density to 2390 kg/m^3. Due to similarities in lithological composition, almost the same densities are characteristic for the Lower Cretaceous (2410 kg/m^3) and the Jurassic (2420 kg/m^3) which are predominantly composed of mudstones/siltstones. The average density of Triassic sediments (2510 kg/m^3) reflects their relatively high degree of compaction compared with the overlying layers, consequent-upon their greater burial depth. The Upper Permian (Zechstein) rock salt has been modelled with an average density of 2300 kg/m^3, reflecting some uncertainties in the shape and composition of this geometrically complex layer. On the other hand, the density of the pure rock salt is lower than 2300 kg/m^3. The density of Upper Permian carbonates and clastics has a relatively high value of 2610 kg/m^3. The highest sediment density (2640 kg/m^3) has been assigned to the strongly compacted Lower Permian - pre-Permian sediments. The above-mentioned densities of the various sedimentary layers in agreement with previously published values for the northern North Sea (e.g., Christiansson et al. 2000, Fichler et al. 2011).

The uppermost crystalline layer comprises gabbro to anorthositic rocks and, consequently, has a high density of 2880 kg/m^3. A higher average density of 3,000 kg/m^3 has been assigned to the magmatic intrusions that are locally present within the middle-upper crust of the study area. The density structure of the upper crystalline crust indicates a decrease of average upper crustal density from 2670 kg/m^3 beneath the greater part of the model area to 2627 kg/m^3 beneath the Horda Platform. The middle crystalline crust of the northern North Sea and adjacent continent is characterised by average densities of 2740-2770 kg/m^3. The assigned density for the lower crystalline crust of Baltica is 2856 kg/m^3. On the other hand, the high-velocity lower crustal layer is characterised by velocities which exceed 6.7-6.8 km/s. Therefore, the average density of this high-velocity, lower crustal layer has been taken as 3060 kg/m^3. In addition, a density of 2930 kg/m^3 has been assigned to high-density middle crust. The assigned densities of the crystalline rocks (Table 12.1) are generally consistent with previous gravity studies within the same region (e.g. Lyngsie & Thybo 2007, Fichler et al. 2011, Maystrenko & Scheck-Wenderoth 2011) and are in the range of the empirical velocity-density relationship within the North Sea (Barton 1986).

A marked velocity change from 6.9-7.1 km/s within the lower crust to more than 8.0-8.3 km/s within the uppermost mantle occurs at the Moho (Christie 1982, Barton & Wood 1984, Iwasaki et al. 1994, Stratford et al. 2009). This prominent change in P-velocities points to a distinct increase of densities within the uppermost mantle compared to the lower crust. Considering the thermal state of the lithospheric mantle, a derived density of the lithospheric mantle is 3222 kg/m^3. Finally, an average density of 3160 kg/m^3 has been assigned to the

uppermost asthenosphere. There, seismic velocities are lower than within the overlying lithospheric mantle (e.g., Gregersen & Voss 2002, Shomali et al. 2006, Eken et al. 2007).

Table 12.1 Densities of the layers of the 3D structural model used during the 3D density modelling.

No	Layer of the 3D structural model	Dominant lithology	Density ρ [kg/m^3]
1	Sea water		1030
2	Tertiary	clastics	2210
3	Upper Cretaceous	carbonates, clastics	2390
4	Lower Cretaceous	clastics	2410
5	Jurassic	clastics	2420
6	Triassic	clastics, carbonates	2510
7	Upper Permian (Zechstein) salt	rock salt	2300
8	Non-salt Upper Permian (Zechstein)	clastics, carbonates, anhydrites	2610
9	Lower Permian - pre-Permian sediments	clastics, carbonates	2640
10	Upper crustal magmatic rocks	gabbro to anorthositic rocks	2880
11	Middle-upper crustal intrusions	intrusive rocks	3000
12	Low-density upper crustal layer	metasediments or granite	2627
13	Upper crustal layer	granite and gneiss	2670
14	Eastern central North Sea rocks	granitoids and/or gneiss	2740
15	Western central North Sea rocks	granitoids and/or gneiss	2770
16	Middle crust of Laurentia and Avalonia	granitoids and/or gneiss	2750
17	Middle crust of Baltica	granitoids and/or gneiss	2740
18	Lower crust of Baltica	metamorphic rocks	2856
19	High-density crust	mafic granulites, gabbros	2930
20	High-density lower crustal layer	gabbros, high-grade metamorphic rocks	3060
21	Lithospheric upper mantle	peridotite	3222

12.3.3 Method

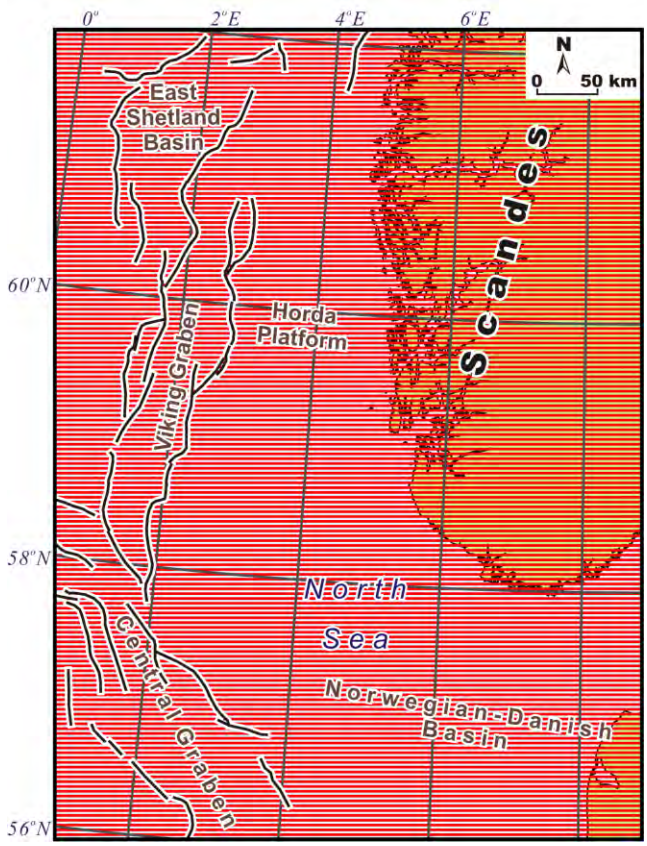

Figure 12.22. Location of the 2D vertical slices through the 3D density model (red lines).

The 3D density modelling has been performed by use of the IGMAS plus software (the Interactive Gravity and Magnetic Application System; Götze 1978, Götze & Lahmeyer 1988, Schmidt & Götze 1998, Götze & Schmidt 2010). Prior to the modelling, a triangulation between structural depth maps is applied along predefined 2D vertical slices to obtain the geometry of the model in 3D. The geometrical approximation for the layers of the 3D model is determined by multiple polyhedra with triangulated planes between the top and the base of each layer and constant densities are assigned to these polyhedra. Finally, the integral gravity effect of all triangulated polyhedra gives the total gravity effect of the 3D model. The procedure of 3D gravity modelling is based on interactive changes of the geometry and density of the layers. In particular, the 3D gravity modelling was carried out by interactive changes of the geometry and densities along 169 E-W-oriented vertical slices through the 3D structural model of the northern North Sea System and adjacent areas (Fig. 12.22). The distance between these 2D working planes is the same as the horizontal resolution of the model, which is 4 km. The 2D working slices are parallel to each other and cross the most important gravity anomalies and the major structural elements of the study area to avoid potential artifacts due to 3D triangulation between the slices. Additionally, the 3D model has been laterally extended in all directions, exceeding the actual model area. Thereby, the major structural features have been prolonged to the extended parts of the 3D structural model to avoid boundary effects.

Furthermore, an inherent non-uniqueness of the approach needs to be mentioned. It is obvious that that numerous density and structural models can be responsible for the same modelled gravity. In the present study, these limitations of the method have been drastically reduced by use of additional constraining data. Besides, the 3D density modelling assumes that the lateral influence of masses is considered in three dimensions, decreasing a number of possible solutions. Sensitivity tests have shown that the modelled gravity response is most sensitive to geometrical modifications of two interfaces where a strong density contrast is present, such as at the base of sediments/the top of crystalline crust and the Moho discontinuity. The depth position of the Moho is relatively well constrained by deep-seismic data over large parts of the modelled area (Fig. 12.19). The top of the crystalline basement is also in agreement with boreholes and seismic data. However, the interface between the pre-Permian sediments and the crystalline rocks is not always properly defined by seismic data and the accuracy of the 3D gravity modelling is strongly dependent on these input data. In addition, similar densities of the highly compacted Lower Permian - pre-Permian sediments and the upper crustal crystalline rocks can also increase the uncertainties in determining the depth to the top of the crystalline rocks by the 3D density modelling within the deepest parts of the study area. Actually, the uncertainties in geometry and densities increase with depth, mostly due to the decreasing resolution of the input data. This is especially true in the case of the depth to the lithosphere-asthenosphere boundary which is the deepest boundary of the model. To remove all these uncertainties, additional data would be required. Lastly, the constant average density assigned to each layer also have an effect on the results of the modelling.

12.3.4 Results of the 3D density modelling

The results of the 3D density modelling demonstrate that the obtained gravity response of the final 3D structural/density model (Fig. 12.23b) is in good agreement with the long-wavelength component of the observed gravity field (Fig. 12.23a) over the area under consideration. The difference between observed and modelled gravity (Fig. 12.23c) demonstrates that some of local gravity anomalies have not been reproduced during the 3D density modelling. Most of these residual misfits are in the range of ±5 mGal. Locally, some short-wavelength misfits between the observed and the calculated gravity anomalies are up to ±25 mGal. On the other hand, these short-wavelength local misfits do not have a marked impact on the regional gravity field and, therefore, do not strongly influence the structure of the study area at the regional scale.

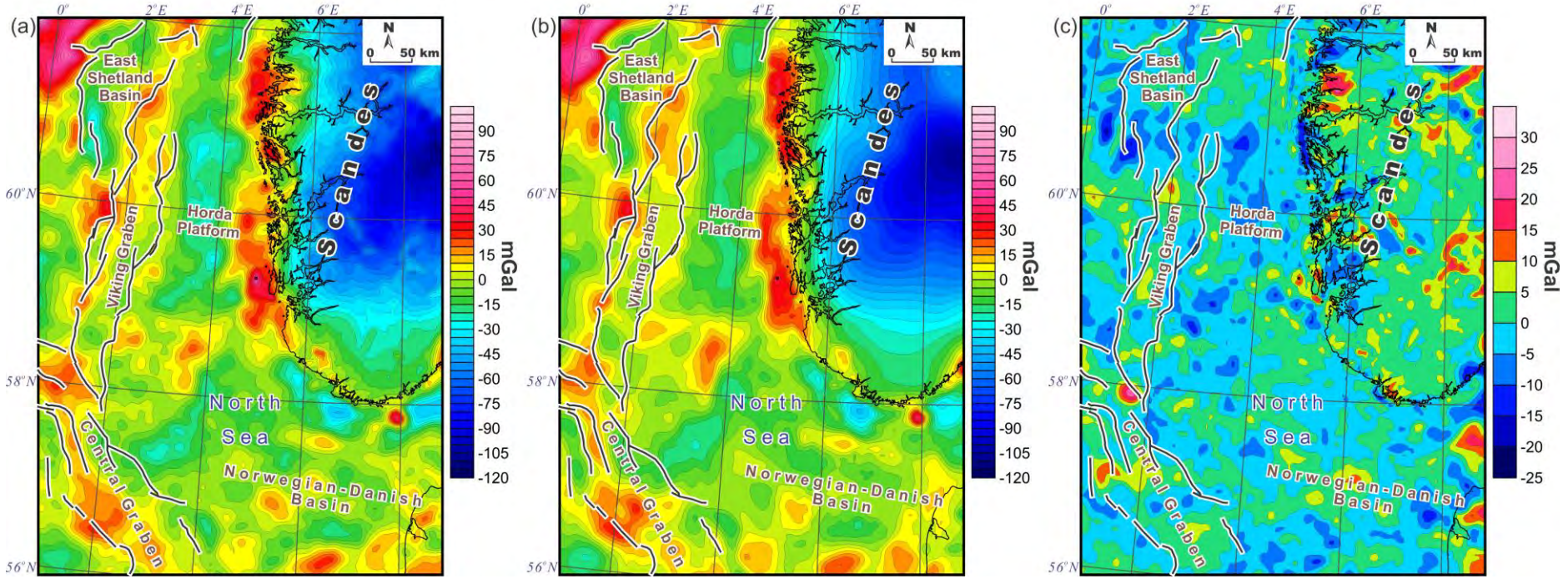

Figure 12.23. (a) Observed gravity anomalies over the study area (Olesen et al. 2010, Andersen et al. 2010). (b) Modelled gravity anomalies. (c) Residual gravity map demonstrating the difference between the observed gravity field (Fig. 12.23a) and the modelled one (Fig. 12.23b).

For the purpose the 3D gravity modelling, the crystalline crust of the study area has been subdivided into several layers.

The modelled upper crystalline crust includes four layers. Within the uppermost crystalline crust, two local layers have been included in the 3D model. These layers are represented by shallow magmatic intrusions (Fig. 12.25) and gabbroic to anorthositic rocks (Fig. 12.24) which are well mapped at the surface along the western coast of Norway. Nevertheless, the distribution of the gabbroic-anorthositic rocks is clearly uncertain within areas covered by thick sediments in the North Sea. Only two middle-upper intrusions have been determined during the gravity modelling (Fig. 12.25); the first intrusion is located near the southern coast of Norway (for details see Olesen et al. 2004) and the second one is modelled within the north-western flank of the East Shetland Basin (the northwestern corner of the model area). On the other hand, this does not mean that there are no other intrusive bodies within the crust of the area under consideration. Some of the intrusions can be smaller than the horizontal resolution of the 3D structural model, whereas the larger intrusive complexes are partially represented by the high-density zones within the crystalline crust (Fig. 12.34). The third upper crustal layer is modelled beneath the Horda Platform (Fig. 12.26). This layer is locally 9-15 km thick on average and is characterised by a low density (2627 kg/m^3) which can correspond to either metasediments or granite. The next upper crustal layer (Fig. 12.27) is characterised by a regional distribution and has a density of 2670 kg/m^3. This regional upper crustal layer is thickest beneath the Norwegian mainland, implying that the total crystalline crust is more dense within the North Sea where thick sedimentary successions are known to occur.

The modelled middle crust of the study area contains four layers with similar densities around 2750 kg/m^3. Prior to the 3D density modelling, the position of the suture zone between Avalonia, Laurentia and Baltica within the central part of the North Sea has been determined according to Lyngsie et al. (2006) and Lyngsie & Thybo (2007). These authors proposed that this upper crustal suture is located beneath the Central and Viking grabens. In addition, Fichler et al. (2011) have suggested that the collision between the Avalonian, Laurentian and Baltican crustal domains occurred within a tectonically complex region, involving at least two island arc chains which were inferred to be present at the western boundary of Baltica during the closure of the Iapetus Ocean in Late Silurian times. Based on this assumption, two middle crustal domains, in addition to the crystalline crust of Baltica, Avalonia and Laurentia, have been included in the model within the central part of the North Sea. The largest middle crustal layers are the middle crust of Baltica (Fig. 12.28) and a narrow zone of similar rocks beneath the eastern parts of the Viking and Central grabens (Fig. 12.29). These two layers have the same density of 2740 kg/m^3, assuming similar lithological compositions and can be represented by granitoids or gneisses. Towards the west, another narrow zone of middle crustal rocks has been integrated into the model beneath the western part of the Viking and Central grabens (Fig. 12.30). These western central North Sea rocks have the highest average density (2770 kg/m^3) that has been assigned to the middle crustal layers (Table 12.1).

According to Fichler et al. (2011), this layer can at least partially correspond to inherited island arc rocks. The thickness of the layer is locally more than 14 km. Finally, the middle

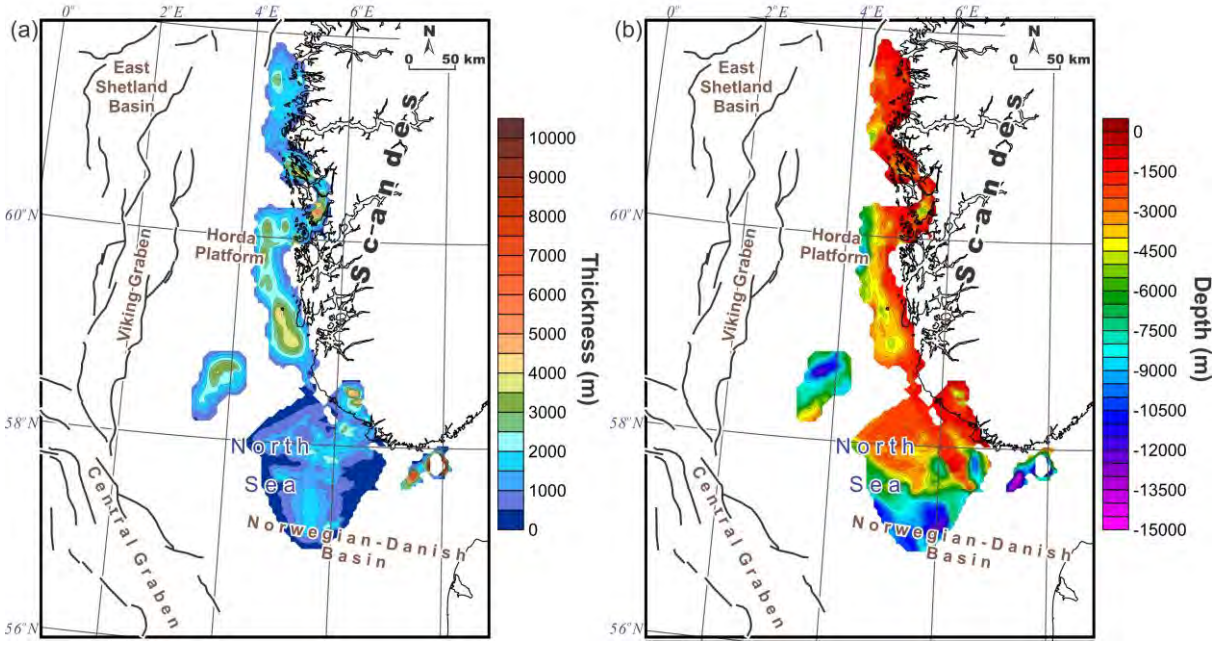

Figure 12.24. Upper crystalline crust: (a) thickness map and (b) structural depth map (base of the layer) of the upper crustal magmatic rocks (layer 10).

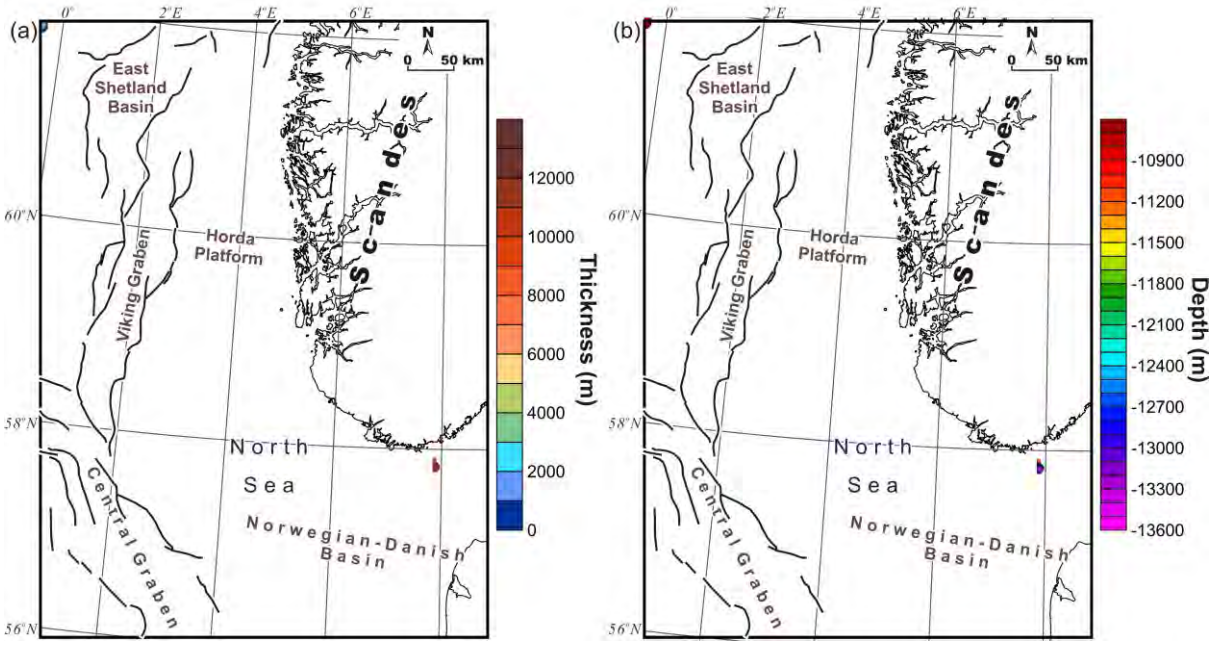

Figure 12.25. Upper crystalline crust: (a) thickness map and (b) structural depth map (base of the layer) of the upper crustal intrusions (layer 11).

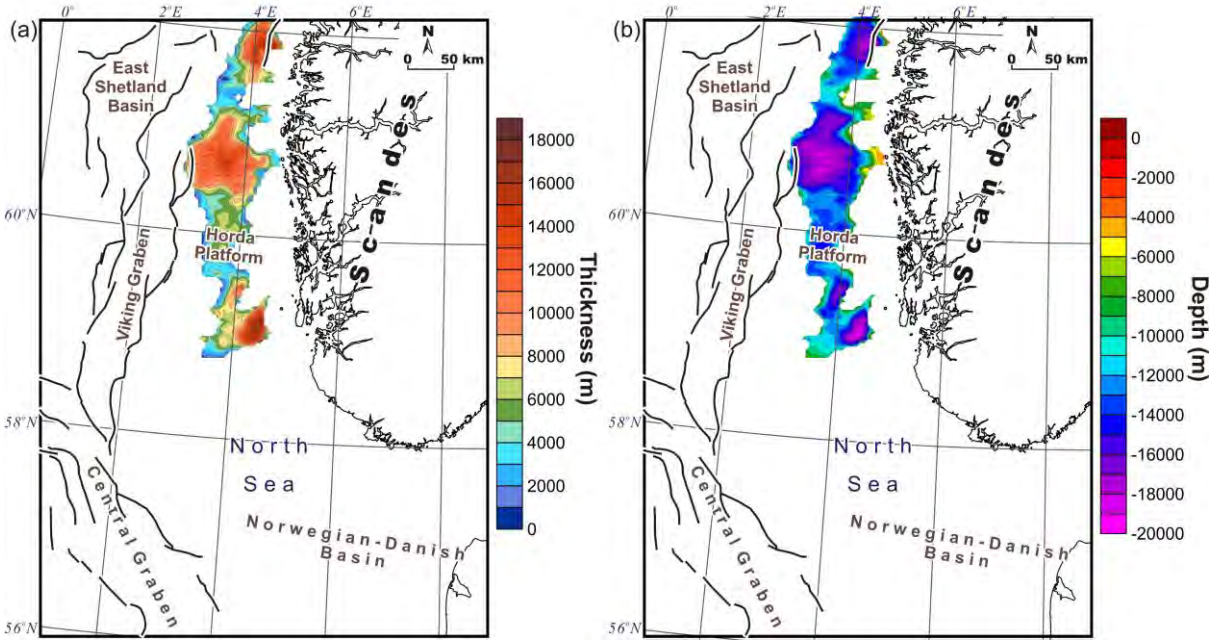

Figure 12.26. Upper crystalline crust: (a) thickness map and (b) structural depth map (base of the layer) of the low-density upper crustal layer (layer 12).

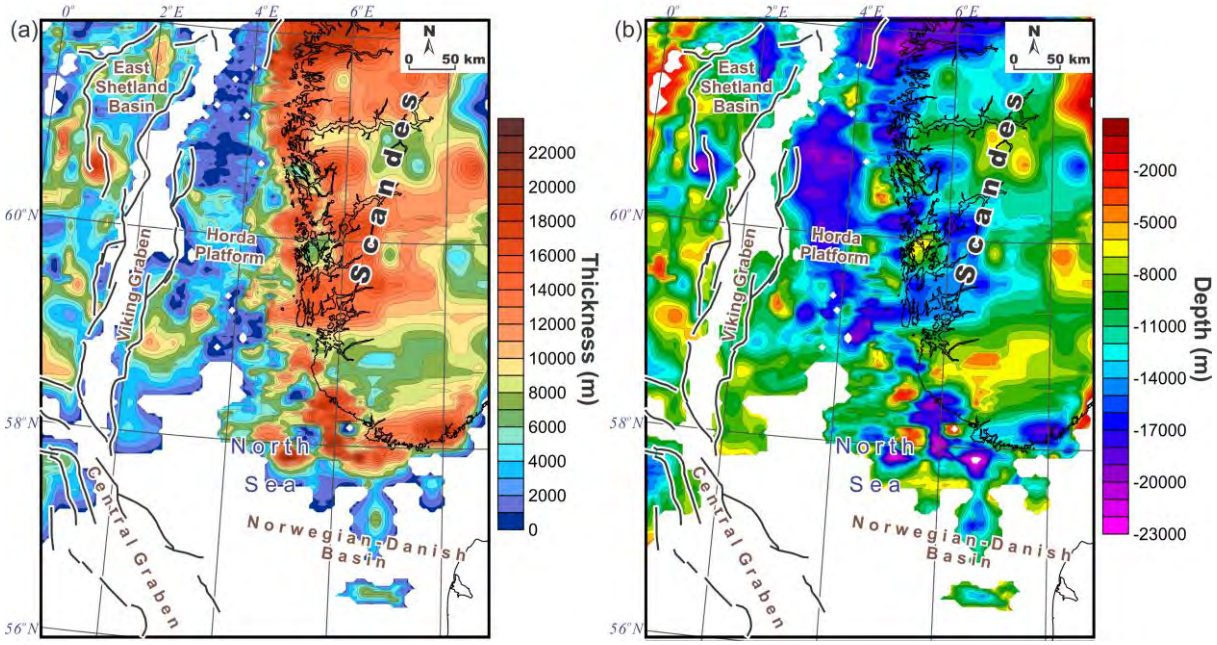

Figure 12.27. Upper crystalline crust: (a) thickness map and (b) structural depth map (base of the layer) of the regional upper crustal layer (layer 13).

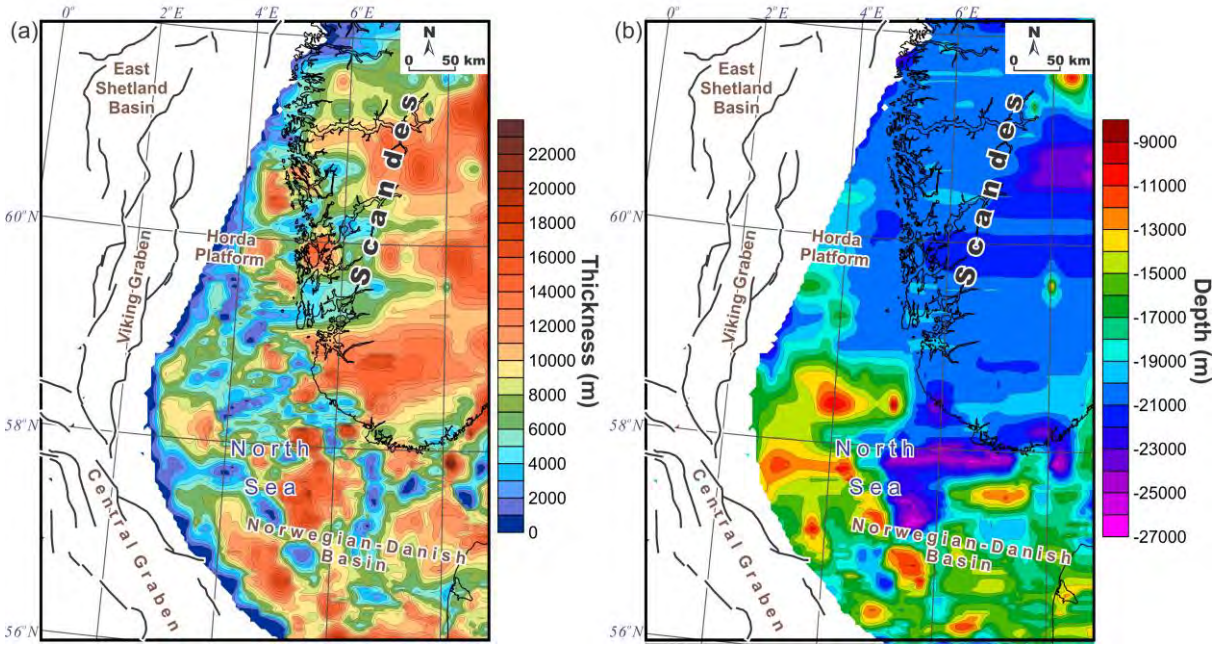

Figure 12.28. Middle crystalline crust: (a) thickness map and (b) structural depth map (base of the layer) of the middle crust of Baltica (layer 17).

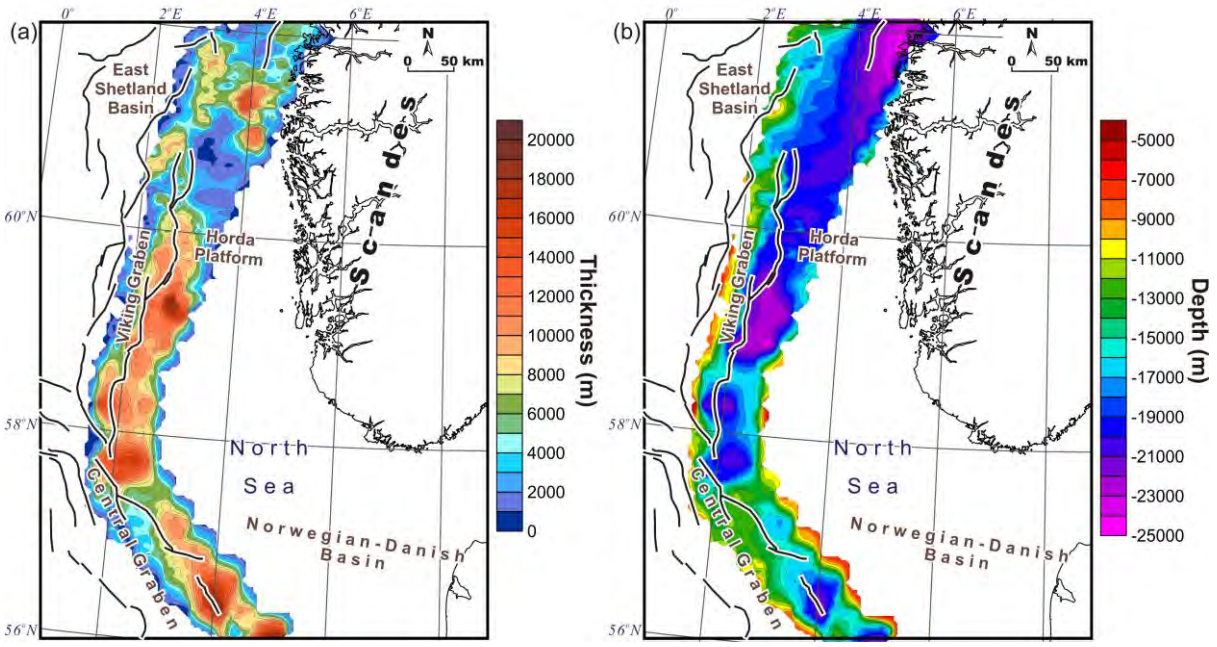

Figure 12.29. Middle crystalline crust: (a) thickness map and (b) structural depth map (base of the layer) of the eastern Central North Sea rocks (layer 14).

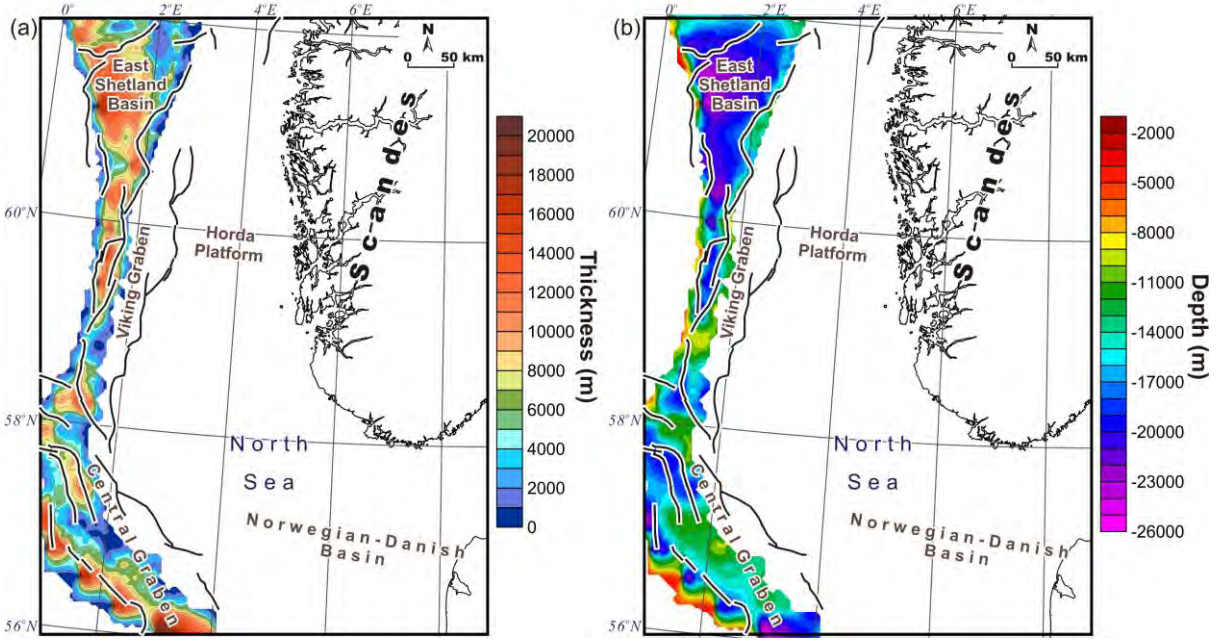

Figure 12.30. Middle crystalline crust: (a) thickness map and (b) structural depth map (base of the layer) of the western Central North Sea rocks (layer 15).

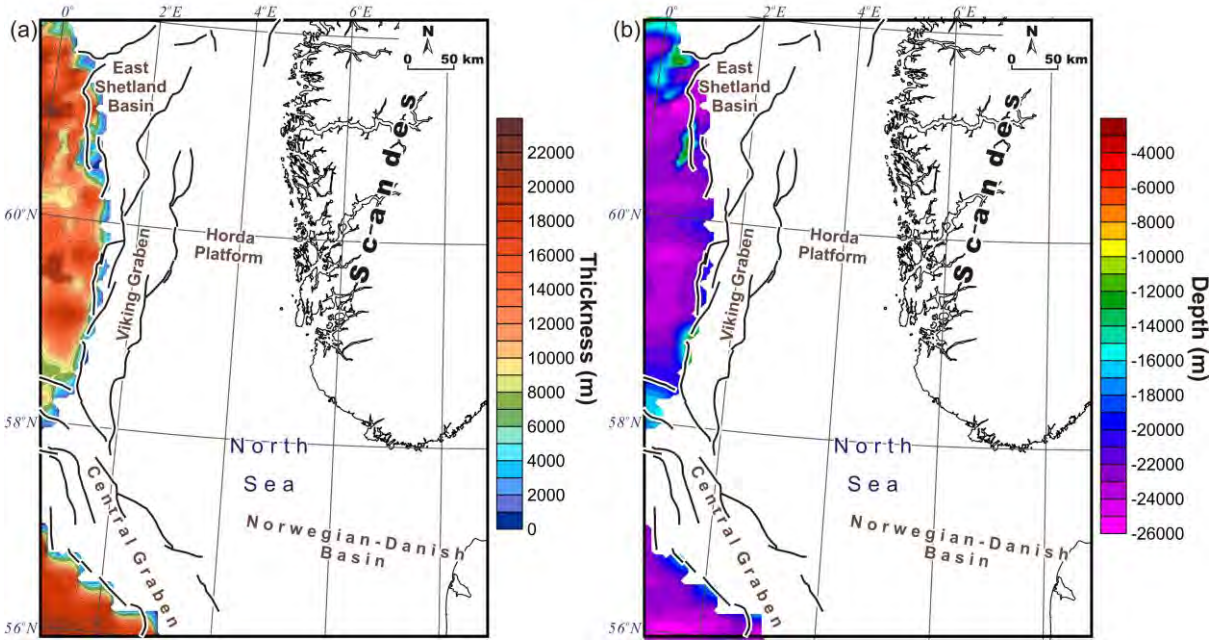

Figure 12.31. Middle crystalline crust: (a) thickness map and (b) structural depth map (base of the layer) of the middle crust of Laurentia and Avalonia (layer 16).

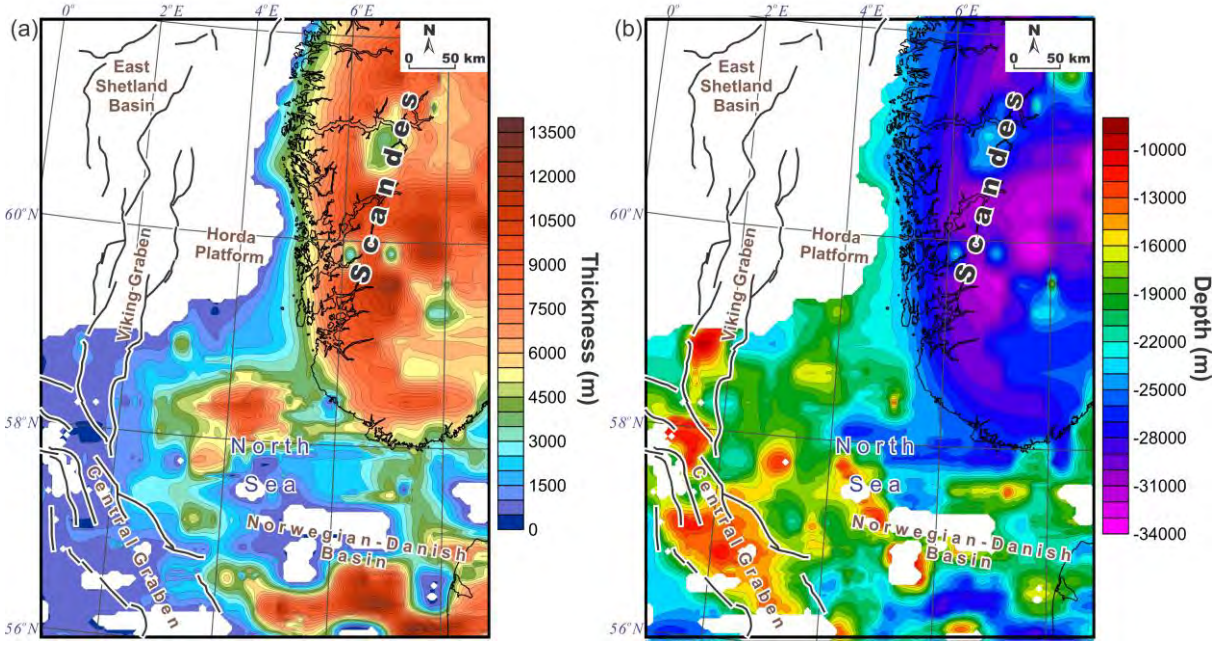

Figure 12.32. *Lower crystalline crust: (a) thickness map and (b) structural depth map (base of the layer) of the lower crust of Baltica (layer 18).*

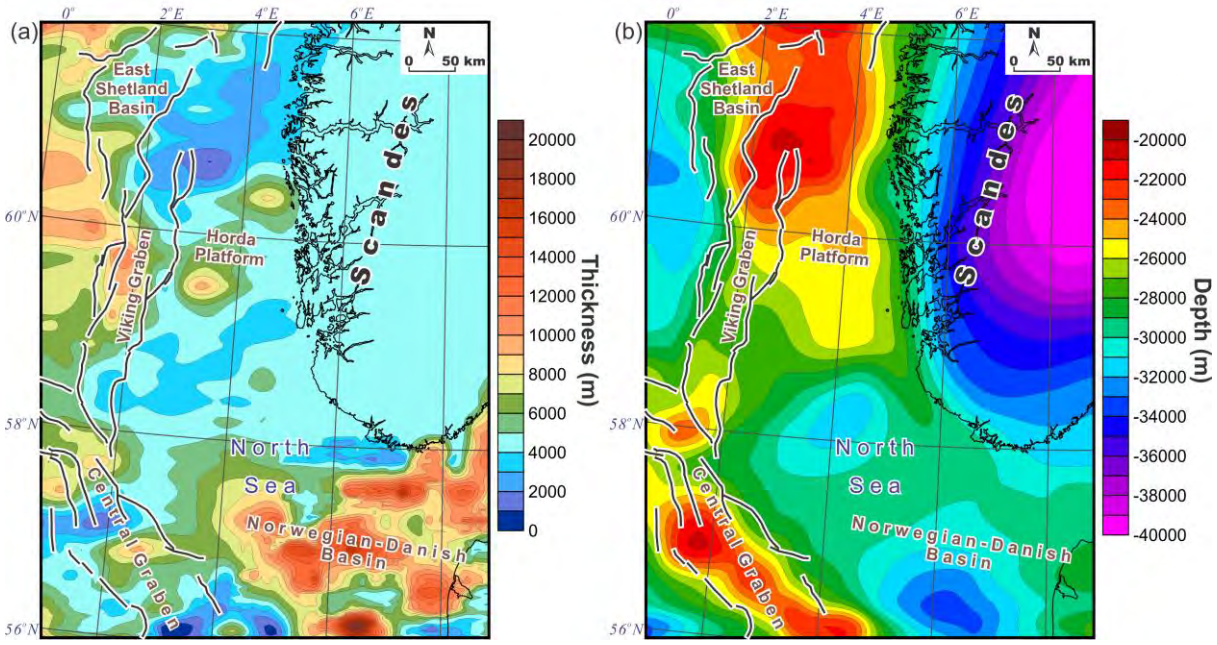

Figure 12.33. *Lower crystalline crust: (a) thickness map and (b) structural depth map (base of the layer; Moho) of the high-density lower crustal layer (layer 20).*

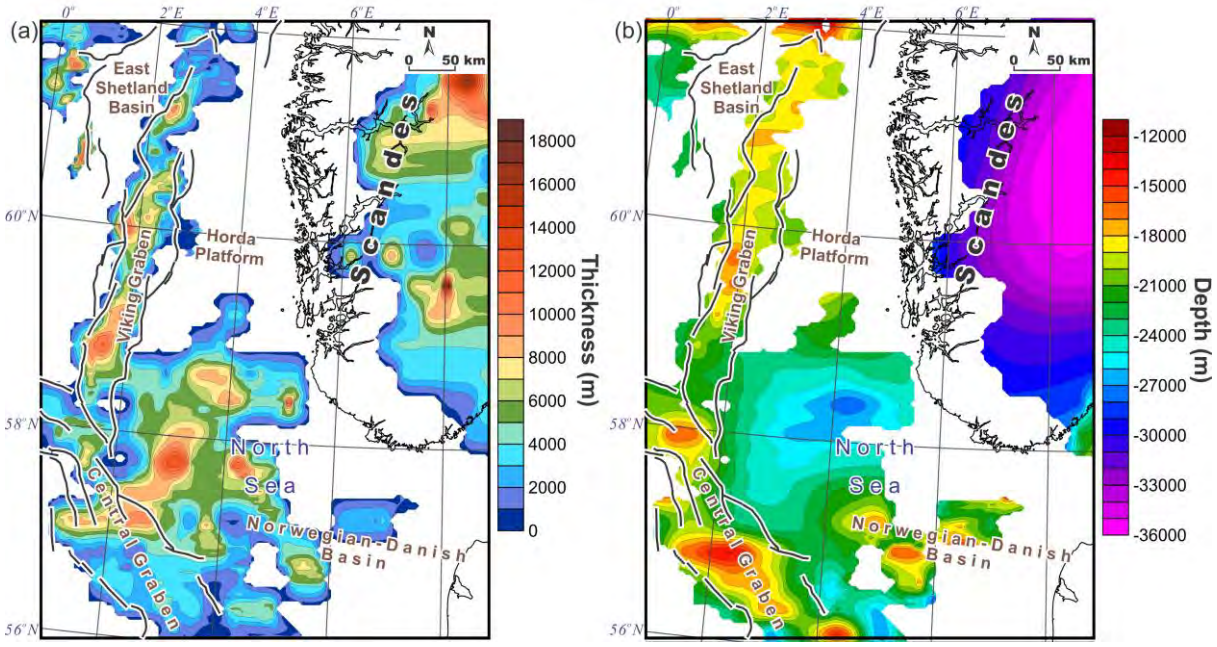

Figure 12.34. Lower crystalline crust: (a) thickness map and (b) structural depth map (base of the layer) of the high-density crust (layer 19).

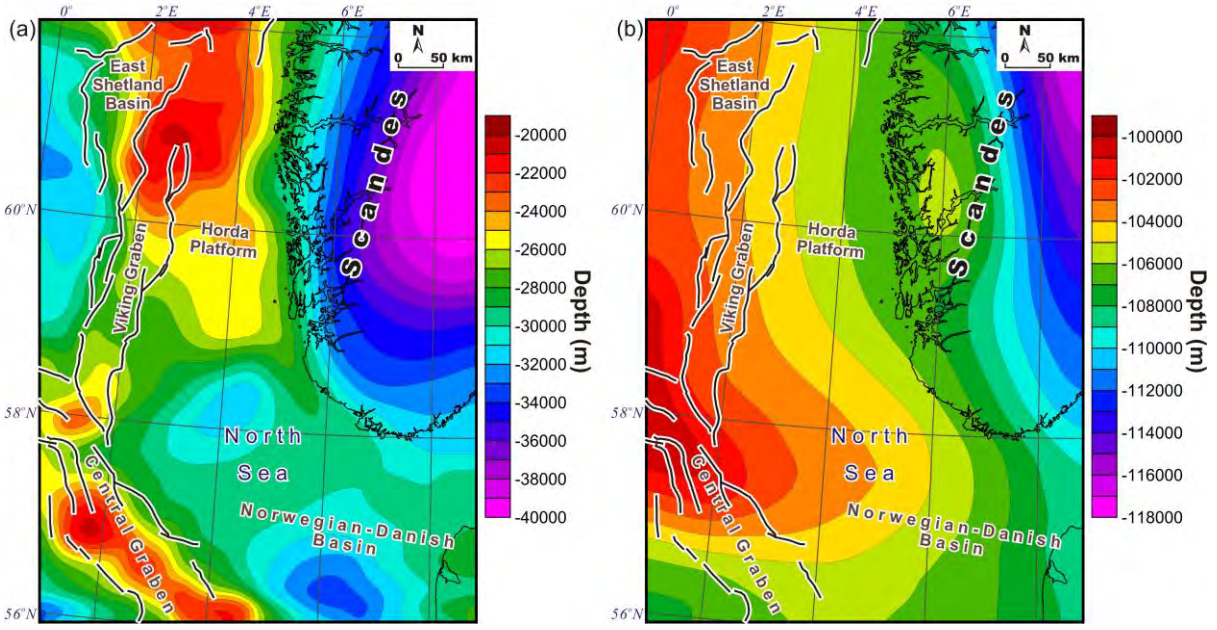

Figure 12.35. (a) Resulting depth to Moho and (b) resulting depth to the lithosphere-asthenosphere boundary.

crystalline crust of Laurentia and Avalonia (Fig. 12.31) has been defined in the westernmost part of the model area. The thickness of the middle crust of Laurentia and Avalonia is 10-15 km on average, and locally reaching more than 20 km.

The modelled lower crust consists of three layers. The first layer is the lower crust of Baltica (Fig. 12.32) which thins markedly from 6-10 km within the Precambrian crustal domain of

Baltica to less than 1 km beneath the Caledonian crustal domains of Laurentia and Avalonia. The second one is the high-density, lower crustal layer (Fig. 12.33) which corresponds to the high-velocity layer where observed P-wave velocities exceed 6.7-6.8 km/s. This layer thickens considerably beneath the Norwegian-Danish Basin (more than 15 km) and the eastern part of the East-Shetland Platform (more than 10 km). The rest of the model area is characterised by relatively thin, high-density, lower crust which is thinner than 5 km beneath the continent. In addition to high-density lower crust, a high-density zone within the crystalline crust (Fig. 12.34) has been modelled to fit the observed and calculated gravity. The prominent feature of this layer is the narrow area of thickening beneath the Viking Graben. There, the high-density crust is characterised by thickened zones which are elongated NE-SW and restricted to the axial part of the graben (Fig. 12.34). In the case of the Viking Graben,

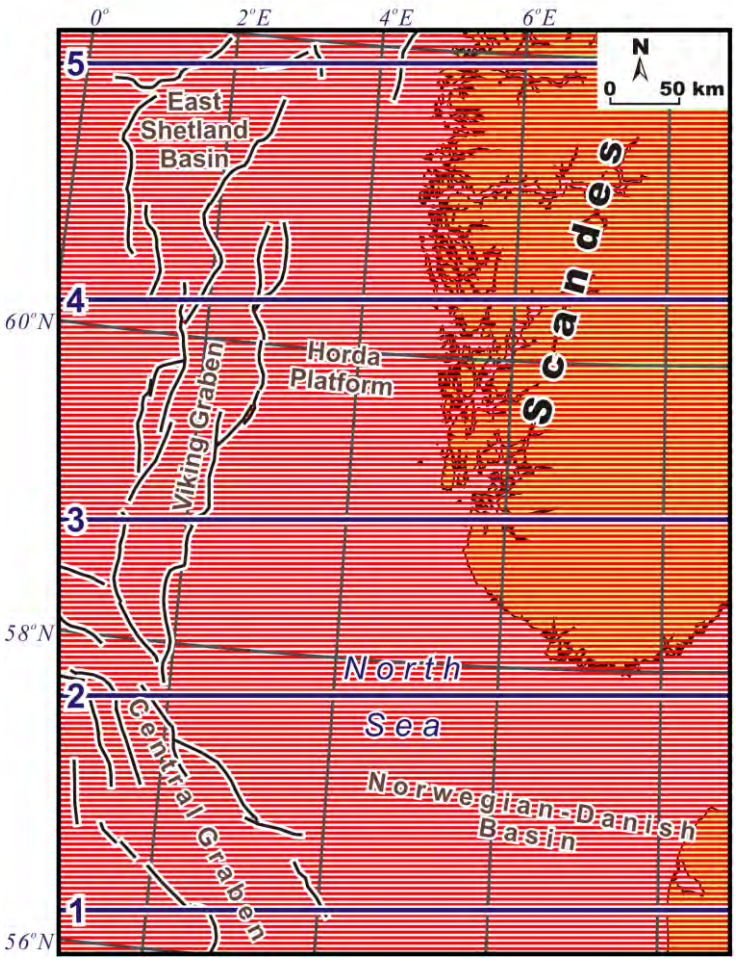

Figure 12.36 *Location of the 2D vertical slices through the 3D density model (red lines). Five selected slices are highlighted by bold blue lines and numbering.*

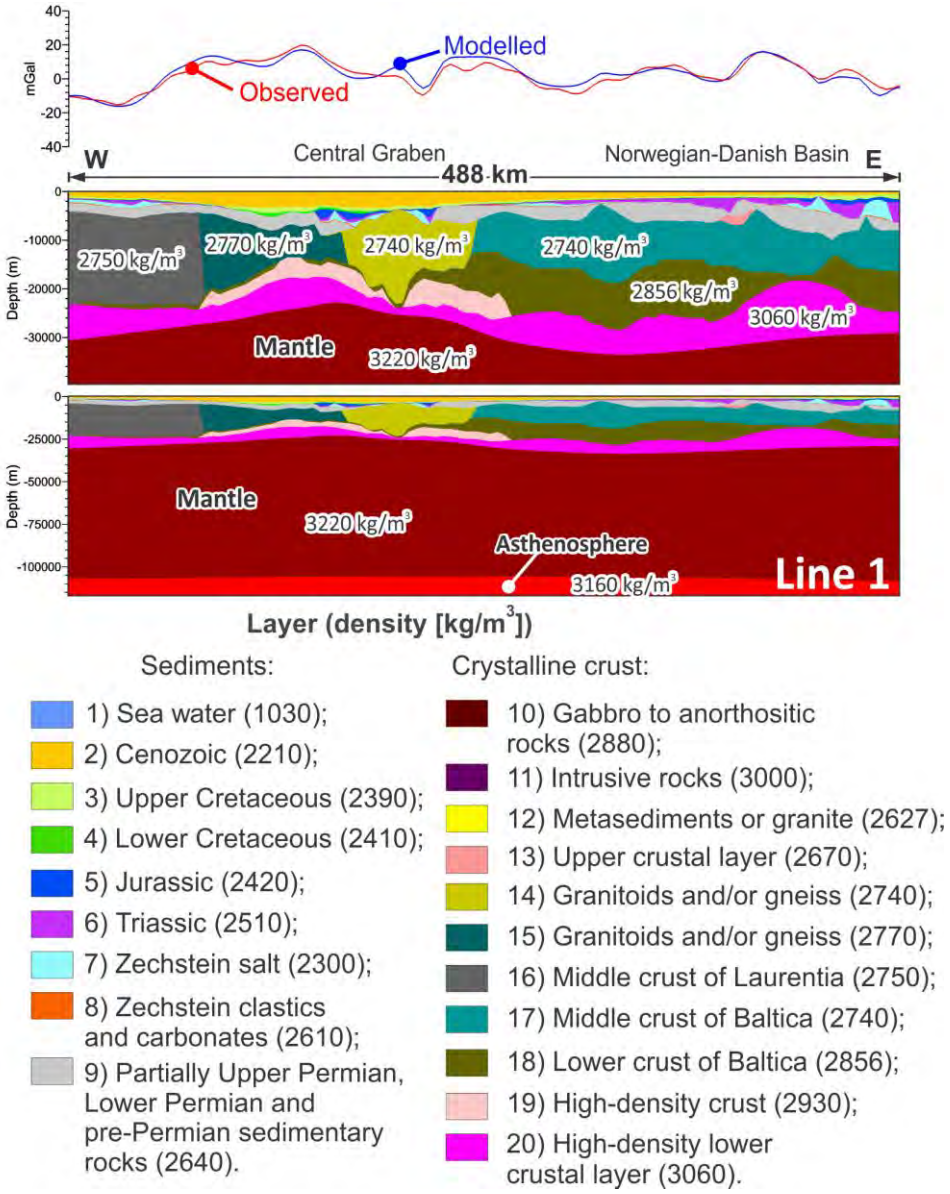

Figure 12.37 *Selected vertical slice 1 through the 3D structural/density model of the northern North Sea and adjacent areas. Layer numbering is the same as in Tables 12.1 and 12.2. The location of this slice is shown in Fig. 12.36.*

the high-density zones may mostly be related to the intermediate intrusions (Fichler et al. 2011) which have a higher density compared to the surrounding crystalline crust. The obtained Moho topography (Fig. 12.35a) and depth to the base of the lithosphere (Fig. 12.35b) correlate clearly with the major tectonic units of the study area. Both boundaries are located deeply beneath the continent. Furthermore, the Moho is prominently uplifted beneath the Central and Viking grabens whereas the lithosphere-asthenosphere boundary is relatively shallow beneath the western part of the model area.

The cross-sectional view of the structure across the major structural units of the study area is shown along five selected 2D vertical slices (Figs. 12.36-12.41). E-W-oriented vertical slice 1 is located within the southern part of the study area (Fig. 12.36), crossing the Central Graben

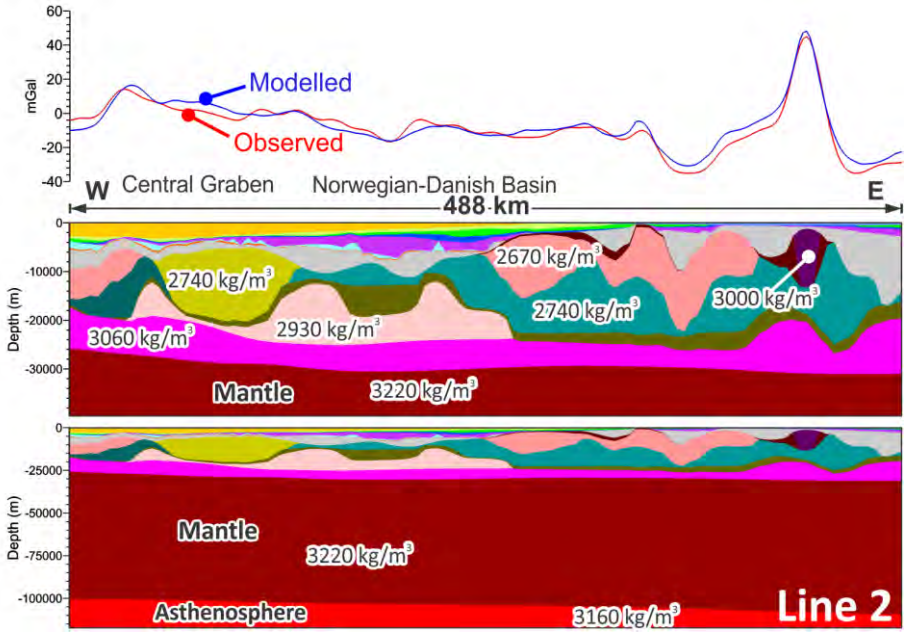

Figure 12.38. Selected vertical slice 2 through the 3D structural/density model of the northern North Sea and adjacent areas (for the legend, see Fig. 12.37). The location of this slice is shown in Fig. 12.36.

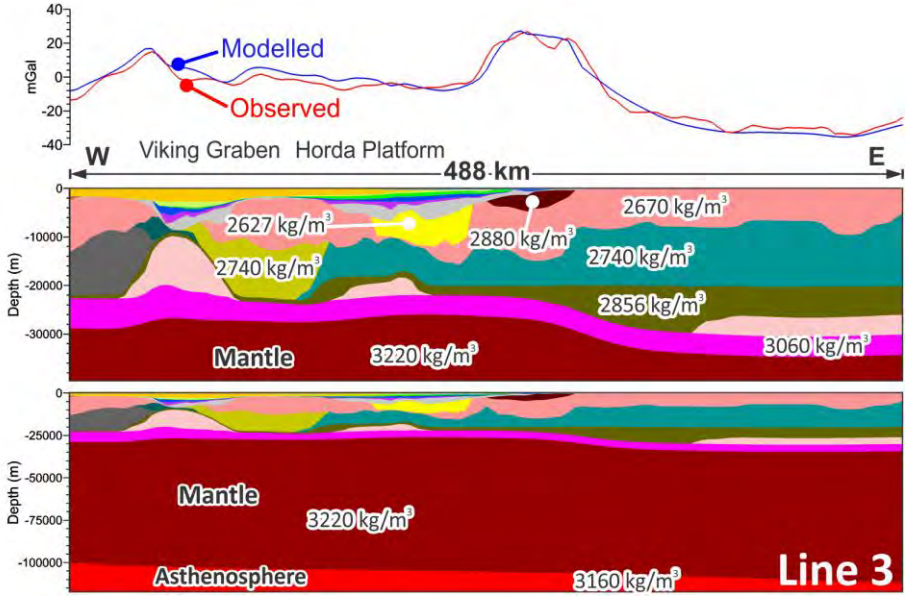

Figure 12.39. Selected vertical slice 3 through the 3D structural/density model of the northern North Sea and adjacent areas (for the legend, see Fig. 12.37). The location of this slice is shown in Fig. 12.36.

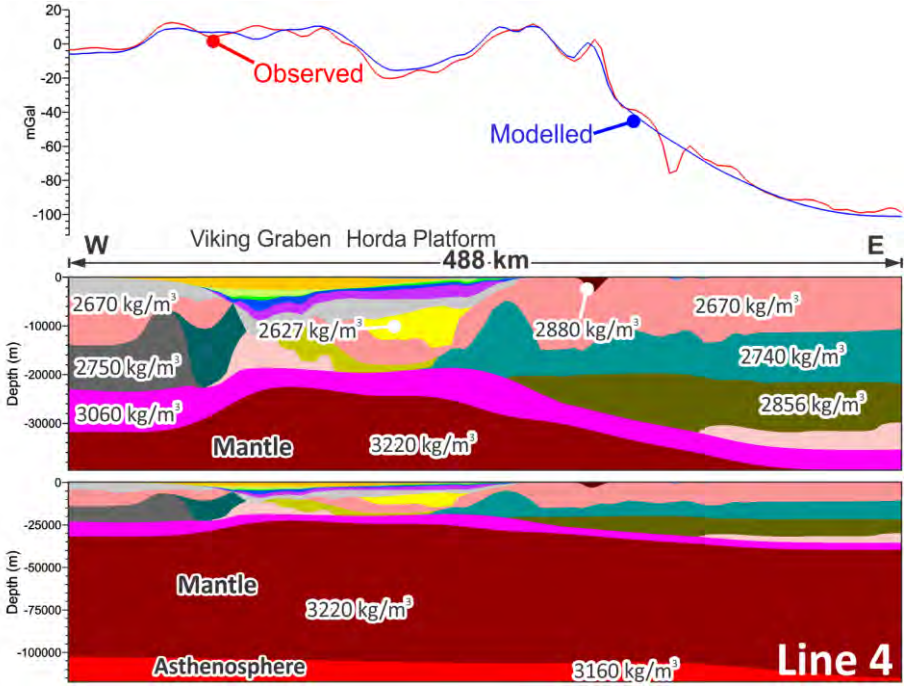

Figure 12.40 *Selected vertical slice 4 through the 3D structural/density model of the northern North Sea and adjacent areas (for the legend, see Fig. 12.37). The location of this slice is shown in Fig. 12.36.*

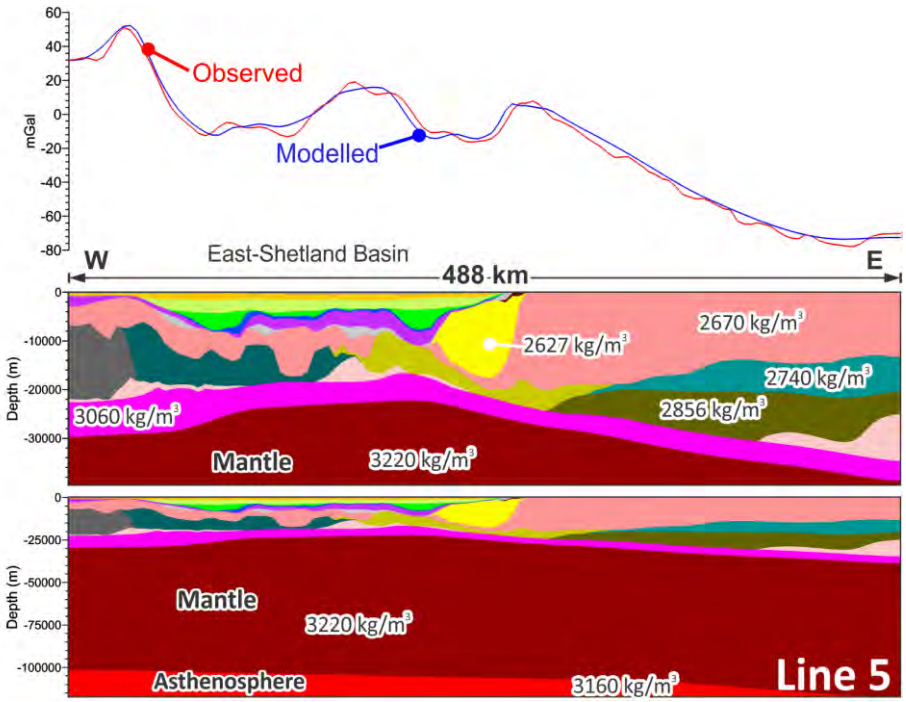

Figure 12.41. *Selected vertical slice 5 through the 3D structural/density model of the northern North Sea and adjacent areas (for the legend, see Fig. 12.37). The location of this slice is shown in Fig. 12.36.*

and the southern part of the Norwegian-Danish Basin. Along this line (Fig. 12.37), a marked uplift of the Moho is observed beneath the Central Graben. To the east, a remarkable thickening of the high-density lower crustal layer occurs beneath the Norwegian-Danish

Basin. In addition, this slice shows a mosaic structure of the crystalline crust in the vicinity of the Central Graben where two middle crustal blocks have been introduced between Precambrian crust of Baltican origin in the east and the Caledonian crustal domain of Avalonia to the west.

Line 2 runs across the northern parts of the Central Graben and the Norwegian-Danish Basin (Fig. 12.36). This slice crosses the prominent gravity high over the northern part of the Norwegian-Danish (Fig. 12.38) where the presence of magmatic intrusions within the middle-upper part of the crystalline crust is necessary in order to fit the observed and modelled gravity.

Towards the north, the third vertical slice (Fig. 12.39) is interesting in terms of different origins of two, high-amplitude, positive gravity anomalies along this line. The first positive anomaly is related to an integral gravity effect of a marked thickening of the high-density crust beneath the Viking Graben and a density contrast between the crystalline rocks within the uplifted western flank and thick sediments in the basin along the steeply dipping marginal fault of the western Viking Graben. On the other hand, the second gravity anomaly is mostly associated with the near-surface, high-density, gabbroic-anorthositic rocks which are well mapped along the southwestern coast of Norway (e.g., Sigmond 2002).

The next slice (Line 4 in Fig. 12.36) crosses the prominent gravity low over the Horda Platform (Fig. 12.21). According to the results of the 3D density modelling (Fig. 12.40), this regional-scale gravity low is partially related to the presence of the low-density upper crustal layer (the yellow body in Fig. 12.40) which can be correlated lithologically with the presence of highly compacted pre-Permian sediments or even metasediments and/or relatively light granite. The last vertical plane (Line 5 in Fig. 12.36) crosses the East Shetland Basin and the northern part of the Viking Graben, showing a wide Moho uplift beneath these basins (Fig. 12.41). In addition, the northern continuation of the low-density upper crustal body is clearly visible within the middle part of the profile.

Based on the results of the 3D density modelling, the input structural data have been refined in terms of the lithosphere-scale 3D structural/density model (Fig. 12.3). The output 3D model includes twenty-one layers: (1) sea water; (2) Tertiary; (3) Upper Cretaceous; (4) Lower Cretaceous; (5) Jurassic; (6) Triassic; (7) Zechstein salt; (8) Zechstein clastics, carbonates and anhydrites; (9) pre-Permian sediments; (10) intrusions; (11) upper crustal magmatic rocks; (12) low-density upper crustal layer; (13) upper crustal regional layer; (14) middle crust of Baltica; (15) eastern central North Sea rocks; (16) western central North Sea rocks; (17) middle crust of Laurentia and Avalonia; (18) lower crust of Baltica; (19) high-density crust; (20) high-density lower crustal layer; (21) lithospheric upper mantle. This data-constrained, 3D structural/density model (Fig. 12.3) has finally been used for the 3D thermal modelling to estimate the present-day thermal state of the northern North Sea and adjacent areas.

12.4 3D thermal modelling

The next step of the 3D analysis was the 3D thermal modelling which has been performed to understand the regional thermal regime within the area under consideration. The lithospheric-scale 3D model, validated by the 3D density modelling, has been used as a realistic approximation of the geometries of the sedimentary infill as well as of the underlying crystalline crust and lithospheric mantle during 3D thermal modelling.

12.4.1 Thermal properties

Prior to the 3D thermal modelling, thermal properties, represented by thermal conductivity and radiogenic heat production, have been assigned constants for each layer (Table 12.2).

The values of thermal conductivity for the sedimentary cover are mostly inferred from the measurements of drillcore samples from the North Sea (Evans 1977) and laboratory measurements of rock samples with similar lithology (Cermak & Rybach 1982). Additionally, thermal properties of the sedimentary infill have been supplemented with published values (Cermak & Rybach 1982, Wollenberg & Smith 1987, Artemieva et al. 2006, Scheck-Wenderoth & Maystrenko 2008) for the crystalline crust and the lithospheric mantle. In particular, thermal conductivity and radiogenic heat production of the upper crystalline rocks are derived from Slagstad (2008) and Slagstad et al. (2008, 2009). Specific heat capacities of the layers taken from the typical values published by Clauser (2011).

The assigned values of these different parameters are also within the range of those measured in the Northeast German Basin (Norden & Förster 2006, Norden et al. 2008) where the major lithological features of the study area are easily recognisable.

12.4.2 Method

The 3D temperature distribution at the subsurface of the structurally complex study area has been modelled by use of the commercial software package COMSOL Multiphysics. COMSOL Multiphysics is a finite-element analysis software package for a variety of physical processes. During the 3D thermal modelling, the Heat Transfer Module was used to simulate the stationary and time-dependent heat transfer in solids by heat conduction, which is assumed to be the dominant mechanism of heat transfer at the regional scale within the study are. Therefore, these simulations have been carried out based on physical principles of the conductive 3D thermal field by solving the heat equation (12.5):

$$\rho C\,(\delta T/\delta t) = \nabla \cdot (k\,\nabla T) + Q \qquad (12.5)$$

Table 12.2 Thermal properties of the layers of the 3D structural model used during the 3D thermal modelling.

No	Layer of the 3D structural model	Dominant lithology	Specific heat capacity C_p [J/kgK]	Thermal conductivity k [W/mK]	Radiogenic heat production S [$\mu W/m^3$]
2	Tertiary	clastics	1180	1.50	0.7
3	Upper Cretaceous	carbonates, clastics	1000	1.95	1
4	Lower Cretaceous	clastics	1180	2.00	1.5
5	Jurassic	clastics	1180	2.10	1.6
6	Triassic	clastics, carbonates	1180	2.10	1.6
7	Upper Permian salt	rock salt	840	3.50	0.3
8	Non-salt Upper Permian (Zechstein)	clastics, carbonates,	1120	1.95	0.8
9	Lower Permian - pre-Permian sediments	clastics, carbonates	1180	2.90	1.6
10	Upper crustal magmatic rocks	gabbro to anorthositic rocks	880	2.70	0.5
11	Middle-upper crustal intrusions	intrusive rocks	880	3.20	0.6
12	Low-density upper crustal layer	metasediments or granite	880	3.05	2.0
13	Upper crustal layer	granite and gneiss	880	3.05	1.7
14	Eastern central North Sea rocks	granitoids and/or gneiss	950	2.70 (2.85-2.95)	0.8 (1-1.3)
15	Western central North Sea rocks	granitoids and/or gneiss	950	2.70 (2.9-3.01)	0.8 (1-1.6)
16	Middle crust of Laurentia and Avalonia	granitoids and/or gneiss	950	2.70	0.8
17	Middle crust of Baltica	granitoids and/or gneiss	950	2.70 (2.9-3.02)	0.8 (1.2-1.4)
18	Lower crust of Baltica	metamorphic rocks	1050	2.60	0.3
19	High-density crust	mafic granulites, gabbros	1100	2.60	0.3
20	High-density lower crustal layer	gabbros, high-grade metamorphic rocks	1100	2.30	0.2
21	Lithospheric upper mantle	peridotite	1200	3.95	0.03

where ρ is the density [kg/m^3], C is the heat capacity [J/kgK], T is the temperature [K], k is the thermal conductivity [W/mK], ∇T is the temperature gradient [K/m], t is the time [s], Q is the heat source (radioactive heat production) [W/m^3], δT is the change in temperature per time interval δt, and $\nabla \cdot$ is the operator giving the spatial variation in temperature. Accordingly, the solution of the heat equation (5) is sensitive to the values of the thermal properties (C, k and Q) as well as the thermal boundary conditions.

The heat flux [W/m^2] has been calculated according to Fourier's law of heat conduction (12.6):

$$q = - k \nabla T \qquad (12.6)$$

where k is the thermal conductivity [W/mK] and ∇T is the temperature gradient [K/m].

The 3D thermal modelling has been performed by means of a finite-element method in 3D which is a suitable approach for a relatively complex geometry like the lithosphere-scale 3D model of the the northern North Sea and adjacent areas (Fig. 12.3). The lateral boundaries are closed to heat transfer, assuming that the temperature gradient is zero across the thermally insulated lateral boundaries. The time-dependent temperatures at the sea floor and the Earth´s

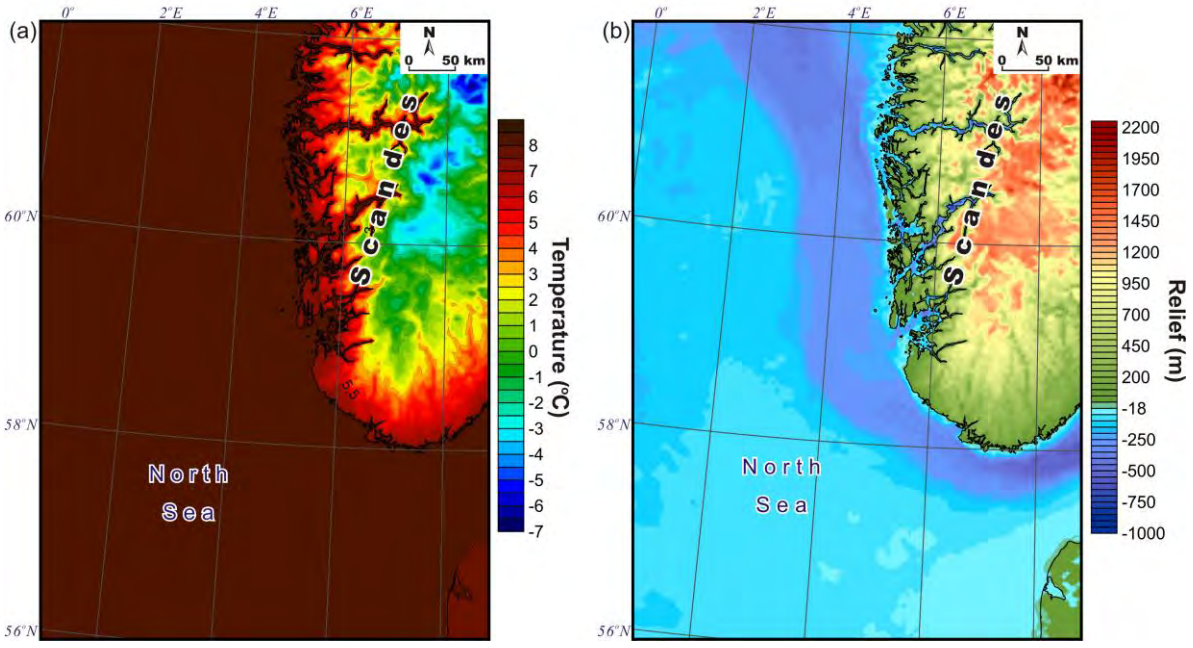

Figure 12.42. *Upper thermal boundary. (a) Temperature: annual average air temperatures 1961-1990 and average sea-bottom temperature of 8oC 1997-2002 (from Tveito et al. 2000 and ICES 2012) and (b) Structural surface: the sea floor and the Earth´s surface (from IOC, IHO, BODC 2003).*

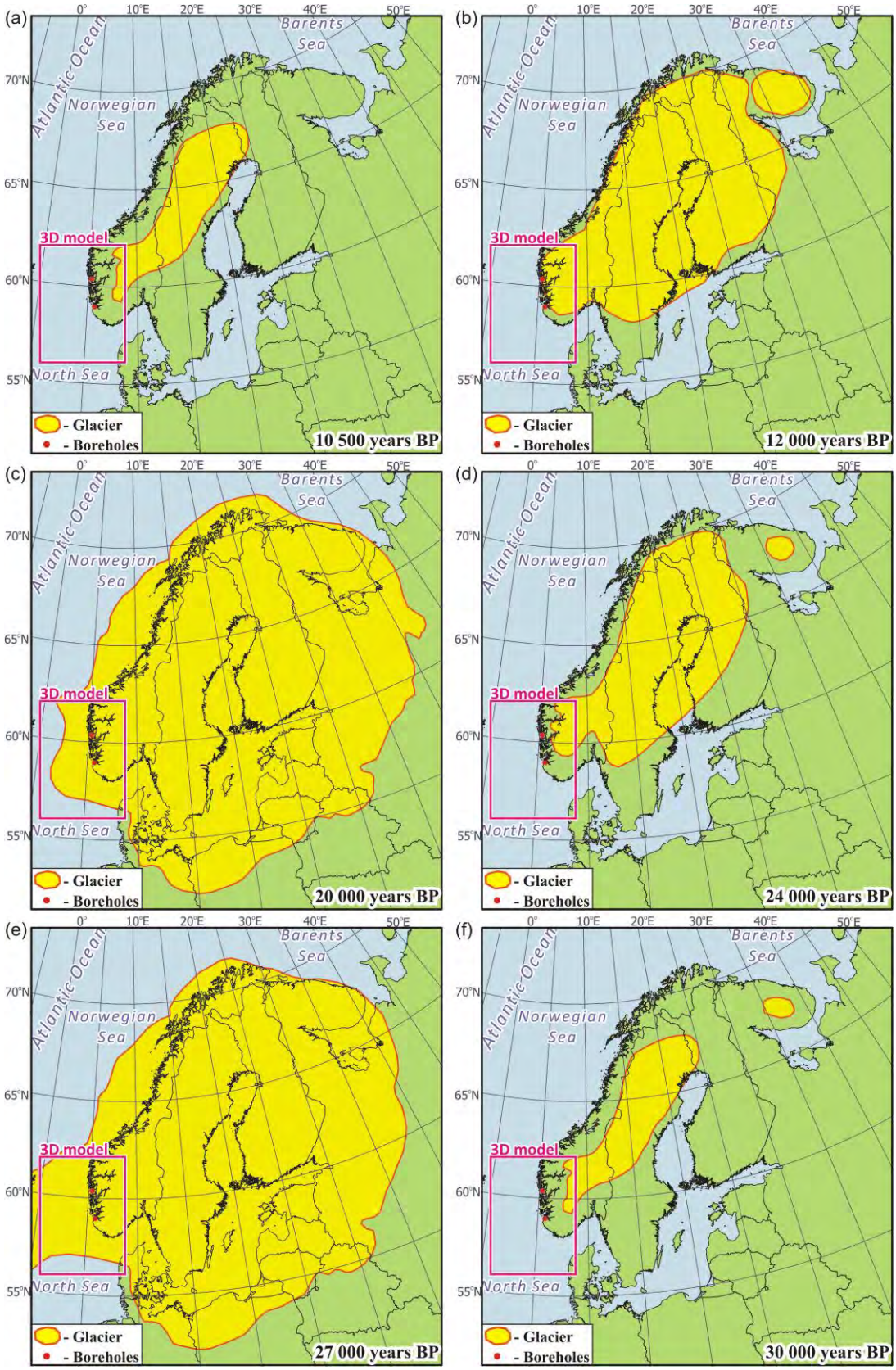

Figure 12.43 *Ice cover during the Weichselian glaciation (after Olsen 2006, Slagstad et al. 2009). The locations of two new boreholes in the Bergen and Stavanger key areas are shown.*

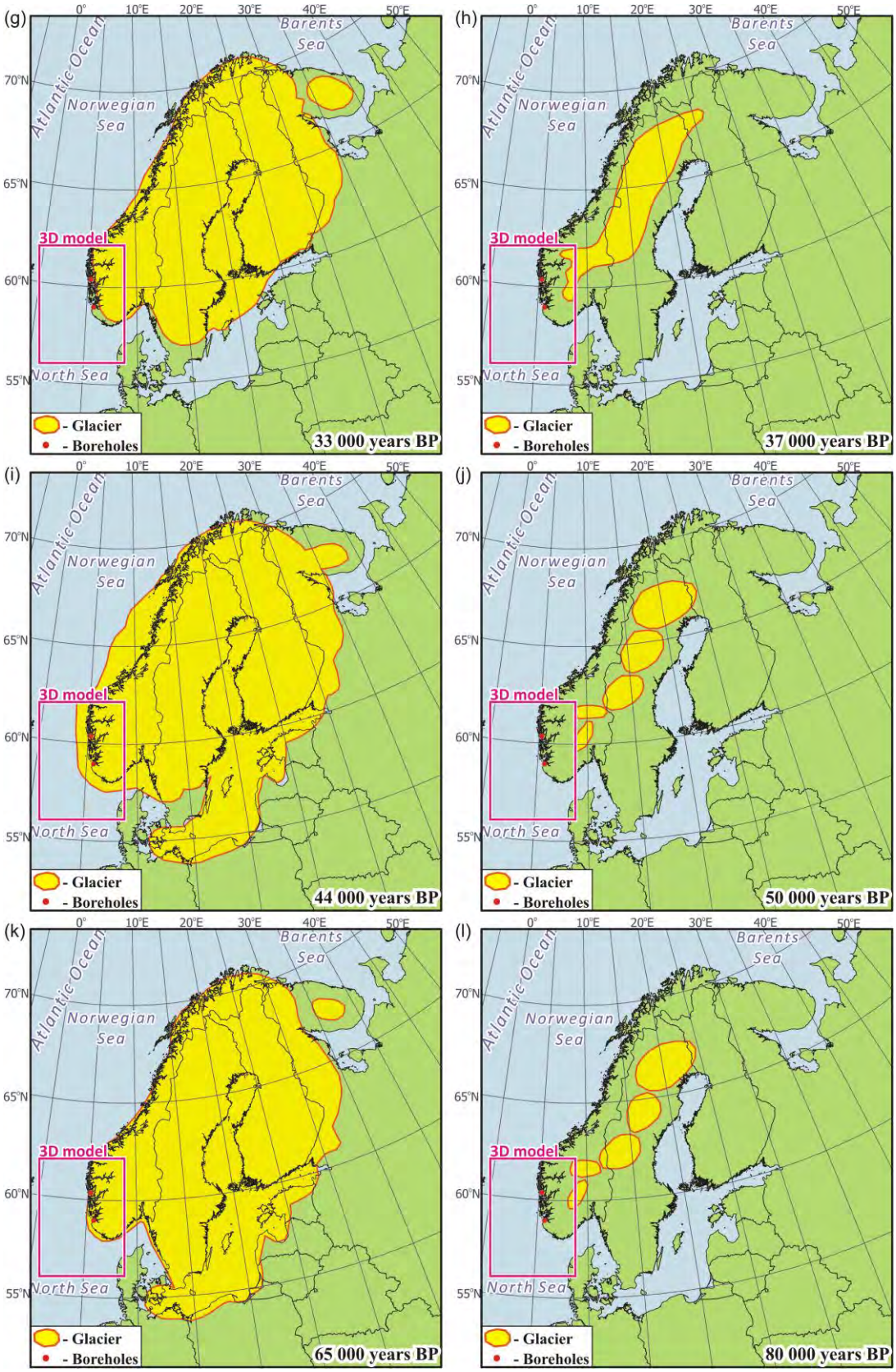

Figure 12.43 Continued. Ice cover during the Weichselian glaciation (after Olsen 2006, Slagstad et al. 2009). The locations of two new boreholes in the Bergen and Stavanger key areas are shown.

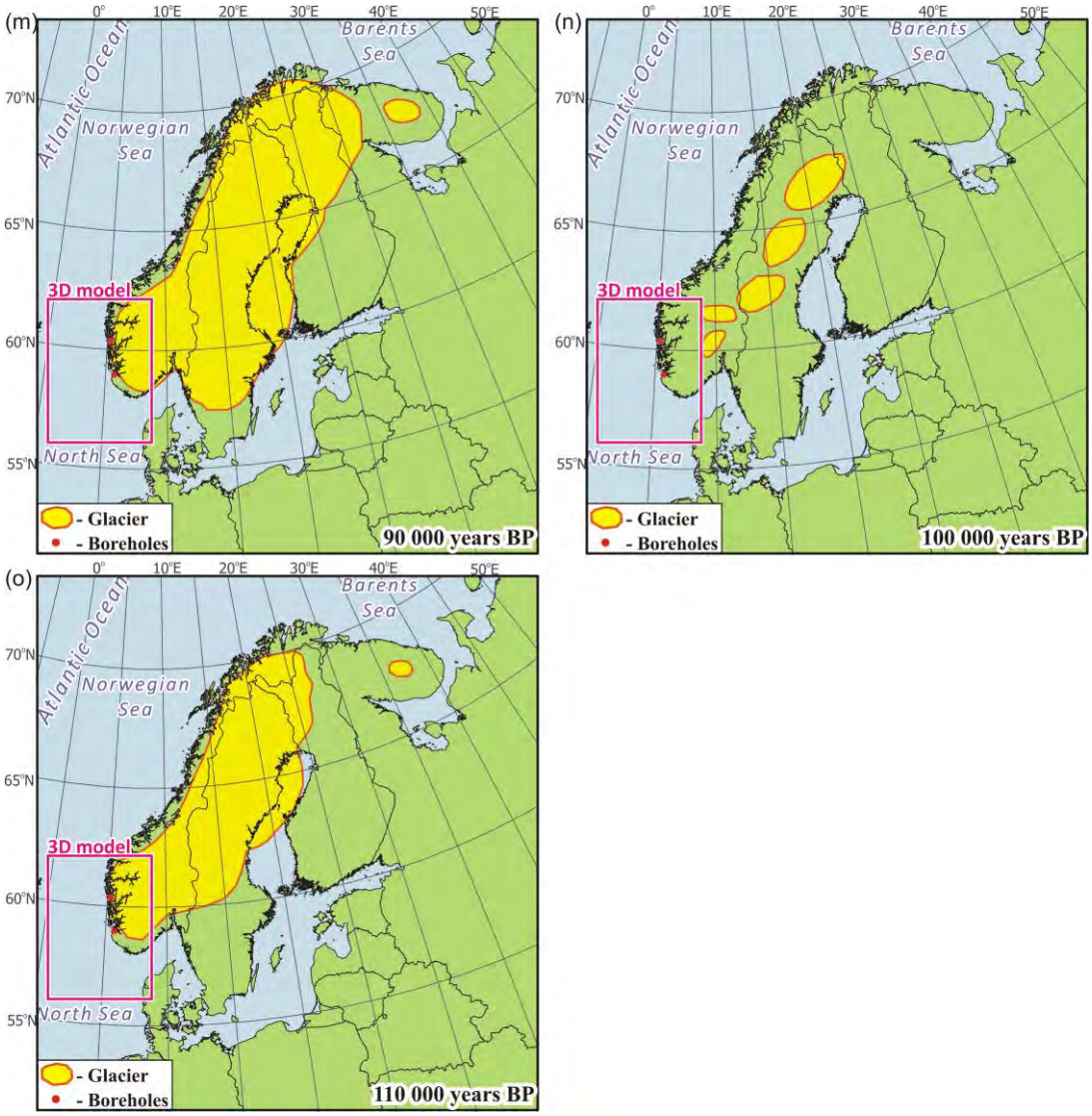

Figure 12.43 *Continued. Ice cover during the Weichselian glaciation (after Olsen 2006, Slagstad et al. 2009). The locations of two new boreholes in the Bergen and Stavanger key areas are shown.*

surface (Fig. 12.42 and 12.44) have been taken as the upper thermal boundary condition whereas the lithosphere-asthenosphere boundary (Fig. 12.35b) has been chosen as a lower thermal boundary which corresponds to the 1300 °C isotherm (e.g., Turcotte & Schubert 2002).

The 3D thermal modelling has been carried out considering the palaeoclimatic changes of the surface temperature during the last 220,000 years before present (BP). During this time interval, the study area was affected by glaciations during the Saalian glacial/Eemian interglacial period (220,000-110,000 years BP) and the Weichselian glacial period (~110,000–10,000 years BP), as well as by the Holocene interglacial period (10,000 years BP to present day). The present-day temperature at the Earth´s surface (Fig. 12.42a) is represented by the annual average air temperatures during 1961-1990, which are taken from the database at the Norwegian Meteorological Institute (Tveito et al. 2000). The temperature at the sea floor has been derived from published values of average bottom temperatures in

winter and in summer within the North Sea during 1997-2002 (ICES 2012). According to these data, the average annual bottom temperature is around 8 °C within the northern part of the North Sea. Palaeotemperature at 8,000 years BP (Fig. 12.44a) has been assumed to be 0.6 °C below the present-day surface temperature (Fig. 12.41a). This difference between the present-day temperature and that at 8,000 years BP has been derived from the reconstructed, area-average, mean annual temperature anomalies for northwestern Europe (Davis et al. 2003). To reconstruct the older palaeoclimatic history within the northern North Sea and adjacent areas, a recent model of temporal ice-cover variations in Scandinavia during the Weichselian glacial period (Olsen 2006) has been used based on maps published by Slagstad et al. (2009). The spatial distribution of an ice cover through time is reproduced in Fig. 12.43. According to these data (Olsen 2006; Fig. 12.43), the northwestern part of the study area was almost continuously covered by a Weichselian ice sheet which could have been up to 3,000 m thick (Siegert et al. 2001). The same palaeoclimatic settings were also applied for the Saalian glacial/Eemian interglacial period (220,000-110,000 years BP), taking into account that climatic conditions were inferred to have been relatively similar during the Weichselian glacial/Holocene interglacial and the Saalian glacial/Eemian interglacial periods (Andersen & Borns 1994, Slagstad et al. 2009). At times when the study area was glaciated, a temperature of -1 °C is assumed at the Earth´s surface beneath the ice cover. This is the same assumption as used by Slagstad et al. (2009) for palaeoclimatic corrections of heat-flux measurements from several sites in Norway. A near-melting point temperature of -1 °C is in agreement with published estimates of the subglacial thermal regime beneath the large polar ice sheets in Antarctica, which can be taken as comparable analogues of ice sheets developed during the Quaternary glacial cycles in Europe. The major aspects of the Antarctic subglacial conditions have been discussed by Pattyn (2010), showing that the mean ice basal temperature is in the range of -1-0 °C for the greater part of Antarctica. Furthermore, an airborne radar survey has detected approximately 100 lakes under the Antarctic ice cap (Price et al. 2002), the largest of which Lake Vostok has already been drilled. Temperature at the sea floor has been taken as 3 °C which is 5 degrees less than the present-day temperature. On the other hand, a more complex scenario has been applied for time intervals when some parts of the study area were free of ice and sea water. For 12,000 years BP, simulated mean annual temperatures for the Younger Dryas (Renssen & Isarin 1998) have been taken as representative temperatures at the Earth´s surface where the ice cover was absent. For the earlier time intervals, annual mean surface temperatures during the Last Glacial Maximum (Schmittner et al. 2011) have been used for the 3D thermal modelling within the sea water/ice free areas. These temperatures (Schmittner et al. 2011) are comparable with other estimations of the surface temperatures during the Last Glacial Maximum (e.g., Otto-Bliesner & Brady 2006, Bartlein et al. 2010, Hofer et al. 2012, Ziemen et al. 2012), demonstrating that the surface air temperature difference could be less than -20 °C compared to the pre-industrial period (present day before the industrial revolution). Temperatures along the marginal parts of the ice cover are unknown in detail and, for that reason, these temperatures have been obtained by simple interpolation

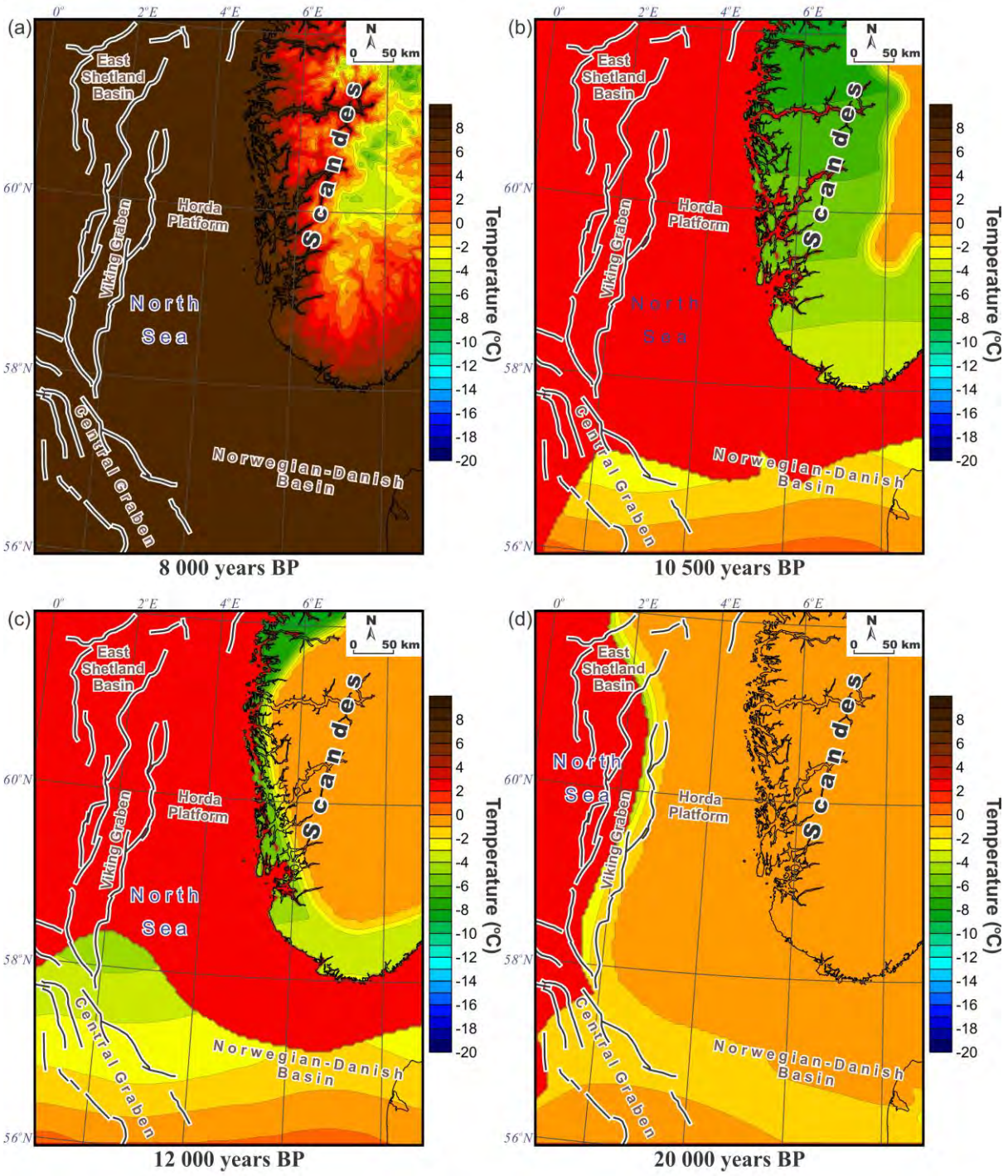

Figure 12.44. *Annual average palaeotemperatures at the sea bottom and the Earth´s surface during the Weichselian glaciation (based on Lambeck 1995, Renssen & Isarin 1998, Isarin & Renssen 1999, Tveito et al. 2000, Davis et al. 2003, Hohl 2005, Gyllencreutz et al. 2006, Schmittner et al. 2011, ICES 2012).*

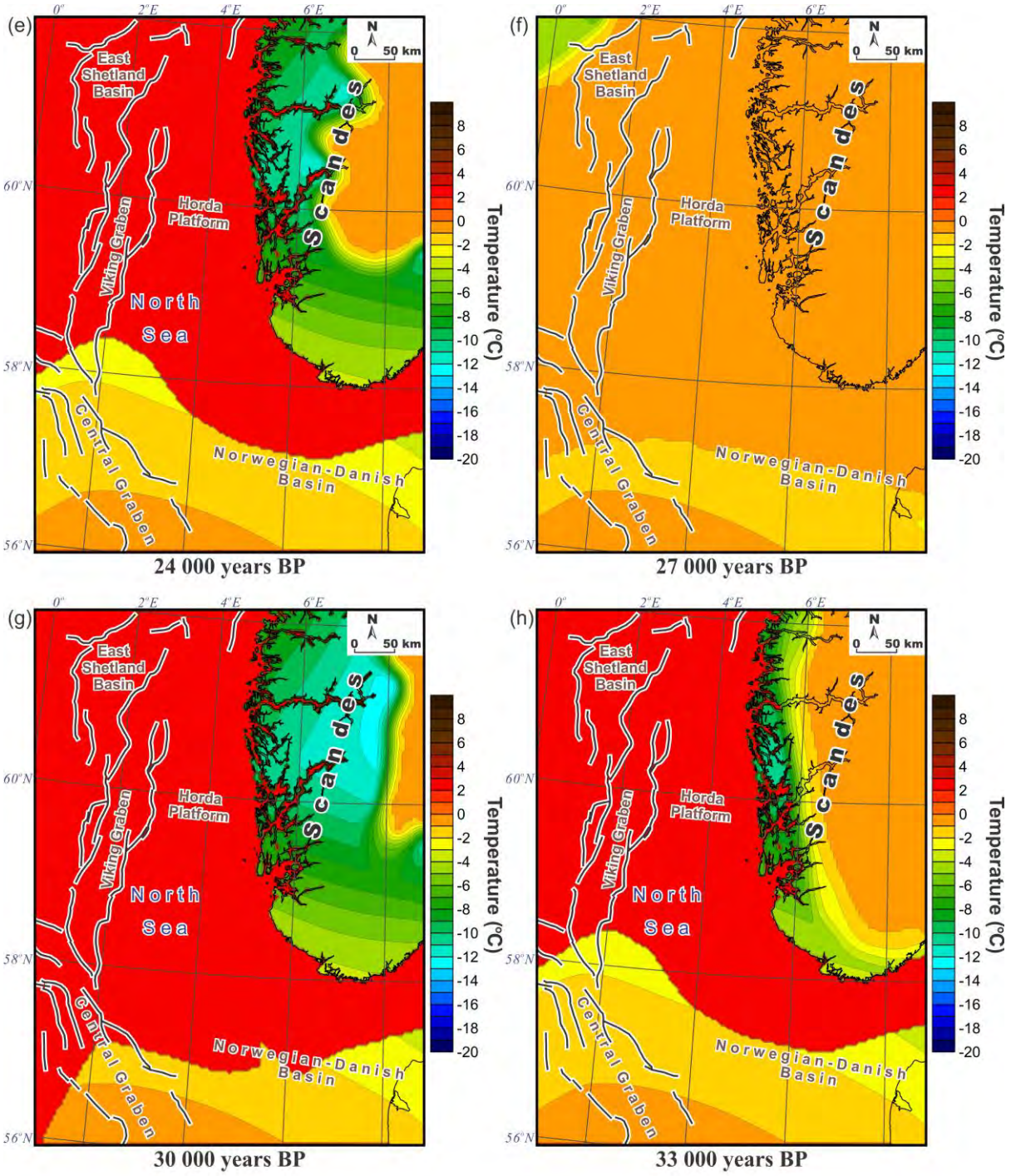

Figure 12.44. Continued. Annual average palaeotemperatures at the sea bottom and the Earth´s surface during the Weichselian glaciation (based on Lambeck 1995, Renssen & Isarin 1998, Isarin & Renssen 1999, Tveito et al. 2000, Davis et al. 2003, Hohl 2005, Gyllencreutz et al. 2006, Schmittner et al. 2011, ICES 2012).

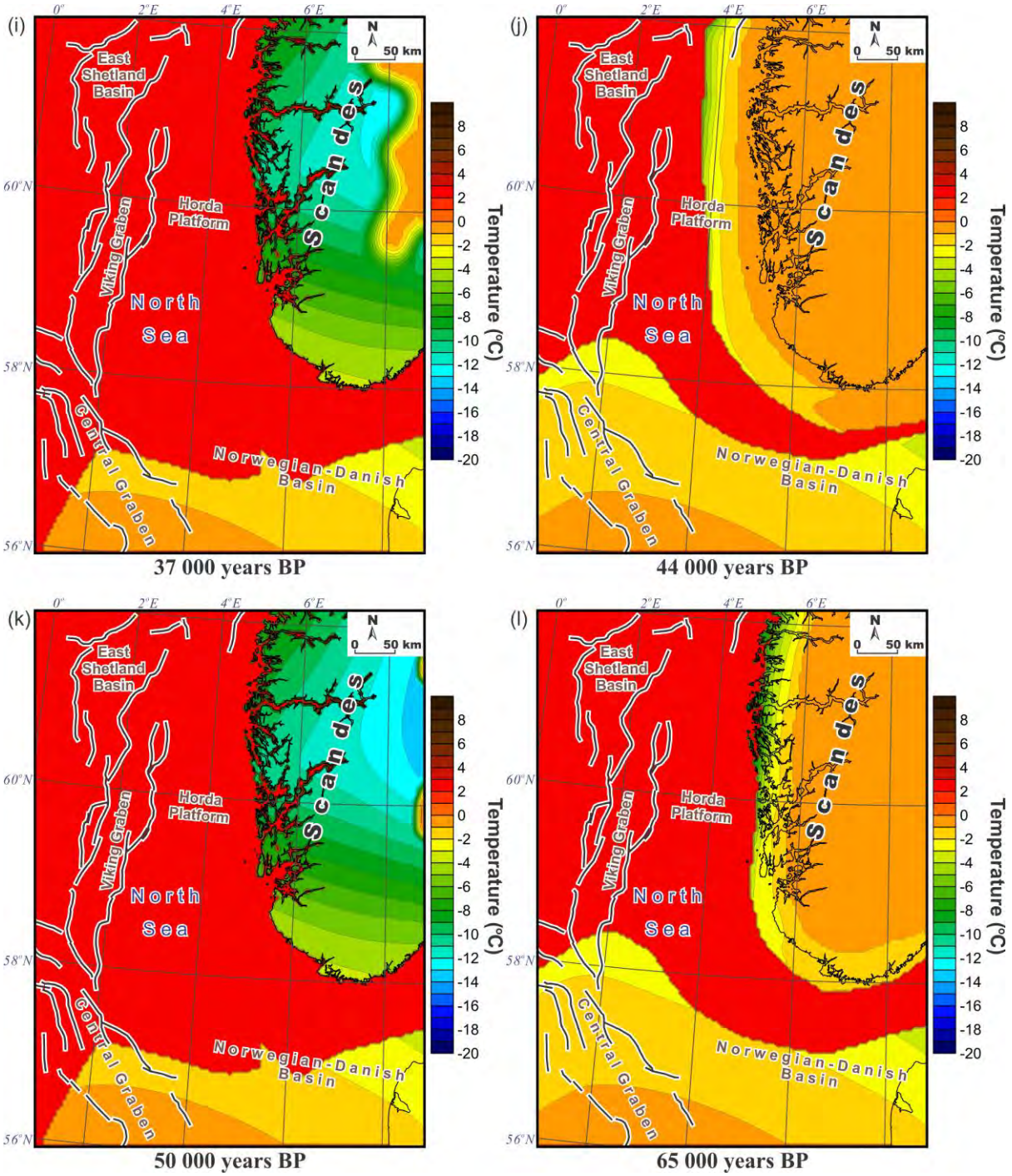

Figure 12.44 *Continued. Annual average palaeotemperatures at the sea bottom and the Earth´s surface during the Weichselian glaciation (based on Lambeck 1995, Renssen & Isarin 1998, Isarin & Renssen 1999, Tveito et al. 2000, Davis et al. 2003, Hohl 2005, Gyllencreutz et al. 2006, Schmittner et al. 2011, ICES 2012).*

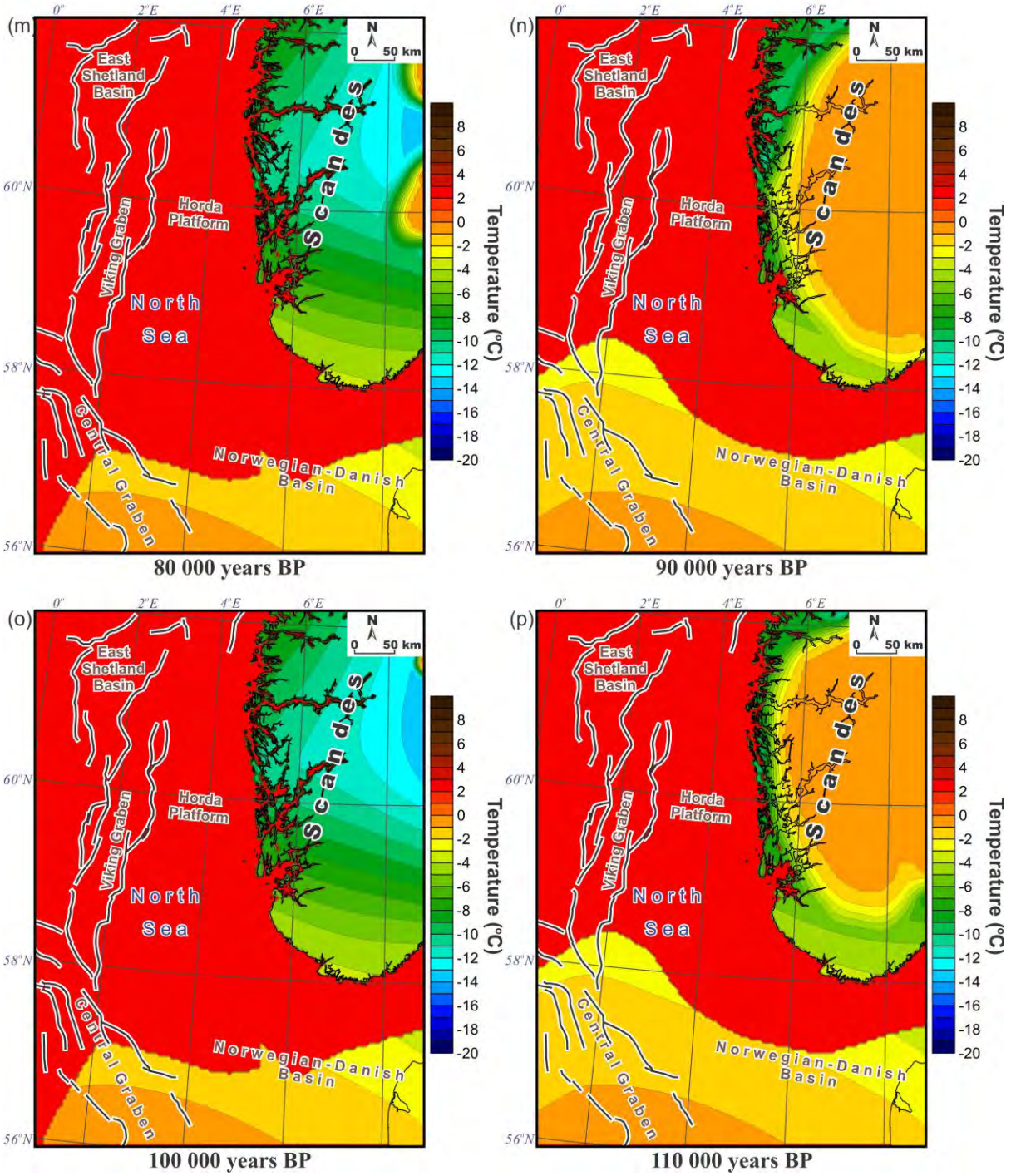

Figure 12.44 *Continued. Annual average palaeotemperatures at the sea bottom and the Earth´s surface during the Weichselian glaciation (based on Lambeck 1995, Renssen & Isarin 1998, Isarin & Renssen 1999, Tveito et al. 2000, Davis et al. 2003, Hohl 2005, Gyllencreutz et al. 2006, Schmittner et al. 2011, ICES 2012).*

between -1 °C beneath the internal parts of the ice sheet and the derived temperature over the remaining land areas (Renssen & Isarin 1998, Schmittner et al. 2011). The position of shorelines within the southern part of the study area is based on palaeogeographical investigations by Lambeck (1995) and Gyllencreutz et al. (2006). Estimations of sea-level changes for 10,000 years BP (Lambeck 1995, Gyllencreutz et al. 2006) were employed when

the size of the ice sheet was similar to that at 10,000 years BP (Fig. 12.43a). This shoreline has been applied for the following time steps: 10,000 years BP (Fig. 12.43a), 30,000 years BP (Fig. 12.43f), 37,000 years BP (Fig. 12.43h), 50,000 years BP (Fig. 12.43j), 80,000 years BP (Fig. 12.43l) and 100,000 years BP (Fig. 12.43n). On the other hand, reconstructed palaeoshorelines for 12,000 years BP (Lambeck 1995, Gyllencreutz et al. 2006) were used when the size of the Weichselian ice sheet was relatively large as it was at 12,000 years BP (Fig. 12.43b). Therefore, the shoreline for 12,000 years BP has been applied for the following time steps: 12,000 years BP (Fig. 12.43b), 20,000 years BP (Fig. 12.43c), 24,000 years BP (Fig. 12.43d), 27,000 years BP (Fig. 12.43e), 33,000 years BP (Fig. 12.43g), 44,000 years BP (Fig. 12.43i), 65,000 years BP (Fig. 12.43k), 90,000 years BP (Fig. 12.43m) and 110,000 years BP (Fig. 12.43o).

The reconstruction of the annual average palaeotemperatures at the sea bottom and the Earth´s surface during the Weichselian and Saalian glaciations demonstrates that the 3D model region is characterised by areas with essentially low palaeotemperatures (Fig. 12.44). In particular, the surface temperature was locally less than -15 °C over the continent where the ice cover was absent or very thin. These low temperatures imply the existence of permanently frozen ground which can reach more than 1-2 km in thickness in some areas of the world (e.g., Dobinski 2011).

12.4.3 Results of 3D thermal modelling

The results of the transient 3D, conductive, thermal modelling provide an overview of the present-day temperature distribution beneath the northern North Sea and adjacent areas of the continent. Major changes in the thermal pattern within the study area are shown by use of selected 2D horizontal slices through the obtained 3D conductive thermal field (Figs. 12.45 & 12.46). Figure 12.45 illustrates the thermal pattern at six depth levels within the upper part of the 3D model where relatively low thermal conductive sediments are present. On the other hand, Figure 12.46 demonstrates the temperature distribution within the deeper part of the study area; near the crust-mantle boundary (Fig. 12.46a, b) and within the lithospheric mantle (Fig. 12.46c, d).

At the regional scale, the mainland is generally colder than the basinal areas of the northern North Sea (Fig. 12.45). Within the upper part of the model, this regional trend of modelled temperatures is related to the high thermal conductivity of crystalline crustal rocks (Table 12.2) which crop out over large parts of the continent. This interaction between the relatively high values of thermal conductivities and structural pattern is responsible for a chimney effect within the areas where the sedimentary cover is absent or very thin. For instance, the chimney

Fig

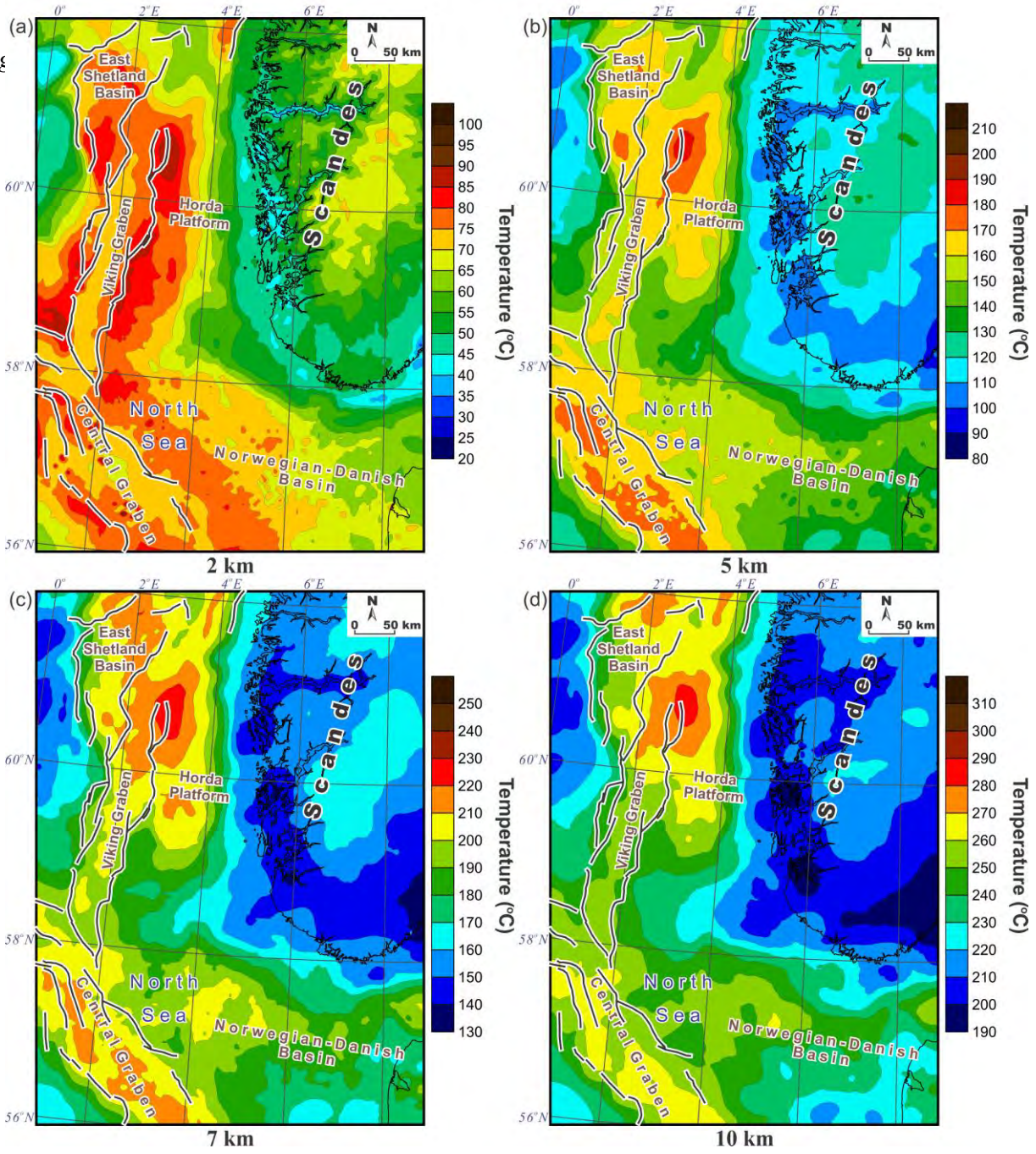
(a)
(b)
(c)
(d)
East Shetland Basin
Viking Graben
Horda Platform
Scandes
North Sea
Central Graben
Norwegian-Danish Basin
0° 2°E 4°E 6°E
60°N
58°N
56°N
N
0 50 km
Temperature (°C)
2 km
5 km
7 km
10 km

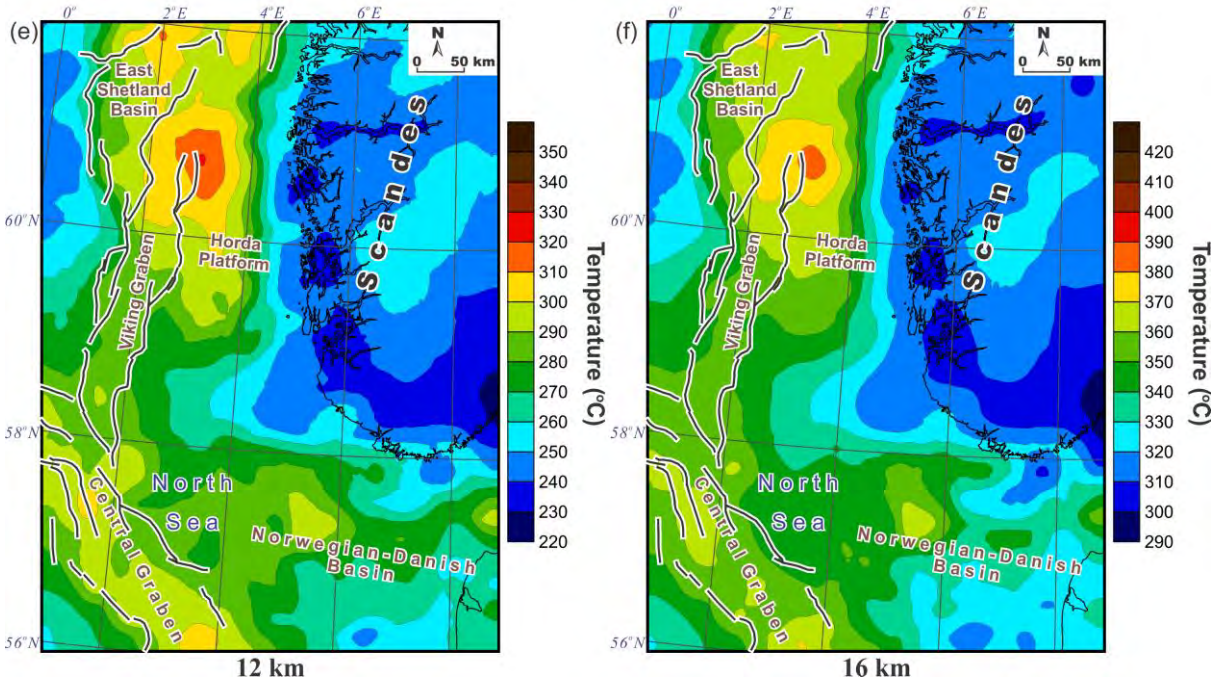

Figure 12.45. Continued. Modelled temperatures within the upper part of the study area. Temperature maps for depths of 2 km (a), 5 km (b), 7 km (c), 10 km (d), 12 km (e) and 16 km (f) extracted from the 3D thermal model.

effect is also clearly recognisable within the East Shetland Platform where the sediments are thinner compared to the East Shetland Basin or the Viking Graben. In contrast, there is a clear correlation between areas with thicker sedimentary successions and areas with higher temperatures (cf. Figs. 12.7-12.13, 12.16 & 12.45). This regional trend of temperature is related to the low thermal conductivity of sediments which increases the heat storage within the areas covered by thick sediments. In other words, the relatively thick, low-conductive sediments reduce the rate of heat transfer, acting like the thermal insulation in a vacuum flask. This thermal effect is especially pronounced within the Central and Viking grabens, and the East Shetland and Norwegian-Danish basins where the thickness of the sedimentary cover is greatest. This thermal blanketing effect of sediments is still recognisable down to a depth of 12-16 km near the base of the sedimentary succession (Fig. 12.45e, f). Furthermore, the effect of increased radiogenic heat production within the upper crustal low-density layer (Fig. 12.26; Table 12.2) is prominent beneath the northern part of the Horda Platform, where the highest temperatures are modelled within the upper part of the 3D model (Fig. 12.45). There, the thickness of the upper crustal low-density layer is more than 10 km (Fig. 12.26).

Locally, the regional pattern of the modelled temperatures is disturbed by Permian salt structures. There are pronounced local temperature increases (see hot spots in Fig. 12.45) in places where the sediments are pierced by salt within the Central Graben and the Norwegian Danish Basin (cf. Figs. 12.2, 12.12 & 12.45a). This is due to the fact that the Upper Permian

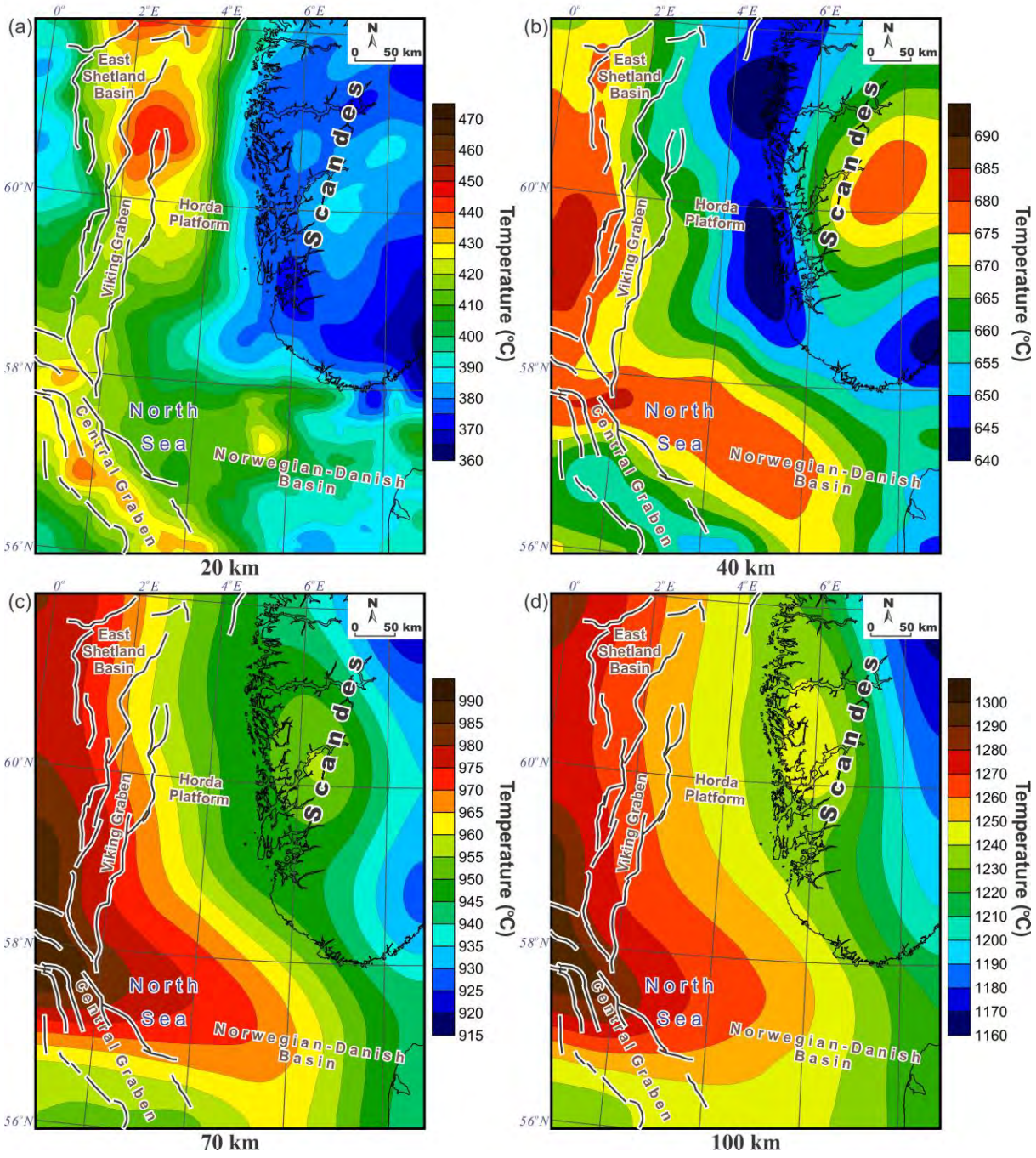

Figure 12.46 Modelled temperatures within the deep part of the study area. Temperature maps for depths of 20 km (a), 40 km (b), 70 km (c) and 100 km extracted from the 3D thermal model.

(Zechstein) salt layer has a much higher thermal conductivity than the surrounding sediments (Table 12.2), causing an increased conductive heat transfer within the salt walls and diapirs. This phenomenon was already observed in salt-bearing basins and has been confirmed by results of numerical modelling (e.g., Selig & Wallick 1966, Jensen 1983, Scheck 1997). In addition, local negative temperature anomalies are observed beneath the salt structures and near the salt base in places where the salt is thick (cf. 12.2, 12.12 and 12.45b, c). Once more, increased conductive heat transfer within the salt gives rise to the thermal anomalies. In this case, they are negative beneath the high-conductive salt layer. This salt-related heat extraction is especially pronounced in the temperature map at depths of 5 km and 7 km within the Central Graben and the Norwegian-Danish Basin where the negative thermal anomalies are located near the base of some salt structures (Fig. 12.45b, c).

The results of the 3D thermal modelling within the deeper parts of the model are shown in Fig. 12.46 by four representative horizontal slices of the 2D temperature distribution at depths of 20, 40, 70 and 100 km. The main feature of the regional pattern in these temperature maps is the transition from a relatively cold, eastern part of the study area to a warm one in the west (Fig. 12.46). At great depths (70-100 km; Figs. 12.46c, d) the temperature distribution roughly reflects the configuration of the lower thermal boundary, which is represented by the base of the lithosphere. Therefore, the configuration of the lithosphere-asthenosphere boundary is the main controlling factor in temperature distribution within the deeper levels of the 3D thermal model. On the other hand, interaction of the crustal and mantle thermal properties already complicates the temperature distribution at the depth of 20-40 km (Figs. 12.46a, b). At the depth of 40 km (Fig. 12.46), the character of temperature distribution is still affected by the increased thickness of the crystalline crust beneath the continent where a positive crust-related thermal anomaly is still recognisable. This is due to the fact that the crystalline crust is characterised by an increased radiogenic heat production in contrast to the mantle material at the same depth level (Table 12.2).

The modelled temperatures and heat flux at the top of the crystalline basement are shown in Fig. 12.47. There is a clear correlation between the depth to the top of the crystalline basement (Fig. 12.15) and the temperature distribution (Fig. 12.47a). Where the top of crystalline rocks is deeply located, the modelled temperatures are high and vice versa (cf. Figs. 12.15 & 12.47a). Therefore, several temperature maxima are located within the deepest parts of the study area in the northern parts of the Viking Graben and the Norwegian-Danish Basin where the modelled temperature is more than 300 °C. In contrast, the distribution of the calculated heat flux at the top of the basement (Fig. 12.47b) demonstrates a general decrease of heat flux values with depth (cf. Figs. 12.15 & 12.47b). This relationship is mostly controlled by the thickness of the crystalline crust which acts as additional heat source due to an increased content of radiogenic elements and, therefore, essentially contributes to a deep heat flux (cf. Figs. 12.47a & 12.48b). Within the deep parts of the Norwegian-Danish Basin and Central and Viking grabens, the lowest values of the heat flux have been obtained, reaching 40 mW/m^2 on average. Conversely, higher positive values of the calculated heat flux (more than 60 mW/m^2) correspond to the areas where the crystalline

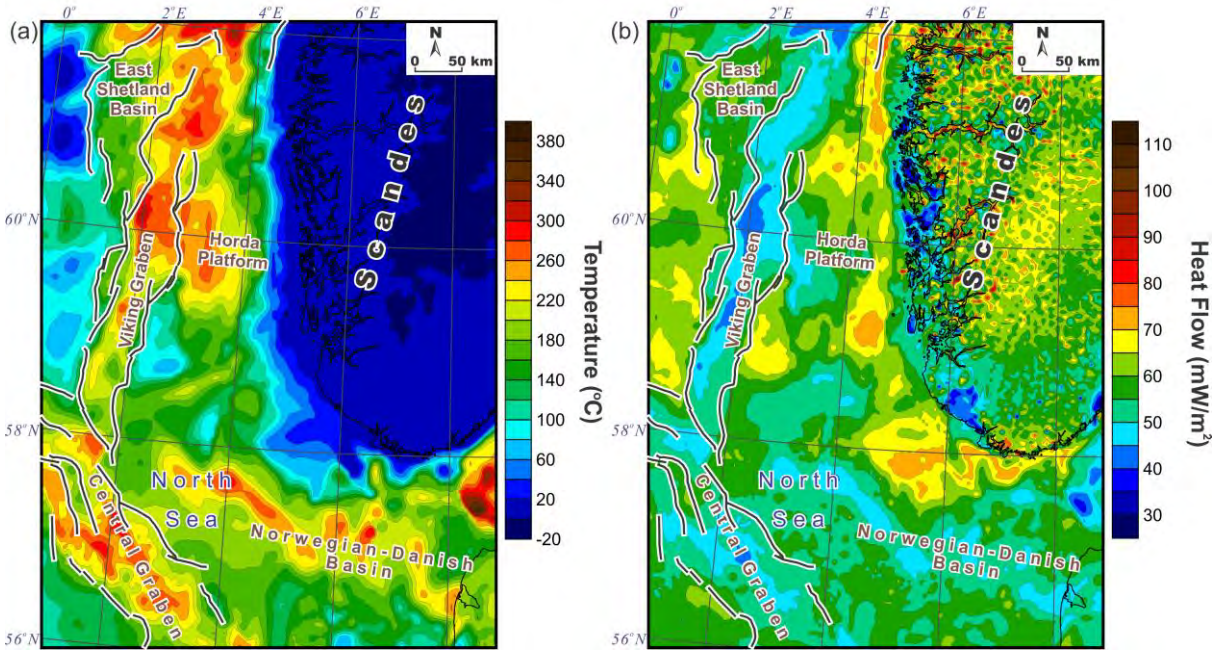

Figure 12.47. Modelled temperatures (a) and heat flux (b) at the top of the crystalline basement.

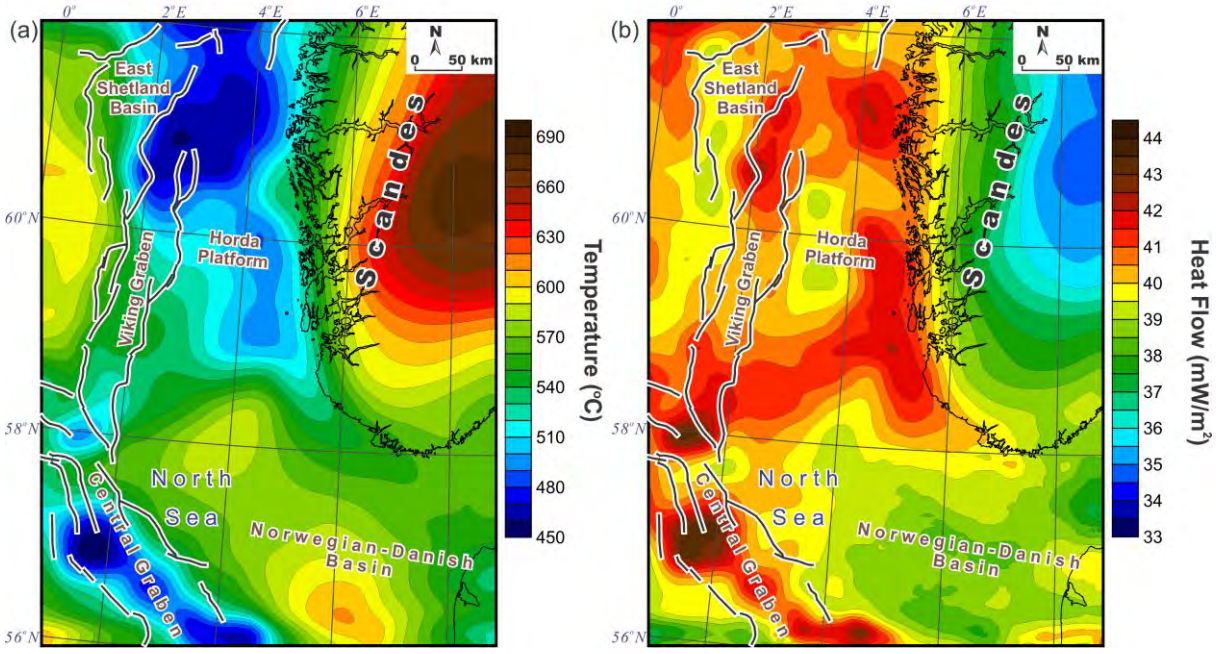

Figure 12.48. Modelled temperatures (a) and heat flux (b) at the Moho.

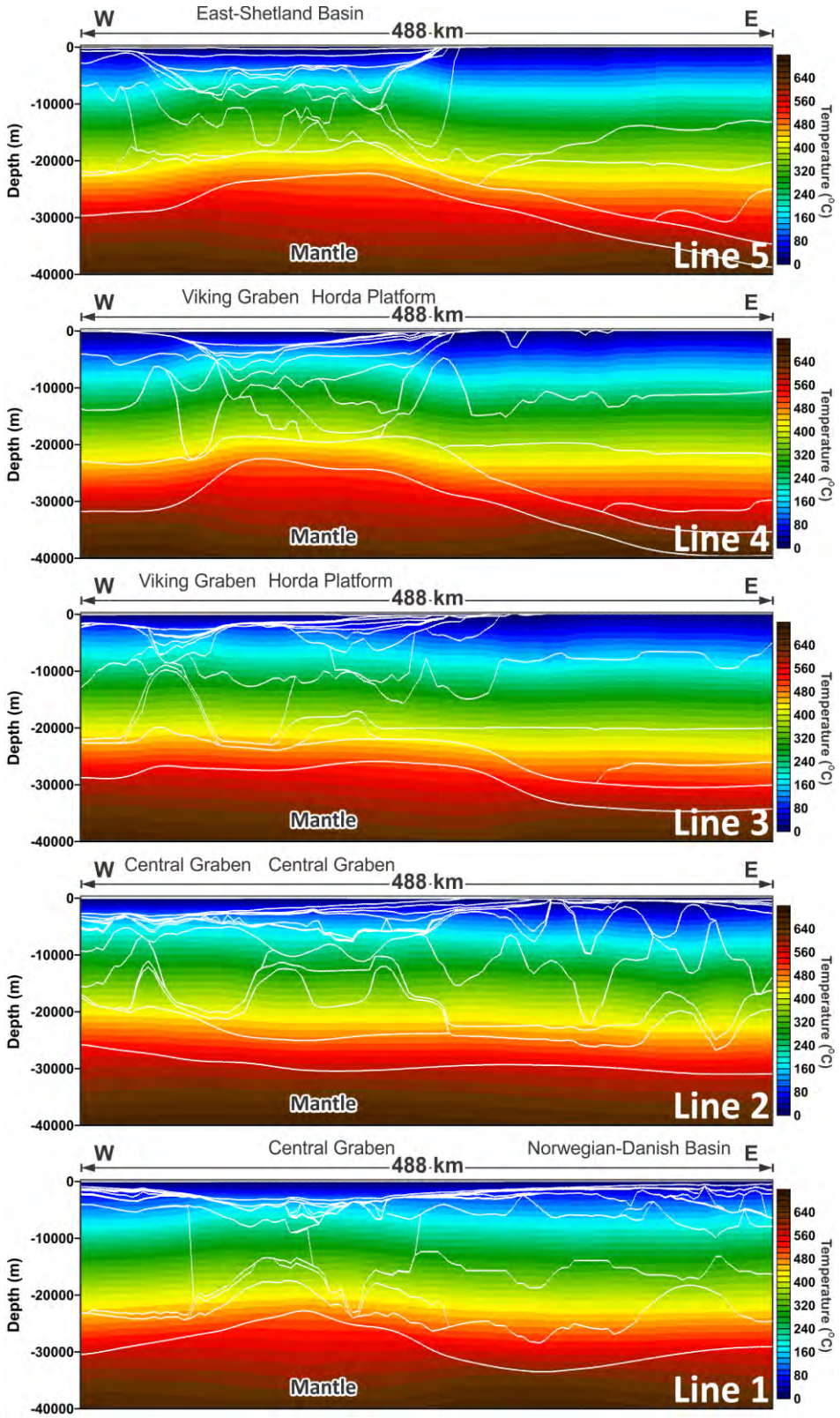

Figure 12.49 Temperature distribution along five selected 2D vertical slices through the lithosphere-scale 3D structural model of the northern North Sea and adjacent areas (for the location of these slices, see Fig. 12.36).

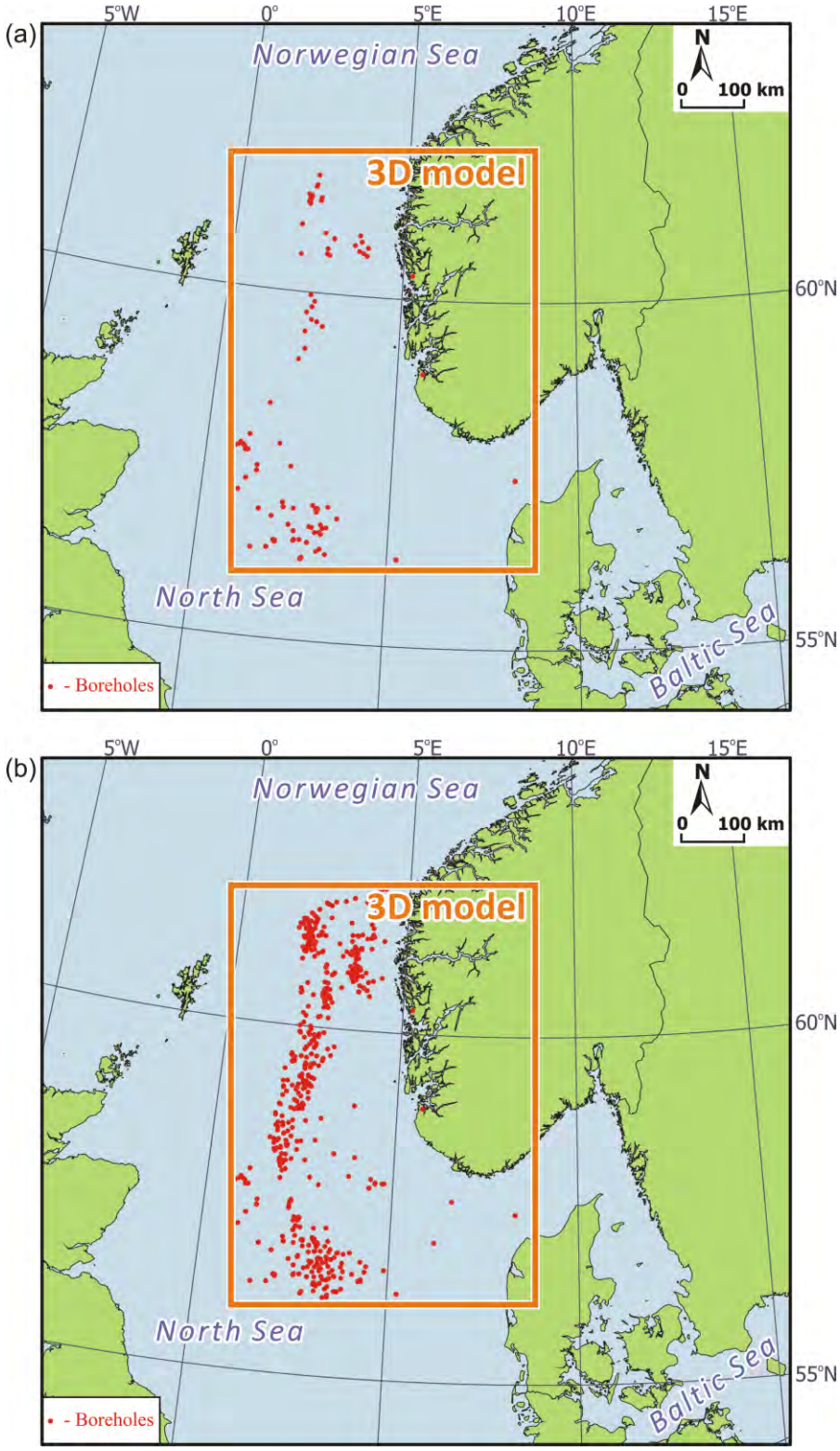

Figure 12.50. Location of the available boreholes. (a) Boreholes with DST (drill stem test) temperatures are only shown within the Norwegian sector of the North Sea. (b) Boreholes with less reliable bottom-hole temperatures (BHT) are also shown within the Norwegian sector of the North Sea.

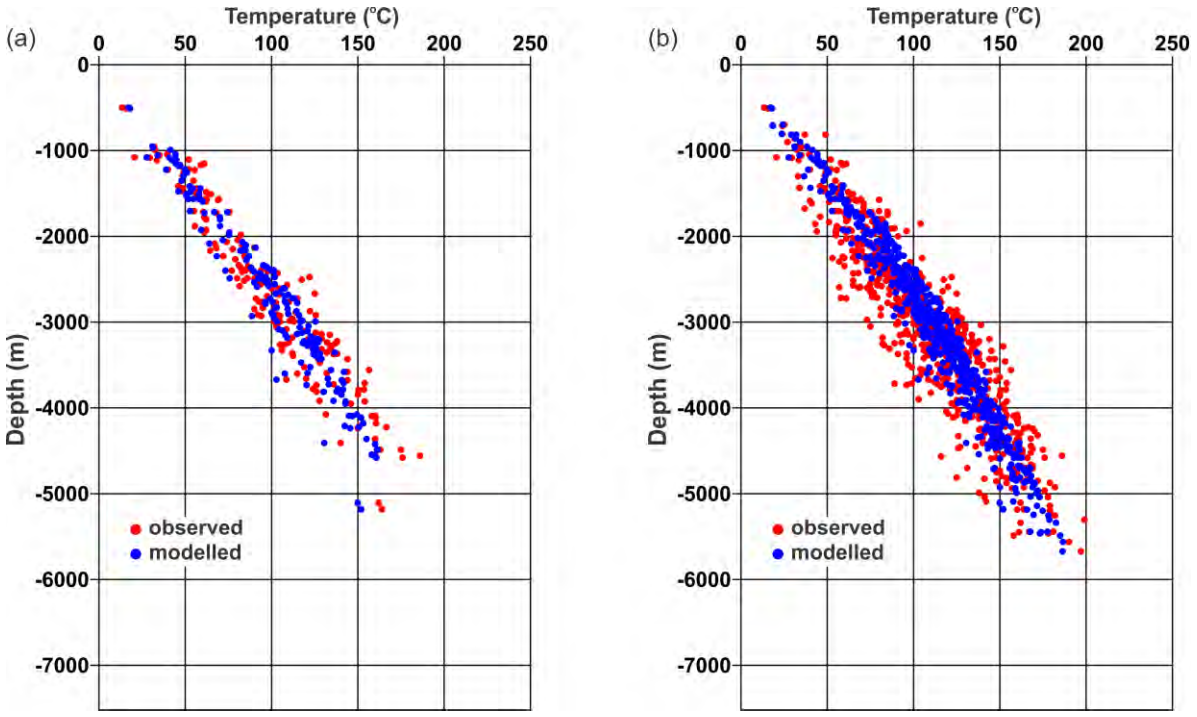

Figure 12.51 *Misfit between the calculated (blue dots) and the observed (red dots) temperatures. (a) Only boreholes with DST (drill stem test) temperatures are used within the Norwegian sector of the North Sea. (b) Boreholes with less reliable bottom-hole temperatures (BHT) are also included within the Norwegian sector of the North Sea.*

basement is uplifted. The complex picture of heat flux over the continent is mostly controlled by abrupt changes in the topography (Fig. 12.42b).

The temperature pattern at the Moho (Fig. 12.48.a) reflects the configuration of the Moho topography (Fig. 12.35a), indicating that the major controlling factor, as in the case of the top of the crystalline basement, is again the depth position of the chosen interface. Consequently, the highest temperature is modelled beneath the mainland, reaching values of more than 650 °C. In contrast, the calculated heat flux is characterised by lowest values (less than 37 mW/m^2) beneath the continent, whereas the highest values (more than 42 mW/m^2) are modelled beneath the central parts of the Central and Viking grabens where the Moho is notably uplifted.

To demonstrate the cross-sectional view at the modelled temperatures, five 2D vertical slices (Fig. 12.49) have been extracted from the 3D thermal model. The locations of these vertical slices are the same as the positions of five representative vertical slices across the 3D density model (Fig. 12.36). The most prominent feature along these cross-sections is that an uplift of the modelled isotherms spatially correlates with the relatively shallow position of the Moho on one hand. On the other hand, the uplift of the isotherms coincides with the areas where thick sediments are present and, thus, there the thermal insulation effect of the sediments is highest. Therefore, a superposition of the chimney effect of the high thermally conductive upper mantle material and thermal blanketing of the low thermally conductive sedimentary

cover results in the increased modelled temperatures within the crystalline crust where the Moho is uplifted and the sedimentary infill is relatively thick. Furthermore, the calculated isotherms are approximately horizontal beneath the mainland, reflecting the subhorizontal structural subdivision of the crystalline crust of the Baltican crustal domain (cf. Figs. 12.39-12.41 & 12.49a, b, c).

The calculated temperature variations within the upper part of the 3D structural model have been compared to temperatures measured in boreholes. The locations of all available boreholes are shown in Fig. 12.50. For the Norwegian sector of the North Sea, positions of the boreholes with only DST (drill stem test) temperatures are shown in Fig. 12.50a, whereas the positions of the boreholes with less reliable bottom-hole temperatures (BHT) are shown in

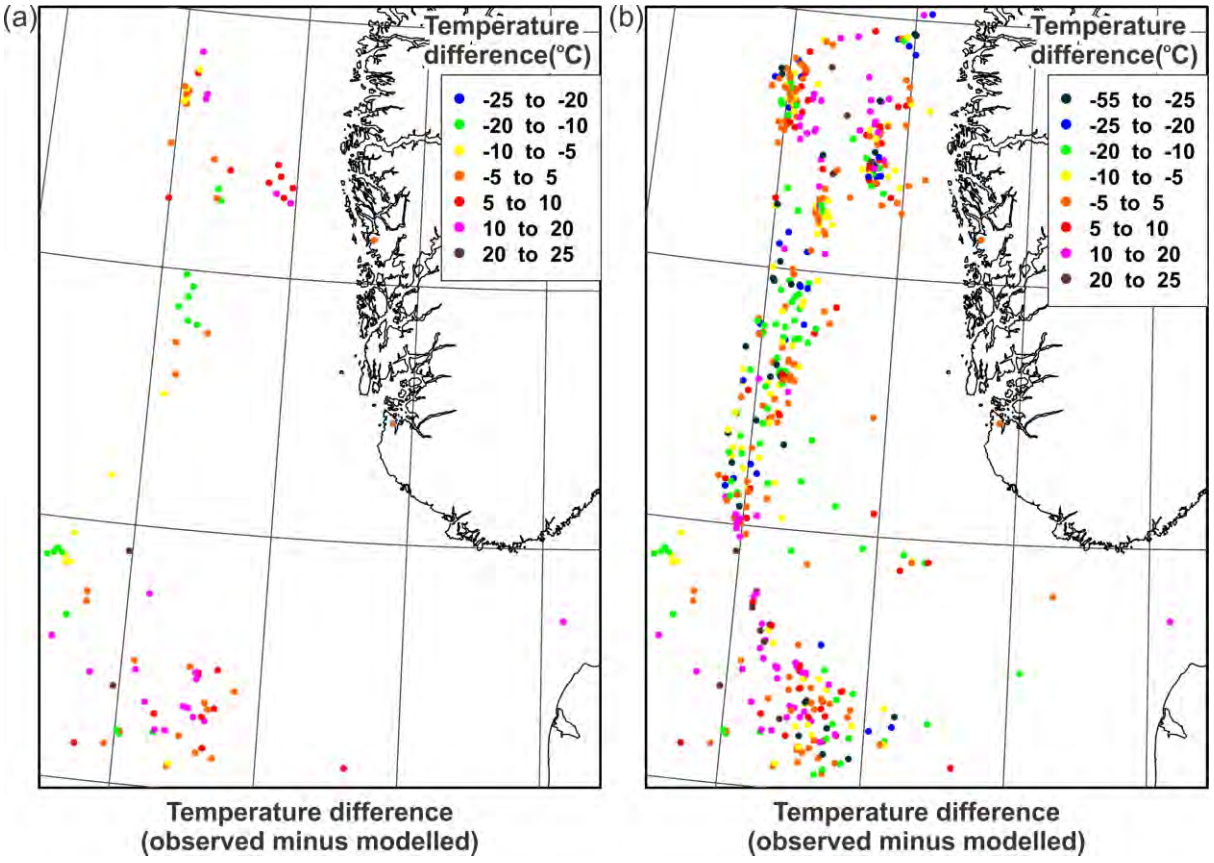

Figure 12.52 *Spatial distribution of temperature difference values (measured temperature minus the modelled one) within the study area. (a) Only boreholes with DST (drill stem test) temperatures are used within the Norwegian sector of the North Sea. (b) Boreholes with less reliable bottom-hole temperatures (BHT) are also included within the Norwegian sector of the North Sea.*

Table 12.3. Difference between modelled temperatures and measured ones (measured values minus the modelled ones) in available deep boreholes. Only DST (drill stem test) temperatures are used within the Norwegian sector of the North Sea.

N	Temperature range	Percentage of values, %	Number of values
1	from -25 to -20	0	0
2	from -20 to -10	17.4	32
3	from -10 to -5	14.1	26
4	from -5 to 5	33.2	61
5	from 5 to 10	14.7	27
6	from 10 to 20	18.5	34
7	from 20 to 25	2.2	4

Table 12.4. Difference between modelled temperatures and measured ones (measured values minus the modelled ones) in available deep boreholes. In addition to DST (drill stem test) temperatures from the Norwegian sector of the North Sea, less reliable bottom-hole temperatures (BHT) are also used.

N	Temperature range	Percentage of values, %	Number of values
1	from -55 to -25	5.1	38
2	from -25 to -20	5.1	38
3	from -20 to -10	16.5	122
4	from -10 to -5	15.0	111
5	from -5 to 5	29.9	221
6	from 5 to 10	12.2	83
7	from 10 to 20	14.6	108
8	from 20 to 25	2.3	17

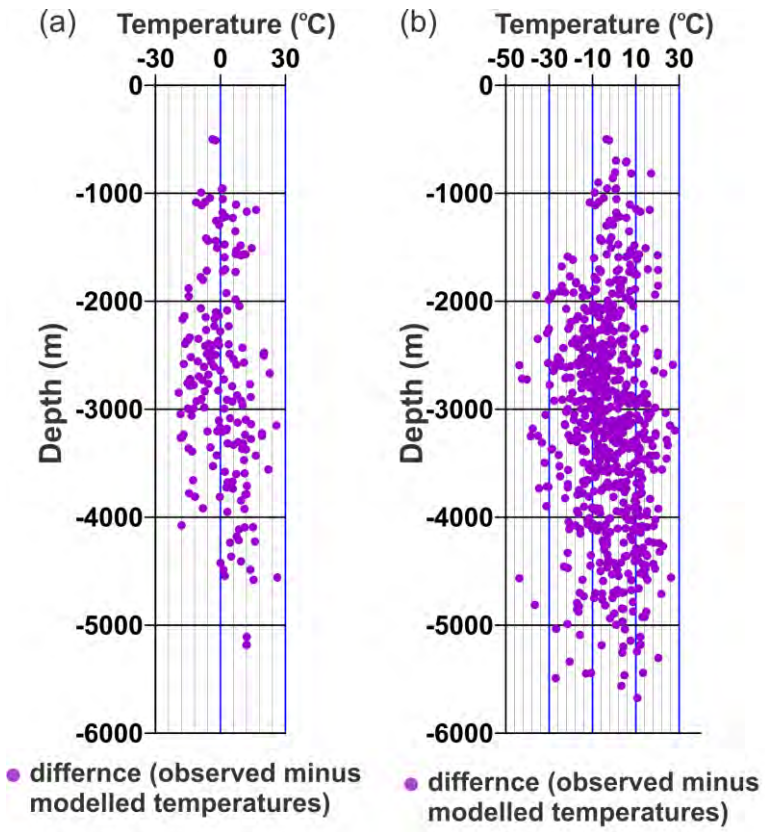

Figure 12.53. Temperature difference values (measured temperature minus the modelled one). (a) Only boreholes with DST (drill stem test) temperatures are used within the Norwegian sector of the North Sea. (b) Boreholes with less reliable bottom-hole temperatures (BHT) are also included within the Norwegian sector of the North Sea.

Fig. 12.51. The difficulty with bottom-hole values is that bottom-hole temperatures (BHT) were measured either during drilling or soon after the drilling process was finished and, therefore, these temperatures contain an element of the thermal disturbance within the boreholes due to circulation of the drilling fluid. For that reason, bottom-hole temperatures (BHT) are unfortunately unreliable. In contrast, drill stem test (DST) temperatures are supposed to be obtained after reaching thermal equilibrium in the boreholes and, therefore, are more reliable for constraining the subsurface thermal regime. However, due to a deficit of drill stem test (DST) data within the Norwegian sector of the North Sea (Fig. 12.50a), bottom-hole temperatures (BHT) have also been used to compare the observed and modelled temperatures. To separate these two datasets with different reliabilities, the results of the comparison are provided separately for drill stem test (DST) temperatures (Figs. 12.51a, 12.52a, 12.53a; Tables 12.3) and for drill stem test (DST) temperatures with bottom-hole temperatures (BHT) in addition (Figs. 12.51b, 12.52b, 12.53b; Tables 12.4).

Comparison of the observed and modelled values of temperature has shown that the results of the 3D thermal modelling are in a reasonable agreement with the general trends of measured temperatures (Fig. 12.51). The detailed analysis (Fig. 12.52; Tables 12.3 and 12.4) demonstrates that large misfits between the modelled and observed temperatures have also

been found. Actually, a large proportion of the differences between the modelled and observed values are in the range of ±10 °C, implying that conduction is the dominant mechanism of heat transfer at the regional scale within the northern North Sea. Some values, however, are much larger than 10 degrees (Fig. 12.53). Based on our knowledge of the internal structure of the North Sea sedimentary basins, these misfits are possibly related to the convective heat transfer which is superimposed on the regional conductive thermal field in some areas where geothermally heated or cooled fluids are present. An additional reason can be related to the horizontal resolution of the 3D model, which is 4 km. This means that some local structural features of the study area could not be resolved in the detail which is necessary for representing the detailed section of particular boreholes in the places where these boreholes are located. Consequently, in these specific locations the measured temperatures cannot be correctly reproduced by 3D thermal modelling.

12.5 Summary

In summary, it can be stated that the integration of all available structural data in combination with the 3D gravity analysis allowed us to evaluate a first-order configuration of the crystalline crust within the northern part of the North Sea and adjacent areas that is consistent with the observed gravity.

Furthermore, the results of the 3D thermal modelling have provided significant progress in our understanding of the first-order characteristics of the conductive thermal field within the northern North Sea and adjacent areas. Therefore, these results have revealed some key features of the present-day thermal state of the study area that are extremely important factors in the exploration for hydrocarbons and in evaluations of the deep geothermal potential of the sedimentary basins.

The crustal and thermal models can be downloaded from NGUs ftp2.ngu.no server. User names and passwords have already been distributed to the Coop partners.

13. 2D CRUSTAL AND THERMAL MODELLING WITHIN THE BERGEN AND STAVANGER AREAS

Yuriy Maystrenko, Harald Elvebakk, Jadranka Kurtic

13.1 Introduction

To understand some of the details of the configuration and heat flux of the crystalline crust, a combined lithosphere-scale 2D density, magnetic and thermal modelling has been performed within two small areas near Bergen and Stavanger (Fig. 13.1). These two areas have been chosen because crystalline rocks with different thermal properties crop out at the Earth's surface within these localities. Granitic rocks with a high content of radiogenic elements are exposed near Bergen and rocks with a relatively low radiogenic heat production occur near Stavanger. Additionally, three boreholes have been drilled there, revealing the structure of the

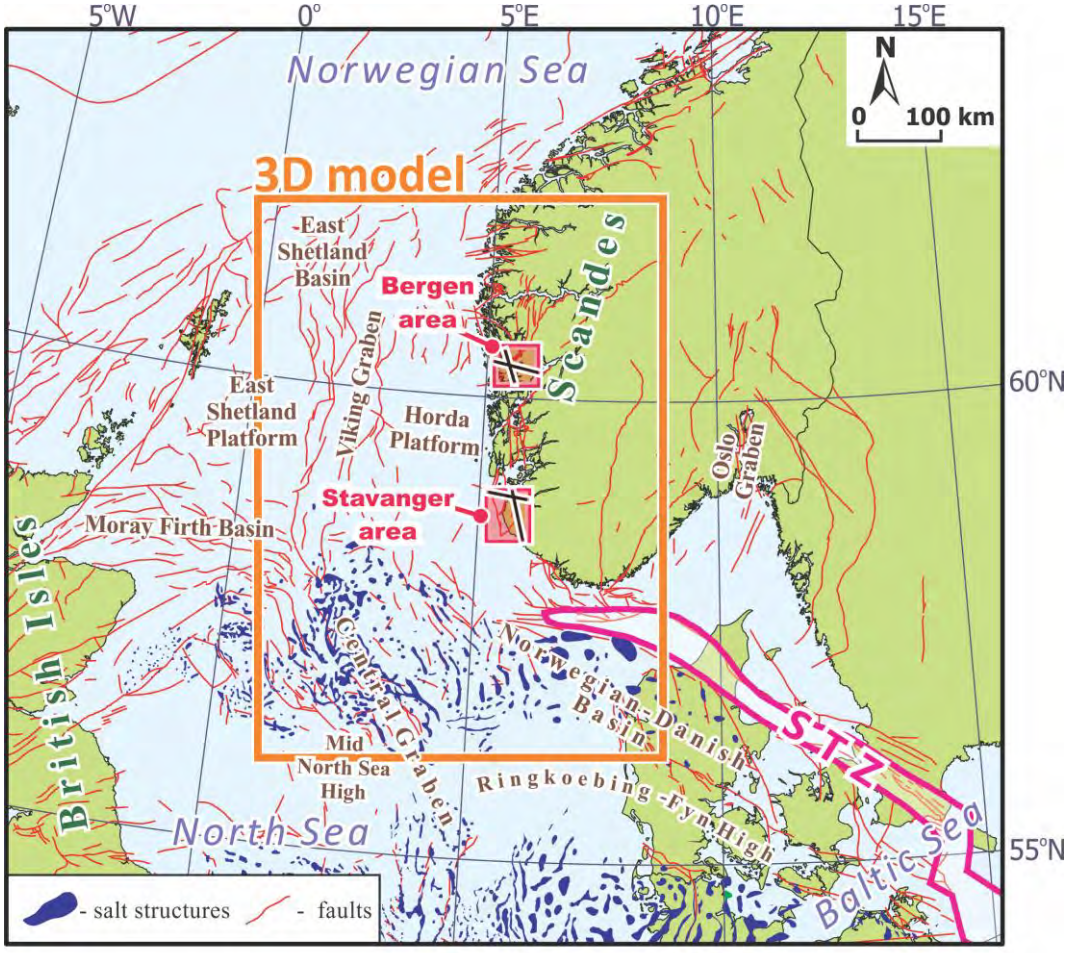

Figure 13.1. Tectonic settings within the main study area with locations of the 2D profiles within the Bergen and Stavanger areas (after Ziegler 1990, Vejbæk & Britze 1994, Lokhorst 1998, Pharaoh 1999, Baldschuhn et al. 2001, Sigmond 2002, Maystrenko et al. 2012). The location of the 3D structural model of the northern North Sea and adjacent areas of the continent is also shown. STZ - Sorgenfrei-Tornquist Zone.

subsurface. The Fyllingsdalen borehole has recently been drilled near Bergen, and the Alstein and Ullrigg boreholes are located near Stavanger. Thermal well logging was carried out in these three boreholes in 2011 and 2012 (Elvebakk & Storrø 2012 this report), allowing to constrain the thermal regime of the subsurface. Moreover, the petrophysical database 'Petro' at NGU provides the measured values of densities, magnetic and thermal properties of crystalline rocks located within these two key areas and the core samples from the 516 m-deep Fyllingsdalen borehole have also been investigated in the laboratory of NGU (Elvebakk & Storrø 2012 this report).

13.2 Geological settings

13.2.1 The Bergen area

The prominent geological feature of the Bergen region is the Bergen Arc System which consists of several Caledonian nappes. These nappes are clearly recognisable on the geological map of the Bergen area (Fig. 13.2a). In the east, the arc is bounded by the extensional Bergen Arc Shear Zone (Wennberg et al. 1998). Previous geological studies demonstrated that the Bergen Arc initially formed during the Caledonian orogeny when different oceanic and continental terranes were amalgamated at the western margin of Baltica palaeocontinent (e.g., Sturt & Thon 1978, Fossen & Dunlap 2005), forming an orogenic wedge over the crystalline rocks of the Precambrian, Baltician crust. During late- or post-Caledonian times, the Bergen region was affected by a major extensional event with localisation of the extensional structures along the Bergen Arc Shear Zone (Boundy et al. 1997). Tectonically, the Bergen Arc represents the hanging-wall of this extensional shear zone (Bingen et al. 2000). Internally, the Bergen Arc System consists of a sequence of Caledonian nappes which overlie the Øygarden Gneiss Complex in the west (Fig. 13.2a). According to rock sample measurements, the Øygarden gneiss complex is characterised by an increased content of radiogenic elements. Values of the radiogenic heat production reach more than 10 $\mu W/m^3$ in places where the Løvstakken granite of the Øygarden complex is present (Fig. 13.2b). According to structural features of the region (Fig. 13.2a), the Løvstakken granite can be traced beneath the Caledonian nappes (Fig. 13.3). Three main Caledonian nappes are recognised. The Lindås Nappe contains mainly anorthosites, gneisses and amphibolites, whereas the Hardangerfjord Nappe is represented by the Gullfjellet Ophiolite Complex where diorites, gabbros and metabasalts dominate. Development of partial eclogitisation within the Lindås Nappe indicates that these rocks were located at great depth near the base of the continental crystalline crust during a Mid Ordovician phase of the Caledonian orogeny at c. 460 Ma (Bingen et al. 2000). The lowest nappe of the Bergen Arc is the Blåmanen Nappe which consists mainly of mylonitised granitic gneisses. Furthermore, some of the nappes also include sedimentary formations. There is thus a clear lithological contrast between the Caledonian nappes and the Løvstakken granite of the Øygarden rock complex that can be used to understand the details of the deep structure within the Bergen region with the help of potential fields and conductive thermal modelling.

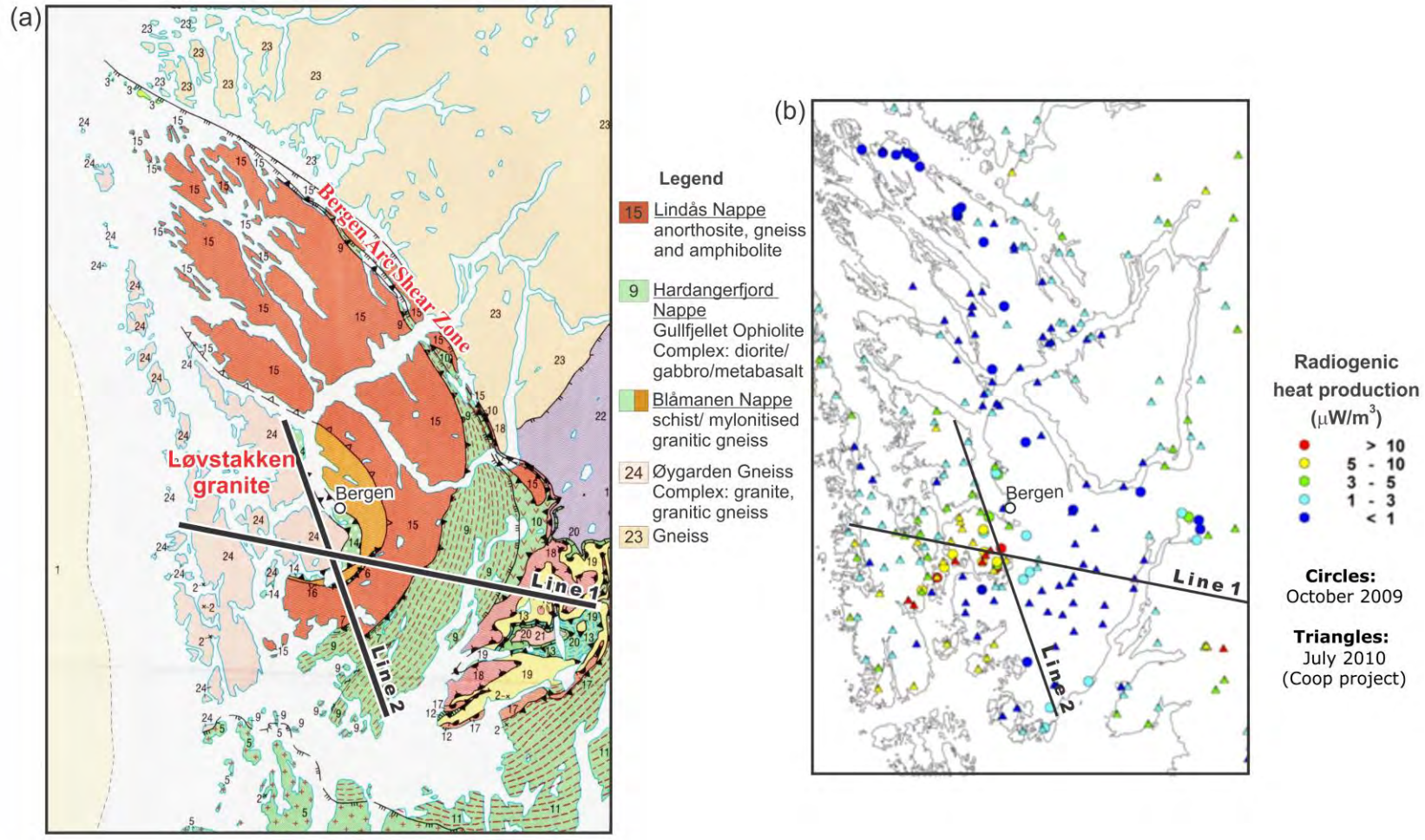

Figure 13.2. (a) Simplified geological map of the Bergen area (after Ragnhildstveit & Helliksen 1997). (b) Location of rock samples with measured values of radiogenic heat production (after Pascal et al. 2011).

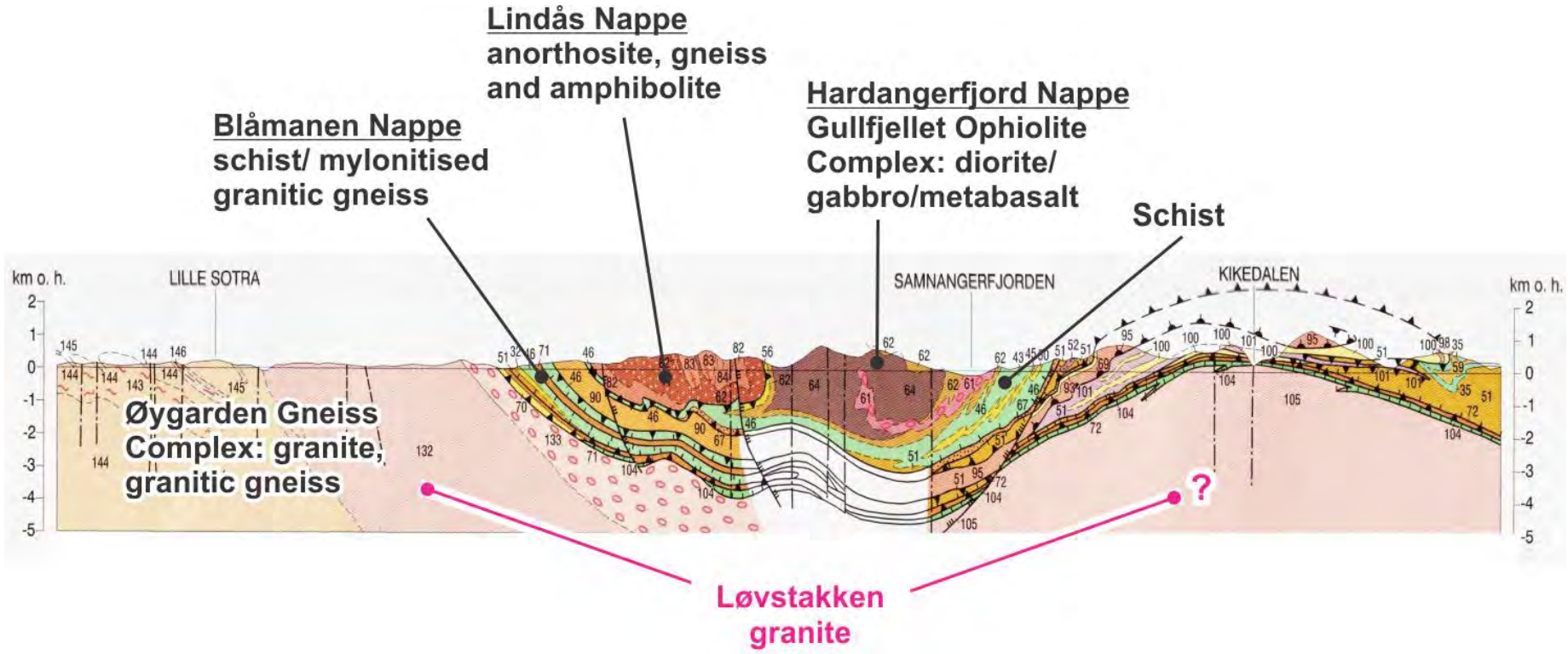

Figure 13.3. Geological cross-section approximately along Line 1 within the Bergen area (after Ragnhildstveit & Helliksen 1997).

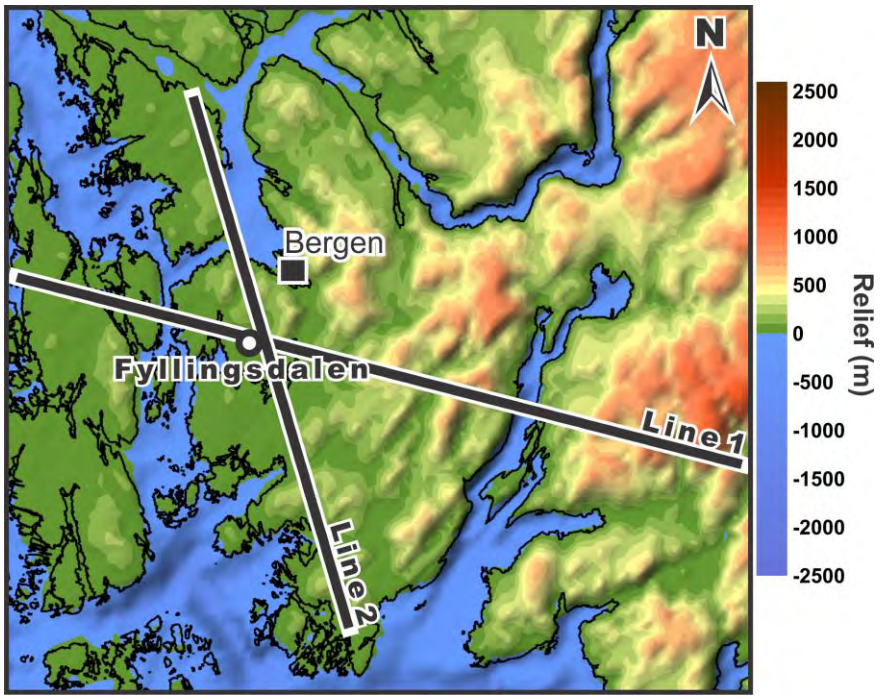

Figure 13.4. Bathymetry and topography within the Bergen area (from the NGU database).

Topographic relief (Fig. 13.4) is present in the form of smoothed landforms in the vicinity of the Fyllingsdalen borehole. In contrast, the eastern part of the Bergen area is characterized by rugged topography which ranges from 500 to 1200 m a. s. l. on average. The bathymetric data show that depths reach down to 700-800 m.

13.2.2 The Stavanger area

The bedrock geology of the Stavanger region is shown in Fig. 13.5. The study area covers the northwestern part of the Sveconorwegian (c. 930 Ma) Rogaland Igneous Province which is recognisable due to a presence of an anorthosite complex (anorthosite and norite rocks) in the south-eastern part of the geological map (Fig. 13.5; Jorde et al. 1995). In general, the Rogaland Igneous Province comprises a wide range of rocks such as norites, anorthosites, granodiorites and granites (see Olesen et al. 2004). The rocks of this anorthosite complex are characterised by a low radiogenic heat production and possibly extend towards the north beneath the crystalline rocks (gneiss, augen gneiss, migmatite, phyllite, biotite-pigeonite granite and granitic gneiss) which occur at the surface. Therefore, the presence of the anorthosite complex with relatively low or normal values of radiogenic heat production implies that the geothermal potential of the Stavanger area has to be lower than that in the Bergen region.

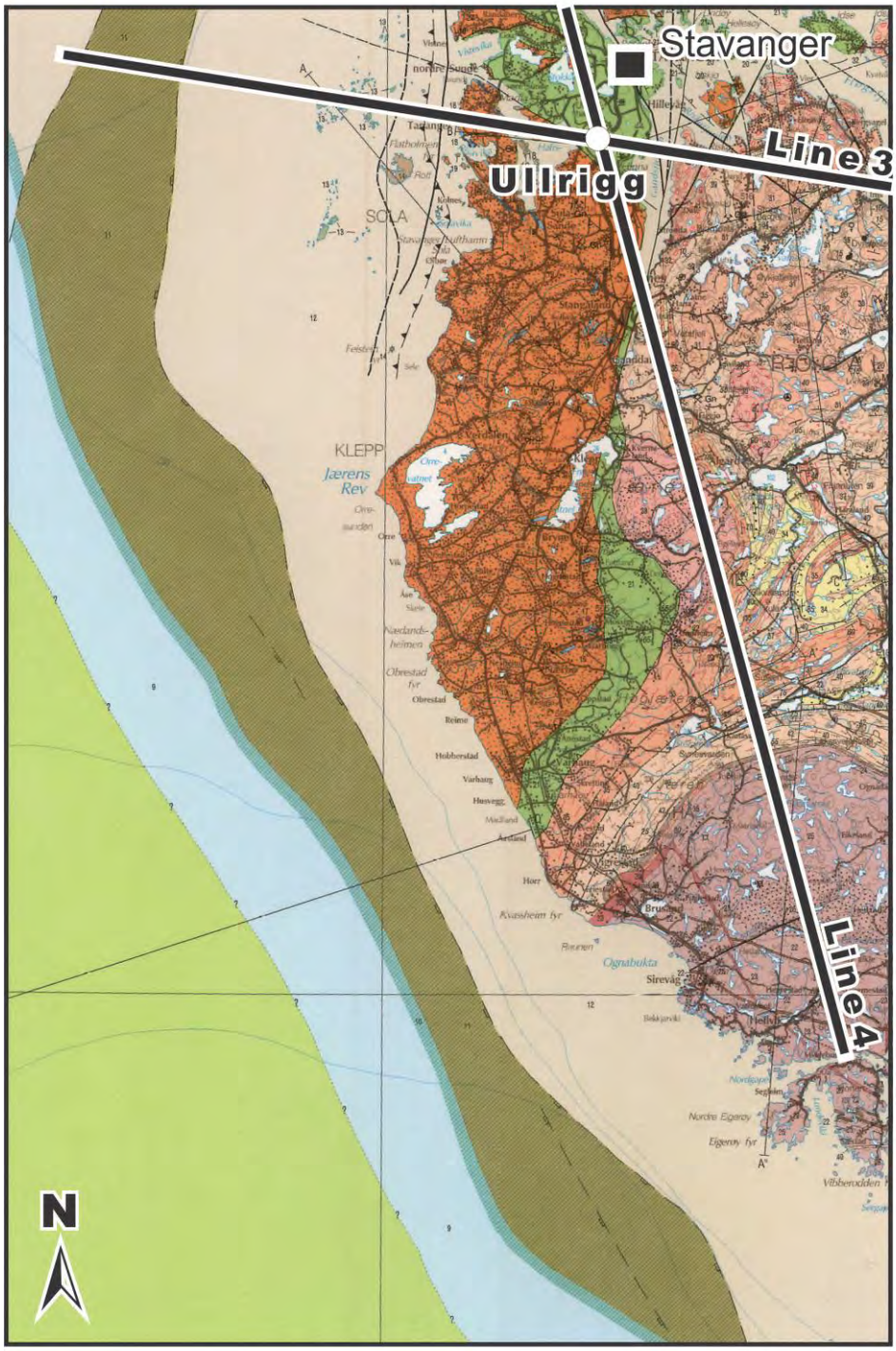

Figure 13.5. Geological map of the Stavanger area (after Jorde et al. 1995).

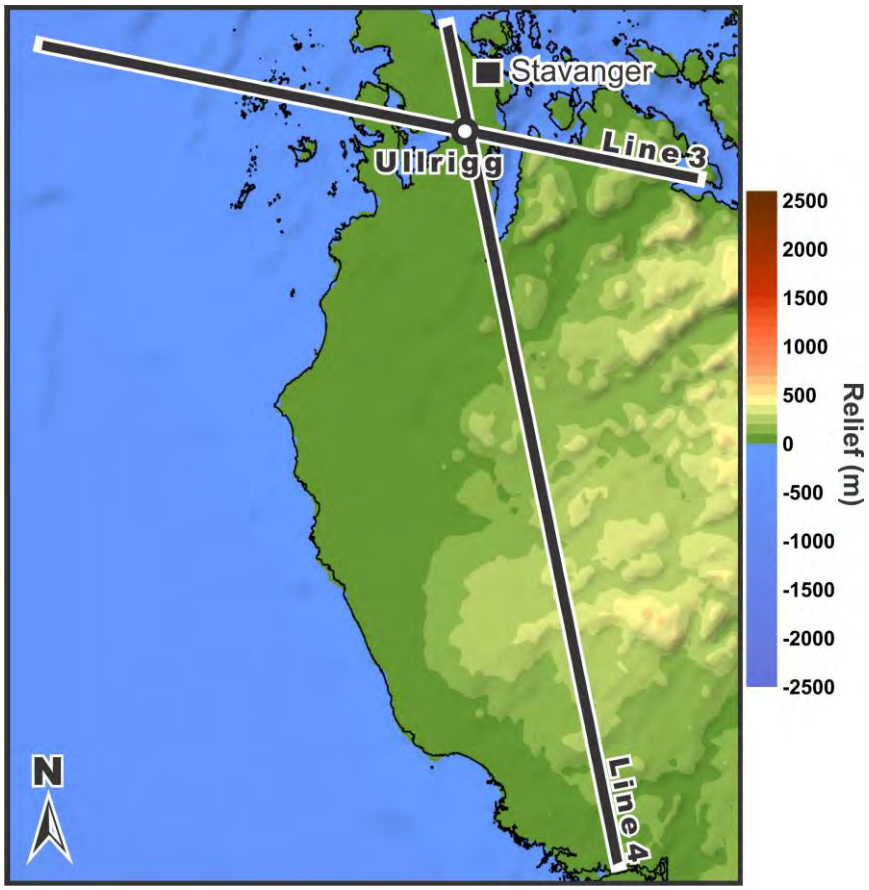

Figure 13.6. Bathymetry and topography within the Stavanger area (from the NGU database).

The topography and bathymetry are comparatively smooth in the vicinity of the Ullrigg borehole (Fig. 13.6). Changes in topography are only notable within the hilly area in the eastern part of the Stavanger peninsula where the relief is 200-400 m above mean sea level.

13.3 Methods

2D density, magnetic and thermal modelling have been applied to reveal the present-day deep structure and thermal state of the crystalline crust within the Bergen and Stavanger areas. 2D gravity and magnetic modelling have been carried out by use of the commercial software package GEOSOFT Oasis montaj, instead of the IGMAS plus software which has been used for the 3D density modelling. During 2D density and magnetic modelling, the GM-SYS Profile Modelling module was used to model the geological structure along four 2D profiles by changing the geometries, densities and magnetic properties of the layers to obtain a fit between the observed potential fields and the modelled gravity and magnetic responses of the 2D models. The advantage of the GM-SYS Profile Modelling relates to an option that a great number of 2D layers/bodies with any polygonal shape can be used to simulate the deep structure of the study areas. Therefore, any geometrical complexity of the geological structure can be accurately represented and tested during the 2D density and magnetic modelling.

Besides, the same geological model can be verified by both 2D gravity and magnetic modelling at the same time. Therefore, GM-SYS Profile Modelling allows us to create complex 2D structural models which are consistent with the observed gravity and magnetic fields.

A 2D temperature distribution has been simulated with the help of the commercial software package COMSOL Multiphysics and, therefore, the theoretical background and methodology are the same as in the case of the 3D thermal modelling that has already been described in Chapter 11 (Maystrenko 2012 this report). The base of the lithosphere has again been chosen as a lower thermal boundary, which corresponds to the 1300 °C isotherm (Turcotte & Schubert 2002). For the upper boundary, annual average air temperatures and time-dependent palaeotemperatures have been applied.

13.4 Datasets and rock properties

13.4.1 Structural data

Geometries of the deep crustal layers (from the Moho to the base of the regional upper crustal layer) and the lithosphere-asthenosphere boundary along the four 2D lines are taken from the 3D structural model of the northern North Sea and adjacent continent (Maystrenko 2012 this report). Therefore, the middle-lower crustal structure and Moho topography are mostly based on the results of forward modelling ray tracing solutions for two deep-refraction seismic lines (Magnus-Rex lines 2 and 3) within southern Norway (cf. Figs. 12.19 & 13.1), published by Stratford et al. (2009). On the other hand, the structure of the upper crust is based on the surface geology (Figs. 13.2 & 13.5) and borehole data. In the case of the Bergen area, results of the interpretation along the geological cross-section in Fig. 13.3 have been taken as the structural model along Line 1. Consequently, the upper crustal structure of Line 2 from the Bergen area is also derived from this geological cross-section (Fig. 13.3). Within the Stavanger area, the upper crustal 2D models along Lines 3 and 4 are based on surface geological data (Fig. 13.5) extrapolated to great depth.

13.4.2 Observed gravity and magnetic fields

The detailed Bouguer gravity anomalies from Rudlang (2011) have been used over the Bergen area (Fig. 13.7). This Bouguer gravity anomaly map has been calculated by use of 71 sampled gravity points measured by NGU during the autumn of 2010 as well as 363 previously measured gravity points taken from the NGU database within the study area. On the other hand, the Bouguer gravity anomalies onshore (Olesen et al. 2010) and the free air

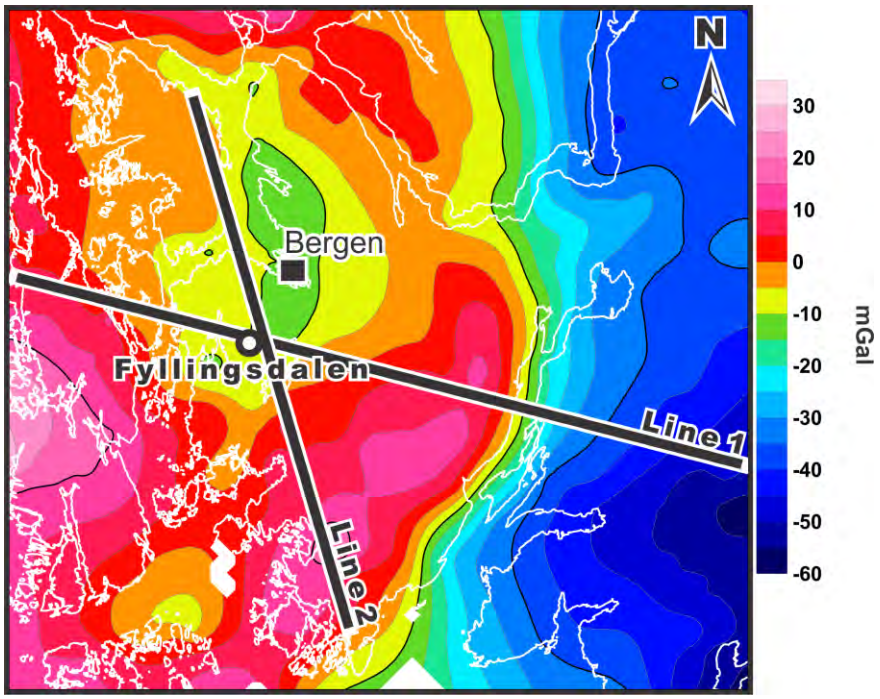

Figure 13.7. Bouguer gravity anomalies (data from Rudlang 2011).

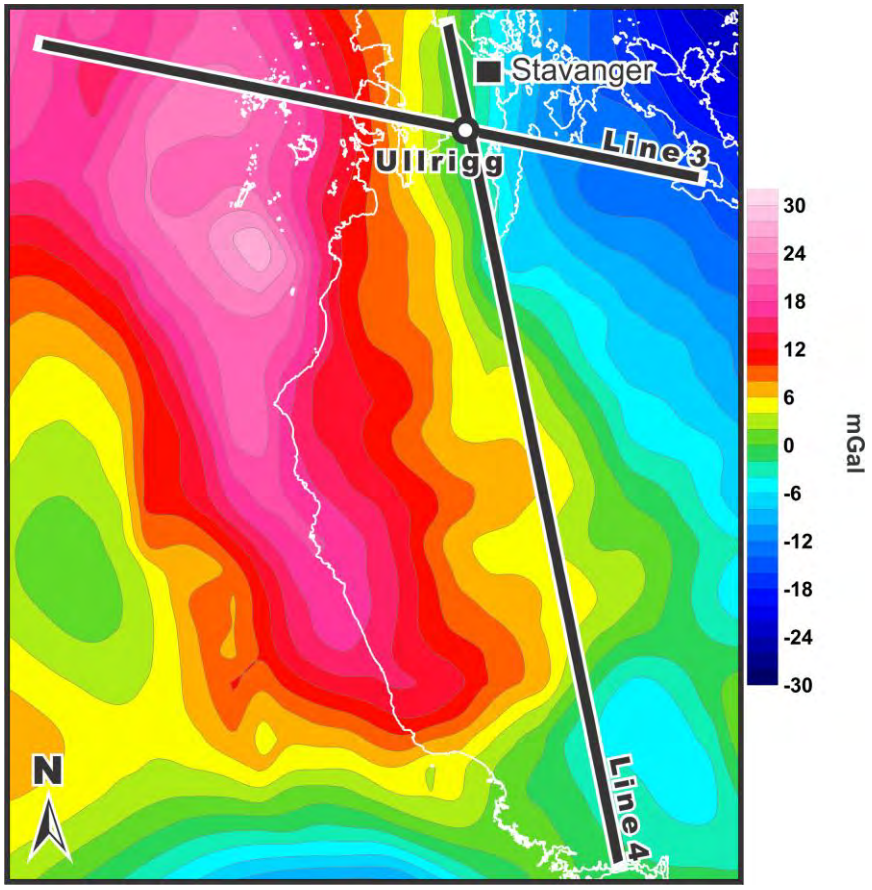

Figure 13.8. Observed gravity anomalies. Gravity data are from the NGU compilation over the continent (Olesen et al. 2010) and the DNSC08GRA global marine gravity field (Andersen et al. 2010).

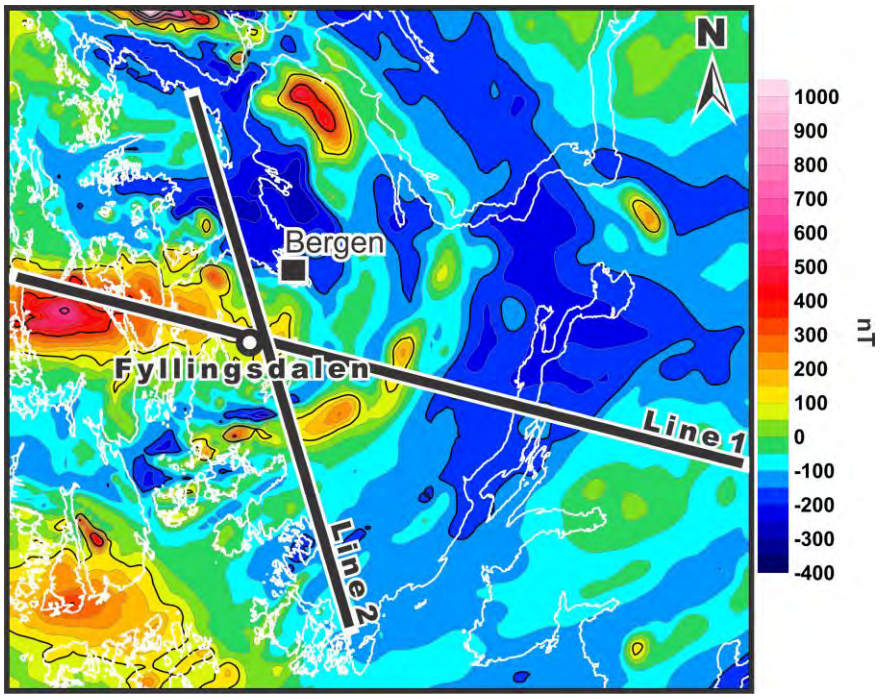

Figure 13.9. Magnetic anomalies (data from Olesen et al. 2010).

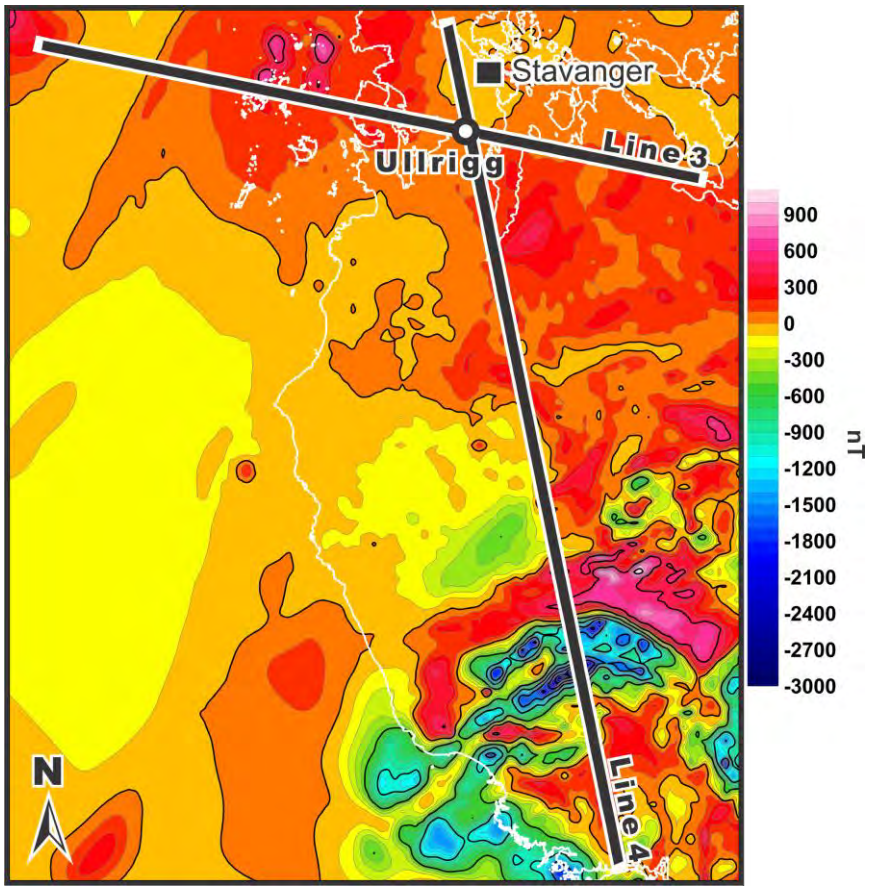

Figure 13.10. Magnetic anomalies (data from Olesen et al. 2010).

gravity anomalies offshore (Andersen et al. 2010) were used for the 2D density modelling within the Stavanger area (Fig. 13.8).

The observed magnetic fields over both the Bergen and the Stavanger areas (Figs. 13.9 & 13.10) have been extracted from the recent magnetic compilation grid over Norwegian territory by Olesen et al. (2010). The total magnetic field is referred to the International Geomagnetic Reference Field (IGRF).

The most prominent feature of the observed gravity and magnetic fields within the Bergen area (Figs. 13.7 & 13.9) corresponds to the presence of a semi-circular, positive gravity anomaly and a series of arcuate magnetic anomalies. These curved anomalies are spatially coincident with the shape of the Caledonian nappes within the Bergen Arc System (cf. Figs. 13.2, 13.7 & 13.9) and they can, therefore, be used to model the geometry of the nappes at depth. The observed gravity field over the Stavanger area is characterised by a NW-SE-trending positive anomaly along the western coastline of the Stavanger peninsula (Fig. 13.8). Values of the observed magnetic anomalies are up to -3000 nT within the southern part of the Stavanger area where there is a strong influence from the remanence within the anorthosite complex.

13.4.3 Densities, magnetic and thermal properties

Final values of the density, magnetic susceptibility, thermal conductivity and radiogenic heat production are shown in Table 13.1 for the Bergen area and in Table 13.2 for the Stavanger area. Densities and thermal properties (thermal conductivity and radiogenic heat production) for the middle-lower crystalline crust and the upper mantle of these areas have been taken from the results of regional-scale 3D density and thermal modelling (Tables 12.1 and 12.2), presented in Chapter 11 (Maystrenko 2012 this report). Values of densities and thermal properties within the middle crystalline crust have been slightly modified to take into account the local conditions within the particular area. Furthermore, the upper crustal densities, magnetic susceptibilities, thermal conductivities and radiogenic heat production (Tables 13.1 and 13.2) are mostly derived from the NGU petrophysical electronic database, called Petro. The average constant values for each layer have been assigned according to the location of the sampling points. When information about the required property is absent within the NGU database, the literature values have been used. In particular, thermal properties have been derived by use of laboratory measurements of rocks with similar lithology from other localities of the world (Cermak & Rybach 1982, Slagstad et al. 2009, Clauser 2011). Magnetic susceptibilities of the middle-lower crystalline crust are adopted from the previously published estimations (e.g., Fichler et al. 2011, Ebbing 2012 this report). Finally, magnetic remanence intensity (0-13 A/m), declination (295^{o}) and inclination (60^{o}) of the anorthosite complex (anorthosite/norite) are based on values for similar rocks within the Rogaland Igneous Province published by Olesen et al. (2004).

Table 13.1 **Final densities, magnetic susceptibilities and thermal properties of the layers within the Bergen area used during the 2D density, magnetic and thermal modelling.**

No	Layer of the 3D structural model	Density ρ [kg/m^3]	Magnetic susceptibility χ_m [SI]	Specific heat capacity C_p [J/kgK]	Thermal conductivity k [W/mK]	Radiogenic heat production S [μW/m^3]
1	Gneiss, amphibolite	2800	0.0011-0.012	880	3.10	1.5
2	Diorite,	3030	0.0005	880	3.20	0.3
3	Schist	2773	0.0004-0.005	880	2.80	2.7
4	Schist, mylonised granitic gneiss	2774	0.0003	880	2.80	1
5	Gneiss	2640	0.012-0.03	880	3.03	1.5
6	Løvstakken granite: upper granite/granitic gneiss	2620	0.0005-0.02	880	3.00	4.5
7	Lower granite, granitic gneiss	2710	0.022-0.052	910	3.00	1.6
8	Middle crystalline crust	2743	0.002-0.041	950	2.70	0.8
9	Lower crystalline crust	2856	0.01	1050	2.60	0.3
10	High-density lower crustal layer	3056	0.006	1100	2.30	0.2
11	Lithospheric upper	3222		1200	3.95	0.03

Table 13.2 Final densities, magnetic susceptibilities and thermal properties of the layers within the Stavanger area used during the 2D density, magnetic and thermal modelling.

No	Layer of the 3D structural model	Density ρ [kg/m^3]	Magnetic susceptibility χ_m [SI]	Specific heat capacity C_p [J/kgK]	Thermal conductivity k [W/mK]	Radiogenic heat production S [μW/m^3]
1	Pre-Permian sediments	2600	0.0011-0.012	1180	2.40	1
2	Biotite-pigeonite granite	2640	0.009-0.029	880	3.00	2.0
3	Charnockite series	2670	0.039-0.059	880	3.10	2.0
4	Plutonic rocks, gabbro	2820	0.015-0.032	880	2.80	0.7
5	Gneiss, augen gneiss, migmatite	2610-2627	0.002-0.038	880	2.90	1.5
6	Phyllite	2810	0.0003	880	2.70	2.0
7	Anorthosite/norite	2840	0.003-0.018	880	2.70	0.3
8	Upper granite/granitic gneiss	2620-2640	0.001-0.020	880	2.90	1.2
9	Lower granite/granitic gneiss	2710-2730	0.0001-0.048	910	2.85	1.0
10	Middle crystalline crust	2744	0.002-0.006	950	2.60	0.7
11	Lower crystalline crust	2856	0.023	1050	2.60	0.3
12	High-density lower crustal layer	3057	0.006	1100	2.30	0.2
13	Lithospheric upper mantle	3222		1200	3.95	0.03

13.5 Results of 2D density and magnetic modelling

13.5.1 The Bergen area

The Fyllingsdalen borehole is located near the intersection point of two modelled lines (Fig. 13.4). According to the drillcore information acquired fromthis borehole, the highly radioactive Løvstakken granite is more than 516 m thick at the place where this layer is cropping out at the surface (Figs. 13.11 & 13.12). 2D density and magnetic modelling were applied to trace the Løvstakken granite at depth within the Bergen area.

Results of the 2D density modelling demonstrate that the semi-circle shaped Lindås Nappe (anorthosites, gneisses and amphibolites) and the Hardangerfjord Nappe (the Gullfjellet Ophiolite Complex: diorites, gabbros and metabasalts) are characterised by high densities (2800 and 3030 kg/m^3, respectively) and that these bodies are represented within the uppermost upper crustal level (Figs. 13.11 & 13.12). It is clear that these two, upper crustal, high-density bodies (the Lindås and Hardangerfjord nappes) create a density contrast which is mostly responsible for the wide positive gravity anomaly over the Bergen area (Fig. 13.7). An approximately 1 km-thick layer of schists underlies the Lindås and Hardangerfjord nappes. The base of the schists is located at a depth that varies from 4800 to 5400 m within the deepest parts along Lines 1 and 2. This uppermost, upper crustal configuration allows us to model the Løvstakken granite (upper granite/granitic gneiss in Figs. 13.11 & 13.12) beneath the Caledonian nappes. The maximum thickness of this granite reaches more than 9 km in the eastern part of Line 1. This relatively low-density (2620 kg/m^3), upper granitic layer is underlain by a more dense (2710 kg/m^3) granitic/granitoid layer. The base of the granitic/granitoid layer has a slightly wavy shape. In contrast, layers of the middle-lower crust are subhorizontal, reflecting the subhorizontal velocity structure along the Magnus-Rex deep-refraction, seismic lines (Stratford et al. 2009), which are located near the Bergen area (Fig. 12.19). In particular, the Moho is almost horizontal along N-S-trending Line 2 and is located at a depth of 30-31 km. On the other hand, the Moho is dipping gently towards the east along the E-W-trending Line 1.

In order to fit the observed and modelled magnetic anomalies, the density-based structure of the upper-middle crystalline crust must include several blocks with different magnetic susceptibilities. This complicated structure of the upper crust is modelled within the central and western parts of Line 1 and within the central part of Line 2. There, observed short-wavelength magnetic anomalies imply the presence of upper crustal blocks with varying values of magnetic susceptibility. Consequently, the modelled layer of the Løvstakken granite has also been subdivided into several blocks during the magnetic modelling. The latter indicates that the lithological composition of this upper granitic layer can vary and, therefore, the additional constraints are required to remove these types of uncertainty. The 2D conductive thermal modelling was the third method which has been used to test the possible configuration of the relatively high-radiogenic Løvstakken granite, and the results of the 2D gravity and magnetic modelling have been used as a structural base during the thermal simulations.

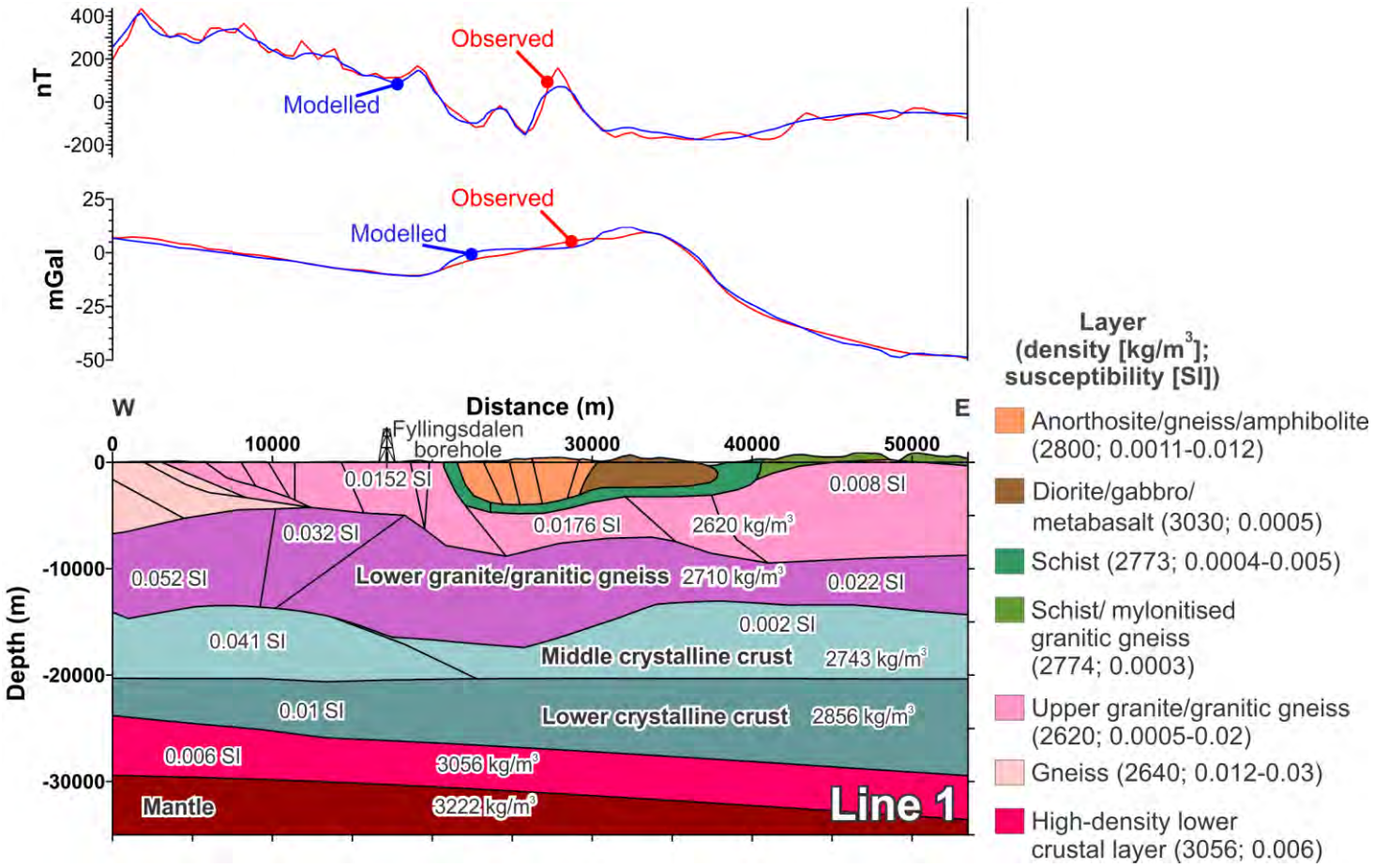

Figure 13.11 Results of the 2D gravity and magnetic modelling along Line 1 within the Bergen area (modified after Rudlang 2011).

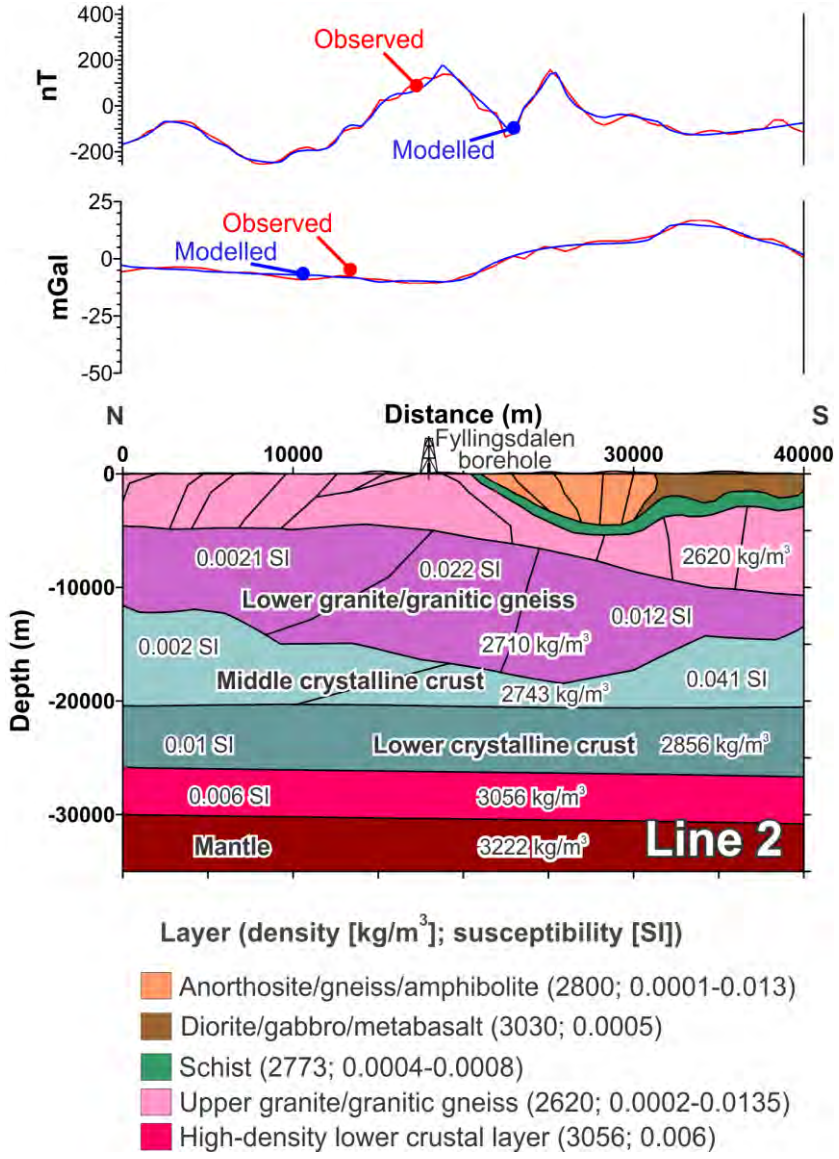

Figure 13.12. Results of the 2D gravity and magnetic modelling along Line 2 within the Bergen area.

13.5.2 The Stavanger area

According to the results of 2D density modelling along Lines 3 and 4, the upper crystalline crust is characterized by the presence of the anorthosite complex (anorthosites and norites) beneath the gneisses and granitic rocks (Figs. 13.13 & 13.14). In addition, the high-density plutonic rocks are modelled near the surface over the gneisses along Line 3. The prominent positive gravity anomaly over the western part of Line 3 is associated with these high-density

plutonic rocks, which has resulted in a strong density contrast within the less dense upper crust. On the other hand, the low-amplitude, positive gravity anomaly over the central part of Line 4 is partially controlled by the density contrast along the upper-middle crustal boundary, which is slightly uplifted within the central part of the line (Fig. 13.14). In addition, the presence of high-density anorthosites and norites beneath the granitic layers is also necessary to fit the observed and modelled gravity within this part of the line.

The Ullrigg borehole is located within the area where the phyllites are exposed at the surface and the modelled upper crustal layer is relatively thin. The total thickness of the phyllite and granitic layer is only around 8000 m near the location of the Ullrigg borehole. On the other hand, the thickest upper crustal layer is modelled within the southern part of Line 4 where the anorthosite complex is underlain by an almost 15 km thick granitic layer. The modelled thickness of the drilled phyllites is in the range of 900-1800 m along both lines. As in the case of the Bergen area, the modelled layers of the middle-lower crust are almost horizontal with a notable dipping of the lower crustal boundaries towards the east along Line 3. There, the Moho dips from a depth of 27-28 km in the west to more than 32 km in the east, reflecting the regional gradient of the Moho depth change from the Meso-Cenozoic basin areas within the North Sea towards the central part of Precambrian Baltica (e.g., Ziegler & Dèzes 2006, Tesauro et al. 2008, Grad et al. 2009, Ebbing & Olesen 2010)

The results of the 2D magnetic modelling show that the distribution of magnetic susceptibilities complicates the structure of the upper crust. Besides, a relatively high intensity of remanence (remanent magnetisation) is required to model the high-amplitude negative magnetic anomalies over the southern part of Line 4 (Fig. 13.14).

The resulting crustal models in Figures 13.13 and 13.14 were used during the thermal modelling to understand the regularities in temperature distribution within the Stavanger area.

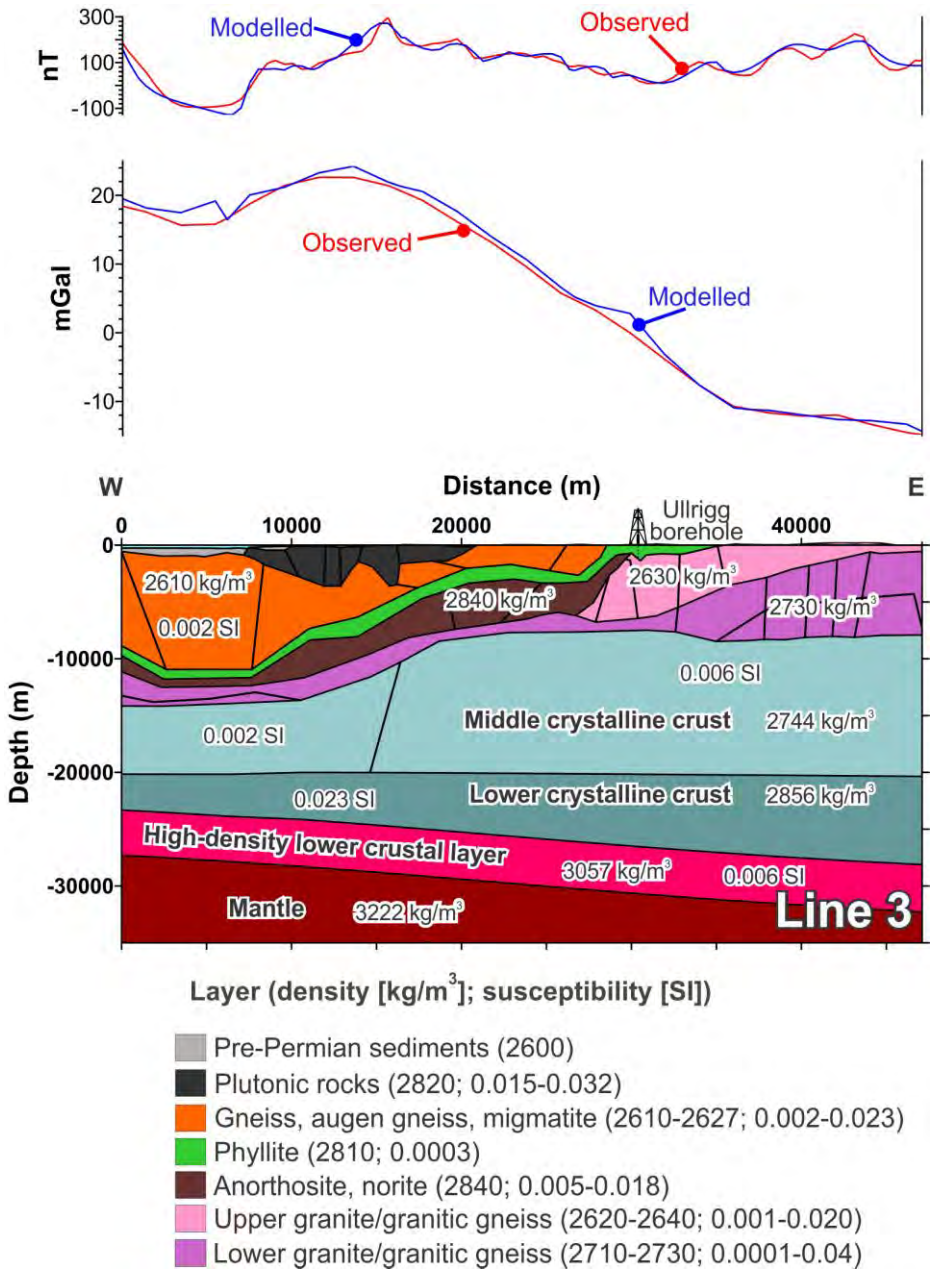

Figure 13.13. Results of the 2D gravity and magnetic modelling along Line 3 within the Stavanger area.

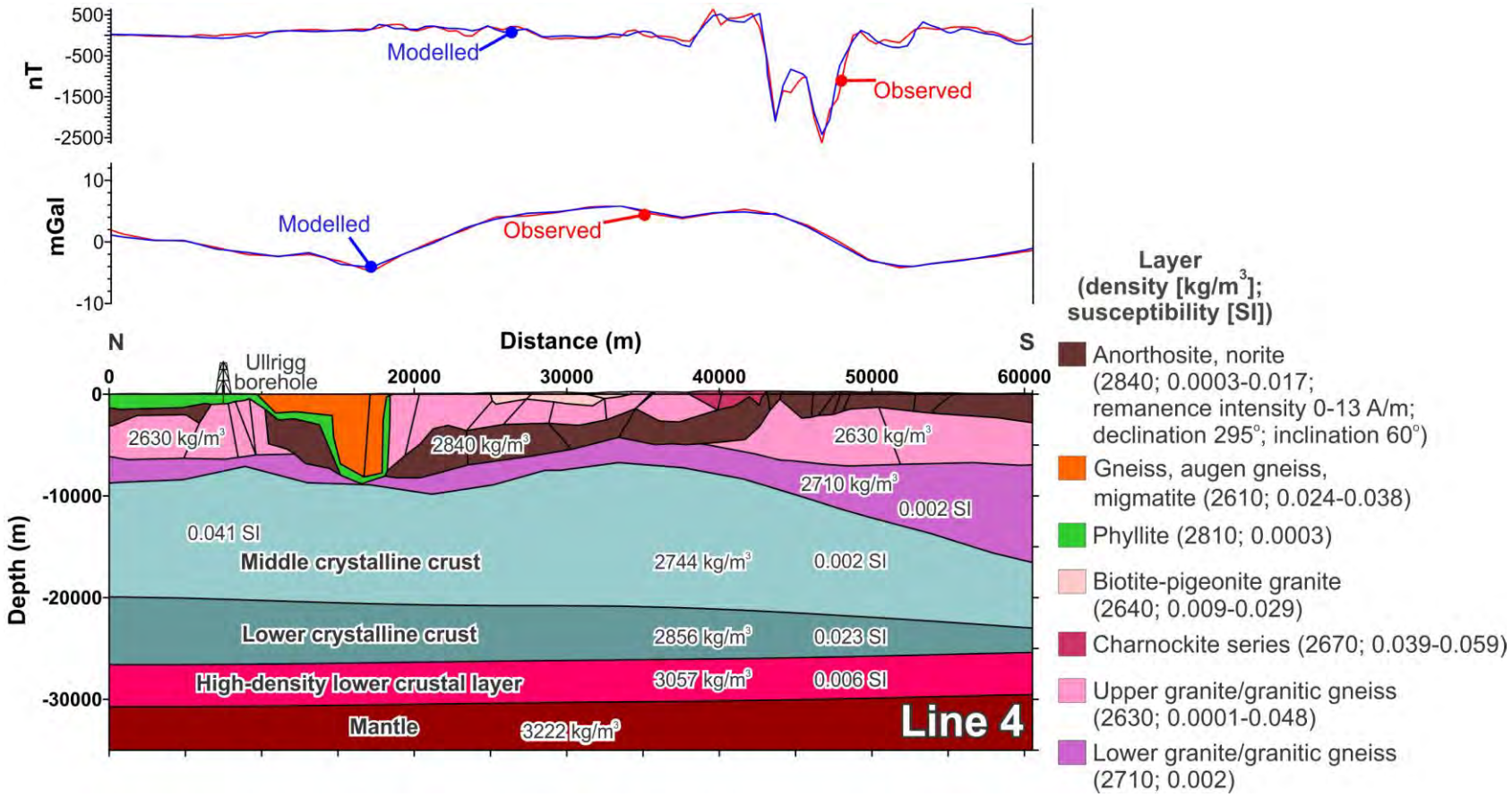

Figure 13.14. Results of the 2D gravity and magnetic modelling along Line 4 within the Stavanger area.

13.6 2D thermal modelling

The next step in the detailed studies within the Bergen and Stavanger areas involved 2D thermal simulations, which have been carried out to reveal the thermal state of the subsurface. Four profiles (Figs. 13.11-13.14), consistent with gravity and magnetics, have been used as a structural skeleton during the 2D thermal modelling. Several testing models have been generated and validated during the 2D thermal modelling to obtain a fit between the modelled and the measured temperatures in two available boreholes. Therefore, the modelling procedure was divided into several steps which are presented below.

13.6.1 Initial thermal models

The starting point of the 2D thermal modelling was an initial thermal model that has been calculated by using the thermal properties in Tables 13.3 and 13.4 for the Bergen and Stavanger areas, respectively.

The relatively high value (4.5 $\mu W/m^3$) of radiogenic heat production has been assigned to the entire upper granite/granitic gneiss layer, believed to represent the distribution of the Løvstakken granite. This value represents an average value of radiogenic heat production from the Løvstakken granite within the Bergen area (Fig. 13.2b), reflecting the high content of radiogenic elements in these rocks (Rudlang 2011). On the other hand, the highest value of radiogenic heat production, 2.4 $\mu W/m^3$, attained within the relatively thin phyllite of the Stavanger area. The rest of the upper crustal rocks in both key areas are characterised by a radiogenic heat production which is not more than 2 $\mu W/m^3$.

The initial thermal models have been calculated assuming steady-state conditions. Therefore, annual average air temperatures during 1961-1990 (Tveito et al. 2000) near the locations of each borehole have been used for the upper thermal boundary at the Earth's surface (Figs. 13.4 & 13.6). In particular, a constant temperature of 6.5 °C and 7 °C has been applied during the 2D thermal calculations at the surface within the Bergen and Stavanger areas, respectively. The base of the lithosphere has been taken as a lower thermal boundary with temperature of 1300 °C.

The calculated distribution of temperatures along Lines 1 and 2 within the Bergen area is shown in Fig. 13.15, and modelled temperatures along Lines 3 and 4 within the Stavanger area are shown in Fig. 13.16. The presence of the layer with an increased radiogenic heat production within the Bergen area is clearly reflected in the modelled temperature distribution, which is characterised by an uplift of isotherms within the upper parts of Lines 1 and 2 towards the areas where the Løvstakken granite is thickest (Fig. 13.15). In contrast, the modelled isotherms are almost horizontal within the Stavanger area (Fig. 13.16) where the assigned radiogenic heat production is not as variable as in the Bergen area (cf. Tables 13.3 and 13.4).

Table 13.3 Initial thermal properties of the layers used during the 2D thermal modelling within the Bergen area.

No	Layer of the 3D structural model	Specific heat capacity C_p [J/kgK]	Thermal conductivity k [W/mK]	Radiogenic heat production S [$\mu W/m^3$]
1	Gneiss, amphibolite	880	3.10	1.5
2	Diorite, gabbro/metabasalt	880	3.20	0.3
3	Schist	880	2.80	2.7
4	Schist, mylonised granitic gneiss	880	2.80	1
5	Gneiss	880	3.03	1.5
6	Løvstakken granite: upper granite/granitic gneiss	880	3.00	4.5
7	Lower granite, granitic gneiss	910	3.00	2.0
8	Middle crystalline crust	950	2.70	0.8
9	Lower crystalline crust	1050	2.60	0.3
10	High-density lower crustal layer	1100	2.30	0.2
11	Lithospheric upper mantle	1200	3.95	0.03

Table 13.4 Initial thermal properties of the layers used during the 2D thermal modelling within the Stavanger area.

No	Layer of the 3D structural model	Specific heat capacity C_p [J/kgK]	Thermal conductivity k [W/mK]	Radiogenic heat production S [$\mu W/m^3$]
1	Pre-Permian sediments	1180	2.40	1
2	Biotite-pigeonite granite	880	3.00	2.0
3	Charnockite series	880	3.10	2.0
4	Plutonic rocks, gabbro	880	2.80	0.7
5	Gneiss, augen gneiss, migmatite	880	2.90	2.0
6	Phyllite	880	2.60	2.4
7	Anorthosite/norite	880	2.70	0.3
8	Upper granite/granitic gneiss	880	3.00	1.7
9	Lower granite/granitic gneiss	910	2.90	1.4
10	Middle crystalline crust	950	2.70	0.8
11	Lower crystalline crust	1050	2.60	0.3
12	High-density lower crustal layer	1100	2.30	0.2
13	Lithospheric upper mantle	1200	3.95	0.03

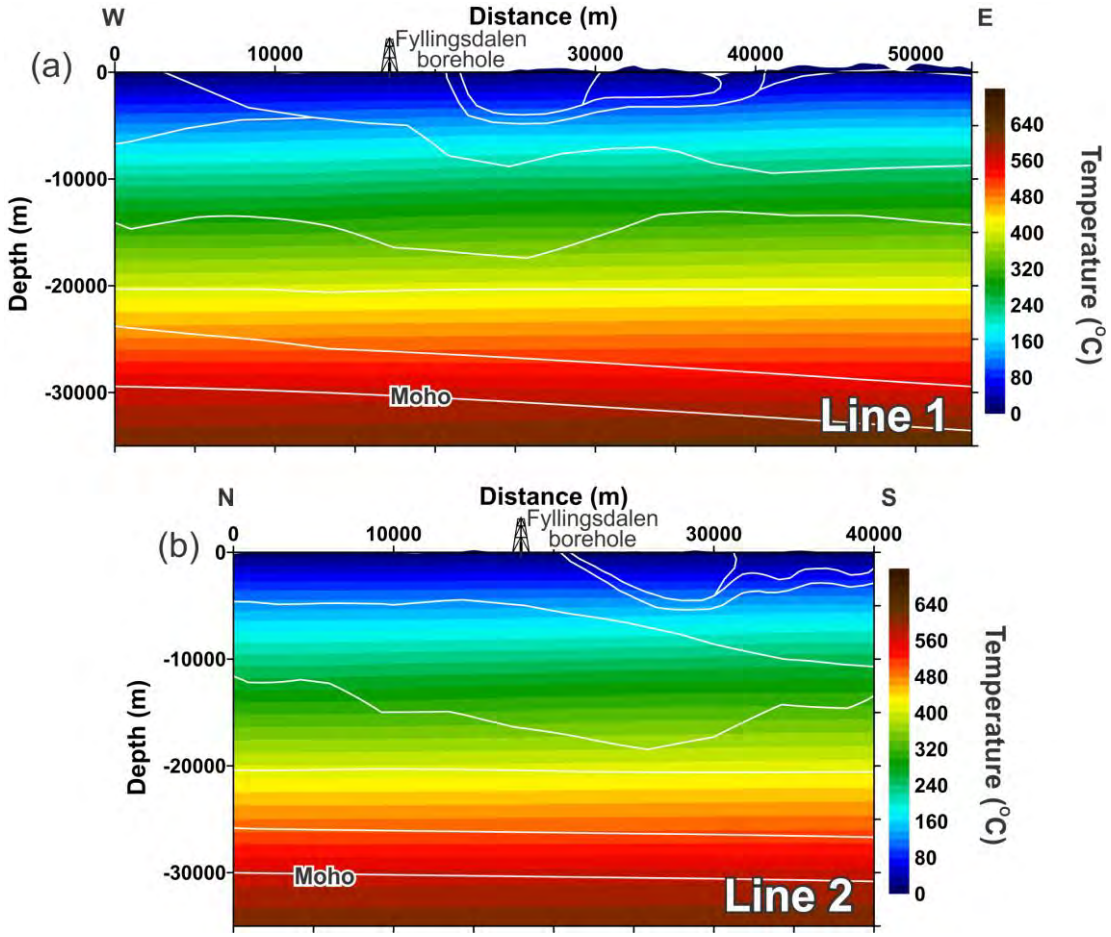

Figure 13.15. 2D thermal models derived by use of the initial thermal properties in Table 13.3. Modelled temperature distribution along Line 1 (a) and Line 2 (b) within the Bergen area.

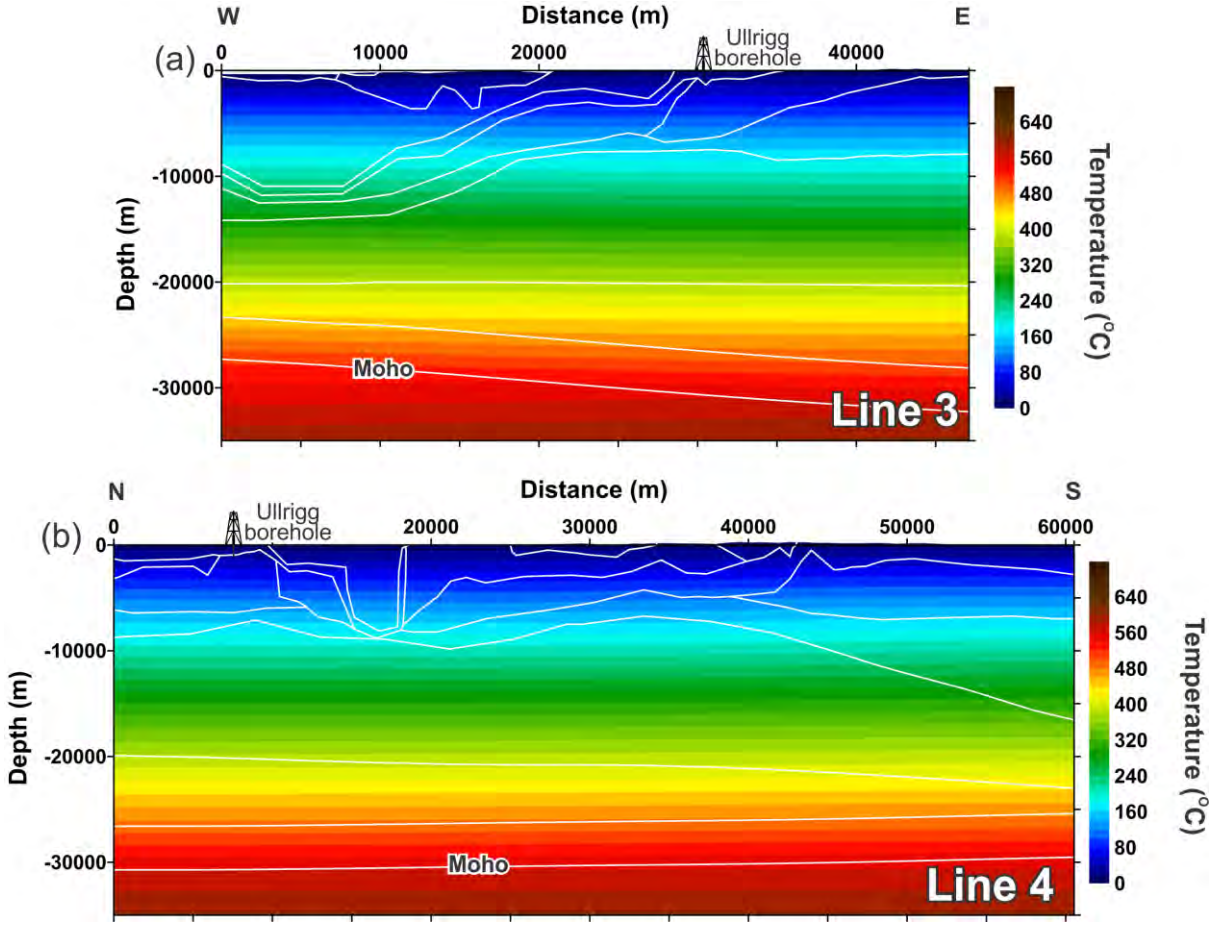

Figure 13.16. 2D thermal models derived by use of the initial thermal properties in Table 13.4. Modelled temperature distribution along Line 3 (a) and Line 4 (b) within the Stavanger area.

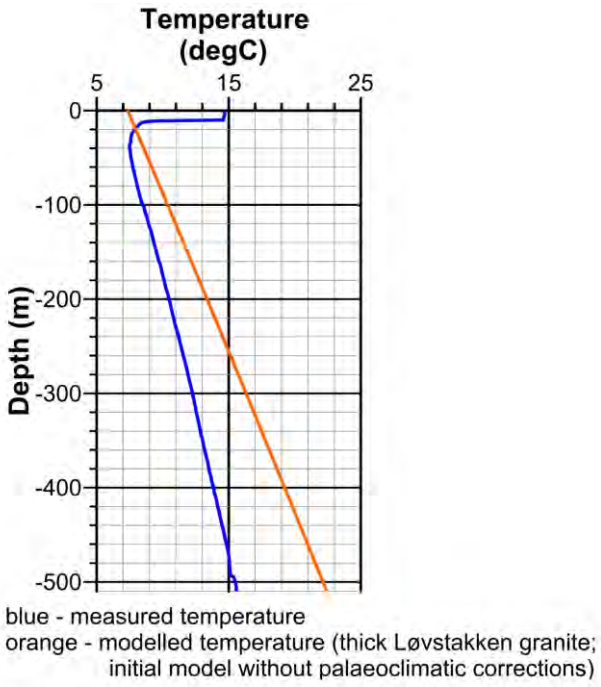

Figure 13.17. The Fyllingsdalen borehole; measured versus modelled temperatures. Modelled temperatures (orange line) are according to the initial values of thermal properties given in Table 13.3.

Comparison with the observed temperature provides the best way to validate the results of the simulations and to find out what has possibly gone wrong in the models. Consequently, the modelled temperatures have been compared with the temperature-depth profiles measured in the Fyllingsdalen and Ullrigg boreholes (Elvebakk & Storrø 2012 this report). The results of the comparison are shown in Figures 13.17 and 13.18. Unfortunately, there are large misfits between the modelled data and the results of the temperature-depth plots. These misfits are more than 7 °C at a depth of 500 m in the case of the Fyllingsdalen borehole, and attain c. 12 °C at a depth of 1000 m in the Ullrigg borehole. Therefore, there is something wrong in both models. It has to be mentioned that the prominent misfits within the uppermost 10-50 m of both boreholes are caused by the seasonal changes of present-day surface temperatures.

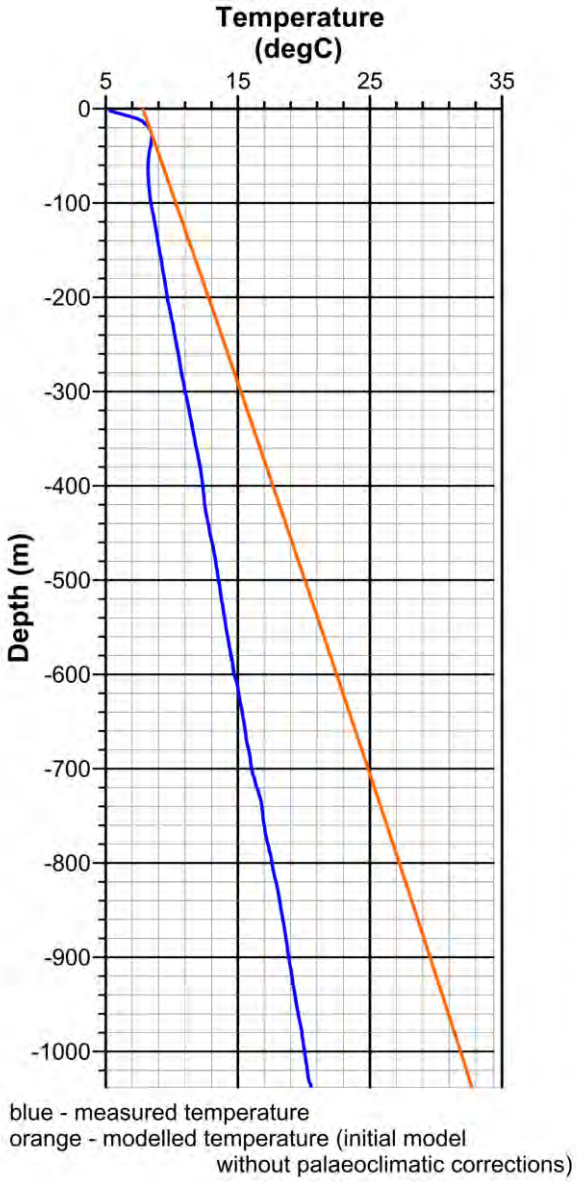

Figure 13.18. The Ullrigg borehole; measured versus modelled temperatures. Modelled temperatures (orange line) are according to the initial values of thermal properties given in Table 13.4.

13.6.2 Reduced basal heat flux at the Moho

One of the easiest solutions to remove the misfits involves a decrease of the deep heat flux. In order to test this hypothesis, several models with a reduced heat flux at the Moho have been evaluated. In the case of the initial model, the heat flux at the Moho is not constant and varies in the range of 30-40 mW/m^2, mostly depending on the thickness of the lithospheric mantle with constant average thermal conductivity. The latter is due to the fact that the lower thermal boundary of the initial model corresponds to a constant temperature (1300 ^{o}C) at the lithosphere-asthenosphere boundary. Therefore, values of heat flux less than 30 mW/m^2 at the Moho have been regarded as the lower thermal boundary instead of the constant temperature at the base of the lithosphere. According to the result of thermal simulations recorded during this step, the best-fit values of the examined 2D models do not allow the heat flux to be higher than 15 mW/m^2 heat flux at the Moho beneath the Bergen and Stavanger regions. The modelled temperatures for the reduced basal heat flux of 15 mW/m^2 at the Moho are shown in Figures 13.19 and 13.20.

Since thermal properties (Tables 13.3 & 13.4) were not modified during this stage of the 2D thermal modelling, the modelled isotherm patterns are very similar to the results which have been obtained in the case of the initial models (cf. Figs. 13.15, 13.16 & 13.19, 13.20). However, the modelled values of temperature with reduced basal heat flux are much lower than those in the initial models. The result of the comparison between the measured temperatures and the calculated temperatures with reduced heat flux demonstrates their general coincidence (Figs. 13.21 & 13.22). The difference is in the range of 2-2.2 ^{o}C.

From theoretical point of view, it is problematic, however, to have values equal to or less than 15 mW/m^2 for the heat flux at the Moho beneath the Bergen and Stavanger regions. According to Fourier's law of heat conduction, the heat flux [W/m2] is defined as (13.1):

$$q = - k\nabla T \qquad (13.1)$$

where k is the thermal conductivity [W/mK] and ∇T is the temperature gradient [K/m].
Therefore, to have low values of heat flux, the thermal gradient and/or the thermal conductivity have to be decreased. The thermal gradient within the lithospheric mantle is predominantly controlled by the position at depth of the lower thermal boundary at the base of the lithosphere which is located at depth of 105-110 km (Fig. 12.35b) beneath these two key regions. In order to have low values of the thermal gradient, the position of the lithosphere-asthenosphere boundary therefore has to be much deeper than 110 km. However, a much deeper base of the lithosphere within these areas is not in agreement with the seismically derived base of the lithosphere reported by Calcagnile et al. (1997) and Geissler et al. (2010), nor with the results of integrated studies by Artemieva et al. (2006) and Maystrenko & Scheck-Wenderoth (2011). Furthermore, Fig. 13.23 shows theoretical estimates of the thermal conductivities plotted versus depth (Hofmeister 1999). The thermal conductivity decreases rapidly in the upper mantle and has a value of less than 2 W/mK under normal upper mantle pressure-temperature conditions. In addition, the thermal conductivity is most likely to

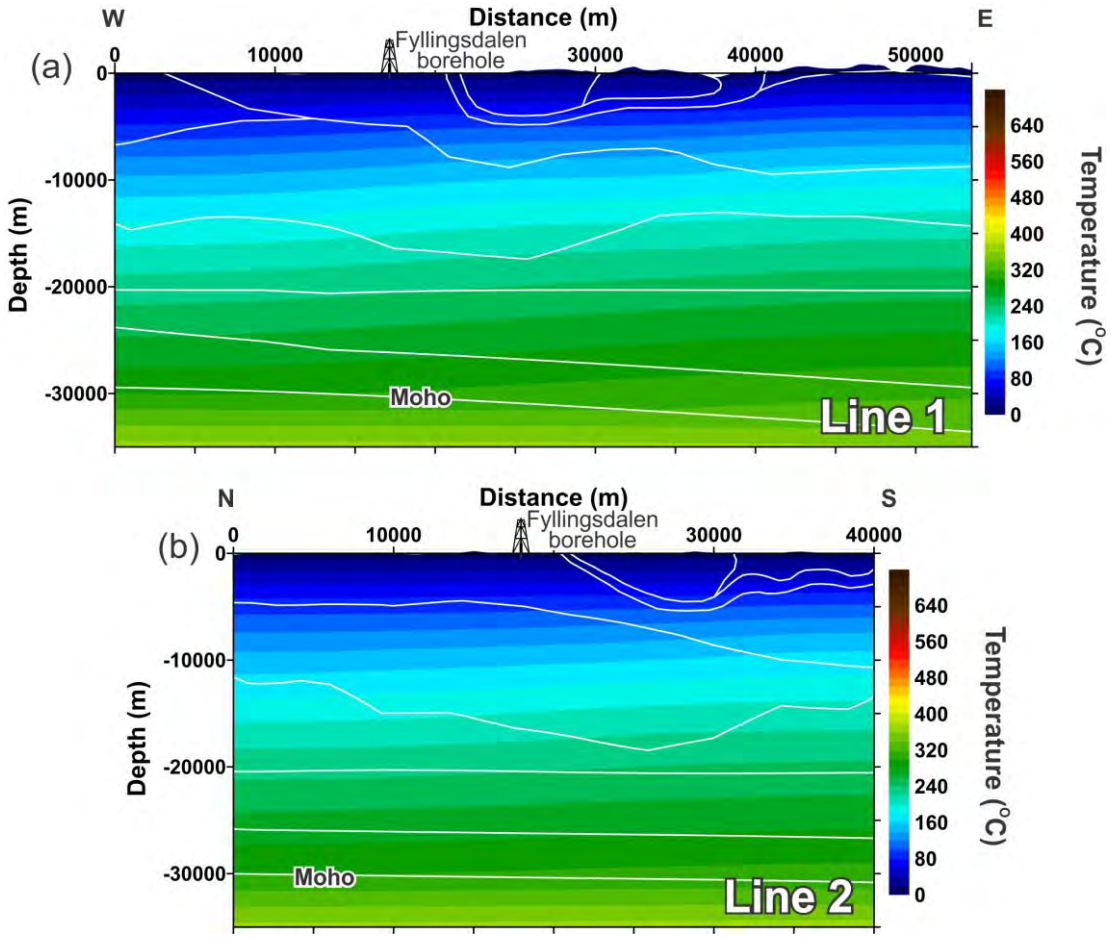

Figure 13.19. 2D thermal models derived by using the initial thermal properties in Table 13.3 and a reduced heat flux (15mW/m2) at the Moho. Modelled temperature distribution along Line 1 (a) and Line 2 (b) within the Bergen area.

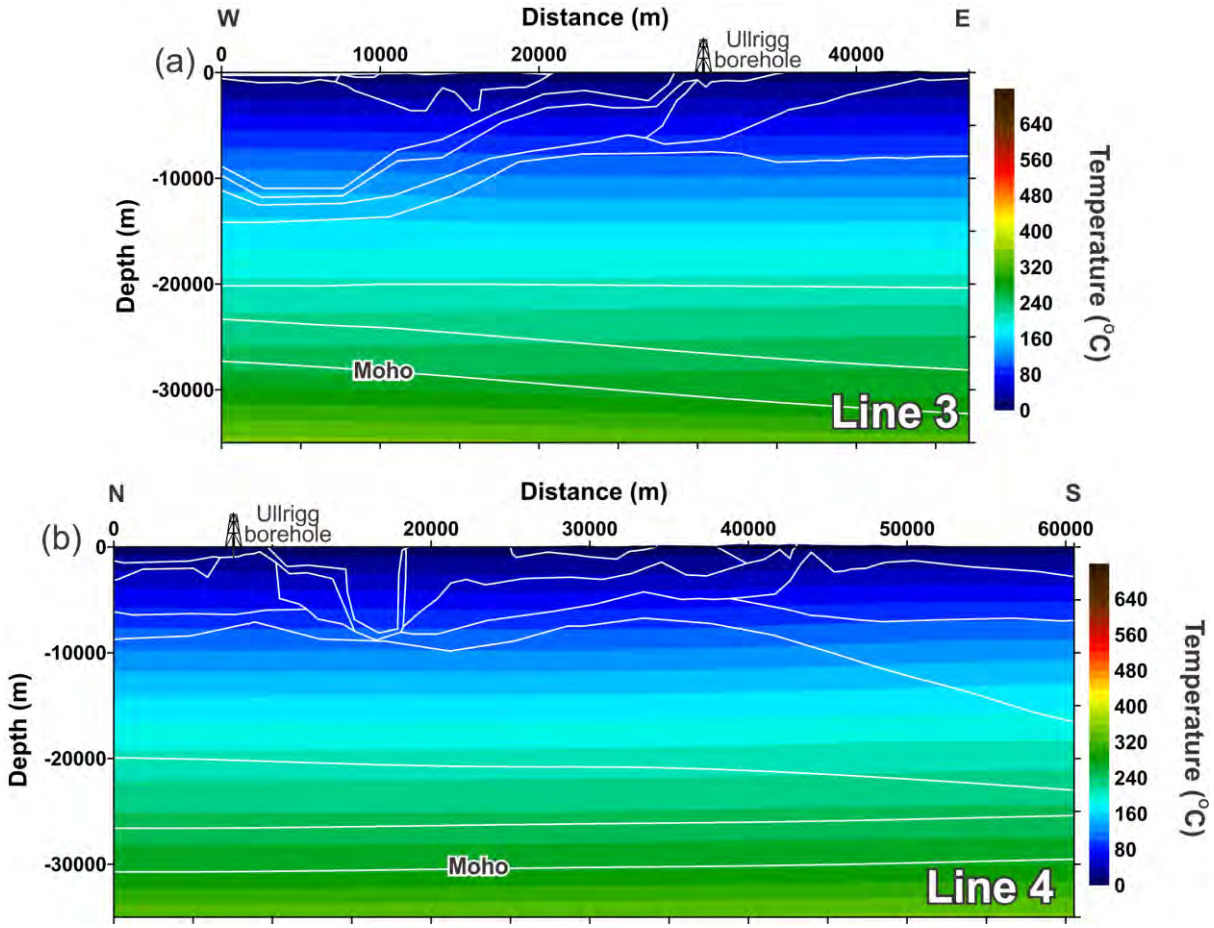

Figure 13.20. 2D thermal models derived by using the initial thermal properties in Table 13.4 and a reduced heat flux (15mW/m2) at the Moho. Modelled temperature distribution along Line 3 (a) and Line 4 (b) within the Stavanger area.

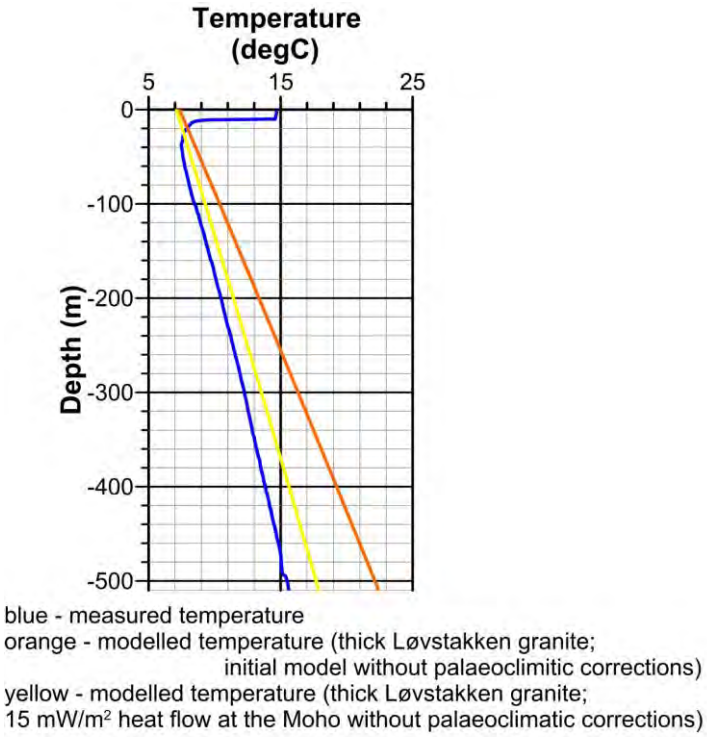

Figure 13.21. The Fyllingsdalen borehole: measured versus modelled temperatures. Modelled temperatures: the orange line is according to initial values of thermal properties in Table 13.3 and the yellow line is according to the same thermal properties with a reduced heat flux (15mW/m2) at the Moho.

have values of 3-4 W/mK within the lithospheric mantle. On the other hand, the thermal conductivity has to be much lower than 2 W/mK within the lithospheric mantle to have a less than 15 mW/m^2 heat flux at the Moho with a reasonable depth to the base of the lithosphere. To conclude, it is extremely unlikely that the basal heat flux at the Moho can reach a value of 15 mW/m^2 or lower beneath the Bergen and Stavanger areas. Thus, another explanation for the low measured temperatures within the Fyllingsdalen and Ullrigg boreholes has to be found.

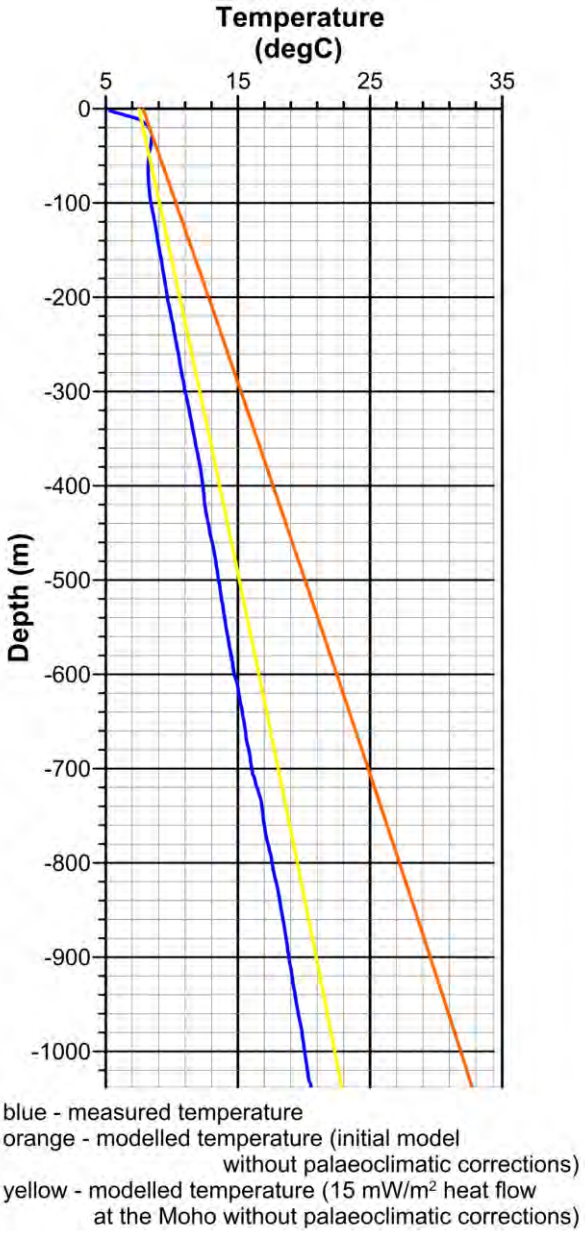

Figure 13.22. The Ullrigg borehole: measured versus modelled temperatures. Modelled temperatures: the orange line is according to initial values of thermal properties in Table 13.4 and the yellow line is according to the same thermal properties with a reduced heat flux (15mW/m2) at the Moho.

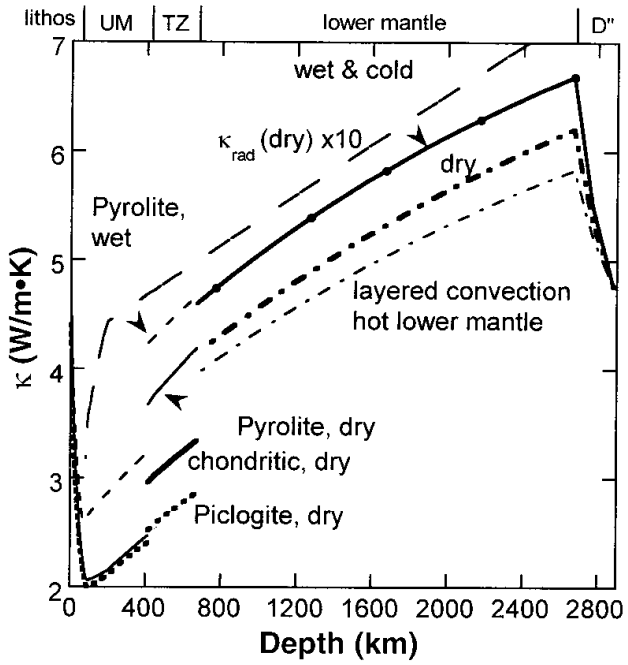

Figure 13.23. Thermal conductivity versus depth in the mantle (reproduced from Hofmeister 1999).

13.6.3 Palaeoclimatic corrections and reduced thermal properties

The Fyllingsdalen and Ullrigg boreholes penetrate only the uppermost part of the crystalline crust whereas the Kola superdeep borehole SG-3, the deepest one in the world, reaches a depth of more than 12 km. This provides an opportunity to obtain experimental data on the thermal regime at a great depth. For instance, the distribution of the temperature gradient and conductive heat flux within the Kola superdeep borehole (Fig. 13.24) demonstrates a considerable decrease of heat flow towards the surface at a depth of 2 km (Popov et al. 1999). A similar situation is also observed in other deep wells within the Scandinavian and Kola peninsulas. According to Kukkonen (1989), Popov et al. (1999), Kukkonen et al. (2011) and others, these significant changes in the shallow heat flux can be related to palaeoclimatic effects and/or convectional heat transfer due to groundwater flow. Kukkonen et al. (1989) suggested that the presence of crustal fracturing creates ideal conditions for deep groundwater flow in the bedrock which can disturb the conductive thermal regime of the subsurface within central areas of the Baltic Shield in Finland. In the case of the Bergen and Stavanger areas, drilling and logging in the Fyllingsdalen and Ulrihgg boreholes indicate the presence of fractures which are good pathways for groundwater circulation (Elvebakk & Storrø 2012 this report). In the Ulrigg borehole, the fracture zone is present at a depth of 300 m and the upper 120 m of the Fyllingdalen borehole is also characterised by highly fractured bedrock. Moreover, the Fyllingsdalen borehole was stopped at 516 m because fractured bedrock caused problems for further drilling operations (Elvebakk & Storrø 2012 this report). Water sampling in the Fyllingsdalen borehole indicates that the chemical composition of the groundwater is

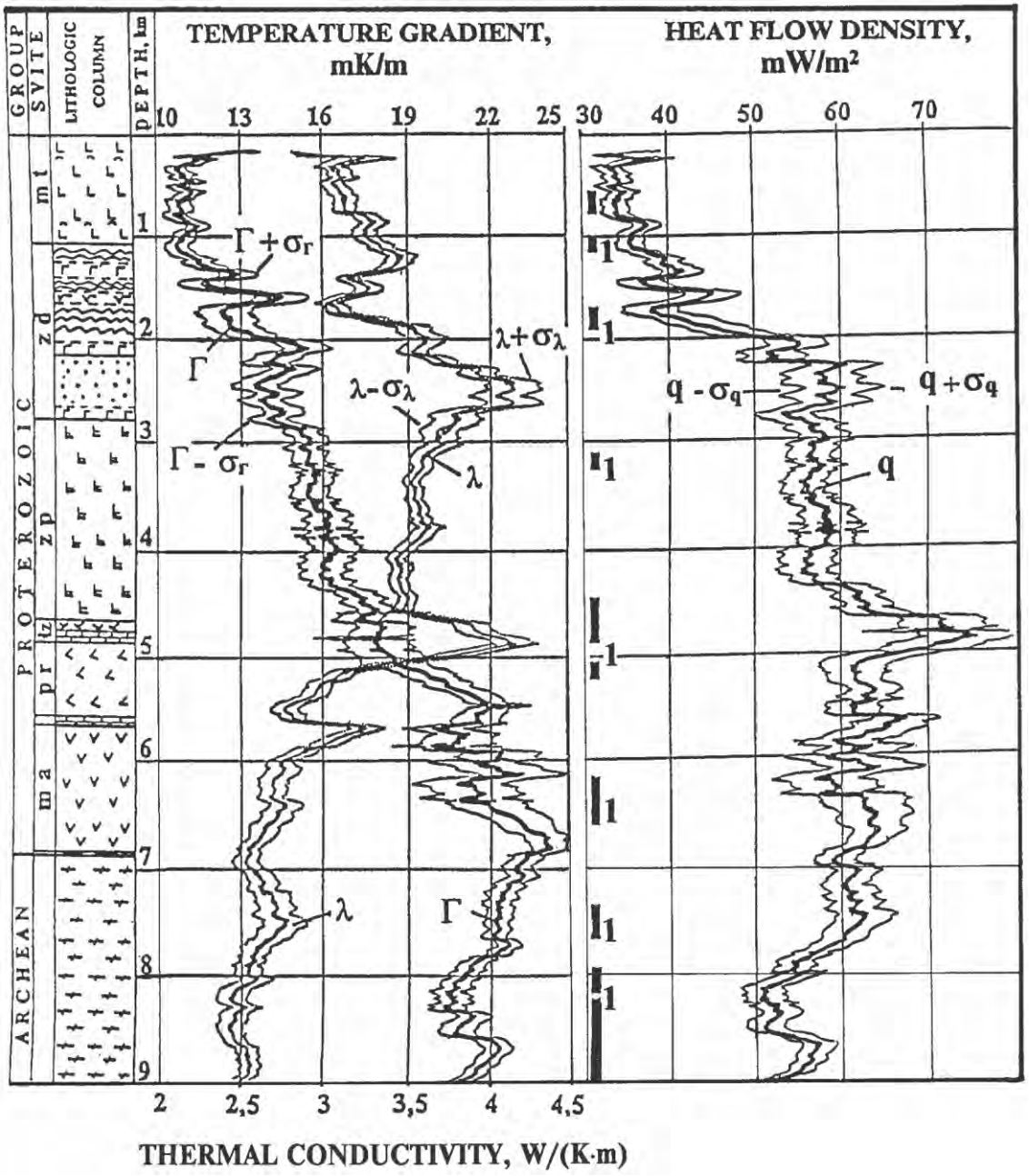

Figure 13.24. Distribution of the temperature gradient (□), effective thermal conductivity (□) of the rocks and conductive heat flux (q) within the Kola superdeep borehole SG-3 (reproduced from Popov et al. 1999).

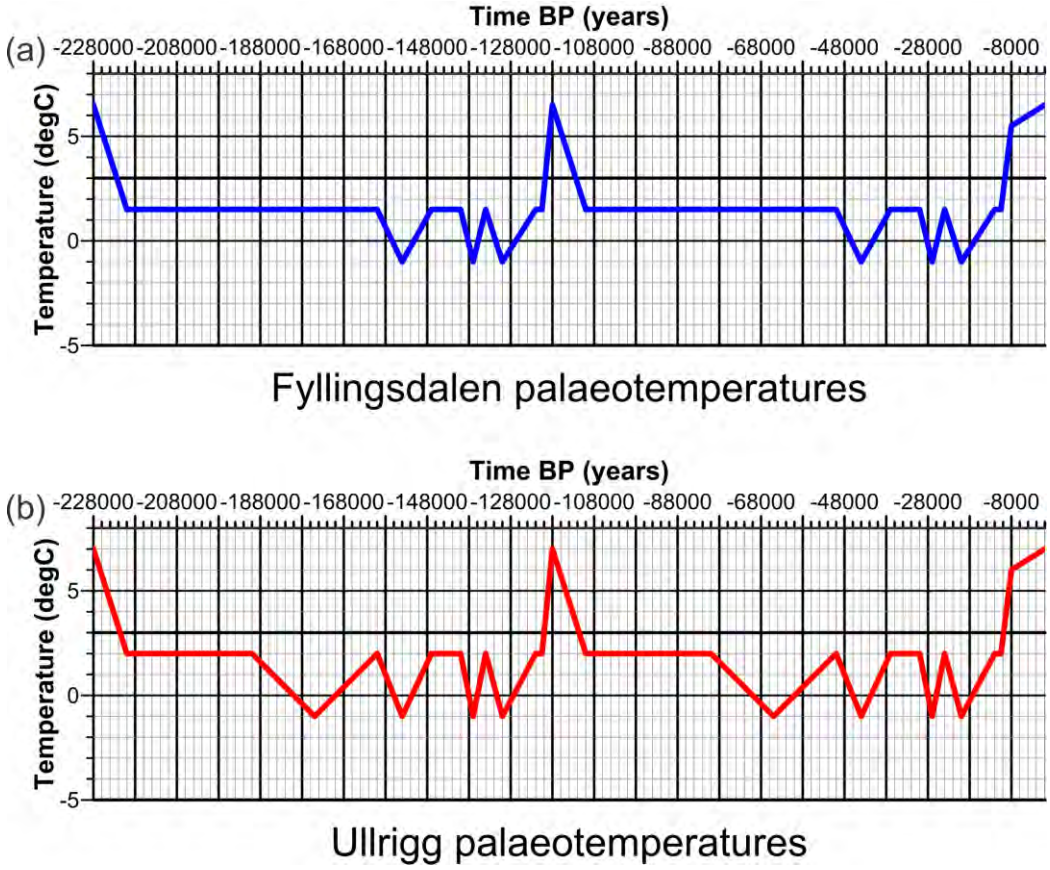

Figure 13.25. Scenario 1 for time-dependent surface temperature according to Slagstad et al. (2009). Palaeotemperatures for the Bergen area (a) and for the Stavanger area (b).

very similar to standard mean ocean water, although the salinity of the groundwater is low (Elvebakk & Storrø 2012 this report). To consider the groundwater influence on the subsurface thermal regime, a convectional thermal model has to be created. However, this kind of model requires additional structural and hydrogeological constraints and, therefore, cannot be executed accurately during the present study. On the other hand, the influence of the palaeoclimatic changes can be examined based on the assumptions of Slagstad et al. (2009) which were used for the palaeoclimatic Scenario 1. The palaeoclimatic history during the last glacial period is derived from a recent model of temporal ice-cover variations in Scandinavia during the Weichselian glaciations (Olsen 2006). Fig. 12.43 shows the limits of the ice cover through time, reproduced from Slagstad et al. (2009). According to Slagstad et al. (2009), at times when the borehole was covered by ice, the temperature at the surface in the vicinity of the borehole is assumed to have been -1 °C. At times when the borehole sites were ice free, a temperature of 5 °C below present-day surface temperatures (Tveito et al. 2000) at each borehole was assumed. In particular, a constant temperature of 1.5 °C has been assumed in the Bergen region and 2 °C for the Stavanger area. The Weichselian glacial (~110,000–10,000 years BP) and Holocene interglacial (10,000 years BP to present day) palaeoclimatic settings were also used for the Saalian glacial/Eemian interglacial period

Table 13.5 Reduced values of thermal properties used during the 2D thermal modelling within the Bergen area.

No	Layer of the 3D structural model	Specific heat capacity C_p [J/kgK]	Thermal conductivity k [W/mK]	Radiogenic heat production S [$\mu W/m^3$]
1	Gneiss, amphibolite	880	3.10	1.5
2	Diorite, gabbro/metabasalt	880	3.20	0.3
3	Schist	880	2.80	2.0
4	Schist, mylonised granitic gneiss	880	2.80	1
5	Gneiss	880	3.03	1.5
6	Løvstakken granite: upper granite/granitic gneiss	880	3.00	4.5
7	Lower granite, granitic gneiss	910	2.90	1.0
8	Middle crystalline crust	950	2.5	0.5
9	Lower crystalline crust	1050	2.3	0.1
10	High-density lower crustal layer	1100	2.1	0.1
11	Lithospheric upper mantle	1200	3.1	0.01

Table 13.6 Reduced values of thermal properties used during the 2D thermal modelling within the Stavanger area.

No	Layer of the 3D structural model	Specific heat capacity C_p [J/kgK]	Thermal conductivity k [W/mK]	Radiogenic heat production S [$\mu W/m^3$]
1	Pre-Permian sediments	1180	2.90	1
2	Biotite-pigeonite granite	880	3.00	2.0
3	Charnockite series	880	3.10	2
4	Plutonic rocks, gabbro	880	2.80	0.5
5	Gneiss, augen gneiss, migmatite	880	2.90	1.5
6	Phyllite	880	2.60	2.0
7	Anorthosite/norite	880	2.70	0.3
8	Upper granite/granitic gneiss	880	3.00	1.4
9	Lower granite/granitic gneiss	910	2.90	1.0
10	Middle crystalline crust	950	2.50	0.5
11	Lower crystalline crust	1050	2.30	0.1
12	High-density lower crustal layer	1100	2.10	0.1
13	Lithospheric upper mantle	1200	3.10	0.01

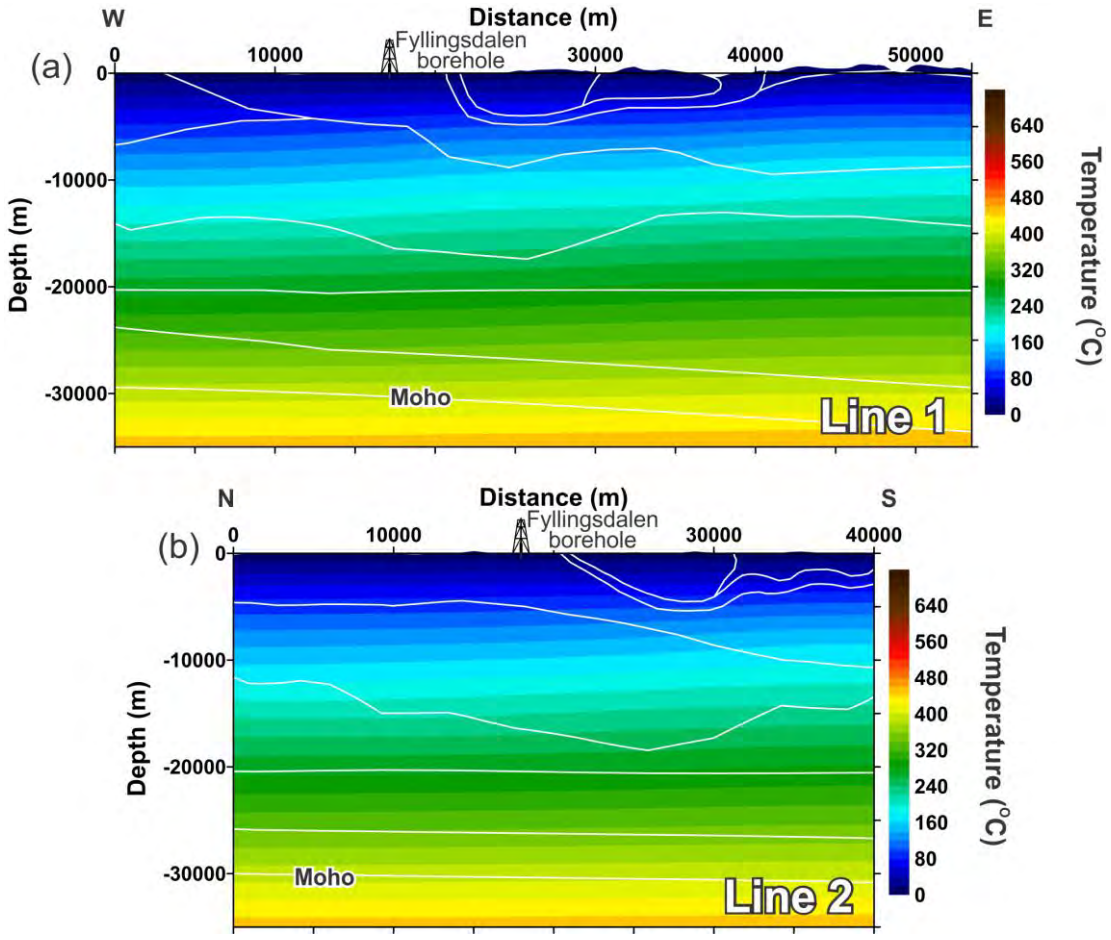

Figure 13.26. 2D thermal models derived by using reduced values of thermal properties in Table 13.5. Modelled temperature distribution along Line 1 (a) and Line 2 (b) within the Bergen area.

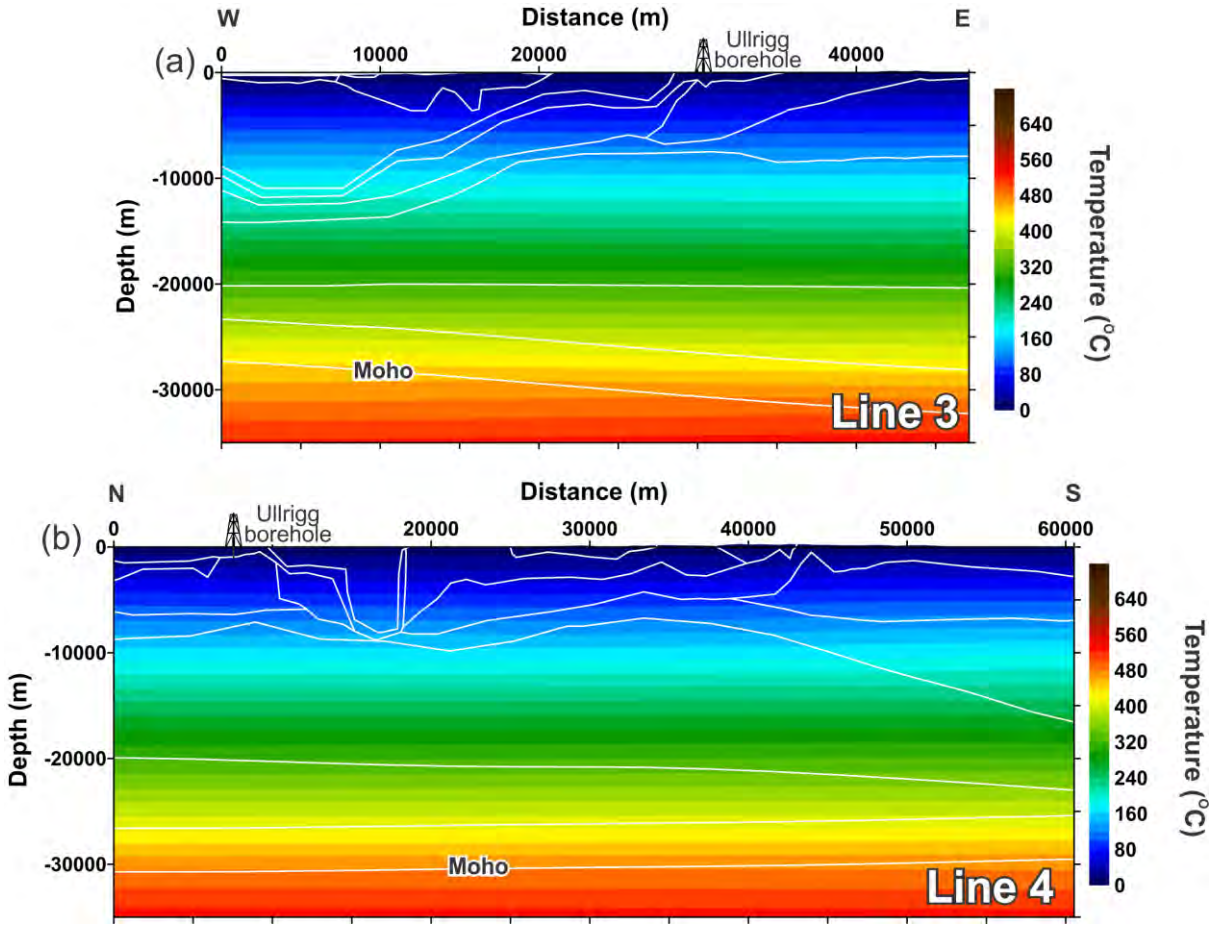

Figure 13.27. 2D thermal models derived by using reduced values of thermal properties in Table 13.6. Modelled temperature distribution along Line 3 (a) and Line 4 (b) within the Stavanger area.

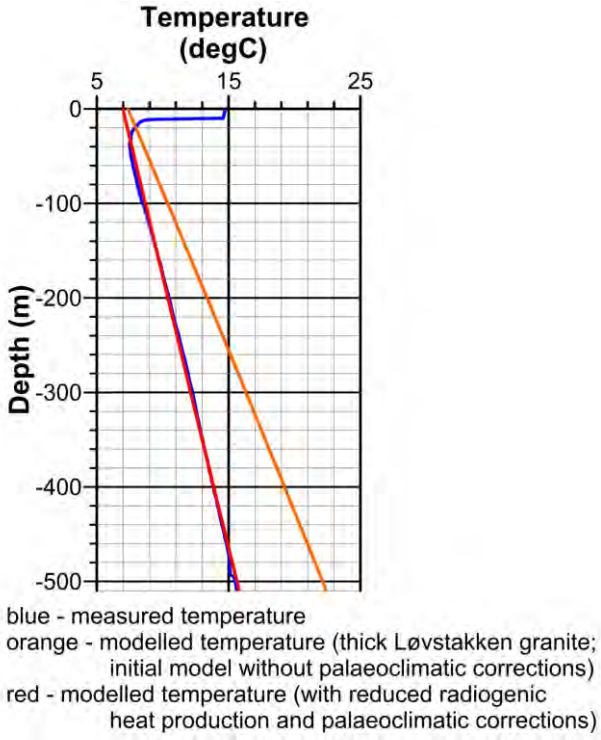

Figure 13.28. The Fyllingsdalen borehole: measured versus modelled temperatures. Modelled temperatures: the orange line is according to initial values of thermal properties in Table 13.3 and the red line is according to reduced values of thermal properties in Table 13.5 with palaeoclimatic corrections.

(220,000-110,000 years BP), taking into account that climatic conditions were relatively similar during the Weichselian glacial/Holocene interglacial and the Saalian glacial/Eemian interglacial periods (Andersen & Borns 1994, Slagstad et al. 2009). The reconstructed, annual, average palaeotemperatures at the Earth's surface according to Scenario 1 are shown in Fig. 13.25 for both boreholes. However, a first run of the transient 2D thermal analysis indicated that the time-dependent upper thermal boundary according to Scenario 1 (Fig. 13.25) does not provide a good fit between measured and modelled temperatures. Therefore, an additional parameterisation of initial thermal properties in Tables 13.3 and 13.4 (radiogenic heat production and thermal conductivity) had to be carried out to remove the misfit between observed and calculated data. To remove the misfit, a significant reduction of the radiogenic heat production is required compared to the initial thermal models (cf. Tables 13.3, 13.4 and 13.5, 13.6). Values of thermal conductivities have also been changed. The calculated temperatures along four profiles are displayed in Figures. 13.26 and 13.27.

A comparison of the measured and modelled plots shows a perfect coincidence in the case of the Fyllingsdallen borehole (Fig. 13.28) and a good fit is also obtained for the Ulrigg borehole (Fig. 13.29).

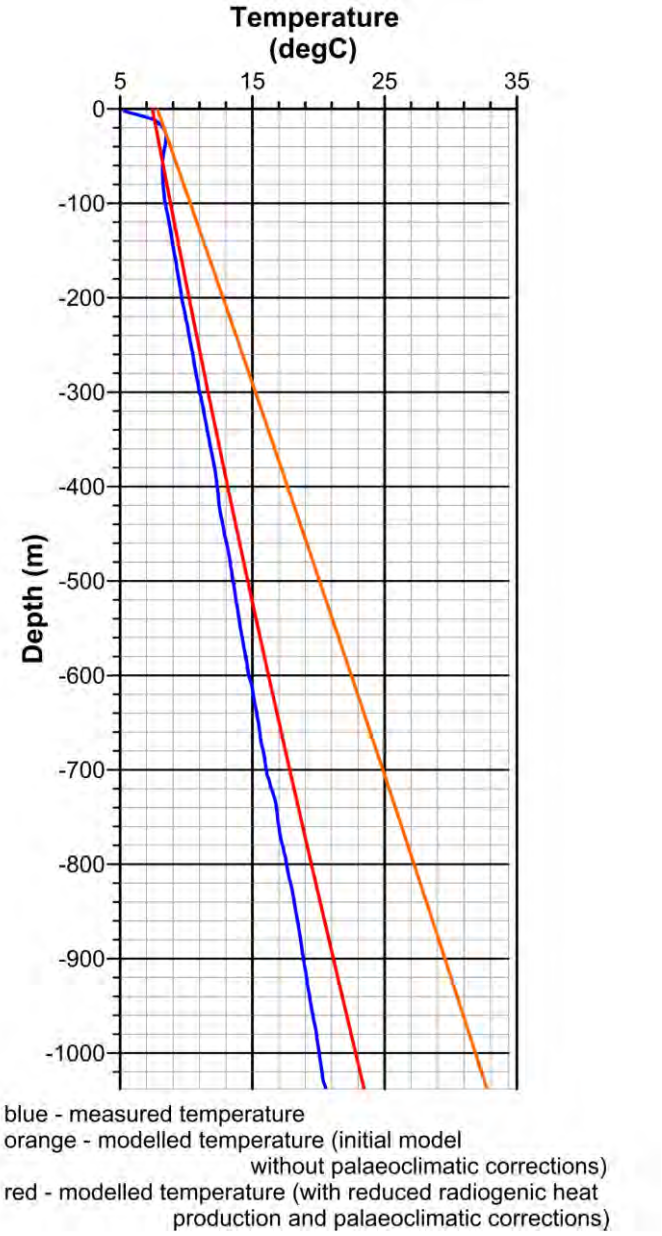

Figure 13.29. The Ullrigg borehole: measured versus modelled temperatures Modelled temperatures: the orange line is according to initial values of thermal properties in Table 13.4 and the red line is according to reduced values of thermal properties in Table 13.6 with palaeoclimatic corrections.

Table 13.7 Reduced values of thermal properties used during the 3D thermal modelling.

No	Layer of the 3D structural model	Dominant lithology	Thermal conductivity k [W/mK]	Radiogenic heat production S [μW/m^3]
2	Tertiary	clastics	1.50	0.7
3	Upper Cretaceous	carbonates, clastics	1.95	1
4	Lower Cretaceous	clastics	2.00	1.5
5	Jurassic	clastics	2.10	1.6
6	Triassic	clastics, carbonates	2.10	1.6
7	Upper Permian	rock salt	3.50	0.3
8	Non-salt Upper Permian (Zechstein)	clastics, carbonates,	1.95	0.8
9	Lower Permian - pre-Permian sediments	clastics, carbonates	2.90	1.0
10	Upper crustal magmatic rocks	gabbro to anorthositic rocks	2.70	0.3
11	Middle-upper crustal intrusions	intrusive rocks	3.20	0.6
12	Low-density upper crustal layer	metasediments or granite	3.00	1.6
13	Upper crustal layer	granite and gneiss	2.95	1.2
14	Eastern Central North Sea rocks	granitoids and/or gneiss	2.50	0.5
15	Western Central North Sea rocks	granitoids and/or gneiss	2.50	0.5
16	Middle crust of Laurentia and Avalonia	granitoids and/or gneiss	2.50	0.5
17	Middle crust of Baltica	granitoids and/or gneiss	2.50	0.5
18	Lower crust of Baltica	metamorphic rocks	2.30	0.1
19	High-density crust	mafic granulites, gabbros	2.40	0.15
20	High-density lower crustal layer	gabbros, high-grade metamorphic rocks	2.10	0.1
21	Lithospheric upper	peridotite	3.10	0.01

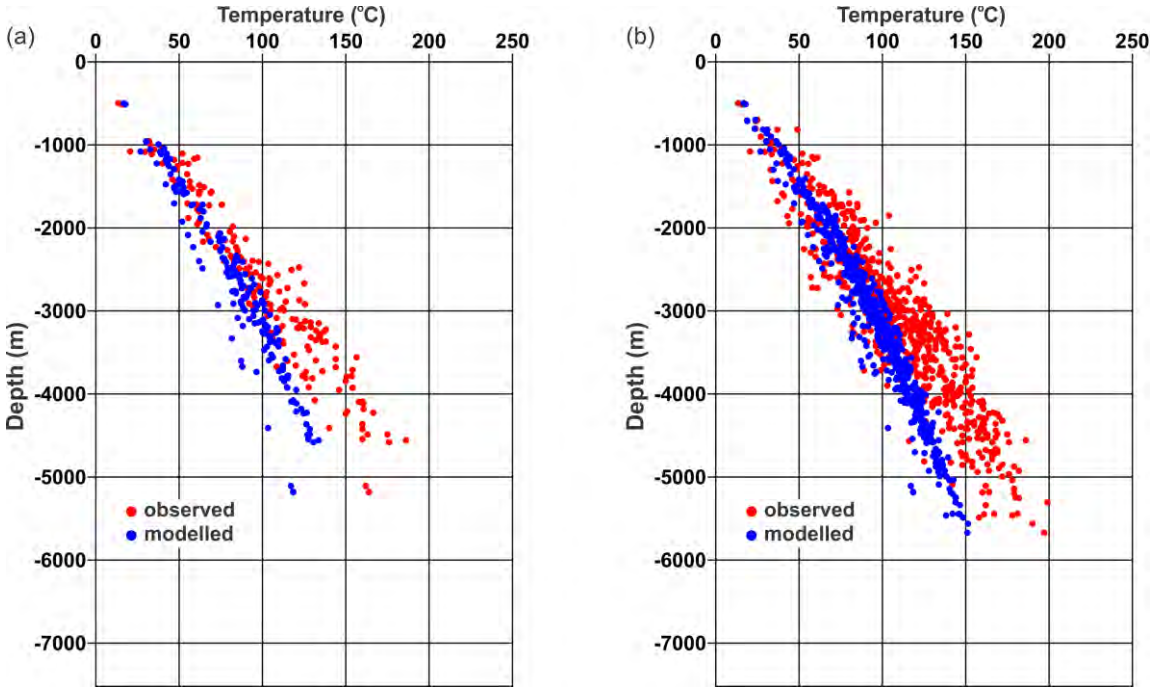

Figure 13.30. Results of steady-state 3D thermal modelling by use of reduced values of thermal properties in Table 13.7. Note the misfit between the calculated (blue dots) and the observed (red dots) temperatures. (a) Only boreholes with DST (drill stem test) temperatures are used within the Norwegian sector of the North Sea. (b) Boreholes with less reliable bottom-hole temperatures (BHT) are also included within the Norwegian sector of the North Sea.

Steady-state 3D thermal calculations with similar reduced thermal properties (Table 13.7) have been carried out in a systematic way so as to be able to verify these results of 2D thermal modelling. The lithospheric-scale 3D structural model (Fig. 12.3; Maystrenko 2012 this report), validated by the 3D gravity modelling, has been used as a structural skeleon during the 3D thermal modelling. For the upper boundary, annual average air temperatures during 1961-1990 (Tveito et al. 2000) and an average sea-bottom temperature of 8 °C during 1997-2002 (ICES 2012) have been chosen. The lithosphere-asthenosphere boundary has been taken as the lower thermal boundary which corresponds to the 1300 °C isotherm. The locations of deep boreholes used for this comparison are shown in Fig. 12.50 and the reliability of the measured data is briefly discussed in Chapter 11 of this report (Maystrenko 2012 this report). Unfortunately, a comparative analysis demonstrates that there is a mismatch between the observed and modeled trends which generally increases with depth (Fig. 13.30). Therefore, the modelling assumptions are once more incorrect and other models have to be examined.

13.6.4 Reduced thickness of the Løvstakken granite

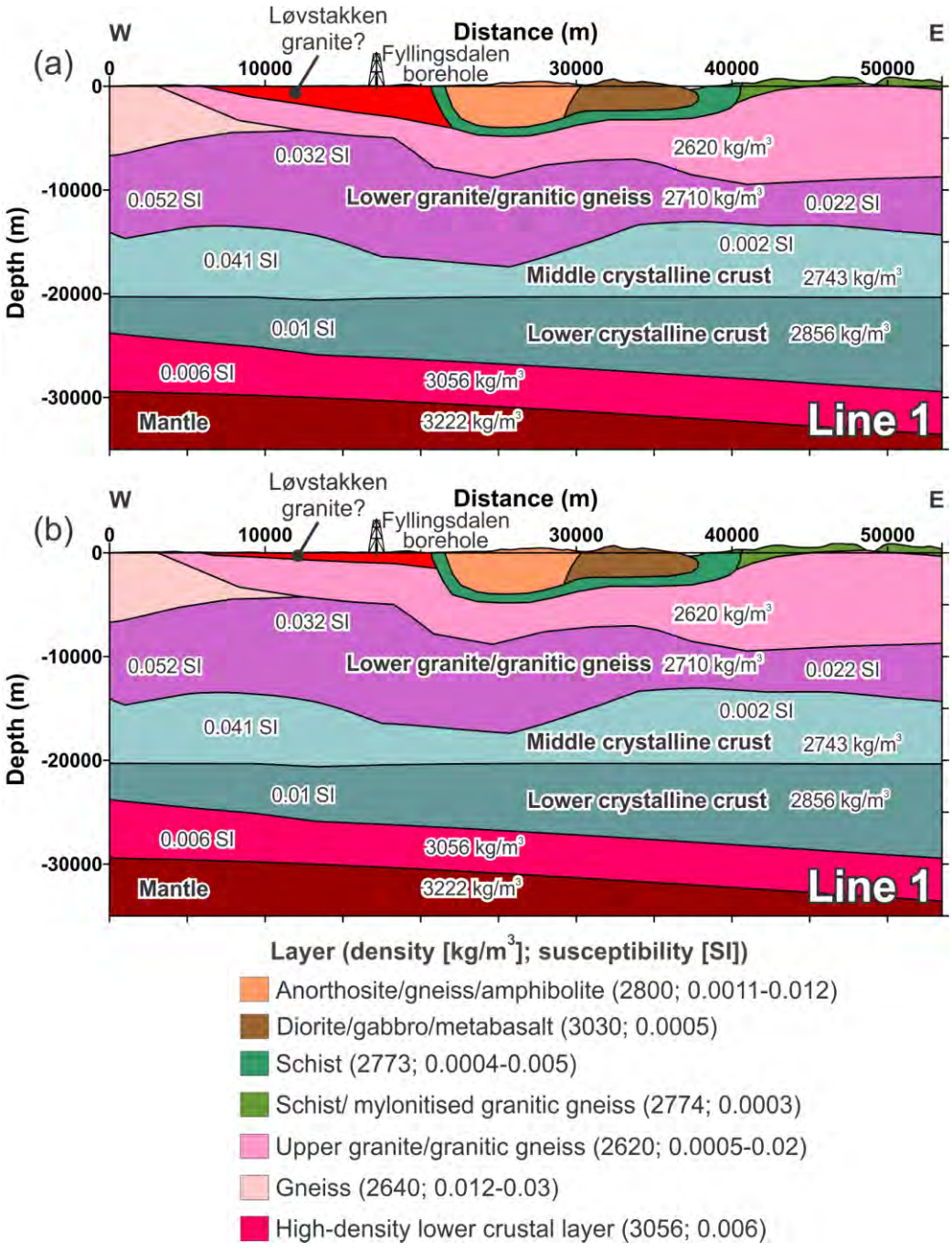

Figure 13.31. Reduced thickness of the Løvstakken granite along Line 1 within the Bergen area: (a) thin Løvstakken granite and (b) very thin Løvstakken granite.

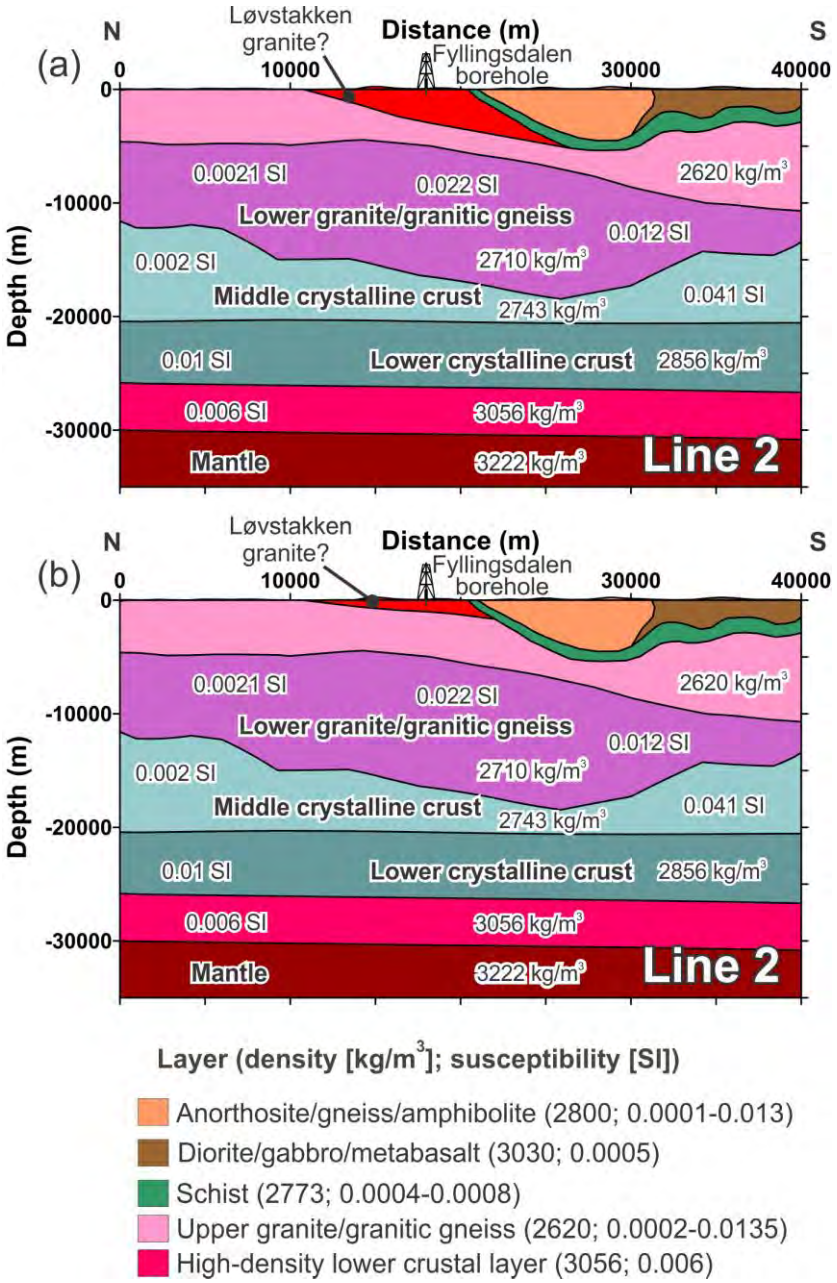

Figure 13.32. Reduced thickness of the Løvstakken granite along Line 2 within the Bergen area: (a) thin Løvstakken granite and (b) very thin Løvstakken granite.

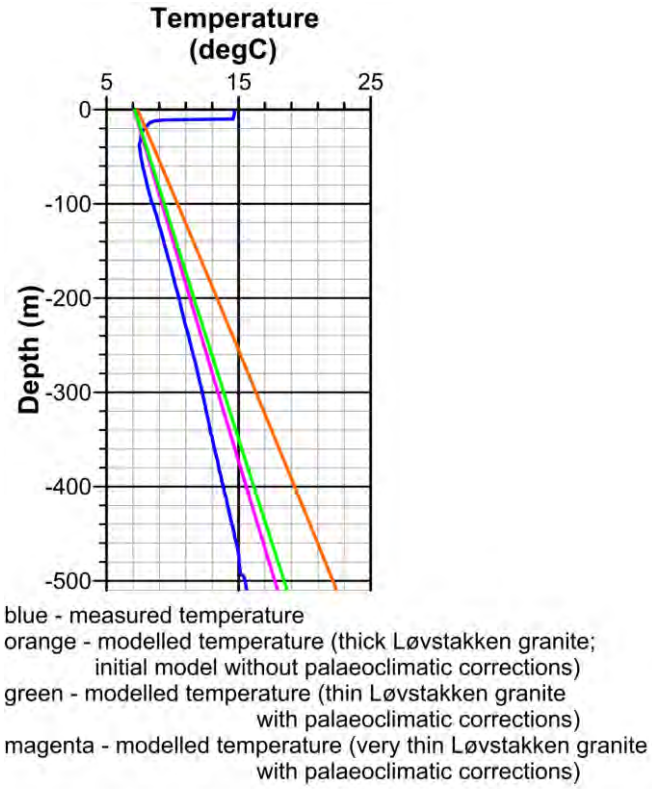

Figure 13.33. The Fyllingsdalen borehole: measured versus modelled temperatures. Modelled temperatures: the orange line is according to initial values of thermal properties in Table 13.3, the green and magenta lines are according to the same values of thermal properties with palaeoclimatic corrections and a reduced thickness of the Løvstakken granite (the green line corresponds to the model in Figures 13.31a and 13.32a, whereas the magenta line corresponds to the model in Figures 13.31b and 13.32b).

For completeness, the influence of changes in geometry of the Løvstakken granite was also examined by decreasing the thickness of this layer. Distribution of this granite was restricted to the area where these rocks crop out at the surface. These simulations were performed in order to understand how these changes affect the results of the 2D thermal modelling.

The modelled temperature-depth profiles were calculated by first using the reduced thickness of the Løvstakken granite in Figures 13.31a and 13.32a, then calculating the same profile with a markedly reduced thickness of this granite as in Figures 13.31b and 13.32b. The results of the modelling (Fig. 13.33) demonstrate only a very slight difference between these two models, whilst a prominent decrease of the misfit is obvious as compared to the initial model. Therefore, this test shows that the thickness reduction of the highly radioactive Løvstakken granite can be a possible option within the Bergen area.

13.6.5 Final model

In the final 2D models, changes of palaeotemperatures during the Weichselian glaciations have been revised in detail and a new scenario (Scenario 2 in Fig. 13.34) has been applied. Scenario 2 is derived from the palaeoclimatic surface temperatures in Fig. 12.44 which have been used during the 3D thermal modelling (Maystrenko 2012 this report). The important point of palaeotemperature restoration corresponds to the locations of both boreholes in relation to the position of the ice cover. The Fyllingsdallen and Ullrigg borehole locations were continuously situated near the margin of the Weichselian ice sheet (Fig. 12.43) and, therefore, these locations could have been affected by cold climatic conditions in the tundra where the annual average air temperature was below zero. In addition, during this final stage of 2D thermal modelling, some thermal properties (Tables 13.8 and 13.9) have been slightly modified.

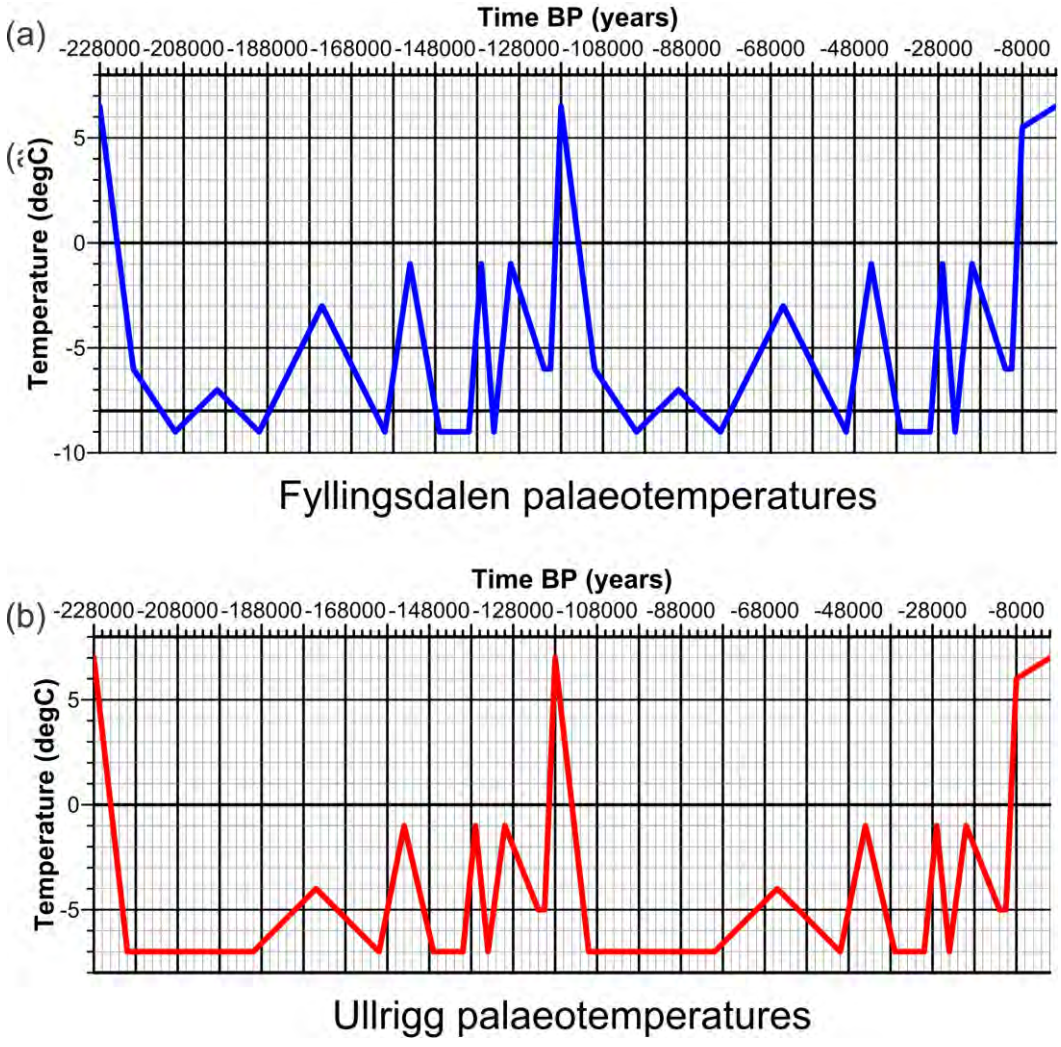

Figure 13.34. Scenario 2 for time-dependent surface temperatures according to the palaeotemperatures in Fig. 12.44 which were used during the 3D thermal modelling (Maystrenko 2012 this report). Palaeotemperatures for the Bergen area (a) and for the Stavanger area (b).

Table 13.8 Final thermal properties of the layers used during the 2D thermal modelling within the Bergen area.

No	Layer of the 3D structural model	Specific heat capacity C_p [J/kgK]	Thermal conductivity k [W/mK]	Radiogenic heat production S [$\mu W/m^3$]
1	Gneiss, amphibolite	880	3.10	1.5
2	Diorite, gabbro/metabasalt	880	3.20	0.3
3	Schist	880	2.80	2.7
4	Schist, mylonised granitic gneiss	880	2.80	1
5	Gneiss	880	3.03	1.5
6	Løvstakken granite: upper granite/granitic gneiss	880	3.00	4.5
7	Lower granite, granitic gneiss	910	3.00	1.6
8	Middle crystalline crust	950	2.70	0.8
9	Lower crystalline crust	1050	2.60	0.3
10	High-density lower crustal layer	1100	2.30	0.2
11	Lithospheric upper mantle	1200	3.95	0.03

Table 13.9 Final thermal properties of the layers used during the 2D thermal modelling within the Stavanger area.

No	Layer of the 2D structural model	Specific heat capacity C_p [J/kgK]	Thermal conductivity k [W/mK]	Radiogenic heat production S [$\mu W/m^3$]
1	Pre-Permian sediments	1180	2.40	1
2	Biotite-pigeonite	880	3.00	2.0
3	Charnockite series	880	3.10	2.0
4	Plutonic rocks, gabbro	880	2.80	0.7
5	Gneiss, augen gneiss,	880	2.90	1.5
6	Phyllite	880	2.70	2.0
7	Anorthosite/norite	880	2.70	0.3
8	Upper granite/graniti	880	2.90	1.2
9	Lower granite/graniti	910	2.85	1.0
10	Middle crystalline	950	2.60	0.7
11	Lower crystalline	1050	2.60	0.3
12	High-density lower crustal	1100	2.30	0.2
13	Lithospheric upper mantle	1200	3.95	0.03

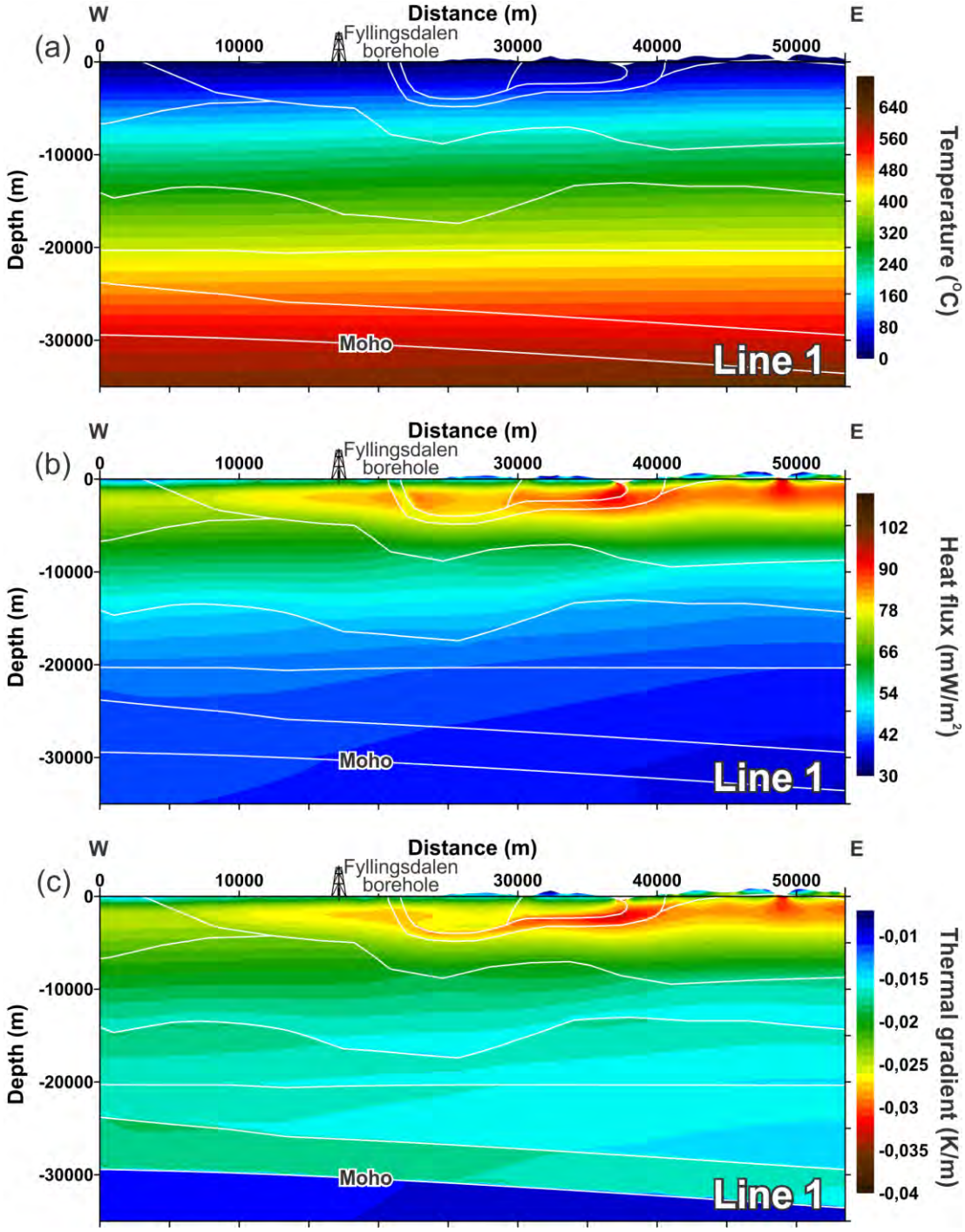

Figure 13.35. Results of the 2D thermal modelling along Line 1 within the Bergen area, using the final thermal properties in Table 13.8 and Scenario 2 for surface palaeotemperatures. Modelled temperature (a), heat flux (b) and thermal gradient (c).

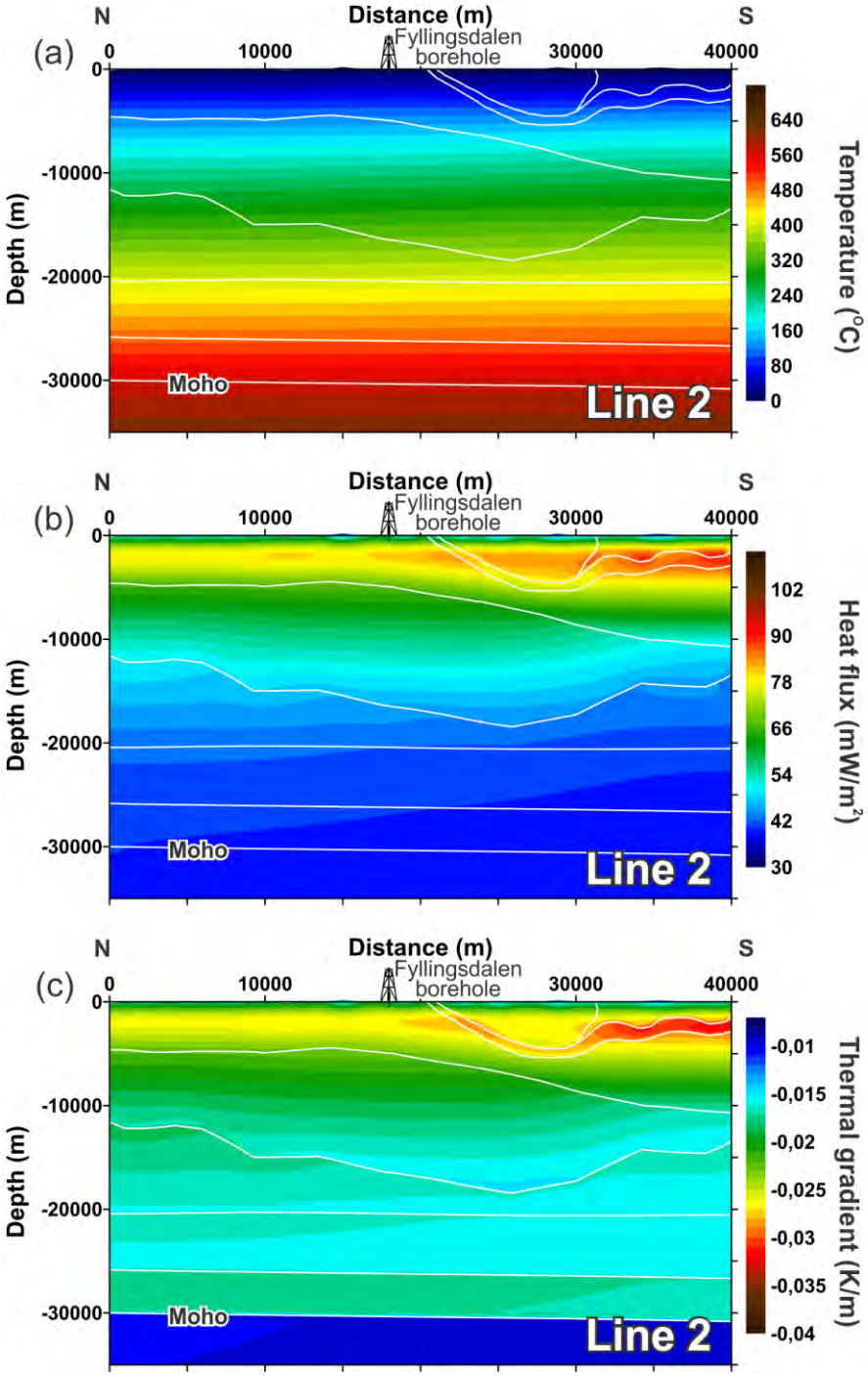

Figure 13.36. Results of the 2D thermal modelling along Line 2 within the Bergen area, using the final thermal properties in Table 13.8 and Scenario 2 for surface palaeotemperatures. Modelled temperature (a), heat flux (b) and thermal gradient (c).

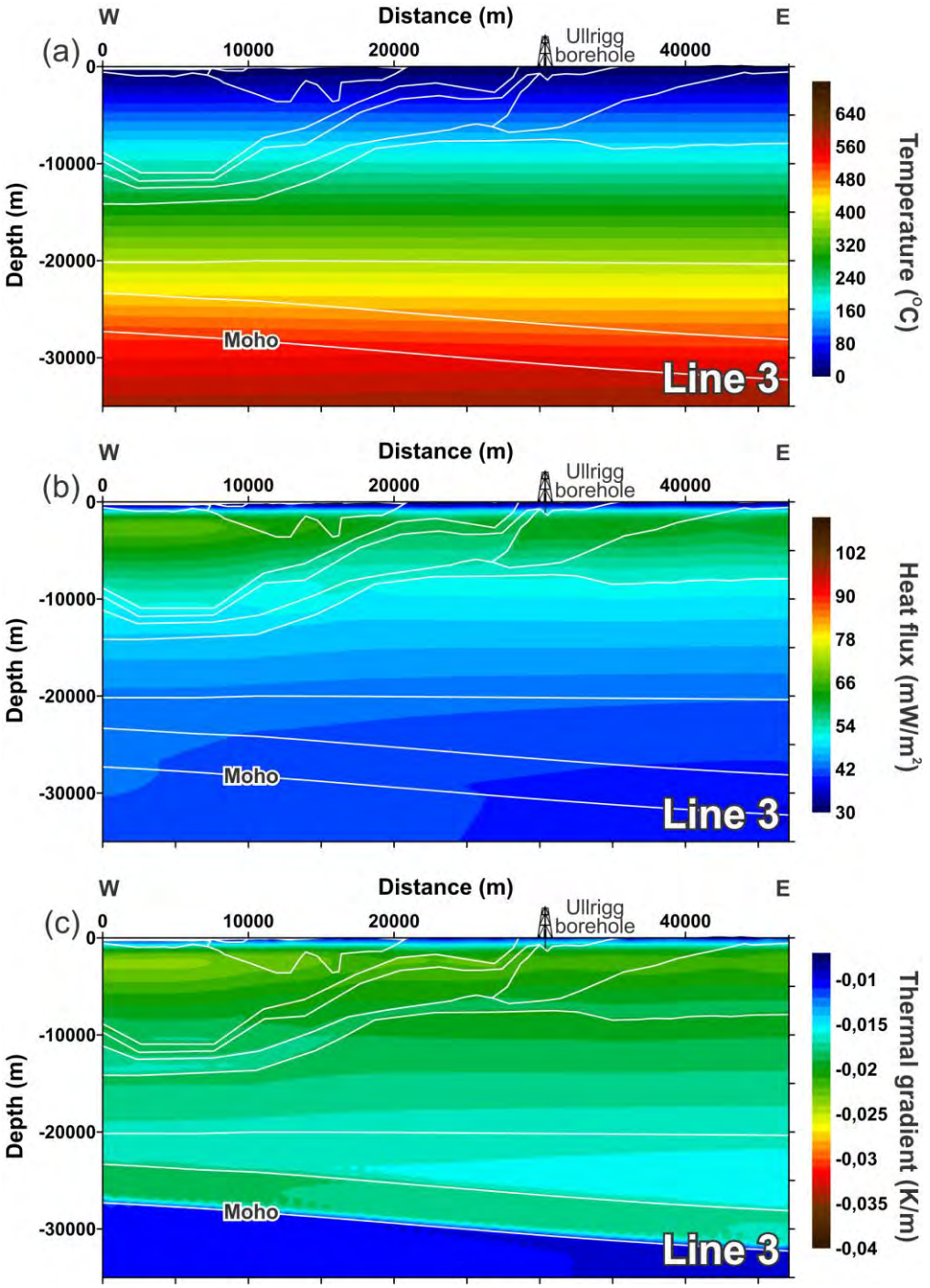

Figure 13.37. Results of the 2D thermal modelling along Line 3 within the Stavanger area, using the final thermal properties in Table 13.9 and Scenario 2 for surface palaeotemperatures. Modelled temperature (a), heat flux (b) and thermal gradient (c).

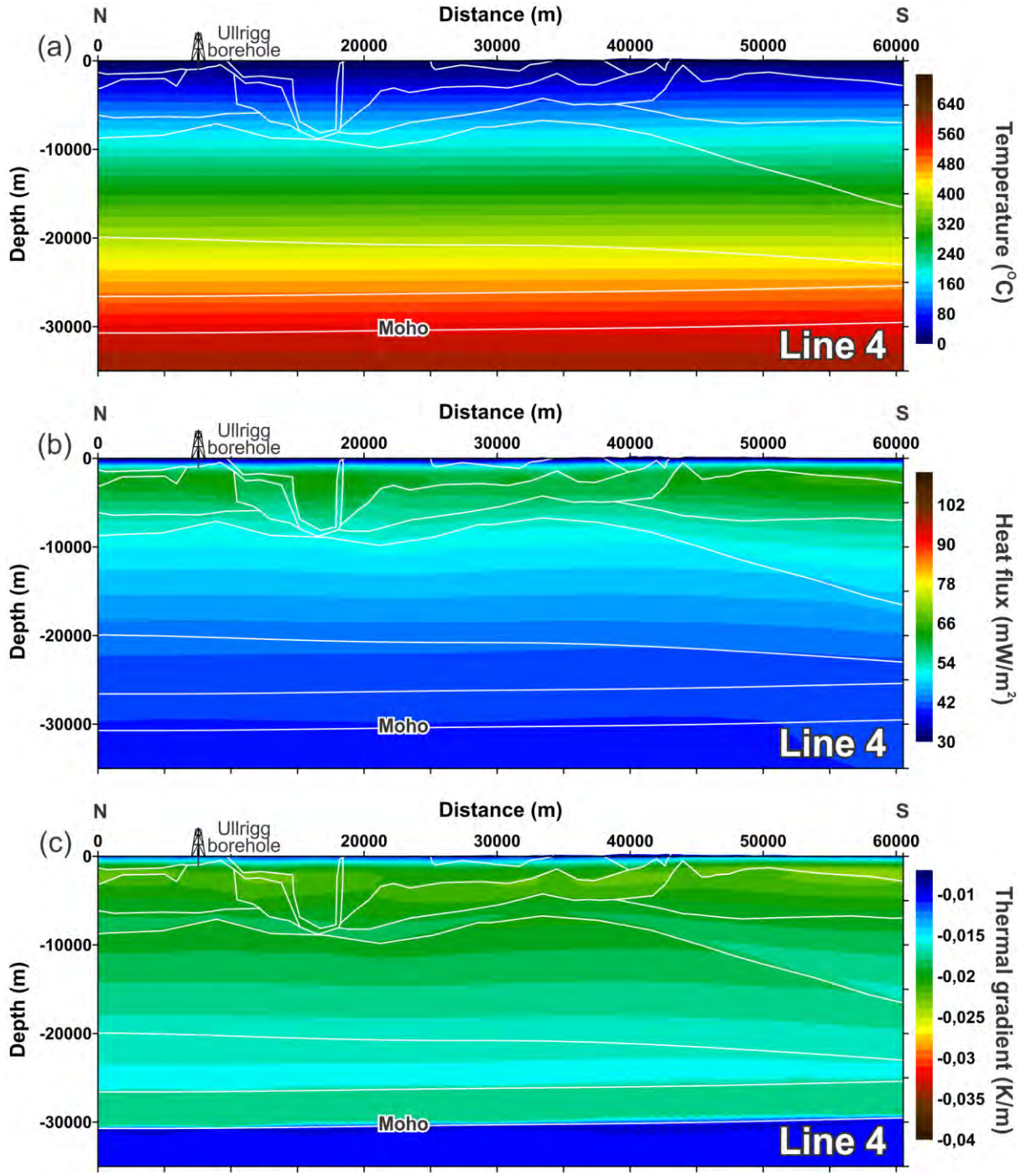

Figure 13.38. Results of the 2D thermal modelling along Line 4 within the Stavanger area, using the final thermal properties in Table 13.9 and Scenario 2 for surface palaeotemperatures. Modelled temperature (a), heat flux (b) and thermal gradient (c).

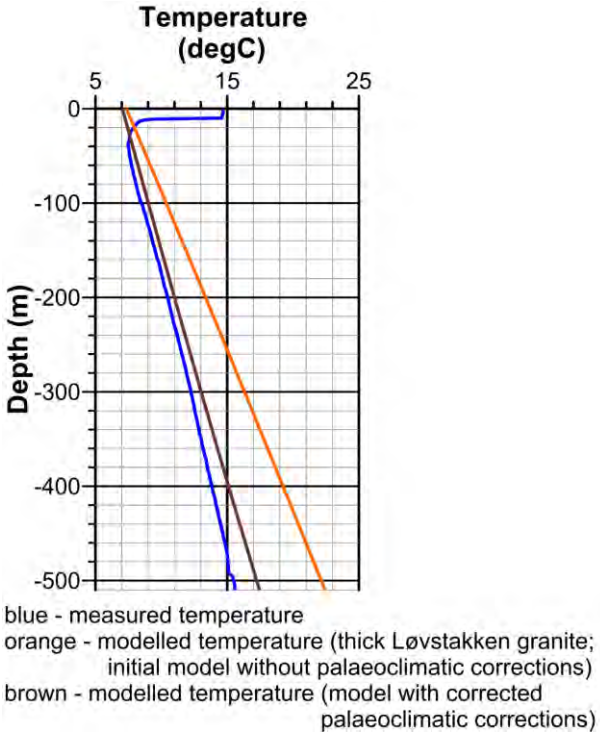

Figure 13.39. The Fyllingsdalen borehole: measured versus modelled temperatures. Modelled temperatures: the orange line is according to initial values of the thermal properties in Table 13.3 and the brown line is according to final values of the thermal properties in Table 13.8.

The results of the thermal modelling for the final models are displayed in Figures 13.35-13.38, showing the 2D distribution of the modelled temperatures, heat flow and thermal gradients. As in the case of the initial models, the modelled temperatures along Lines 1 and 2 within the Bergen area are high within the upper parts of Line 1 and 2 towards the areas where the Løvstakken granite is thickest (Fig. 13.35a & 13.35b). The calculated heat flux is also high within areas where the presence of the relatively thick Løvstakken granite is modelled (Figs. 13.35b & 13.36b). The same is true for the temperature gradient which also follows this structural pattern. On the other hand, the modelled isotherms are subhorizontal within the Stavanger area (Fig. 13.37a & 13.38a). The heat flux is relatively low within the anorthosites, norites and phyllites which are characterised by a lower thermal conductivity compared to the surrounding granites and gneisses (Table 13.9). In general, the obtained heat flux beneath the Stavanger area is lower than the modelled one within the upper crystalline crust of the Bergen area (cf. Figs. 13.35b, 13.36b & 13.36b, 13.37b).

The comparison of measured and calculated temperature depth profiles (Fig. 13.39 & 13.40) demonstrates a relatively good fit when Scenario 2 is used for the palaeoclimatic perturbations. The residual misfit is still around 2 °C. This misfit can partially be related to the fact that a convectional heat transfer due to groundwater circulation within fractured crystalline rocks has not been considered in the final thermal models. The other possible reasons for the misfit are either an inaccuracy in the structural models or uncertainties in the values of the thermal properties.

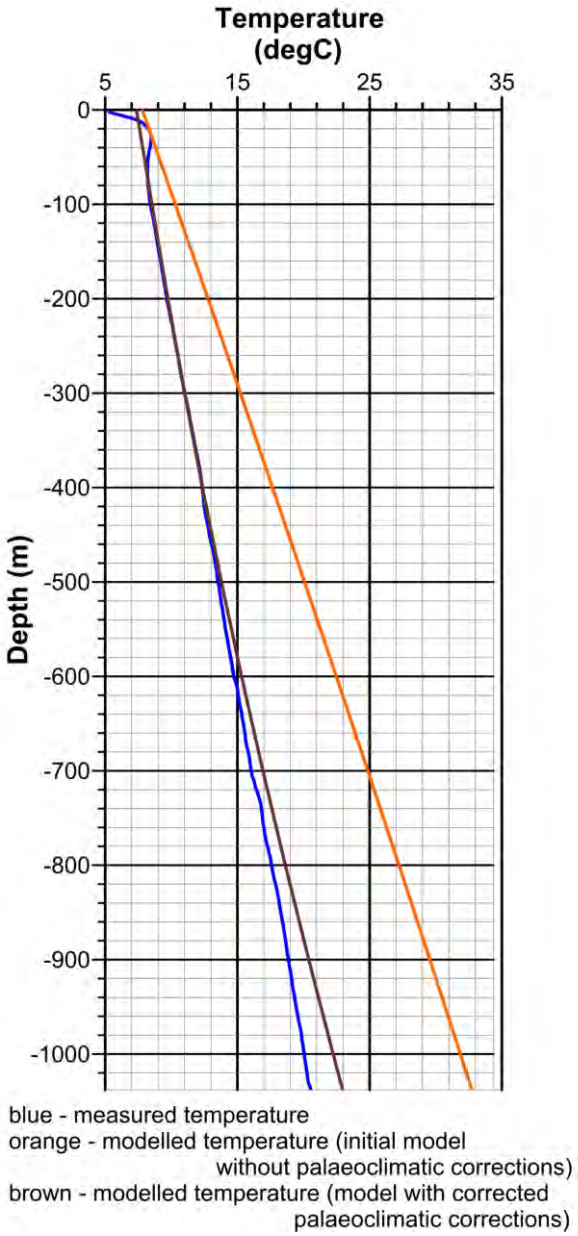

Figure 13.40. The Ullrigg borehole: measured versus modelled temperatures. Modelled temperatures: the orange line is according to initial values of the thermal properties in Table 13.4 and the brown line is according to final values of the thermal properties in Table 13.9.

13.7 Heat-flow calculations

The heat-flow calculations, and topographic and palaeoclimatic corrections have been carried out following the approach described by Slagstad et al. (2009).

Values of thermal conductivities were obtained from measurements of thermal properties on rock core sampling from the Fyllingsdalen borehole (Fig. 13.41 and 13.43). On the other hand, average constant thermal conductivities from the Ullrigg borehole (Figs. 13.42 & 13.44) are derived from the petrophysical database Petro at NGU, based on rock samples with the same lithology as those located at the surface in the vicinity of this borehole. Values of the thermal gradient were averaged by running-mean averages within depth intervals of 20 and 100 m. The same procedure has been applied for thermal conductivities in the Fyllingsdalen borehole. Heat flux values have been calculated using Fourier's law of heat conduction (Equation 13.1). The heat flux, therefore, was calculated as the product of thermal gradients and conductivities and was also plotted with 20 m and 100 m averaging. Afterwards, the calculated values of heat flux had to be corrected for the changes in topography and palaeothermal regime.

According to Slagstad et al. (2009), the topographic corrections are based on topographic models with a horizontal resolution of 100 m and a vertical resolution of 1 m. At the locations of both boreholes, a 10×10 km block was constructed by use of the finite element method in COMSOL Multiphysics software. The constructed blocks have a vertical thickness of 5 km plus the digital elevation data which represent the upper surface of these blocks. The lower surface of the blocks is flat at a depth of 5 km. The boreholes were placed at the centre of the blocks. The surface temperature has been set to decrease according to a function of elevation by 6.5 °C km^{-1}. The lower thermal boundary is represented by the heat flux at the base of the blocks which has been set to be 50 mW/m^2. In these models, constant and homogeneous thermal conductivities have been assigned, based on the measured conductivities from each borehole. A value of 3 W/mK was used for the Fyllingsdalen borehole and 2.8 W/mK was assigned for the Ullrigg borehole. Finally, the topographic corrections on heat flow were calculated to be positive (increased heat flow) beneath topographic lows or negative (reduced heat flow) beneath topographic highs (Slagstad et al. 2008). The calculated topographic corrections are rather minor, reaching values of up to 4 mW/m^2 in the Fyllingsdallen borehole. In the Ullrigg borehole, these values are in the range -1-1 mW/m^2.

The palaeoclimatic corrections were also calculated by use of the finite element method in COMSOL Multiphysics software. This has been done based on 1D models with average homogeneous thermal conductivities (3 W/mK for the Fyllingsdalen borehole and 2.8 W/mK for the Ullrigg borehole) and a constant basal heat flux of 50 mW/m^2. A surface temperature has been set to vary according to the palaeoclimatic Scenarios 1 (Fig. 13.25) and 2 (Fig. 13.34) within each borehole. It should be mentioned that the most reasonable is the second Scenario, although Scenario 1 has to be shown for the sake of completeness of the present study.

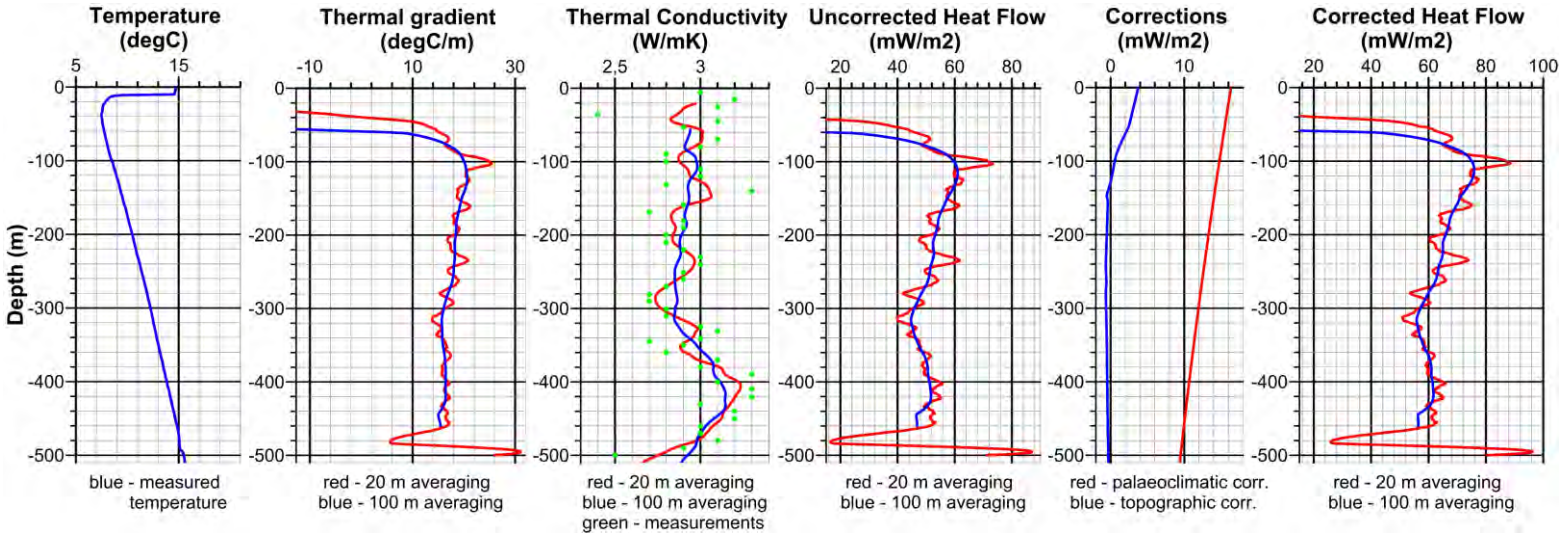

Figure 13.41. Plots showing measured temperature (Elvebakk & Storrø 2012), thermal gradient (Elvebakk & Storrø 2012), thermal conductivity, uncorrected heat flow, corrections (topographic and palaeoclimatic) and corrected heat flow it the Fyllingsdalen borehole. Green dots are the measured thermal conductivities based on drillcore data. Palaeoclimatic corrections are according to Scenario 1 in Fig. 13.25a (Slagstad et al. 2009).

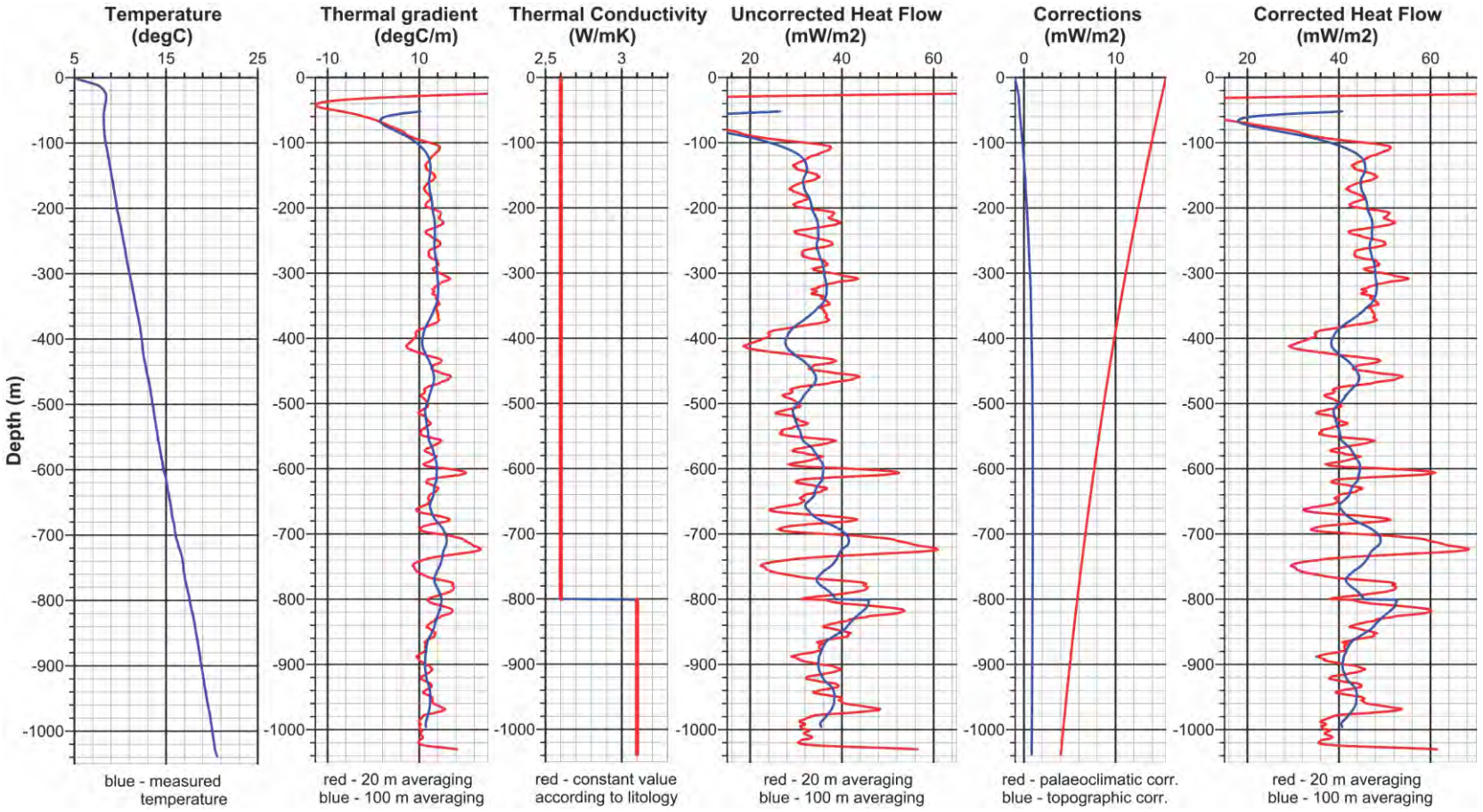

Figure 13.42. Plots showing measured temperature (Elvebakk & Storrø 2012), thermal gradient (Elvebakk & Storrø 2012), thermal conductivity, uncorrected heat flow, corrections (topographic and palaeoclimatic) and corrected heat flow in the Ullrigg borehole. Average values of thermal conductivities are based on surface samples with the same lithology. Palaeoclimatic corrections are according to Scenario 1 in Fig. 13.25b (Slagstad et al. 2009).

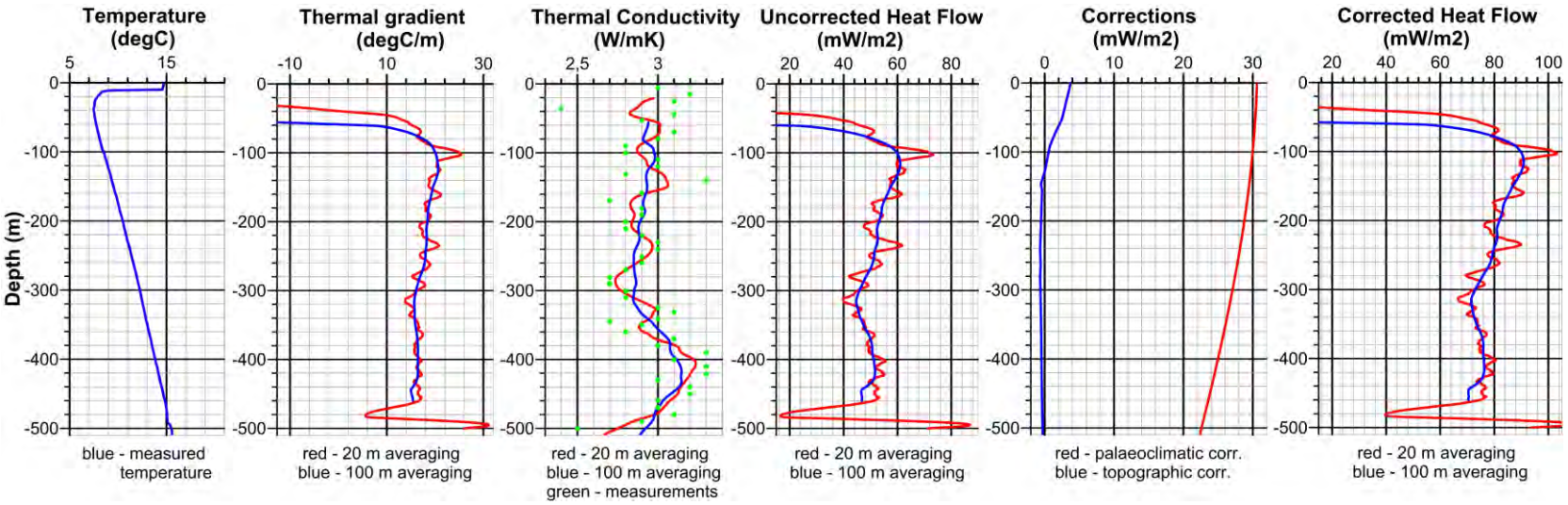

Figure 13.43. Plots showing measured temperature (Elvebakk & Storrø 2012), thermal gradient (Elvebakk & Storrø 2012), thermal conductivity, uncorrected heat flow, corrections (topographic and palaeoclimatic) and corrected heat flow in the Fyllingsdalen borehole. Green dots are the measured thermal conductivities based on drillcore data. Palaeoclimatic corrections are according to Scenario 2 in Fig. 13.34a.

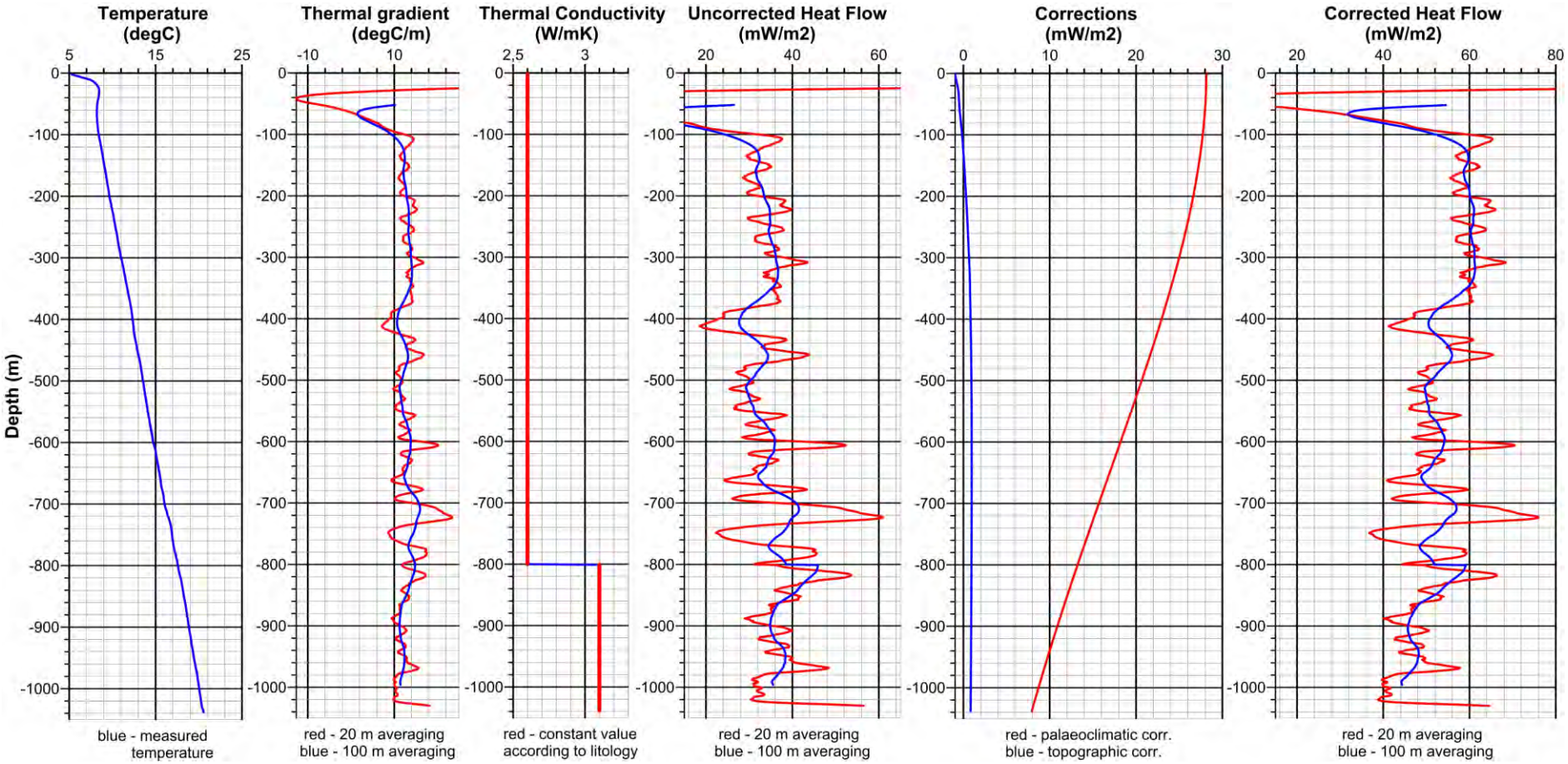

Figure 13.44. Plots showing measured temperature (Elvebakk & Storrø 2012), thermal gradient (Elvebakk & Storrø 2012), thermal conductivity, uncorrected heat flow, corrections (topographic and palaeoclimatic) and corrected heat flow in the Ullrigg borehole. Average values of thermal conductivities are based on surface samples with the same lithology. Palaeoclimatic corrections are according to Scenario 2 in Fig. 13.34b.

Table 13.10 Uncorrected and corrected average heat flux for the Fyllingsdalen borehole.

Palaeo-climatic scenario	Averaging interval [m]	Depth interval [m]	Data range: uncorrected heat flux [mW/m^2]	Average uncorrected heat flux [mW/m^2]	Data range: corrected heat flux [mW/m^2]	Average corrected heat flux [mW/m^2]
Scenario 1	20	300-450	39-55	50	50-65	59
Scenario 1	100	300-450	44-51	49	55-61	59
Scenario 2	20	300-450	39-55	50	66-81	74
Scenario 2	100	300-450	44-51	49	70-76	74

Table 13.11 Uncorrected and corrected average heat flux for the Ullrigg borehole.

Palaeo-climatic scenario	Averaging interval [m]	Depth interval [m]	Data range: uncorrected heat flux [mW/m^2]	Average uncorrected heat flux [mW/m^2]	Data range: corrected heat flux [mW/m^2]	Average corrected heat flux [mW/m^2]
Scenario 1	20	400-996	18-60	35	29-68	43
Scenario 1	100	400-996	27-45	35	38-52	43
Scenario 2	20	400-996	18-60	35	36-76	51
Scenario 2	100	400-996	27-45	35	44-59	51

The results of the calculations are shown in Figures 13.41 and 13.42 according to Scenario 1, whereas Figures 13.43 and 13.44 demonstrate the results which were obtained according to Scenario 2. Palaeoclimatic corrections are more than 15 mW/m^2 within the uppermost parts of the boreholes according to Scenario 1, and are around 30 mW/m^2 in the case of Scenario 2. The difference is almost double.

In the case of Scenario 1, the average heat flow within the Fyllingsdallen borehole has been calculated from depth of 300 m to 450 m, where the thermal gradient is relatively stable. The depth interval 440-996 m has been chosen to calculate the average value of heat flow within the Ullrigg borehole. The obtained values of heat flux are shown in Tables 13.10 and 13.12. Consequently, the corrected heat flux is 59 mW/m^2 within the Fyllingsdalen borehole and 43 mW/m^2 within the Ullrigg borehole according to palaeoclimatic Scenario 1. The obtained corrected heat fluxes according to Scenario 2 are higher than previous values and are equal to 74 mW/m^2 within the Fyllingsdalen borehole and 51 mW/m^2 within the Ullrigg borehole.

13.8 Summary

In summary, it can be stated that four lithosphere-scale 2D structural models have been constructed for the Bergen and Stavanger areas. These 2D models integrate a combination of all available shallow and deep datasets derived by 3D modelling of three observables, gravity, magnetics and temperature, and thus represent detailed modern knowledge about the structure of these two key areas.

It is important to note that the influence of the palaeoclimatic perturbations is relatively high and is still recognisable at the subsurface within the Bergen and Stavanger areas in terms of reduced uppermost crustal temperatures as a result of continuous cooling since the last glaciations.

Finally, the calculated heat flux is higher within the Bergen area than that in the Stavanger area (cf. Tables 13.10 and 13.11). This difference is mostly controlled by the presence of the Løvstakken granite in the Bergen area with its relatively high radiogenic heat production.

14. HEAT FLOW MAP OF NORWAY

Yuriy Maystrenko, Odleiv Olesen, Trond Slagstad, Harald Elvebakk

In order to understand the relationship between the regional pattern of the heat flow and the major tectonic units of the area under consideration, a heat flow map of Norway and adjacent areas has been built. Construction of the heat flow map has been carried out using a regional-scale dataset from Slagstad et al. (2009) and recently released heat flow data (Pascal & Midttømme 2006, Pascal 2009, Pascal et al. 2010, Rudlang 2010, Müller 2012, Maystrenko 2012). According to the map in Fig. 14.1, the data coverage is dense enough over large parts of the study area to be used for the regional-scale heat flow map. The most dense heat flow datasets are situated within the Mid-Norwegian continental margin where several profiles and sites with shallow measurements of the heat flow are located (Langseth & Zielinski 1974, Sundvor et al. 1987, 1989, Ritter et al. 2004). Onshore, these shallow measurements have been supplemented by recently obtained values of the heat flow within the deep boreholes where drill stem test (DST) temperatures and, partially, bottom-hole temperatures are available (Balling 1992, Balling et al. 2006, Pascal & Midttømme 2006, Pascal 2009, Rudlang 2010, Müller 2012). In addition, the data from Eldholm et al. (1999) have been used at the Norwegian continental margin. Within the mainland, the published literature values from Swanberg et al. (1974), Heier & Grønlie (1977), Eriksson & Malmqvist (1979), Järvimäki & Puranen (1979), Puranen et al. (1968), Malmqvist et al. (1983), Lindqvist (1984), Kukkonen (1987, 1988, 1989), Eldholm et al. (1999), Hurter & Haenel (2002), Mottaghy et al. (2005) have been extended by using new measurements of the heat flow in the frames of the Kontiki (Olesen et al. 2007b, Slagstad et al. 2009) and the HeatBar (Pascal et al. 2010) projects. Furthermore, newly calculated heat flow values in the Fyllingsdalen and Ullrigg boreholes from the present study (Maystrenko 2012) have been also used. Therefore, the data, obtained from a variety of datasets, provide a basis for a regional evaluation of the heat flow distribution within the study area in relation to the large-scale tectonic units of northern Europe. All datasets were compiled together and interpolated by using a minimum curvature gridding method with a horizontal resolution of 10 km to obtain the new heat flow map of Norway and adjacent areas (Fig. 14.2).

The obtained heat flow map (Fig. 14.2) shows that the regional pattern is locally disturbed by the short wavelength signals. This is especially pronounced at the Mid-Norwegian continental margin where the large amount of the input data is restricted to relatively small area and, therefore, some local peaks are still recognisable on the map. In order to remove the influence of the local structures, all wavelengths of the interpolated heat flow smaller than 50 km have been filtered out. The result of filtering is shown in Fig. 14.3.

There is a correlation between the thickness of the crust (Fig. 12.17) and the deep heat flow distribution (Fig. 14.3). Where the base of the crust and lithosphere are deeply located, the interpolated heat flow is generally low and vice versa. Actually, thickness of the crust is

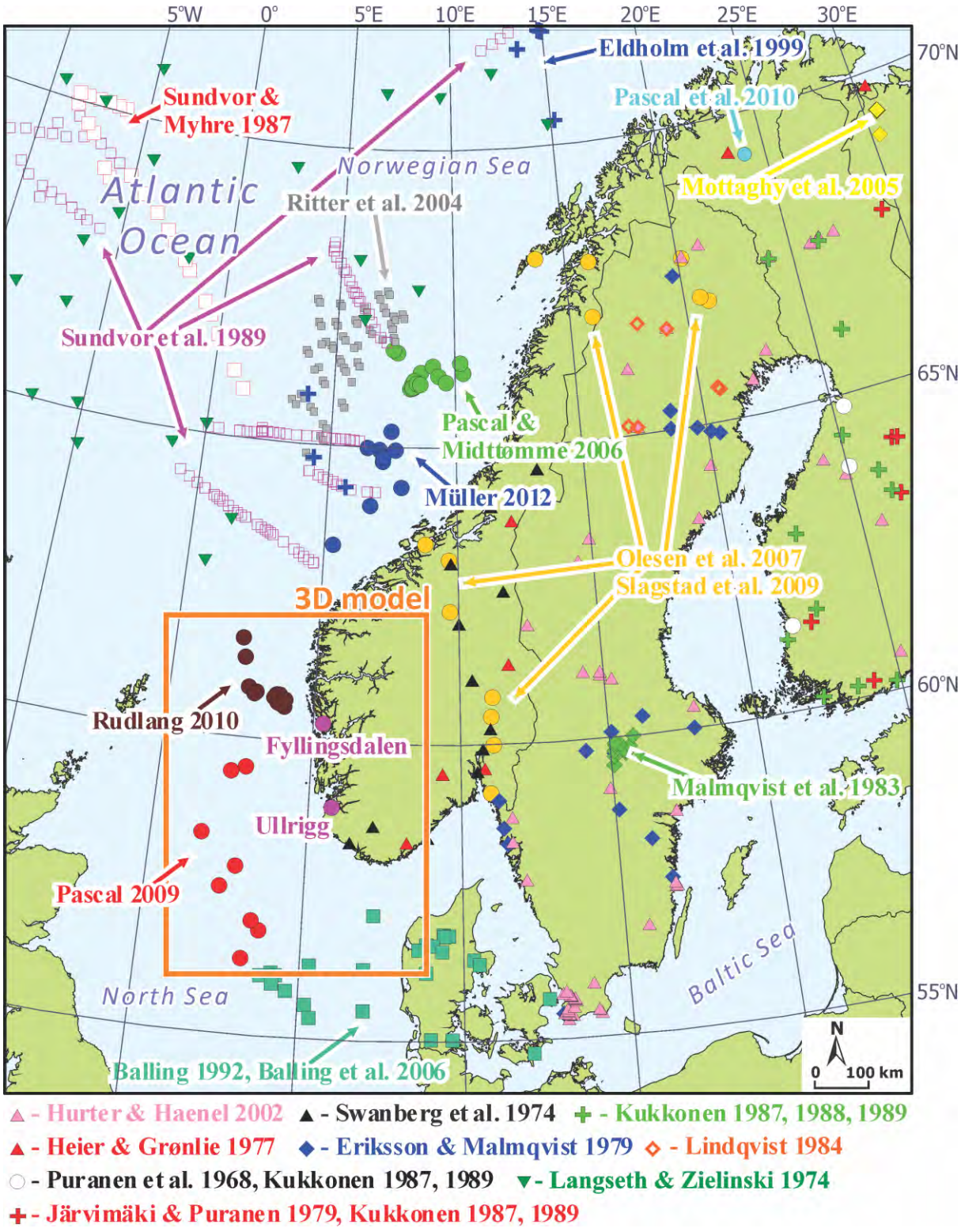

Figure 14.2. Datasets used for the heat flow map of Norway and adjacent areas.

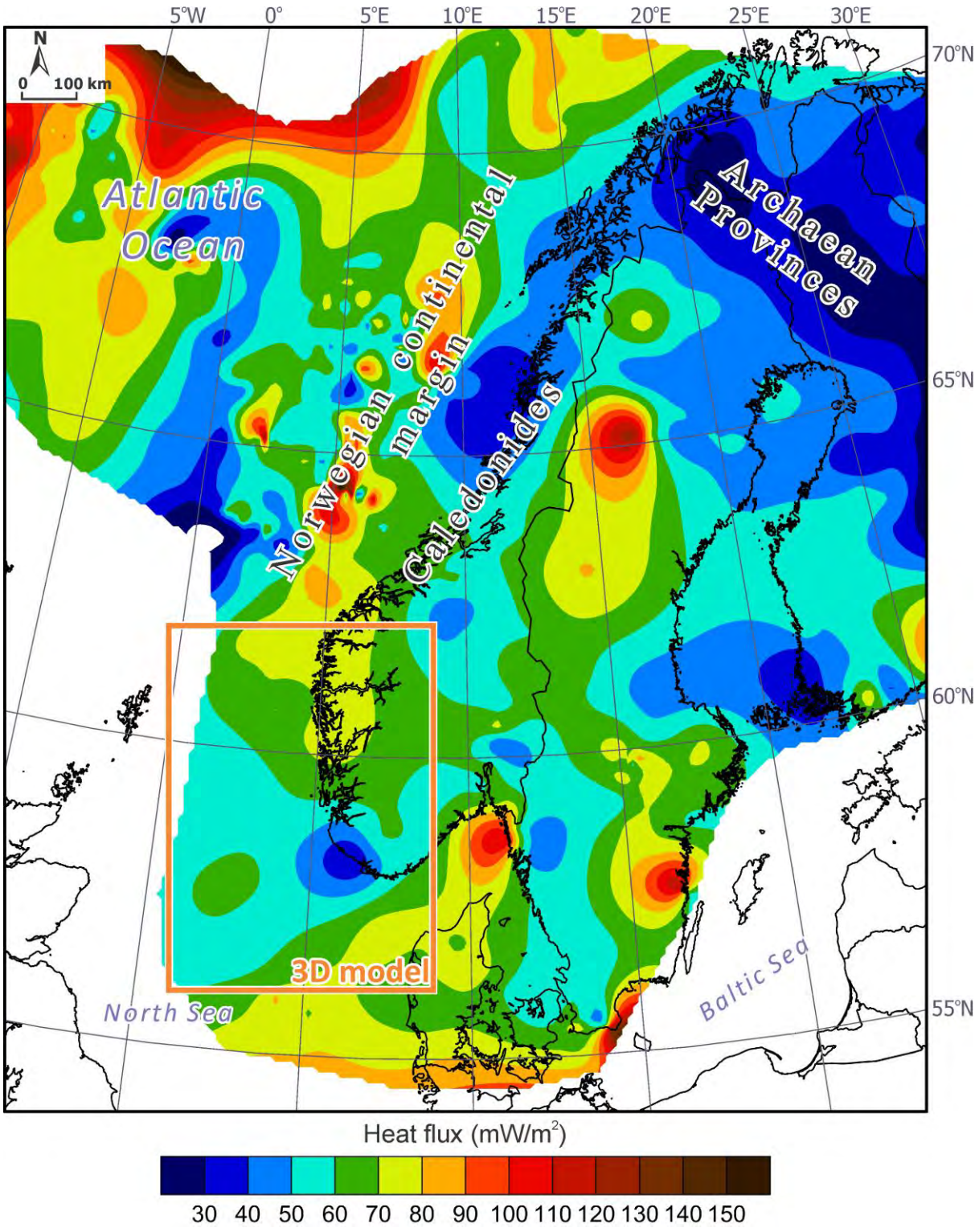

Figure 14.2 Heat flow map of Norway and adjacent areas.

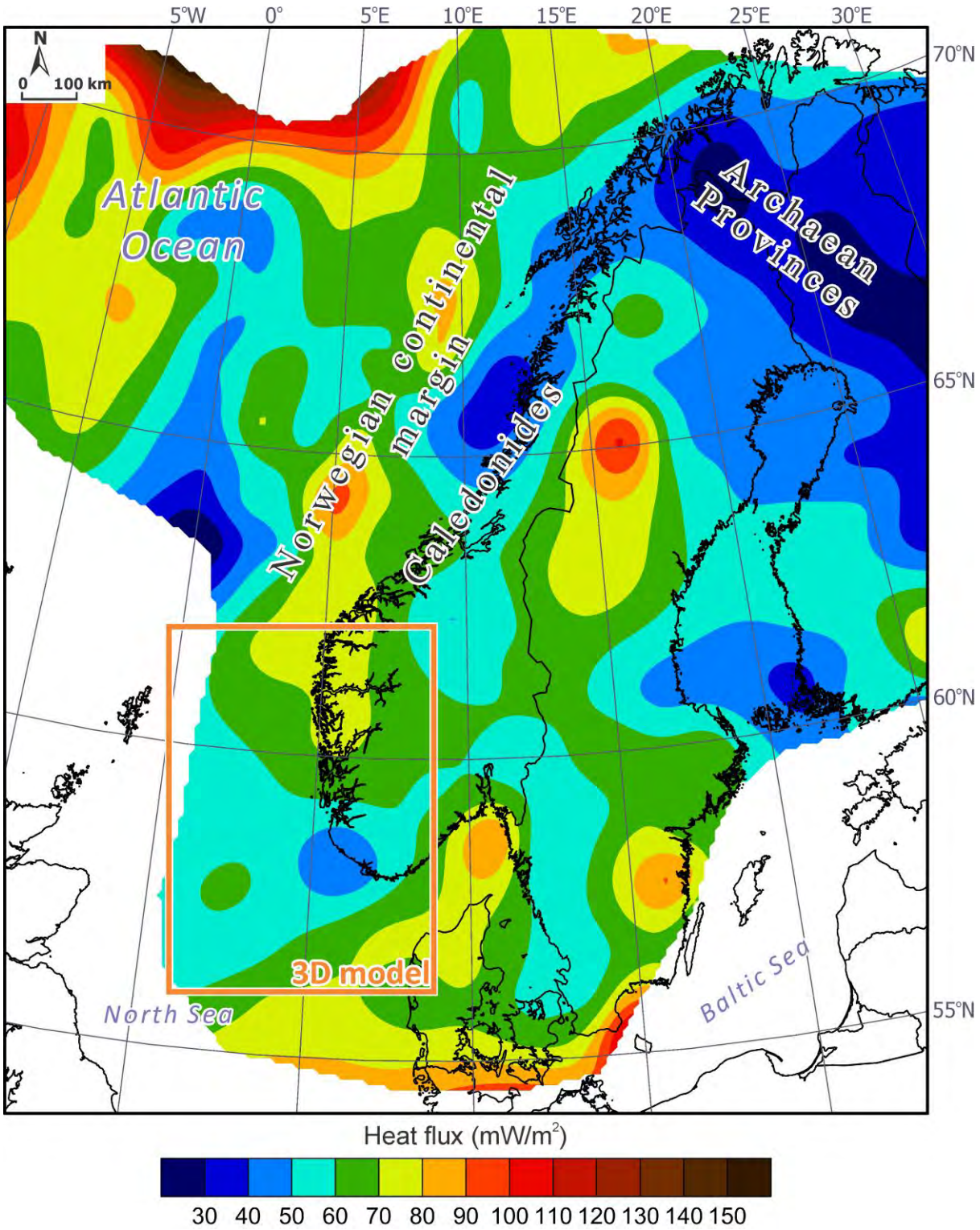

Figure 14.2. Low-pass filtered heat flow map of Norway and adjacent areas. Wavelengths smaller than 50 km are filtered out.

controlled by the age of the crust. Therefore, the pronounced heat flow minimum is located within the oldest parts of the study area in the north of Scandinavia where the Achaean core of the Fennoscandian Shield is present. There, the heat flow is less than 30 mW/m^2. On the other hand, the heat flow maxima over the mainland complicate this regional trend of the deep heat flow in places where the crystalline rocks are characterised by the high content of radioactive elements and, thus, the increased radiogenic heat production.

Within the northern North Sea, the obtained values of the heat flux are in the range of 40-50 mW/m^2 on average. Towards the north, the Norwegian continental margin is characterised by the higher heat flow compared to the North Sea and reach more than 80 mW/m^2 within the areas where the influence of the vertical fluids migration can be significant (e.g., Ritter et al. 2004). Increasing of the heat flow is also observed towards the Mid-Atlantic Ridge.

15. CONCLUSIONS

1) The AMAGER mapping indicates that the Norwegian strandflat is an exhumed, weathered and peneplaned surface. We conclude that this Late Triassic to Early Jurassic surface was modified and levelled during Pleistocene erosion.
2) This base level surface was preserved beneath Late Jurassic and Cretaceous sediments until the Neogene.
3) The heat generation of the mainland basement rocks varies by almost one order of magnitude, from less than 1 $\mu W/m^3$ to more than 7 $\mu W/m^3$.
4) The observed thermal gradients are 16.5 $^{\circ}$C/km in Fyllingsdalen and 13 $^{\circ}$C/km at Ullandhaug.
5) Tentative palaeoclimatic corrections for Fyllingsdalen and Ullandhaug vary from 15 to 30 mW/m² (i.e., 20-40 % of the original heat-flow values).
6) Two different scenarios show corrected heat-flow values which vary from 43 to 51 mW/m² at Ullandhaug and from 59 to 74 mW/m² in Fyllingsdalen.
7) The increased heat flow in Fyllingsdalen is attributed to high values of radiogenic heat production within the Løvstakken granite.
8) The observed low heat flow in the Stavanger area indicates that the Rogaland Igneous Province extends to the north as well as to the west below the Egersund Basin, as also revealed by the observed negative aeromagnetic anomalies.
9) Granites rocks with high radiogenic heat production generate, on the other hand, a higher heat flow in the Fyllingsdalen area to the west of Bergen. The aeromagnetic map shows that the Løvstakken granite extends to the west below the Stord Basin and will consequently cause an increased temperature within this basin.
10) The observed and modelled heat flow is strongly controlled by the lithology and structures in the crust. The temperature at a depth of 5 km in the Egersund and Stord basins is, for example, estimated to c. 155° and 170°C, respectively, a difference which is mainly due to varying heat production in the basement rocks. The heat-producing granites beneath the Stord Basin can locally give an even higher temperature.
11) A large number of Quaternary sand channels has been mapped in the Norwegian North Sea to the west of the Norwegian Channel.
12) The existing subcrop map along the west coast of Norway has been corrected.
13) Onshore, several regional and coinciding gravity and magnetic anomalies can be attributed to lower crustal rocks transported to the upper crust as extensional domes and core complexes during late phases of the Caledonian orogeny.
14) The Nordfjord-Sogn Detachment Zone continues to the south into the Bergen Arc Shear Zone.
15) The Hardangerfjord Shear Zone bends to the south at the coast and continues southwards along Karmsundet.
16) The Sveconorwegian Kongsberg-Bamble suture zone continues across the Skagerrak into the Kattegat.
17) The new aeromagnetic compilation reveals a large number of detailed onshore-offshore structures.

16. OUTLOOK AND RECOMMENDATION FOR COOP PHASE II

1. Extend the airborne geophysical mapping northwards and eastwards to Mid Norway and the mountainous part of southern Norway (Fig. 16.1) with two new surveys: TRAS-13 (Trøndelag Region Airborne Survey 2013) and STAS-13 (Stavanger-Trondheim Aeromagnetic Survey 2013).
2. Generate a new crustal and thermal model of the Mid Norway onshore-offshore area.
3. Check the possibility that the observed high heat flow on the Haltenbanken can be attributed to a westward extension of the Transcandinavian Igneous Belt (TIB) occurring on the mainland of Trøndelag.
4. Improve the existing North Sea crustal model by integrating the magnetic data into the model.
5. Extend the AMAGER mapping of deep weathering to the strandflat of Mid Norway.
6. Extend the heat-production mapping to Mid Norway.
7. Harmonise the heat-production data based on airborne radiometrics with heat production calculated from chemical analysis of bedrock samples.
8. One of the uncertainties in the heat-flow calculations and temperature modelling is the contribution of the palaeoclimatic effect. We suggest, therefore, to extend the temperature logging of the Ullrigg well at Ullandhaug in Stavanger to a vertical depth of c. 1600 m. NGU has recently acquired a new winch and a 2000 m cable for the logging tools and we plan to carry out the new logging in March 2013.
9. It has not been possible to trace the known Permo-Triassic dykes on the new high-resolution aeromagnetic map. Follow-up fieldwork is needed to find out if this phenomenon is related to the small width of the dykes (a few decimetres) or to a low magnetisation.
10. Integrate the onshore-offshore faults with the new compilation of 1:250,000 bedrock maps along the coast.
11. Carry out a micropaleontological study of the NPD core sample from well 25/12-1 to find a more accurate date. Seismic interpretations may indicate a Triassic age rather than the Devonian age indicated in the original well log.

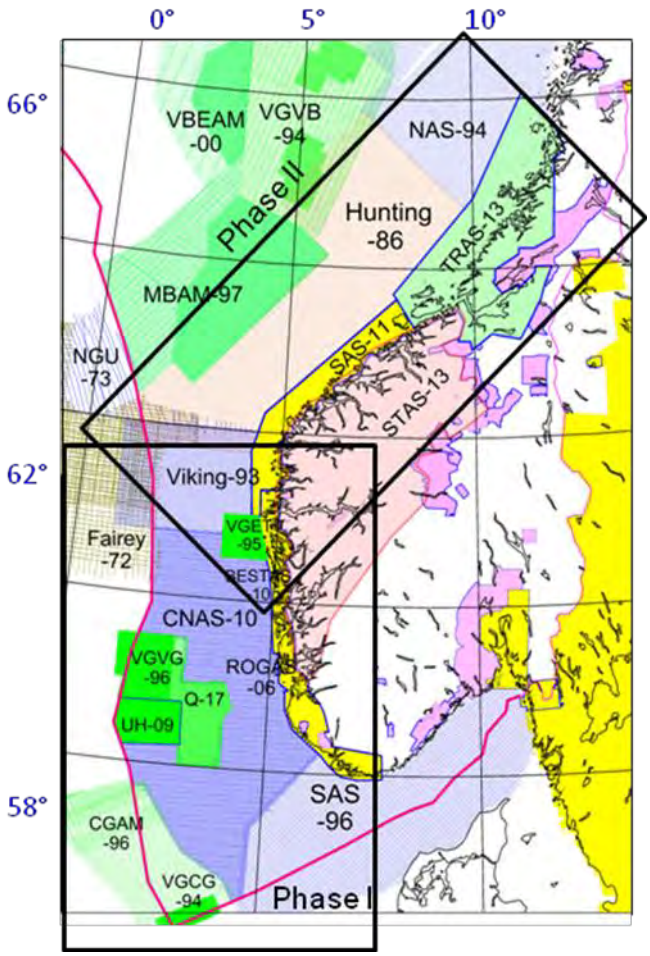

Figure 16.1. Overview map showing the existing surveys and the planned TRAS-13 and STAS-13 surveys within the Coop Phase I and II areas. The TRAS-13 (Trøndelag Region Airborne Survey 2013) is a combined aeromagnetic and radiometric survey with a line spacing of 250 m and 60 m flight altitude. The STAS-13 (Stavanger-Trondheim Aeromagnetic Survey 2013) will be flown with a line spacing of 1 km and a regional draping at 230 m altitude.

Acknowledgements

Fugro Airborne Surveys from Johannesburg in South Africa, Novatem from Mont-Saint-Hilaire in Québec and Fly Taxi Nord in Tromsø carried out the airborne surveys. Drillcon Core Group from Nora in Sweden carried out the core drilling in Fyllingsdalen. The NTNU and University of Tromsø students Iryna Podtykan, Kjetil Skrede, Therese Rudlang and Ingrid Skrede collected bedrock samples and made gamma spectrometer measurements in the Bergen and Stavanger regions. Clea Fabian, Melanie Mesli and Kjetil Skrede carried out the measurements of density and magnetic properties in NGUs laboratory. Bjørn Willemoes-Wissing at NGU analysed the thermal conductivity of the samples from the Fyllingsdalen drillcore and samples from the vicinity of the Ullrigg drill site. Ana Banica, Tomm Berg and Bente Kjøsnes at NGU carried out chemical analysis of groundwater samples from the Fyllingsdalen drillhole. BayernGas Norge, BKK, ConocoPhillips Norge, Det norske oljeselskap, Eni Norge, E.ON E&P Norge, GdF Suez E&P Norge, Lundin Norway, Maersk Oil Norway, NGU, Noreco, Oljedirektoratet, Repsol Exploration Norge, RWE Dea Norge, Statoil, Total E&P Norge, VNG Norge and Wintershall Norge financed the study. The sponsor representatives Mats Andersson, Morten Bergan, Dag Bering, Tom Bugge, Michele Marco Comisso, Christine Fichler, Grim Gjeldvik, Christian Gram, Ebbe Hartz, Henning Hovland, Astrid Haavik, Robert P. Johannessen, Ivar B. Kristvik, Jan Erik Lie, Anne-Lise Jensen Lysholm, Ingrid Magnus, Kathrin Mälzer, Chris Parry, Morten Sand, Reinert Seland, Marie Schneider, Inger Flesland Strass, Jan Strømmen, Stephen Tarran, Filippos Tsikalas, Alastair Welbon, Tor Atle Wicklund and Alv Aanestad followed the progress of the project and gave advice during the different stages of the work tasks. PGS Multiclient (Volker Dirks) gave permission to include maps from their North Sea Digital Atlas (NSDA) in the present Coop Phase I report. TGS-NOPEC Geophysical Company (Reidun Myklebust) permitted us to display the Utsira High Aeromagnetic Survey 2009 (UHAM-09) and the two seismic lines, NSR06-31174 and NSR06-31142-2 in the present report. Exploro (Tomas Kjennerud) and Det norske oljeselskap (Tom Bugge) allowed us to utilise confidential heat-flow data from the southern North Sea. Åse Minde compiled the report. David Roberts read the report and improved the English text. We express our sincere thanks to all these persons, companies and institutions.

REFERENCES

Ahmad, J. & Schmitt, D. 2006: Reservoir characteristics of a Quaternary channel: Incorporating rock physics in seismic and DC resistivity surveys. *Abstract, 2006 CSPG CSEG Convention*, 306-314

Andersen, B.G. & Borns Jr., H.W. 1994: The Ice Age World. Scandinavian University Press (Universitetsforlaget AS), Oslo. 208 pp.

Andersen, O. B., & Knudsen P. 1998: Gravity anomalies derived from the ERS-1 satellite altimetry, Kort og Matrikelstyrelsen, Copenhagen.

Andersen, O. B., Knudsen P., & Berry P. 2010: The DNSC08GRA global marine gravity field from double retracked satellite altimetry, *Journal of Geodesy, Volume 84, Number 3, DOI: 10.1007/s00190-009-0355-9.*

Andersen, T.B., Torsvik, T.H., Eide, E.A., Osmundsen, P.T. & Faleide, J.I. 1999: Permian and Mesozoic extensional faulting within the Caledonides of Central Norway. Journal of the Geological Society, London, 156, 1073-1080.

Andreoli, M. A. G., Hart, R. J., Ashwal, L. D. & Coetzee, H. 2006: Correlations between U, Th content and metamorphic grade in the Western Namaqualand Belt, South Africa, with implications for radioactive heating of the crust. *Journal of Petrology 47*, 1095-1118.

Archie, G.E. 1942: The electrical resistivity log as an aid in determining some reservoir characteristics. *Petroleum Technology 5,* 1422 – 1430.

Artemieva, I.M., Thybo, H. & Kaban, M.K. 2006: Deep Europe today: geophysical synthesis of the upper mantle structure and lithospheric processes over 3.5 Ga. *In* Gee D.G. & Stephenson, R.A. (eds.), European Lithosphere Dynamics, *Geol. Soc, London, Mem.* 32, The Geological Society Publishing House, Bath, pp. 11-41. doi: 10.1144/GSL.MEM.2006.032.01.02.

Bainbridge, G., Musselman, C., Whitehead, N. & McDonald, N. 2002: Euler 3D Deconvolution (v5.1.5). Processing, analysis and visualization system for 3D inversion of potential field. Tutorial and User guide. *Geosoft Manual*, 66 pp.

Baldschuhn, R., Binot, F., Fleig, S. & Kockel, F. 2001: Geotektonischer Atlas von Nordwest-Deutschland und dem deutschen Nordsee-Sektor - Strukturen, Struckurenwicklung, Paläogeographie. *Geologisches Jahrbuch A* 153, 1-88, 3 CD-Rs.

Balling, N. 1992: Denmark. *In* Hurtig, E., Cermák, V., Hänel, R. & Zui, V. (eds), *Geothermal Atlas of Europe*, Vol. Hermann Haack, Gotha, pp. 25-28.

Balling, N., Breiner, N. & Waagstein, R., 2006: Thermal structure of the deep Lopra-1/1A borehole in the Faroe Islands. *Geological Survey of Denmark and Greenland Bulletin* 9, 91-107.

Barbosa, V.C.F., Silva, J.B.C. & Medeiros, W.E. 2000: Making Euler deconvolution applicable to small ground magnetic surveys. *Journal of Applied Geophysics* 43(1), 55-68.

Bartlein, P.J., Anderson, K.H., Anderson, P.M., Edwards, M.E., Mock, C.J., Thompson, R.S., Webb, R.S., Webb III T. & Whitlock, C. 1998: Palaeoclimate simulations for North America over the past 21,000 years: Features of the simulated climate and comparisons with palaeoenvironmental data. *Quaternary Science Reviews* 17, 549-585.

Barton, P. & Wood, R. 1984: Tectonic evolution of the North Sea basin: crustal stretching and subsidence. *Geophys. J. R. astr. Soc.* 79, 987-1022, doi: 10.1111/j.1365-246X.1984.tb02880.x.

Barton, P.J. 1986: The relationship between seismic velocity and density in the continental crust - a useful constraint?. *Geophys. J. R. astr. Soc.* 87, 195-208, doi: 10.1111/j.1365-246X.1986.tb04553.x.

Bea, F., Montero, P. & Zinger, T. 2003: The nature, origin, and thermal influence of the granite source layer of Central Iberia. *Journal of Geology 111*, 579-595.

Bingen, B., Davis, W.J. & Austrheim. H, 2000: Zircon U-Pb geochronology in the Bergen arc eclogites and their Proterozoic protoliths, and implications for the pre-Scandian evolution of the Caledonides in western Norway. *Geological Society of America Bulletin* 113, 640-649.

Bjørkum, P.A., Oelkers, E.H., Nadeau, P.H., Walderhaug, O. & Murphy, W.M. 1998: Porosity prediction in quartzose sandstones as a function of time, temperature, depth, stylolite frequency, and hydrocarbon saturation. AAPG Bulletin – American Association of Petroleum Geologists 82, 637-648.

Blakely, R. 1995: Potential Theory in Gravity and Magnetic Applications. *Cambridge University Press*, 461 pp.

Blakely, R.J. & Simpson, R.W. 1986: Approximating edges of source bodies from magnetic or gravity anomalies. *Geophysics* 51, 1494-1498.

Bockelie, J.F. & Nystuen, J.P. 1985: The southeastern part of the Scandianvian Caledonides. *In*: Gee, D.G. & Sturt, B.A. (eds.) *The Caledonian Orogeny - Scandinavia and related areas.* John Wiley & Sons, Chichester, 69-88.

Boundy, T.M., Mezger, K. & Essene, E.J. 1997: Temporal and tectonic evolution of the granulite-eclogite association from the Bergen Arcs, western Norway. *Lithos* 39, 159-179.

Brigaud, F., Vasseur, G. & Caillet, G, 1992: Thermal state in the north Viking Graben (North Sea) determined from oil exploration well data, *Geophysics. 57, 1*, 68-88.

Britze, P. & Japsen, P. 1991: The Danish Basin. "Top Zechstein" and the Triassic (two-way traveltime and depth, thickness and interval velocity). Geological map of Denmark 1: 400 000. Geological Survey of Denmark, Map Series 31.

Bryhni, I. & Sturt, B.A. 1985: Caledonides of southwestern Norway. *In*: Gee, D.G. & Sturt, B.A. (eds.) *The Caledonian Orogeny - Scandinavia and related areas.* John Wiley & Sons, Chichester, 89-107.

Bøe, R. & Bjerkli, K. 1989: Mesozoic sedimentary rocks in Edøyfjorden and Beitstadfjorden, central Norway: implications for the structural history of the Møre-Trøndelag Fault Zone. *Marine Geology 87*, 287-299

Bøe, R., Mørk, M.B.E., Roberts, D. & Vigran, J.O. 2005: Possible Mesozoic sediments in fault and brecciation zones detected in Frøyfjorden, Mid Norway. *Norges geologiske undersøkelse Bulletin 443,* 29–35.

Bøe, R., Fossen, H. & Smelror, M. 2010: Mesozoic sediments and structures onshore Norway and in the coastal zone. *Norges geologiske undersøkelse Bulletin 450*, 15-32.

Calcagnile, G., Del Gaudio, V. & Pierri, P. 1997: Lithosphere-asthenosphere system in shield areas of North America and Europe. *Annals of Geophysics* 40 (5), 1043-1056, DOI: 10.4401/ag-3850.

Carstens, H. 2012: Torghatthullet, et resultat av mange prosesser. *GEO 15, 8,* 26-29.

Čermak, V. & Rybach, L. 1982: Thermal properties: Thermal conductivity and specific heat of minerals and rocks, *In* Angenheister, G., (ed.), Landolt-Börnstein, *New Series, Geophysics and space research*, Volume 1, subvolume A: Berlin, Springer, p. 305–343.

Childers, V. A., McAdoo, D. C., Brozena, J. M. & Laxon, S. W. 2001: New gravity data in the Arctic Ocean - Comparison of airborne and ERS gravity. *Journal of Geophysical Research* ***106****(B5)*.

Christiansson, P., Faleide, J. I. & Berge, A. M. 2000: Crustal structure in the northern North Sea from deep seismic reflection and refraction data. In: A. Nøttvedt et al. (eds): *Dynamics of the Norwegian Margin*. The Geological Society of London Special Publication, 167, 15-40.

Christie, P.A.F. 1982: Interpretation of refraction experiments in the North Sea, *Phil. Trans. R. Soc. Lond.* A, 305, 101–112, doi: 10.1098/rsta.1982.0028.

Clauser, C. 2011: Thermal storage and transport properties of rocks, *In* Gupta, H. (ed.), Heat capacity and latent heat, *Encyclopedia of Solid Earth´s Geophysics, 2nd ed.* Vol. 2, 1423-1431.

Clauser, C. & Huenges, E. 1995: *Thermal Conductivity of Rocks and Minerals, Rock Physics and Phase Relations, A Handbook of Physical Constants,* AGU reference shelf 3.

Cooper, G.R.J. & Cowan, D.R. 2006: Enhancing potential field data using filters based on the local phase. *Computers & Geosciences 32 (10)*, 1585–1591.

Davies, J., Mushayandebvu, M. & Smith, R. 2004: Magnetic detection and characterization of Tertiary and Quaternary buried channels. *SEG Expanded Abstracts 23*, 734, 4 pp.

Davis, B.A.S., Brewer, S., Stevenson, A.C., Guiot, J. & Data Contributors 2003: The temperature of Europe during the Holocene reconstructed from pollen data. *Quaternary Science Reviews* 22 (15-17), 1701-1716.

Davis, M.W. 2010: A receiver function study of the crust and mantle beneath the British Isles. *Ph.D. Dissertation*, University of Cambridge, Robinson College, 192 pp.

Davis, M.W., White, N.J., Priestley, K.F., Baptie, B.J. & Tilmann, F.J. 2012: Crustal structure of the British Isles and its epeirogenic consequences. *Geophys. J. Int.* 190, 705-725, doi: 10.1111/j.1365-246X.2012.05485.x.

Dobinski, W. 2011: Permafrost. *Earth´s-Science Reviews* 108, 158–169.

Dragoi-Stavar, D., & Hall S. 2009: Gravity modeling of the ocean-continent transition along the South Atlantic margins. *Journal of Geophysical Research (Solid Earth), 114(B13), 09401.*

Ebbing, J. & Olesen, O. 2010: New compilation of to basement and basement thickness for the Norwegian continental shelf reveals the segmentation of the passive margin system. *In* Vining, B.A. & Pickering, S.C. (eds.) Petroleum Geology: From mature basins to new frontiers. *Proceedings of the 7th Petroleum Geology Conference. Petroleum Geology Conference Series 7*, Geological Society of London, 885-897.

Ebbing, J., Gernigon, L., Pascal, C., Olesen, O. & Osmundsen, P.T. 2009: A discussion of structural and thermal control of magnetic anomalies on the mid-Norwegian margin. *Geophysical Prospecting 57*, 665-681.

Eldholm, O., Sundvor, E., Vogt, P.R., Hjelstuen, B.O., Crane, K., Nilsen, A.K. & Gladczenko, T.P. 1999: SW Barents Sea continental margin heat flow and Håkon Mosby Volcano. *Geo-Marine Letters 19*, 29–37.

Elvebakk, H. 2011: Sammenstilling av resistivitet, seismiske hastigheter og naturlig gammastråling i norske bergarter. *NGU Rapport 2011.042.*

Eken, T., Shomali, Z.H., Roberts, R. & Bödvarsson, R. 2007: Upper-mantle structure of the Baltic Shield below the Swedish National Seismological Network (SNSN) resolved by teleseismic tomography. *Geophys. J. Int.* 169, 617-630, doi: 10.1111/j.1365-246X.2007.03351.x.

Elvebakk, H. & Saintot, A. 2011: Geofysisk logging av borehull på Alstein, Randaberg kommune, Rogaland. *NGU Rapport 2011.032.* Florio, G., Fedi, M. & Pasteka, R. 2006: On the application of Euler deconvolution to the analytic signal. *Geophysics 71(6)*, L87-L93.

Erickson, D. 2004: Crustal structure beneath an exposed eclogite terrain, southwestern Norway: inferred from wide-angle seismic techniques. *Master Thesis University of Wyoming*, USA.

Eriksson, K.G. & Malmqvist, D. 1979: A review of the past and present investigations of heat flow in Sweden. *In* Cemak, V. & Rybach, L. (eds.), *Terrestrial Heat Flow in Europe*. Springer, Berlin, 267-277.

Evans, T.R. 1977: Thermal properties of North Sea rocks. *The Log Analyst* 8, 3-12.

Falkum, T. 1982: Geologisk kart over Norge, berggrunnskart Mandal – M 1:250.000. Norge geologiske undersøkelse, Trondheim.

Fichler, C., T. Odinsen, H. Rueslatten, O. Olesen, J.E. Vindstad, & Wienecke, S. 2011: Crustal inhomogenetics in the Northern North Sea from potential field modeling: Inherited structure and serpentinites?, Tectonophysics, 510, 172-185 (2011), doi: 10.1016/j.tecto.2011.06.026.

Flem, B., Grimstvedt, A., Slagstad, T. & Skår, Ø. 2005:. Bulkanalyse av Th og U i bergartsprøver med LA-ICP-MS. Metodebeskrivelse. *NGU Rapport 2005.031*.

Fossen, H. 1998: Advances in understanding the post-Caledonian structural evolution of the Bergen area, West Norway. *Norsk Geologisk Tidsskrift 78,* 33-46.

Fossen, H. & Dunlap W.J. 1999: On the age and tectonic significance of Permo-Triassic dikes in the Bergen-Sunnhordland region, southwestern Norway. *Norsk Geologisk Tidsskrift* 69, 169-178.

Fossen, H. & Hurich, C.A. 2005: The Hardangerfjord shear zone in SW Norway and in the North Sea; a large-scale low-angle shear zone in the Caledonian crust. *Journal of the Geological Society, London,*162, 675-687.

Fossen, H., Mangerud, G., Hesthammer, J., Bugge, T. & Gabrielsen, R.H. 1997: The Bjorøy Formation: A newly discovered occurrence of Jurassic sediments in the Bergen Arc System. *Norsk Geologisk Tidsskrift 77,* 269-287.

Furnes, H. & Lippard, S.J. 1983: Devonian lavas from Solund, West Norway. Field relationships and geochemistry. *Norges geologiske undersøkelse Bulletin 382,* 1-16.

Færseth, R. 1996: Interaction of Permo-triassic and Jurassic extensional fault-blocks during the development of the northern North Sea. Journal of the Geolgical Society, London, 153, 931-944.

Geissler, W.H., Sodoudi, F. & Kind, R. 2010: Thickness of the central and eastern European lithosphere as seen by S receiver functions. *Geophys. J. Int.* 181, 2, 604-634, doi: 10.1111/j.1365-246X.2010.04548.x.

Geosoft 2010a: Montaj MAGMAP filtering, 2-D frequency domain processing of potential field data, Extension for Oasis Montaj v7.1. Geosoft Incorporated, 79 pp.

Geosoft 2010: Oasis montaj v7.1 MAGMAP Filtering. 2D frequency domain processing of potential Field Data tutorial. *Geosoft Incorporated,* 70 pp.

Geosoft 2010b: OASIS Montaj v7.2 Mapping and processing system, The core software platform for working with large volume spatial data. Quick start tutorials. Geosoft Incorporated, 325 pp.

Geosoft 2011: Oasis montaj v7.3 Mapping and processing system. The core software platform for working with large volume spatial data. Quick start tutorials. *Geosoft Incorporated,* 289 pp.

Gernigon, L., Marello, L., Mogaard, J.O., Werner, S.C. & Skilbrei, J.R. 2007: Barents Sea Aeromagnetic Survey BAS - 06: Acquisition-processing report and preliminary interpretation. NGU Report 2007.035, Geological Survey of Norway, Trondheim, 142 pp.

Ghienne, J. F. & Deynoux, M., 1998: Large-scale channel fill structures in Late Ordovician glacial deposits in Mauritania, Western Sahara. *Sedimentary Geology 119*, 141-159.

Gjelle, S., Gustavson, M., Qvale, H. & Skauli, H. 1985: Berggrunnsgeologisk kart Melfjorden 1928 III, 1:50 000, foreløpig utgave. Norges geologiske undersøkelse, Trondheim.

Götze H.-J. & Schmidt, S. 2010: IGMAS+: A new 3D gravity, FTG and magnetic modeling software tool: *ASEG-PESA Airborne Gravity Workshop, Expanded Abstracts*, 91-96, ISBN 978-1-921781-17-9.

Götze, H.J. & Lahmeyer, B. 1988: Application of three-dimensional interactive modeling in gravity and magnetics. *Geophysics* 53, 1096-1108.

Götze, H.J. 1978: Ein numerisches Verfahren zur Berechnung der gravimetrischen Feldgrößen drei-dimensionaler Modellkörper. *Arch. Met. Geoph. Biokl. Ser.* A(25), 195-215.

Grad, M., Tiira, T. & ESC Working Group 2009: The Moho depth map of the European Plate. *Geophys. J. Int.* 176, 279-292, doi: 10.1111/j.1365-246X.2008.03919.x.

Gregersen, S. & Voss, P. 2002: Summary of project TOR: delineation of a stepwise, sharp, deep lithosphere transition across Germany-Denmark-Sweden. *Tectonophysics 360*, 61-73, doi:10.1016/S0040-1951(02)00347-5.

Gunn, P.J. 1997: Application of aeromagnetic surveys to sedimentary basin studies, *Journal of Australian Geology & Geophysics 17***,** 133-144.

Gyllencreutz, R., Backman, J., Jakobsson, M., Kissel, C. & Arnold, E. 2006: Post Glacial Palaeoceanography in the Skagerrak. *The Holocene 16*, 975-985.

Hartz, E.H., Martin, M.W., Andresen, A. & Andersen, T.B. 2002: Volcanic rocks in the Devonian Sound Basin, Western Norway: large landslides of Silurian (439 Ma) rhyolites. *Journal of the Geological Society, London,* 159, 121-128.

Heier, K.S. & Grønlie, G. 1977: Heat flow-heat generation studies in Norway. *In* Saxena, S.K. & Bhattacharji, S. (eds.), *Energetics of geological processes*. Springer-Verlag, New York, 217–235.

Helland, A. 1885: Om jordens løse afleiringer. Meddelelse fra Den naturhistoriske Forening i Kristiania, pp. 27–42.

Hofer, D., Raible, C.C., Dehnert, A. & Kuhlemann, J. 2012: The impact of different glacial boundary conditions on atmospheric dynamics and precipitation in the North Atlantic region. *Climate of the Past Discussions* 8(1), 935-949, DOI 10.5194/cp-8-935-2012

Hofmeister, A.M. 1999: Mantle values of thermal conductivity and the geotherm from phonon lifetimes. *Science 283*, 1699-1706.

Hohl, V. 2005: Northern European long term climate archives. *Technical Report TR-05-01*, Swedish Nuclear Fuel and Waste Management Co, Stockholm, Sweden.

Hossack, J.R. 1984: The geometry of listric growth faults in the Devonian basins of Sunnfjord, W. Norway. *Journal of the Geological Society, London,* 141, 629-637.

Hsu, S.-K. 2002: Imaging magnetic sources using Euler's equation. *Geophysical Prospecting 50*, 15-25.

Hurter, S. & Haenel, R. (eds.) 2002: Atlas of geothermal resources in Europe. *EC publ. no. EUR 17811*, Luxembourg.

ICES 2012: Factors affecting the distribution of North Sea fish, http://www.google.no/url?sa=t&rct=j&q=&esrc=s&source=web&cd=1&cad=rja&ved=0CGIQFjAA&url=http%3A%2F%2Fwww.ices.dk%2Fmarineworld%2Ffishmap%2Fpdfs%2Ffactors.pdf&ei=5xwyUOPvJ5KN4gSl_YGwAQ&usg=AFQjCNFP7NOm.

IAEA. 1991: Airborne Gamma Ray Spectrometer Surveying. *Technical Reports Series No.323*

Ihlen, P.M., lneson, P.R. & Mitchell, J. G. 1978: K-Ar dating of clay-mineral alteration associated with ore deposition in the northern part of the Oslo Region. *In* Neumann, E.-R. & Ramberg, I. B. (eds.) *Petrology and Geochemistry of Continental Rifts.* Dordrecht, D. Reidel Publ. Comp., 255-264.

Ihlen, P.M., Ineson, P.R., Mitchell, J.G. & Vokes, F.M. 1984: K-Ar dating of dolerite dykes in the Kongsberg-Fiskum district, Norway, and their relationships with the silver and base metal veins. *Norsk Geologisk Tidsskrift 64*, 87-96.

Ineson, P.R., Mitchell, J.G. & Vokes, F.M. 1975: K-Ardating of epigenetic mineral deposits: An investigation of the Permian metallogenic province of the Oslo Region, southern Norway. *Economic Geology 70*, 1426-1436.

Ineson, P.R., Mitchell, J. G. & Vokes, F.M. 1978: Further KAr determinations on clay mineral alteration associated with fluorite deposition in southern Norway. *In* Neumann, E.-R. & Ramberg, I. B. (eds.) *Petrology and Geochemistry of Continental Rifts,* Dordrecht, D. Reidel Publ. Comp., 265-275.

IOC, IHO & BODC 2003: Centenary Edition of the GEBCO Digital Atlas, published on CD-ROM on behalf of the Intergovernmental Oceanographic Commission and the International Hydrographic Organization as part of the General Bathymetric Chart of the Oceans; British Oceanographic Data Centre, Liverpool, UK.

Iwasaki, T., Sellevoll, M.A., Kanazawa, T., Veggeland, T. & Shimamura, H. 1994: Seismic refraction crustal study along the Sognefjord, south-west Norway, employing ocean-bottom seismometers, *J. Geophys. Int. 119*, 791–808.

Jackson, C. A-L. & Larsen, E. 2008: Temporal constraints on basin inversion provided by 3D seismic and well data: a case study from the South Viking Graben, offshore Norway. *Basin Research 20*, 397-417.

Jackson, C.A-L., Kane, K.E. & Larsen, E. 2010: Structural evolution opf minibasins on the Utsira High, northern North Sea; implications for Jurassic sediment dispersal and reservoir distribution. *Petroleum Geoscience 16*, 105-120.

Japsen, P. 1993: Influence of lithology and Neogene uplift on seismic velocities in Denmark; implications for depth conversion of maps. *AAPG Bulletin* 77, 194-211.

Japsen, P. 1994: Retarded compaction due to overpressure deduced from a seismic velocity/depth conversion study in the Danish Central Trough, North Sea. *Marine and Petroleum Geology* 11, 715-733.

Japsen, P. 1998: Regional velocity-depth anomalies, North Sea Chalk: a record of overpressure and Neogene uplift and erosion. *AAPG Bulletin* 82, 2031-2074.

Japsen, P. 1999: Overpressured Cenozoic shale mapped from velocity anomalies relative to a baseline for marine shale, North Sea. *Petroleum Geoscience 5*, 321-336.

Japsen, P. & Langtofte, C. 1991a: The Danish Basin. “Base Chalk” and the Chalk Group (Two-Way Traveltime and Depth, Thickness and Interval Velocity), Geological Map of Denmark 1:400 000. Geological Survey of Denmark, Copenhagen, Map Series 29.

Japsen, P. & Langtofte, C. 1991b: The Danish Basin. "Top Trias" and the Jurassic-Lower Cretaceous (two-way traveltime and depth, thickness and interval velocity). Geological map of Denmark 1: 400 000. Geological Survey of Denmark, Map Series 30.

Japsen, P., Bonow, J.M., Chalmers, J.A., & Rasmussen, E.S. 2008: Norges fjelde - rodløse realiteter. *Geologisk Nyt 2*, 38-40.

Jaupart, C. & Mareschal, J.-C. (2003). Constraints on crustal heat production from heat flow data. In: Rudnick, R. L. (ed.) *The Crust*. Oxford: Elsevier-Pergamon, 65-84.

Jensen, K. 1983: Calculations on the thermal conditions around a salt diapir. *Geophys. Prospecting* 31, 481–489.

Johnston, S., Hacker, B.R. & Ducea, M.N. 2007: Exhumation of ultrahigh-pressure rcoks beneath the Hornelen segment of the Nordfjord-Sogn Detachment Zone, western Norway. *Geological Society of America Bulletin*, 119, 1232-1248.

Jorde, K., Sigmond, E.M.O. & Thorsnes, T. 1995: Geologisk kart over Norge, berggrunnskart Stavanger – M 1:250.000. Norges geologiske undersøkelse, Trondheim.

Järvimäki, P. & Puranen, M. 1979. Heat flow measurements in Finland. *In* V. Cermák & L. Rybach (eds.), *Terrestrial Heat Flow in Europe*. Springer, Berlin, pp. 172-178.

Karlstrom, K. E. & Williams, M. L. 1998: Heterogeneity of the middle crust: Implications for strength of continental lithosphere. *Geology 26*, 815-818.

Keating, P. & Pilkington, M. 2004: Euler deconvolution of the analytic signal and its application to magnetic interpretation. *Geophysical Prospecting* 52(3), 165-182.

Kellett, R., 2007: A geophysical facies description of Quaternary channels in northern Alberta. *CSEG Recorder 32*, 10, 51-55

Kelly, A., England, R.W. & Maguire, P.K.H. 2007: A crustal seismic velocity model for the UK, Ireland and surrounding seas. *Geophys. J. Int.* 171, 1172-1184, doi: 10.1111/j.1365-246X.2007.03569.x.

Kildal, E.S. 1970: Geologisk kart over Norge, berggrunnskart Måløy – M 1:250.000. Norges geologiske undersøkelse, Trondheim.

Killeen, P. G. & Heier, K. S. 1975: Radioelement distribution and heat production in Precambrian granitic rocks, southern Norway. *Det Norske Videskaps-Akademi, I. Mat.-Naturv. Klasse. Skrifter, Ny Serie 35*, 1-32.

Klemperer, S.L. & White, N. 1989: Coaxial stretching or lithospheric simple shear in the North Sea? Evidence from deep seismic profiling and subsidence. *In* Tankard, A. & Balkwill, H.R. (eds.), Extensional Tectonics and Stratigraphy of the North Atlantic Margins. *Am. Assoc. Pet. Geol. Mem.,* 511-522.

Krogh, E.J, 1977: Evidence of Precambrian continent-continent collision in Western Norway. *Nature 267*, 17-19.

Kukkonen, I. 1987: Vertical variation of apparent and palaeoclimatically corrected heat flow densities in the central Baltic Shield. *Journal of Geodynamics* 8, 33-53.

Kukkonen, I. 1988: Terrestrial heat flow and groundwater circulation in the bedrock in the central Baltic Shield. *Tectonophysics* 156, 59-74.

Kukkonen, I.T. 1989: Terrestrial heat flow and radiogenic heat production in Finland, the central Baltic Shield. *Tectonophysics* 164, 219-230.

Kukkonen, I. T., Rath, V., Kivekäs, L., Šafanda, J. & Cermak, V. 2010: Geothermal studies of the Outokumpu Deep Drill Hole, Finland: Vertical variation in heat flow and palaeoclimatic implications. *Physics of the Earth and Planetary Interiors* 188, 9-25.

Kyrkjebø, R., Gabrielsen, R.H. & Faleide, J.I. 2004: Unconformities related to the Jurassic-Cretaceous synrift-postrift transition of the northern North Sea. Journal of the Geological Society, London, 161, 1-17.

Lambeck, K. 1995: Late Devensian and Holocene shorelines of the British Isles and North Sea from models of glacio-isostatic rebound. *Journal of the Geological Society of London* 152, 437-448.

Langseth, M.G. & Zielinski, G.W. 1974: Marine heat flow measurements in the Norwegian-Greenland Sea and in the vicinity of Iceland. *In* Kristjansson, L. (ed.), *Geodynamics of Iceland and the North Atlantic Area*, Vol. Reidel, Dordrecht, pp. 277-295.

Larsen, E., Sejrup, H.P., Janocko, J., Landvik, J.Y., Stalsberg, K. & Steinsund, P.I. 2000: Recurrent interaction between the Norwegian Channel Ice Stream and terrestrial-based ice across southwest Norway. *Boreas* 29, 185–203.

Lassen, A. & Thybo, H. 2012: Neoproterozoic and Palaeozoic evolution of SW Scandinavia based on integrated seismic interpretation. *Precambrian Research 204-205*, 75-104

Lauritzen, S.E. 2013: Recent mapping and studies in marine abrasion caves in Torghatten, Brønnøy. *In* Nakrem, H.A. & Haukdal, G. (eds.) *Vinterkonferansen 2013, Oslo, January 8-10, 2013. NGF Anstracts and Proceedings of the Geological Society of Norway 1. 2013,* p 80.

Lie, J.E., Grandal, E. & Sørlie, R. 2012: The basement structure, discoveries and reservoir potential on the southern Utsira High. *In* Hendriks, B. and Haukdal, G.K. (eds.) Onshore-offshore relationships on the North Atlantic Margin. *Abstracts and Proceedings of the Geological Society of Norway 2*, 54-56.

Lindqvist, J.G. 1984: Heat flow density measurements in the sediments of three lakes in. Northern Sweden. *Tectonophysics 103*, 121.

Lokhorst, A. 1998: The Northwest European GasAtlas. Netherlands Institute of Applied Geoscience TNO, Haarlem, the Netherlands.

Longva, O. & Thorsnes, T. (eds.) 1997: Skagerrak in the past and at the present—an integrated study of geology, geochemistry, hydrography and microfossil ecology. *Norges Geologiske Undersøkelse Special Publication 8*, 100.

Lutro, O. 2012. Detailed bedrock map from the BESTAS10 - SAS11 area. *Norges geologiske undersøkelse, Trondheim.*

Luyendyk, A. 1997: Processing of airborne magnetic data. *AGSO Journal of Australian Geology and Geophysics 17(2)*, 23-30.

Lyngsie, S.B. & Thybo, H. 2007: A new tectonic model for the Laurentia-Avalonia-Baltica sutures in the North Sea: A case study along MONA LISA profile 3. *Tectonophysics 429*, 201-227, doi:10.1016/j.tecto.2006.09.017.

Lyngsie, S.B. & Thybo, H., Rasmussen, T.M. 2006: Regional geological and tectonic structures of the North Sea area from potential field modeling. *Tectonophysics 413*, 147-170, doi:10.1016/j.tecto.2005.10.045.

Malmqvist, D., Larson, S., Landström, O. & Lind, G. 1983: Heat flow and heat production from the Malingsbo granite, central Sweden. *Bull. Geol. Inst. Univ. Uppsala* 9, 137-152.

Marson, I. & Klingele, E. E. 1993: Advantages of using the vertical gradient of gravity for 3-D interpretation. *Geophysics 58*, 1588-1595.

Mauring, E. & Kihle, O. 2006: Leveling aerogeophysical data using moving differential median filter. *Geophysics, 71,* L5–L11.

Maystrenko, Y. 2012: 2D crustal and thermal modelling within the Bergen and Stavanger areas. *This report*.

Maystrenko, Y.P. & Scheck-Wenderoth, M. 2011: Deep structure of the Central European Basin System and adjacent areas based on integrated 3D gravity and 3D thermal analyses. EGU General Assembly, memory stick: *Geophysical Research Abstracts*, Vol. 13, EGU2011-3588-2, Vienna, Austria.

Maystrenko, Y.P., Bayer, U. & Scheck-Wenderoth, M. 2012: Regional-scale structural role of Permian salt within the Central European Basin System, In Alsop, G.I., Archer, S.G., Hartley, A.J., Grant, N.T., Hodgkinson, R. (Eds), Salt Tectonics, Sediments and Prospectivity. *Geological Society, London, Special Publications* 363, 409-430.

McBride, J.H. & England, R.W. 1999: Window into the Caledonian orogen: Structure of the crust beneath the East Shetland platform, United Kingdom. *Geological Society of America Bulletin* 111, 1030-1041, doi: 10.1130/0016-7606(1999)111<1030:WITCOS>2.3.CO;2.

Midttømme, K., Sættem, J., Roaldset, E. & Zielinski, G. 1995: Thermal Conductivity of Unconsolidated Sediments from the Vøring Basin, Norwegian Sea, *EAEG Extended Abstracts. 2,* 57 Conference, Glasgow, May/June 1995.

Midttømme, K & Roaldset, E. 1999: Thermal conductivity of sedimentary rocks: uncertainties in measurements and modelling. *In* Aplin, A.C., Fleet, A.J. & Macquaker, J.H.S. (eds.) *Muds and Mudstones: Physical and Fluid Flow Properties.* Geological Society, London, Special Publications 158, 45-60.

Miller, H.G. & Singh, V. 1994: Potential field tilt—a new concept for location of potential field sources. *Journal of Applied Geophysics 32*, 213–217.

Mjelde, R., Goncharov, A. & Müller, R.D. 2012: The Moho: Boundary above upper mantle peridotites or lower crustal eclogites? A global review and new interpretations for passive margins, Tectonophysics, doi:10.1016/j.tecto.2012.03.001.

Mogensen T., E. & Korstgard, J. A. 2003: Triassic and Jurassic transtension along part of the Sorgenfrei-Tornquist Zone in the Danish Kattegat. *In* Surlyk, F. & Ineson, J. R. (eds.) *The Jurassic of Denmark and Greenland*. Geological Survey of Denmark and Greenland Bulletin 1, 439-458.

Mosar, J. 2003: Scandinavia's North Atlantic passive margin. *Journal of Geophysical Research 108*, 2360-2377.

Mosar, J., Osmundsen, P.T., Sommaruga, A., Torsvik, T.H. & Eide, E.A. 2002: Greenland-Norway separation: a geodynamic model for the North Atlantic. *Norwegian Journal of Geology 82*, 281–298.

Mottaghy, D., Schellschmidt, R., Popov, Y.A., Clauser, C., Kukkonen, I.T., Nover, G., Milanovsky, S. & Romushkevich, R.A. 2005: New heat flow data from the immediate vicinity of the Kola super-deep borehole: vertical variation in heat flow confirmed and attributed to advection. *Tectonophysics* 401, 119–142.

Müller, C. 2012. Heat Flow Calculation on Halten Terrace. *This report*.

Mushayandebvu, M.F., Lesur, V., Reid, A.B. & Fairhead, J.D. 2004: Grid Euler deconvolution with constraints for 2D structures. *Geophysics 69(2)*, 489-496.

Nadeau, P.H., Bjørkum, P.A. & Walderhaug, O. 2005: Petroleum system analysis: Impact of shale diagenesis on reservoir fl uid pressure, hydrocarbon migration and biodegradation risks. *In* Doré,

A. G. & Vining, B. (eds.) *Petroleum Geology: North-West Europe and Global Perspectives - Proceedings of the 6th Petroleum Geology Conference,* 1267-1274. Geological Society, London.
Nasuti, A., Aarset, M., Brönner, M., Koziel, J. & Lauritsen, T. 2012: Central North Sea Aeromagnetic Survey 2010 (CNAS-10) data acquisition and processing. *NGU Report 2012.023*, 36 pp.
NITG 2004: Geological Atlas of the Netherlands - onshore (1:1000000). Netherlands Institute for Applied Geoscience TNO - National Geological Survey (Utrecht): 103 pp.
Norden, B. & Förster, A. 2006: Thermal conductivity and radiogenic heat production of sedimentary and magmatic rocks in the Northeast German Basin. *AAPG Bulletin* 90, 939–962.
Norden, B., Förster, A. & Balling, N. 2008: Heat flow and lithospheric thermal regime in the Northeast German Basin. *Tectonophysics 460*, 215–229.
Norton, M.G. 1987: The Nordfjord-Sogn detachment, W. Norway. *Norsk Geologisk Tidsskrift* 67. 93-106.
Norwegian Petroleum Directorate (NPD) 2011: The NPD's fact pages; well data summary sheets: http://factpages.npd.no/FactPages/Default.aspx?nav1=wellbore&nav2=PageView|Exploration|All&nav3=6753 . (November 2011)
Novatem internal report 2012: Fixed-wing magnetic and radiometric survey of the Stad Region in Western Norway. *C11089, Airborne survey for NGU - Stad project, Norway 2012.*
Nyland, B., Jensen, L.N., Skagen, J., Skarpnes, O. and Vorren, T.O. 1992: Tertiary uplift and erosion in the Barents Sea: magnitude, timing and consequences. *In* Larsen, R. M., Brekke, H., Larsen, B. T. & Talleraas, E. (eds.) *Structural and tectonic modeling and its applications to Petroleum Geology,* 153-162. Elsevier, Amsterdam.
Olesen, O., Reitan, M. & Sæther, P.O. 1993. Petrofysisk database PETBASE 3.0, Brukerbeskrivelse. *Norges geologiske undersøkelse Internal Report, 93.023*.
Olesen, O., Smethurst, M.A., Torsvik, T.H. & Bidstrup, T. 2004: Sveconorwegian igneous complexes beneath the Norwegian–Danish Basin. *Tectonophysics 387*, 105-130.
Olesen, O., Dehls, J.F., Ebbing, J., Henriksen, H., Kihle, O. & Lundin, E. 2007a: Aeromagnetic mapping of deep-weathered fracture zones in the Oslo Region – a new tool for improved planning of tunnels. *Norwegian Journal of Geology 87*, 253-267.
Olesen, O., Balling, N., Barrère, C., Breiner, N., Davidsen, B., Ebbing, J., Elvebakk, H., Gernigon, L., Koziel, J., Lutro, O., Midttømme, K., Nordgulen, Ø., Olsen, L., Osmundsen, P.T., Pascal, C., Ramstad, R.K., Rønning, J.S., Skilbrei, J.R., Slagstad, T. & Wissing, B. 2007b: KONTIKI Final Report, CONTInental Crust and Heat Generation In 3D. *NGU Report 2007.042*, 438 pp.
Olesen, O., Brönner, M., Ebbing, J., Gellein, J., Gernigon, L., Koziel, J., Lauritsen, T., Myklebust, R., Sand, M., Solheim, D. & Usov, S. 2010: New aeromagnetic and gravity compilations from Norway and adjacent areas – methods and applications. *Petroleum Geology Conference series 7,* 559-586.
Olesen, O., Bering, D., Brönner, M., Dalsegg, E., Fabian, K., Fredin, O., Gellein, J., Husteli, B., Magnus, Ch., Rønning, J.S., Solbakk, T., Tønnesen J.F. & Øverland, J.A. 2012: Tropical Weathering In Norway, TWIN Final Report. *NGU Report 2012.005*, 188 pp.
Olesen, O., Bungum, H., Dehls, J.F., Lindholm, C., Pascal, C. & Roberts, D. 2013: Neotectonics, seismicity and contemporary stress field in Norway – mechanisms and implications. *In* Olsen, L. & Slagstad T. (eds.) *Quaternary Geology of Norway – landscape development, glacier variations, sediments and neotectonics.* NGU Special Publications 13, in press.
Olsen, L. 2006: Fennoscandia M-LWeichselian glacial variations - much more than just local ice-margin fluctuations. In: Peltonen, P., Pasanen, A. (eds.), The 27th Nordic Geological Wintermeeting. *Bulletin of the Geological Society of Finland, Special Issue. Geological Society of Finland,* Oulu, Finland, p. 118.
Ormaasen, D.E. 1976: *Geochemistry and petrology of the mangeritic rocks in Lofoten–Vesterålen.* Cand. real./M.Sc. thesis, University of Oslo.
Osmundsen, P.T., Andersen, T.B., Markussen, S. & Svendby, A.K. 1998: Tectonics and sedimentation in the hanging wall of a major extensional detachment: the Devonian Kvamshesten Basin, western Norway. *Basin Research 10*, 213-234.
Otto-Bliesner, B.L., Brady, E. Clauzet, G. Tomas, R., Levis, S. & Kothavala, Z. 2006: Last glacial maximum and Holocene climate in CCSM3. *J. Climate 19*, 2526-2544.
Pascal, C. 2009: Erogen 08: Heat flow determinations in the Norwegian-Danish Basin. *NGU Report 2009.046*.

Pascal, C. & Midttømme, K. 2006: Impact of recent glacial erosion on subsurface temperatures: the Mid-Norwegian Margin. *NGU Report 2006.088*.

Pascal, C., Rudlang, T., Skrede, I. & Gellein, J. 2011: Assessing the thermal state of the Norwegian North Sea. Presentation at the North Sea Crustal Onshore-Offshore Project meeting, Trondheim February 16th, 2011, 24 slides.

Pascal, C., Aarseth, M., Ebbing, J., Lauritsen, T., Lutro, O. & Olesen, O. , 2010: Quantitative assessment of geothermal resources in the Oslo and Bergen Regions. *NGU Report 2010.054*

Pascal, C., Balling, N., Barrère, C., Davidsen, B., Ebbing, J., Elvebakk, H., Mesli, M., Roberts, D., Slagstad, T. & Willemoes-Wissing, B. 2010: HeatBar Final Report 2010, Basement Heat Generation and Heat Flow in the western Barents Sea - Importance for hydrocarbon systems. *NGU Report 2010.030*.

Pattyn, F. 2010: Antarctic subglacial conditions inferred from a hybrid ice sheet/ice stream model, *Earth´s Planet. Sci. Lett.* 295, 451-461.

Pavlis, N. K., Holmes, S. A., Kenyon, S. C., & Factor, J. K. 2012: The development and evaluation of the Earth Gravitational Model 2008 (EGM2008), *Journal of Geophysical Research, 117, B04406, doi:10.1029/2011JB008916.*

PGS Reservoir 2003. North Sea Digital Atlas - Version 2.0 (NSDA-2.0), *Industrial report*, PGS Reservoir, Berks, UK.

Pharaoh, T.C. 1999: Palaeozoic terranes and their lithosphere boundaries within the Trans-European Suture Zone (TESZ): a review. *Tectonophysics* 314, 17-41, doi:10.1016/S0040-1951(99)00235-8.

Pilkington, M., Miles, W. F., Ross, G. M. & Roest, W. R. 2000: Potential-field signatures of buried Precambrian basement in the Western Canada Sedimentary Basin: The Lithoprobe-Alberta basement transect-Le transect Lithoprobe du socle Albertain. *Canadian Journal of Earth Sciences – Revue Canadienne des Sciences de la Terre 37*, 1453-1471.

Popov, Y.A., Pevzner, S.L., Pimenov. V.P. & Romushkevich, R.A. 1999: New geothermal data from the Kola superdeep well SG-3. *Can Geotech J* 306(3-4), 345-366.

Price, P.B., Nagornov, O.V., Bay, R., Chirkin, D., He, Y., Miocinovic, P., Richards, A., Woschnagg, K., Koci, B. & Zagorodnov V. 2002: Temperature profile for glacial ice at the South Pole: implications for life in a nearby subglacial lake. *Proc Natl Acad Sci USA* 99, 7844-7847.

Puranen, M., Järvimäki, P. Hämäläinen, U. & Lehtinen, S. 1968: Terrestrial heat flow in Finland. *Geoexploration* 6, 151-162.

Raade, G. 1973: *Distribution of radioactive elements in the plutonic rocks of the Oslo region.* Mineralogical-Geological Museum. Cand real. thesis. University of Oslo, 162 pp.

Ragnhildstveit J. & Helliksen D. 1997: Geologisk kart over Norge, berggrunnskart Bergen – M 1:250.000. Norges geologiske undersøkelse, Trondheim.

Ragnhildstveit, J., Naterstad, J., Jorde, K. & Egeland, B. 1998: Geologisk kart over Norge, berggrunnskart Haugesund – M 1:250.000. Norges geologiske undersøkelse, Trondheim.

Ranalli, G. & Murphy, D. C. 1987: Rheological stratification of the lithosphere. *Tectonophysics 132*, 281-295.

Ravat, D., Wang, B., Wildermuth, E. & Taylor, P. T. 2002: Gradients in the interpretation of satellite-altitude magnetic data; an example from central Africa. Earth's gravity and magnetic fields from space. *Journal of Geodynamics 33*, 131-142.

Reid, A., Allsop, J., Granser, H., Millet, A. & Somerton, I. 1990: Magnetic interpretation in three dimensions using Euler deconvolution. *Geophysics 55*, 80-91.

Renssen, H. & Isarin, R.F.B. 1998: Surface temperature in NW Europe during the Younger Dryas: AGCM simulation compared with temperature reconstructions. *Climate Dynamics 14*, 33-44.

Ritter, U., Zielinski, G.W., Weiss, H.M., Zielinski, R.L.B. & Sættem, J. 2004: Heat flow in the Vøring Basin, Mid. Norwegian Shelf. *Petroleum Geoscience 10,* 353-365.

Rise, L. & Rokoengen, K. 1984: Surficial sediments in the Norwegian sector of the North Sea between 60°30'N and 62°N. *Marine Geology* 56, 287–317.

Roberts, D. & Gee, D.G. 1985: An introduction to the structure of the Scandinavian Caledonides. *In*: Gee, D.G. & Sturt, B.A. (eds.) *The Caledonian Orogeny-Scandinavia and related areas.* John Wiley & Sons, Chichester, 55-68.

Rokoengen, K. & Rønningsland, T.M. 1983: Shallow bedrock geology and Quaternary thickness in the Norwegian sector of the North Sea between 60°30'N and 62°N. *Norsk Geologisk Tidsskrift 63*, 83–102.

Rudlang, T. 2010: *Determination of heat flow in exploration wells, North Sea.* Project Assignment, Petroleum Geology, TGB 4560, NTNU, 58 p.

Rudlang, T. 2011: Heat flow and deep underground temperature in the Bergen region. *Master of Science Thesis*, Petroleum Geology, TGB 4900, NTNU, Trondheim, Norway, 75 pp..

Rybach, L. 1988: Determination of heat production rate. In: Hänel, R., Rybach, L. & Stegena, L. (eds.) *Handbook of Terrestrial Heat-Flow Determination*. Dordrecht: Kluwer Academic Publishers, 125-142.

Salisbury, R.S.K., Denley, M.R. & Douglas, G. 1996: The value of integrating existing 3D seismic into shallow gas studies. *Offshore Technology Conference, Houston,* 305–317.

Sandiford, M. & McLaren, S. 2006: Thermo-mechanical controls on heat production distributions and the long-term evolution of the continents. *In* Brown, M. & Rushmer, T. (eds.) *Evolution and Differentiation of the Continental Crust*: Cambridge University Press, 67-91.

Scheck, M. 1997: Dreidimensionale Strukturmodellierung des Nordostdeutschen Beckens unter Einbeziehung von Krustenmodellen. *STR97/10* GeoForschungsZentrum Potsdam, 125 pp..

Scheck-Wenderoth, M. & Maystrenko Y. 2008: How warm are passive continental margins? A 3D lithosphere-scale study from the Norwegian margin. *Geology* 36(5), 419-422.

Schmidt, S. & Götze, H.-J. 1998. Interactive visualization and modification of 3-D models using GIS functions. *Phys. Chem. Earth´s 23*, 289-295, doi:10.1016/S0079-1946(98)00027-5.

Schmittner, A., Urban, N.M., Shakun, J.D., Mahowald, N.M., Clark, P.U., Bartlein, P.J., Mix, A.C. & Rosell-Mele, A. 2011: Climate Sensitivity Estimated from Temperature Reconstructions of the Last Glacial Maximum. *Science*. 334, 1385-1388, DOI http://dx.doi.org/10.1126/science.1203513

Sejrup, H.P., King, E., Aarseth, I., Haflidason, H. & Elverhøi, A. 1996: Quaternary erosion and depositional processes: Western Norwegian fjords, Norwegian Channel and North Sea Fan. *In* De Batist, M. & Jacobs, P. (eds.), *Geology of siliciclastic seas*. Geological Society of London, Special Publication 117, 187–202.

Sejrup, H.P., Larsen, E., Haflidason, H., Berstad, I.M., Hjelstuen, B.O, Jonsdottir, H.E., King, E.L., Landvik, J., Longva, O., Nygård, A., Ottesen, D., Raunholm, S., Rise, L., Stalsberg, K. 2003. Configuration, history and impact of the Norwegian Channel Ice Stream. *Boreas 32*, 18–36.

Selig, F. & Wallick, G.C. 1966: Temperature distribution in salt domes and surrounding sediments. *Geophysics 31*, 346–361.

Shomali, Z.H., Roberts, R.G., Pedersen, L.B. & the TOR Working Group 2006: Lithospheric structure of the Tornquist Zone resolved by nonlinear P and S teleseismic tomography along the TOR array. *Tectonophysics 416*, 133-149, doi:10.1016/j.tecto.2005.11.019.

Siegert, M.J., Dowdeswell, J.A., Hald, M. & Svendsen, J.I.. 2001: Modelling the Eurasian ice sheet through a full (Weichselian) glacial cycle. *Global and Planetary Change 31*, 367-385.

Sigmond, E. M. O. 1996. Geologisk kart over land- og havomrader i Nordvest-Europa, M 1:4 mill. *Norges geologiske undersøkelse, Trondheim.*

Sigmond, E.M.O. 2002: Geological map, land and sea areas of Northern Europe, Scale 1: 4 million, Geological Survey of Norway.

Silva, I.A.B.C. & Barbosa, V.C.F. 2003: 3D Euler deconvolution: Theoretical basis for automatically selecting good solutions. *Geophysics 68(6)*, 1962-1968.

Skilbrei, J.R. 1989: Structure of the Jotun Nappe Complex, southern Norwegian Caledonides: Ambiguity of gravity modelling and reinterpretation. *NGU Report 89.169,* 26 pp.

Skibrei, J.R., Olesen, O., Osmundsen, P.T., Kihle, O., aaro, S. & Fjellanger, E. 2002: a study of the basement structures and onshore-offshore correlations in Central Norway. *Norwegian Journal of Geology 82,* 263-279.

Skår, Ø. 2002: U-Pb geochronology and geochemistry of early Proterozoic rocks of the tectonic basement windows in central Nordland, Caledonides of north-central Norway. *Precambrian Research 116*, 265-283.

Slagstad, T. 2008: Radiogenic heat production of Archaean to Permian geological provinces in Norway. *Norwegian Journal of Geology 88*, 149-166.

Slagstad, T., Barrére, C., Davidsen, B. & Ramstad, R. K. 2008: Petrophysical and thermal properties of pre-Devonian basement rocks on the Norwegian continental margin. *Geological Survey of Norway Bulletin 448*, 1–6.

Slagstad, T. & Barrère, C. 2007: Appendix B – Photographs of NPD and StatoilHydro cores. *In* Olesen et al. (eds) *KONTIKI Final Report, CONTInental Crust and Heat Generation In 3D.* NGU Report 2007.042, 401-438.

Slagstad, T. & Davidsen, B. 2007: Age and composition of basement rocks in the North Sea and Norwgian Sea and implications for the continuity of the Caledonian–Appalachian orogenic belt. *In* Olesen et al. (eds) *KONTIKI Final Report, CONTInental Crust and Heat Generation In 3D.* NGU Report 2007.042, 181-222.

Slagstad, T., Midttømme, K., Ramstad, R.K. & Slagstad, D. 2008: Factors influencing shallow (< 1000 m depth) temperatures and their significance for extraction of ground-source heat. *In* Slagstad, T. (ed.), Geology for Society, *Geological Survey of Norway Special Publication* 11, 99–109.

Slagstad, T., Balling, N., Elvebakk, H., Midttømme, K., Olesen, O., Olsen, O. & Pascal, C. 2009: Heat-flow measurements in Late Palaeoproterozoic to Permian geological provinces in south and central Norway and a new heat-flow map of Fennoscandia and the Norwegian–Greenland Sea. *Tectonophysics 473*, 341–361.

Slagstad, T., Davidsen, B. & Daly, J.S. 2011: Age and composition of crystalline basement rocks on the Norwegian continental margin: offshore extension and continuity of the Caledonian–Appalachian orogenic belt. *Journal of the Geological Society, London 168*, 1167–1185

Slagstad, T., Roberts, N.M.W., Marker, M., Røhr, T.S. & Schiellerup, H. 2012: A non-collisional, accretionary Sveconorwegian orogen. *Terra Nova* (in press)

Smart, J., 2000: Seismic expressions of depositional processes in the upper Ordovician succession of the Murzuq Basin SW Libya. *In* Sola, M.A. & Worsley. D. (eds.) *Geological Exploration in Murzuq Basin,* Elsevier Science, 397-415.

Solli, A. & Nordgulen, Ø. 2006: Berggrunnskart over Norge og kaledonidene i Sverige og Finland. Målestokk 1:2 million. Norges geologiske undersøkelse, Trondheim.

Stalsberg, K., Larsen, E., Ottesen, D. & Sejrup, H.P. 2003: Middle to Late Weichselian Norwegian Channel Ice Stream deposits and morphology on Jæren, southwestern Norway and the eastern NorthSea. *Boreas 32*, 149–166.

Stavrev, P. & Reid, A. 2007: Degrees of homogeneity of potential fields and structural indices of Euler deconvolution. *Geophysics 72(1)*, L1-L12.

Storvoll, V., Bjørlykke K. & Mondol N.H. 2005: Velocity-depth trends in Mesozoic and Cenozoic sediments from the Norwegian shelf. *AAPG Bulletin* 89(3), 359-381.

Stratford, W., Thybo, H., Faleide, J.I., Olesen, O. & Tryggvason, A. 2009: New Moho Map for onshore southern Norway. *Journ. Geophys. Int. 178*, 1755-1765.

Sturt, B.A. & Thon, A. 1978: A major early Caledonian igneous complex and a profound unconformity in the Lower Palaeozoic sequence of Karmøy, southeast Norway. *Norsk Geologisk Tidsskrift 55*, 221-228.

Sundvor, E. & Myhre, A.M. 1987: Heat flow measurements: Jan Mayen Ridge and Norway Basin. *Seismo-Series* 9, Seismological Observatory, University of Bergen.

Sundvor, E., Myhre, A.M. & Eldholm, O. 1989: Heat flow measurements on the Norwegian continental margin during the FLUNORGE project. *University of Bergen Seismo-Series* 27.

Swanberg, C.A., Chessman, M.D., Simmons, G., Smithson, S.B., Grønlie, G. & Heier, K.S. 1974: Heat flow – heat generation studies in Norway. *Tectonophysics* 23, 31–48.

Tesauro, M., Kaban, M.K. & Cloetingh, S.A.P.L. 2008: EuCRUST-07: A new reference model for the European crust. *Geophys. Res. Lett.* 35(5), L05313, doi:10.1029/2007GL032244.

Thomas, D.W. & Coward, M.P. 1996: Mesozoic regional tectonics and South Viking Graben formation: evidence for localized thin-skinned detachments during rift development and inversion. *Marine and Petroleum Geology 13*, 149-177.

Thompson, D.T. 1982: EULDPH: A new technique for making computer-assisted depth estimates from magnetic data. *Geophysics* 47, 31-37.

Torsvik, T. H. & Olesen, O. 1988. Petrophysics and Palaeomagnetism. Initial Report of the Norwegian Geological Survey Laboratory. *Norges geologiske undersøkelse Report 88.171.*

Turcotte, D. L. & Schubert, G. 1982: *Geodynamics: Application of Continuum Physics to Geological Problems*. New York: John Wiley and Sons Inc.

Turcotte, D.L. & Schubert, G. 2002: Geodynamics (2nd edition): Cambridge, Cambridge University Press, 456 p.

Tveito, O.E., Førland, E., Heino, R., Hanssen-Bauer, I., Alexandersson, H., Dahlström, B., Drebs, A., Kern-Hansen, C., Jónsson, T., Vaarby Laursen, E. & Westman, Y. 2000. Nordic temperature maps. *DNMI-Report 09/00 KLIMA*, 54 pp.

Vejbaek, O.V. & Britze, P. 1994. Geological map of Denmark 1: 750,000. Top pre-Zechstein (two-way traveltime and depth). Sub- and supercrop map. Geological Survey of Denmark, Map Series 45. 3 maps and 8 pp.

van der Vegt, P., Janszen, A., & Moscariello, A. 2012: Tunnel valleys: current knowledge and future perspectives. *Geological Society of London Special Publications 368*, doi 10.1144/SP368.13.

Wennberg, O.P., Milnes, A.G. & Winsvold, I. 1998: The northern Bergen Arc Shear Zone - a oblique-lateral ramp in the Devonian extensional detachment system of western Norway. *Norsk Geologisk Tidsskrift 78*, 169–184.

Werner, S. 1953: Interpretation of magnetic anomalies of sheet-like bodies. *Sveriges Geologiska Årsbok 43, 6*, 130 pp.

Wilberg, R. 1989: Data for malmsonering for Bordvedåga-forekomsten, analyser fra Be-mineraliseringer og regional geologi i Høgtuva-området. *NGU Report 89.097,* 67 pp.

Wollenberg, H.A. & Smith, A. R. 1987: Radiogenic heat production of crustal rocks: an assessment based on geochemical data. *Geophysical Research Letters 14(3)*, 295-298.

Ziegler, P. 1990. *Geological Atlas of western and central Europe (2 ed.)*. Shell International Petroleum Maatschappij BV, The Hague, the Netherlands.

Ziegler, P.A. & Dèzes, P. 2006: Crustal evolution of Western and Central Europe, *In* Gee D.G. and Stephenson, R.A. (eds.), European Lithosphere Dynamics, *Geol. Soc, London, Mem. 32*, 43-56.

Ziemen, F., Rodehacke, C. & Mikolajewicz, U. 2012: LGM ice sheets simulated with a complex fully coupled ice sheet - climate model. EGU General Assembly, memory stick: *Geophysical Research Abstracts 14*, EGU2012-6277, Vienna, Austria.

Øverland, J.A., Bering, D., Brönner, M., Dalsegg, E., Fredin, O., Magnus, C. & Solbakk, T. 2012: Lista. *In* Olesen, O., Bering, D., Brönner, M., Dalsegg, E., Fabian, K., Fredin, O., Gellein, J., Husteli, B., Magnus, Ch., Rønning, J.S., Solbakk, T., Tønnesen J.F. & Øverland, J.A. (eds.) *Tropical Weathering In Norway, TWIN Final Report.* NGU Report 2012.005, 37-46.

Heat Flow Calculation on Halten Terrace

Christian Müller & Yuriy Maystrenko

16.1 Well examination

1.1 Studied Wells

Within the framework of this study ten exploration wells have been examined (Table 1). The main objective was the calculation of local thermal conductivity and heat flow to obtain reliable values along the Mid-Norwegian margin. All wells are located in petroleum fields on or close to the Halten Terrace (Fig. 1). A lot of exploration drilling has been done there in the last few decades and allows us to choose the most suitable wells. Our first selection criterion was the availability of DST-temperatures. These values are published on the website of NPD. Furthermore an equidistant coverage within the fields was pursued.

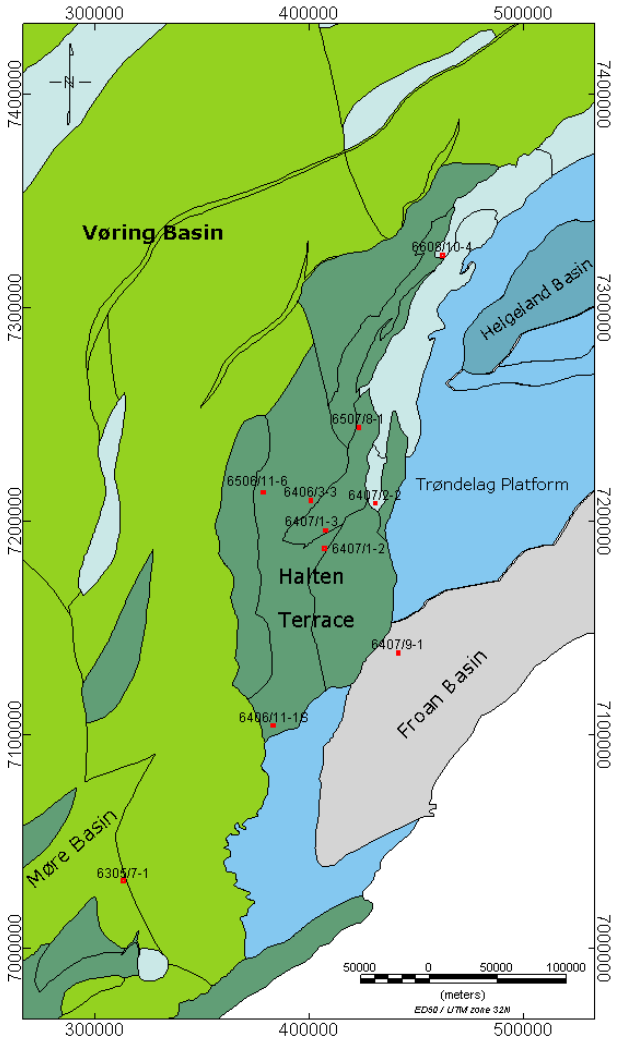

Figure 1. Location plot of examined wells

The methodology and calculation workflow follows the procedure outlined by Therese Rudlang [6]. Therefore a detailed description of the encountered lithologies is needed containing the percentaged fraction of the minerals. For a few wells these are available on the

NPD website, found in the completion report of the respective well (sometimes in the geochemical information). In the case of missing information the required lithologies were obtained by a request to Statoil, Norske Shell and BP Norge. Large gaps or only rough information led to elimination of the respective well.

Table 1. Exploration wells used for calculation. Information taken from the NPD website.

Field	Geological unit	Well number	UTM-zone	NS UTM [m]	EW UTM [m]
Draugen	Froan Basin	6407/9-1	32	7138488.30	441548.41
Heidrun (southern part)	Halten Terrace	6508/8-1	32	7244164.64	423003.38
Kristin	Halten Terrace	6506/11-6	32	7213786.47	378448.14
Norne (eastern part)	Revfall Fault Complex	6608/10-4	32	7324847.23	462006.74
Ormen Lange	Møre Basin	6305/7-1	31	7028228.30	613145.72
Tyrihans	Halten Terrace	6407/1-2	32	7187495.23	406877.13
		6407/1-3	"	7195989.53	407531.49
Åsgard	Halten Terrace				
(central part)		6406/3-3	32	7209958.99	400545.31
(eastern part)		6407/2-2	"	7208716.22	430730.79
No Field	Halten Terrace	6406/11-1S	32	7104524.70	383011.32

1.2 Preparation of input files:

The first step is to register the intervals of the logs into an excel sheet. Therefore, the given RKB (Rotary Kelly Bushing) depths have to be adjusted to the depth below sea level (BSB).

$$BSB = RKB - KBE - \text{water depth}$$

Information about KBE (Kelly bushing elevation) and water depth are published at the NPD Factpage for the respective well.

Afterwards, the encountered groups and formations for the different depths were filled in. Brigaud et al. (1992) established a table containing codes for most stratigraphical units of the Northern Viking Graben. Groups and formations of one geological period are labelled with the same code. These codes are linked to measured thermal conductivities of samples from the respective period (Table 3). This approach takes ongoing diagenetic processes into account, which lead to different thermcal properties of sedimentary rocks in the lithological units

(Rudlang 2010). Due to proximity of the Viking Graben to the Møre and Vøring Basin and the presence of mostly the same groups, the table was also used for calculations performed in this study. For units which were not mentioned the formation code of the corresponding period was used (Table 2).

Table 2. Stratigraphical units in the survey area. The basic concept is taken from Brigaud et al. (1992). The respective codes are connected to the time of deposition as well as Table 3, containing the thermal conductivities.

Period	Groups	Sedimentary Formations	Code
Eocene to present	Nordland	Naust	1
		Kai	1
	Hordaland	Brygge	1
Paleocene	Rogaland	Tare	2
		Tang	2
Upper Cretaceous	Shetland	Springar	3
		Nise	3
		Kvitnos	3
Lower Cretaceous	Cromer Knoll	Lysing	4
		Lange	4
		Lyr	4
Upper to Middle Jurassic	Viking	Spekk	5
		Melke	5
	Fangst	Garn	5
Lower Jurassic	Båt	Ror	6
		Tilje	6

Afterwards, the percentaged fractions of every interval and the respective thermal conductivity value for the matrix of the respective lithology have to be registered. Brigaud et al. (1992) published an attempt which provides the thermal conductivity for the major lithologies (such as sandstone, shale …) depending on the stratigraphic group. These values are based on several laboratory measurements from previous investigations and proposed for the Viking Graben. As before these values were also chosen for this calculation because of proximity to this area and the presence of mostly the same groups (Table 3).

Table 3. Matrix thermal conductivities of sedimentary rocks for respective lithological unit, values in W/mK. Taken from Brigaud et al. (1992)

Formation Code	Sandstone	Carbonates	Shales
1	6.12	3.38	2.07
2	6.66	3.28	2.08
3	6.27	3.28	2.29
4	6.27	3.28	2.2
5	6.99	3.7	2.49
6	6.99	3.33	2.46

Table 4. Further values for encountered lithofacies. Dolomite, organic matter (usually lignite) and volcanic tuffs are taken from Brigaud et al. (1992), and the value for pyrite from Midttømme et al. (1998).

	Dolomite	Organic Matter	Volcanic Tuffs	Pyrite
λ [W/mK]	5.30	1.00	2.00	19.2

For the first one hundred metres of the wells the lithological description was usually missing. In this case, these values were estimated. Therefore, the underlying percentaged fractions and adjacent wells were considered. As rough evidence the study of Midttømme (1995) can be used. The investigated samples from the first 4 m of the Vøring Basin are mostly described as clayey sediments and had a measured thermal conductivity ranging between 0.8 – 1.1 W/mK (these are not matrix thermal conductivities).

Furthermore in some parts the intersected intervals showed fractions that appear partly as a pure bulk. In this case the thermal conductivity of the respective lithofacies was used (Table 4). In addition some fractions cannot directly assigned to one of the major sedimentary rocks from Table 3. In these cases an estimated thermal conductivity was calculated taking into account the single fractions, using the equation from Brigaud et al. 1992:

$$k = \prod_{i=1}^{m} k_{ci}^{xi}, \quad (1)$$

where k_{xi} is the volumetric fraction, and k_{ci} is the conductivity of the individual component.

The theoretical bulk conductivity was then calculated (eq. 1) using the percentaged fraction and matrix conductivity of the respective lithofacies. In addition the porosity has to be calculated. Here, the decreasing porosity due to compaction was taken into account (eq. 2 – Sclater and Christie (1980)).

$$f = f_0 * e^{-cz}, \quad (2)$$

with f_0 as surface porosity, depth z and compaction coefficient c.

Sclater and Christie (1980) provided values of lithology-dependent parameters for the North Sea (Table 5), which were also used in this study. For fractions assigned as a mixture of two main sedimentary rocks (like marl, mixture of carbonates and shales) the parameters were calculated as the average of their percentaged fractions. The "bulk" porosity was achieved by the repeated use of eq. 1, again taking into account the percentaged fractions of the respective porosities. Due to the missing values of surface porosity and cementation coefficient of the lithofacies pyrite, organic matter and volcanic tuffs, have these fractions have not been considered for porosity calculation. As these lithologies were encountered in only small intervals of max. 5 m and they have little influence on the calculated heat-flow values.

Table 5. Lithology-dependent parameters for normally pressured sedimentary rocks from North Sea, f_0 – surface porosity, C – compaction coefficient. Additionally mentioned are the densities assumed for sediment grains in the respective lithologies (Sclater & Christie 1980).

Lithology	f_0	C, x 10^{-5} cm^{-1}	P_{sg}, g/cm^3
Shale	0.63	0.51	2.72
Sand	0.49	0.27	2.65
Chalk	0.7	0.71	2.71
Shaley sand / Silt	0.56	0.39	2.68

For completeness, the thermal conductivity at in situ conditions was achieved. Water was assumed to fill the whole pore space with a thermal conductivity of 0.6 W/mK. For calculation, the expression found by Andrews-Speed et al. (1994) was used:

$$k_{pr} = k_w^{\varphi} * k_r^{1-\varphi} \quad (3)$$

with bulk saturated conductivity of porous rock k_{pr}, conductivity of pore fulid k_w and the conductivity of the solid component k_r.

2. Heat-flow calculation

To calculate the heat flow, a program written in C by Pascal (2010) was used. It is a simple 'trial and error' algorithm which takes into account the temperature dependency of the respective thermal conductivities to calculate the heat flow corrected for temperature. Two input files are required. The first called 'conductivities' contains the BSB depth, theoretical bulk conductivity (k_matrix) and the 'correct porosity'. The second one called 'input' contains the DST temperature and a starting average heat-flow value. In the beginning, the program reads the input files and stores the values into several arrays. Afterwards, the temperature-corrected thermal conductivities of matrix and water on the sea floor are calculated with the assumption of 0^0C at the sea floor. These values are required as input parameters for the 'Sass-function' which is used for the following temperature correction of thermal bulk conductivity:

$$k_{Mat_i}(T) = \frac{k_{Mat_i}(0)}{1.007 + \left(0.0036 - \frac{0.0072}{k_{Mat_i}(0)}\right) * T}$$

with

$$k_{Mat_i}(0) = \left(1.007 + 25 * \left(0.0037 - \frac{0.0074}{k_{Mat_i}(25)}\right)\right) * k_{Mat_i}(25)$$

The next step is the iterative calculation for every interval. In the end, the achieved temperature at the bottom of the last interval is compared to the DST temperature. If there is a misfit, the starting heat-flow value is corrected by a small value and the iteration workflow starts again with the new heat-flow value to calculate temperature and corrected thermal conductivities. The program stops when a difference of less than 0.1 between calculated and measured DST temperature is obtained. As a result, a text file is generated containing temperature and thermal conductivity values from sea floor to DST depth.

In order to assume the sensitivity of the calculated heat-flow values, which could be affected by errors in matrix conductivity and porosity, 100.000 Monte-Carlo simulations were run for each well. In the beginning, the program perturbs the parameters for thermal conductivity and porosity. Afterwards, one loop of heat-flow calculations (like the first program) is run. Then it perturbs the parameters and starts the next loop of the calculation. In the end, the output file contains the 100,000 values of calculated heat flow. For statistical evaluation of the achieved heat-flow values, mean, median and standard deviations were calculated (Table 6).

Table 6. Final results of heat flow and statistical calculation.

Well-No	DST Depth in m	T_bottom In °C	Heat Flow Median in mW/m²	Heat Flow Mean in mW/m²	Standard deviation
6305/7-1	2048	89.94	71.5	71.51442	1.165665
6406/3-3	3668	136.03	57.1	57.0932	0.745646
6406/11-1S	3364	138.93	65.6	65.58937	0.812288
6407/1-2	3267	133.95	64.15	64.15595	0.691104
6407/1-3	3325	131.17	62.65	62.62952	0.569642
6407/2-2	2200	91.02	60.4	60.43237	1.006354
6407/9-1	1365	68.21	67.17659	67.15	1.102931
6506/11-6	4265	167.65	66.65	66.63425	0.725609
6507/8-1	2034	81.1	56.7	56.7257	0.700423
6608/10-4	2177	93.94	61.85	61.86239	0.78901

Figure 2 shows the obtained heat flows for the examined wells. The values represent the median of the average heat flow for the respective well. For better visualization, the values were sorted into 5 groups.

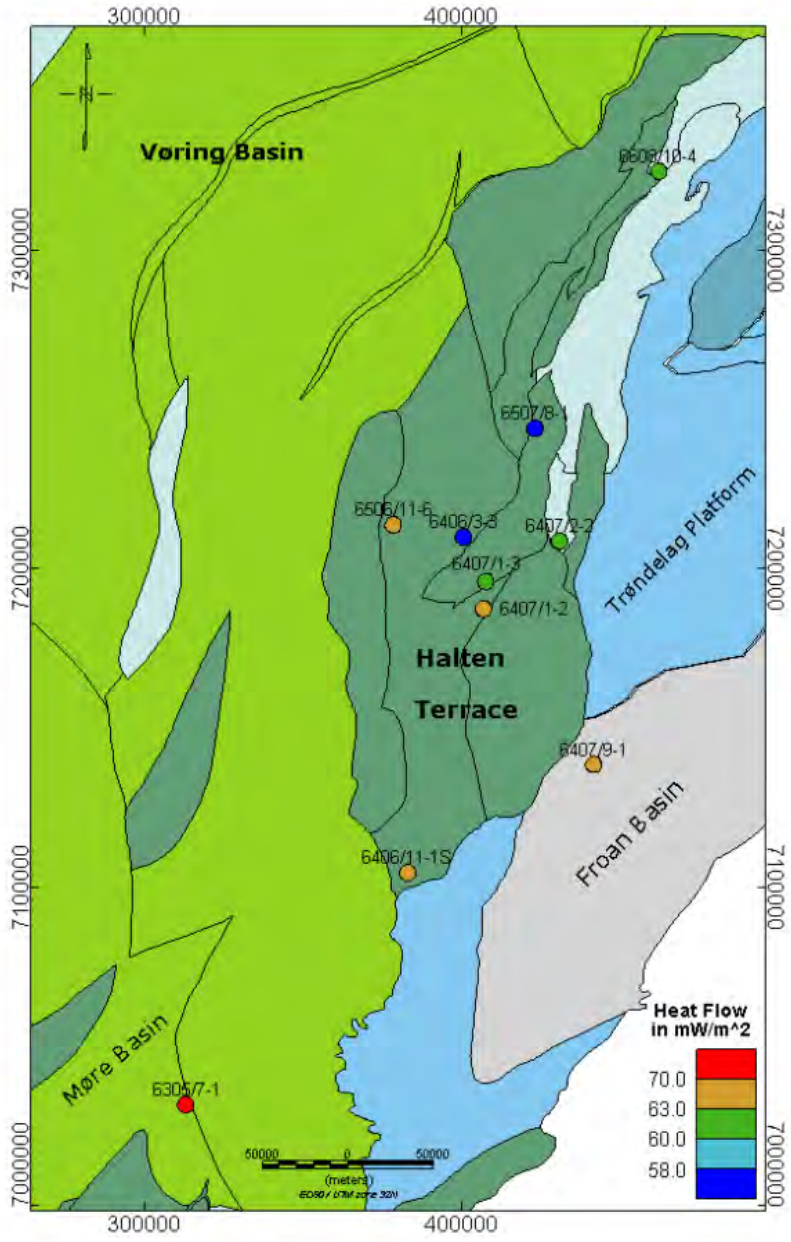

Figure 2. Classified heat flow values for every well.

CHEMICAL ANALYSIS GROUNDWATER SAMPLES FROM FYLLINGSDALEN

INSTRUMENT: **Radiometer Titralab 94 / CDM 210 Conductivity meter**

METODE: **Metodeoppsettet er beskrevet i NGU-SD 3.6: Bestemmelse av ledningsevne**
ANALYSENE UTFØRES ETTER NORSK STANDARD - NS-ISO 7888

NEDRE BESTEMMELSESGRENSE: **0.05 mS/m** **(1 mS/m = 10 μS/cm)**

ANALYSEUSIKKERHET:

Måleområde (mS/m)	Usikkerhet
0.05 - 1.0*	± 20 % rel.
1.0 - 2.0	± 8 % rel.
2.0 - 5.0	± 4 % rel.
5.0 - 140	± 2 % rel.

Oppgitte usikkerheter har dekningsfaktor 2 (2 standardavvik), noe som tilsvarer et konfidensintervall på 95 %.

*. Resultater under 1 mS/m kan bli påvirket av atmosfærisk karbondioksyd og ammoniakk

PRESISJON: **Det kjøres rutinemessig kontrollprøver, som føres i kontrolldiagram (X-diagram). Disse kan forevises om ønskelig.**

ANTALL PRØVER: 4

ANMERKNINGER:

1. Elektrisk konduktivitet ved 25° C er beregnet med automatisk temperaturkompensasjon. Temperaturverdier oppgitt i resultattabellen tilsvarer prøvetemperatur under måling.
2. Analyseobjekt omfattes ikke akkreditering.

Gjengivelse av analysedata skal skje på en slik måte at meningsinnholdet i rapporten ikke endres.

Ferdig analysert	03.07.2012	Tomm Berg
	Dato	OPERATØR

Analysedato	Prøvetatt	Prøve id.	Kommune	Ledn.-evne	Temp.
				mS/m	°C
02.07.2012	15.06.2012	1. Fyllingsdalen dybde 35m	Bergen	76.8	21.9
02.07.2012	15.06.2012	2. Fyllingsdalen dybde 110m	Bergen	220	21.9
02.07.2012	15.06.2012	3. Fyllingsdalen dybde 454m	Bergen	763	21.9
02.07.2012	15.06.2012	4. Fyllingsdalen dybde 496m	Bergen	855	21.9

Analysedato	Prøvetatt	Prøve id.	Kommune	pH
				pH
02.07.2012	15.06.2012	1. Fyllingsdalen dybde 35m	Bergen	9.00
02.07.2012	15.06.2012	2. Fyllingsdalen dybde 110m	Bergen	10.27
02.07.2012	15.06.2012	3. Fyllingsdalen dybde 454m	Bergen	10.18
02.07.2012	15.06.2012	4. Fyllingsdalen dybde 496m	Bergen	9.60

INSTRUMENT: **Radiometer Titralab 94 / Glasselektrode pHC 2701-8 "Red Rod"**

METODE: **pH: Metodeoppsettet er beskrevet i NGU-SD 3.5: Bestemmelse av pH. Utførelsen følger NS 4720**

ANALYSEUSIKKERHET: **± 0.20 pH**
Oppgitt usikkerheter har dekningsfaktor 2 (2 standardavvik), noe som tilsvarer et konfidensintervall på 95 %.

PRESISJON: **Det analyseres rutinemessig kontrollprøver som føres i kontrolldiagram (X-diagram). Disse kan forevises om ønskelig.**

ANTALL PRØVER: 4

ANMERKNINGER: Analyseobjekt omfattes ikke akkreditering.

Gjengivelse av analysedata skal skje på en slik måte at meningsinnholdet i rapporten ikke endres.

Ferdig analysert	03.07.2012	Tomm Berg
	Dato	OPERATØR

INSTRUMENT: **Dionex Ionekromatograf 120 DX**
METODE: Metodeoppsettet er beskrevet i NGU-SD 3.4: IC-analyse av anioner

NEDRE BESTEMMELSESGRENSER (LLQ) OG ANALYSEUSIKKERHETER (1 mg/l = 1 ppm):

	F^-	Cl^-	NO_2^-*	Br^-	NO_3^-	PO_4^{3-}	SO_4^{2-}
LLQ:	0.05 mg/l	0.1 mg/l	0.05 mg/l	0.1 mg/l	0.05 mg/l	0.2 mg/l	0.1 mg/l
Usikkerhet LLQ – 30*LLQ	20 %	20 %	20 %	20 %	20 %	20 %	20 %
Usikkerhet > 30*LLQ	10 %	10 %	10 %	10 %	10 %	10 %	10 %
INFO: 30*LLQ =	1.5 mg/l	3 mg/l	1.5 mg/l	3 mg/l	1.5 mg/l	6 mg/l	3 mg/l

Oppgitte usikkerheter har dekningsfaktor 2 (2 standardavvik), noe som tilsvarer et konfidensintervall på 95 %.

*) NGU-lab er ikke akkreditert for NO_2^-

PRESISJON : Det analyseres rutinemessig kontrollprøver som føres i kontrolldiagram (X-diagram). Disse kan forevises om ønskelig.
ANTALL PRØVER: 4

ANMERKNINGER: Analyseobjektet omfattes ikke akkreditering. Klorid-konsentrasjon er bestemt i prøver som var fortynnet til et hensiktsmessig nivå.
Alle andre anioner er bestemt i ufortynnete prøver og rapporterte verdier er kun informative.
I enkelte prøver er interferensen fra klorid veldig intens og noen anioner kunne ikke måles.

Gjengivelse av analysedata skal skje på en slik måte at meningsinnholdet i rapporten ikke endres.

Ferdig analysert	28. jun. 2012	Bente Kjøsnes
	Dato	OPERATØR

Prøve ID	F^- [mg/l]	Cl^- [mg/l]	NO_2^- [mg/l]	Br^- [mg/l]	NO_3^- [mg/l]	PO_4^{3-} [mg/l]	SO_4^{2-} [mg/l]
Bergen Fyllingsdalen 35m	0.25	157		0.59	0.32	0.48	35.0
Bergen Fyllingsdalen 110m	1.18	575		1.98	0.38	0.75	120
Bergen Fyllingsdalen 450m	0.58	2200		7.79	0.41		390
Bergen Fyllingsdalen 496m	0.54	2500		9.08			450

INSTRUMENT: **ICP-AES type Perkin Elmer Optima 4300 Dual View**

NEDRE BESTEMMELSESGRENSER (LLQ) OG HØYESTE MÅLEOMRÅDE VED VANNANALYSER

(For vannprøver som fortynnes blir deteksjonsgrensene automatisk omregnet) **(1 mg/l = 1 ppm)**

	Si mg/l	Al mg/l	Fe mg/l	Ti mg/l	Mg mg/l	Ca mg/l	Na mg/l	K mg/l	Mn mg/l	P mg/l	Cu mg/l	Zn mg/l	Pb mg/l	Ni mg/l	Co mg/l	V mg/l
LLQ	0.02	0.02	0.002	0.001	0.05	0.02	0.05	0.5	0.001	0.05	0.005	0.002	0.005	0.005	0.001	0.005
Høyeste målegrense	5	50	50	5	100	100	250	20	5	10	5	5	5	5	5	5

	Mo mg/l	Cd mg/l	Cr mg/l	Ba mg/l	Sr mg/l	Zr mg/l	Ag mg/l	B mg/l	Be mg/l	Li mg/l	Sc mg/l	Ce mg/l	La mg/l	Y mg/l	As mg/l	Sb mg/l
LLQ	0.005	0.0005	0.002	0.002	0.001	0.002	0.005	0.02	0.001	0.005	0.001	0.02	0.005	0.001	0.01	0.005
Høyeste målegrense	5	10	50	5	5	5	1	5	5	5	5	5	5	5	20	5

ANALYSEUSIKKERHET:

i) Nedre måleområde (LLQ - 5*LLQ):

± 50 rel. %: As, Sb (S, Se, Sn) ± 37.5 rel. %: K, Pb

± 25 rel. %: Ag, Al, B, Ba, Be, Ca, Cd, Ce, Co, Cr, Cu, Fe, La, Li, Mg, Mo, Mn, Na, Ni, P, Si, Sc, Sr, Ti, V, Y, Zn, Zr

ii) Øvre måleområde (> 5*LLQ):

± 20 rel. %: As, Sb (S, Se, Sn) ± 15 rel. %: K, Pb

± 10 rel. %: Ag, Al, B, Ba, Be, Ca, Cd, Ce, Co, Cr, Cu, Fe, La, Li, Mg, Mo, Mn, Na, Ni, P, Si, Sc, Sr, Ti, V, Y, Zn, Zr

Oppgitte usikkerheter har dekningsfaktor 2 (2 standardavvik), noe som tilsvarer et konfidensintervall på 95 %

PRESISJON: **Det analyseres rutinemessig kontrollprøver som føres i kontrolldiagram (X-diagram). Disse kan forevises om ønskelig.**

ANTALL PRØVER: 4 (2 analyseoppsett)

ANMERKNINGER: Prøvene er saltrike og analyseoppsett avviker fra akkreditert metode

Na-konsentrasjon er utenfor måleområdet og derfor rapporterte verdier utenfor dette området anses som semikvantitative.

Prøvene er forbehandlet på 2 (to) ulike måter pga. utfelling: (1) Prøvene anmerket F/S er surgjort etter filtrering.

(2) Prøvene anmerket S/F er surgjørt og filtrert etter 2 dager.

Prøvene anmerket 450m og 496m fortynnes til analyse 2 ganger pgs. høyt innhold i Na.

Ferdig analysert	27.jun.12	Ana Banica
	Dato	OPERATØR

Prøve ID	Si [mg/L]	Al [mg/L]	Fe [mg/L]	Ti [mg/L]	Mg [mg/L]	Ca [mg/L]	Na [mg/L]	K [mg/L]	Mn [mg/L]	P [mg/L]	Cu [mg/L]	Zn [mg/L]	Pb [mg/L]	Ni [mg/L]	Co [mg/L]	V [mg/L]
Bergen Fyllingsdalen 15.06.2012_F/S_35m	0.147	1.43	<0.002	<0.001	1.87	5.53	137	8.82	0.0029	<0.05	<0.005	0.0107	<0.005	<0.005	<0.001	<0.005
Bergen Fyllingsdalen 15.06.2012_F/S_110m	1.41	12.7	0.0061	<0.001	0.424	6.37	390	18.9	<0.001	<0.05	0.0222	0.0071	<0.005	<0.005	<0.001	0.0069
Bergen Fyllingsdalen 15.06.2012_F/S_450m	3.17	<0.04	<0.004	<0.002	9.10	44.9	1450	64.8	<0.002	<0.1	<0.01	0.0052	<0.01	<0.01	<0.002	0.0121
Bergen Fyllingsdalen 15.06.2012_F/S_496m	3.37	<0.04	<0.004	<0.002	30.2	65.1	1750	80.6	<0.002	<0.1	<0.01	0.0058	<0.01	<0.01	<0.002	0.0117
Bergen Fyllingsdalen 15.06.2012_S/F_35m	0.241	2.87	1.45	0.0028	2.01	6.46	132	8.35	0.0353	<0.05	0.0367	6.31	<0.005	0.0062	<0.001	<0.005
Bergen Fyllingsdalen 15.06.2012_S/F_110m	2.68	14.9	2.05	0.0101	0.903	10.6	402	19.2	0.0454	0.059	0.640	2.07	<0.005	<0.005	<0.001	<0.005
Bergen Fyllingsdalen 15.06.2012_S/F_450m	6.42	6.12	1.34	0.0426	17.0	47.8	1360	61.6	0.0343	0.124	0.0707	0.929	<0.01	<0.01	<0.002	<0.01
Bergen Fyllingsdalen 15.06.2012_S/F_496m	7.01	8.15	1.05	0.0145	41.0	65.3	1540	68.5	0.0742	0.185	0.0439	3.09	<0.01	<0.01	<0.002	0.0119

Mo [mg/L]	Cd [mg/L]	Cr [mg/L]	Ba [mg/L]	Sr [mg/L]	Zr [mg/L]	Ag [mg/L]	B [mg/L]	Be [mg/L]	Li [mg/L]	Sc [mg/L]	Ce [mg/L]	La [mg/L]	Y [mg/L]	As [mg/L]	Sb [mg/L]
0.0682	<0.0005	<0.002	0.0490	0.0641	<0.002	<0.005	0.064	<0.001	0.0063	<0.001	<0.02	<0.005	<0.001	<0.01	<0.005
0.0813	<0.0005	<0.002	0.0171	0.0694	<0.002	<0.005	0.247	<0.001	<0.005	<0.001	<0.02	<0.005	<0.001	<0.01	<0.005
0.0552	<0.001	<0.004	0.0850	0.595	<0.004	<0.01	0.519	<0.002	0.0184	<0.002	<0.04	<0.01	<0.002	<0.02	<0.01
0.0537	<0.001	<0.004	0.101	0.834	<0.004	<0.01	0.451	<0.002	0.0158	<0.002	<0.04	<0.01	<0.002	<0.02	<0.01
0.0620	<0.0005	0.0078	0.0646	0.0650	<0.002	<0.005	0.072	<0.001	0.0068	<0.001	<0.02	<0.005	<0.001	<0.01	<0.005
0.0643	<0.0005	0.0162	0.0429	0.0847	0.0023	<0.005	0.222	<0.001	<0.005	<0.001	<0.02	<0.005	<0.001	<0.01	<0.005
0.0497	<0.001	0.0096	0.0876	0.576	<0.004	<0.01	0.454	<0.002	0.0209	<0.002	<0.04	<0.01	0.0021	<0.02	<0.01
0.0447	<0.001	0.0076	0.0899	0.722	<0.004	<0.01	0.446	<0.002	0.0192	<0.002	<0.04	<0.01	<0.002	<0.02	<0.01

Appendix C

AGE DATING OF BASEMENT ROCKS IN THE NORTH SEA AND THE NORWEGIAN SEA

Trond Slagstad & Børre Davidsen

Data reproduced from Slagstad & Davidsen (2007) in the Kontiki Final Report (Olesen et al. 2007). The results are partly published by Slagstad et al. (2011).

Zircon was separated from 11 basement samples from exploration wells in the North Sea and Norwegian Sea. The samples were provided by the Norwegian Petroleum Directorate (D. Bering pers. comm. 2005) and the separation was carried out using standard techniques including heavy liquids, magnetic separation and final hand picking under a binocular microscope. Zircons from 10 samples were analysed at by laser ablation–inductively coupled plasma–mass spectrometry (LA–ICP–MS) at the Geological Survey of Norway and 8 samples were analysed by secondary ion mass spectrometry (SIMS) at the Nordsim laboratory in Stockholm. Seven of the samples have been analysed using both techniques. The details of the analysing procedure are described by Slagstad & Davidsen (2007) and Slagstad et al. (2011).

The majority of samples are of magmatic rocks with ages ranging from 463 to 421 Ma; two samples are of metasedimentary rocks that most likely constitute parts of Caledonian nappes (see below); and two samples are of Proterozoic gneisses that probably represent an offshore continuation of the Western Gneiss Region (Fig. 1). The offshore Caledonian basement appears to consist of magmatic and metasedimentary rocks that can be correlated with rocks in tectonostratigraphically high (i.e., Upper and Uppermost Allochthons) nappes within the Scandinavian Caledonides (Fig. 2). Slagstad & Davidsen (2007) made also a correlation with the 'Caledonian' magmatism in Scotland and East Greenland as well as within the Appalachian orogen in North America.

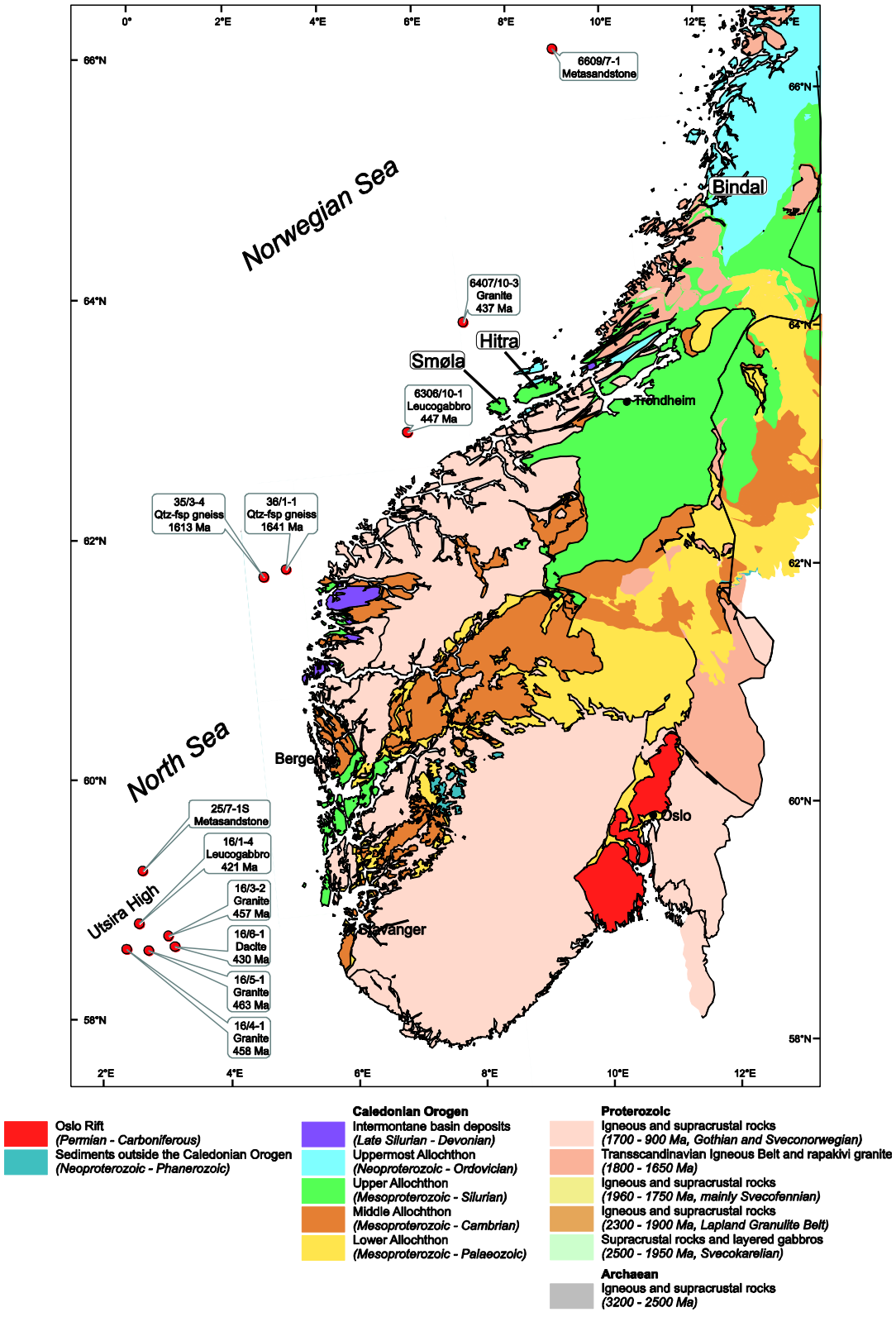

Figure 1. Simplified geological map of South and Central Norway (modified after Solli and Nordgulen (2006) with locations and ages of samples selected for geochronological analysis.

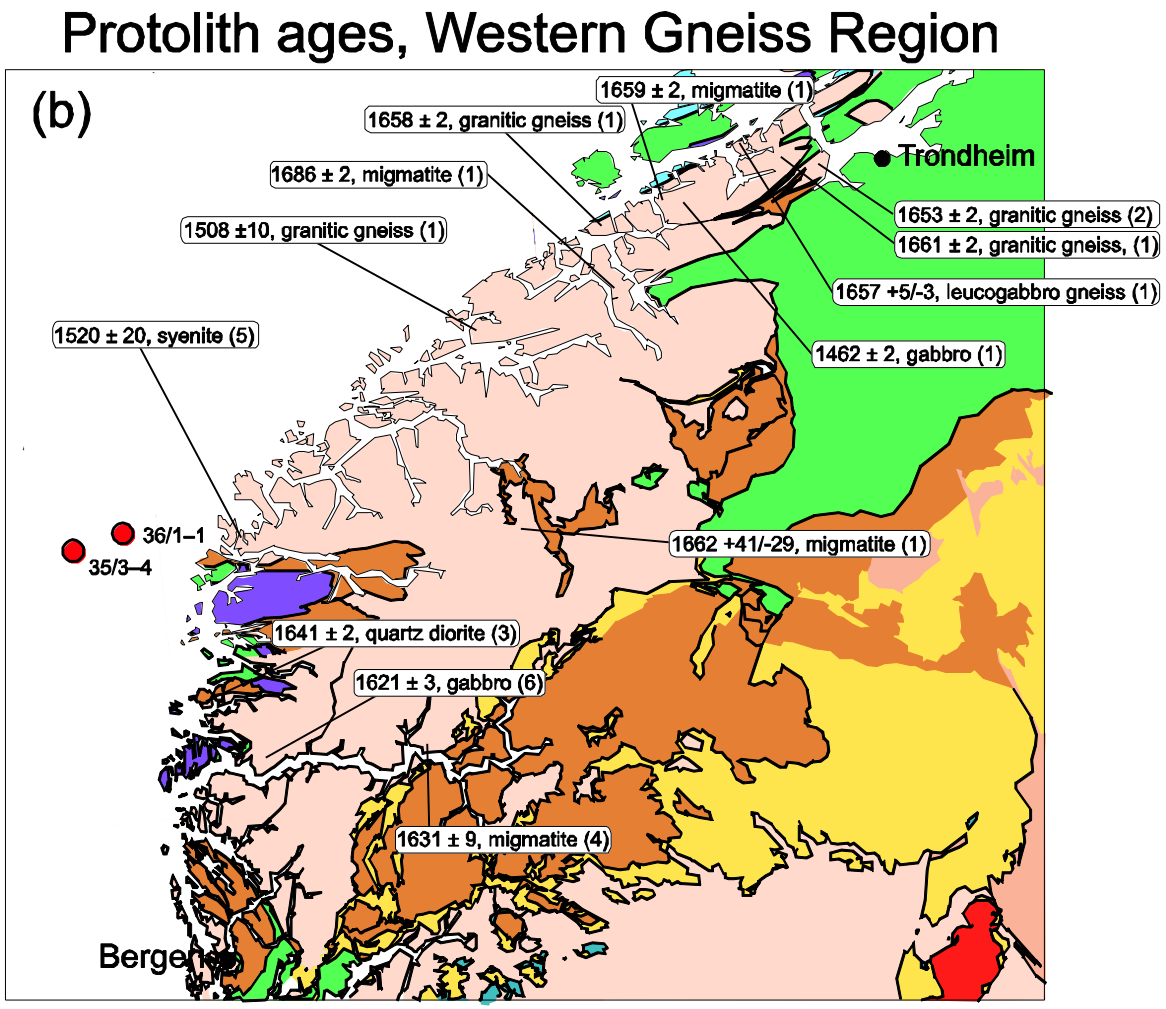
Protolith ages, Western Gneiss Region
(b)
1659 ± 2, migmatite (1)
1658 ± 2, granitic gneiss (1)
1686 ± 2, migmatite (1)
1508 ±10, granitic gneiss (1)
1520 ± 20, syenite (5)
1653 ± 2, granitic gneiss (2)
1661 ± 2, granitic gneiss, (1)
1657 +5/-3, leucogabbro gneiss (1)
1462 ± 2, gabbro (1)
Trondheim
36/1–1
35/3–4
1662 +41/-29, migmatite (1)
1641 ± 2, quartz diorite (3)
1621 ± 3, gabbro (6)
1631 ± 9, migmatite (4)
Bergen

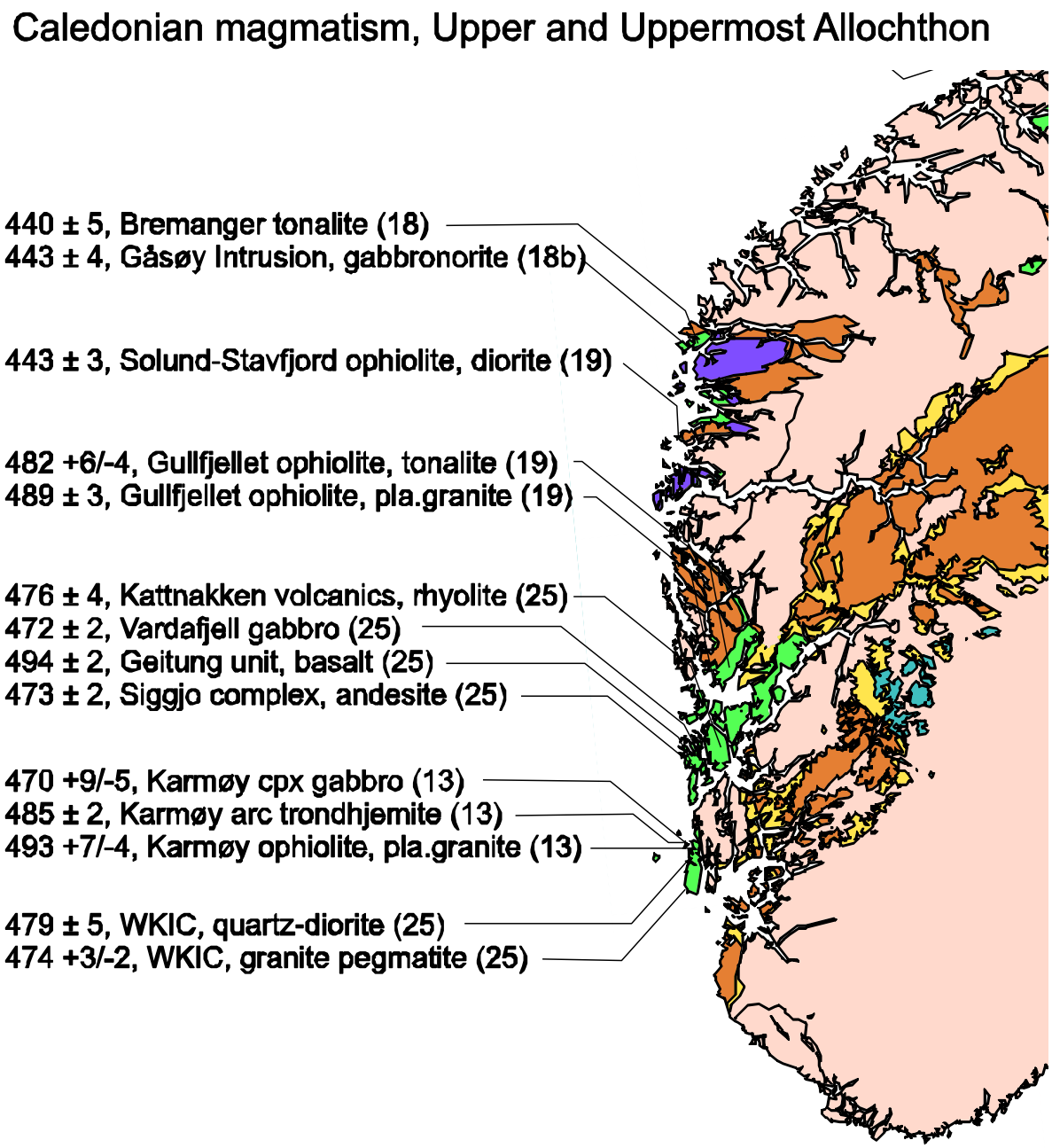

Figure 2. (previous page) (a) Simplified geological map of Norway (modified after Solli and Nordgulen (2006)) showing published U–Pb age data from Caledonian magmatic rocks in the Norwegian Caledonides. References in parentheses are presented in Table 10.2 in the Kontiki report (Olesen et al. 2007b, Slagstad & Davidsen 2007). (b) U–Pb protolith ages from the Western Gneiss Region (from compilation by Skår 2000). The numbered references are listed in Slagstad & Davidsen (2007).

PETROPHYSICAL DATA AND PHOTOGRAPHS OF NPD AND STATOIL CORES

Trond Slagstad and Cécile Barrère

The basement samples stored at the national core repository at NPD were measured in NGUs petrophysical laboratory within the frame of the KONTIKI project. The results are published by Slagstad et al. (2008) and the petrophysical data from the North Sea and the Norwegian Sea are listed below (Figs. 1 & 2, Table 1)

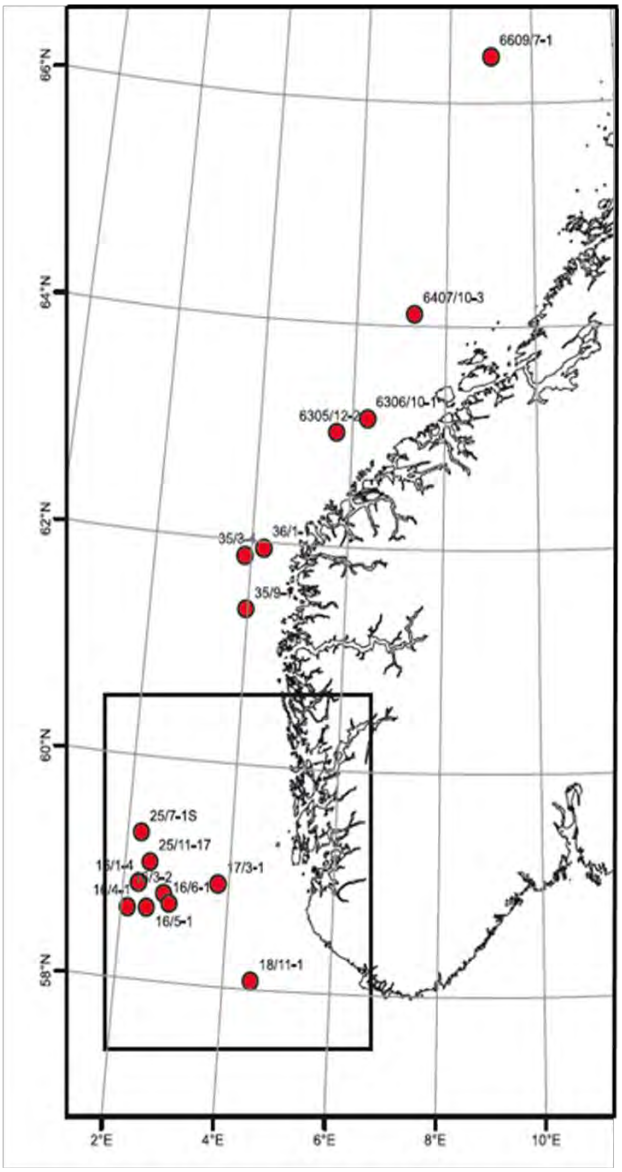

Figure 1. Map showing the locations and names of wells from which basement samples have been obtained (Slagstad et al. 2008).

Well name	Sample depth (m)	Area	Top Basement depth (m)	Sample depth below Top Basement (m)	North	East	Lithology	Density (kg m^{-3})	Magnetic suscept. (10^{-6} SI)	Magnetic remanence (10^{-3} A m^{-1})	Electrical resistivity (ohm*m)
16/1-4	1937.0	North Sea	1864.0	73.0	58° 51' 55.20'' N	2° 17' 56.12'' E	Gabbro	2765	448.4	32.1	130
16/3-2	2017.7	North Sea	2015.0	2.7	58° 47' 12.80'' N	2° 47' 34.70'' E	Granite	2680	949.7	48.8	39845
16/4-1	2907.4	North Sea	2885.0	22.4	58° 38' 18.33'' N	2° 8' 17.03'' E	Altern. qtzite/siltstone	2778	221.3	2.8	3829
16/4-1	2908.6	North Sea	2885.0	23.6	58° 38' 18.33'' N	2° 8' 17.03'' E	Granite	2646	88	6.9	11075
16/5-1	1929.3	North Sea	1925.0	4.3	58° 38' 53.66'' N	2° 29' 39.69'' E	Granite	2662	179.8	11.3	403
16/6-1	2059.7	North Sea	2055.0	4.7	58° 42' 06.00'' N	2° 54' 44.00'' E	Porph. volcanic rock	2591	181.1	9.5	768
17/3-1	2849.5	North Sea	2811.0	38.5	58° 55' 02.50'' N	3° 48' 21.33'' E	Breccia	2750	553.3	10.3	1100
17/3-1	2850.7	North Sea	2811.0	39.7	58° 55' 02.50'' N	3° 48' 21.33'' E	Breccia	2661	58.3	0	14854
18/11-1	2082.3	North Sea	2060.0	22.3	58° 4' 21.30'' N	4° 32' 00.10'' E	Porph. volcanic rock	2639	207.4	2.2	1465
25/7-15	3548.2	North Sea	n.a.	n.a.	59° 18' 35.23'' N	2° 16' 05.37'' E	Brecciated siltstone	2683	1406.8	68.7	110
25/7-15	3554.3	North Sea	n.a.	n.a.	59° 18' 35.23'' N	2° 16' 05.37'' E	Qtz-rich sandstone	2722	48.8	9.2	553
25/11-17	2259.5	North Sea	2243.0	16.5	59° 3' 26.66'' N	2° 29' 06.59'' E	Metasiltstone	2666	291.6	0	415
35/3-4	4088.3	North Sea	4069.0	19.3	61° 51' 54.54'' N	3° 52' 26.99'' E	Bt-gneiss	2773	234.1	0	2288
35/9-1	2313.6	North Sea	2313.6	0.0	61° 23' 07.95'' N	3° 59' 03.72'' E	Breccia	2619	286.4	0	38
36/1-1	1588.7	North Sea	1568.0	20.7	61° 56' 40.36'' N	4° 15' 43.86'' E	Granitic gneiss	2676	104.3	5.2	835
6305/12-2	3158.3	Norwegian Sea	3145.0	13.3	63° 1' 11.39'' N	5° 40' 06.44'' E	Brecciated siltstone	2740	456.8	9.6	198
6306/10-1	3158.5	Norwegian Sea	2989.0	169.5	63° 9' 26.32'' N	6° 19' 41.45'' E	Quartz diorite	2767	2836.2	58.6	363
6306/10-1	3159.2	Norwegian Sea	2989.0	170.2	63° 9' 26.32'' N	6° 19' 41.45'' E	Quartz diorite	2732	1001.7	20	1403
6407/10-3	2972.1	Norwegian Sea	2959.0	13.1	64° 6' 11.66'' N	7° 18' 11.43'' E	Granite	2631	1186.7	108.9	11622
6609/7-1	1944.7	Norwegian Sea	1912.0	32.7	66° 24' 56.49'' N	9° 1' 14.91'' E	Brecciated silt-/ sandstone	2622	14.7	0	958
6609/7-1	1945.8	Norwegian Sea	1912.0	33.8	66° 24' 56.49'' N	9° 1' 14.91'' E	Altern. silt-/sandstone	2580	24.6	11	1121

Table 1. Petrophysical properties of basement samples from the North Sea and the Norwegian Sea (Slagstad et al. 2008). Note that the magnetic susceptibility is low for all samples and reveals an occurrence of paramagnetic minerals but a very low content of ferromagnetic minerals such as magnetite, hematite and magnetite.

Photgraphs from Slagstad & Barrère (2007) in the Kontiki Final Report (Olesen et al. 2007) are included below. The sample locations are shown in Figure 1.

NPD core samples

16/1-4, 1937m Utsira High, North Sea

Medium- to coarse-grained, undeformed gabbro (leucogabbro). The gabbro is strongly altered and saussuritised and contains a few small, calcite-filled veins and vugs.

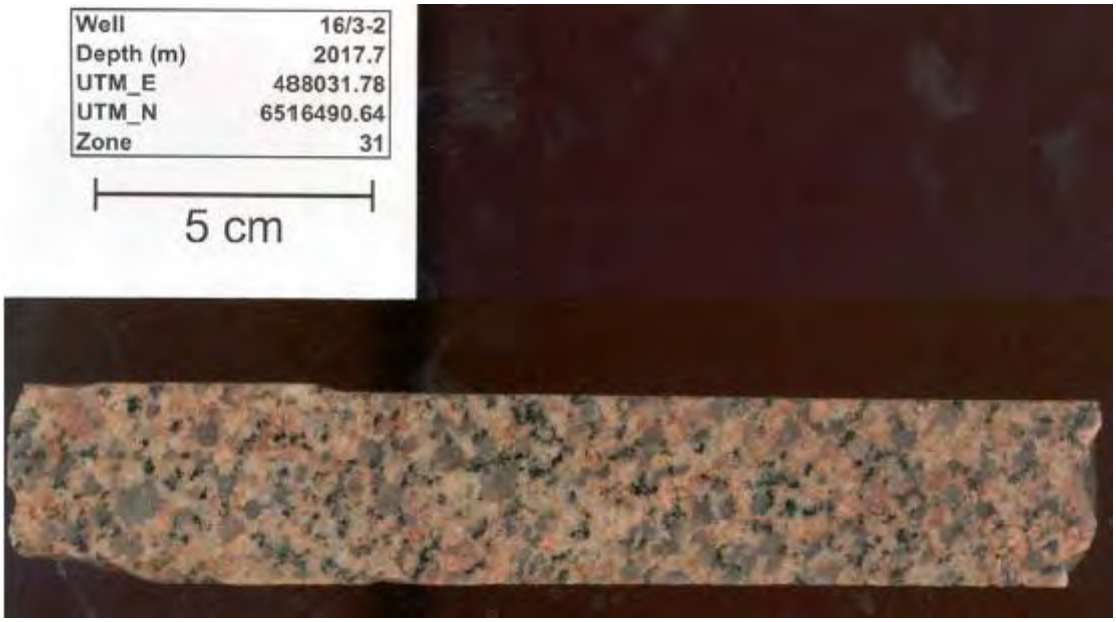

16/3-2, 2017.7m North Sea

Medium-grained, red granite consisting of fine-grained, whitish-red to red feldspar and coarser (<1 cm) irregular, but generally rounded, grains of quartz. The granite is unfoliated and spotted with 1–4 mm black, unoriented specks of hornblende, homogeneously distributed in the rock.

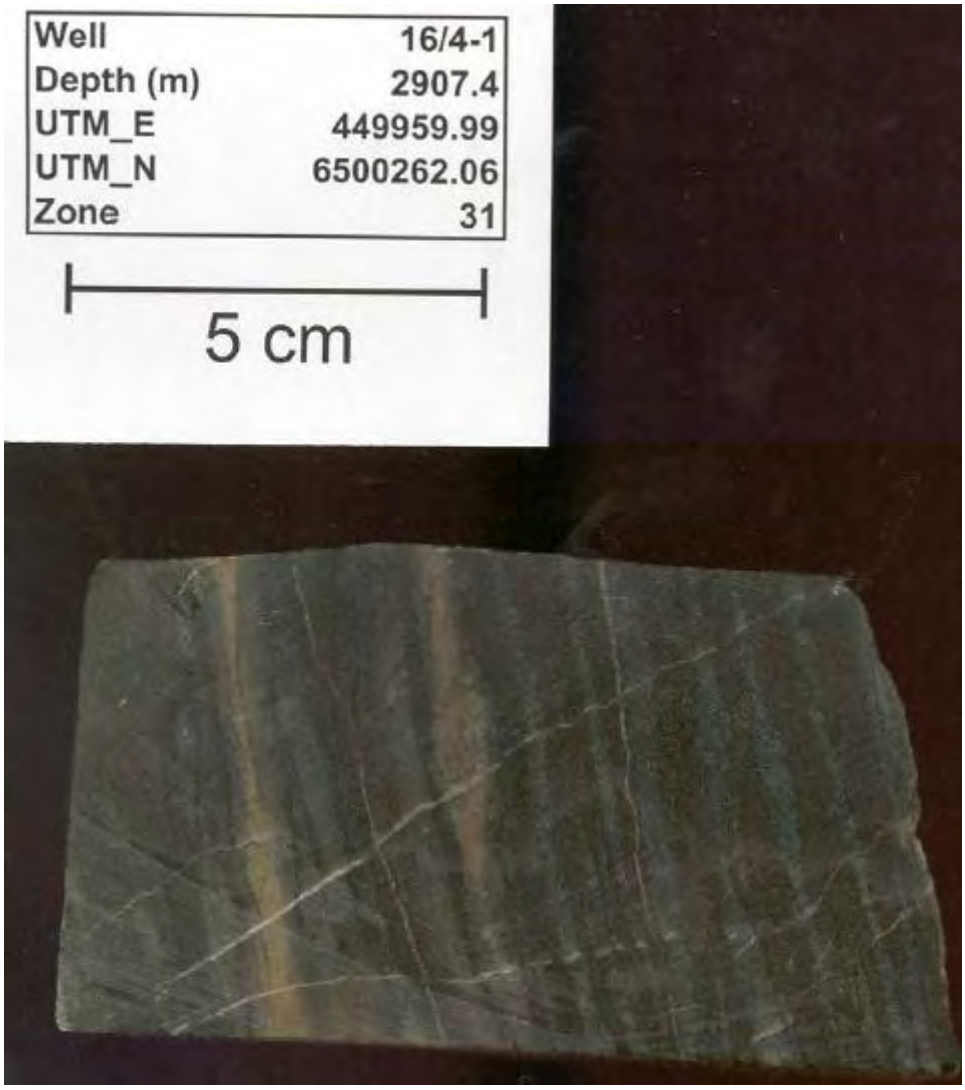

16/4-1, 2907.4m Utsira High, North Sea

Compositely layered, fine-grained, light grey quartzite and dark grey siltstone. Layer thickness varies from c. 1 mm up to several cm. The rock is criss-crossed by thin, calcite-filled veins, dominantly subvertical, although subhorizontal veins are also found. The subvertical veins appear to form en echelon patterns, and some of the veins are only developed in the quartzite but are not visible in the siltstone. This effect is most likely caused by differences in rheology of the two rock types. Some cm-thick, green to orange layers, slightly oblique to the layering in the rock, appear to consist of epidote and albite (?) and are most likely metasomatic.

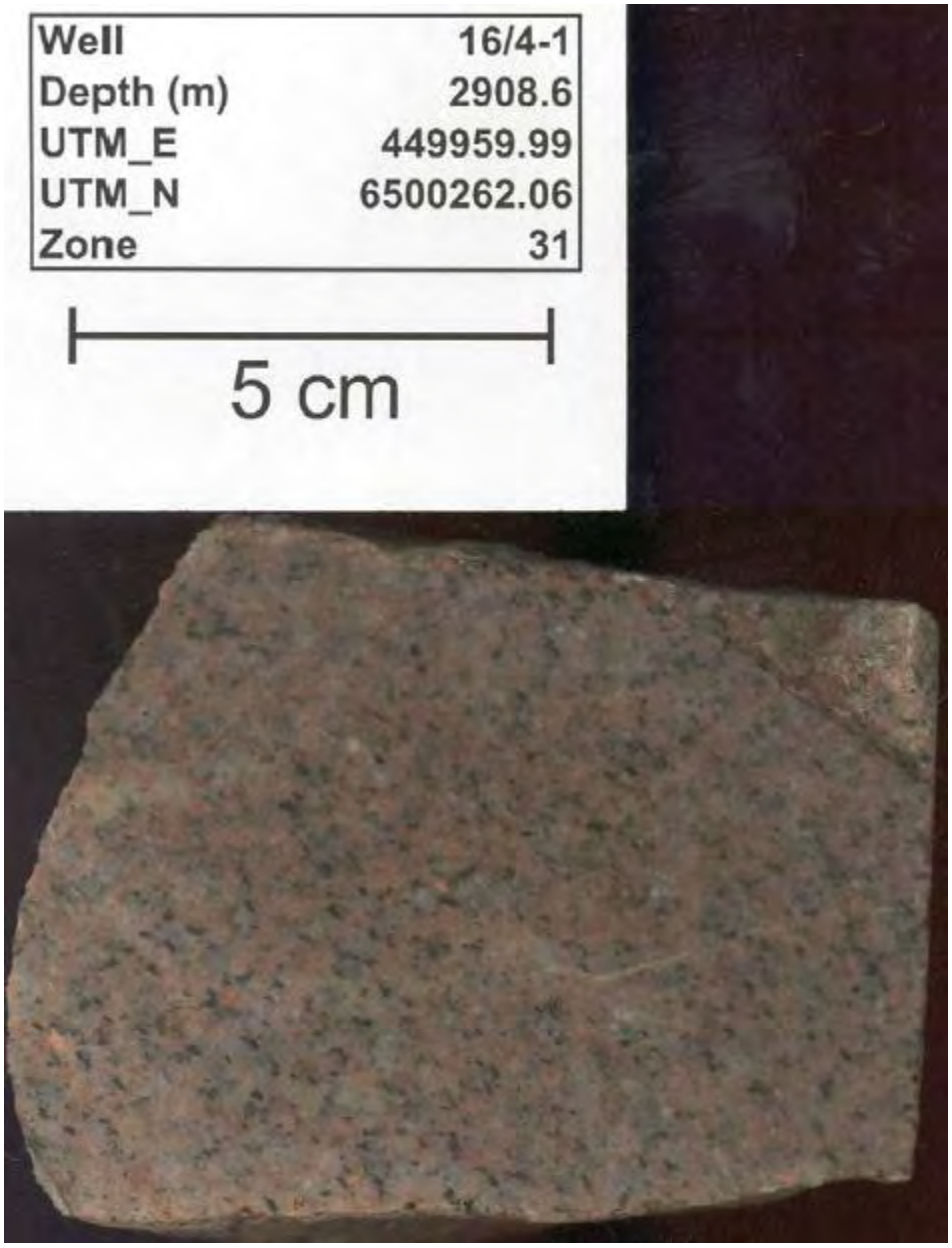

16/4-1, 2908.6m Utsira High, North Sea

Fine-grained granite, grey with a reddish hue. The granite is unfoliated and spotted with 1–3 mm, black, unoriented specks of hornblende, homogeneously distributed in the rock.

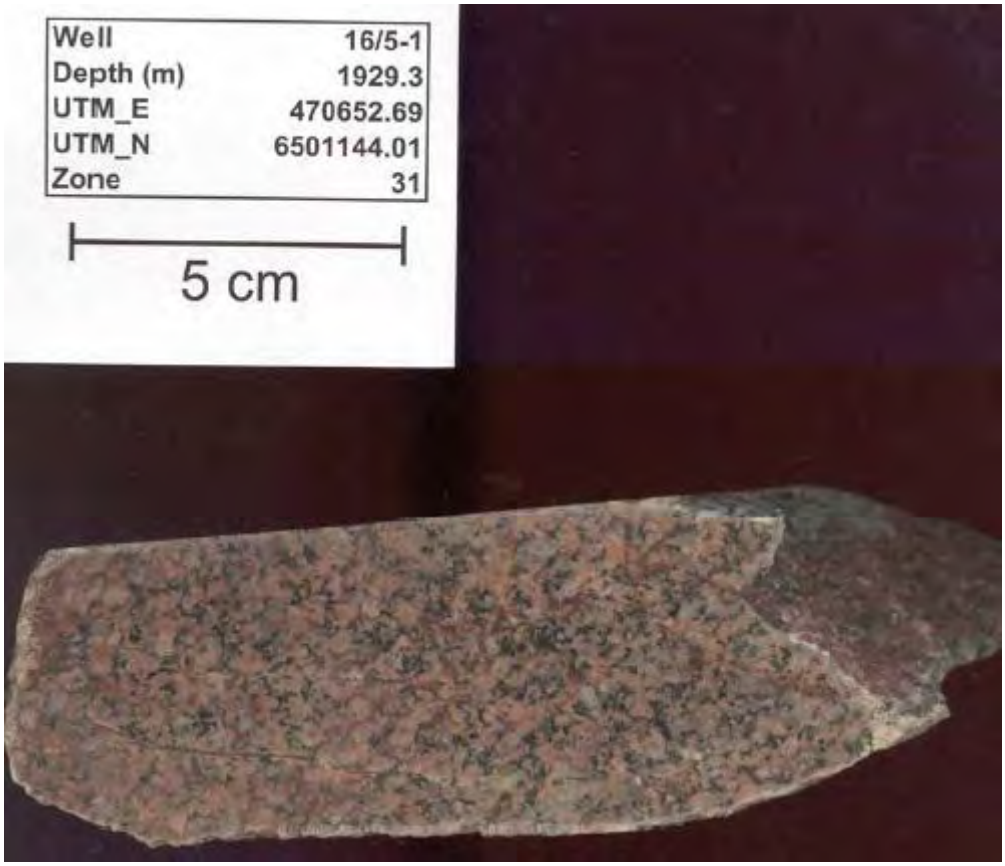

16/5-1, 1929.3m Utsira High, North Sea

Fine-grained, unfoliated, dark red granite with intergrown, irregular (i.e., in matrix) hornblende. There are some cracks in the sample with discontinuous, thin, bleached margins, indicating some alteration.

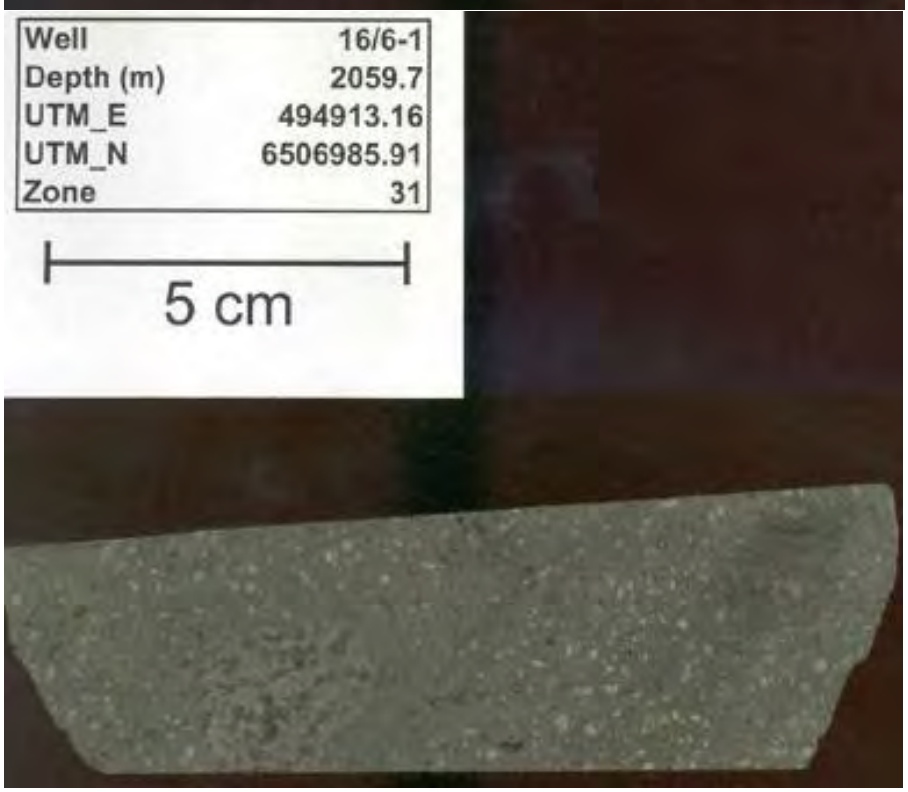

16/6-1, 2059.7m Utsira High, North Sea

Fine-grained, undeformed, grey volcanic rock with abundant small (<2 mm) phenocrysts of plagioclase and more rarely quartz, and specks of hornblende(?), set in a fine-grained, feldspar-rich (+some quartz) groundmass. The rock also contains a small (c. 4 cm) inclusion of slightly coarser grey rock, probably a xenolith.

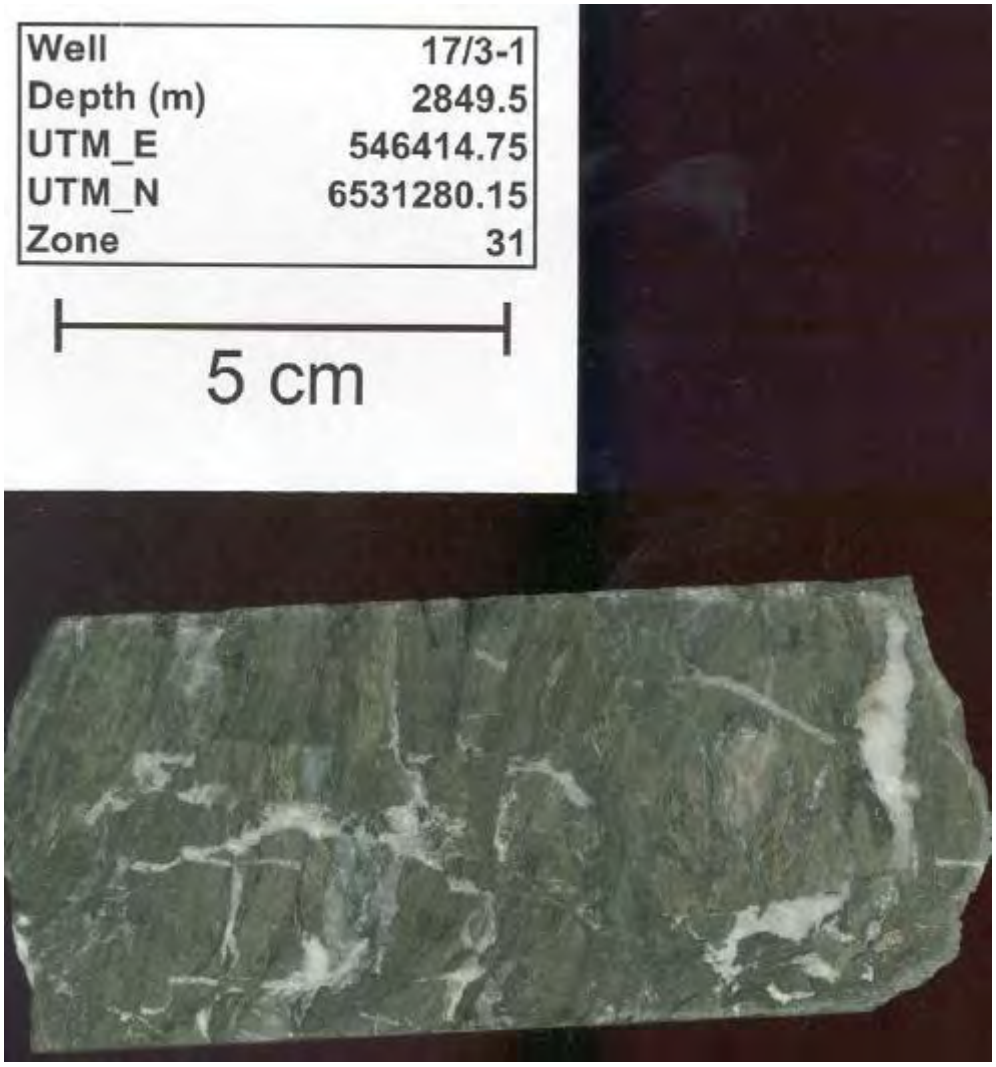

17/3-1, 2849.5m Stord Basin, North Sea

Dark green fault breccia with abundant calcite-filled veins and vugs. The rock appears to contain quite abundant chlorite and possibly epidote, but little quartzofeldspathic material, making it distinct from the other sample from this core (at 2850.7m).

From NPD's Fact-page: "…drilled […] in metamorphic basement rock, dated 410 My".

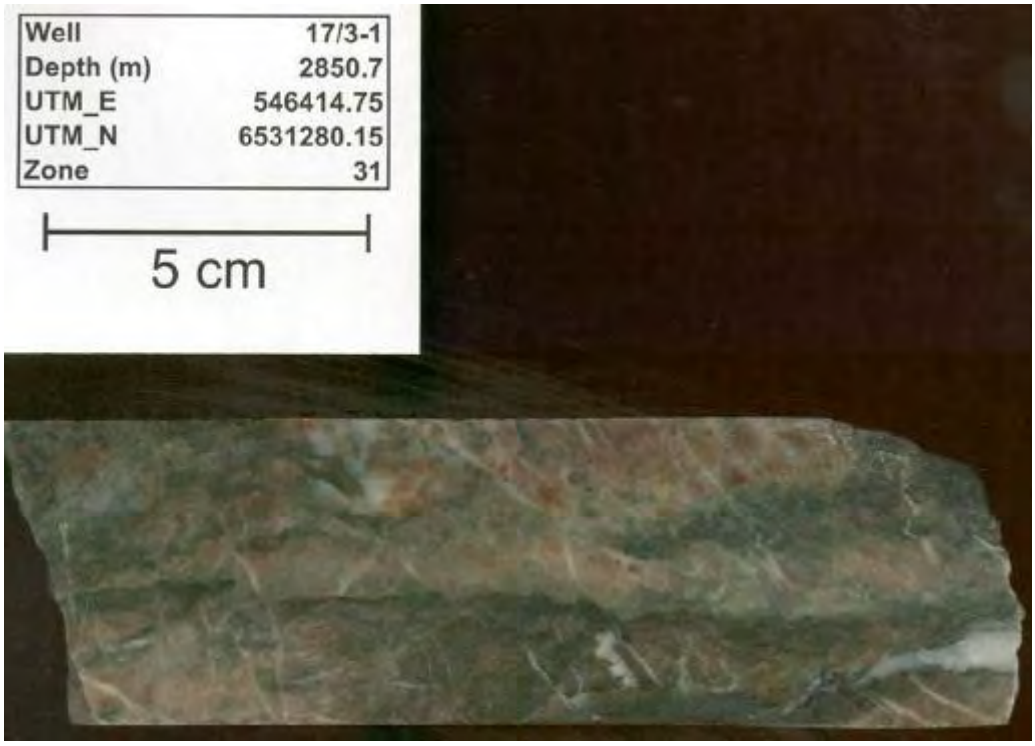

17/3-1, 2850.7m Stord Basin, North Sea

Fault breccia consisting predominantly of medium-grained feldspar, altered feldspar and epidote, as well as layers/inclusions of mafic material. The breccia is cross-cut by numerous calcite-filled veins, some of which offset the breccia, and microveins.

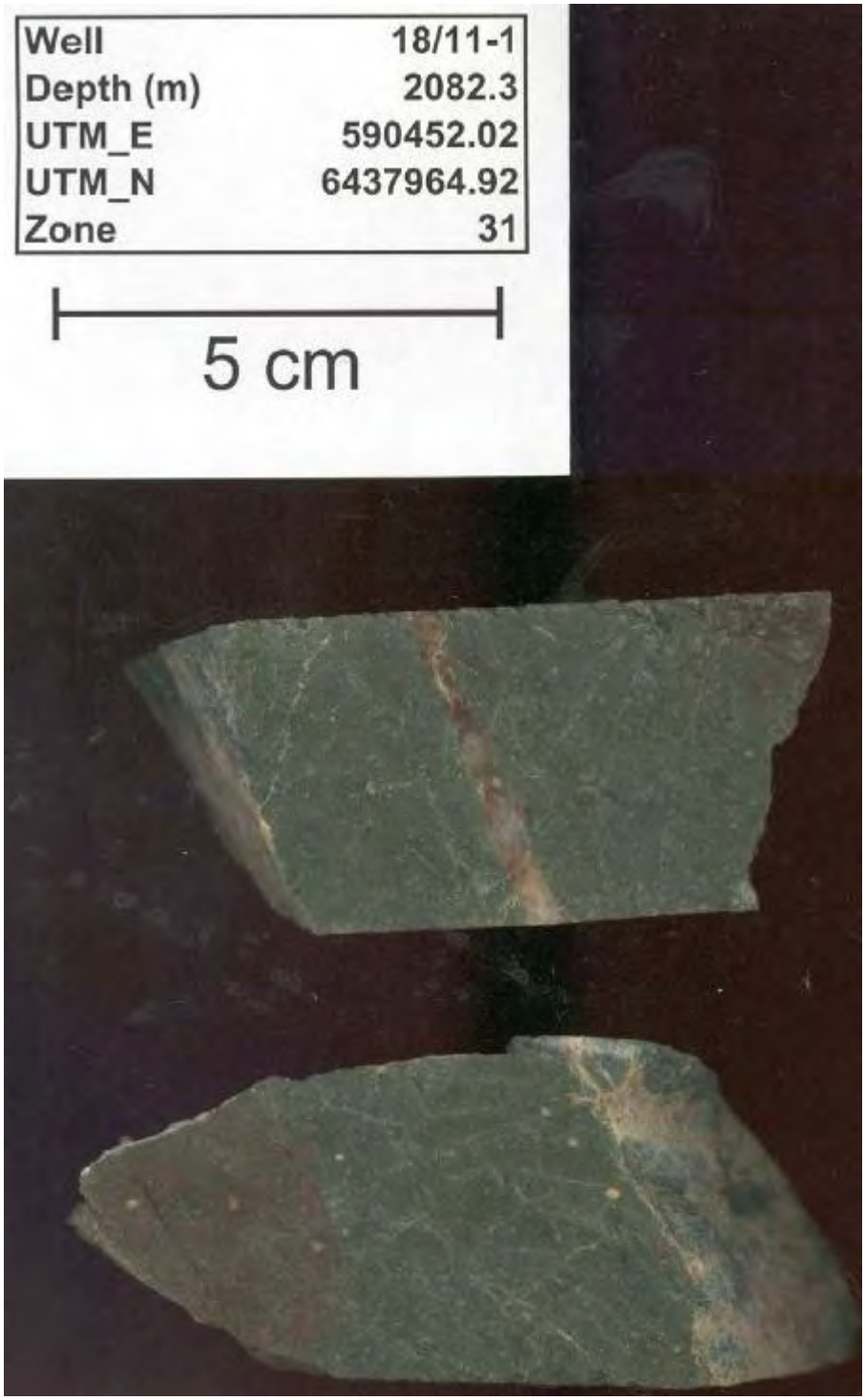

18/11-1, 2082.3m Stavanger Platform, North Sea

Dark green, volcanic rock with plagioclase phenocrysts, typically 1–2 mm across, set in a fine-grained, feldspar-rich (+some quartz) groundmass. The rock is criss-crossed by numerous, white, hairline veins that locally are calcite-filled.

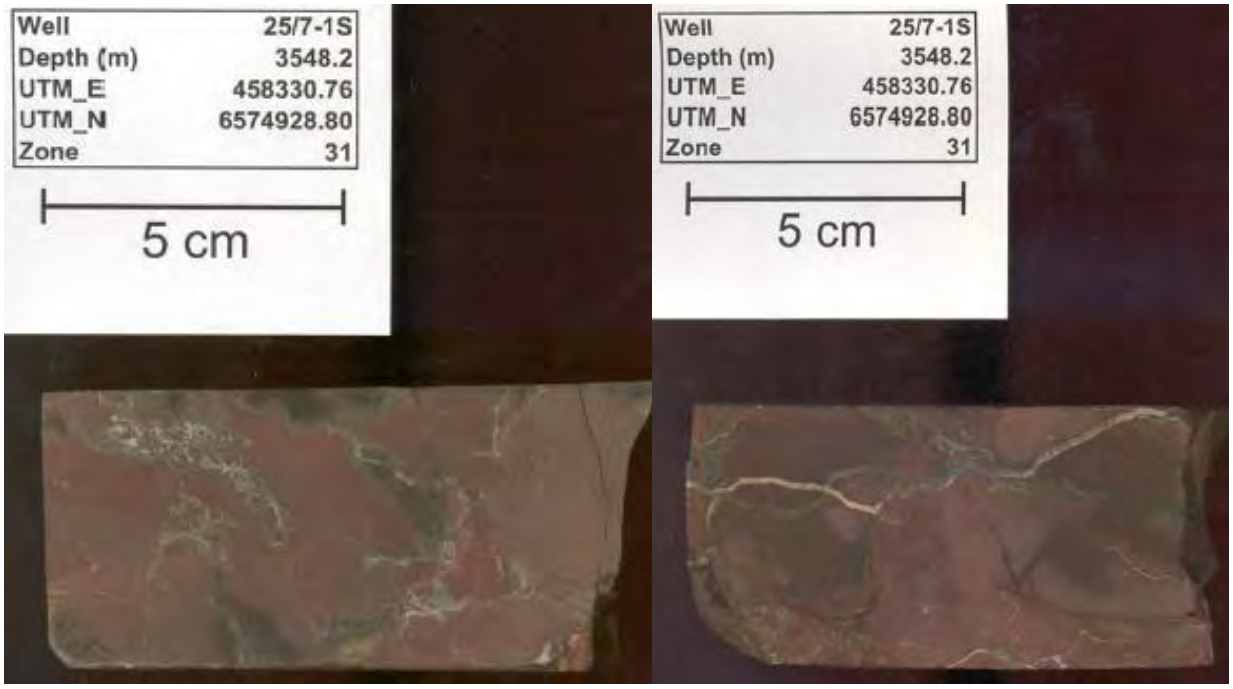

25/7-1S, 3548.2m North Sea

Breccia with irregular fragments typically c. 5 cm long of dark red, microcrystalline, calcareous siltstone(?). The fragments have slightly rounded edges. The groundmass consists of some microcrystalline, calcareous, dark green rock, and several irregular patches of microcrystalline, calcareous, dark red rock that appear to transect calcite-filled veins which in turn cut the siltstone fragments. The dark red siltstone and microcrystalline patches are difficult to distinguish, but in general the former appears slightly coarser grained.

25/7-1S, 3554.3m North Sea

Faintly banded, fine-grained, grey quartz-rich sandstone. The sandstone is criss-crossed by numerous thin veins, with dark green, white or brown infilling. The brown infilling is calcareous.

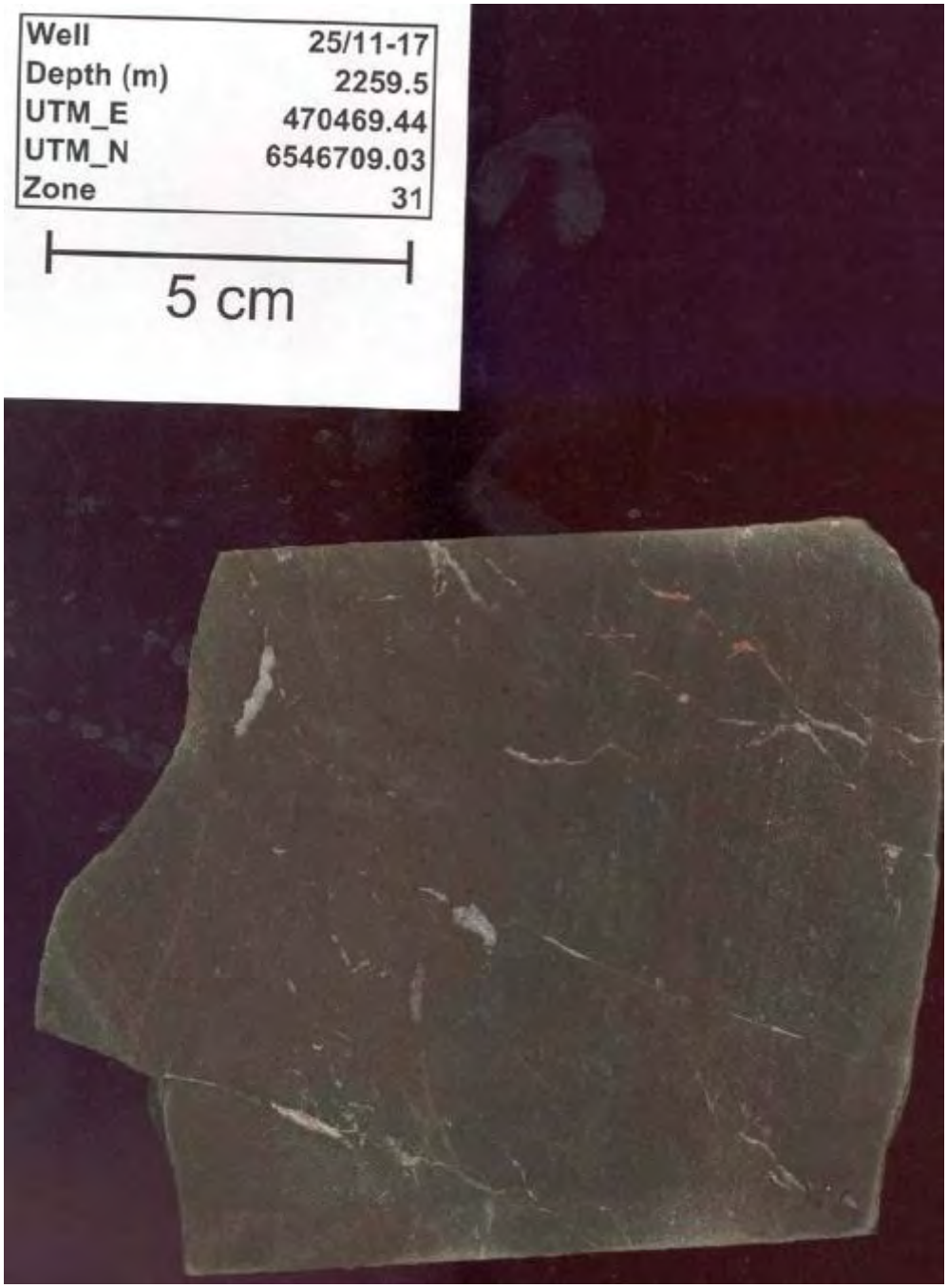

25/11-17, 2259.5m Balder/Grane area, North Sea

Microcrystalline to fine-grained, dark brown to grey siltstone with numerous short (<2 cm), irregular veins and vugs filled with white and more rarely red material, identified as calcite, and possibly some zeolite.

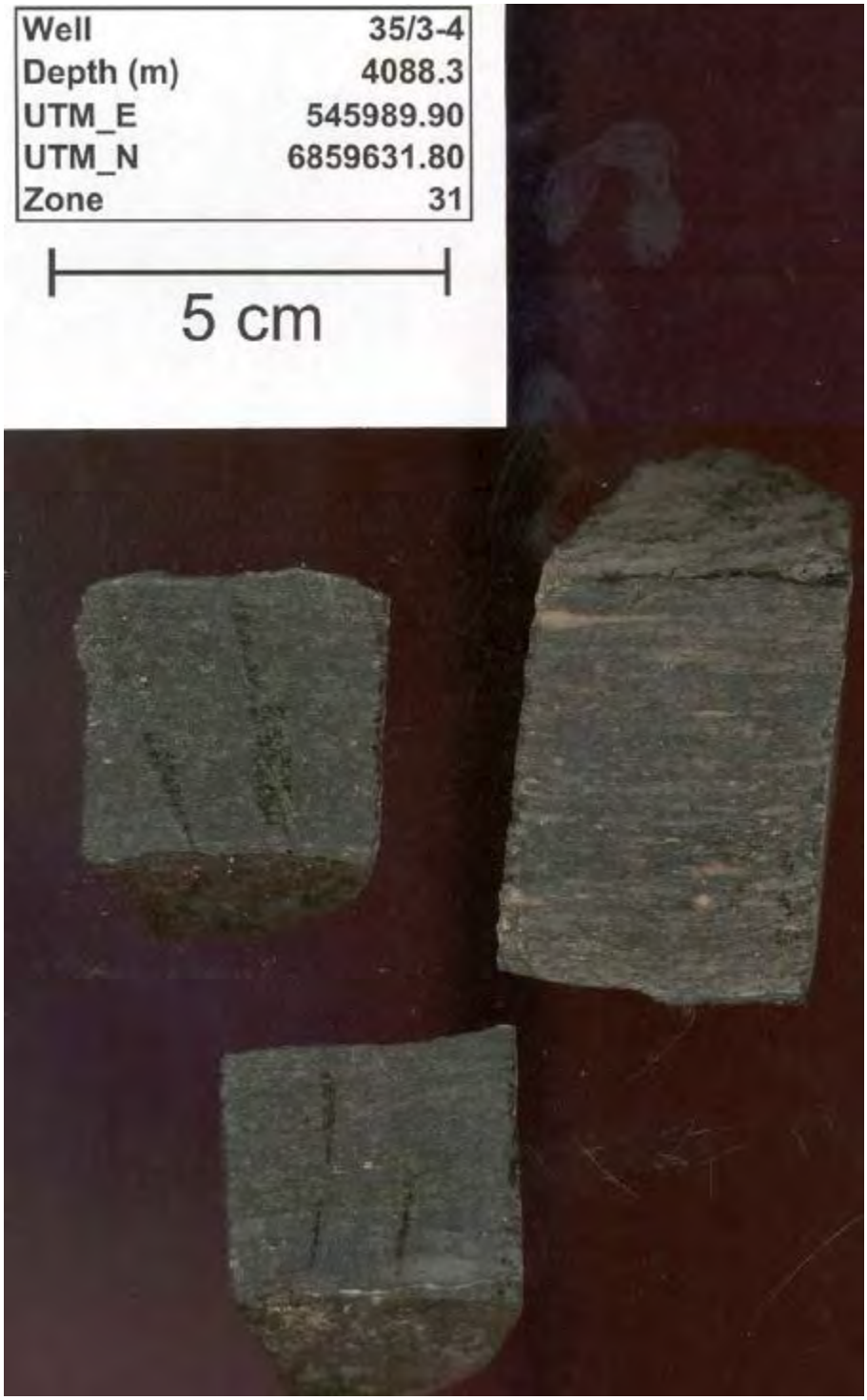

35/3-4, 4088.3m North Sea

Fine-grained, dark grey, quartz-rich mica schist with several, concordant, mm-sized patches and veins of granitic(?) material. The rock contains a fair amount of pyrite, some with well-developed crystal faces, typically 1–2 mm across but locally up to 5 mm.

From NPD's Fact-page: "…before reaching basement rocks of Caledonian age".

35/9-1, 2313.6m North Sea

Fine-grained, dark green breccia. Colour varies from light grey, green, dark green to dark grey, giving the rock a speckled appearance. The light grey and green material is calcareous. The breccia contains some mm-thick, calcite-filled veins. No larger clasts can be observed.

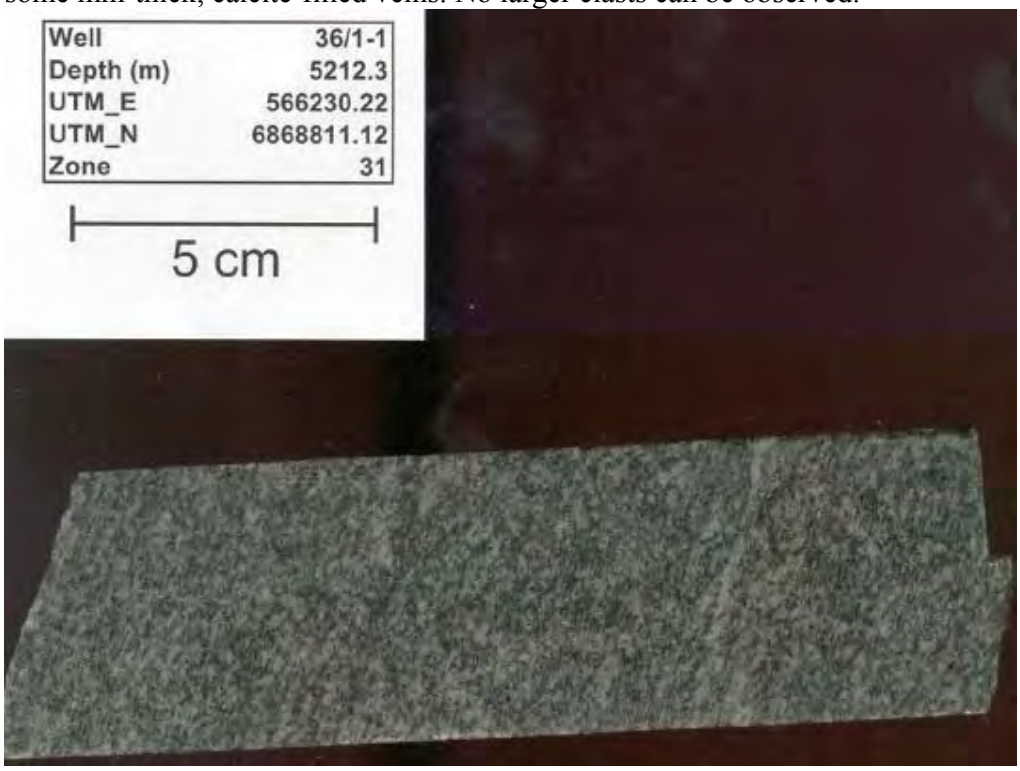

36/1-1, 5212.3m, North Sea

Fine-grained, grey, biotite-epidote-bearing granitic gneiss. Abundant biotite laths impart the gneiss with a strong foliation.

6305/12-2, 3158.3m Norwegian Sea

Grey fault(?) breccia consisting dominantly of angular fragments of siltstone, separated by thin "veins" of dark material. Some fragments of quartz and some calcite that appears to pre-date brecciation. Numerous calcite-filled veins and vugs. The breccia appears to contain abundant chlorite.

6306/10-1, 3158.5m Frøya High, Norwegian Sea

Fine- to medium-grained, unfoliated leucogabbro with a few calcite-filled cracks. The gabbro is strongly altered and saussuritised.

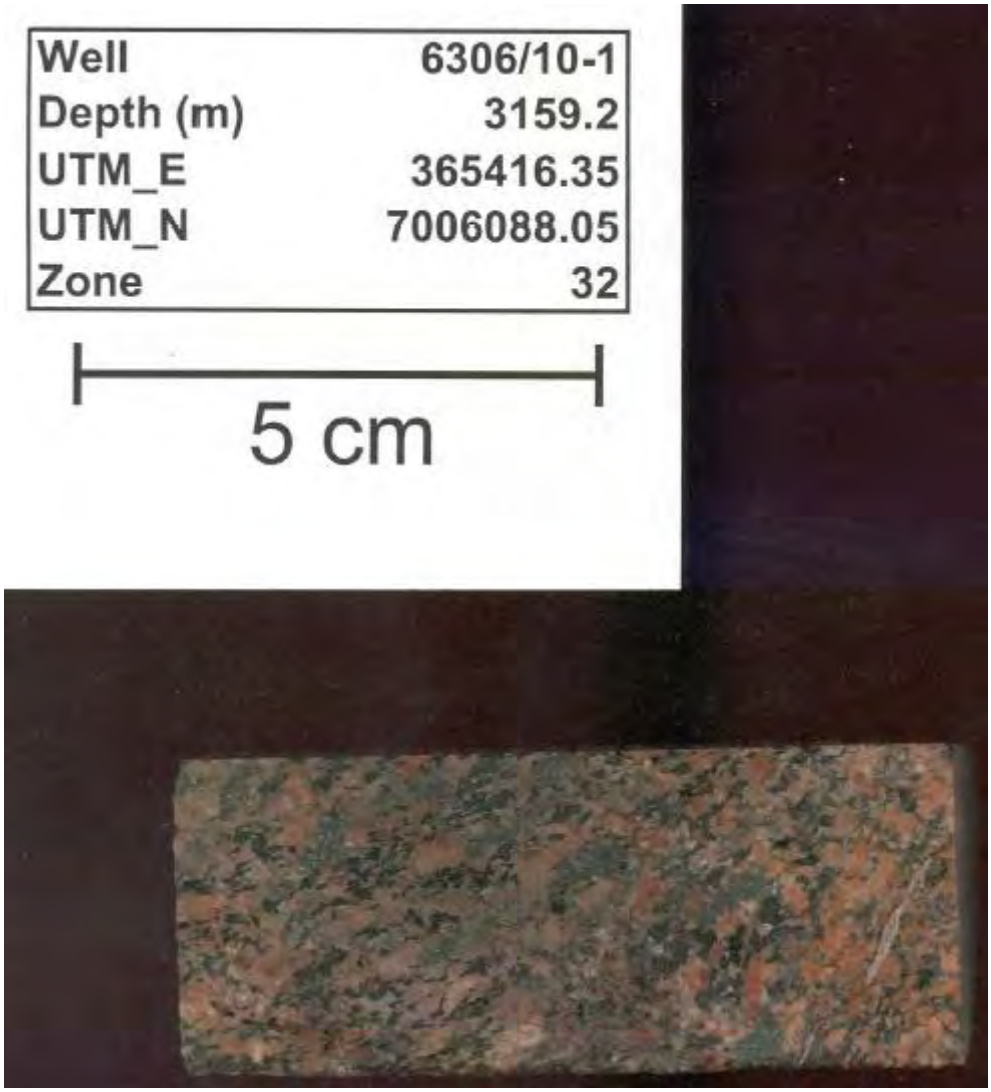

6306/10-1, 3159.2m Frøya High, Norwegian Sea

Fine- to medium-grained, unfoliated leucogabbro with a few calcite-filled cracks. The gabbro is strongly altered and saussuritised.

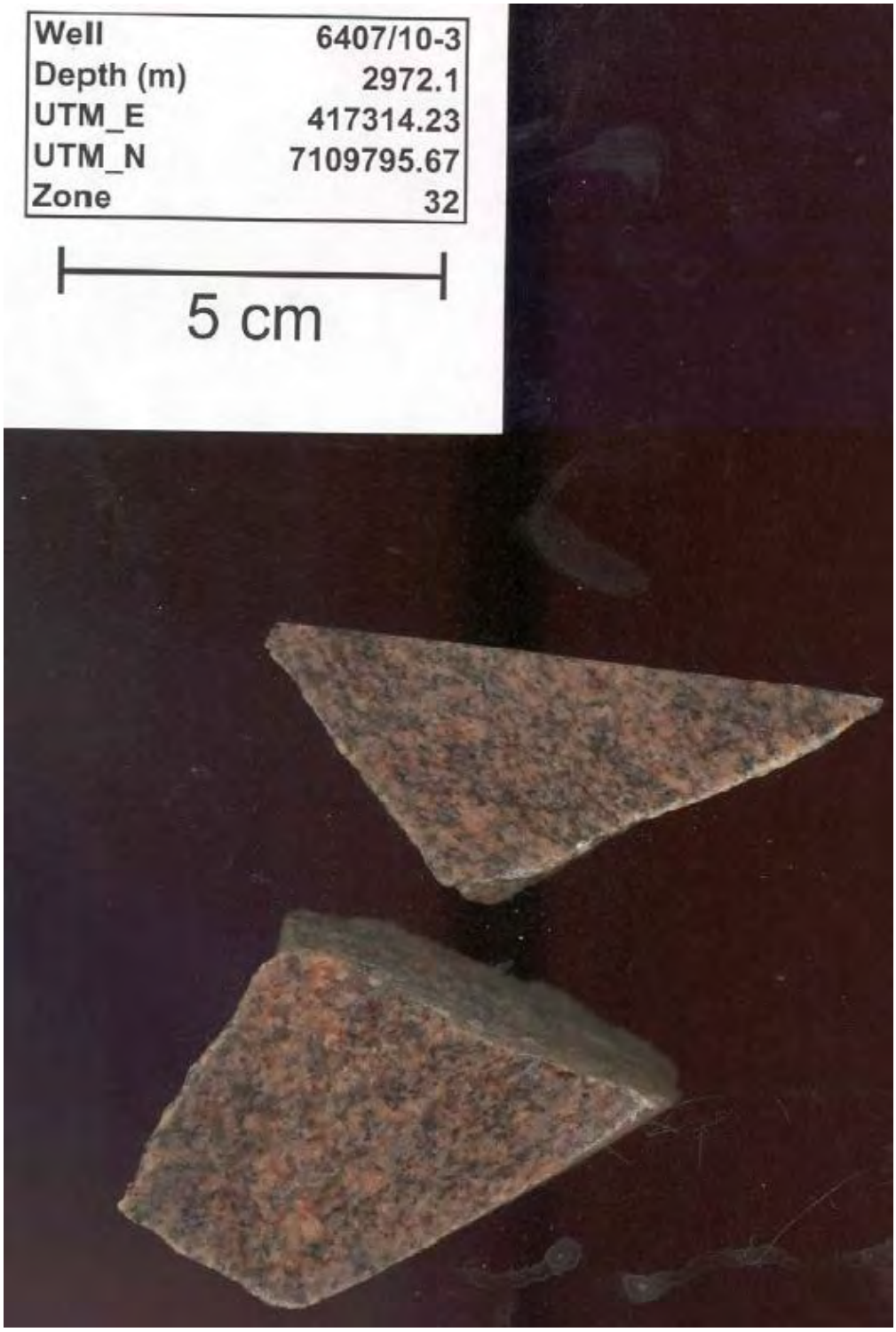

6407/10-3, 2972.1m Norwegian Sea
Fine-grained, unfoliated, dark red granite with small specks (<1 mm) of hornblende.

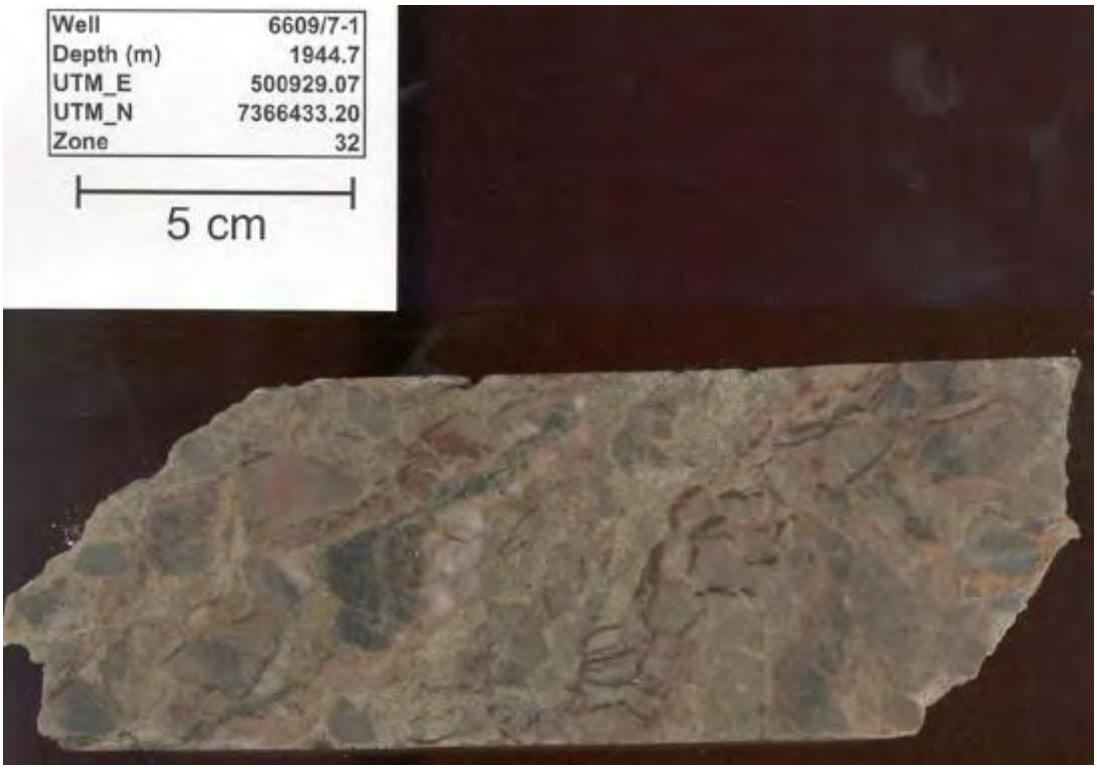

6609/7-1, 1944.7m Norwegian Sea

Breccia with angular fragments of fine-grained, quartz-rich sandstone and siltstone. The quartzite is grey with a reddish hue, and the fragments range in size from a few mm up to several cm. The matrix consists of crumbly, microcrystalline, green material, and minor amounts of red to brown calcareous material.

6609/7-1, 1945.8m Norwegian Sea

Laminated metasediment consisting of layers, typically < 1 cm thick, of microcrystalline sandstone/quartzite(?) with a orange hue, and thinner layers of grey, microcrystalline siltstone(?). The rock is extensively cracked with calcite-filled veins. It is possible that the sandstone/siltstone is calcareous, but the large number of small calcite-filled veins makes it difficult to discern which part of the rock fizzes when exposed to HCl.

Beskrivelse til geologisk kart over Norge 1:250000, Måløy

E. Sigmond Kildal
Utgitt 1970

1.1 GEOLOGISK OVERSIKT

Kartbladet Måløy omfatter fem av de seks vestnorske devonfeltene, og deres underlag av forskjellige metamorfe bergarter. De predevonske bergarter har vært utsatt for en gjennomgripende kaledonsk deformasjon og metamorfose. Dette gjør det meget vanskelig å utrede de tektoniske/ stratigrafiske forhold, men følgende bergarts-komplekser er forsøkt utskilt:

yngst 5. Bergarter av devonsk alder.
4. Bergarter av kambro-silurisk alder.
3. Metamorfe suprakrustalbergarter antatt avsatt i den kaledonske geosynklinal. (Senprekambrisk til kambro-silurisk alder)
2. Overskjøvne charnockittiske bergarter, mindre intrusiver og inneslutninger i gneisene. (Ukjent alder).
Eldst 1. Basalgneiskomplekset. (Kaledonsk omdannede, overveiende prekaledonske bergarter).

Kvartskeratofyr fra Solund og muligens enkelte diabasganger er yngre enn devonavsetningene. (Sand- og grusavsetninger fra kvartærtiden er ikke avmerket på kartet). Landskapet er preget av trange fjorder og daler som skjærer seg inn i landmassen. Det markerte relieff er et resultat av den tertiære landhevning og den derav følgende sterke erosjon, både i tertiær tid og ved breenes arbeide under de kvartære istider.

BERGARTSBESKRIVELSE

1. Basalgneiskomplekset. (Kaledonsk omdannede, overveiende prekaledonske bergarter).

Basalgneiskomplekset omfatter intrusiver, migmatitter og gneiser av varierende typer. Omkring Førde og på begge sider av Sognefjord er bergartene oftest middels- til grovkornet, ofte med flytefolder og med hyppig opptredende pegmatittårer. Gneisbeltet fra Myklebust (nord for Åfjord) og østover til Hestadfjord består også av lyse, finkornede kvarts-feltspat-bergarter, disse kan være opprinnelige suprakrustale bergarter (meta-arkoser). Det er vanskelig å skille disse fra lignende yngre bergarter, – den stratigrafiske inndeling i dette området er derfor stedvis usikker. Sonen av øyegneis syd for Nordfjord og diverse intrusivbergarter ved Tangen syd for Sognefjord hører sannsynligvis også til basalgneiskomplekset.

2. Overskjøvne charnockittiske bergarter, mindre intrusiver og inneslutninger i gneisene. (Ukjent alder).

Nord for Nordfjord finnes større områder med mangerittiske bergarter, mineralassosiasjon: granat-plagioklas-orthoklas med disthen eller klinopyroksen. Syd for Førdefjord har vi et større område av mangerittsyenitt. Begge disse mangerittkomplekser har en tektonisk posisjon som kan svare til de overskjøvne Jotundekker i det sentrale Sør-Norge. Syd for Hestadfjord finnes et mindre forkastningsområde med kvartsrike charnockittiske bergarter, hvis opprinnelse og tektoniske posisjon er uklar. I og over de metamorfe suprakrustalbergarter nord for Eikefjord opptrer kvartsfattige gneiser med soner og inneslutninger av anorthositt, serpentinitt og gabbro, De kvartsfattige gneiser har relikter av granat og mikroperthitt som antyder at de har vært charnockittiske før metamorfosen satte inn. Generelt finnes i de metamorfe supra-krustalbergarter små inneslutninger av eklogitt, granatamfibolitt og serpentinitt. Soner med anorthositt er funnet på nordre halvdel av kartbladet.

3. Metamorfe suprakrustalbergarter. (Antatt avsatt i den kaledonske geosynklinal. Senprekambrisk til kambrosilurisk alder).

Nord for den store forkastning ved Standal. (Standalforkastningen S. F.).

I Nordfjord er den dominerende bergart en granodiorittisk, båndet gneis med soner av øyegneis og granittisk gneis av forskjellig opprinnelse. Områder hvor den granodiorittiske gneis inneholder rikelig med soner av glimmerskifer, kvartsitt og amfibolitt er her skilt ut med grønn bunnfarve på kartet. Mellom Nordfjord og Standalsforkastningen finnes over basalgneis (basalgneis opptrer her øst for kartbladet) et kompleks av båndet kvarts–biotitt–plagioklas–gneis med soner av glimmerskifer, feltspatholdig kvartsitt, meta-arkose og øyegneis. Lokalt finnes også dolomittførende glimmerskifer og dolomittmarmor.

Syd for Standalsforkastningen.

Fra Førdefjord og sydover til kartgrensen ligger en lagserie av meta-arkose med soner av gneis, øyegneis, kvartsitt, glimmerskifer og noe amfibolitt over basalgneiskomplekset. Over disse ligger mørke, båndete kvartsfattige, plagioklas–biotitt–gneiser (metagråvakker, antatt derivert fra andesittiske/basaltiske vulkanitter) og amfibolitt. I disse bergarter opptrer soner av glimmerskifer, grønnskifer, øyegneis og kvartsitt. Det er en jevn overgang fra disse bergarter til de overliggende antatte kambro-siluriske grønnsteiner og grønnskifre.

I området øst for Vadheimsfjord og ved Fuglsetfjord opptrer tallrike kvartsittsoner i gneisene, den mektigste av disse har en maksimal bredde på ca. 2000 meter. Mellom Førdefjord og Standals-forkastningen er stratigrafien mere usikker. Her opptrer amfibolittiske skifre, biotittrike gneiser og meta-arkoser med soner av kvartsitt og øyegneis.

4. Bergarter av kambrosilurisk alder.

Grønnstein og grønnskifer er overveiende metabasalter og metatuffer. Grønnsteinene viser ofte overganger til gabbrolignende bergarter. Glimmerskifrene er vesentlig karbonatførende kvarts–muskovittskifre, noen inneholder granater. Ved Åfjord i Hyllestad er det granat–disthen–glimmer-skifre med overgang til gneiser. I Berlepollen på Bremanger finnes granat–staurolitt–skifer. Kvartsittene er mer eller mindre skifrige, grå eller hvite, og fører vekslende mengder med feltspat, muskovitt og kvarts. På Bremanger er kvartsittene brune grunnet høyt biotittinnhold. Fyllonitter finnes nord for Håsteinens devonfelt. Disse er antagelig dannet ved en mekanisk deformasjon av glimmer-skifre og metagråvakker. Kvarts, albitt, mikroklin, kloritt, muskovitt og kalkspat er hovedmineralene. Fyllonittene inneholder lag av grønnskifer. Kalkstein/marmor finnes ved Hyllestadfjorden, på Atløy og nord for Håsteinens devonfelt; på Frøya kun små marmorlinser.

5. Bergarter av devonsk alder.

Det er fem områder med avsetninger fra devontiden: Hornelen, Håsteinen, Kvamshesten, Bulandet, Værlandet og Solund. Fossilfunn daterer avsetningene til mellomdevon. Foruten sandstein er det breksjer og konglomerater med bollemateriale av varierende sammensetning. Sedimentene er avsatt i kontinentale innsynkningsområder begrenset av forkastninger.

Hornelens devonfelt består vesentlig av grønn sandstein med marginale breksjer og konglomerater,- areal 64 x 24 km^2. Sedimentserien har en tilsynelatende mektighet på over 20000 meter, og dette forklares ved en skjev innsynkning med en gradvis forskyvning av sedimentasjons-bassenget. Bølgeslagsmerker, tørkesprekker, krypespor og regndråpeavtrykk viser at avsetningen fant sted på grunt vann.

Håsteinens devonfelt består av tildels meget grove konglomerater og breksjer, - lengst i vest finnes litt sandstein. Enkelte steder består sedimentene av sammenkittet rasmateriale, blokker på 2 x 3 x 2 m er målt flere steder. Mektigheten er over 1000 meter.

Kvamshestens devonfelt består av tre ledd: 1) Basalbreksje og basalkonglomerat. 2) Rød og grønn sandstein. 3) Rød sandstein og konglomerat. Sedimentenes karakter viser at sedimentasjonen stort sett har foregått i takt med en etappevis

innsynkning av bassenget. Mektigheten er ca. 2500 meter.

Bulandet og Værlandets devonfelt består vesentlig av konglomerat, litt sandstein finnes i Sørværet. Mektigheten er over 2500 meter.

Solunds devonfelt består av konglomerat og sandstein, – sandstein finnes sørlig i de sentrale partier. Avsetningene er trolig vifteformede elveavsetninger med transport fra sydøst. Beregnet mektighet er 5200 meter.

Plutonske bergarter/intrusiver.

I basalgneiskomplekset opptrer partier med massive granittiske bergarter, noen av disse antas å være kaledonske intrusiver. (Førdeområdet).

I de metamorfe suprakrustaler er det intrudert flere granitter ved Førdefjorden, ved Bygstad, og på sydsiden av Sognefjorden. En rekke steder finnes det porfyrgranitt/øyegneis med intrusive relasjoner til sidebergartene. Gabbro opptrer flere steder, og er eldre enn de nevnte porfyrgranitter. Charnockittiske bergarter, tilsynelatende intrusive, opptrer hyppig. Kaledonske eller postkaledonske diabasganger finnes ved Kinn, Moldvær og Sandvik. Ultrabasitt (olivinstein nord for Nordfjord, serpentinitt syd for Nordfjord) og eklogitt opptrer som linseformede inneslutninger,

I bergarter av kambro-silurisk alder er det intrusiv gabbro på den sydlige del av Frøya, på Tviberg, på Atløy, mellom Eikefjord og Brufjord og i Solund. I Solund er gabbro trolig blitt skjøvet over devonavsetningene. På Bremangerland er det intrusjoner av kvartsdioritt, og i Hyllstad og på Svanøy av granodioritt.

FOSSILER

Kambro-siluriske fossiler

Atløy: På to steder på vestsiden er funnet koraller og enkrinittstilker i marmorlag i fyllitt. Sannsynlig alder er øvre ordovicium – undre silur. (5a-6c)

Frøya: Ved Nesje er det fossillignende tegninger i marmor (N.-H. Kolderup 1928). Ved Mulevikja lenger syd fant Reusch (1881) graptolittlignende tegninger i mørk skifer.

1.1.1 Devonske fossiler:

Hornelens devonfelt: Plantefossiler er funnet ved Svartevann ved Gjegnalundbreen. Følgende plantefossiler er funnet: *Thursophytom milleri, Damsonites ellenae, Hyenia, Pectinophyton norvegicum, Barrandeina kolderupi* og *Broeggeria norvegica*. Fiskefossilene er *krossopterygier* som er vanskelig å artsbestemme bortsett fra *Gyroptychius kiæri*. Sannsynlig alder er undre del av mellomdevon.

Kvamshestens devonfelt: Plantefossiler er funnet en rekke steder, disse ligner meget på Hornelens plantefossiler.

Sørværet: Funn av *Psilophyton* på Lamholmen tyder på at avsetningene er noe eldre enn Hornelens og Kvamshesten devonfelter.

ALDERSBESTEMMELSE

Radiologisk datering, kalium-argon metoden

Granodiorittisk bandet gneis: (biotitt), Totland i Nordfjord. 372 mill. år.

Mangerittiske bergarter (mikroperthitt) Deknepoll i Nordfjord 427±12 mill. år, 406±12 mill. år. **

Eklogitt (lys glimmer) Almenningen i Nordfjord 451±10 mill. år, 445±9 mill. år, 441±9 mill. år. **

Eklogitt (amfibol) Almklov 1850 mill. år. *

*Mc Dougall I. and Green, D. H., 1964

**Bestemmelser utført av F. M. Consultants L. T. D. Herne Bay, Kent, England.

ØKONOMISK GEOLOGI

Tidligere gruver og brudd:

Svovelkis og kobberkis: Svanøy, Grimelien og Vågedalen ved Flokenes.

Ilmenitt: Sørdal ved Gjølanger

Takskifer og steinbrudd: *Granat-disthen-skifer* (kvernstein): Åfjord i Hyllestad. *Kvartsitt:* Nordsiden av Dalsfjorden. *Kalkstein:* Åfjord i Hyllestad. *Kvartsdioritt:* Bremanger. *Kleberstein:* Svanøy

Nåværende gruver og brudd:

Olivinstein: Almklovdalen nord for Nordfjord. Årsproduksjonen i 1969 var 121000 tonn olivinsand.

1.2 Hydrogeologi:

De predevonske bergarter gir lite vann ved brønnboringer, vanligvis 0-600 l/time. Fra devonske bergarter har vi få hydrogeologiske data, men boringer antas å kunne gi noe større vannmengder. Vannets kvalitet er vanligvis god.

1.3 UTVALGT LITTERATUR

Forkortelser:

B. M.: Bergens Museum Aarbok. Naturvitenskapelig rekke.

B. U.: Universitetet i Bergen. Årbok. Naturvitenskapelig rekke.

N. G. T.: Norsk Geologisk Tidsskrift,

N. G. U.: Norge geologiske undersøkelse,

BRYHNI, I. 1964: Relasjonen mellom senkaledonsk tektonikk og sedimentasjon ved Hornelens og Håsteinens devon.. N. G. U. 223.

– 1966. Reconnaissance studies of gneisses, ultrabasites, eclogites and anorthosites in outer Nordfjord, Western Norway. N. G. U. 241.

GJELSVIK, T. 1951: Oversikt over bergartene i Sunnmøre og tilgrensende deler av Nordfjord. N. G. U. 179.

Høeg, O. A. 1966: Norges fossile flora. Universitetsforlaget.

IRGENS, M., HIORTDAHL, TH. 1864: Om de geologiske forhold paa kyststrekningen af Nordre Bergenhus Amt. Universitetsprogram for 2. halvaar 1864, Christiania.

JARVIK, E. 1949: On the middle Devonian Crossopterygians from the Hornelen field in Western Norway. B. U. 1948.. r. 8.

KOLDERUP, C. F. 1916: Bulandets og Værlandets konglomerat og sandstensfelt. B. M. 1915-16. Nr 8.

– 1923: Kvamshestens devonfelt. B. M. 1920 – 21. Nr. 4.

– 1925: Haasteinens devonfelt. B. M. 1923 – 24. Nr. 11.

– 1926: Solunds devonfelt. B. M. 1924 – 25. Nr. 8.

– 1927: Hornelens devonfelt. B. M. 1926. Nr. 6.

KOLDERUP, N. H. 1921 Der Mangeritsyenit und umgebende Gesteine in Söndfjord im westlichen Norwegen. B. M. 1920 – 21. Nr. 5.

– 1928. Fjellbygningen i strøket mellom Nordfjord og Sognefjord. B. M. 1928. Nr. 1.

– 1960. The relationship between Cambro-Silurian schists and the gneisscomplex in the Deep-Caledonides of Sogn and Fjordane, West Norway. Guide to excursions no. A 5 and no. C 2, Int. geol. Congr. Oslo 1960.

McDOUGALL, I. and GREEN, D. H. 1964: Excess radiogenic argon in pyroxenes and isotopic ages on minerals from Norwegian eclogites. N. G. T. 44 pp. 183-195.

NATHORST, A. G. 1915: Zur Devon flora des westlichen Norwegens. B. M. 1914 – 15. Nr. 9.

NILSEN, T. H. 1968: The relationship of sedimentation to tectonics in the Solund Devonian district of South Western Norway. N. G. U. 259.

REUSCH, H. 1881: Konglomerat-sandstensfelterne i Nordfjord, Söndfjord og Sogn. Nyt Magazin for Naturvidenskaberne. Bind 26.

SKJERLIE, F. J. 1968: The pre-Devonian rocks in the Askvoll-Gaular area and adjacent districts, Western Norway. N. G. U. 258.

For geologisk oversikt og flere referanser anbefales:

HOLTEDAHL, O., 1953: Norges geologi. N. G. U. 164.

– 1960: Geology of Norway. N. G. U. 208.

BESKRIVELSE TIL GEOLOGISK KART OVER NORGE - 1: 250.000, BERGEN

Jomar Ragnhildstveit og Dag Helliksen

GEOLOGISK OVERSIKT

Kartet viser berggrunnens oppbygning som i området består av:

l Grunnfjell og andre underlagsbergarter fra proterozoisk tid (105-149).
2 Bergarter fra kambrosilurisk tid (17-65, 104), dannet etter at grunnfjellet var slitt ned til et lavlandsområde.
3 Bergarter fra proterozoisk og kambrosilurisk tid, framskjøvet under den kaledonske fjellkjededannelsen (17-104).
4 Bergarter dannet etter den kaledonske fjellkjededannelsen (1-15).

Grunnfjellet og de andre underlagsbergartene (105-149) i området er ca 1800 til 900 millioner år. De yngste bergartene er hovedsakelig granitter, dannet i etterkant av den svekonorvegiske fjellkjededannelsen som fant sted for ca 1150-1000 millioner år siden. Grunnfjellet ble deretter utsatt for erosjon og begynte etter hvert å sprekke opp vest for kartområdet. Oppsprekkingen førte til at grunnfjellet for ca 600 millioner år siden var delt i to kontinentplater, Grønland-Amerikaplaten i vest og den fennoskandiske platen i øst. Kontinent-platene begynte sakte å drive fra hverandre. Mellom platene ble Iapetushavet (Protoatlanteren) dannet, og det ble dannet ny havbunnsskorpe fra smelter som kom opp langs midthavsryggen. I kambrisk tid var grunnfjellet i Sør-Norge slitt ned til et ganske flatt lavlandsområde som ble oversvømt av havet. Slam og leire ble avsatt i havet i kambrosilurisk tid, nå omdannet til glimmerskifer (104). I ordovicisk tid begynte de to kontinentene å drive mot hverandre igjen slik at havet etterhvert lukket seg. Sammenpressingen førte til den kaledonske fjellkjededannelsen. En liten del av havbunns-skorpen, samt bergarter avsatt oppå skorpen ble skjøvet på land tidlig under fjellkjededannelsen, for ca 470-450 millioner år siden og finnes nå i *Hardangerfjorddekket (18-65).* Havbunnsskorpen ble deretter overleiret av sedimentære bergarter som Mobergkonglomeratet (31) og dets overliggende, fossilførende kalkstein (30) fra ashgilltiden (ca 449-443 millioner år). Fossiler viser at sedimentasjonen i alle fall fortsatte til inn i tidligsilurisk tid. Deretter ble det en kraftig kontinent-kontinent-kollisjon mellom Grønland-Amerikaplaten og den fenno-skandiske platen for ca 425 millioner år siden. Under kollisjonen ble Grønland-Amerikaplaten trolig skjøvet litt innover den Fennoskandiske platen, noe som førte til sterk deformasjon og stedvis til mer enn dobling av skorpetykkelsen. Berggrunnen nordvest for Hardangerfjorden ble sterkt påvirket av denne siste kaledonske kollisjonsfasen, og består av en komplisert oppbygd stabel av skyvedekker (17-104) som er skjøvet over de proterozoiske underlags-bergartene (106-149). Underlagsbergartene nordvest for Hardangerfjorden (106-149) ble også for det meste sterkt deformert under denne siste kollisjonsfasen, men er likevel trolig stedegne eller tilnærmet stedegne bergarter, antatt sammenhengende med grunnfjellet sørøst for Hardangerfjorden. Grunnfjellet sørøst for Hardangerfjorden (105) ble bare kaledonsk deformert nær den overliggende skyvegrensen.

Dekkeoppbygningen startet muligens med at Hardangerfjorddekket ble skjøvet oppå en dypt erodert kontinentrand. Både *Lindåsdekket (73-88)* og enkelte *flak innen Hardangerfjorddekket (66-67)* består av bergarter som kan ha blitt løsrevet fra den dypt eroderte fennoskandiske? kontinentranden som

Hardangerfjorddekket ble skjøvet over. Under den videre skyvning, antatt med Hardangerfjorddekket over Lindåsdekket, løsnet etter hvert også andre bergarter fra den underliaoende kontinentskorpen. Dette gjelder de proterozoiske bergartene i *Blåmans- (89-91*), *Mjånes- (92), Slettafjell- (93-96) og Grasbergdekket (97-103),* som alle gled lett på den underliggende, karbonholdige, kaledonske glimmerskiferen (104). Under den siste fram-skyvningsfasen førte folding, imbrikasjoner og andre tektoniske avskjæringer til at Hardangerfjord-dekket havnet i forskjellige nivåer i dekkestabelen. Dekket ligger f. eks. klart under andre dekker i Bergensområdet og inntar forskjellige posisjoner ellers i området. Hardangerfjorddekket er ut fra dette den øverste tektonostratigrafiske enheten i området og derfor plassert øverst av dekkene i tegnforklaringen. Det er imidlertid også indikasjoner på at Lindåsdekket kan være den øverste tektonostratigrafiske enheten.

Den nydannede kaledonske fjellkjeden ble straks utsatt for gravitasjonskrefter og strekning, og den begynte å slites ned av erosjon og tektoniske prosesser, ofte kalt den postorogene kollapsfasen. Først ble dekkene skjøvet noe tilbake mot nordvest i tidlig- til mellomdevonsk tid. Deformasjonen var mange steder så kraftig at den helt overpreger eldre strukturer. Dette gjelder særlig i Øygards-komplekset, Bergsdalen tektoniske enhet og de sørøstlige delene av det nordvestre gneisområdet. Sent under og etter tilbakeskyvningen ble det dannet folder og strekningsforkastninger som 'Foldegrøften' /Hardangerfjordskjærsonen langs Hardangerfjorden, og Bergensbue-strukturen vest for Samnangerfjorden-Fensfjorden (se snitt A'A"). Erosjonsprodukter fra fjellkjeden ble avsatt som tidlig- til mellomdevonske sedimenter i forkastningsbetingede bassenger som f. eks. *Solundbassenget (15).* Videre strekning førte til at kontinentet begynte å sprekke opp, og langs enkelte av de nord-sørgående sprekkene kom det opp mørke *gangbergarter (14)* i permisk til juraisk tid (274-162 mill. år). Under den videre strekningen og erosjonen ble det kontinuerlig avsatt *sedimenter fra triasisk til kvartær tid (13-1)* på sokkelen. Oppsprekkingen førte til at kontinentskorpen på nytt ble delt i to vest for kartområdet, og de to delene begynte å drive fra hverandre for knapt 60 mill. år siden. Mellom kontinentene ble Norskehavet dannet, og havet har siden vokst som følge av nydanningen av havbunnsskorpe langs den midtatlantiske spredningsryggen: Sedimentasjonen på sokkelen og erosjonen av kystområdene vil trolig fortsette i millioner av år.

INNDELING OG BESKRIVELSE AV BERGARTENE

STEDEGNE TIL NÆR STEDEGNE BERGARTER FRA PROTEROZOISK TID (105-149)

Grunnfjellet (148-149) sørøstligst på kartet, ved Løfallstrand, tilhører det sørnorske grunnfjellsområdet og består av gabbro gjennomsatt av tallrike diabaser, kvartsdioritt til tonalitt og yngre, massiv granitt. Grunnfjellet er deformert nær den overliggende, kaledonske skyvegrensen.

De proterozoiske underlagsbergartene (105-147) nordvest for Hardangerfjorden er for det meste sterkt kaledonsk deformert med mange skjærsoner. Stedvis kan bergartene være kortskjøvet. Bergartene er blottlagt i områder der overliggende dekker er erodert vekk, og områdene har litt forskjellige kaledonske trekk. *Kikedalskomplekset (105)* (Kikedalsvinduet) består for det meste av granitt som kan være sammenhengende med granitt sørøst for Hardangerfjorden. I nærheten av den overliggende skyvegrensen og andre kaledonske/postkaledonske skjærsoner er granitten deformert og omdannet til båndet mylonittgneis. *Bergsdalen tektoniske enhet*

(106-116) består av sedimentære bergarter (kvartsitt, kvartsskifer, konglomerat, m.m.), vulkanske bergarter (basalt, andesitt, dacitt, ryolitt) og dypbergarter (granitt, granodioritt, kvartsdioritt, gabbro). Enheten antas å være sammenhengende med Kikedalskomplekset. Disse overflatebergartene er sannsynligvis en nordvestlig fortsettelse av Ullensvanggruppens bergarter i grunnfjellet på Folgefonnshalvøya. Nordvestgrensen til Bergsdalen tektoniske enhet er en skjærsone eller mindre skyvegrense med sørøstlig fall, markert med kaledonsk glimmerskifer i nordøst og fyllonittisert, proterozoisk amfibolitt i sørvest. I den underste delen av enheten er det innblandet grå gneis av antatt samme type som finnes videre nordvestover i det nordvestre gneisområdet. Dette sees mer tydelig på nabokartet i øst. I *det nordvestre gneisområdet (*117-131) preges berggrunnen av migmatittiske gneiser (131) og grå monzogranittisk til granodiorittisk biotitt-gneis (124). De migmatittiske gneisene er av flere generasjoner hvorav de eldste muligens kan ha dannet et underlag for overflatebergarter i området. De migmatittiske gneisene varierer fra lyse, røde, granittiske, til biotitt- og amfibolrike. De yngste er knyttet til granittdannelse i antatt svekonorvegisk tid. Den grå gneisen (124) er forholdsvis ensartet over store områder. De fleste steder er den svakt båndet og med enkelte granittiske årer tilnærmet parallelt med foliasjonen og båndingen. I områder med ellers sterk kaledonsk deformasjon, kan det lokalt finnes områder hvor bergarten er ganske massiv med granittårer på kryss og tvers. Stedvis har den grå gneisen (124) blitt migmatittisert (f.eks. vest for Romarheimsfjorden). Den inngår derfor stedvis blant de migmatittiske gneisene på kartet. Den grå gneisen (124) og de grå til røde granodiorittiske til granittiske bergartene (119-122) er stort sett antatt å være dypbergarter. De er stedvis relativt kvartsrike, og for en stor del trolig dannet ved oppsmelting av skorpebergarter som har inneholdt overflatebergarter. Spredte grovkornete kvartsitter (128-129) i enheten er uoppsmeltede deler av overflatebergartene. Den kaledonske deformasjonen har stedvis ført til at bergarter av forskjellig opprinnelse, fra migmatitter til mer ensartede gneiser, er omdannet til grå, båndet gneis (124) og kartlagt som sådan. I den sørøstlige delen av enheten er det en sørøstfallende gneisbenkning med senkaledonske, asymmetriske folder som viser nordvestlig vergens, lik folder i Bergsdalen tektoniske enhet. Lengre nordvest er deformasjonen mer variabel med enkelte brede forskifringssoner hvor det etter hvert dukker opp eklogittiserte gabbroer og amfibolitter (127) som viser at bergartene der ble presset ned på relativt stort skorpedyp under den kaledonske fjellkjede-dannelsen. En tynn sone av finkornet kvartsitt og amfibolitt med epidotknoller (117-118) på nørdøstsiden av Austfjorden er bergarter fra antatt kambrosilurisk tid som er skjøvet og nedfoldet i gneisene. *Øygardskomplekset (132-147)* er muligens sammenhengende med bergartene i det nordvestre gneisområdet. Over store områder opptrer lyse til mørke grå, for det meste kaledonsk båndete biotittgneiser av tonalittisk til grano-diorittisk sammensetning (143-144, 146), altså litt forskjellig fra den grå, overveiende monzo-granittiske gneisen (124) i det nordvestre gneisområdet. Grå gneis har gitt aldere (Rb-Sr) på opptil ca 1750 millioner år. Gneisene er stedvis migmatittiske, og gjennomsatt av ulike gabbroer og noritter (138-141) og enda yngre, røde, granittiske (132-137), stedvis migmatittiske dypbergarter. Finkornet amfibolitt (145-146) og litt kvartsitt (142) opptrer stedvis sammen med finkornet tonalittisk gneis, særlig på Askøy, og kan være omdannede overflatebergarter. Kvartsitt og kvartsrike gneiser finnes også spredt i Øygarden og på Sotra. I den basiske Kauslandsagmatitten på Sotra (147) er det funnet spor etter

granulittfaciesmineralogi i agmatittblokker som inneholder de antatt eldste strukturene i det området. Bergartene er omdannet under amfibolitt- og grønnskiferfaciesforhold, for det meste sterkt deformert, og har stort sett slakt østlig fall og en kraftig øst-sørøststupende strekningslineasjon.

BERGARTER SKJØVET UNDER DEN KALEDONSKE FJELLKJEDEDANNELSEN

Kortskjøvne bergarter fra kambrosilurtiden (104) ligger stedvis over de stedegne til nær stedegne proterozoiske underlagsbergartene. De består av gråsvart, karbonholdig- til grågrønn glimmerskifer med kvartslinser og inneholder stedvis granat. Mellom glimmerskiferen og underlagsbergartene finnes det noen få steder også tynne benker av kvartsitt og/eller kalkstein, antatte rester etter stedegne avsetninger fra kambro-ordovicisk tid.

Grasberg- og Slettafjelldekket (93-103) består av grunnfjellsbergarter fra proterozoisk tid, tilsvarende de som finnes i Bergsdalen tektoniske enhet. Slettafjelldekket ligger over Grasbergdekket, stedvis med en tynn, mellomliggende glimmerskifer (97) og/eller kvartsitt (93) fra antatt kambrosilurisk tid.

Mjånesdekket (92) består vesentlig av monzogranittisk gneis som er aldersbestemt til ca 1485 millioner år. Det ligger på samme måte som Slettafjelldekket tektonostratigrafisk over Grasbergdekket og under Hardangerfjorddekket, men er foldet rundt og under Grasbergdekket. Disse dekkene utgjør de sørligste delene av det som har blitt kalt Bergsdalsdekkene eller Vossadekkekomplekset.

Blåmansdekket (89-91) består av migmatitt og migmatittisk gneis (90-91) fra proterozoisk tid, og litt kvartsitt (89) som ble avsatt på det migmatittiske underlaget. Blåmansdekkets tektonostratigrafiske posisjon antas å være over, eller tilsvarende Grasberg-, Slettafjell-, og Mjånesdekket.

Lindåsdekket (73-88) synest å danne en buet, senkaledonsk synformstruktur med tidlig-kaledonske, tette til isoklinale folder. Bergartene er fra proterozoisk tid og er inndelt i *Holsnøysuiten (73-79)* og et kompleks av kaledonsk omdannede varianter av Holsnøysuitens bergarter samt eldre og yngre bergarter (80-88). Holsnøysuiten består av antatt opprinnelige dypbergarter som ble fullstendig omkrystallisert, under granulittfacies høygrads-metamorfose, under den svekonorvegiske fjellkjededannelsen. Omdanningen skjedde i de dypeste delene av jordskorpen (ca 800-900°C, < 10 kbar), trolig kort tid etter at bergartene ble dannet. Granulittfaciesmineraler viser aldre fra ca 1150 til ca 900 millioner år. De eldste bergartene i suiten er anortositt og gabbro. Disse ble gjennomsatt av tonalittiske, monzodiorittiske, syenittiske og granittiske bergarter. En tonalitt er aldersbestemt til ca 1035 millioner år. Granulittfacies-dypbergarter kalles charnockitter, og klassifiseres litt forskjellig fra vanlige dypbergarter. De navngis vanligvis ved å legge til hypersten (ortopyroksen) i bergarts-navnet da bergartene normalt inneholder dette mineralet, f. eks. hyperstengranitt. Man kan også bruke spesialnavn på slike bergarter, f. eks. mangeritt og jotunitt. Mangeritt (74) ble først beskrevet fra Manger og er en hyperstenmonzonitt til monzodioritt med mesopertittisk feltspat. Dypbergartene i Holsnøysuiten må ha trengt inn i eldre bergarter (80-88, også kalt 'bakgrunns-komplekset'), men det er usikkert i hvor stor grad de eldre bergartene er til stede i enheten. Komplekset inneholder imidlertid eldre, mulige kvartsitter (86), selv om opprinnelsen til dem er noe usikker. Flere svært langstrakte anortosittsoner kan

representere ganger i eldre bergarter, og det er også funnet tynne soner av godt bevart mangeritt omgitt av gneis. De yngre bergartene er omdannede granitter (80), antatt dannet under eller i etterkant av den svekonorvegiske fjellkjededannelsen. Bergartene i Holsnøysuiten ble også utsatt for eklogittfacies høygradsomdanning langs enkelte skjærsoner dypt i den kaledonske fjellkjeden, under høy temperatur (ca 650°C) og svært høyt trykk (>15kbar), på ca 60 kms dyp. Aldersbestemmelser kan tyde på at dette skjedde for ca 450 millioner år siden. Eklogittiserte bergarter finnes særlig på Holsnøy og i mindre grad langs strøkfortsettelsen helt til Fleslandsområdet. Etter eklogittiseringen ble bergartene de fleste steder omdannet og deformert høyere opp i skorpen under amfibolitt- og grønnskiferfacies metamorfose, på samme måte som omdanningen i de andre dekkene.

Hardangerfjorddekket (18-72) består vesentlig av havbunnsskorpebergarter dannet for ca 490 til ca 470 millioner år siden og bergarter avsatt oppå havpunnsskorpen før og etter at skorpedelene ble skjøvet på land som såkalte ofiolittkomplekser for mellom 470 og 450 millioner år siden. Videre skyvning i sensilurisk tid førte til oppdeling av dekket i en rekke tektoniske enheter som nå finnes i forskjellige områder og tektoniske nivåer. I Os-Samnangerområdet er det påvist mange tektoniske enheter som inneholder deler fra ofiolittkomplekset. *Gullfjelkomplekset (61-65)* er det største og mest intakte ofiolittkomplekset, med bergarter dannet for ca 490 millioner år siden, trolig i nærheten av en øybue som et såkalt suprasubduksjonstype ofiolittkompleks. Sammen med de eldste delene av Samnangerkomplekset (43-53), som også består av ofiolittkompleksbergarter, danner disse et underlag for de andre bergartene. Ofiolittkomplekser kjennetegnes ved den lagdelte oppbygningen som en havbunnsskorpe antas å ha, nemlig med ultramafiske bergarter (65) underst, derover ulike gabbrovarianter og dioritt (63-64), med økende antall og tetthet av diabaser (62) oppover i skorpen og basaltisk putelava (62) øverst. Putestrukturene ble dannet under bråkjølingen som fant sted da lavaen rant ut på havbunnen og viser at den nå omdannede putelavaen nordover langs Samnangerfjorden er svakt overbikket mot sørøst. Før havbunnsskorpebergartene ble skjøvet på land, ble Gullfjellkomplekset gjennomsatt av en tonalitt (61), ca 482 millioner år, og andre dypbergarter som f. eks. Stolmaplutonen (26), som kan være ca 472 millioner år. *Samnangerkomplekset* (43-53) omfatter bergarter øst og nord for Samnangerfjorden, dannet før avsetningen av Osgruppen, samt liknende bergarter av mer usikker alder ellers i dekket. Komplekset inneholder mange tektoniske avskjæringsplan, stedvis markert med innskjøvne proterozoiske gneisflak (66-72) eller tallrike linser av serpentinitt (53). Opprinnelig utgjorde serpentinitt, gabbro, dioritt og basalt (51-52) for det meste ofiolittfragmenter, men serpentinittene ble under skyvningen også presset inn i andre bergarter som glimmerskifer (46) og grønnskifer (51). Glimmerskifrene i komplekset er grønne, grå, eller svarte og karbonrike. Konglomeratsoner innen komplekset (47, 50) inneholder boller av ofiolittkompleksbergarter, stedvis også turmalinitt- og spessartinkvartsitt-boller, og er stedvis assosiert med tynne marmorsoner. Konglomerat og breksje med ultramafiske bruddstykker finnes i bergarter jevnført med Samnangerkomplekset ved Baldersheim. Sandstein og konglomerat med boller av kvarts og kvartsitt? (43) finnes nord for Sævillvatnet i Samnanger, på Bjørnatrynet sørvest for Os og på Varaldsøy (rett øst for kartbladgrensen), og er av usikker alder. Siden Samnangerkomplekset grenser mot flere proterozoiske gneisflak, er det rimelig å anta at det innen komplekset også finnes glimmerskifer som opprinnelig ble avsatt

på det kontinentale gneisunderlaget. *Varaldsøykomplekset* (57-60) inneholder også ultramafiske lag, gabbro og diabaser (60) underst. Derover ligger det grønnskifer (59) som antas opprinnelig å ha vært basaltiske til andesittiske tufter. Deretter ble det avsatt ryolitt til dacitt som nå er omdannet til kvartskeratofyr (57). Oppbygningen tyder på at Varaldsøykompleksets bergarter (57-60) utgjorde en øybue som ble bygget opp over havbunnsskorpen.

Vinkeldiskordant over ofiolitt- og øybuebergartene, ble det avsatt vesentlig sedimentære bergarter, hovedsakelig i forbindelse med bassengutvikling. Dette gjelder bergartene i Osgruppen (28-31) som ligger over Gullfjell-/Samnanger-komplekset, Storetveitgruppen (32) som ligger over antatte ofiolittbergarter i Bergensområdet, Mundheims-gruppen (33-38) som ligger over Varaldsøy-komplekset, og Lunnøygruppen (39-42) som ligger over antatte ofiolittbergarter i Møkster-Austevoll-området. I Osgruppen er det funnet fossiler, og lagrekken er blottet i tre tette synklinaler; Hegglandsdal-, Os- og Ulven-synklinalen. Underst i *Osgruppen (27-31)* ligger Mobergkonglomeratet (31) med boller fra det underliggende Gullfjellkomplekset, for det meste bestående av gabbro, grønnstein, amfibolitt og glimmerskifer, men også boller av omdannet kiselstein og hvit kalkstein. Over konglomeratet ligger Vallaformasjonen (30) med marine sedimenter som fyllitt/glimmerskifer, fossilførende kalkstein og marmor. Fossilene er fra ashgilltiden (ca 449-443 millioner år siden) og består av gastropoder og cephalopoder samt koraller og krinoidestilker. Kalksteinen og det underliggende konglomeratet kan følges nordover til Osterøy og sørover til Stord, Bømlo og Karmøy. Sedimenter (29) avsatt over Valla-formasjonen er bevart i Ulvensynklinalen (Skardfjells-, Vaktdals- og Gjertrudsberg-formasjonen) og Hegglandsdals-synklinalen (Hegglandsdalsformasjonen). De består av grunnmarine avsetninger som konglomerat, sand-stein og fyllitt. Vaktdalsformasjonen består hoved-sakelig av fyllitt, til dels kalkspatholdig, med graptolitt- og korallfossiler fra mellomllandovery-tiden.
Skardfjellsformasjonen er øverste formasjon i Ulvensynklinalen og består av konglomerat med overliggende, urein kvartsitt. Konglomeratet inneholder for det meste kvartsittboller, men stedvis også boller av serpentinitt, sandstein, fyllitt og tonalitt. Lokalt er det funnet skjellfossiler nær Skardfjells-formasjonens undergrense. Sedimentene i Os-gruppen er gjennomsatt av enkelte mørke gang-bergarter (27, lamprofyr), og det finnes også grønnstein (28) høyt oppe i gruppen. Osgruppen ble antatt avsatt etter at ofiolitt- og øybuebergartene var skjøvet på land og erodert. *Storetveitgruppen (32)* er jevnført med Osgruppen ut fra tilstedeværelsen av konglomerat med overliggende marmor underst i gruppen. *Mundheimsgruppen (33-38)* kan følges fra Strandebarmsområdet, over Varaldsøy og Ølve til den nordøstlige delen av Tysnes. Den består vesentlig av ulike sedimenter fra grunnmarine basalavsetninger til turbiditter og dyphavs-avsetninger antatt dannet under utviklingen av et ensimatisk? øybuebasseng. Basalavsetningene (38) består av konglomerat og gråvakke med boller av grønnstein, gabbro, trondhjemitt, dioritt, kiselstein m.m., stedvis også av turmalinitt og spessartin-kvartsitt (coticule). Over basalavsetningene ligger det marmor (37), stedvis med små krinoidestilker. Over marmoren ligger det mektige avsetninger av fyllitt, glimmerskifer og sandstein (35) samt enkelte lag av kiselstein (34). Fyllitten er for det meste grå til svart og karbonrik. Høyt oppe i Mundheims-gruppen finnes også litt grønnstein og grønnskifer (33) på samme måte som i Osgruppen. På den nordligste delen av Tysnes er Mundheimsgruppen avsatt oppå antatte ofiolittkompleksbergarter, og det er nærliggende å jevnføre basalavsetningene

der med Mobergformasjonen, forbundet via den sørveststupende Bjørnefjordsantiklinalen. På tross av visse likhetstrekk med Osgruppen er Mundheimsgruppen muligens eldre, ut fra sammenligninger med bergarter og aldersbestemmelser på øyene videre sørvestover. *Lunnøygruppen (39-42)* har også vært antatt å være av samme alder som Osgruppen. Bergartene i gruppen er imidlertid gjennomsatt og stedvis migmatittisert av Stolmaplutonen (26) som trolig er eldre enn Osgruppen. Karakteristiske avsetninger som turmalinitter og spessartinkvartsitt (coticule) er funnet i basalavsetningene både i Lunnøygruppen, Mundheimsgruppen og flere steder i Samnangerkomplekset.

Fanaskifrene (56) og Lyseklosterskifrene (54-55) danner smale soner av sedimentære og vulkanske bergarter antatt avsatt i ordovisisk tid. Fanaskifrene fortsetter i en smal sone helt nord til Sørfjorden. I den nordlige delen antas marmoren i enheten å tilsvare Vallaformasjonen i Osgruppen.

Sunnhordlandssuiten (18-26) består av dypbergarter antatt dannet i tre forskjellige faser. Stolmaplutonen (26) tilhører den eldste fasen, og består av gabbro og dioritt som for det meste er oppbygd av lagganger. Stolmaplutonen er trolig ca 472 millioner år ut fra sammenligning med den aldersbestemte Vardafjellgabbroen på Bømlo. Rekstraplutonen (21-22) tilhører neste fase, og består av granodioritt og kvartsdioritt. Håkremonzogranitten, Drønamonzogranitten og Korsnesgranitten tilhører den siste fasen, og er aldersbestemt til ca 430 millioner år. Stedvis ble sidebergartene oppsmeltet da dypbergartene kom på plass. Sandstein ble f. eks. oppsmeltet, og senere deformert til granittisk gneis (25) under framskyvningen, og det ble også dannet andre deformerte bergarter (23-24).

Gneisflak fra proterozoisk tid i Hardangerfjorddekket (66-72) kan inndeles i underliggende såleflak og innskjøvne flak. Heimstadflaket (72) og det underste av Mindeflakene (70-71) danner gneissåler i bunnen av Hardangerfjorddekket. Flakene består av blastomylonitt og mylonitt, samt bånd og soner av kvartsitt som er tektonisk blandet med skifre fra kaledonsk tid. De innskjøvne gneisflakene (66-69) er omgitt av bergarter tilhørende Samnanger-komplekset og opptrer særlig i Samnanger. Flere av gneisflakene i Samnanger består av omdannede charnockitt-/granulittbergarter.

STEDEGNE SENKALEDONSKE TIL POSTKALEDONSKE BERGARTER (1-15)

På fastlandet finnes det sandsteiner, konglomerater og breksjer (15) fra devonsk tid, avsatt i forkastningsbetingede bassenger knyttet til den sen- til postkaledonske strekningen beskrevet i oversikten. Noen få steder på Sotra og rundt Sævareidfjorden finnes det mørke, nord-sørstrykende gangbergarter, såkalte lamprofyrer (14). Lamprofyrene er fra perm- og juratiden, aldersbestemt til ca 274-162 millioner år, og knyttet til oppsprekkingen av kontinentskorpen forut for dannelsen av Norskehavet for ca 60 millioner år siden. Lamprofyrene har inneslutninger av spinell-lherzolitt og må derfor ha kommet fra relativt stort dyp i skorpen (70-80 km?). På sokkelen har det under jevn innsynkning og noe forkastningsaktivitet kontinuerlig blitt avsatt sedimentære bergarter (1–13) fra mesozoisk tid til nåtid. Bergartene består av sand-, silt-, leir- og slamstein til dels rike på organisk materiale. Bergartene på sokkelen er kjent for sine olje- og gassforekomster som særlig er knyttet til de organisk rike skifrene fra senjuraisk tid (se økonomisk geologi). Utbredelsen til de underliggende, proterozoiske og kaledonske bergartene på sokkelen er lite kjent. Utviklingen på sokkelen, og

sammenhengen med fastlands-geologien, kommer ellers frem på snitt A-A'.

OMDANNING

Trykk- og temperaturavhengig omdanning i bergartene kalles metamorfose og er til dels behandlet under bergarts-beskrivelsene. Grunnfjellet sørøst for Hardangerfjorden, Kikedalskomplekset, Bergsdalen tektoniske enhet og Øygardskomplekset ble i proterozoisk tid for det aller meste omdannet under lav- til middelgrads metamorfose. Under den kaledonske fjellkjededannelsen ble grunnfjellet sørøst for Hardangerfjorden, Kikedalskomplekset og den overliggende kambrosiluriske glimmer-skiferen (104) omdannet under lavgrads-forhold (biotitt- til nær almandinsone), mens Bergsdalen tektoniske enhet og Øygardskomplekset stedvis nådde opp i middelgrads metamorfose. Nordvestre gneisområde ble i den nordvestre delen utsatt for kaledonsk eklogittfacies metamorfose. Blant skyvedekkene som inneholder proterozoiske bergarter, er Lindåsdekkets omdanning klart forskjellig fra de andre dekkene. Lindåsdekkets bergarter ble utsatt for granulittfacies høygradsmetamorfose under den svekonorvegiske fjellkjede-dannelsen, og i tillegg eklogitt-facies høygradsmetamorfose under den kaledonske fjellkjededannelsen langs enkelte skjærsoner. De andre dekkene viser tilsvarende proterozoisk metamorfose som underlagsbergartene (lav- til middelgrad), mens den kaledonske metamorfosen deres stort sett er lavgrad. Hardangerfjorddekkets bergarter ble omdannet to ganger under den kaledonske fjellkjededannelsen. Først lavgradsomdanning trolig i forbindelse med at dekket ble skjøvet på land og derfor kun observert i bergarter som er eldre enn Osgruppen. Deretter ble bergartene på ny utsatt for lavgradsomdanning, men under litt høyere trykk og temperatur enn under den første omdanningen slik at det ble dannet relativt almandinrike granater. Stedvis nådde metamorfosen opp i middelgrad med dannelsen av kyanitt og oligoklas. Eksempler på dette finnes i Fanaskifrene, nordre del av Samnanger og ved Baldersheim. I Austevoll-Møksterområdet ble bergartene stedvis også høytemperaturomdannet da de ble gjennomsatt av dypbergarter. Etter den kaledonske, prograde metamorfosen ble alle bergartene i området retrogradert i varierende grad ved lavgrads metamorfose, med kloritt- karbonat- og epidot-dannelse.

STRUKTURGEOLOGI

Bergartene på fastlandet ble for det meste deformert og omdannet til gneiser, mylonitter eller skifre under den kaledonske fjellkjededannelsen og den etterfølgende devonske strekningen. Snittet A'-A" viser hovedtrekkene i dekkeoppbygningen med Lindåsdekket som den øverste dekkeenheten og i prinsippet med samme dekkeoppbygning under Lindåsdekket både mot vest og øst. Lindåsdekket ligger over bergarter tilhørende Hardangerfjord-dekket i vest representert med Heldalsskifrene og i øst med bergartene i Os-Samnangerområdet. Under der ligger Blåmansdekket i vest og tilsvarende dekker i øst representert med Slettafjelldekket, Grasbergdekket og Mjånesdekket. Under der igjen ligger bergarter tilhørende Hardangerfjorddekket, med Bergensområdet i vest og Hålandsdalsområdet i øst. Begge steder er det underst dekkesåler av gneis og kvartsitt, hhv det underste av Mindeflakene i vest og Heimstadflaket i øst. Disse gneis-kvartsittsålene er begge steder antatt uttynnede deler av hhv Blåmansdekket og Grasbergdekket-Slettafjelldekket. Under disse gneis-kvartsittsålene ligger det stedvis kambrosilurisk glimmerskifer. Underst ligger de proterozoiske underlagsbergartene, representert med Øygardskomplekset i vest og Kikedals-komplekset, Bergsdalen tektoniske enhet og det sørnorske grunnfjellsområdet i øst. På snitt A'-A", rett øst for kryssningspunktet med snitt B-B', er det inntegnet en stor, idealisert, liggende fold. Her danner Grasbergdekket kjernen i en

foldenese som lukker seg mot sørøst og er omgitt av Hardangerfjord-dekket, med Samnangerområdet på oversiden av folden, Hardangerfjord-området i foldeom-bøyningen og Hålandsdalsområdet på undersiden av folden. Hardangerfjord-dekket i Hålandsdals-området kiler ut nordover langs snitt B-B' slik at Grasbergdekket blir liggende rett på glimmerskiferen (104) over Bergsdalen tektoniske enhet. Vestover langs snitt A-A', kan derimot Hardangerfjorddekket tenkes å ligge under de andre dekkene helt til Bergensområdet. Imidlertid har bergartene langs dette idealiserte snittet blitt avskåret av imbrikasjoner og dupleksdannelser under fremskyvningen slik at det neppe er en kontinuerlig forbindelse. Den etterfølgende devonske strekningsfasen førte til dannelsen av såkalte postorogene kollapsstrukturer som er godt utviklet i området. Langs snitt B-B', nordover fra kryssningspunktet med snitt A-A", er det nordøststrykende bergartsgrenser og skjærsoner med sørøstlig fall som tydelig viser at dekkene er tilbakeskjøvet mot nordvest. Denne typen strukturer dominerer også i hele Øygardskomplekset, men der med tilbakeskyvning mot vest-nordvest. Fra Vaksdalsområdet og videre sørvestover til Bergen sees imidlertid ikke disse strukturene. Der ligger skyvedekkene i en stor, buet synformstruktur, en halvgrabenstruktur kalt Bergensbuestrukturen, som ble dannet sent under- til etter tilbakeskyvningen. I en sone rundt den nordøstlige til østlige kontakten til Bergensbuestrukturen er det dannet karakteristiske folder med akser som er parallelle med buestrukturen. Foldene overpreger tilbakeskyvningsstrukturene i Vaksdalsområdet og ble dannet da deler av dekkene ble nedforkastet mot nordvest slik at Bergensbuestrukturen ble dannet. Langs Austfjorden foregikk dette som en skrå venstrehåndsforkastning relativt til gneisunderlaget nordøst for fjorden. Det er flere slike strekningsforkastninger nær Bergensbuestrukturens konvekse østgrense. De eldste forkastningene er foldet, mens de yngste er rettere og assosiert med friksjonsbreksjer, kataklasitter og psevdotachylitter og kutter gjennom dekkebergartene. Under Haukanes-flaket er det en slik ung, buet forkastning som har ført til utkiling av de underliggende deler av Hardangerfjorddekket rett sør for snittlinjen. Knyttet til denne forkastningen er to mindre nordøst-sørveststrykende forkastninger lengre nordvest, en over Gullfjellet og en nordvest for Gullfjellet. Begge disse forkastningene dør ut mot nordøst da de trolig er bundet til hengblokken over Haukanesforkastningen. Det finnes også flere mindre forkastninger tilnærmet parallelle med disse to lengre nordvest i Lindåsdekket. De devonske bergartene nordvestligst i Fensfjorden og videre nordover er avsatt i forkastningsbetingede bassenger knyttet til denne devonske streknings-fasen. En mer rettlinjet halvgraben-struktur er Hardangerfjordskjærsone ('foldegrøften') langs Hardangerfjorden, antydet på snittet B-B'. Denne er på samme måte som Bergensbuestrukturen både en folde- og forkastningsstruktur. Forkastningen er for det meste skjult av de overliggende dekkene som skled ned i halvgrabenstrukturen sent under tilbake-skyvningen. Størrelsen på Hardangerfjord-skjærsonen er derfor vanskelig å anslå, men trolig er grunnfjellet langs nordvestsiden av Hardangerfjorden nedforkastet minst en kilometer. Forkastninger knyttet til Hardangerfjordskjærsonen kutter også opp gjennom dekkene, f. eks. fra nordøstlige delen av Tysnes og nordøstover til Skogseidvatnet, en forkastning som mot sørvest går inn i Sunnhordlandsforkastningen på Tysnes. Sunnhordlandsforkastningen har en buet forkastningsflate med sørveststupende akse der hengblokken har glidd mot vest eller sørvest omtrent samtidig med dannelsen av Hardangefjordskjærsonen og Bergensbuestrukturen. Mellom

Hardangerfjord-skjærsonen og Bergens-buestrukturen danner Fusahalvøya som følge av disse halvgrabenstrukturene en slakt sørvest-stupende antiklinal, kalt Bjørnefjords-antiklinalen. Via denne folden bindes bergarter i Hardangerfjord-dekket langs Hardangerfjorden sammen med tilsvarende bergarter i Os-Samnangerområdet. Enda yngre strukturer er svært åpne øst-vest rettede folder, trolig dannet sent under dannelsen av foldegrøften og Bergensbuene. Disse sees både i underlagsbergartene og i dekkene. Enda yngre strukturer er knyttet til den begynnende oppsprekkingen langs kysten, forut for åpningen av Norskehavet, og senere under utviklingen av Norskehavet. Disse strukturene er hovedsakelig nordnordvest-sørsørøst til nordsør-strykende, steile sprekker og forkastninger som er best utviklet på Sokkelen (se f. eks. snitt A-A'). Forkastningene kan ha blitt reaktivert flere ganger, noen så sent som etter siste istid, men da i tilfelle med bare svært små forkastningssprang.

ØKONOMISK GEOLOGI

Malmforekomster

For tiden er det ingen økonomisk drivverdige malmer i området. Tidligere har det vært drift flere steder på forekomster av kobber, nikkel og jern, og prøvedrift på gull. Malmforekomstene er knyttet til Lindåsdekket, og grønnstener-gabbro i Hardangerfjorddekket, særlig i Varaldsøy-komplekset.

lndustrimineraler og -bergarter

Det er ingen større brudd i drift. En rekke forekomster som har vært i drift, særlig på kalkstein, kvartsitt og skifer, er i de senere år nedlagt. For tiden er det vel ti pukkverk som er i drift, der noen få driver med eksport.

Olje og gass

Trollfeltet er et av verdens største utenskjærs gassfelt med i alt 1370 millioner tonn utvinnbare oljeekvivalenter (t.o.e.), derav 94% gass. Målt i 1.o.e. tilsvarer dette 20% av de påviste, utvinnbare ressurser på norsk sokkel og over 40% av de påviste, utvinnbare gassresurser, eller ca 1% av verdens påviste gassressurser. Feltet ble påvist i 1979 og produksjonen startet i 1996. Strukturelt ligger Trollfeltet på nordvestkanten av Hordaplattformen (Bergenshøyden), ved overgangen til østkanten av Vikinggrabenen. Kildebergarten til hydrokarbonene er hovedsakelig organisk rik leirstein fra senjuraisk tid (Kimmeridge clay/Draupneformasjonen).
Hydrokarbonforekomstene finnes i Vikinggruppens grunnmarine sand- og siltsteiner som har opp til 34% porøsitet og som er fra mellom- til senjuraisk tid. Hydrokarbonene holdes tilbake på grunn av roterte forkastningsblokker som er forseglet av tette kappebergarter av leirstein-kalkrik leirstein fra senjuraisk til tertiær tid. *Bragefeltet er* et oljefelt med vel 40 millioner tonn utvinnbare oljeekvivalenter, derav 95% olje. Dette. tilsvarer drøyt 1 % av de påviste utvinnbare oljeressursene. Bragefeltet ble påvist i 1980, og feltet kom i produksjon i 1993.

HYDROGEOLOGI

Borebrønner i grunnfjellsbergartene gir vanligvis 400-2000 liter vann i timen og sjelden over 7000 l/t. Basiske bergarter som grønnskifer, gabbro og amfibolitt, samt glimmerskifere gir sjelden over 700 l/t. Grunnvann i fjell gir vanligvis bedre drikkevannskvalitet enn overflatevann.

ISOTOPALDERSBESTEMMELSER:

(Medhenvisning til bokser i tegnforklaringen)

14 K-Ar total-bergart og mineraler; ca. 162-274 mill. år (Færseth, R.B. o.a. 1976: *Lithos 9).*

18 Rb-Sr total-bergart; 430±6 mill. år (Fossen, H. og Austrheim, H. 1988: *NGU-bull. 413).*

20 Rb-Sr total-bergart; 430±10 mill. år (Andersen, T.B. & Jansen, Ø. 1987: *NGT 67).*

61 Øybuetilknyttet tonalitt: U-Pb zirkon; 482+6/-4 mill. år (Dunning, G. & Pedersen, R.B. 1988.. *Contrib. Mineral. Petrol. 88).*

65 Tonalittdifferensiat: U-Pb zirkon; 489±3 mill. år (Dunning, G. & Pedersen, R.B. 1988: *Contrib. MineraL Petrol 88).*

74 U-Pb zirkon; 944±6 mill. år, nedre skjæringspunkt, & Rb-Sr retrograde mineraler; 409:18 mill. år (Austrheim, H. o.a., i Austrheim, H. 1*990: Dr. philos. avhandl., Univ. i Oslo).*

77 ^{238}U-^{206}Pb granat-plagioklas-klinopyroksen alder til anortosittkoronitt; konkordant 1151,2±417 mill. år (Burton, K.W. o.a. 1995, E.Pl.Sci.Lett. 133). U-Pb zirkon-alder til gjennomsettende tonalitt; 1035±12 / 418±9 mill. år, øvre/nedre skjæringspunkt (Austrheim, H. o.a., i Austrheim, H. 1990: *Dr. philos. avhandl., Univ. i Oslo).* Sm-Nd granulittfaciesmineraler; ca. 896-912 mill. år (Cohen, A.S. o.a. 1988, *Contrib. Mineral Petrol. 98).* ^{40}Ar-^{39}Ar fengittalder, eklogittisert skjærsone, 350°C avkjølingsalder; 448±5 mill. år. (Boundy, T. M. o.a. 1992: *The American Geophysical Union 1992 Fall meeting, abstract).*

92 U-Pb zirkon; ca 1485 mill. år. (Pedersen, R.B. og Ragnhildstveit, J. 1996, *upubl)*

131-144 Rb-Sr total-bergart; 1400±100 mill; 890±150 mill. år; 1750±60 mill. år, (Sturt, B.A. o.a. 1975: *Nature, 253).*

FOSSILER:

29) Vaktdalsformasjonen: Graptolitter (Rastrites, Monograptus, Glyptograptus, Diplograptus, Climacograptus): Tidligsilurisk alder (midtre Llandovery, etasje 6b); (Reusch, H. 1882: Christiania. Ryan, P.D. & Skevington, D. 1976: *NGU 324).*

30) Vallaformasjonen: Koraller, Krinoidestilker, Gastropoder, Cephalopoder: Senordovicisk alder (Ashgill, etasje 5a); (Kolderup, C.F. & Kolderup, N._H. 1940: *Bergens Mus. skr. 20).*

REFERANSER:

Trykte publikasjoner og kart:

Andersen, T.B., Bering, D.H., Fossen, H. Ingdahl, S.E., Jansen, Ø.J., Rykkelid E. & Thon, A. 1988: Berggrunnskart AUSTEVOLL 1115-2 - M 1:50.000, foreløpig utg. *NGU*

Askvik, H. 1971: Gabbroic and quartzdioritic intrusions in gneisses on southern Askøy, West Norwegian Caledonides. *NGU 270.*

Bering, D.H., Rykkelid, E. & Fossen, H. 1988: Berggrunnskart MARSTEIN 1115-3 – M 1:50.000, foreløpig utg. *NGU.*

Færseth, R.B., Thon, A., Larsen, S.G., Sivertsen, A. & Elvestad, L. 1977: Geology of the lower Palaeozoic rocks in the Samnanger-Osterøy area, Major Bergen Arc. *NGU 334.*

Foslie, S. 1955: Kisdistriktet Varaldsøy-Ølve i Hardanger og bergverksdriftens historie. *NGU 147*

Fossen, H. 1989: Geology of the Minor Bergen Arc, West Norway. *NGU bull. 416.*

Fossen, H. & Thon, A. 1988: Berggrunnskart BERGEN 1115-1- M 1:50.000, foreløpig utg. *NGU.*

Indrevær, G. & Steel, R.J. 1975: Some aspects of the sedimentary and structural history of the Ordovician and Devonian rocks of the westernmost Solund Islands, West Norway. *NGU 317.*

Ingdahl, S.E. 1989: The Upper Ordovician-Lower Silurian rocks in the Os area, Major Berge Arc, Western Norway. *NGT 69.*

Kildal, E.S. 1965: Note on the geology of the archipelago NW of Bergen («Øygarden») *NGU245.*

Kolderup, C.F. & Kolderup, N.H. 1940: Geology of the Bergen Arc system. *Bergens Mus. skr. 20.*

Kvale, A. 1945-47: Petrologic and structural studies in the Bergsdalen quadrangle, Western Norway, part I, II. *Bergens Mus. Årb. 1945-47.*

Naterstad, J., Ragnhildstveit, J., Ingdahl, S.E. & Rundhovde, E., 1992: Berggrunnskart FUSA 1215-3 - M 1:50.000, foreløpig utg. NGU.

Ragnhildstveit, J. & Naterstad, J., 1993: Berggrunnskart SAMNANGER 1215-4 - M 1:50.000, foreløpig utg. NGU.

Ryan, P.D. & Skevington, D. 1976: A reinterpretation of the Late Ordovician-Early Silurian stratigraphy of the Dyvikvågen and Ulven-Vaktdal areas, Hordaland, Western Norway. NGU 324.

Upubliserte verk og kart:

Austrheim, H. 1978: The metamorphic evolution of the granulite facies rocks of Radøy, with special emphasis on the rocks of the.mangerite complex. Unpubl. cand. real. thesis, Univ. of Bergen.

Austrheim, H. 1990: Fluid induced processes in the lower crust as evidenced by Caledonian eclogitization of Precambrian granulites. Unpubl Dr. philos. thesis, Univ. of Oslo.

Bøe, R. 1978: The Major Bergen Are in the northern part of the Lindås peninsula; Petrography, Geochemistry and Structural geology. Unpubl. cand. real. thesis, Univ. of Bergen.

Bering, D. 1984: Tektonometamorf utvikling av Øygarden gneiskompleks i Sund, Sotra. Upubl cand. real. oppg., Univ. i Bergen.

Forster, J.J. 1980: Basement/cover relationships in the Bergsdalen area, Central South West Norway. Ph. D. thesis, Bedford College.

Fossen, H. 1986: Structural and metamorphic development of the Bergen area, West Norway. Unpubl cand. scient. thesis, Univ. of Bergen.

Fossen, H. 1992: Devonian extensional deformation in the Caledonian orogen, Southern Norway. Unpubl Ph D. thesis, Univ. of Minnesota.

Færseth, R.B. 1971: Geologiske undersøkelser i Samnanger, Store Bergensbue. Upubl. cand. real oppg., Univ. i Bergen.

Gray, J. 1978: Structural history and Rb-Sr geochronology of Eksingedalen, West Norway. Ph. D. thesis, Univ. of Aberdeen.

Henriksen, H. 1979: Structural geology and metamorphism on the Northern Osterøy. Unpubl. cand. real thesis, Univ. of Bergen.

Hopper, F.W.M. 1980: The structural and metamorphic development of the Bergen Arc/Bergsdalen gneisses of Osterøy, S.W. Norway. Unpubl. Ph D. thesis, Bedford College.

Iden, I.K. 1974: Bergensbuenes bergarter i området mellom Knarvik og Eikangervåg,

Lindåshalvøya. Upubl. cand. real. oppg., Univ. i Bergen.

Inderhaug, J.E. 1975: Liafjellområdets geologi. Upubl. cand. real. oppg., Univ. i Bargen.

Ingdahl, S.E. 1985: Stratigraphy, structural geology and metamorphism in the Os area, Major Bergen Arc. Unpubl. cand. scient. thesis, Univ. of Bergen.

Johns, C.C. 1981: The geology of Northern Sotra; Precambrian gneisses west of the Bergen Arcs, Norway. Unpubl. Dr. Philos. thesis, Bedford College.

Larsen, S.G. 1974: Geologiske undersøkelser i østlige Samnanger, Ytre Bergensbue, Vest Norge. Upubl. cand. real. oppg., Univ. i Bergen.

Naterstad, J. & Jorde, K. 1981. Basement-cover relationships in Southern Norway Hardangervidda to Karmøy (preliminary guide). Uppsala Caledonide Symp. Excursion nr. B6.

Qvale, H. 1978: Geologisk undersøkelse av et kaledonsk serpentinittfelt ved Baldersheim i Hordaland. Upubl. cand. real. oppg., Univ. i Oslo.

Ragnhildstveit, J. 1987: Geologien i Fusaområdet, Hordaland, Vest-Norge. Upubl. cand. scient. oppg., Univ. i Oslo.

Rundhovde, E. 1987: Tektonostratigrafi og strukturell utvikling i Lukksund-området, søraust for Bjørnafjorden, Sunnhordland. Upubl. cand. scient. oppg., Univ. i Bergen.

Rykkelid, E. 1987: Geologisk utvikling i Møkster/Selbjørn-området. Upubl. cand. scient. oppg., Univ. i Bergen.

Sivertsen, A. 1975: En geologisk undersøkelse av Bruvikfeltet på Osterøy - en del av den store Bergensbue. Upubl. cand. real. oppg., Univ. i Bergen.

Thon, A. 1973: Geologiske undersøkelser i Samnanger, ytre Bergensbue. Upubl. cand. real. oppg., Univ. i Bergen.

Øvreng, O. 1969: Geologiske undersøkelser i området Liafjell-Bjørnetrynet i Os. Upubl. cand. real. oppg., Univ. i Bergen.

BESKRIVELSE TIL GEOLOGISK KART OVER NORGE - 1: 250.000 HAUGESUND

Jomar Ragnhildstveit og Bernt Egeland

GEOLOGISK OVERSIKT OG UTVIKLINGSHISTORIE

Kartet viser en oversikt over bergartene i området og omfatter:

1. Grunnfjell, stedegne bergarter fra proterozoisk tid (131-174).
2. Stedegne bergarter fra kambrosilurisk tid avsatt oppå grunnfjellet (129-130).
3. Proterozoiske og kambrosiluriske bergarter, skjøvet inn over grunnfjellet for vel 400 millioner år siden, under den kaledonske fjellkjededannelsen (14-128).
4. Stedegne bergarter dannet etter den kaledonske fjellkjededannelsen (1-12).

Grunnfjellet (131-174) består av en rekke forskjellige bergarter, dannet i forskjellige faser for ca 1750 til ca 850 millioner år siden. De eldre bergartene ble stedvis omdannet til gneiser og skifre, både før og under den svekonorvegiske fjellkjededannelsen for ca 1200-1000 millioner år siden. Etter dannelsen ble grunnfjellet utsatt for en lang periode med erosjon og strekning. Den store kontinentplaten som grunnfjellet tilhørte sprakk etter hvert opp, og for ca 600 millioner år siden ble platen delt i to vest for kartområdet. Kontinentplatene drev deretter sakte fra hverandre (se evt oppslagsverk om «platetektonikk») og Iapetushavet, også kalt Protoatlanteren, ble dannet mellom platene samtidig som ny havbunnsskorpe ble dannet fra basaltisk smelte som steg opp langs midthavsryggen under havet. Under denne lange strekningsfasen ble grunnfjellet erodert ned til et stort sletteland som til slutt ble oversvømt av havet. *Stedegne bergarter fra kambrosilurisk* (129-130) representerer omdannede sedimenter som ble avsatt i dette havet over grunnfjellet. Strekningen stoppet opp og ble etterfulgt av en sammenpressingsfase. Denne førte først til kollisjon mellom havbunnsskorper, med dannelse av øybue- og ofiolittkomplekser (suprasubduksjonstype) for ca 495 til ca 480 millioner år siden. Deretter ble det kollisjon mellom havbunnsskorpen og kontinentskorpen, langs en såkalt aktiv kontinentrand. De siste havbunnsskorpebergartene ble dannet for ca 470 millioner år siden. En liten del av havbunnsskorpebergartene ble skjøvet på land som ofiolitt- og øybuekomplekser, trolig en gang for mellom 470 og 449 millioner år siden, mens mesteparten forsvant ned under kontinentskorpen i en såkalt subduksjonssone. Det ble avsatt hovedsakelig sedimentære bergarter oppå de overskjøvne havbunnsskorpebergartene, i et senordovicisk til silurisk randbasseng. Havbunnsskorpebergartene ble også gjennomsatt av siluriske, ca 430 millioner år gamle dypbergarter. Både havbunnsskorpebergartene, deres overliggende overflatebergarter og de yngre gjennomsettende dypbergartene, finnes nå som overskjøvne ordoviciske til siluriske bergarter i *Hardangerfjorddekket (14-103).* Når det ikke var mer havbunnsskorpe igjen mellom kontinentene ble det en kraftig kontinent-kontinent-kollisjon, noe som førte til dannelsen av den kaledonske fjellkjeden for ca 425-400 millioner år siden. Hardangerfjorddekket ble da skjøvet lengre mot sørøst (?), og rev under skyvningen med seg en del av grunnfjellsunderlaget, kalt *Skorpeflaket (103). Boknafjorddekket (104-115*) *og Storheidekket (116-126)* er også løsrevne deler av grunnfjellet, skjøvet fra nordvest (?), stedvis med påliggende rester av kambrosiluriske bergarter. Når dekkene ble skjøvet videre sørøstover (?), over grunnfjellet og dets overliggende kambrosilurbergarter, ble deler av kambrosilurbergartene også revet med og skjøvet, og finnes nå underst i dekkestabelen, kalt *Visteflaket og tilsvarende flak (127-128).*

Etter at den kaledonske kompresjonen stoppet opp, ble den høye kaledonske fjellkjeden utsatt for erosjon og tektoniske prosesser som følge av gravitasjonskrefter og ny strekning. Flere strekningsforkastninger ble dannet, f.eks. langs Hardangerfjorden. Erosjonsprodukter fra den kaledonske fjellkjeden ble først avsatt i forkastningsbetingede bassenger i devonsk tid. Det er usikkert om det stedvis finnes rester av devonske bergarter på sokkelen, og det har vært vurdert om Utslættefjellformasjonen (14) kan være av devonsk alder. *Sedimentære bergarter fra mesozoisk til kvartærtid (1-11)* er i alle fall avsatt i store mengder på sokkelen, og litt i Skudenesfjorden. Strekningen førte til en ny oppsprekking og deling av kontinentplaten vest for kartområdet. Denne oppsprekkingen er lett å se i området. Langs enkelte av de nordsørgående sprekkene har mørke *gangbergarter fra permisk til juraisk tid (12)* trengt opp, særlig i Sunnhordland. For ca 60 millioner år siden og fram til i dag, har de to kontinentplatene drevet fra hverandre. Mellom platene ble Norskehavet og Atlanteren dannet. Havene har siden vokst som følge av at det foregår nydannelse av havbunnsskorpe langs den midtatlantiske spredningsryggen. I samme tidsrom har det også pågått en kontinuerlig sedimentasjon på kontinentalsokkelen som følge av erosjonen av kystområdene.

INNDELING OG BESKRIVELSE AV BERGARTENE

GRUNNFJELL, STEDEGNE BERGARTER FRA PROTEROZOISK TID (131-174)

Grunnfjellet er blottlagt over store områder sørøst for Hardangerfjorden, der overliggende bergarter er fjernet av erosjon.

Overflatebergartene (166-174) består av sedimentære og vulkanske bergarter som trolig er eldre enn ca 1505 millioner år. Underlaget som overflatebergartene ble avsatt på er ikke med sikkerhet funnet innenfor kartet, og bergartene er derfor kanskje de eldste i området. Bergartene er mange steder overdekket eller gjennomsatt av dypbergarter, og til dels sterkt deformert, foldet og omdannet, slik at den opprinnelige lagrekken er lite kjent. De sedimentære bergartene består for det meste av grå til grønn fyllitt og sandstein. Det finnes også konglomerater som vanligvis er rike på vulkanske boller, mens gneisboller ikke er funnet. I tillegg finnes karbonatholdig skifer og tynne kvartsitt- og marmorlag. De vulkanske bergartene er fra basiske til intermediære og sure, lokalt med agglomerat. De er til dets porfyriske og blærerike, mens putelava ikke er funnet. Overflatebergartene er best bevart i den nordlige delen av kartet i området Skånevik-Bjoa. Øst for Skånevik ligger basiske vulkanitter over kryssjiktet sandstein, med yngre lag mot nordøst i sandsteinen. Det er likevel trolig for enkelt å anta at basiske vulkanitter og vulkansk deriverte sedimenter generelt ligger over eldre sedimenter i området. Lengre sørover på kartet er overflatebergartene mer omdannet og deformert til heterogene skifre, glimmerskifer, glimmergneis, kvarts-feltspatskifer og -gneis, amfibolitt og hornblendeskifer. Disse er særlig forskifret eller forgneiset rundt de yngre, gjennomsettende dypbergartene.

Dyp- og gangbergartene (131-165) utgjør størsteparten av grunnfjellet og har på tross av store variasjoner i sammensetning, deformasjon og omdanning fra sted til sted, trolig en relativt enkel utviklingshistorie. Utviklingen startet med dannelsen av basiske komplekser. Det basiske komplekset nordøst for Skånevik omfatter ultramafiske kumulater, jern- og titanrik gabbro, lagdelt gabbro, leukogabbro, anortositt og diabaser. Det er usikkert om diabasene kan ha vært tilførselsganger til vulkanittene øst for Skånevik. Grå til grågrønne dyp- og gangbergarter av tonalitt til dioritt og monzogranitt har gjennomsatt det basiske komplekset ved Skånevik, og stedvis ført til dannelsen av

intrusivbreksjer og lokal migmatittisering. De grå intrusivene kuttes stedvis selv av gabbroer og diabaser. Grå til grågrønne tonlitter og kvartsdioritter, samt mindre mengder dioritt, granodioritt og monzogranitt (151-160) danner i tillegg store og små plutoner ellers i området. De grå dypbergartene er for det meste middelskornete, massive til folierte bergarter som ikke er særlig rekrystallisert, men stedvis forgneiset eller forskifret. De grå til grågrønne intrusivene har mange steder også ført til omfattende kontaktomdanning av omgivende overflatebergarter. De synes å vise en utvikling fra gabbro til dioritt, kvartsdioritt og tonalitt, og stedvis videre til granodioritt og monzogranitt. En monzogranitt (innen felt 152) er aldersbestemt til ca 1505 millioner år. Det er mulig at alle de basiske og grå til grågrønne intrusivene beskrevet over, ble dannet i et relativt kort tidsrom under en eller flere magmatisk pulser for vel 1500 millioner år siden. Etter at disse bergartene stedvis ble deformert og foldet, ble de gjennomsatt av diabaser, som for øvrig også har gjennomsatt deler av bergartene beskrevet under.

Etter dannelsen av de grå, overveiende tonalittiske intrusivene, fulgte en lengre periode med intrusjon av vesentlig granitter og granodioritter, og dannelsen av migmatitter. Disse varierer nå fra nyrekrystalliserte gneiser, til massive granitter (131-150). De folierte til gneisaktige, granittiske til granodiorittiske plutonene, har i mange tilfeller kommet på plass mer som diapirer med betydelig deformasjon av sidebergartene. Ålfjordmigmatitten (148), er en stor granittisk til granodiorittisk pluton, for det meste migmatittisk, med tallrike inneslutninger av omgivende bergarter, og delvis omgitt av en smal øyegneis-sone. Tallrike, oftest runde eller ovale granittkropper og pegmatitter av varierende størrelse, danner mer massive partier både i de store granittiske til granodiorittiske plutonene og også ellers i området, særlig på Haugesunds-halvøya. Granittene er folierte til massive, med ulik sammensetning og tekstur fra grå biotittrike, til lyse røde. Den største av de unge granittene er den runde, massive, Ulvanosgranitten (134), som varierer fra porfyrisk til grovkornet og storkornet. Ulvanosgranitten og andre unge granitter antas å være dannet for ca 950-850 millioner år siden, i etterkant av den svekonorvegiske fjellkjededannelsen.

STEDEGNE BERGARTER FRA KAMBROSILURISK TID (129-130)

Sedimentære bergarter fra antatt vesentlig kambrosilurisk tid ble avsatt på det nederoderte grunnfjellet. Rester av bergartene er stedvis bevart i en tynn sone mellom grunnfjellet og de overskjøvne bergartene. Enkelte steder, i små forsenkninger i grunnfjellet, ble det avsatt basalkonglomerat, stedvis godt bevart f.eks. sørover fra Yrkefjorden. De fleste steder er det imidlertid en hvit til svakt blåaktig kvartsitt underst med et tynt marmorlag over. Videre oppover i lagrekken opptrer kalkspatholdig til karbonrik til sandig fyllitt.

VISTEFLAKET OG TILSVARENDE FLAK (127-128)

Den underste av de overskjøvne enhetene består av glimmerskifer, Ryfylkeskifrene (127), stedvis med en proterozoisk gneissåle (128). Glimmerskiferen ble opprinnelig avsatt på det nederoderte grunnfjellet og antas å være fra kambrosilurisk tid. Den er gråsvart til grågrønn, inneholder gjerne hvite, håndstore kvartslinser, og kan være granatholdig i motsetning til den underliggende, stedegne fyllitten. Skyvegrensen mot den underliggende fyllitten er de fleste steder vanskelig å kartlegge der den ikke markeres av en gneissåle.

STORHEIDEKKET OG BOKNAFJORDDEKKET (104-126)

Begge dekkene består av proterozoiske, opprinnelige grunnfjellsbergarter, stedvis med rester etter påliggende kambrosilurbergarter (104). I Nedstrandsområdet ligger *Boknafjorddekket* over *Storheidekket* (navn fra det tilgrensende Sauda-kartet) med en kaledonsk glimmerskifer imellom. Det er imidlertid usikkert om Boknafjorddekket virkelig danner et eget stort dekke slik tolkningen på kartet viser, eller om det henger sammen med Storheidekket, bare med innstokket glimmerskifer langs skjærsoner og mindre skyveforkastninger. Bergartene i Boknafjorddekket viser stedvis sterk proterozoisk deformasjon og folding, med kuttende, antatt unge proterozoiske granittpegmatitter, som kun kan være svakt kaledonsk deformert. Dypbergartene i Boknafjorddekket består overveiende av tonalittisk gneis, mens overflatebergartene, *Rennesøygruppa (111-115)*, for det meste består av finkornet amfibolitt, for det meste antatt omdannet basalt, lava og/eller tuff, stedvis med lag av kvartsitt (omdannet kiselstein?), og soner av kvarts- og feltspatrike gneiser. Glimmergneisene består delvis av omdannede, leirrike sedimenter stedvis med bevarte sedimentære strukturer. Boknafjorddekket viser store likheter med bergarter som finnes i grunnfjellet nord på Haugesundshalvøya. Øst for Boknafjorden består *Storheidekket* overveiende av lys grågrønn, saussurittisert, kvarts-feltspatrik gneis (126) som vesentlig er tolket å være omdannet tonalitt/trondhjemitt til granodioritt. I gneisen er det stedvis funnet spredte mesoperthittkorn (xenokrystaller?). Gneisene, særlig i de lavere delene av dekket, er generelt mer kaledonsk deformert og saussurittisert enn tilsvarende bergarter i Boknafjorddekket. De skjøvne, proterozoiske bergartene nord for Vindafjorden er jevnført med Storheidekket.

HARDANGERFJORDDEKKET (14-103) er det øverste og lengst skjøvne dekket og består overveiende av ordoviciske til siluriske bergarter. Beskrivelsen bygger på tilgjengelig litteratur, og den detaljerte inndelingen er valgt for å vise mulige jevnføringer fra område til område. Sideveis variasjoner, tektoniske avskjæringer og begrenset blotningsgrad har gjort oppbyggingen av en mer generell stratigrafi vanskelig.

Dyp- og gangbergarter:
Karmøy- og Lyklingofiolitten (sensu stricto, 98-102) utgjør de eldste delene av havbunnsskorpen og er ca 495-490 millioner år gamle. De to ofiolittfragmentene har en oppbygning som kjennetegner havbunnsskorpen; ultramafiske bergarter, ulike gabbrovarianter og dioritt underst gjennomsatt av diabasganger og tonalitt i de øvre delene, og med Visnesgruppas basalt (54) øverst. Denne basalten er antatt dannet fra den eldste av fire påviste diabasgenerasjoner i Karmøy-ofiolittkomplekset (sensu lato). Karmøyofiolitten ble gjennomsatt av *dyp- og gangbergarter (80-97*) i tidlig- og mellomordovicisk tid. *Sauøy-trondhjemitten (91)* er f.eks. aldersbestemt til ca 485 millioner år, og boninittiske diabaser av 2. og 3. generasjon ble dannet hhv. før 485 og mellom 485 og 479 millioner år siden, og antas å representere to forskjellige rift-spredningsfaser. *Utsirakomplekset (93-195)* består vesentlig av gabbro og tonalitt, og har vært utsatt for middels- til høygrads omdanning. Komplekset har antagelig tilhørt undre del av en tidligordovicisk øybueskorpe. *Vest-Karmøysuiten (84-90)*, har antagelig også trengt inn og størknet i undre del av en øybueskorpe. Suiten består av kvartsdioritt til tonalitt og granitt som er ca 479-474 millioner år gamle. Bergartene er antatt å ha sammenheng med oppsmelting av subduserte sedimenter fra kontinentskorpen (S-granitter), noe som støttes av at det er funnet inneslutninger av arkeiske zirkoner i dem. De er derfor trolig dannet nær en gammel kontinentskorpe. Kalkalkaline bergarter, som er antatt

dannet i den siste fasen i havbunns-skorpeutviklingen, størknet for ca 470 millioner år siden. Det gjelder *Vardafjellgabbroen (76-79),* ca 472 millioner år, *Feøygabbroen (83)* ca 470 millioner år, og *Stolmaplutonen (74-75)* av antatt samme alder og delvis samme oppbygning som Vardafjellgabbroen. Som beskrevet i oversikten, ble disse havbunnsskorpebergartene deretter skjøvet på land. Vardafjellgabbroen og Stolmaplutonen utgjør den eldste bergartsgenerasjonen i *Sunnhordlands-suiten (67-79),* mens *Rolvsnesgranodioritten (68-69)* tilhører den yngste. Bergarter som antas å være dannet samtidig med Rolvsnesgranodioritten er aldersbestemt til ca 430 millioner år. Altså ble Rolvsnesgranodioritten dannet etter at havbunns-skorpebergartene var skjøvet på land.

Overflatebergarter:
Visnesgruppa (54) er den laveste stratigrafiske enheten på Karmøy. Den finnes stedvis bevart i forkastningsbetingede blokker. Gruppen består av basalt (MORB til IAT type), som rant ut på havbunnen for det meste som putelava, trolig i forbindelse med første diabasgenerasjon i Karmøyofiolittkomplekset, for ca 495-490 millioner år siden. *Torvastadgruppa (33-41*) er antatt å være avsatt oppå Visnesgruppa, men kontakten er senere tektonisert. Bergartene er antatt avsatt i et tidlig- til mellomordovicisk (indre) øybuebasseng (MORB-lignende og kalkalkalin til alkalin vulkanisme), og viser for en stor del samme geokjemiske utvikling som dyp- og gangbergarter i Karmøyofiolittkomplekset.
Torvastadgruppa er inndelt i fire formasjoner: Midtøyformasjonen (41) er vulkanske bergarter som kan tilsvare 2. og 3. diabasgenerasjon i Karmøyofiolittkomplekset, og består vesentlig av vulkanoklastiske avsetninger og noe lava av basaltisk til andesittisk sammensetning (både IAT, MORB-lignende, alkaline og kalkalkaline typer). Velleformasjonen (40) består hovedsakelig av kalkalkaline, klinopyroksenrike, pyroklastiske og vulkanoklastiske avsetninger som kan tilsvare Feøygabbroen. Vikingstadformasjonen (38-39) består av alkalibasaltisk grønnstein samt litt kiselstein. Grønnsteinen har stedvis pulestrukturer og ligner geokjemisk på den 4. og siste diabasgenerasjonen i Karmøyofiolittkomplekset.
Hålandsformasjonen (33-37) er den øverste enheten på Karmøy og består for det meste av grå fyllitt og arkose i veksling med litt kiselstein. Lagrekken på Bømlo starter med *basalt (57)* som antatt tilsvarer Visnesgruppa. *Geitungenheten (48-50)* er avsatt diskordant over Lyklingofiolitten (sensu stricto), og består for det meste av basalt stedvis med putestrukturer, i veksling med kvartskeratofyr. Sistnevnte er geokjemisk lik trondhjemittene i enheten. Geitungenheten er ca 494 millioner år, altså omtrent samme alder som Karmøyofiolitten, og synest geokjemisk å være dannet i en umoden øybue (IAT), muligens tilsvarende undre del av Midtøyformasjonen på Karmøy. *Varaldsøykomplekset (51-53)* og vulkanske bergarter nordvest for Siggjargruppa på Stord, er ut fra begrensede geokjemiske analyser jevnført med Geitungenheten. Diskordant over Geitungenheten ligger *Søre Lyklingholmenheten (47),* som for det meste består av sedimentær breksje og stedvis konglomerat, muligens avsatt langs en bruddsone i en umoden øybue. Enheten inngår som øverste ledd i det som i litteraturen er kalt Lykling ofiolittkompleks. *Siggjargruppa (42-45)* ble avsatt på land, oppå bergartene i Lykling ofiolittkompleks, etter at sistnevnte var blitt deformert og stedvis overbikket. Gruppen består hovedsakelig av basiske, intermediære og sure vulkanske bergarter med mindre innslag av sedimentære bergarter. Stedvis finnes et basalkonglomerat, Erlandsvassformasjonen (45). Vulkanittene i Siggjargruppa er høy-

kalium kalkalkaline, antatt dannet ved en aktiv kontinentrand. På kartet omfatter Siggjargruppa også den antatt tilsvarende Kattnakkagruppa. Vulkanittene er ca 476 og 473 millioner år gamle, altså av tilnærmet samme alder som Vardafjell- og Feøygabbroen. Vardafjell-gabbroen har gjennomsatt Siggjargruppa (T. Andersen, muntl. inf.), trolig før havbunnsskorpe-bergartene (inkludert Vardafjell-gabbroen,) ble skjøvet på land. Siggjargruppa er imidlertid også tolket å være avsatt i et intrakontinentalt miljø etter at havbunnsskorpebergartene var skjøvet på land. *Grutlefjordgruppa (30-32)* er avsatt diskordant på Lyklingofiolitten og Siggjargruppa, og på grunn av senere erosjon, bare bevart i kjernen av synklinaler. Underste del av gruppen, Sagvassformasjonen (31-32), begynner med et lokalderivert konglomerat stedvis med en overliggende marmor. I motsetning til tidligere tolkning antas nå formasjonen å være dannet før ashgilltiden (H. Brekke, muntl. inf.). Derover følger et tykt konglomerat. Øverste del av gruppen, Eriksvassformasjonen (30), består vesentlig av basaltisk lava avsatt på land. Geokjemisk er lavaen ganske lik tilsvarende bergarter i Siggjargruppa. *Langevåggruppa (22-29)* har tektonisk kontakt mot Siggjargruppa og Grutlefjordgruppa, og har derfor noe usikker alder og stratigrafisk posisjon. Krekjebærformasjonen (29), som er den underste enheten i Langevåg-gruppa, består hovedsakelig av mafisk, kalkalkalin, vulkaniklastisk breksje og noe lava med fenokrystaller av klinopyroksen. Den er avsatt på land og ligner svært på tilsvarende avsetninger i Torvastadgruppa (Velleformasjonen). Den overliggende Kyrkjetuftformasjonen (26-28) består av undersjøiske vulkanoklastiske massestrømmer, turbidittavsetninger, tuft, slamstein og kiselstein. Derover følger Vorland- og Stavanesformasjonen (25) som begge består av grønn fyllitt og sandstein, antatte turbidittavsetninger, i veksling med omdannet putelava og massiv grønnstein (tholeiittisk/alkalin) som geokjemisk er forskjellig fra Krekjebærformasjonen.

Sagvågformasjonen (25) på Stord og videre nordøstover til Tysnes), består av forskjellige grønnskifervarianter, som dels kan være fra et høyere stratigrafisk nivå enn Agdesteinformasjonen? Hesthaugformasjonen (25) er den tykkeste kiselsteinsenheten i Langevåggruppa. Vespestadformasjonen er den øverste enheten i Langevåggruppa på Bømlo, og antatt å tilsvare Agdestein-, og Ådlandsformasjonen på Stord. Vespestadformasjonen (kun boks 24) består av svart fyllitt og grå til hvite sandsteinslag, antatt turbidittavsetninger. Kiselstein er ikke observert i formasjonen. Ådlandsformasjonen (kun boks 24) består av svart fyllitt med kvartsårer og -linser. Høyere opp i enheten veksler fyllitten med grå sandsteinslag. Agdesteinformasjonen (22-23) ligger over Ådlandsformasjonen og består av grå sandstein og sandig fyllitt, stedvis med lag av kiselstein. Toppen av Langevåggruppa sees ikke. Langevåggruppa er antatt å representere utviklingen av et randbasseng. Agdestein-, Vespestad- og Ådlandsformasjonen tilsvarer trolig øverste del av Hålandsformasjonen i Torvastadgruppa. *Dyvikvåg-gruppa (14-15)* på *Stord, Bergeseidgruppa (16)* på Bømlo og *Skudenesgruppa (17-21)* på Karmøy er jevnførbare enheter. Alle representerer tidsekvivalente avsetninger over den viktige regionale mellom- til senordoviciske vinkel-diskordansen. Bergartene er avsatt på omdannede havbunnsskorpebergarter. De tre gruppene starter alle med et konglomerat med boller fra dette underlaget. Over konglomeratene ligger kalkstein som inneholder fossiler; koraller, gasiropoder, brachiopoder, krinoidestilker, bryozoer, mm., fra senordovisisk, ashgill tid. Høyere opp, i Dyvikvåggruppa (Vikanesformasjonen, 15), er det også funnet fossiler fra tidligste silurtid (undre llandovery), representert med blant annet en rikholdig

graptolittfauna. Sedimentasjonen der må følgelig ha fortsatt til inn i silurtiden. Utslettefjellformasjonen (14) utgjør øverste enhet i Dyvikvåggruppa. Konglomeratet inneholder boller av både granitt- og kvartsittisk materiale. Granittbollene er for en stor del antatt å stamme fra Sunnhordlandssuiten, og konglomeratet er derfor enten fra silurisk eller muligens tidlig- til mellomdevonsk tid.

Ånugloskifrene (59-64) og Bremneskomplekset (65-66) er overflatebergarter av mer usikker stratigrafisk posisjon. Bremneskomplekset ligger mellom Vardafjellgabbroen og Rolvsnes-granodioritten, og består av mer eller mindre migmatittisert arkose, glimmerskifer, kvartsitt og kalkstein og med metamorfe mineraler som granat, kordieritt og sillimanitt. Migmatittiseringen fant sted da bergartene ble gjennomsatt av Vardafjellgabbroen, og bergartene må følgelig være eldre enn ca 470 millioner år. Ånugloskifrene opptrer i et underliggende flak, *Borgundøyflaket*, innen Hardangerfjorddekket. Bergartene består av sedimenter og vulkanitter som er avsatt på antatt havbunnsskorpebergarter.

Skorpeflaket (103) består av mylonittiske gneiser fra proterozisk tid. Det ble skjøvet inn i Hardangerfjorddekket sent under framskyvningen, og ble dermed en del av dekket.

GANGBERGARTER FRA PERMISK TIL JURAISK TID (12)

En rekke nord-sørgående, svarte gangbergarter, lamprofyrer, finnes særlig i Sunnhordland. Gangbergartene er ca 162-274 millioner år gamle, og kom på plass i forbindelse med oppsprekking av kontinentskorpen, forut for åpningen av Norskehavet. Det er funnet inneslutninger av spinell-lherzolitt i bergartene, som defor må ha kommet fra relativt stort dyp (70-80 km ?).

SEDIMENTÆRE BERGARTER FRA MESOZOISK TIL KVARTÆRTID

De sedimentære bergartene på sokkelen avspeiler en kontinuerlig tilførsel av materiale fra land, samtidig med jevn innsynkning av bassengområdet. Kartleggingen er basert på seismiske linjer, og tolkning og inndeling av bergartene i enheter er sammenholdt med informasjon fra borhull i tilgrensende områder. Kun et grunt borhull nord for Utsira finnes innenfor kartbladet. Bergartene har hovedstrøkretning nord-sør parallelt med kysten og slakt fall mot vest. Unntak er de 50-250 meter tykke, flattliggende sedimentene av kvartær og senpliocen alder som ligger med klar vinkeldiskordans mot de underliggende bergartene. Kartet framstiller berggrunnsgeologien slik den framkommer under denne sedimentpakken. I området øst for ca 4,50º antas de yngste bergartene å ligge direkte på eldre, vesentlig kambrosiluriske bergarter, som gir en typisk ujevn havbunnstopografi, mange steder gjennomsatt av forkastninger. De kambrosiluriske bergartene langs kystsonen er skilt fra de yngre sedimentære bergartene i vest med en markert brattkant mot vest. Denne danner østskråningen av Norskerenna, og synest å ha vært en aktiv forkastningssone i flere ulike faser, den siste i sentertiær. Store deler av kartbladet utenskjærs ligger innenfor Norskerenna, som er et morfologisk hovedtrekk i denne del av Nordsjøen. Det er ikke mulig ut fra den seismiske kartleggingen å bestemme alderen til de eldste sedimentære bergartene. Muligheten er imidlertid til stede for at sedimentære bergarter fra mellom- og tidligjuraisk tid, samt triastiden finnes umiddelbart vest for de omdannede bergartene i kystsonen. Også bergarter fra mulig devonsk til karbonsk tid kan være nedforkastet lanqs denne sonen. En betydelig del av den mesozoiske lagpakken synest å bestå av sedimenter avsatt i *senjuraisk* tid, og de organisk rike skifrene nær overgangen jura/kritt kan med letthet følges regionalt på seismiske snitt i

Nordsjøen. Skiferen er hovedkildebergarten for olje og gass i Nordsjøen, men er antagelig lite utviklet innen kartbladet, hvor det antagelig har vært et avsetningsmiljø med rask tilførsel av sedimenter fra land. Siden dybden til overgrensen av juralagrekken er så viktig i oljesammenheng, viser kartet også dybdekoter til grenseflaten mellom jura- og krittbergartene, målt i toveis gangtid, dvs tiden det tar for en lydpuls å nå ned til renseflaten og opp igjen, målt i millisekunder. I *tidlig krittid* synes innsynkningen å avta, og de vanligste sedimenttypene er trolig silt og leire med innslag av mergel, kalkstein og sandstein. *I senkrittid* ble det avsatt en tynn (50-150 m mektig) lagpakke av kalkstein og mergel. Hele *tertiær* kjennetegnes ved en jevn tilførsel av materiale og rolig innsynkning av bassenget. Havnivåendringer har medført enkelte brudd i sedimentasjonen, og avsetningsmiljøet har vekslet fra dype og landnære havavsetninger til strandavsetninger. De *paleocene* avsetningene i dette området antas å bestå av leirstein og siltstein i veksling med litt sandstein og kalkstein. Avsetningene er relativt mektige og trolig kan litologi og mektighet avspeile tektoniske bevegelser som har hatt sammenheng med åpningen av Norskehavet. Også vulkansk aktivitet er et karakteristisk trekk for den seinere delen av paleocen i Nordsjøen. Prøver som er tatt fra Balderformasjonen, viser en leirskifer vekslende med sandige askelag, stedvis med innslag av kalkstein, dolomitt og sideritt. Hovedvulkansenteret har antagelig ligget nord for de britiske øyer, men vulkansk aktivitet er også kjent fra Skagerrak. De *eocene* bergartene antas delvis å ha blitt avsatt under transgresjonsfaser, og består hovedsakelig av leirskifer i veksling med lag av sandstein, siltstein og noe kalkstein. Litologisk vil ikke bergarter fra *oligocentiden* skille seg særlig ut fra den underliggende lagpakken, men en kan forvente et større innslag av grovklastisk materiale som følge av havnivåendringer knyttet til jordskorpebevegelser. Borhullsprøver fra den *miocene* lagpakken har vist vekslende lag med delvis konsolidert leir-, silt- og sandstein. Den yngste, flattliggende, *senpliocene* lagpakken overleirer de skråstilte bergartene med en mektighet mellom 50 og 250 m. Informasjon fra omkringliggende borhull angir en senpliocen alder på denne vinkeldiskordansen. Grenseflaten viser helning østover mot overgangssonen til de underliggende, omdannede kambrosilurbergartene. Den representerer således en periode med kraftig elve- eller grunthavserosjon, hvor de mest motstandsdyktige bergartene har dannet oppstikkende partier (se snittet). Under videre sedimentasjon i sentertiær og kvartær tid er forkastningssonen mellom de omdannede og de sedimentære bergartene blitt aktivert med innsynkning langs denne. Sedimentene over vinkeldiskordansen nord for kartbladet, varierer fra sand overleiret av mer finkornet materiale i senpliocen tid til morenemateriale og leire i den kvartære lagpakken. Mesozoiske bergarter (10) er også avsatt i et forkastningsbetinget basseng i Skudenesfjorden.

BERGARTENES OMDANNING

Bergartene i grunnfjellet ble i proterozoisk tid omdannet under lavt til middelstrykk og middels til høy temperatur ved en kombinasjon av regional- og kontaktmetamorfose. Særlig intrusjonene av tonalitt til dioritt, men også granitt-migmatitt massivene, forårsaket kontaktmetamorfosen. Metamorfe mineraler omfatter klorittoid, andalusitt, granat, sillimanitt, kyanitt, staurolitt, kordieritt, og lokalt antofyllitt, og omdanningen kommer lokalt opp i høy middelgrad (høy amfibiolittfacies metamorfose). På Bokn, sørvest for en skjærsone, finnes stedvis svakt charnockittiske, granittiske til tonalittiske bergarter (159) med blå kvarts, fiolett feltspat, lokalt mesoperthittisk feltspat, og med amfibolittbånd som inneholder

klinopyroksen og antatte psevdomorfoser etter ortopyroksen. Bergartene der er massive til båndete, dels åremigmatitter, og kan tilsvare de charnockittiske og granittiske migmatittene i grunnfjellet sørover fra Høgsfjorden (sør for kartet). De *stedegne til nær stedegne kambrosilurbergartene* er omdannet under midtre grønnskiferfacies-forhold (biotittsone), trolig med en svak økning i metamorfosen mot nord. Tilsvarende bergarter innen *Visteflaket og tilsvarende flak* er omdannet under litt høyere trykk/temperaturforhold (øvre grønnskiferfacies) og består av en grovere glimmerskifer som stedvis har spessartin-almandingranater, og generelt sett en svakt økende omdanningsgrad nordvestover og oppover i tektonostratigrafien. *Boknafjorddekkets og Storheidekkets* bergarter viser omtrent samme proterozoiske metamorfose som grunnfjellet på Haugesundshalvøya. Enkelte steder rett øst og sør for kartet, inneholder imidlertid bergarter tilsvarende Storheidekket, partier med bevarte proterozoiske granulittbergarter, lokalt massive høy-temperatur charnockittbergarter. Den kaledonske omdanningen vises ved stedvis retrogradering, særlig i de underste og mest deformerte delene av Storheidekket der gneisene for det meste er svakt grønne som følge av saussurittisering.

I Hardangerfjorddekket ble de tidlig-ordoviciske ofiolittbergartene omdannet under varierende grønnskiferfacies-forhold (biotittsone) og erodert før de senordoviciske sedimentene ble avsatt. Unntak er bergarter i Utsirakomplekset og Bremneskomplekset, som viser middels- til høygrads kontaktmetamorfose. Under den videre deformasjonen og skyvningen ble bergartene på ny utsatt for grønnskiferfacies omdanning, fra klorittsone i sør til biotittsone i nord, og stedvis med senkaledonsk retrogradering.

STRUKTURGEOLOGI

Grunnfjellet viser for det meste en svak til moderat proterozoisk deformasjon, med unntak av de unge massive granittene. I den nordøstlige delen av kartet er hovedstrøkretningen nordvest-sørøst. Det vanligste proterozoiske strukturelementet ellers er store plutoner omgitt av sterkere deformerte dyp- og overflatebergarter, dels deformert da plutonene kom på plass. Kaledonsk deformasjon har i økende grad påvirket grunnfjellet sørvestover med forskifring og forgneising langs skjærsoner, særlig i nærheten av skyvegrensene.

Hovedtrekkene i den kaledonske dekkeoppbygningen framgår av nøkkel-kartet og oversikten over, med den usikkerheten som er nevnt tidligere om forholdet mellom Boknafjord- og Storheidekket. Det finnes flere mindre skyveforkastninger og tektoniske enheter enn det som er vist på kartet, både mulige kortskjøvne grunnfjellsbergarter (139), skyvegrenser og imbrikasjoner innen Visteflaket og tilsvarende bergarter, og skyvegrenser innen Hardangerfjorddekket.

Etter framskyvningen av dekkene ble grunnfjellet langs Hardangerfjorden nedfoldet og nedforkastet mot nordvest langs strukturer som er kalt Foldegrøften og Hardangerfjordskjærsonen. Det går også en forkastning parallelt med dette langs den sørøstlige delen av Bømlo, Stord og Tysnes, kalt Sunnhordlandsforkastningen. I Ølen-Nedstrand-Boknafjordområdet ble det i samme tidsrom dannet en buet forsenkning/nedfoldning i grunnfjellet, kalt Ølen-Nedstrand forsenkningen. Yngre NNV-SSØ- til nord-sør- strykende forkastninger av flere generasjoner, finnes mange steder, eksempelvis langs Karmsundet og videre sørover i Skudenesfjorden, med mesozoiske bergarter nedforkastet i en halvgraben. Flere, særlig NNVSSØ- til nord-sør-strykende forkastninger er reaktivert etter istiden (postgiasiale forkastninger) med

forkastningssprang trolig på opp til ca 10 meter for enkelte forkastninger. Slike forkastninger er påvist langsVindafjorden-Sandeidsfjorden- Øis-vågen og vestligst i Yrkelorden, ved Ølen med bevegelse på ca 1 mm/år, de siste årene. Trolig har det også vært reaktivering langs andre forkastninger. Det er også registrert en relativt høy jordskjelvsaktivitet i Sunnhordland de siste årene med styrke på opp til 4,5 på Richterskalaen.

ØKONOMISK GEOLOGI

Malmforekomster: Kobber- og svovelkis-forekomster opptrer en rekke steder knyttet til gabbro/grønnnskifer i Karmøy- og Lykling-ofiolitten. Både på Karmøy og Bømlo har det vært gruvedrift på kobberkisforekomstene. Visnes kobberverk var i drift fra ca 1880 til 1972. På Feøy har det vært gruvedrift på nikkel fra magnetkis. På Bømlo har det også vært gullgruvedrift på kvartsganger. På Stord er det nedlagte svovelkisgruver i grønnskifer (f.eks. Stordø kisgruver nedlagt 1968), og også på Huglo (Tveit). I Vindafjord er det en nedlagt thorium og uranmineralgruve (Thors gruve) i en pegmatitt-gang, som også har vært drevet på glimmer.

Industrimineraler og -bergarter: Marmor og kalksteinsbrudd har vært drevet på Moster, Vikanes og Huglo. Flere steder i grunnfjellet i Sveio har det vært små skifer- og granittbrudd. Granittbrudd finnes også flere andre steder, f.eks. Rubbestadneset og Espevik. Det finnes en rekke pukkverk, det største (gigantpukkverk) ligger nord for Tau.

HYDROGEOLOGI

Borebrønner i de granittiske til tonalittiske dypbergartene gir vanligvis fra 400-2000 liter i timen og sjelden over 7000 l/t. Basiske bergarter (gabbro, amfibolitt, basaltiske bergarter), glimmerskifer, fyllitt, gir som regel minst vann, vanligvis 0-300 l/t og sjelden over 700 l/t, men «trykking» kan øke kapasiteten noe, f.eks. i de basiske bergartene i Boknafjordområdet. Borhull i eller nær sprekkesoner vil som regel også øke brønnens kapasitet.

ALDERSBESTEMMELSE AV BERGARTER VED HJELP AV RADIOGENE ISOTOPER

Et utvalg av aldersbestemmelser er oppført med henvisning til bokser i tegnforklaringen:

12 K-Ar totalbergart og mineraldateringer: 162-274 mill. år (Færseth, R.B. et al. 1976. Lithos 9).

42 U-Pb zirkon: 476±4 mill. år (ryolitt/Kattnakkagruppa): 473±(2 mill. år (ryolitt/Siggjargruhpapnad) i (Pedersen, R.B. & Dunning, G.R., i Pedersen, R.B. 1992. Dr. philos. avhandl. Univ. i Bergen). Rb-Sr totalbergart; 455±5 mill. år (Kattnakkagruppa, Priem, H.N.A. & Torske, T 1973. NGU 300.); 464±16 mill. år (Siggjargruppa, Furnes, H. et al. 1983. Geol. Mag. 120).

49 U-Pb zirkon: (andesitt) 494±2 mill. år (Pedersen, R. B. 1992. Dr. philos. avhandl., Univ. i Bergen).

69 Bergart som antatt tilsvarer Rolvsnesgranodioritten: Rb-Sr totalbergart; 430±10 mill. år (Andersen, TB. & Jansen, Ø. 1987. NGT 67); 430±6 mill. år (Fossen , H. & Austrheim, H. 1988. NGU bull. 413).

76 U-Pb zirkon: 472±2 mill. år (Pedersen, R.B. 1992, Dr. philos. avhandl., Univ. i Bergen).

83 U-Pb zirkon: 470 +9/-5 mill. år (Dunning, G.R. & Pedersen, R.B. 1988. Contrib. Mineral. Petrol. 98).

85 U-Pb zirkon: 474+3/-2 mill. år (Pedersen, R. B. 1992. Dr. philos. avhandl., Univ. i Bergen).

90 U-Pb zirkon: 479±5 mill. år (Pedersen, R. B. 1992. Dr. philos. avhandl., Univ. i Bergen).

91 U-Pb zirkon: 485±2 mill. år (Dunning, G.R. & Pedersen R.B. 1988. Contrib. Mineral. Petrol. 98).

98 U-Pb zirkon: 493+71-4 mill. år (Dunning, G.R. & Pedersen R.B. 1988. Contrib. Mineral. Petrol. 98).

152 U-Pb zirkon: 1505.1±1.4 mill. år (Ragnhildstveit, J. og Tucker, B. foreløpig aldersbestemmelse, under arbeid).

UTVALGT LITTERATUR, KART OG UPUBLISERTE VERK:

Amaliksen, K.G. 1983: The geology of the Lykling ophiolitic complex, Bømlo, SW Norway. *Unpubl cand real. thesis, Univ. of Bergen.*

Andersen, TB. & Jansen, Ø.J. 1987: The Sunnhordland Batholith, W. Norway: Regional setting and internal structure, with emphasis on the granitoid plutons. *NGT 67, 159-183.*

Birkeland, T. 1981: The geology of Jæren and adjacent districts. A contribution to the Caledonian nappe tectonics of Rogaland, Southwest Norway. *NGT 61, 213-235.*

Brekke, H. 1983. The Caledonian geological patterns of Moster and Southern Bømlo. Evidence for Lower Palaeozoic magmatic arc development. *Unpubl. cand. real. thesis, Univ of Bergen.*

Brekke, H., Amaliksen, K.G., Færseth, R.B., Jorde, K., Naterstad, J., Nilsen, E., Nordås, J., Ragnhildstveit, J. & Ree, R., 1993: Berggrunnskart BØMLO 11 14-2, M 1:50.000, foreløpig utgave. NGU.

Brekke, H., Furnes, H., Nordås, J. & Hertogen, J. 1984: Lower Pajaeozoic convergent plate margin volcanism on Bømlo, SW Norway, and its bearing on the tectonic environments of the Norwegian Caledonides. *J. geol. soc. London 141,1015-1032.*

Broch, O.A., Isachsen, F., Isberg, O. og Strand, T 1940: Bidrag til Skudnessedimentenes geologi. *NGU 155.*

Færseth, R.B. & Solli, A. 1982: Berggrunnskart HUSNES 1214-4, M 1:50.000. *NGU.*

Færseth, R.B. 1982: Geology of Southern Stord and adjacent Islands, Soutwest Norwegian Caledonides. *NGU 371, 57-112.*

Færseth, R.B., Andersen, T.B., Nielsen, P.E., Nordås, J., og Ragnhildstveit, J. 1993: Berggrunnskart FITJAR 11 14-1, M 1:50.000, foreløpig utgave. *NGU.*

Hansen, B., Lund, T., Sturt, B.A. & Thon, A. 1989: Berggrunnskart UTSIRA 11 13-4, M 1:50.000, foreløpig utgave. *NGU.*

Hansen, H. & Lund, T. 1984: The geology of Utsira, SW Norway. *Unpubl. cand. scient. thesis, Univ. of Bergen.*

Jorde, K., Naterstad, J., Pedersen, R.B., Solli, T. & Ragnhildstveit, J. 1993: Berggrunnskart HAUGESUND 11 13-1, M 1:50.000, foreløpig utg. *NGU.*

Kvale, A. 1937: Et kaledonsk intrusiv - og effusivfelt på Stord. *Bergens mus. Årb. Naturvitensk. rekke 1, 43 s.*

Ledru, P. 1980: Evolution structurale et magmatique du complexe plutonique de Karmøy (sud-ouest des Calédonides norvégiennes). *Bull. Soc. géol. mineral. Bretagne, Xll, 2: 1-106.*

Müller, G. & Wurm, F. 1969: Die gesteine der inselgruppe Randøy-Fogn. Beiträge zur metamorphose und zum aufbau der kambro-silurischen gesteine des Stavangergebietes 1. *NGT 49, 1-97.*

Müller, G. & Wurm, F. 1970: Die Gesteine der Halbinsel Strand. NGU 267, 1-55.

Müller, G. & Wurm, F. 1970: Die Gesteine der Inseln des Sentralen Boknfjords. NGU267,61-90.

Müller, G. & Wurm, F. 1974: Berggrunnskart STRAND 1213-2, M 1:50.000, foreløpig utgave. NGU.

Nielsen, P.E. 1990: Geologiske relasjoner mellom Bremneskomplekset og Sunnhordlandsbatolitten, Bømlo, Vest-Norge. Upubl. Cand scient. oppg., Univ. i Oslo.

Nilsen, E. 1984: En petrografisk og strukturgeologisk undersøkelse av Auklandshamnområdet, Sunnhordland. Upubl. cand. real oppg., Univ i Oslo.

Nordås, J. 1985: A volcanological and geochemical study of the lower palaeozoic Lykling ophiolitic complex and Siggjo complex, central Bømlo, Western Norway. Unpubl cand. real. thesis, Univ. of Bergen.

Nordås, J., Amaliksen, K.G., Brekke, H., Suthren, R.J. & Furnes, H., Sturt, B.A.,

Robins, B. 1985: Lithostratigraphy and petrochemistry of Caledonian rocks on Bømlo, Southwest Norway. In: Gee, D.G. & Sturt, B.A.: The Caledonide orogen Scandinavia and related areas. 679-692.

Pedersen, R.B. 1982: The Karmøy ophiolite plutonic suite. Unpubl. Cand real.thesis, Univ. of Bergen.

Pedersen, R.B. 1992: Geochronology, Geochemistry and Petrogenesis of Caledonian Ophiolite Complexes. Unpubl. Dr philos. thesis, Univ. of Bergen,

Ree, R. 1981: En petrografisk og strukturgeologisk undersøkelse av Valevågområdet, Sunnhordland. Upubl. Cand real. oppg., Univ. i Oslo.

Reusch, H. 1888: Bömmelöen og Karmöen med omgivelser, Kristiania, 422 8.

Riis, F 1977: En petrografisk - strukturgeologisk undersøkelse av Nedstrandområdet, Ryfylke. Upubl. cand. real. oppg., Univ. i Oslo.

Rokoengen, K. & Sørensen, S. 1990. Late Jurassic sedimentary bedrock north of Utsira, offshore western Norway. NGT 70, 61-63.

Solli, A., Naterstad, J. & Andresen, A. 1978: Structural succession in a part of the outer Hardangerfjord Area. NGU 343, 39-51.

Sørbye, R.C. 1964: Anthophyllite-cordierite-gneisses in the basal rock complex of the Haugesund peninsula, Western Norway. NGT 44, 323-340.

Sørbye, R.C. 1948: Geological studies in the north-eastern part of the Haugesund peninsula, W. Norway. Univ. i Bergen årbok, Naturv rekke 6.

Tellefsen, J.E. 1982: En petrografisk og strukturgeologisk undersøkelse av Mosterøy, Bru og Sokn i Boknfjorden, Rogaland. Upubl. candrealoppg., Univ. i Oslo.

Tellefsen, J.E., Wurm, F., Jorde, K., Naterstad, J. og Birkeland, T. 1990: Berggrunnskart RENNESØY 1213-3, M. 1:50.000, foreløpig utgave. NGU.

Thon, A. 1980: Steep shear zones in the basement and associated deformation of the cover sequence on Karmøy, SW Norwegian Caledonides. J Struct geol 2, 75-80.

Thon, A., Magnus, C. & Breivik, H. The stratigraphy of the Dyvikvågen Group, Stord: A revision. NGU 359, 31-42.

Vollan, J.R. 1988: Strukturell utvikling av det subkambriske peneplanet nord for Kårstø i Ryfylke. Upul candscient.oppg. Univ i Tromsø.

Vollset, J. & Dore, A.G. 1984: A revised Triassic and Jurassic lithostratigraphic nomenklatur for the Norwegian North Sea. NPD-bulletin 3, pp. 1-53.

BESKRIVELSE TIL GEOLOGISK KART OVER NORGE STAVANGER 1:250.000

Knut Jorde, Ellen M.O. Sigmond, Tove Thorsnes

Geologisk oversikt

Berggrunnen innen kartbladet omfatter (fra eldst til yngst):

Grunnfjell, stedegne bergarter fra jordens urtid

Grunnfjellet består av: 1) omdannede bergarter av ulik opprinnelse, i første rekke ulike gneiser og migmatitter, 2) en gruppe omdannede overflatebergarter kalt Gjesdalssuprakrustalene og 3) yngre dypbergarter og gangbergarter som har trengt som en smelte inn i de eldre bergartene. Over disse ligger:

Bergarter fra jordens urtid og oldtid

Underst ligger Ryfylkeskifrene, disse består vesentlig av leirskifre som er omdannet til fyllitt. Noen av leirskifrene ble avsatt på grunnfjellsoverflaten og er fra kambrosilurisk lid, andre kan være overskjøvne, eldre skifre. Over disse ligger Jærdekkekompleksets bergarter som består overveiende av glimmergneis gjennomsatt av enkelte kropper av granodiorittt. Øverst ligger Karmsunddekkets grønnstein og kloritt-muskovittskifer Begge disse dekkene er skjøvet inn over Ryfylkeskifrene.

Over disse er avsatt ute på kontinentalsokkelen:

Bergarter fra jordens middeltid og nytid

Disse består av svakt hellende sandstein, siltstein, kalkstein og leirstein, med tynne lag av vulkansk aske fra karbon- til tertiærtiden. Øverst ligger flattliggende kvartære avsetninger.

Beskrivelse av bergartene (fra eldst til yngst)

Grunnfjell, stedegne bergarter fra jordens urtid (prekambrium)

Omdannede bergarter av ulik opprinnelse fra mellomproterozoisk tid (42-36). *Numrene i parentes viser til numrene i tegnforklaringen.*

Bergartene er gneiser og migmatitter, som er så sterkt omdannet at det er vanskelig å fastslå både deres opprinnelse og deres aldersforhold til Gjesdalssuprakrustalene. Typiske bergarter er charnockittisk gneis, dvs. en hyperstenførende granittisk gneis (42), båndet gneis med veksling av lyse og mørke bånd (41 og 40) og granittisk gneis (37). Omdannelsen har stedvis vært så omfattende at bergartene har smeltet, og gått over til migmatittisk gneis med diffus båndning (39), eller en granatrik, båndet gneis (38). Den båndete gneisen kan inneholde serpentinitt eller kleberstein (36).

Gjesdalssuprakrustalene (35-33)

Gjesdalssuprakrustalene har fått sitt navn etter Gjesdal kommune, der de utgjør en stor del av berggrunnen. Bergartene er overveiende av sedimentær opprinnelse. I likhet med gneisene som er nevnt over, er de sterkt omdannet, og opptrer nå som lys, granittisk gneis med moderat utviklet båndning (35) og kvartsrik, diopsidførende gneis (34). En sone med uren marmor (33) nord for Gjesdal er bevart som en isolert rest innenfor de båndete, migmatittiske gneisene.

Dypbergarter yngre enn Gjesdals-suprakrustalene (32-25)

En grovkornet øyegneis (32) finnes i en bred sone øst for Gandsfjorden. Gneisen er en foliert porfyrgranitt.

Middels- til grovkornet granitt og granodioritt (31) danner berggrunnen i

store deler av området mellom Ålgård og Hommarsåk.
Disse er overveiende massive, stedvis svakt folierte, og inneholder spredte partier med båndet gneis og granatrike soner. Granitten og granodioritten opptrer mange steder i veksling med den båndete, migmatittiske gneisen, stedvis er det en gradvis overgang mellom dypbergarter og gneiser. Slike feltforhold viser at dypbergartene kan være helt eller delvis dannet ved oppsmelting av gneisene selv.

Lys, middelskornet granitt (30) opptrer både som partier i de migmatittiske gneisene, og i større, ensartede bergartskropper.

Vest for Ålgård ligger Sjelsetmassivet, en stor gjennomsettende kropp av forskjellige typer granitt som gjennomgående er lite deformert. Hovedbergarten er biotittgranitt (29). Denne er gjennomsatt av charnockitt (pigeonittgranitt og fayalittgranitt, 28 og 27). Biotittgranitten er ca 985 millioner år. Charnockitten er noe yngre, 930-900 millioner år og antas å ha sammenheng med dypbergartene i Bjerkreim-Sokndalmassivet sørvest for anortositten. Charnockitten antas å være dannet på dypere nivå i jordskorpen enn biotittgranitten.

Det store Egersund-Ogna-massivet består av grovkornet anortositt (25) og noritt (26), som har trengt inn i de omgivende gneisene. Bergartene er dannet ved oppsmelting på stort dyp (omlag 40 km) og har hatt en meget høy temperatur (950º C) da de gjennomsatte de andre gneisene. Massivet danner en domformet bergartskropp som også strekker seg ut under havbunnssedimentene utenfor kysten. Massivet består av en sentral, massiv del og en ytre randsone av mer folierte bergarter. Anortositten er meget ensformig og består av store krystaller av feltspat (plagioklas An_{40-50}), med spredte kjempe-krystaller av plagioklas og enkelte pyroksener. Anortositten gir dårlig jordsmonn ved forvitring, særlig er fosforinnholdet lavt. Dette fører til at dyr som beiter i anortosittområdet må ha fortilskudd for å unngå mangelsykdommer.

Gangbergarter (24-22)
Foliert noritt (24) opptrer som en lag-gang i gneisene umiddelbart utenfor Egersund-Ogna-massivet. En serie av ganger av monzonitt (23) og diabas (22) gjennomsetter massivets bergarter.

Bergarter fra jordens urtid og oldtid overskjøvet under den kaledonske fjellkjededannelse

Ryfylkeskifrene (21)
Glinsende, gråsvart til grønnlig grå fyllitt (21) danner berggrunnen i området mellom Stavanger og Hafrsfjorden og i området mellom Tunheim og Varhaug. Fyllitten er stedvis rik på kvartseitler, og inneholder soner med kvartsrik fyllitt, kvartsitt, noe meta-arkose, samt svarte, karbonførende lag.

Det antas at de fleste fyllittene er kambrosiluriske og avsatt på grunn-fjellsoverflaten, andre kan være prekambriske og skjøvet inn over de underliggende grunnfjellsbergartene under dannelsen av den kaledonske fjellkjeden.

Jærdekkekompleksets bergarter (20-13)
Mørkegrå glimmergneis (19) utgjør hoveddelen av de overskjøvne gneisene på Jæren. Bergarten er en mørk, muskovitt-biotittgneis med lag av amfibolitt (16), kvartsitt og glimmerskifer, samt spredte soner av marmor og kalksilikatgneis (18). Gneisen er av sedimentær opprinnelse, mens amfibolitten er en omdannet dag- eller gangbergart. To små kropper av omdannet eklogitt (17) ved Garborg kan være skjøvet opp fra undre del av jordskorpen eller fra den underliggende mantelen fordi de viser spor av høyere omdannelse enn de omgivende dekkebergarter.

Partier av mer massive dypbergarter opptrer som en del av dekkekomplekset. Bergartene varierer i mineralsammen-setning, og omfatter granodioritter, granitter og tonalitter. Nord for Tananger er to kropper av granodioritt (15) skilt ut som en egen bergart, i resten av Jærdekkekomplekset er de tre bergartstypene slått sammen (20). Dypbergartene er stedvis moderat foliert, stedvis finbåndet. De er mer massive enn glimmergneisen, og danner de markerte kollene mellom Hafrsfjorden og Gandsfjorden. Grensene mellom disse bergartene og glimmergneisen er stedvis sterkt deformert , men i enkelte områder er det klart at ihvert fall den siste generasjonen av dypbergartene er trengt inn i glimmergneisene. Ved Tananger kan varme-påvirkningen fra dypbergartene ha vært så sterk at de omgivende bergarter har blitt kontaktomdannet, idel det er funnet vesuvian i gneisene.

Karmsunddekkets bergarter (14-13)
Øyene vest for Jæren består av gabbro og grønnstein (14) og kvarts-kloritt-muskovittskifer med lag av kvartsitt og kalkstein (1 3). Bergartene er lite undersøkt, men de kan være den sørlige fortsettelsen av dekkebergartene på Karmøy. Disse er delvis omdannede basalter, sedimenter og gabbro som utgjør en gammel kambrosilurisk havbunns-skorpe.

Bergarter fra jordens urtid, middeltid og nytid (12-1).

Fjellgrunnen utenskjærs består i et belte utenfor kysten av de samme prekambriske og kaledonske bergartene som på land, men lenger vest dekkes disse av yngre sedimenter (se kart og dybdesnitt D). Nær kysten har grunnfjellet et ujevnt relieff og er gjennomsatt av store forkastninger med sprang-høyder som kan være over 1000 meter. Forkastningene ble hovedsakelig dannet i karbon og perm, i vest også i trias-tidligjura,og de skiller det norske, stabile området med tykkjordskorpe fra Nordsjøen med sin tynne skorpe og jevne innsynkning.

I dybdesnitt D ser vi at grunnfjellsjordskorpen har sunket inn og dannet en trauformet forsenkning som er fyllt av avsetninger fra **karbon-og permtiden (Il).**

I **triastiden** ble store mengder sedimenter (10) fra fastlandet avsatt på elveslettene og i innsjøer i det flate lavlandsområder som Nordsjøen var den gang. Deretter fikk vi dannet den utjevnede overflaten som jurasedimentene er avsatt på.

Fra **juratiden** mangler avsetninger fra tidligjura. De mellomjuraiske sedimentene består av elve- og deltaavsetninger hvor materialet stammer fra fastlandet (10). I senjura trengte havet inn over det tidligere flate landområdet. Den marine skiferen fra senjura, som i sentrale og nordlige Nordsjøen er hovedkildebergarten for olje og gass, er imidlertid lite utviklet innenfor kartområdet. Her finnes i stedet en veksling av leirstein, sandstein og siltstein (9).

I **krittiden** var det ingen bevegelse langs forkastningene, men den jevne innsynkningen av bassengene fortsatte, og sedimentene ble følgelig avsatt i et havområde. I tidligkritt ble det avsatt sedimenter av ulik karakter, noe som skyldes vekslende havnivå. Det ble avsatt silt og leire med innslag av mergel, kalkstein og sandstein (8). I senkritt var havnivået høyt og stabilt og det ble avsatt kalkstein og mergel (7). Tykkelsen av sedimentene fra senkritt avtar fra 500-600 meter i sør til 50-60 meter i nord. Dette kan gjenspeile avsetningsbassengets utbredelse i senkritt, eller være et resultat av senere erosjon i tidligtertiær.

Tertiærtiden var preget av jevn tilførsel av sedimenter fra fastlandet og en rolig innsynkning av bassenget. På grunn av endringer i havnivået ble sedimentene

tidvis avsatt i dype havbassenger, tidvis i strandsonen (6-2).

I **paleocen** ble det avsatt leir-og siltstein med lag av sandstein og kalkstein (6). Et lag av vulkansk aske i toppen av Balderformasjonen (5) danner grensen mellom paleocen og eocen. Dette askelaget har antagelig kommet fra et vulkansenter nord for De britiske øyer, askelaget er et godt ledelag som kan følges over størstedelen av Nordsjøen.

I **eocen** trengte havet igjen inn over større områder. Avsetningene fra denne tiden er leirskifer i veksling med lag av sandstein, siltslein og kalkstein (4).

I **oligocen** er sedimentene (3) noe mer grovkornet på grunn av at havdypet igjen var mindre. I **miocen** opptrer vekslende leir-, silt-, og sandstein (2).

Sedimenter fra **pilocen** er ikke funnet innenfor kartbladet, men finnes like vest for kartkanten.

I korte perioder av **kvartærtiden** var havområdet dekket av is. Avsetningene fra denne tiden er marin leire, silt og usortert morenemateriale (1).

Alle sedimentene fra juratiden til og med miocen (10-2), heller svakt mot VSV, dette er et resultat av en.jevn innsynkning av Nordsjøbassenget og en tilsvarende hevning av Norges fastland. Dybdesnitt D viser at disse skråstilte lagene er blitt erodert (nedslitt), før de kvartære sedimentene (1) ble avsatt, grensen danner en vinkeldiskordans. Erosjonen antas å være et resultat av at isbreene under enkelte av de eldre istidene i kvartær tidvis strakte seg ut i Nordsjøen, og der skrapte vekk de underliggende sedimentene. De kvartære sedimentene (1) ble deretter avsatt oppå denne erosjonsflaten.

Bergartenes omdannelseshistorle

Ut fra aldersbestemmelser og mineralselskap kan en skissere følgende omdannelsesforløp:

Den eldste fasen i **grunnfjellet** (M_0) er presvekonorvegisk, ca. 1500 mill. år, og er en metamorf og/eller magmatisk fase.

De neste faser er sveko-norvegiske. Den eldste (M_2) er ca 1200 mill. år. Dette er en fase med en generell amfibolittfacies-omdannede i Sør-Norge, men i kartområdet er sporene etter denne delvis visket ut av de senere høytemperaturfasene.

Den følgende fasen (M_3) fant sted for ca. 1050 mill. år siden. Omdannelsen skjedde under høy temperatur og middels trykk (granulittfacies til amfibolittfacies), og hadde sammenheng med dannelsen av de store massivene av anortositt og noritt.

Fase M_4 er ca 950 mill. år og forårsaket en omdannelse under forhold som tilsvarer undre granulittfacies/øvre amfibolittfacies. Denne omdannelsen er antatt å henge sammen med inntrengningen av dypbergarter rett øst for kart-bladgrensen.

Ryfylkeskifrene er stedvis omdannet under betingelser som svarer til øvre grønnskiferfacies, stedvis undre grønnskiferfacies avhengig av tektonisk stilling. Senere har det skjedd en tilbakeskridende omdannelse i lavere grønn-skiferfacies.

Den eldste omdannelsen kan være prekambrisk eller kaledonsk, den yngste er kaledonsk.

Jærdekkekompleksets bergarter(19, 18, 16 og15) er generelt omdannet under betingelser som svarer til midtre amfibolittfacies antagelig i prekambrisk tid. Enkelte antatt yngre granitter og granodioritter (20) inneholder bl.a. hypersten, og har en alder på ca 960 mill. år, bergartene er derfor omdannet under

granulittfacies-betingelser i prekambrisk tid. Eklogittene (1 7) har en relikt mineralogi som viser til eklogittfacies-omdanning, denne fasen er eldste omdannelsesfase i Jærdekkekomplekset.

Karmsunddekkets bergarter er omdannet under grønnskiferfacies-betingelser under den kaledonske fjellkjededannelse.

Deformasjonshistorie

Bergartene i grunnfjellet er i stor utstrekning blitt sammenfoldet og sammenskjøvet dypt nede i jordskorpen under høye temperaturer. Dette har gitt bergartene et plastisk foldet preg. Det plastiske preget ses både i bergartene rundt anortositt-massivet og i grunnfjellsgneisene generelt. Variasjon i foliasjonsretningene er de fleste steder mere et resultat av inntrengning av dypbergarter enn av regional deformasjon.

Ryfylkeskifrene og de kaledonske dekkebergartene er påvirket av minst to hoveddeformasjoner. Den eldre deformasjonen kan observeres som isoklinalfolder med NV-SØ-rettede foldeakser og intens lineasjon i alle de kompetente bergartene, og antas i det vesentligste å være prekambrisk. Den yngre fase med Ø-V til ØNØ-VSV-rettede foldeakser gjør seg mest gjeldene i skifrene, og antas å være kaledonsk. Disse foldene har mange steder akseplan med fall mot S og SSØ, og viser en relativ skyvebevegelse mot N og NNV, og kan representere en tilbakeskyvning i en sen kaledonsk fase. Del er få direkte spor elter den generelle kaledonske hoved-overskyvning mot S og SØ.

Etter den kaledonske fjellkjedefoldningen ble landmassen brutt opp av forkastninger langs steile plan med ulike retninger. Forkastningenes alder kan variere fra devon til nåtid.

Langs Gandsfjorden er det påvist bevegelser på knapt en mm pr. år. Aktiv bevegelse på ca en mm er også påvist i Vindafjord nord for kartet, og langs en forkastning som følger anortositt-gneisgrensen øst for kartet. Langs denne siste forkastningen synker anortositt-massivet 2 mm pr år i forhold til gneisene.

Utenskjærs (snitt D) har jordskorpen blitt utsatt for strekning, og deler av grunnfjellet nær kysten har sunket inn i løpet av karbon- og permtiden. Lenger vest i snittet ses en av de store forkastningene som førte til innsynkningen i de sentrale delene av Nordsjøen i løpet av mellomjura til tidligkritt-tiden.

Isotop-aldersbestemmelser

Grunnfjell

Charnockittisk åre i Undheimleuconoritten 1028±77 mill. år (dannelsesalder, Rb-Sr)[1)]. Sjelsetgranitten 985±165 mill. år (dannelsesalder, Rb-Sr) [1)]. Fase med (kvarts) mangeritt i Bjerkreim-Sokndal-lopolitten 944 mill. år (dannelsesalder, Sm-Nd plagioklasisokron)[2)], 928±50 mill. år (dannelsesalder, Rb-Sr)[3)], og 910-930 mill. år (dannelsesalder, U-Pb zirkon)[4)]. Sjelset-charnockitten 900-930 mill. år (dannelsesalder, Rb-Sr) [1)].

Ryfylkeskifrene

Fyllitt nær Stavanger 540±100 mill. år (metamorfosealder, Rb-Sr) [5)].

Kaledonske dekkebergarter

Båndet gneis 995±30 mill. år (metamorfosealder, Rb-Sr) [5)].

1) Maijer et al. 1994, N.G.T. 74, 2) Barling et al. 1993, Terra Nova 5, 3) Wielens et al. 1981, N.G.U. 359, 4) Pasteels et al. 1979, Lithos 12, 5) Roddick & Jorde 1981, N.G.U. 365.

Fossiler

Det er ikke påvist fossiler på land innen kartbladet, men det er funnet mellomkambriske fossiler i en mørk skifer

avsatt i en grop i grunnfjellet i bunnen av Ryfylkeskifrene på Ritland, (nordøst for kartbladet). Silurfossiler er funnet i skifre i Karmsunddekket på Karmøy (nord for kartbladet).

Industrimineraler og -bergarter

Steinbrudd

Det er steinbrudd i drift på anortositt (22), granitt (31) og i overskjøvne gneiser (19). Det meste av steinen brukes til pukk og tilslag til asfalt. Det har vært tatt ut stein fra granodioritt (15) til moloen i Tananger. Det har i tillegg vært mindre drift på marmor og kvarts i Gjesdalsuprakrustalene (33 og 34) og på kleberstein (36), alle sørøst for Auglend.

Gruver, ertsforekomster og skjerp

Det har vært gruvedrift på nikkel i anortositt (25) ved Homse gruve. Forøvrig har det vært skjerpet i mindre målestokk på hematitt i kvartsbreksje og kobber i gneis (39) i fjellene nordøst for Auglend. Det har også vært skjerpet på uran i granitt (31), og på kobber i glimmergneis (19) i Jærdekke-komplekset.

Hydrogeologi

Brønnboringer i grunnfjellsbergartene gir vanligvis fra 100-2000 l/time pr. bore-brønn.

Fyllitt og glimmerskifer gir lite vann, vanligvis 0-300 l/time. Hydraulisk trykking kan imidlertid øke kapasiteten noe.

De overskjøvne glimmergneiser i Jærdekke-komplekset vil antagelig gi noe mindre vann-mengder enn grunnfjells-bergartene.

(Kvartære avsetninger, spesielt i forbindelse med vassdrag, kan gi store vannmengder, flere titusen l/time).

*Beskrivelse av borehullet på Tananger (se snitt B) **

Borehullet på Tananger ble boret i 1989-90 av Norsk Agip A/S og brukes som et ledd i opplæring av boredekksarbeidere. Hullet er 1241 meter dypt, målt fra boredekket. Et slikt hull gir geologisk informasjon av ulike slag. Boreslammet som pumpes ut av hullet frakter med seg borekaks (knust steinmateriale), som utgjør et sett med små bergartsprøver. Bergartenes fysiske egenskaper, som egenvekt, porøsitet, naturlige radioaktivitet og lydhastighet, samt lagenes helning, kan måles ("logges") med elektriske måleinstrumenter som senkes ned i hullet. Resultatene av målingene tegnes som loggkurver som viser variasjonene av de fysiske egenskapene mot dypet i hullet.

Geologien i borehullet på Tananger kan belyses med kurvene som viser variasjon i gammalogg) og egenvekt (tetthetslogg). Den første som kommer fra uran, thorium og radioaktive isotoper av kalium. Disse forekommer i små mengder i de fleste bergarter. Tetthetsloggen registrerer bergartenes egenvekt ved å måle refleksjon og endring av nøytronstråling.

De to loggkurvene viser at det er ensartet glimmergneis (19) ned til omlag 550 meters dyp. Fra 550 m til omlag 900 m er det veksling av granodioritt og granitt (sammenfattet som granulitt), amfibolitt og gneis, disse tolkes som en del av glimmergneisen (19). Bergartene fra 900 m til bunnen av hullet tolkes som granodioritt, granitt m.fl. (20), med et tynt lag av marmor (18) i ca 1080 m dyp.

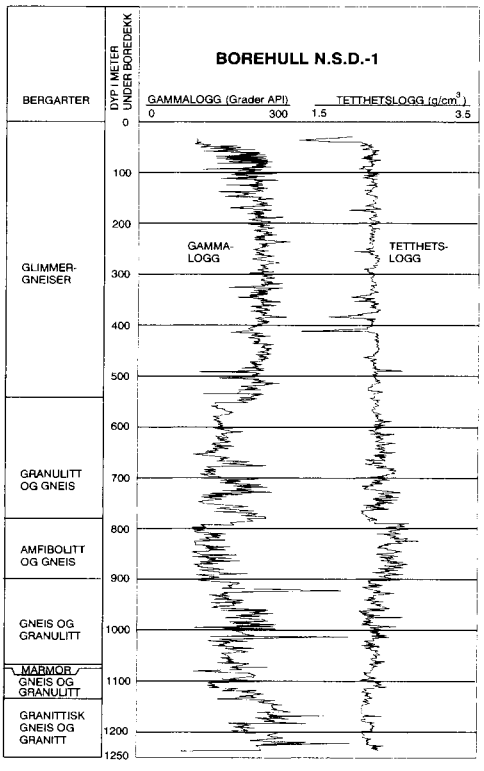

Utvalgt litteratur

Anundsen, K., Grimstveit, L., Harsson, B.G. & Holsen, J. 1994: Prezise measurements of active faulting in southwest Norway. Tectonophysics, in press.

Birkeland, T. 1981: The geology of Jæren and adjacent districts. A contribution to the Caledonian nappe tectonics of Rogaland, southwestern Norway. Nor. Geol. Tidsskr. 61, 213-235.

Deegan, C.E. & Scull, B.J. 1977: A standard lithostratigraphic nomenclature for the Central and Northern North Sea. Inst. Geol. Sci. Rep. 17/25 & Norw. Petr. Dir. Bull. 1, 1-36.

Glennie, K.W. 1984: The structural Framework and the Pre-Permian History of the North Sea Area. 1: Glennie, K.W. (red) Introduction to the Petroleum Geology of the North Sea. Blackwell Scientific Publ. 236 p.

Maijer, C.& Padget, P. (red) 1987: The geology of southernmost Norway: an excursion guide. Nor. Geol. Unders. Spec. Publ. 1.

Maijer, C., Verschure, R.D. & Visser, D. 1994: Strontium isotope study of two supposed satellite massifs of the Egersund Anorthosite Complex: The Sjelset Igneous Complex and the Undheim Leuconorite. Nor. Geol. Tidsskr. 74, 58-69.

Michot, P. 1960: La geologie de la catazone: le probleme des anorthosites, la palingenese basique et la tectonique catazonale dans le Roqaland meridional (Norvege meridionale). Nor. Geol. Unders. 212g, 1-54.

Olsen, R.G. & Strass, I.F. 1982: The Norwegian-Danish Basin. Norw. Petr. Dir. Paper 31, 1-76.

Rokoengen, K. & Rønningsland T.M. 1983: Shallow bedrock geology and Quaternary thickness in the Norwegian sector of the North Sea between 60° N and 62° **N** Nor. Geol. Tidsskr. 63, 83-102.

Vollset, J. & Dore, A.G. 1984: A revised Triassic and Jurassic lithostratigraphic nomenclature for the Norwegian North Sea. Norw. Petr. Dir. Bull. 3, 1-53.

* Knut Kirkemo i Norsk Agip A/S har beskrevet borehullet på Tananger, og firmaet Schlumberger har foretatt den omfattende data-sammenstillingen av alle målte parametre som ligger til grunn for typebestemmelsene av bergartene satt opp til venstre for loggene.

Beskrivelse til geologisk kart over Norge 1:250 000, Mandal

Torgeir Falkum
Utgitt 1982

GEOLOGISK OVERSIKT

Berggrunnen innen kartbladet Mandal kan inndeles i 5 hovedenheter:

1.Agderkomplekset, som er et gneis-migmatittkompleks og består av de eldste bergartene: migmatittiske båndgneiser, granittiske gneiser og øyegneiser med mindre mengder av andre bergarter. De er alle deformert og metamorfosert.

2.Telemarksuitens bergarter består av omdannede (metamorfe) sedimentære og vulkanske bergarter, bl.a. båndete kvartsitter og amfibolitter.

3.Granittiske dypbergarter som gjennomsetter bergartene i Agderkomplekset og Telemarksuiten. De fleste er yngre, udeformerte granitter. De eldste kan være noe deformert og metamorfosert.

4.Egersundkompleksets dypbergarter består av en magmatisk suite av basiske til sure bergarter som noritt, gabbro, anortositt, syenitt og pyroxengranitt.

5.Gangbergarter. De fleste er doleritt-(diabas) eller lamprofyrganger av prekambrisk alder, og finnes for det meste i kartets vestlige del eller langs kysten, mens enkelte ganger av permisk alder finnes i den sydøstlige delen i kyststrøket fra Mandal til Kristiansand.

BERGARTSBESKRIVELSE OG GEO-TEKTONISK UTVIKLING

Grunnfjell (prekambrisk alder).

Agderkompleksets eldste bergarter er migmatittiske båndgneiser, granittiske gneiser og øyegneiser. Båndgneisene består av vekslende lyse og mørke lag med tykkelse fra en millimeter og opp til flere meter. De lyse lag er gneiser av varierende sammensetning fra alkalifeltspat-granittisk over granittisk (som er det vanligste) til granodiorittisk og tonalittisk. De mørke lag består av amfibolitt med eller uten pyroxen og biotitt/hornblendegneiser. Disse båndgneisene er sterkt deformert og ofte migmatittiske, og metamorfosegraden er de fleste steder amfibolittfacies.

De fleste av disse gneisene ble sannsynligvis dannet under den svekokarelske fjellkjededannelse for omtrent 2 milliarder år siden. Dette gneisunderlag ble så utsatt for strekkrefter fram til neste fjellkjede-dannelse som begynte for 1200 millioner år siden. Denne oppsprekningen av jordskorpen førte til innsynkning i bassenger med avsetning av sedimentære og vulkanske bergarter **(Telemarksuitens bergarter).** Kontinentets kyst har antagelig ligget i strøket fra Arendal til Stavanger, og de omdannede sedimentære bergartene ved Kristiansand og Faurefjell er avsatt i dette kystnære grunthavsområdet. Granat-cordieritt-sillimanittskifer og -gneiser er antagelig omdannede sedimenter opp-rinnelig avsatt i havet som leire.

Disse bergarter er avsatt før den neste store oppsprekningsperiode for 1200 millioner år siden. Basaltiske smelter fløt inn i disse sprekker og er senere omdannet til amfibolittlag. Denne fase betraktes som innledningen til den sveko-norvegiske fjellkjededannelsen, som varte ca 350 m. år. I denne perioden ble havbunnsplaten skjøvet fra vest mot øst inn under det daværende sydnorske kontinent. Dette førte til at strekk-kreftene ble avløst av sammenpresningskrefter og bergartene ble foldet sammen i tette isoklinalfolder med skifrighet utviklet parallelt med akseplanet. Alle tidligere planstrukturer ble ved denne deformasjon foldet parallelt med denne første sveko-norvegiske foliasjon. Samtidig steg temperaturen og bergartene omkrystalliserte til amfibolittfacies-gneis, amfibolitt, kvartsitt, marmor og granat-cordieritt-sillimanittgneis. På et senere tidspunkt ble båndgneiskomplekset i Flekkefjordområdet gjennomsatt av norittiske ganger. Disse noritter er foldet og metamorfosert til pyroxenamfibolitter. De folierte pyroxenmonzonitter og charnockitter er også dannet i denne

periode, sannsynligvis samtidig med enkelte små ultramafiske kropper. Noe senere ble hele området gjennomsatt av store granittbatholitter. Disse ble foldet under den andre deformasjonsfase og finnes nå som de fin- til middelskornete granittiske gneiser. De dekker nå meste-parten av den sentrale og nordvestlige delen av kartbladet. Etter den andre deformasjonsfasen ble området på ny gjennomsatt av batholitter med porfyrisk granitt. Disse er deformert til øyegneiser og stripete gneiser under den tredje deformasjonsfase og foldet i store isoklinalfolder med akseplan som heller mot øst, og foldeakser som stuper mot syd. Den andre fases store isoklinalfolder er foldet på nytt av de senere deformasjonsfaser og har derfor ofte sammenfallende akseplan med tredje fases folder selv om foldene kan ha øststupende foldningsakser. I Agderkomplekset trengte endel granittbatholitter seg inn i området øst og vest for Kvinesdal. Dette foregikk enten på et sent stadium under tredje fases bevegelser eller umiddelbart etter at disse var avsluttet. En av disse granitter er Hommegranitten som har en Rb-Sr alder på 997 millioner år, denne tolkes som en inntrengningsalder. Disse granitter er deformert av fjerde fases folder og omkrystallisert under amfibolittfacies betingelser. Den fjerde fases folder har steiltstående N-S akseplan og både nord- og sydstupende foldeakser.

Disse folders amplitude er mindre enn de tidligere folders amplitude, de fleste steder i størrelsesorden 50-200 meter, mens de eldre folder vanligvis er opp til flere kilometer store.

Den femte og siste deformasjonsfase førte til åpne øst-vest folder med steile akseplan uten omkrystallisering av bergartene.

De granittiske dypbergarter utgjør en gruppe granitter som er trengt inn i de omgivende bergarter etter at deformasjonsbevegelsene er stanset (post-kinematiske granitter). Den eldste granitten som ikke er blitt deformert under en regionalmetamorfose, er Holumgranitten med en Rb-Sr alder på 980 millioner år. Dette tolkes som en inntrengningsalder og det kan derfor sluttes at siste regionalmetamorfose i Flekkefjordsområdet fant sted for omtrent 1000 millioner år siden. Etter at deformasjonsprosessen var stanset trengte kalkalkaline hornblende- eller biotittgranitter inn i bergartene i de sentrale deler av kartet, mens leukonoritter og charnockitter gjennomsatte bergartene i Egersundskomplekset. Denne fase stabiliserte den sydnorske del av jordskorpen og foregikk over en periode på 100 til 150 millioner år. De eldste er små legemer av kvartsdioritt og porfyrisk biotittgranitt som kan være svakt deformert. Deretter trengte de store hornblende- og biotittgranitter inn og de finnes i en sone fra Farsund-Lyngdal området og NNØ-over. Enkelte av disse granitter omvandlet sidestenen i så sterk grad at det ble dannet agmatitter. Deretter trengte enkelte røde alkalifeltspatgranitter seg inn samtidig med endel granitt-pegmatitter.

Egersundkompleksets bergarter i vest består av basiske til sure dypbergarter som ble dannet i tidsrommet fra 1200 til 900 millioner år siden. De dypbergarter som er eldre enn 1000 millioner år er deformert og metamorfosert. De store anortositt-massivene i Egersundsområdet består av anortositt med opp til flere meter store krystaller av plagioklas. Dessuten finnes leukonoritt og noritt, stedvis som linser i selve anortositten. Dette bergartskompleks er flere steder forskifret ut mot grensen. Egersund-Ogna massivet er antagelig det eldste, og det blir gjennomsatt av bergartene i Håland-Helleren massivet. Disse gjennomsetter den eldre del av den Y-formede synformstruktur som inneholder bergartene i Bjerkrheim-Sokndal lopolitten. Den eldste del er deformert og består av pyroxenmonzonitt og monzonitt og kvartsmargeritt. De store anortosittmassiver og den eldste del av Bjerkreim-Sokndal lopolitten trengte sannsynligvis inn i gneiskomplekset for

1080 til 1050 millioner år siden. De omgivende gneiser er blitt kontaktmetamorfosert i granulittfacies i en 10-20 kilometer bred sone rundt lopolitten. Metamorfosegraden avtar til amfibolittfacies lengre mot nord og øst.

Leukonoritt og charnockitt er de yngste bergarter som trengte inn i Egersundkomplekset og disse er tilslutt gjennomsatt av pegmatittårer med mange sjeldne mineraler (Hidra). Tilsvarende finnes mange sjeldne pegmatittmineraler i Evje-Ivelands-området.

Deretter ble området hevet og erosjonen satte inn. Omlag 800 millioner år tilbake virket den syd-norske delen av jordskorpen som et stivt underlag. I dette underlaget trengte det inn svermer av dolerittganger, særlig i Egersundsområdet og i Hunnedalen.

I paleozoisk tid ble det nordvestre området påvirket av den kaledonske fjellkjededannelse og en svak metamorfose kan ses i form av nydannet biotitt.

I permisk tid ble bergartene i kyststrøket fra Mandal til Kristiansand gjennomsatt av dolerittganger og lamprofyrer.

RADIOMETRISKE ALDERSBESTEMMELSER

Følgende utvalgte aldersbestemmelser viser de viktigste begivenheter i områdets geologiske utvikling. Følgende konstanter er anvendt: $^{87}Rb = 1.42 * 10^{-11}$ år^{-1}; $^{238}U = 1.55125*10^{-10}$ år^{-1}; $^{235}U = 9.8485*10^{-10}$ år^{-1}

Synkinematiske bergarter:

Charnockittisk migmatitt, Drangsdalen (usikker alder): Rb-Sr alder 1453±60 mill. år[1)]. Øyegneis, Sletthei, Evje: Rb-Sr alder 1348±80 mill. år[2)]. Pyroxenmonzonitt, Gloppurdi: Rb-Sr alder 1181 ±70 mill. år[1)]. Granittisk gneis, Syrtveit, Evje: Rb-Sr alder 1120±31 mill. år). Pyroxenmonzonitt, Botnavatnet, metamorfosealder: U-Pb alder 1070±30 mill. år[7)]. Øyegneis, Sirdal: U-Pb alder 1030±35 mill år[7)]. Øyegneis, Fennefoss: Rb-Sr alder 1026±57 mill. år[2)]. Granittisk gneis, Homme: Rb-Sr alder 997±14 mill år[5)]

Postkinematiske bergarter:

Biotittgranitt, Holum: Rb-Sr alder 980±33 mill. år[6)]. Granitt, Høvringsvatn: Rb-Sr alder 945+53 mill. år[2)]. Pyroxen (kvarts) monzonitt, Bjerkreim-Sokndal: Rb-Sr alder 928±50 mill. år[7)]. Hornblende granitt, Lyngdal: U-Pb alder 950±53 mill. år[2)]. Hornblende granitt. Lyngdal: Rb-Sr alder 912±36 mill. år[3)]. Monzonittisk gang, Høvringsvatn: Rb-Sr alder 900±53 mill. år[2)]. Charnockittganger, Hidra: U-Pb alder på zirkon 931±10 mill. år[4)]. Charnockittganger, Hidra: Rb-Sr alder 892±25 mill. år[4)]. Charnockitt, Farsund, U-Pb alder på zirkon 920-940 mill. år[4)]). Charnockitt, Farsund (usikker alder: Rb-Sr alder 834±39 mill. år[5)].

1) Versteeve 1975, NGU 318. 2) Pedersen 1981, BSS Danmark 29. 3) Pedersen & Falkum 1975, Chem. Geol. 15.4) Pasteels et al. 1979, Lithos 12. 5) Falkum & Pedersen 1979, NGT 59. 6) Wilson et al. 1977, NGT 57. 7) Wielens et al. 1980, NGU 359. 8) Pasteels & Michot 1975, NGT 55.

ØKONOMISK GEOLOGI

Gruver og ertsforekomster

Det har vært gruvedrift på nikkel ved Flat i Evje, molybden på Knaben, Kvina og Flottorp, wolfram i Ørsdalen og titan (ilmenitt) i Blåfjell-Storgangen. Det drives fremdeles på Tellness-noritten etter ilmenitt i dagbrudd. Enkelte små kobberforekomster ved Byglandsfjorden er også blitt drevet.

Stein- og mineralbrudd

Det brytes kvarts, feltspat og glimmer fra pegmatitter i Evje-Iveland, og anortositt og leukonoritt ved Rekefjord til pukk. Gamle kjente pegmatittforekomster er Rømteland og mange brudd på Hidra.

UTVALGT LITTERATUR

Barth, T.F.W. 1960: Precambrian of Southern Norway. In Holtedahl, O. (ed.), Geology of Norway. Norges geol. Unders. 208, 48.

Demaiffe, D., Duchesne, J.C. and Hertogen, J. 1979: Trace element variations and isotopic composition of charnockitic acidic rocks related to anorthosites (Rogaland, S.W. Norway). In Ahrens, L.H. (ed.), Origin and distribution of the elements. Pergamon Press, 417-429.

Duchesne, J.C. 1978: Quantitative modelling of Sr, Ca, Rb, and K in the Bjerkreim-Sogndal layered lopolith (S.W.Norway). Contrib. Mineral. Petrol. 66, 175-184.

Esmark, J, 1823: Om noritformationen. Mag. f. Naturvidensk. 1, 205-215.

Falkum, T. 1966: Structural and petrological investigations of the Precambrian metamorphic and igneous charnockite and migmatite complex in the Flekkefjord area, Southern Norway. Norges geol. Unders., 242, 19-25.

Falkum, T. and Petersen, J.S. 1980: The Sveconorwegian orogenic belt, a case of Late-Proterozoic plate-collision. Geol. Rundschau, 69, 622-647.

Falkum, T., Wilson, J.R., Petersen, J.S. and Zimmermann, H.D. 1979: The intrusive granites of the Farsund area (S. Norway) and their relations with the Precambrian metamorphic envelope. Norsk geol. Tidsskr. 59,125-139.

Hermans, G.A.E.M., Tobi, A.C., Poorter, R.P.E. and Maijer, C. 1975: The high-grade metamorphic Precambrian of the Sirdal-Ørsdal area, Rogaland/Vest-Agder, Southwest Norway. Norges geol. Unders. 318, 51-74.

Keilhau, B.M. 1840: Reise i Lister und Mandals Amt i Sommeren 1839. Nyt Mag. f. Naturvidensk. 2, 333-400.

Kjerulf, T. 1883: Om gang-gjennomskjæringer ved Ekersund. Nyt Mag. f. Naturvidensk. 27, 300-303.

Kolderup, C.F. 1897: Die Labradorfelse des westlichen Norwegens: 1. Die Labradorfelsgebiet bei Ekersund und Soggendal. Bergens Museum Aarborg (1896), No. 5, 224 p.

Michot, P. 1969: Geological environments of the anorthosites of south Rogaland, Norway. In lsachsen, Y. W. (ed.), Origin of Anorthosite and Related Rocks. New York State Mus. Sci . Serv. Mem. 18, 411-423.

Michot, J. and Michot, P. 1969: The problem of anorthosites: The South-Rogaland igneous complex, Southwestern Norway. In lsachsen, Y.W. (ed.), Origin of Anorthosits and Related Rocks. New York State Mus. Sci. Serv. Mem. 18, 399-410.

Petersen, J.S. 1977: The Migmatite Complex near Lyngdal, southern Norway, and related granulite metamorphism. Norsk geol. Tidsskr. 57, 65-83.

Roelandts, I and Duchesne, J.C. 1979: Rare-earth elements in apatite from layered norites and iron-titanium oxide ore-bodies related to anorthosites (Rogaland, S,W. Norway). In Ahrens, L.H. (ed.), Origin and distribution of the elements. Pergamon Press, 199-212.

Tobi, A.C. 1965: Fieldwork in the charnockitic Precambrian of Rogaland (SW Norway). Geol. en Mijnbouw 44, 208-217.

NGU
Norges geologiske undersøkelse
Geological Survey of Norway

Norges geologiske undersøkelse
Postboks 6315, Sluppen
7491 Trondheim, Norge

Besøksadresse
Leiv Eirikssons vei 39, 7040 Trondheim

Telefon 73 90 40 00
Telefax 73 92 16 20
E-post ngu@ngu.no
Nettside www.ngu.no

Geological Survey of Norway
PO Box 6315, Sluppen
7491 Trondheim, Norway

Visitor address
Leiv Eirikssons vei 39, 7040 Trondheim

Tel (+ 47) 73 90 40 00
Fax (+ 47) 73 92 16 20
E-mail ngu@ngu.no
Web www.ngu.no/en-gb/